Establishing Structure-Function Relationships for the Catalytic Reduction of Carbon Dioxide with Chromium-Based Molecular Catalysts with Redox Mediators

Amelia Grace Reid
Marietta, Georgia

B.S. Chem., Chemistry, University of Georgia, 2019

A Dissertation presented to the Graduate Faculty
of the University of Virginia in Candidacy for the degree of
Doctor of Philosophy

Department of Chemistry

University of Virginia
May 6, 2024

Abstract

As the atmospheric concentration of carbon dioxide (CO_2) continues to rise, new strategies for the conversion of waste CO_2 to value-added products are of the upmost importance. While the electrocatalytic reduction of CO_2 has been studied for several decades, improvements are still needed for implementation on an industrial scale. First-row transition metal catalysts are of interest due to their lower cost and high abundance on Earth compared to metals such as platinum. Until the last several years, no catalysts with a chromium (Cr) metal center capable of the CO_2 reduction reaction (CO_2RR) with quantifiable efficiencies had been reported. The first Cr-centered catalyst for the CO_2RR contained a redox-active 2,2′-bipyridine-based N_2O_2 ligand framework. To understand the structure-function relationship of the ligand framework on catalysis, four additional Cr-centered catalysts are discussed with modified bpy-based N_2O_2 or terpyridine-based N_3O ligand frameworks. All of the catalysts are quantitatively selective for the reduction of CO_2 to carbon monoxide (CO) and the most active of the series has a turnover frequency (TOF) of 9.29 s^{-1}.

The development of co-electrocatalytic systems utilizing redox mediators (RMs) is of growing interest as a general strategy for the improvement of electrocatalytic small molecule conversion. RMs assist in the transfer of electron equivalents from the electrode to the catalytic active site providing a kinetic improvement to the overall reaction. A series of dibenzothiophene-5,5-dioxide (DBTD)-based RMs are investigated with the Cr-based complexes to provide a foundational understanding of the co-catalytic activity and mechanism. All co-catalytic systems maintain selectivity for CO and enhance the TOF of the parent catalyst by up to 142-fold. The RMs are proposed to operate via an inner-sphere electron transfer mechanism where the RM formally binds to the Cr center during co-catalysis. This key intermediate is stabilized by a pancake bonding (PB) interaction between the redox-active ligand backbone and the RM, which is also aided through dispersion interactions and a dative covalent interaction between the sulfone and Cr center. Through the analysis of electroanalytical experimental data and computational studies, the kinetic and thermodynamic properties which enhance or weaken the PB interaction are evaluated through iterative synthetic modification.

Copyright Information

Chapters 1, **2**, **3**, and **4** are modified versions of published work which have been reproduced in accordance with the American Chemical Society and the Royal Society of Chemistry Journal Publishing Agreements. Proper citation for each chapter is given below and on the first page of each chapter within this thesis.

Chapter 1:
Reid, A. G.; Machan, C. W., *Journal of the American Chemical Society* **2023**, *145* (4), 2013-2027.

Chapter 2:
Reid, A. G.; Hooe, S. L.; Moreno, J. J.; Dickie, D. A.; Machan, C. W., *Inorganic Chemistry* **2022**, *61* (43), 16963-16970.

Chapter 3:
Reid, A. G.; Moreno, J. J.; Hooe, S. H.; Baugh, K. R.; Thomas, I. H.; Dickie, D. A.; Machan, C. W., *Chemical Science* **2022**, *13*, 9595-9606.

Chapter 4:
Reid, A. G.; Moberg, M. E.; Koellner, C. A.; Moreno, J. J.; Hooe, S. L.; Baugh, K. R.; Dickie, D. A.; Machan, C. W., *Organometallics* **2023,** *42* (11), 1139-1148.

Chapter 5 contains material for an upcoming publication and has been incorporated with consent of all current contributing authors. These authors include Megan E. Moberg, Ethan A. Zelenke, Diane A. Dickie, and Charles W. Machan.

Chapter 6:
Reid, A. G.; Machan, C. W., *Journal of the American Chemical Society* **2023**, *145* (4), 2013-2027.

Acknowledgements

While I am incredibly proud of the scientific work and writing that is contained in these pages which represent years of incredibly hard work, this is probably the section that means the most to me. It is no secret to those in my life that I love being around people whenever I can and that I also don't shy away from a sentimental moment to tell those people how much they mean to me. There are so many people who have made an impact on me along the way and have led me to where I am now as a person. I hope that everyone knows how much their support truly means to me.

First, I want to acknowledge all the teachers who encouraged my curiosity and love of learning while I was growing up. Specifically, Ms. Gillenwater, Ms. LeCroy, and Ms. Lancee for teaching me things that I still think about on an almost daily basis as I navigate both my research and the real world. You all made me excited to go to school and encouraged me during years of my life that were not always easy. I also want to thank my two high school chemistry teachers, Ms. Garcia and Ms. Danielson. Without both of you I would not have fallen in love with chemistry and would not have had the strong foundation in the subject that has allowed me to be successful.

While at the University of Georgia, I worked with incredible chemists who made me realize what I could achieve. I want to thank the late Prof. Charles Kutal who helped me to realize that chemistry was fun after a tough first semester of college. I am also thankful that he gave me my first opportunity to teach as an undergraduate which sparked my love for mentorship. I will forever be thankful for Prof. Todd Harrop for giving me an opportunity to do undergraduate research. The time that you took weekly to meet with me about my research progress and plan for the week gave me the skills that have been pivotal to my success in graduate school. You also gave me wonderful advice during the process of applying to and picking a place for grad school that I frequently share with others and will carry with me through all major career decisions in my life. I also want to thank my first in-lab research mentor Dr. Phan Truong. I am appreciative of all the

time you took to teach me how to do research while also writing your Dissertation and working on your defense. Your encouragement is the reason I decided to pursue a PhD and believed I could write and defend this seemingly scary book.

The people that make up UVA Chemistry were the reason that I decided to pursue grad school here. I am thankful for the many wonderful professors that have mentored me (Dr. Gunnoe, Dr. Gilliard, Dr. Zhang, Dr. Zhu, and Dr. Davis) and for the faculty that I have had the privilege of working with for departmental events and student organizations (Dr. Pires, Dr. Venton, and Dr. Hsu). I am thankful to have built relationships with and been supported by the staff in the department over the years as well. To Earl Ashcraft, Diane Dickie, Cindy Knight, Seth Matula, and Ed de Bary, thank you for all that you have done over the years whether it was quickly answering a question, helping me troubleshoot an instrument, or just being around to talk when I was having a hard day, I am incredibly grateful for all of you.

I could not have made it through grad school without the wonderful friends that I have made in this department. To Seamus, Kim, Joe, and Hazel, we have all grown so much together over the last five years and your friendship has made me a better person. I will forever cherish the memories of True American and hours of conversation around the fire. I also want to thank all of your partners, Katie, Keenan, and Dylan for becoming some of my closest friends and for all the support they have provided to all of us while only sometimes acting bored when we talk about work. Hannah and Zoë, I am so grateful for how close we have become in the last year. You two have always been willing to help when I need something for an event, and you are always down for a spontaneous dinner, concert, or road trip to DC. Our fun dinners and adventures have helped to keep me sane during some of the hardest times in my life the last year. I also want to thank Kaeleigh Olsen and Kelsie Wentz for their mentorship and support during my first few years of grad school. Having female role models just a few years ahead of me in the program that welcomed me with open arms helped so much to build my confidence. Thank you to Parker

Ballard-Kyle for helping remind me to breathe when I get stressed and always making me laugh with a Housewives reference.

To the Machan Lab, past and current members, thank you for making the lab and our offices a fun place to be over the last five years. Thank you to Shelby for being my mentor and handling my million and half questions with patience, including giving me reaction set-up advice via Facetime during lab shutdowns. During your time here, you taught me not just how to do good science, but also how to navigate the personal struggles that come along with grad school. Thank you to Asa Nichols for being like an older brother in the lab, always willing to help or fix something but with lots of teasing and jokes mixed in too. Thank you to the previous postdocs in the lab, Juanjo and Connor, for teaching me how to think about science differently and imparting your expertise. To the wonderful undergrads that I have had the privilege to mentor over my time here, Kira, Adam, Alex, and Ethan. Thank you for teaching me about UVA and putting up with my sometimes lack of patience in the lab. I am so proud of each one of you and I can't wait to see what else you accomplish. To James Sappington, it was so much fun to sit next to you in the office and talk about so many random things and spend the summer of 2021 watching all of the Olympics and talking about swimming.

To my fellow MEEMMAS (Megan, Emma, Elizabeth, Mary Jo, Mollie, and Sameeta), thank you for your role in making the Machan Lab what it is right now. It is such a unique and special experience to work in lab with all women who are smart, talented, hardworking, and also some of my best friends. I haven't taken a second for granted. To Sameeta Sahoo, my current desk neighbor, thank you for all your advice about science and life. You can always tell when something is bothering me and know exactly how to help me feel better. Mary Jo, my fellow Georgia Girl, thank you for understanding all my particular ways and wanting to keep them in place in lab just as much as I do. Mollie, my fellow SEC alum, thank you for always talking football with me and reminding us all to take things a little less seriously sometimes. To Elizabeth, Glizzy, thank you for being my fellow pop-culture queen and also always being down for a coffee run and afternoon

chat. Ms. Megan, I will forever be thankful for your friendship. From weekly trivia nights (one day We Will Be Back) and watching softball games together to mentoring you in the lab, you have been there for me through so much and I am glad I gave you a second chance after you took so long to answer my first email. When I needed you the most you dropped everything to be there for me and I hope you know how much I value your friendship. I am so proud of the scientist you have become and the way you have stepped into your role in the lab. I look forward to seeing all the amazing work you do in the future!

Of course, I also must thank our fearless leader, Charlie Machan. You have been and continue to be a wonderful mentor that has taught me so much about science and leadership. I feel very lucky to have a PI that helps us grow our technical skills in lab and professional skills we need for the real world. Thank you for encouraging me when I doubt myself and my abilities. Without your push I probably wouldn't have even applied for awards I ended up receiving. You always helped to calm my nerves and dealt with the tears in your office that thankfully have been less frequent as I have found my footing in graduate school. The way you and Amanda invited us to spend time with your family meant so much, especially in the lonely post-pandemic times. I might miss your kids even more than you when I leave Charlottesville.

I also have to thank the many people who have supported me and kept me sane outside of work for many years. To my dance teachers growing up (Ms. Marsha, Mr. Gerry, Ms. Bethany, Ms. Jennifer, Ms. Marie, and Ms. Marina), thank you for creating a space for me to escape the stress of my life and teach me lessons that became applicable to school. I also must thank the UGA Dance Department and the Charlottesville Ballet Academy for being the space that I could decompress during my undergraduate and graduate careers. Thank you to my CRETS family, Alana, Jessica, Victoria, Rebecca, Aracely, Tiffany, and my twin, Ashley. Ashely, thank you for taking a chance on eighteen-year-old Amelia and giving me my first job and the constant support you have been ever since. Thank you to my Delta Gamma sisters, Rachel, Clair, Victoria, Callie, Kendall, Mona, and Clary. Your friendships have pushed me to be a better person and have had

a profound impact on my faith. Thank you to my Tuesday Night Ladies from The Point Church, Kati, Booke, Caitlin, Arigaa, Marianna, Ashely, and Natasha. The only thing I would change about my time at UVA is finding all of you sooner. Thank you for your support over what has been the hardest year of my life personally while also juggling the pressure of grad school.

Thank you to Gillian Moss for being my first combo scientist dancer friend and encouraging me through so many big transitions through the years. Thank you to Jamie Williams Lowe, the Taylor Swift to my Abigail. I don't know where I would be today without you and your family's love and support. Thank you to Emma Nichols, my friend since middle school and freshman roommate, for always grounding me when I am in an emotional spiral and being a listening ear whenever I need it. Thank you to Emily Fischer and Stacy Schonhardt, from 306 at The Deeg to The B's in Apt 23, you two have been there for me in so many difficult moments. From comforting me after failing my first organic chemistry test or helping me wash my hair after surgery, to laughing over scaring each other, so many Hallmark movies, and Friday night Kroger runs, you two have been there for all the highs and lows. I am forever grateful to call you my friends and sisters!

Thank you to my entire family for their support over the years. Thank you to Aunt Allison and Uncle William for treating me to many meals while you were visiting and spending hours watching swim meets at the AFC together. Thank you to Kate for getting dinner with me whenever both of our crazy schedules aligned. It has been so much fun to live in the same place as you for the last few years and get a front-row seat to all the amazing things you have accomplished. Thank you to brother, Garrett, for never letting my head get too big and being one of the only people who will respond to my UGA football texts at any hour. Thank you to my Nana for being an inspiration for what a strong woman looks like. Without you no one in our family would have achieved many of the things we have accomplished. Thank you to my Dad for being the only person in my family to try and understand what I do on a daily basis and asking me questions that frequently stump me. I am so grateful that I have someone who cares enough to ask and will challenge me in the way my work truly applies to the greater good. To my Mom, my best friend

and confidant, I do not know what I would do without you. I have you to thank for everything from believing that I could accomplish this before I did to answering every tearful phone call after a long day in lab. I am so thankful to know that you are always in my corner to cheer me on and pick me up when I need it.

And thank you to Emma Cook, my labmate, roommate, best friend, and soul sister. I do not know how I got so lucky to have you as a friend and go through this phase of life with you. It is hard to even explain the bond and friendship that we share, and I am going to have to keep this brief, so I am not a crying mess. We have done just about everything together from traveling to conferences, troubleshooting equipment, practicing presentations, planning department events, watching Bravo, eating so much takeout during the pandemic, visiting wineries, and going to concerts. Thank you for both literally and metaphorically picking me up in my weakest moments over the last five years. There is no one else that I would have wanted by my side through it all.

Dedication

This Dissertation is dedicated to my parents,

Dianne D. Reid and Stephen W. Reid

Thank you both for always believing in me. I love you.

.

Table of Contents

Abstract 2

Copyright Information 3

Acknowledgements 4

Dedication 10

List of Abbreviations 14

List of Figures 16

List of Tables 19

Chapter 1: Introduction 20

1.1 Rising Energy Demands and Atmospheric Carbon Dioxide Concentrations 21

1.2 Electrocatalytic Small Molecule Conversion 21

1.3 The CO_2 Reduction Reaction (CO_2RR) 22

1.3.1 Challenges of the CO_2RR 23

1.3.2 Electrochemical Concepts Relevant to the Development of Molecular Catalysts for the CO_2RR 24

1.4 Molecular Catalysts Capable of the CO_2RR 26

1.5 Chromium-Centered Molecular Catalysts for the CO_2RR 28

1.6 Redox Mediators (RMs) in Homogeneous Co-electrocatalysis 29

1.6.1 Biological Mediators 30

1.6.2 Synthetic Mediators 31

1.6.3 Recent Examples of RMs in Homogeneous Co-electrocatalysis 33

1.6.4 Critical Analysis of Homogeneous Redox Mediator Development 47

1.7 Outline of Research Chapters 55

1.8 References 56

Chapter 2: Homogeneous Electrocatalytic Reduction of CO_2 by a CrN_3O Complex: Electronic Coupling with a Redox-Active Terpyridine Fragment Favors Selectivity for CO 66

2.1 Abstract 67

2.2 Introduction 67

2.3 Results 69

2.4 Mechanistic Insight via Computational (DFT) Analyses 74

2.5 Discussion 80

2.6 Conclusions 82

2.7 Supplementary Information 83

2.8 References....118
Chapter 3: Inverse Potential Scaling in Co-electrocatalytic Activity for CO_2 Reduction Through Redox Mediator Tuning and Catalyst Design....122
3.1 Abstract....123
3.2 Introduction....123
3.3 Results....127
3.3.1 Electrochemistry of Cr Catalysts....127
3.3.2 Electrochemistry of Redox Mediators....131
3.3.3 Co-electrocatalysis Under Protic Conditions....133
3.4 Computational Studies....138
3.5 Discussion....141
3.6 Conclusion....145
3.7 Supporting Information....145
3.8 References....241
Chapter 4: Comparisons of bpy and phen Ligand Backbones in Cr-Mediated (Co-)Electrocatalytic CO_2 Reduction....246
4.1 Abstract....247
4.2 Introduction....247
4.3 Results....250
4.3.1. Electrochemistry of Cr Catalysts....250
4.3.2 Co-Electrocatalysis Under Protic Conditions....255
4.3.3 Computational Studies....258
4.3.4 Proposed Mechanism....263
4.4 Discussion....264
4.5 Conclusion....267
4.6 Supplementary Information....267
4.7 References....299
Chapter 5: Improving Co-Electrocatalytic Carbon Dioxide Reduction by Optimizing the Relative Potentials of Redox Mediatory and Catalyst....303
5.1 Abstract....304
5.2 Introduction....304
5.3 Results....306
5.3.1 Electrochemistry of Cr Catalysts....307
5.3.2 Co-catalytic Activity....308
5.4 Discussion and Conclusions....311

5.5 Supplementary Information 313
5.6 References:.....350
Chapter 6: Summary and Outlook.....354
6.1 Summary and Conclusions of Completed Research.....355
6.2 Future Directions.....357
6.3 Outlook on the Field 359
6.4 References.....362

List of Abbreviations

AOR	alcohol oxidation reaction
Ar	argon
BDE	bond dissociation enthalpy
BDFE	bond dissociation free energy
BNTD	benzonaphthothiophene-7,7-dioxide
Bpy	bipyridine
CO	carbon monoxide
Co	cobalt
CO_2	carbon dioxide
CO_2RR	carbon dioxide reduction reaction
Cp^*_2Co	cobaltocene
CPE	controlled potential electrolysis
Cr	chromium
CV	cyclic voltammetry
DBTD	dibenzothiophene-5,5-dioxide
DMF	*N,N*-dimethylformamide
e^-	electron
E^0	thermodynamic minimum
EPTM	electron-proton transfer mediator
ET	electron transfer
Fc	ferrocene
FE	faradaic efficiency
Fe	iron
FOWA	foot-of-the-wave analysis

GC	glassy carbon
H^+	proton-coupled electron transfer
H_2O	water
H_2O_2	hydrogen peroxide
HAT	hydrogen atom transfer
HCOOH	formic acid
HER	hydrogen evolution reaction
HOMO	highest occupied molecular orbital
HOR	hydrogen oxidation reaction
k_{obs}	observed rate constant
Mn	manganese
N_2	dinitrogen
N_2RR	nitrogen reduction reaction
NH_3	ammonia
Ni	nickel
NICS	nuclear independent chemical shift
O	oxygen
ORR	oxygen reduction reaction
PB	pancake bonding
PCET	proton-coupled electron transfer
phen	phenanthroline
PhOH	phenol
PT	proton transfer
RDS	rate-determining step
RM	redox mediator

Ru	ruthenium
$TBAPF_6$	tetrabutylammonium hexafluorophosphate
TEMPO	2,2,6,6-tetramethyl-1-piperidine *N*-oxyl
THF	tetrahydrofuran
TOF	turnover frequency
TON	turnover number
TPTD	triphenylothiophene-4,4-dioxide
tpy	terpyridine
TS	transition state
TSEC	through-space electronic conjugation
η	overpotential

List of Figures

Figure 1.1. Schematic depicting possible strategies for the electrochemical conversion of CO_2.

Figure 1.2. Bond angle CO_2 compared to activated CO_2 bound to a metal center.

Figure 1.3. Two most common $2e^-/2H^+$ pathways for the CO_2RR which determines selectivity between CO and HCOOH and competitive HER pathway.

Figure 1.4. General structures of selected previous CO_2RR catalysts containing first-row transition metal centers.

Figure 1.5. Structure of Cr(^{tbu}dhbpy)Cl(H_2O) catalyst reported by Hooe *et al.*

Figure 1.6. Mitochondrial electron transport chain highlighting redox mediators (1,4-dihydronicotinamide adenine dinucleotide (NADH), flavin adenine dinucleotide ($FADH_2$), dihydroubiquinone H_2UQ, and iron–sulfur clusters (FeS)) which assist in the reduction of O_2 to H_2O.

Figure 1.7. General inner- versus outer-sphere electron transfer mechanisms with a RM, independent of proton transfer.

Figure 1.8. (**A**) Structures from the redox cycle of 2,2,6,6-tetramethyl-1-piperidine *N*-oxyl (TEMPO), (**B**) the Cu(bpy)$(OTf)_2$ (bpy = 2,2′-bipyridine; OTf = $CF_3SO_3^-$) complex, and (**C**) the intermediate species formed following the rate-limiting deprotonation of the alcohol substrate (benzyl alcohol in this example).

Figure 1.9. Proposed catalytic cycle for oxidation of 2-propanol by Ir(PNP)$(H)_2$, where PNP is bis[2-diisopropylphosphino)ethyl]amide, in the presence of the phenoxyl radical mediator.

Figure 1.10. Co-electrocatalytic cycle proposed by McLoughlin *et al.* for isopropanol (iPrOH) oxidation by a Ru-centered transfer hydrogenation catalyst paired with a metal-based HAT acceptor $Ru^{III}N$. Following HAT between RuH and $Ru^{III}N$, the resulting Ru^{I} and $Ru^{II}NH$ products can be regenerated by the electrode to close the cycle.

Figure 1.11. Calculated thermodynamics and kinetics of synchronous PCET and asynchronous PCET (PT–ET) between P_3^BFeNNH and [Cp*(*exo*-η^4-C_5Me_5H)Co][OTf] to generate $P_3^BFeNNH_2$. Note: k_{rel} for ET is defined as 1 M^{-1} s^{-1}.

Figure 1.12. Plausible mechanistic pathway accounting for the tandem reductive electrocatalysis discussed herein, consistent with the data described in the text.

Figure 1.13. The structures of the Co(salophen) catalyst (**A**) and *p*-hydroquinone (H_2Q) and 2-chlorohydroquinone (2-ClH_2Q) EPTMs (**B**) from Ref 48. The relevant hydrogen atom transfer (HAT) and proton-coupled electron transfer (PCET) steps proposed (**C**) in the reduction of the Co(III) superoxide intermediate.

Figure 1.14. Structure of Mn(^{tbu}dhbpy)Cl catalyst developed in our lab, where (^{tbu}dhbpy)$(H)_2$ is 6,6′-di(3,5-di-*tert*-butyl-2-hydroxybenzene)-2,2′-bipyridine and summary of results in Ref 96.

Figure 1.15. Structures of the iron tetraphenylporphyrin ([Fe(TPP)]$^+$) catalyst and RM with the highest activity for the CO_2RR in Ref 98.

Figure 1.16. Structures of both Cr-based catalysts and RMs from Refs. 45 and 99.

Figure 1.17. Mechanism for aerobic alcohol oxidation by the Cu(bpy)/TEMPO system proposed from hybrid functional DFT methods by Ryland *et al*. in Ref. 151.

Figure 1.18. Previously proposed mechanism for CO_2RR by [Fe(TPP)]$^+$.

Figure 2.1. Comparison of the electronic structure of the active states for bpy- and tpy-based Cr complexes capable of mediating homogeneous electrocatalytic CO_2 reduction to CO.

Figure 2.2. (**A**) Molecular structure of [tpy^{tbu}phoH]^0 obtained from single-crystal X-ray diffraction studies. All non-phenol H atoms have been removed for clarity. Crystals were grown by slow cooling a saturated hexane solution of the ligand. (**B**) Molecular structure of 1 obtained from single-crystal X-ray diffraction studies.

Figure 2.3. Comparison of the CVs of 1.0 mM **1** under Ar and CO_2 saturation conditions with and without 0.1 M PhOH.

Figure 2.4. Molecular geometry and spin density plots of $^3_0\mathbf{Cr}^{-1}$ (**A**) and $^3_0\mathbf{Cr(CO_2)}^{-\mathbf{1}}$ (**B**).

Figure 2.5. Free energy profile of the electrocatalytic CO_2RR cycle for **1**.

Figure 2.6. Molecular geometries of $^3_1\mathbf{TS2}^{-1}$ (**A**) and $^4_0\mathbf{TS3}^{-1}$ (**B**).

Figure 3.1. Overview of protic CO_2 reduction co-electrocatalysis, through-space electronic conjugation, and pancake bonding interactions relevant to the results presented here.

Figure 3.2. Molecular structure of Cr(^{tbu}dh^{tbu}bpy)Cl(H_2O) (**2**) obtained from single-crystal X-ray diffraction studies.

Figure 3.3. (**A**) Structures of Cr(^{tbu}dhbpy)Cl(H_2O) **1** and Cr(^{tbu}dh^{tbu}bpy)Cl(H_2O) **2**, where S is a solvent adduct of water or DMF. (**B**) Comparison of CVs for different Cr catalysts (1.0 mM) under CO_2 saturation conditions and 0.1 M PhOH.

Figure 3.4. (**A**) Structures of redox mediators dibenzothiophene-5,5-dioxide (DBTD), triphenylothiophene-4,4-dioxide (TPTD), 2,8-dimesityldibenzothiophene-5,5-dioxide (Mes_2DBTD), and 2,8-diphenyldibenzothiophene-5,5-dioxide (Ph_2DBTD). TPTD, Mes_2DBTD, and Ph_2DBTD obtained from single-crystal X-ray diffraction studies. (**B**) Comparison of CVs for different RMs (2.5 mM) under Ar saturation.

Figure 3.5. CVs of 1.0 mM Cr(^{tbu}dhbpy)Cl(H_2O) **1** (**A**) or Cr(^{tbu}dh^{tbu}bpy)Cl(H_2O) **2** (**B**) with 2.5 mM DBTD (black), TPTD (red), Mes_2DBTD (green), and Ph_2DBTD (blue) as the RM and 0.1 M PhOH under CO_2 saturation conditions.

Figure 3.6. Correlation between computed DMF displacement energies and TOF.

Figure 3.7. Molecular geometry of the $^{4}_{0}\mathbf{Cr(CO_2H)(Ph_2DBTD)}^{-2}$ adduct (**A**) DFT-calculated spin density (**B**) Kohn-Sham orbital projection of SOMO (**C**) and $SOMO^{-1}$ (**D**).

Figure 3.8. Proposed catalytic mechanism for co-electrocatalytic CO_2 reduction by Cr and RM under protic conditions where Cr is **1** or **2** and RM is DBTD, TPTD, Ph_2DBTD, or Mes_2DBTD.

Figure 4.1. Overview of thermodynamic and kinetic effects which play a role in pancake bonding between Cr catalyst and sulfone RM and the advantages of the new phen ligand framework presented in this work.

Figure 4.2. Molecular structure of Cr(^{tbu}dhphen)Cl(H_2O) (**2**) obtained from single-crystal X-ray diffraction studies.

Figure 4.3. Structures of Cr catalysts discussed in this paper where S is either a H_2O or DMF solvent molecule.

Figure 4.4. (A) Comparison CVs of Cr(^{tbu}dhphen)Cl(H_2O) **2** under Ar and CO_2 saturation conditions with and without 0.6 M PhOH. (**B**) Comparison CVs of Cr(^{tbu}dhbpy)Cl(H_2O) **1** and Cr(^{tbu}dhphen)Cl(H_2O) **2** under CO_2 saturation with 0.6 M PhOH.

Figure 4.5. The structures of DBTD and Ph_2DBTD (**A**). CVs of 1.0 mM Cr(^{tbu}dhbpy)Cl(H_2O) **1** (**B**) or Cr(^{tbu}dhphen)Cl(H_2O) **2** (**C**) in the absence (black) and presence of 2.5 mM DBTD (red) or Ph_2DBTD (blue) as the RM and 0.5 M PhOH under CO_2 saturation conditions.

Figure 4.6. Molecular geometry of $^{4}_{0}\mathbf{Cr}^{-1}$ with H atoms omitted for clarity (**A**) Kohn-Sham orbital projection of SOMO (**B**), $SOMO^{-1}$ (**C**), and $SOMO^{-2}$ (**D**).

Figure 4.7. Proposed catalytic mechanism for electrocatalytic CO_2 reduction by Cr and co-electrocatalytic reduction of CO_2 by Cr and RM where Cr **1** or **2** and RM is DBTD or Ph_2DBTD.

Figure 4.8. Molecular geometry of $^{4}_{0}\mathbf{Cr(CO_2H)(Ph_2DBTD)}^{-2}$ where Cr is the phen based complex **2** (**A** and **B**) or the *tert*-butyl substituted bpy complex **3** (**C** and **D**) with select H atoms removed for clarity.

Figure 5.1. Structures of Cr catalysts and RMs discussed here.

Figure 5.2. Molecular structure of BNTD obtained from single-crystal X-ray diffraction studies.

Figure 5.3. (**A**) CVs of Cr(^{tbu}dh^{tbu}bpy)Cl(H_2O) **3** and 2.5 mM BNTD alone and together under CO_2 saturation conditions with 0.5 M PhOH demonstrating the shift in catalytic potential.

Figure 6.1. Potential new N_2O_2 ligand frameworks and DBTD-based RMs.

Figure 6.2. Proposed sulfone-based EPTMs.

Figure 6.3. Overview of the ways in which RMs can interact with the catalytic species and parameters dictating this role.

List of Tables

Table 2.1. Results from CPE experiments under CO_2 saturation conditions.

Table 3.1. Results of CPE experiments with PhOH under CO_2 saturation conditions.

Table 3.2. Calculated free energies of $[RM]^-$ ligand displacement reaction summarized by **Eq (3.1)**, calculated free energies of activation for the rate-limiting C−OH bond cleavage step and experimental redox potentials of the RMs vs Fc^+/Fc.

Table 4.1. Results of CPE experiments with PhOH under CO_2 saturation conditions.

Table 4.2. Calculated activation and reaction free energies for CO_2 binding by $[Cr(^{tbu}dhbpy)]^-$ and $[Cr(^{tbu}dhphen)]^-$.

Table 4.3. Calculated free energies of $[RM]^-$ ligand displacement reaction summarized by **Eq (4.1)**, calculated free energies of activation for the rate-limiting C−OH bond cleavage step and CO_2 binding.

Table 5.1. Results of CPE Experiments with PhOH under CO_2 Saturation Conditions

Chapter 1

Introduction

Portions of this chapter originally published in:

Reid, A. G.; Machan, C. W., *Journal of the American Chemical Society* **2023**, *145* (4), 2013-2027.

1.1 Rising Energy Demands and Atmospheric Carbon Dioxide Concentrations

As the global energy demand continues to increase due to rising populations and the continued modernization of the developing world, the atmospheric concentration of carbon dioxide (CO_2) is also expected to rise. In 2019, the atmospheric concentration of CO_2 was the highest it had been in the last two million years and these concentrations continue to increase with the burning of fossil fuels.[1] In the last decade, the rate of increase in CO_2 concentrations has slowed due in part to the development and implementation of renewable energy technologies such as wind, solar, and hydroelectric power.[1, 2] While these strategies have certainly made a difference, they suffer from inherent issues related to harnessing the energy they generate: the time and locations where these technologies can generate the most power generally do not align with when and where the largest demand exists.[3] In order to adequately address these challenges and mitigate the effects of increased greenhouse gas emissions, new energy technologies are necessary.[4]

1.2 Electrocatalytic Small Molecule Conversion

Small molecule conversion by homogeneous electrocatalysts is of continuing importance to the mitigation of the problems associated with climate change and increased global energy demand. Reactions such as the alcohol oxidation reaction (AOR),[5] nitrogen reduction reaction (N_2RR),[6] oxygen reduction reaction (ORR),[7] and carbon dioxide reduction reaction (CO_2RR)[8] all involve the transformation of stable, abundant molecules to value-added chemicals or energy. Homogeneous electrocatalysts are compelling because they are generally active at ambient conditions (standard temperature and pressure) and have well-defined active sites, which make them amenable to mechanistic study and iterative synthetic modification. Using inspiration from a variety of electrocatalytic systems, the work presented in this thesis focuses on the development of new electrocatalytic systems for the conversion of CO_2.

1.3 The CO_2 Reduction Reaction (CO_2RR)

The electrochemical reduction of CO_2 can be used to address the issues discussed above in two possible methods (**Figure 1.1**). The first converts CO_2 into a carbon-containing product that can be used directly as a fuel that could be stored or used immediately. When the use of these fuels is paired with carbon capture technology,[9] a closed-carbon loop is created. This strategy results in no net change in the atmospheric CO_2 concentration and would alleviate reliance on current petrochemical resources. Another strategy relies on the conversion of CO_2 into commodity chemicals to be used in chemical industry. In this situation, the capture of CO_2 in the flue gas released during production could be converted into a starting material for the same process which has the potential to both limit the environmental impact of releasing CO_2 into the atmosphere and allow for savings by converting current waste into a useable starting material.[4] Importantly, in order for either strategy to have significant impact they much also be paired with a renewable energy source to create the electrical energy required for the conversion of CO_2.

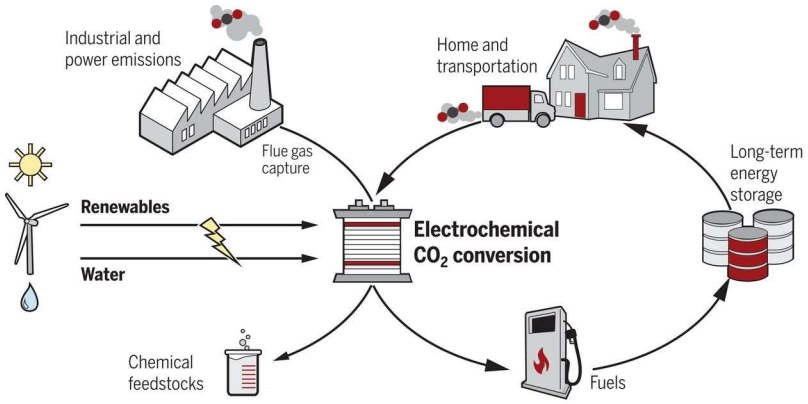

Figure 1.1. Schematic depicting possible strategies for the electrochemical conversion of CO_2.From De Luna, P.; Hahn, C.; Higgins, D.; Jaffer, S. A.; Jaramillo, T. F.; Sargent, E. H., What would it take for renewably powered electrosynthesis to displace petrochemical processes? *Science* **2019,** *364* (6438), eaav3506. Reprinted with permission from AAAS.

1.3.1 Challenges of the CO_2RR

While the reduction of CO_2 to value-added products is an attractive strategy, the development of these systems is non-trivial due to the high chemical stability of CO_2 (**Figure 1.2**) and the variety of possible carbon-containing products (**Table 1.1**). As depicted in **Figure 1.2**, CO_2 is a linear molecule which allows for the electrons in the highest occupied molecular orbitals (HOMOs) to be highly delocalized across the molecule. However, due to the electronegativity of the oxygen atoms, the carbon is electrophilic and susceptible to nucleophilic attack which activates CO_2 and bends the molecule changing the O–C–O bond to 120 degrees.[10] This initial reaction step is difficult and accompanied by a high reaction barrier, such that many systems suffer from high overpotentials (discussed below, an electrochemical parameter related to the kinetic barrier).[8] In many cases, this high thermodynamic stability is overcome by performing the reaction under protic conditions, in order to avoid high energy intermediates by favoring proton-coupled electron transfer (PCET) steps.[11]

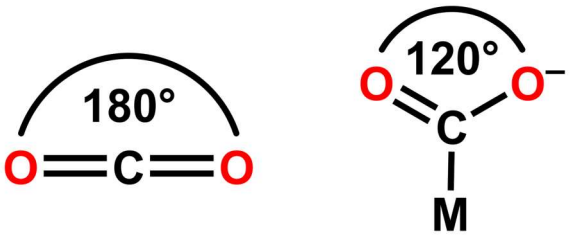

Figure 1.2. Bond angle CO_2 compared to activated CO_2 bound to a metal center.

There are a variety of possible reaction pathways for the CO_2RR by molecular catalysts, with the two-electron/two-proton ($2e^-/2H^+$) products, carbon monoxide (CO) or formic acid (HCOOH) being the most common.[12] Generally, whether the reduced metal center of a catalyst active site binds CO_2 or a H^+ first differentiates between these two products (**Figure 1.3**). If the reduced metal center binds CO_2, an overall anionic intermediate forms which is then protonated to give $[M–COOH]^+$. With the addition of another electron and proton a metal carbonyl is formed with water (H_2O) as a co-product. Alternatively, if the reduced metal center binds a H^+ to yield a

metal hydride, $[M–H]^+$, CO_2 can insert into the M–H bond and formic acid becomes the eventual product. Due to the formation of the metal hydride in the formic acid-producing pathway, the competitive hydrogen evolution reaction (HER) can be observed if acid pK_a is not carefully considered.[13]

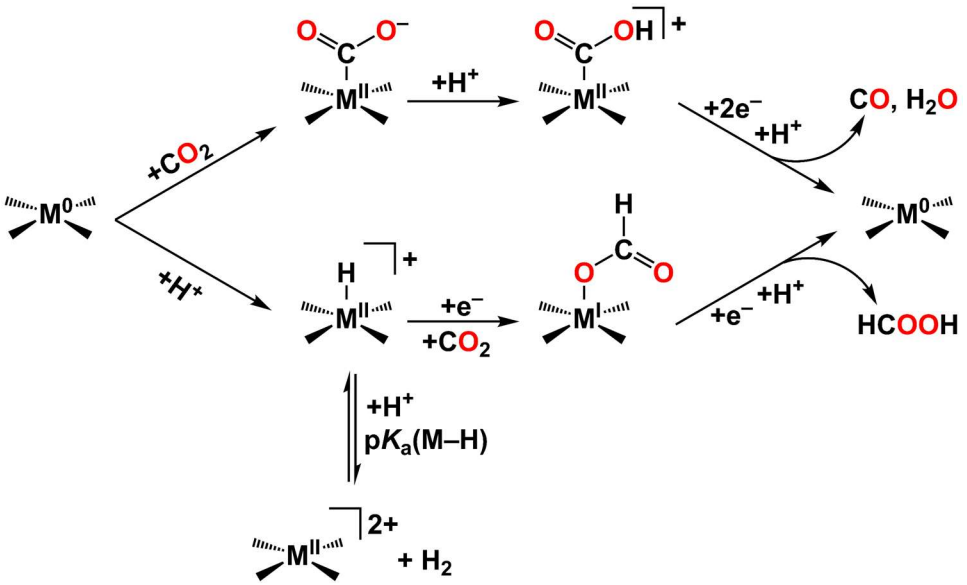

Figure 1.3. Two most common $2e^-/2H^+$ pathways for the CO_2RR which determines selectivity between CO and HCOOH and competitive HER pathway.

1.3.2 Electrochemical Concepts Relevant to the Development of Molecular Catalysts for the CO_2RR

Molecular CO_2RR catalysts are reported under a variety of conditions, therefore, it is necessary to define metrics to compare catalysts in the literature. To compare selectivities between catalysts, Faradaic efficiency (FE) is used. FE relates the number of moles of product formed to the number of moles of electrons passed during an electrochemical experiment, by accounting for the stoichiometry of electrons required for the formation of a given product. In other words, this value gives the percentage of electrons passed during an experiment that go towards the formation of a specific product.[14] It is expected that for a stable electrocatalyst that the sum of the FEs for all products is 100%. If this is not the case, the catalyst is likely unstable and some of the electrons passed during the experiment are leading to the degradation of catalyst and therefore a loss of efficiency.

In order for CO_2RR catalysts to be effective in mitigating some of the challenges discussed above, they must also be energy efficient. The overpotential (η) of a catalyst is the property that defines the energy beyond the thermodynamic minimum ($E^0_{CO_2}$) required to drive an electrochemical reaction at appreciable rates. As such, it represents the additional work required beyond the minimum amount to achieve appreciable rates. The potential where catalysis occurs for a molecular catalyst is best defined by using the potential where half the catalytic current is observed ($E_{cat/2}$).[15-17] The overpotential of a molecular CO_2RR catalyst is thus defined by **Eq (1.1)**.

$$\eta = \left|E_{cat/2} - E^0_{CO_2}\right| \qquad \textbf{Eq (1.1)}$$

The activity of a molecular electrocatalyst is defined by its turnover frequency (TOF) which can be derived from observed rate constant (k_{obs}) of the reaction.[18] Both k_{obs} and TOF are measured per unit time and in homogeneous electrocatalysis the standard unit is s^{-1}. It is important to differentiate the use of TOF and turnover number (TON): TON is frequently used to describe the total lifetime of a catalyst and is a unitless value, corresponding to an experiment run until catalytic activity is no longer observed. Cyclic voltammetry (CV) experiments can be used to calculate the TOF of the reaction using either the ratio of catalytic to non-catalytic current under kinetically limited conditions, or by a technique known as foot-of-the-wave analysis (FOWA). CV techniques can be greatly beneficial for such analysis, since the experiments have a short timescale and are a non-destructive measurement that requires only a small sample of catalyst. However, these techniques assume either that the system can be placed in a pure kinetic regime (limited only by the intrinsic catalyst performance) with Nernstian behavior and no side phenomena, or require a specific relationship between a reversible Faradaic feature with the catalytic one, which greatly limits the systems to which they can applied.[16, 17, 19] An alternative technique relies on a larger-scale controlled potential electrolysis (CPE) experiment (so called

preparative conditions) which requires more materials and longer timescales, but generally provides a more accurate determination of the TOF.[16, 17] The CPE experiment can also provide useful information regarding the stability of a molecular catalyst over longer time periods, depending on how performance changes over the course of an experiment.

Using the integrated expression of current for a homogeneous electrocatalytic response, an equation for k_{obs} can be solved (**Eq (1.2)**) where J is specific current density for a given product (A/cm^2), F is Faraday's constant (C/mol), R is the ideal gas constant (J/mol/K), T is the temperature (K), E_{app} is the potential applied during the CPE experiment (V), and $E_{1/2}$ is the standard potential of the catalyst (V), n_{cat}^{σ} is the number of electrons in the catalytic process (σ = 1 under the assumption that all electrons are delivered to the catalyst by the electrode or σ = 0.5 corresponds to homogeneous electron transfer occurring between catalyst molecules in solution),[20] $[cat]$ is the concentration of the catalyst (mol/cm^3), and D_{cat} is the diffusion coefficient of the catalyst (cm^2/s). With k_{obs} in hand, he TOF$_{CPE}$ of a catalytic system at a given potential can be calculated using **Eq (1.3)**.

$$k_{obs} = \frac{J^2\left(1+\exp\left[\frac{F}{RT}(E_{app}-E_{1/2})\right]\right)^2}{F^2(n_{cat}^{\sigma}[cat])^2 D_{cat}} \qquad \textbf{Eq (1.2)}$$

$$TOF = \frac{k_{obs}}{1+\exp\left[\frac{F}{RT}(E_{app}-E_{1/2})\right]} \qquad \textbf{Eq (1.3)}$$

1.4 Molecular Catalysts Capable of the CO_2RR

Keeping in mind the significant scale of the problems associated with CO_2 discussed above that we seek to address and mitigate; the discussion here will focus on the most widely studied molecular catalysts that contain first-row transition metal centers. First-row transition metals are more abundant than precious metals, making them more cost-effective options for scalable systems.[4] One of the earliest examples of a first-row transition metal catalyst for the

CO_2RR is $[Ni(cyclam)]^{2+}$ where cyclam is 1,4,8,11-tetraazacyclotetradecane (**Figure 1.4**).[21-23] This singular catalyst has been the subject of study for decades now because it is highly selective for the production of CO and is able to operate in aqueous conditions. Many studies of $[Ni(cyclam)]^{2+}$ have used a mercury (Hg) electrode, which presents a safety hazard and is not feasible for use when scaling up the reaction. Studies have shown that using a glassy carbon (GC) working electrode is possible, but the activity of the catalyst is not as high as when the Hg electrode is used.[24] Additionally, the $[Ni(cyclam)]^{2+}$ catalyst is prone to CO poisoning, eventually forming the highly toxic $Ni(CO)_4$ complex, although this can be limited by the addition of CO scavengers.[25]

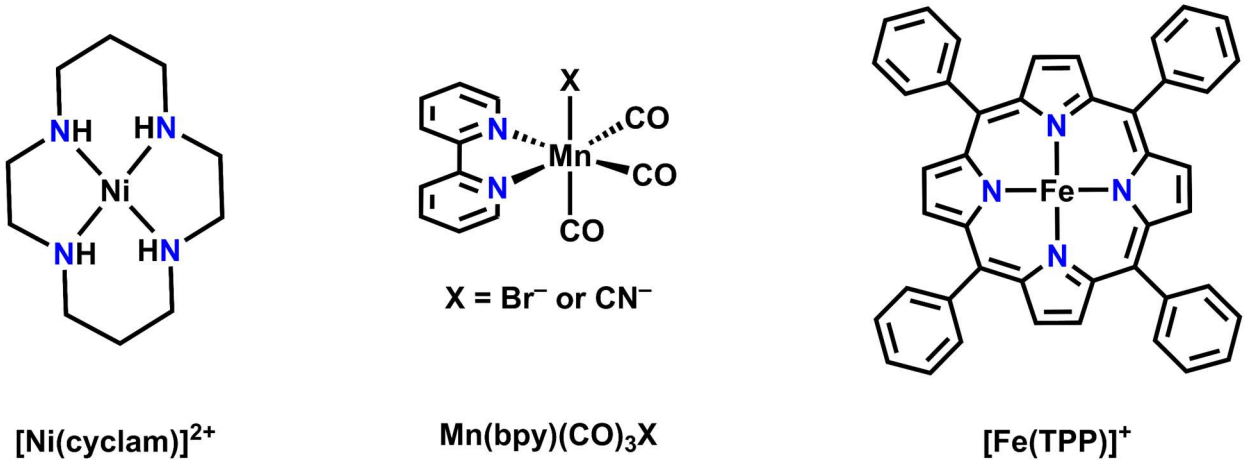

Figure 1.4. General structures of selected previous CO_2RR catalysts containing first-row transition metal centers.

While carbonyl-containing transition metal catalysts supported by 2,2′-bipyridine (bpy)-based ligands have been studied for several decades with a variety of metal centers,[26-29] it was not until 2011 that Mn-centered catalysts were first reported for the CO_2RR (**Figure 1.4**).[30] $Mn(bpy)(CO)_3Br$ is selective for the formation of CO in the presence of weak Brønsted acids, but the activity of this parent catalyst is limited by the formation of a Mn–Mn dimer complex as an intermediate to the active species. Further study of similar Mn-centered catalysts has focused on the design of substituted ligand frameworks to improve the activity: by substituting bulky groups onto the bpy ligand framework, dimer formation is inhibited which in turn increases the observed

activity for the CO_2RR. [31] Additionally, the dimer can be prevented from forming by substituting the bromide ligand for a cyanide (CN) group (**Figure 1.4**).[32]

Finally, iron tetraphenylporphyrin ($[Fe(TPP)]^+$; **Figure 1.4**) and its derivatives have been extensively studied as CO_2RR catalysts for several decades.[33] The parent $[Fe(TPP)]^+$ catalyst is still among one of the most active and selective catalysts for the CO_2RR, with CO as a product.[34, 35] Many derivatives of the parent TPP ligand framework have been synthesized to further improve the activity and understand the catalytic mechanism. The substitution of –OH groups and fluorine atoms on the phenyl ring at the *meso* position were both shown to increase the efficiency of the catalyst by increasing the activity while also decreasing the overpotential.[35] Other work has also seen larger modifications such as the addition of secondary-sphere amide groups which increase the activity by stabilizing intermediates via hydrogen bonding[36-38] and the use of hangman structures which both act to lower the barrier for CO_2 activation.[39] The molecular catalyst with the highest activity reported to this point (TOF = 10^6 s^{-1}) is an iron porphyrin catalyst with charged trimethylanilinium groups substituted in *ortho* positions on the *meso* phenyl rings of the base $[TPP]^{2-}$ framework.[34] The cationic functional groups stabilize the intermediate Fe–CO_2 adduct through Coulombic interactions, providing both a significant increase in activity and a decrease in overpotential. A more detailed discussion of the mechanism of $[Fe(TPP)]^+$ can be found below in **Section 1.6.4.3**.

1.5 Chromium-Centered Molecular Catalysts for the CO_2RR

For decades, it was thought that a catalyst with a chromium (Cr) metal center would not be capable of catalyzing the CO_2RR. It was reasoned that later transition metal complexes with higher *d*-electron counts will have frontier orbitals with more d_{z^2} character than Cr making them more nucleophilic.[13] As discussed above, the activation of CO_2 is difficult and requires a nucleophilic attack on the carbon of CO_2 to bend the molecule and activate it for possible transformation. Tory *et al.* reported a series of catalysts, $M(bpy)(CO)_4$ where M = Cr, Mo, and W

which demonstrated that the Cr analogue had an electrochemical response, but the activity was so low that no FE was reported.[40] A $Cr(CO)_6$ complex was also reported by Grice and Saucedo, but again no selectivity or activity data was reported.[41]

In 2019, Hooe *et al.* reported the first Cr-centered molecular catalysts capable of the CO_2RR with quantitative FE.[42] The catalyst, Cr(^{tbu}dhbpy)Cl(H_2O), where (^{tbu}dhbpy)$^{2-}$ is 6,6′-di(3,5-di-tert-butyl-2-hydroxybenzene)-2,2′-bipyridine, (**Figure 1.5**) has a high selectivity for CO as a product with a FE_{CO} = 96 ± 8% at a relatively low overpotential of 110 mV. The incorporation of the redox non-innocent bpy into the ligand framework has been shown to play a key role in achieving this high selectivity with appreciable activity.[43, 44] The active catalytic intermediate is proposed to be a Cr(II) metal center that is antiferromagnetically coupled to a bpy-based radical. Since the two electrons by which the catalyst is reduced are shared between the metal center and ligand framework, the binding of CO_2 to the metal center over H^+ is promoted through the limited sigma character of the frontier orbitals on the Cr center. The TOF_{CPE} of this catalyst is reported as 4.35 s^{-1} at an applied potential of –2.1 V versus ferrocenium/ferrocene (Fc^+/Fc),[45, 46] which is not competitive with the state-of-the-art catalysts discussed above. The development of new Cr-centered catalysts for the CO_2RR with substituted ligand frameworks and redox mediators to improve activity is the subject of this thesis.

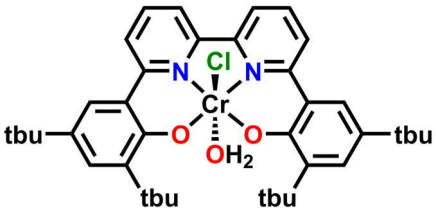

Figure 1.5. Structure of Cr(^{tbu}dhbpy)Cl(H_2O) catalyst reported by Hooe *et al* in Ref 42.

1.6 Redox Mediators (RMs) in Homogeneous Co-electrocatalysis

Much of the previous work in molecular electrocatalysis has relied on iterative changes to both the metal center and ligand framework. However, in many reports, these systems still require

large energy input due to the high overpotentials required to achieve relevant activity. Even in reports with low overpotentials, the activity does not meet what is necessary for implementation into larger scale technologies. Therefore, new strategies for improving this activity must be implemented.

1.6.1 Biological Mediators

In biological systems, nature overcomes significant thermodynamic and kinetic challenges through the use of redox mediators (RMs), which shuttle electron equivalents to active sites where the interconversion of energy and chemical bonds occurs. When the transfer of electrons is accompanied by the transfer of protons, these are referred to as electron-proton transfer mediators (EPTMs).[47, 48] For example, quinones are found in a variety of organisms because of their ability to facilitate reversible proton-dependent redox reactions to and from metallocofactors, which has the added benefit of protecting against the formation of potentially reactive radical intermediates.[49] During mitochondrial respiration, ubiquinone (UQ) assists in shuttling electrons and protons to several of the active sites in the electron transport chain (**Figure 1.6**).[50] Many enzymes also rely on iron–sulfur clusters (FeS) distributed throughout their interior matrix to deliver electrons from the surface of the protein structure to a buried active site within the enzyme.[51, 52] These enzymes have evolved so that the energetic difference in oxidation states of each cluster serves as a driving force for electron transfer (ET), harnessing the ability of the cofactors to exist in a variety of redox configurations without having to electronically couple each site directly.[53, 54] This is a requirement because redox-active sites are generally spatially isolated in biological systems and their tertiary structures are static relative to the movement of electrons, protons, and small molecule substrates.

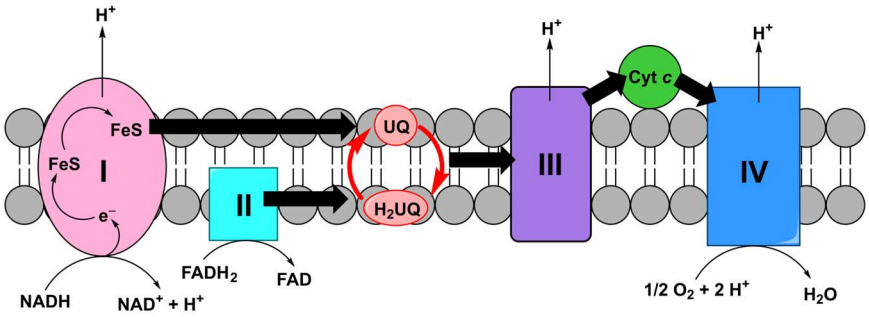

Figure 1.6. Mitochondrial electron transport chain highlighting redox mediators (1,4-dihydronicotinamide adenine dinucleotide (NADH), flavin adenine dinucleotide ($FADH_2$), dihydroubiquinone H_2UQ, and iron–sulfur clusters (FeS)) which assist in the reduction of O_2 to H_2O.

1.6.2 Synthetic Mediators

Inspired by these electron cascades, bioelectrocatalytic systems have been developed that utilize small molecule RMs to deliver electron equivalents to the active sites of enzymes.[55, 56] Electrochemical glucose sensors that previously relied on the energy-intensive oxidation of hydrogen peroxide (H_2O_2) have been modified to instead use osmium- and ferrocene-based compounds as RMs, which improves their efficiency and stability.[57, 58] Several other biosensors that use cytochrome *c* as the mediator have also been developed for the detection of small molecules such as H_2O_2[59] and bilirubin.[60] Fuel cells that rely on co-catalysis with mediators have also been developed for the cathode[61-64] or anode[65] as well as for both half-cell reactions.[66-68] Similar to the way organic molecules have been implemented into biosensors, methyl viologen has been used as a RM with a nitrogenase enzyme catalyst for the reduction of nitrogen to ammonia as the cathodic half-reaction of a hydrogen fuel cell.[69] Importantly, in all of these examples, matching the redox potential of the mediator and the enzyme within 50 mV is necessary for optimal efficiency and activity.[51] This is due to a reliance on outer-sphere ET during the reaction (which necessitates a favorable thermodynamic driving force[70, 71]) and the need to avoid competing ET pathways which lower selectivity (**Figure 1.7**). While the addition of RMs into such

systems has allowed for increased stability, this type of outer-sphere ET can still react with other small molecules present in the reaction medium[57] leading to long-term instability and inefficiency.

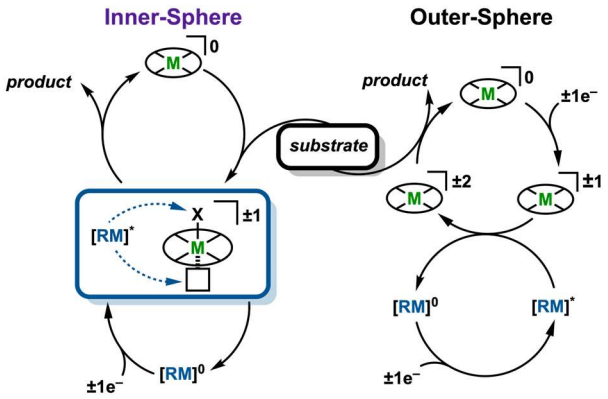

Figure 1.7. General inner- versus outer-sphere electron transfer mechanisms with a RM, independent of proton transfer, where X = substrate and [RM]* = activated mediator.

The use of RMs, commonly ferrocene (Fc) derivatives,[72-74] has been explored in electrosynthesis, where in contrast to the systems described previously, the RM shuttles electron equivalents in a catalytic fashion via an outer-sphere reaction to transform substrates into reactive intermediates.[75, 76] Other examples use nitroxyl radicals as EPTMs in transformations that rely on a hydrogen atom transfer (HAT) step, where proton and electron movement are directly coupled during direct interaction with the substrate, sometimes when both substrate and EPTM are bound to the same metal center.[77-80] Additionally, RMs have been implemented in photocatalysis to assist in photosensitizer activation[81-86] and in systems for heterogeneous CO_2RR to improve activity and selectivity.[87, 88] Although this approach has been recognized as a basic research need for catalysis science, there remains a relatively limited number of homogeneous electrochemical systems with RMs in spite of their potential to improve selectivity, activity, and energy efficiency through thermodynamic and mechanistic analysis.[89] This section includes discussion of examples of RMs in homogeneous co-electrocatalysis, analysis of the key thermodynamic components of these systems, and strategies we believe to be important for further optimization of co-electrocatalytic systems in the future.

1.6.3 Recent Examples of RMs in Homogeneous Co-electrocatalysis

Despite the limited number of reports involving the use of RMs in homogeneous electrocatalysis, the known systems cover a wide scope of energy-relevant small molecule transformations involving AOR,[47, 90, 91] N_2RR,[92, 93] the hydrogenation of unsaturated organic molecules,[94] hydrogen oxidation (HOR),[95] ORR,[48, 96, 97] and CO_2RR.[45, 46, 98-100] Here, the current known examples of co-electrocatalytic systems where (1) both the catalyst and RM are homogeneous molecular species and (2) at least one of the two is redox-active and regenerated by the electrode are described. There are additional examples of co-catalytic systems for small molecule transformation that rely on similar properties, but do not meet both sets of criteria and are therefore not discussed in detail here.[76, 101, 102] The term 'co-electrocatalytic' is meant to encompass that these transformations are both electrocatalytic and require a co-catalytic component to occur; this description does not require that any individual component is also intrinsically catalytic under the described conditions, although this can be the case.

1.6.3.1 RMs in the Alcohol Oxidation Reaction (AOR)

The first example of co-electrocatalytic AOR is a report by Badalyan and Stahl on the use of 2,2,6,6-tetramethyl-1-piperidine *N*-oxyl (TEMPO) as an EPTM with a (2,2′-bipyridine)Cu(II) triflate catalyst for the AOR (**Figure 1.8**).[47] While TEMPO has been widely reported as an electrocatalyst for alcohol oxidation, these systems rely on a $H^+/2e^-$ $TEMPO^+$/TEMPOH redox process, which occurs at very oxidizing electrode potentials, making the process relatively energy intensive.[103-107] The co-electrocatalytic system utilizes the lower energy TEMPO/TEMPOH couple to facilitate a HAT reaction when paired with the Cu catalyst, thanks to the activation of the alcohol substrates when coordinated to the Cu metal center. The authors demonstrated that while co-electrocatalysis occurs at the Cu(II/I) redox potential, the nitroxyl radical is necessary for catalysis due to its role as a hydrogen atom acceptor from a Cu(II)-alkoxide intermediate, the formation of which is the rate-limiting step of the reaction.

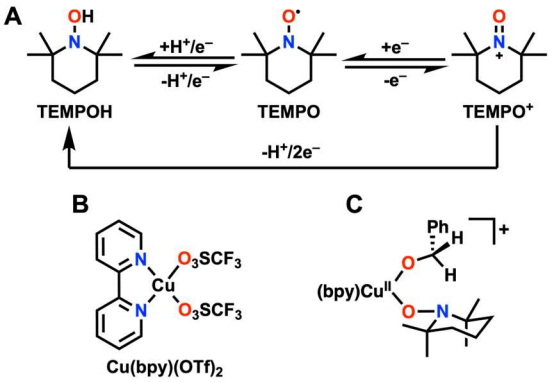

Figure 1.8. (**A**) Structures from the redox cycle of 2,2,6,6-tetramethyl-1-piperidine *N*-oxyl (TEMPO), (**B**) the Cu(bpy)(OTf)$_2$ (bpy = 2,2′-bipyridine; OTf = $CF_3SO_3^-$) complex, and (**C**) the intermediate species formed following the rate-limiting deprotonation of the alcohol substrate (benzyl alcohol in this example) in Ref 47.

The Waymouth Group has published two co-electrocatalytic systems for the AOR, the first of which by Galvin and Waymouth uses an Ir(PNP)(H)$_2$ complex, where PNP is bis[2-diisopropylphosphino)ethyl]amide, (**Figure 1.9**) with several electron-rich phenol derivatives as the EPTM.[90] The authors rationalized that activity for the AORs of interest could be achieved at lower overpotentials by eliminating the need to directly oxidize relatively stable metal-hydride (M–H) species, since the energy-intensive oxidative deprotonation of these intermediates is generally the limiting kinetic step of the intrinsic catalytic cycle. They found that the addition of a phenol derivative to a solution containing the Ir(PNP)(H)$_2$ pincer catalyst led to a significant shift in oxidation potential to much lower energy (more negative potential for the oxidation event which initiates catalysis) due to the interception of the M–H intermediate. The proposed catalytic cycle depends on a HAT step, where a phenoxyl radical accepts a hydrogen atom from the M–H. In total, two successive HAT steps are necessary to complete the catalytic cycle, each of which could represent the rate-determining step (RDS) of the reaction (**Figure 1.9**). By examining a series of phenol-based molecules as the EPTM, Galvin and Waymouth were able to demonstrate that as the pK_a of the phenol becomes more acidic, the observed oxidation potential of the corresponding phenoxide decreases (shifts to more negative potentials) in a manner that can be used to tune the operating potential of the co-catalytic system.

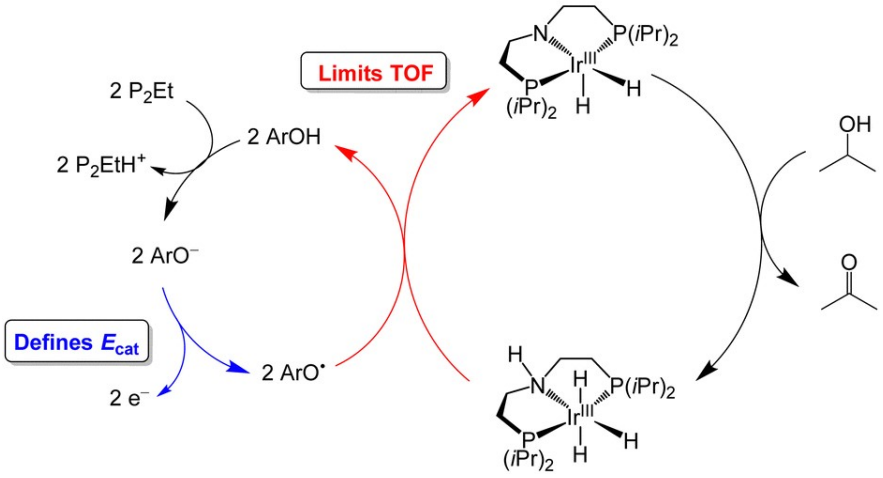

Figure 1.9. Proposed catalytic cycle for oxidation of 2-propanol by Ir(PNP)$(H)_2$, where PNP is bis[2-diisopropylphosphino)ethyl]amide, in the presence of the phenoxyl radical mediator. Reproduced from Ref. 108 with permission from the Royal Society of Chemistry.

Shortly following this report, McLoughlin *et al.* disclosed a second co-catalytic system for the AOR using an efficient Ru-based ketone transfer hydrogenation catalyst and a Ru-centered EPTM, **Ru^{III}N** (**Figure 1.10**).[91] Under thermal catalytic conditions, the catalyst can oxidize isopropanol to acetone in order to drive the reduction of ketone substrates, generating a Ru(II) hydride intermediate **RuH**. They found that the electrocatalytic oxidation of isopropanol could be achieved if an electrode poised at suitably oxidizing potentials was substituted for the ketone substrate,[109] noting that the two-electron, one-proton oxidation of the intermediate Ru(II) hydride complex **RuH** was likely to be the RDS of the catalytic cycle. Subsequently, inspired by previous work,[47, 80] McLoughlin *et al.* reasoned that the introduction of a suitable hydrogen atom acceptor could again access an appreciable catalytic response at less oxidizing potentials (lower overpotentials) by circumventing the stepwise removal of a proton and electron during the oxidation of the key metal hydride intermediate.[91] In order to implement this strategy, the authors developed a set of guidelines for the selection of an EPTM with the appropriate thermodynamic properties: (1) the bond dissociation free energy (BDFE) of the relevant M–H intermediate must be similar to that of the EPTM–H bond, (2) the $E_{1/2}$ and pK_a of the EPTM must be close to the thermodynamic potential for the AOR, (3) the EPTM must be oxidized at more negative potentials

than the targeted M–H intermediate, and (4) the pK_a of the EPTM–H should be in the range where the HER is unfavorable. The system functioned as intended, lowering the overpotential for isopropanol oxidation by ca. 450 mV, in spite of the limited knowledge of relevant thermodynamic parameters in the THF operating solvent, which precluded definitive thermodynamic positioning of several reaction steps. Additionally, high Faradaic efficiency of the desired product was maintained with minimal HER observed.

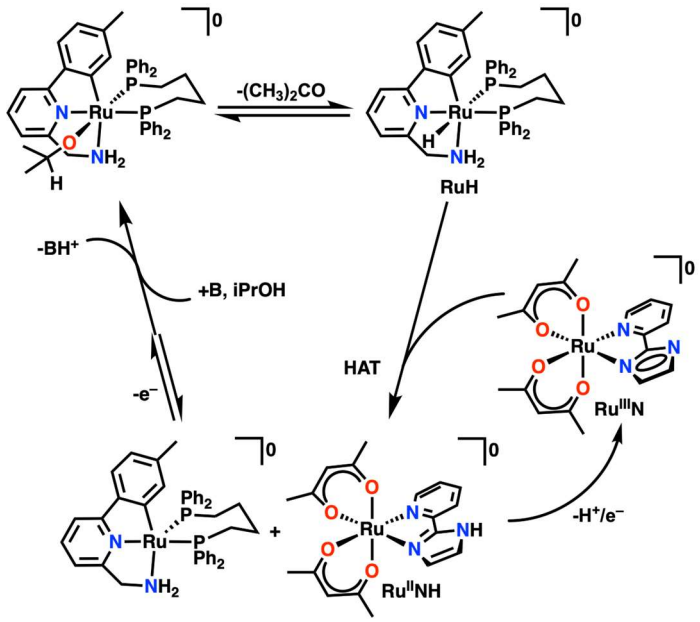

Figure 1.10. Co-electrocatalytic cycle proposed by McLoughlin *et al.* for isopropanol (iPrOH) oxidation by a Ru-centered transfer hydrogenation catalyst paired with a metal-based HAT acceptor $Ru^{III}N$. Following HAT between RuH and $Ru^{III}N$, the resulting Ru^{I} and $Ru^{II}NH$ products can be regenerated by the electrode to close the cycle.

1.6.3.2 RMs in the Nitrogen Reduction Reaction (N_2RR)

Leveraging extensive work on the reduction of N_2 with chemical reducing agents by the Peters group[110, 111] Chalkley *et. al* were able to develop a homogeneous co-catalytic system with a Co-based EPTM for N_2RR in 2018.[92] Previously, in 2017 Chalkley *et al.* reported that $P_3^BFe^+$, where P_3^B = tris(*o*-diisopropylphosphinophenyl)borane, was a competent catalyst for the reduction of N_2 to ammonia (NH_3) with dihydrogen as a co-product when cobaltocene (Cp^*_2Co) was used as the chemical reductant in the presence of acid.[112] In the subsequent 2018 report, it was

established that the Cp^*_2Co EPTM could be electrochemically recycled during co-electrocatalytic N_2RR with $P_3{}^BFe^+$.[92] The authors discovered that the rate of catalysis was dependent on the pK_a of the acid used because the protonation of the EPTM to form $Cp^*(\eta^4\text{-}C_5Me_5H)\text{-}Co^+$ was essential to the co-electrocatalytic cycle. This activated cationic Co-based EPTM was proposed to possess C–H bonds weak enough to position it as a PCET reagent capable of generating N–H bonds during catalysis (**Figure 1.11**). A more recent study of this EPTM by the same group shows the generality of this approach to co-electrocatalytic systems by substituting the Fe-based catalyst for other transition metals that bind N_2. This report establishes the excellent generality of this approach, as all systems function co-electrocatalytically, however, competitive HER is observed in all cases.[93]

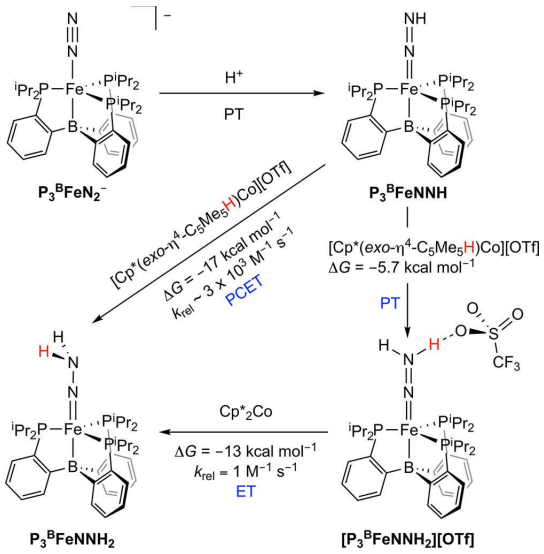

Figure 1.11. Calculated thermodynamics and kinetics of synchronous PCET and asynchronous PCET (PT–ET) between $P_3{}^BFeNNH$ and $[Cp^*(exo\text{-}\eta^4\text{-}C_5Me_5H)Co][OTf]$ to generate $P_3{}^BFeNNH_2$. Note: k_{rel} for ET is defined as 1 M^{-1} s^{-1}. Reprinted with permission from J. Am. Chem. Soc. 2018, 140, 6122–6129. Copyright 2018 American Chemical Society.

1.6.3.3 RMs in the Hydrogenation of Unsaturated Substrates

The electrocatalytic hydrogenation of unsaturated organic molecules can proceed via a M–H intermediate; however, at reducing potentials these intermediates can also rapidly be reduced again to lead to competitive HER. However, a recent study by Derosa *et al.* exploits the

use of the same class of Co-based EPTM described in Section 2.2 to circumvent this issue by forming a M–H intermediate at more positive potentials than those required for HER.[94] To achieve this, a Ni-centered catalyst, $[P_4^{Me}Ni^{II}]^{2+}$, was paired with $[CpCoCp^{NMe2}]^{+}$ as an EPTM (**Figure 1.12**). For this Ni-based catalyst, the two-electron reduction potential of Ni^{II} to Ni^{0} generates a species which can be protonated by an acid of sufficient strength to form a readily reduced Ni^{II}–H. This means that, at a comparable potential to the Ni^{II}/Ni^{0} reduction, the reduction of Ni^{II}–H to Ni^{I}–H can occur, which initiates HER in the presence of the external acid. At potentials which are more positive than those required for Ni^{II}/Ni^{0} and Ni^{II}–H/Ni^{I}–H reduction, the Co-based EPTM is protonated and reduced to generate its activated form, $[CpCoCp^{NHMe2}]^{+}$, which can transfer a hydrogen atom equivalent via a PCET step to $[P_4^{Me}Ni^{II}]^{2+}$, forming $[P_4^{Me}Ni^{III}–H]^{2+}$. Under the conditions required for the reduction of the Co-based RM, the product Ni^{III}–H hydride species is rapidly reduced to a Ni^{II}–H, but the applied potentials are not reducing enough to complete the Ni^{II}–H/Ni^{I}–H reduction. The result is that the intermediate compound Ni^{II}–H is available and capable of hydride transfer to unsaturated substrates like methyl phenylpropiolate under conditions which limit competitive HER. Like the examples for the N_2RR discussed above, all of the systems tested showed some competitive HER even at the less reducing potentials, which is likely a consequence of the presence of multiple species with BDFEs weaker than H_2, *vide infra*.

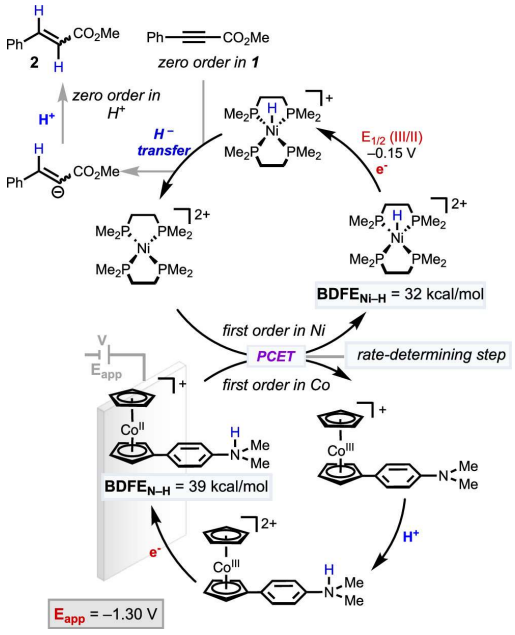

Figure 1.12. Plausible mechanistic pathway accounting for the tandem reductive electrocatalysis discussed herein, consistent with the data described in the text. Reprinted with permission from *J. Am. Chem. Soc.* **2022**, 144,20118-20125. Copyright 2022 American Chemical Society.

1.6.3.4 RMs in the Hydrogen Oxidation Reaction (HOR)

The only example reported for the HOR involves the use of an Fe-centered catalyst, $[Fe(P^{Et}N^{Ph}P^{Et})–(CO)_3]^+$, where $P^{Et}N^{Ph}P^{Et}$ is $(Et_2PCH_2)_2NMe$, and a Cr-based EPTM.[95] The Cr-centered EPTM exists in an equilibrium between its dimeric form, $[Cp^*Cr(CO)_3]_2$, and a 17-electron species, $Cp^*Cr(CO)_3$. The slowest reaction step in the co-electrocatalytic cycle is the homolytic activation of H_2 by two equivalents of $Cp^*Cr(CO)_3$ to generate an intermediate chromium hydride in a purely thermal step. The resultant $Cp^*Cr(CO)_3H$ complex can transfer a hydrogen atom equivalent to the monocationic $[Fe(P^{Et}N^{Ph}P^{Et})–(CO)_3]^+$ to form an $[Fe–H]^+$ which can quickly be deprotonated by added base to generate a formally Fe(0) species. The formally Fe(0) species is oxidized at the electrode to close the cycle, regenerating all components and dictating the required operating potential. Analysis of the reaction components revealed that the chosen base, 2-methylpyridine, was not basic enough to deprotonate the chromium hydride. Further, control testing showed that the oxidation of $Cp^*Cr(CO)_3$ and $Cp^*Cr(CO)_3H$ occurred at

potentials more positive than that of the $[Fe(P^{Et}N^{Ph}P^{Et})–(CO)_3]^{+/0}$ redox event which initiated co-electrocatalysis, meaning that no electrochemical activation of the Cr species occurs as a part of the reaction cycle. Although no BDFEs were reported for any of the hydride species proposed, the observation of facile hydrogen atom transfer from Cr to Fe suggests that this reaction could be favored thermodynamically.

1.6.3.5 RMs in the Oxygen Reduction Reaction (ORR)

Anson and Stahl published a study on Co(salophen) as the catalyst for the ORR with *p*-benzoquinone (BQ) as an EPTM (**Figure 1.13**).[48] This study was a follow-up to an earlier study on the mechanism of Co(salophen)-catalyzed oxidation of *p*-hydroquinone (the reduced form of BQ) under aerobic conditions.[113] In contrast to the intrinsic inactivity of some of the catalysts in the AOR system discussed above, the Co(salophen) metal complex catalyzes the ORR in the absence of the EPTM, producing hydrogen peroxide (H_2O_2; the $2e^-/2H^+$ product). However, when *p*-hydroquinone is present, the system selectivity shifts from H_2O_2 to H_2O (the $4e^-/4H^+$ product) and an increase in rate is observed. Both changes are explained by the authors' proposed mechanism: a Co(III)-superoxide intermediate reacts initially with H_2Q via HAT, which is followed by a PCET step that leads to the formation of H_2O. This pathway for H_2O formation avoids the production of H_2O_2, an undesirable product in polymer electrolyte membrane fuel cells,[114] while also increasing the rate of the ORR. The authors also found that using an EPTM with a more positive reduction potential, 2-chlorohydroquinone ($2\text{-}ClH_2Q$), increased the rates of catalysis relative to BQ used at the same more positive potential.

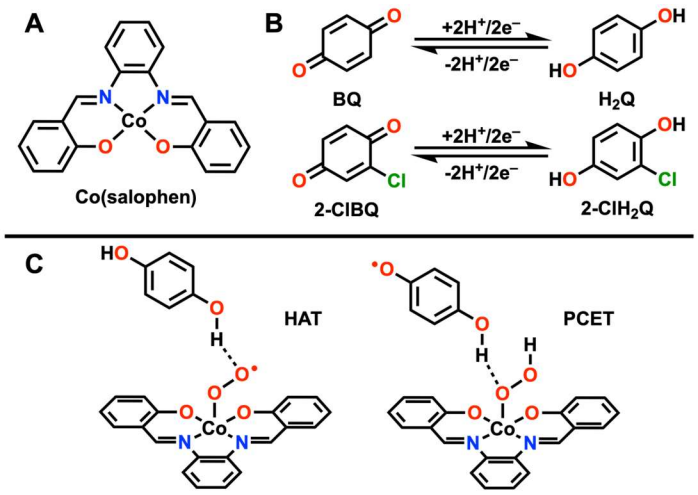

Figure 1.13. The structures of the Co(salophen) catalyst (**A**) and *p*-hydroquinone (H_2Q) and 2-chlorohydroquinone ($2\text{-}ClH_2Q$) EPTMs (**B**) from Ref 48. The relevant hydrogen atom transfer (HAT) and proton-coupled electron transfer (PCET) steps proposed (**C**) in the reduction of the Co(III) superoxide intermediate.

Inspired by the work of Anson and Stahl,[48] our lab has also studied the use of benzoquinone (BQ) as an EPTM with a Mn-centered catalyst, Mn(^{tbu}dhbpy)Cl where (^{tbu}dhbpy)$(H)_2$ is 6,6′-di(3,5-di-*tert*-butyl-2-hydroxybenzene)-2,2′-bipyridine (**Figure 1.14**).[96] In this example, a change in the intrinsic selectivity of the catalyst for H_2O_2[115, 116] to favor H_2O is observed when BQ and 2,2,2-trifluoroethanol (TFEOH) are present in solution. BQ is typically reduced by two electrons in a stepwise fashion under aprotic conditions in non-aqueous solvents, but in the presence of TFEOH the reduced species are stabilized by hydrogen bonding interactions, shifting to a two-electron reduction as the reduction potential of the second electron shifts to more positive potentials than the first reduction (potential inversion). In the co-catalytic system with Co(salophen), Anson and Stahl used AcOH as the proton donor, which is strong enough to fully protonate the benzoquinone dianion under standard thermodynamic conditions; under our chosen reaction conditions, TFEOH should only monoprotonate the same dianion.[117-126] However, at high proton donor concentrations, the solvent mixture becomes non-ideal, as a cluster of proton donors forms around the initially favored monoprotonated species, which was assessed by electrochemical means to have an approximate formulation of $[HQ(TFEOH)_4(TFEO)_1]^{2-}$.[118, 127, 128]

In this non-covalent assembly, it is possible to form a hydrogen bond-stabilized H_2Q species, $[H_2Q(TFEOH)_3(TFEO)_2]^{2-}$ that functions as an EPTM to a Mn(III) superoxide intermediate, intercepting the intrinsic catalytic mechanism and shifting product selectivity from H_2O_2 to H_2O. We found that although this electrogenerated non-covalent EPTM assembly is more reactive[129] than *p*-hydroquinone generated under the conditions reported by Anson and Stahl with a much stronger acid,[48] its co-catalytic function was the same, resulting in a shift in product selectivity from H_2O_2 to H_2O and an increase in the observed activity. Under our reported co-electrocatalytic conditions[96] we proposed that the consumption of the reduced EPTM results in the delivery of one proton and two electrons overall, accompanied by the release of additional proton donors to complete the reaction: the strong association of 2,2,2-trifluoroethanol in the cluster will weaken rapidly as the hydrogen bond-stabilized *p*-hydroquinone cluster is oxidized.

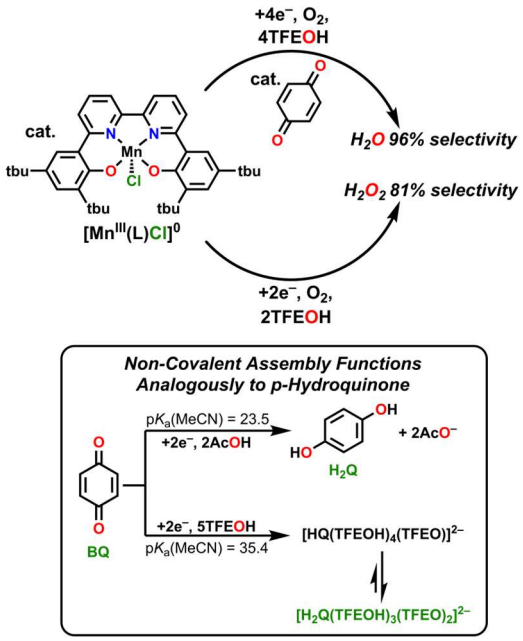

Figure 1.14. Structure of Mn(^{tbu}dhbpy)Cl catalyst developed in our lab, where (^{tbu}dhbpy)$(H)_2$ is 6,6′-di(3,5-di-*tert*-butyl-2-hydroxybenzene)-2,2′-bipyridine and summary of results in Ref 96. Reproduced from Ref. 130 with permission from the Royal Society of Chemistry.

A co-electrocatalytic system for the ORR that does not contain a transition-metal-centered catalyst or RM was published by Gerken and Stahl based on the combination of the nitroxyl

mediator TEMPO and NO_x species.[97] Nitric oxide (NO) can react with half an equivalent of dioxygen to form nitrogen dioxide (NO_2) in a reaction that is both thermodynamically favorable and kinetically facile. TEMPO, when added to the system, is oxidized by NO_2 in the presence of trifluoroacetic acid to give an equivalent of H_2O, while generating $TEMPO^+$ and nitrite (NO_2^-) as co-products. Based on literature precedent, under the protic reaction conditions NO_2^- is thought to self-dimerize and be protonated twice to release H_2O with the formation of N_2O_3, which can dissociate to regenerate NO and NO_2. $TEMPO^+$ is then reduced at the electrode to close the co-electrocatalytic cycle. Interestingly, although it is possible for TEMPOH (which can also be oxidized by NO_2) to form in solution via the acid-assisted disproportionation of TEMPO, the primary implied redox cycling is $TEMPO^{+/0}$, meaning that TEMPO is proposed to function primarily as a RM and not as an EPTM. Neither component is a competent ORR catalyst individually, but the combination of NO_x and TEMPO takes advantage of facile and thermodynamically favorable reactivity to mediate the reaction at much more positive potentials than is possible with homogeneous transition-metal-based catalysts. The authors went on to demonstrate the generality of this approach by achieving co-electrocatalysis with 4-acetamidoTEMPO (ACT), 3-carbamoyl-2,2,5,5-tetramethyl-1-pyrrolidinyl-N-oxyl (3-CARP), and 9-azabicyclo[3.3.1]nonane-N-oxyl (ABNO). Although all systems showed good stability and activity for the ORR, under the electrochemical conditions tested, the system was limited by the loss of NO_x species to the gaseous headspace of the cell.

1.6.3.6 RMs in the CO_2RR

Inspired by biological systems, which accumulate and distribute protons and electrons to metallocofactors during catalysis, Smith *et al.* reported the first example of an EPTM for homogeneous co-electrocatalysis for the CO_2RR in 2019 using the well-studied iron tetraphenylporphyrin ($[Fe(TPP)]^+$) catalyst with a series of nicotinamide adenine dinucleotide (NADH) analogues as the EPTM. (**Figure 1.15**).[98] Consistent with a co-electrocatalytic response,

the addition of the EPTM leads to a greater catalytic rate for the optimized co-catalytic system than the intrinsic activity of $[Fe(TPP)]^+$ (13-fold increase) under the same conditions. This system does not see a change in selectivity when the EPTM is added; the exclusive CO_2 reduction product remains CO. The series of EPTMs that were tested by the authors allowed them to identify two trends for EPTM selection: (1) the EPTM must be capable of mediating the transfer of both protons and electrons and (2) the closer the reduction potentials of the EPTM and catalyst are to one another, the more of an activity enhancement during co-electrocatalysis.

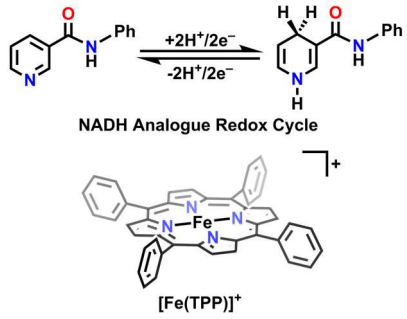

Figure 1.15. Structures of the iron tetraphenylporphyrin ($[Fe(TPP)]^+$) catalyst and RM with the highest activity for the CO_2RR in Ref 98.

Further, this study by Smith *et al.* showed through testing with control compounds that while both electron transfer and proton transfer were implicated, when combined in the same EPTM the enhancement effect was greater than the sum, suggesting a more complex mechanism. This point is important, since it had been established previously[36, 131] that the inclusion of hydrogen bond donors in solution has a positive effect on the CO_2RR. Mechanistic experiments suggested that the pyridine-based EPTMs were reduced by an *ECEC* mechanism (where *E* and *C* are electron transfer and chemical reaction steps, respectively), with potential inversion for the second reduction event favored at high concentrations of proton donor: at high proton donor concentrations the species formed after the initial reduction and protonation is more easily reduced than the starting pyridine species. Although this potential inversion by definition establishes the thermodynamic conditions required for a disproportionation reaction to be viable (EPTM(I)+EPTM(I)⇌EPTM(II)+EPTM(0)),[132] additional control compounds suggested that radical

mechanisms were unlikely to assist in catalysis. This is an important point because radical nicotamides have much lower BDFE values than the fully reduced compounds[133] and could potentially react as HAT reagents. Thus, the results of Smith *et al.* imply the possibility of a two-electron redox event, accompanied by one or two protons in a concerted way.More recently, Dey *et al.* reported a system for the reduction of CO_2 to HCOOH using Mn(bpy)$(CO)_3$Br[31, 134] and an FeS cluster as an EPTM.[100] Interestingly, this system also employs a HAT step in the reaction mechanism to avoid inefficient stepwise electron and proton transfer steps, but in this case the authors sought the formation of a M–H species. Therefore, the BDFEs of the EPTM–H and M–H species, as well as the pK_a of the acid used, were important thermodynamic values to consider. Similar to other studies discussed here, the authors were able to alter reaction selectivity and the rate of product formation when using the EPTM in comparison to the intrinsic catalytic properties of the Mn-based complex. In this case, the Mn-centered catalyst is selective for CO under electrochemical conditions,[31] but in the presence of the FeS cluster EPTM, the selectivity shifts to HCOOH. This is due to the EPTM promoting the formation of Mn^{I}(bpy)–H at more positive potentials than $[Mn^{0}(bpy^{\bullet-})]^{-}$ forms, the latter species being the initial step of the electrocatalytic reduction of CO_2 to the alternative CO product (**Figure 1.3**).[8]

Motivated by the elegant examples discussed above, we have been investigating small molecules with reduction potentials near the catalytic potential of a Cr catalyst developed in our group.[42, 43] Our initial studies focused on RMs with more negative reduction potentials than the Cr catalyst under the basic premise that to drive electron transfer during CO_2RR, downhill reactions would offer the most benefit. During our screening process, we observed that the greatest current enhancement of Cr(^{tbu}dhbpy)(H_2O)Cl (**Figure 1.16A**) arose with sulfone-based RMs (**Figure 1.16B** and **12C**). It should be emphasized that the role of the sulfone is to shuttle electron equivalents only and does not involve an associated proton transfer, functioning as an RM instead of an EPTM. We initially identified the ability of the Cr-catalyst to catalyze the reduction of CO_2

with dibenzothiophene 5,5-dioxide (DBTD) as a RM.[45, 46] The combination of Cr(^{tbu}dhbpy)(H_2O)Cl and DBTD catalyzes the reductive disproportionation of CO_2 to CO and carbonate (CO_3^{2-}) under aprotic conditions. Since the ability to catalyze the reduction of CO_2 under aprotic conditions is not inherent to either the catalyst or RM, we concluded that the electron transfer was occurring via an inner-sphere pathway where the reduced RM binds to Cr during the catalytic cycle in order for the electron transfer from the RM to the catalyst to occur. DFT calculations indicated that Cr-sulfone bond formation, dispersion effects, and through-space conjugation (TSEC)[135] between the bpy-backbone of the ligand and DBTD stabilized the key intermediate prior to the RDS. In TSEC, a single electron is shared between two π systems of appropriate symmetry and orientation.[135] Although an increase in activity also occurred under protic conditions when Cr(^{tbu}dhbpy)(H_2O)Cl and DBTD were combined, we were unable to exclude the possibility that the reduced DBTD RM acted as an outer-sphere electron transfer reagent, since it was reduced at potentials negative of where the Cr-based complex displayed intrinsic CO_2RR activity.

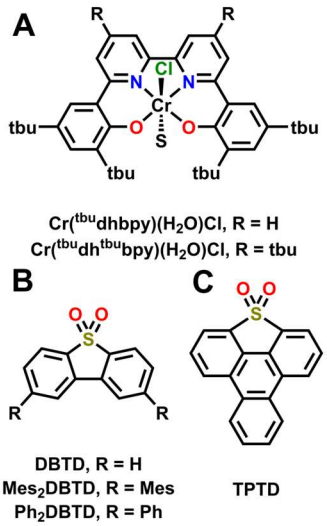

Figure 1.16. Structures of both Cr-based catalysts and RMs from Refs. 45 and 99.

This is in contrast to the work by Smith *et al.* where the greatest increase in co-catalytic activity is observed when the EPTM is reduced at a potential slightly positive of the catalyst. We attribute this difference in potential requirements to the large difference in the upper-limit TOF

values of $[Fe(TPP)]^+$ in comparison to our $Cr(N_2O_2)$ catalyst. Given the significant intrinsic activity of $[Fe(TPP)]^+$, the mediator must be in an activated form prior to potentials where the intrinsic catalytic cycle occurs, such that the co-elecytrocatalytic cycle is competitive. The comparatively lower intrinsic activity of our $Cr(N_2O_2)$ catalyst allows the co-electrocatalytic pathway to be competitive, even though it is accessed at more negative potentials than those required to produce a catalytically competent Cr species.

In the initial co-electrocatalytic studies, we proposed that the protic mechanism relied on pancake bonding (PB), where π systems share two electrons that are antiferromagnetically paired. Since it is known that PB can be improved by synthetically increasing the delocalization of the participating radical as well as increasing steric protection,[136-139] we examined protic reaction conditions with a new Cr-based complex and three additional sulfone-containing RMs which varied in their steric properties and electronic structure (**Figure 1.16**).[99] The results of this study are discussed in **Chapter 3** of this thesis.

1.6.4 Critical Analysis of Homogeneous Redox Mediator Development

Based on these examples, we can highlight key observations and preliminary conclusions about desirable properties for RMs in molecular co-catalytic systems. Much like the use of thermodynamic positioning in natural systems to establish energy gradients, electron transfer events (with or without a proton) in artificial systems rely on reactions which are at least isoergic, but preferably exergonic in the forward direction. It should be emphasized that while the primary function of a *catalyst* is not to create favorable thermodynamics for catalytic reactions, but rather to render them kinetically accessible, the thermodynamic positioning of all elementary reaction steps can impact speciation relevant to the catalytic process and consequently the observed activity.[140] Therefore, the key challenge to developing a co-catalytic system is to critically assess how the slowest and least efficient steps of the system can be supplanted with alternative routes.

The distinct advantage of the co-catalytic approach is the ability to *independently* select the properties of the secondary component without synthetically modifying the catalyst of interest. In single-component electrocatalysts, modification of the ligand framework to include electron-donating or electron-withdrawing functional groups will impact the standard reduction potential of the catalytic center. To a first approximation, the standard potential of a catalytic center can be linked to the observed activity in a basic linear free energy relationship, since the thermodynamic positioning of intermediates and kinetic barriers of interest can depend on the same intrinsic properties that dictate reduction potential.[141] The caveat to this generalization is that this type of "scaling relationship" can only rigorously occur within a catalyst "family" where the mechanism remains consistent. Several synthetic strategies for circumventing this link between standard reduction potential and activity have been developed,[36, 142-144] the majority of which rely on manipulating secondary-sphere effects based on positioning charge and hydrogen-bond donors. A strategy for improving the activity and selectivity of a catalytic system that does not require systematic synthetic modifications of the ligand framework is relatively attractive in terms of time and cost.

As a predictive tool, the Bordwell equation has been used to determine X–H bond strengths via a thermodynamic scheme that uses acid strength and standard reduction potential,[145] most commonly in combination with a solvent-dependent correction for the one-electron reduction potential of H^+.[146] Initially, Bordwell *et al.* used the data from the solution-phase thermochemical cycle to estimate bond dissociation enthalpies (BDEs);[146] however, since this initial implementation it is more common to determine BDFEs from these data. BDEs correspond to the enthalpy associated with homolytic bond cleavage in the gas phase, whereas BDFEs incorporate the effects of solvation relevant to homogeneous reactions, including enthalpic and entropic components. Where possible, we have tried to use BDFE values to describe our analysis of the reaction chemistry, although it is important to note that these are not always available. We

also note that the Mayer group has recently proposed to recalibrate these values by referencing PCET potentials against the standard potential of the $2H^+/H_2$ couple in the solvent of interest.[133, 147] For PCET redox couples with an equivalent number of proton and electron transfers, they argue that the use of the potential for H_2 gas formation as the reference state can produce a value which is largely independent from solvent and solution conditions and can even be conceptually described as the free energy of hydrogenation, which has significant utility in the context of thermochemical cycles. Lastly, for multisite-PCET reactions where the electrons and protons are not spatially co-located at some point in the reaction coordinate, the Bordwell equation can also be used to determine an "effective" BDFE value.[148]

1.6.4.1 Requirements for Relative EPTM X–H Bond Strength in Co-electrocatalysis

Independent of the preferred thermodynamic reference state, the known examples of co-electrocatalysis generally leverage the generation of relatively weak sacrificial X–H bonds for reductive processes (such that the desired product bond is stronger) and comparatively strong ones relative to the substrate bond of interest for oxidative processes. In the pioneering example by Badalyan and Stahl,[47] TEMPO•/TEMPOH cycling (BDFE 66 kcal/mol in MeCN[133]) during the oxidative conversion of alcohols to aldehydes only becomes feasible upon the inclusion of a Cu complex as co-catalyst. As described above, mechanistic studies showed that deprotonation of the Cu(II)-coordinated alcohol is rate-limiting under optimized catalytic conditions, prior to a net hydride transfer ($H^+/2e^-$) from the resultant Cu(II) alkoxide. As a representative example, we shall consider the MeOH oxidation activity reported for this co-electrocatalytic system. The BDFE of the O–H moiety in MeOH has been estimated to be 96.4 kcal/mol[133] and the expected weakening induced by coordination[149] does not appear to be sufficient to generate net hydrogen atom donation to [TEMPO•]. By comparison, the known C–H BDEs of MeOH[150] are weaker (96.1 ± 0.2 kcal/mol) than the O–H BDE (104.6 ± 0.7 kcal/mol). However, for the reaction to proceed an intermediate Cu(II) methoxide species should experience the net loss of $H^+/2e^-$ to generate

formaldehyde under these conditions. Based on the applied potential, Badalyan and Stahl excluded a two-electron, one-proton $TEMPO^+$/TEMPOH-based reaction cycle, which is catalytically competent at more oxidizing potentials.

Prior computational studies on the aerobic system by Ryland *et al.* suggested that the mechanism proceeded via a six-membered transition state involving an O–coordinated $TEMPO^•$ leading to a Cu(I)-coordinated $[R_2N(H)O]$ intermediate (**Figure 1.17**). This $[R_2N(H)O]$ species is a valence tautomer of TEMPOH which rearranges to the latter as part of a thermodynamically favorable net dissociation reaction.[151] Since the formation of Cu^I and TEMPOH is proposed to be thermodynamically favorable, the C–H substrate bond must be weakened through coordination, given the significant thermodynamic differences described above. We speculate here that the viability of this co-catalytic system at the Cu(II)/Cu(I) redox potential could then imply the existence of a redox equilibrium being established between formally $[Cu(II)(OMe^–)]^+$ and $[Cu(I)(OMe^•)]^+$ configurations. Equilibrium electron transfer involving the Cu center would weaken the C–H bonds of the methoxide, rendering the net transfer of a proton and an electron to the co-catalyst $TEMPO^•$ more thermodynamically viable. Thus, the favorable driving force of each step would be consistent with the authors' proposal of net hydride abstraction from the intermediate Cu(II) methoxide being distributed as an electron to the Cu(II) center and a proton and electron to $[TEMPO^•]$.[47] This mechanistic interpretation is based on the thermodynamic inaccessibility of $[TEMPO]^–$ and $[TEMPOH]^+$ under reaction conditions as established by the authors, in conjunction with the low bond BDE of 21.1 kcal/mol estimated for $[H–CH_2O^•]$.[152] This analysis also reconciles with the observation that thermodynamic driving force is almost always a primary determinant in HAT reactivity.[153] An alternative way to consider an inner-sphere redox continuum in this context is as a spin polarization effect on the alkoxide when coordinated to the d^9 Cu(II) center that makes net HAT from $[Cu(II)(OMe^–)]^+$ to coordinated $TEMPO^•$ feasible when coupled with Cu(II) reduction with corresponding C═O bond formation in the formaldehyde product.[153, 154]

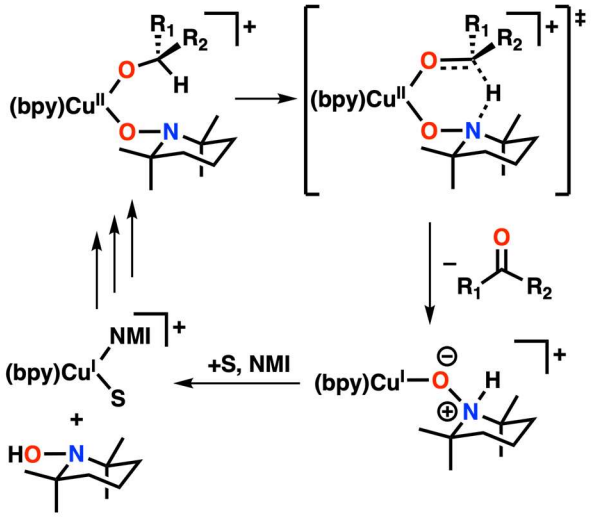

Figure 1.17. Mechanism for aerobic alcohol oxidation by the Cu(bpy)/TEMPO system proposed from hybrid functional DFT methods by Ryland *et al*. in Ref. 151 NMI = *N*-methylimidazole; S = acetonitrile; R_1 = H, alkyl, aryl; R_2 = alkyl, aryl.

Aerobic oxidation reactions like the Cu/TEMPO system can be an entry point to co-catalytic systems since they generally involve electron and proton transfer to a substrate via a mediator, which is recycled by O_2 during the reaction. The Co(salophen)/*p*-hydroquinone demonstrated by Anson and Stahl is an alternative version of this, where a co-electrocatalytic system for the ORR can be achieved when an electrode serves as the source of electrons instead of oxidizable substrates.[48] Although HAT involving the EPTM was shown to play a role in the mechanism of ORR (**Figure 1.13**), the role of O–H BDFE in the reaction was not directly examined. While 2-chloro-*p*-benzoquinone was tested for comparison with *p*-hydroquinone as an EPTM, the computationally estimated BDFE of its O–H bond in DMSO of 84.7 kcal/mol is comparable to that of 83.4 kcal/mol predicted for *p*-hydroquinone at the same level of theory.[155] Although the use of 2-chloro-*p*-benzoquinone results in greater rates of catalysis at more positive potentials than *p*-benzoquinone, as the authors point out this is likely due to the ability to generate greater amounts of 2-chloro-*p*-hydroquinone relative to *p*-hydroquinone at the chosen operating potential.[48] Thus, it is the relative concentration of the activated mediator which results in an increased catalytic response, instead of a difference in BDFE. However, the known role of HAT in

the co-electrocatalytic activity implies that generating hydroquinones with lower O–H BDFEs could be a route to increased activity in future studies.

1.6.4.2 Directing Selectivity for ETPMs with Weak X–H Bonds

There is an important limiting factor to targeting a specific reaction driving force for HAT or concerted proton-electron transfers, depending on desired product selectivity. The formation of weak X–H bonds in an EPTM, while desirable for activating relatively inert substrates, can lead to the competitive evolution of H_2. This parasitic pathway is evident in the work of Chalkley *et al*., who identified that C–H bonds with a calculated BDFE of 31 kcal/mol form when $CoCp^*_2$ is combined with ammonium-based acids.[92] Generating an activated EPTM which contains an X–H bond with low BDFE is essential to achieving N_2RR to NH_3 mediated by Fe tris(phosphino)borane complexes: the gas phase reduction of N_2 with three equivalents of H_2, requires an average BDFE of 49.9 kcal/mol.[133] Although the BDFE value for H_2 is not known in the diethyl ether solvent used by Chalkley *et al.* during co-electrocatalysis, its value in the related ethereal solvent THF is 52.0 kcal/mol.[147] Therefore, in all cases during electrocatalytic N_2RR the thermodynamically preferred formation of H_2 occurred, in some instances with competitive Faradaic efficiency to the desired NH_3 product.[92] Given the existing knowledge of the reaction landscape for the multistep transformation of N_2 to NH_3, potential opportunities exist for kinetic interception strategies that could outcompete competitive H_2 formation in the future.[92, 93, 110, 112]

Galvin and Waymouth[90] and McLoughlin *et al.*[91] have demonstrated the validity of this approach in the development of two transition-metal-catalyzed catalyst systems for the AOR. For the example reported by McLoughlin *et al.,* knowledge of the intrinsic mechanism of the mononuclear catalytic cycle mediated by the Ru complex was valuable, as metal hydride BDFEs generally fall in a relatively narrow range, which enabled more targeted selection of an EPTM.[156, 157] Thus, an additional Ru-based complex capable of HAT at a ligand-based radical reported by Wu *et al.*[158] could be identified with suitable properties for enabling co-electrocatalysis. In order

to avoid the energetic penalty of oxidizing the Ru-based catalyst twice, the EPTM needed to be oxidized at more negative potentials than the Ru(II) hydride intermediate, possess a pK_a that was too weak to protonate the intermediate Ru(II) hydride to generate dihydrogen, and have a BDFE similar enough to the hydride to thermodynamically favor HAT from the Ru(II) hydride. Selecting a suitable EPTM was possible because some of these values vary relatively little across solvents (e.g., metal hydride BDFE[156, 157]) and other thermodynamic parameters can scale reasonably well across solvents (e.g., pK_a[159]). It is worth noting that this approach can also result in mechanistic changes[160] and the best approach for success is undoubtedly one where experimentally measured values under relevant conditions have been established *a priori*. The design rules described by McLoughlin *et al.* are nonetheless quite effective for narrowing the EPTM screening process. Importantly, this strategy is generalizable to reductive processes as well: Dey *et al.* utilized a similar strategy based on the knowledge of M–H BDFEs to identify a RM that would generate M–H species *en route* to the reduction of CO_2 to formic acid.[94]

1.6.4.3 Redox Potential Requirements for Co-electrocatalysis

In contrast to these studies is the work of Smith *et al.,*[98] where the fundamental reaction step differs from a conventional HAT or a concerted proton and electron transfer step. The role of pyridine derivatives to act as catalysts for CO_2 reduction inspires debate;[88] however, Smith *et al.* focused on the generation of dihydropyridines which did not have sufficient hydricity to react with CO_2 on their own.[161, 162] Therefore, as a design principle, the mediator was to transfer protons and electrons to the intermediates generated when CO_2 binds to $[Fe(TPP)]^{2-}$ in the presence of proton donors. In the proposed mechanism for the CO_2RR mediated by $[Fe(TPP)]^{+}$, catalysis is initiated upon the generation of an 'Fe(0)' species at the electrode, $[Fe(TPP)]^{2-}$ (**Figure 1.18**).[163] Upon CO_2 binding, the resultant $[Fe(TPP)(\bullet CO_2)]^{2-}$ adduct is stabilized by an equilibrium hydrogen bonding interaction with the proton donor in solution K_{AH_1}, *nota bene* at low concentrations of added acid the catalytic current becomes second-order with respect to [acid]. This stabilization impacts K_{CO2},

particularly in ligand frameworks with positioned charged moieties or proton and hydrogen bond donors, which can have profound effects on the observed electrocatalytic response and caused a change in mechanism.[36, 142, 164] Subsequently, a second proton donor association triggers electron transfer from the Fe center, with concomitant bond cleavage to generate the H_2O co-product and a formally Fe(II) carbonyl species. The release of CO then occurs via a comproportionation reaction with $[Fe(TPP)]^{2-}$, completing the cycle.

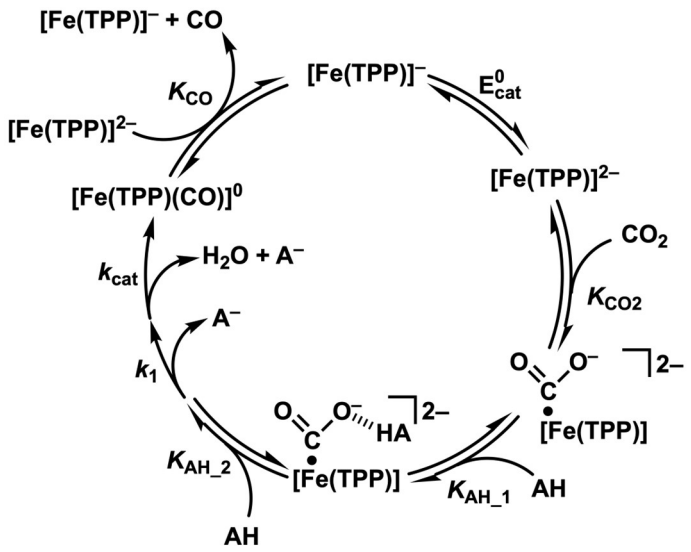

Figure 1.18. Previously proposed mechanism for CO_2RR by $[Fe(TPP)]^{+}$.[165]

Since an increase in catalytic current is observed when the reducible pyridine derivatives are added to the reaction, we can speculate that it is the rate-determining C–OH bond cleavage event that is being impacted. One possibility is that the favorable association of the EPTM to $[Fe(TPP)(\bullet CO_2)]^{2-}$ through hydrogen-bonding interactions supplants K_{AH_1} and the non-covalent interaction of the activated EPTM (a theoretical two-proton and two-electron donor) with metal-bound substrate can shunt the catalytic cycle directly back to $[Fe(TPP)]^{2-}$ with CO and H_2O loss. Since these conditions include PhOH, which serves as a competent proton donor for the catalytic cycle depicted in **Figure 1.18**, there are likely to be contributions from the overlapping catalytic and co-catalytic mechanisms in the observed current. Modulation of EPTM equilibrium

association to $[Fe(TPP)(\bullet CO_2)]^{2-}$ relative to K_{AH_1} would then be expected to shift the observed catalytic rate through control of the relative concentrations of the two possible active species in solution. This proposal is supported by the observation that the reduction potential of the EPTM needs to be slightly positive of that for the catalyst for the greatest enhancement to occur. Generating the reduced RM at potentials positive of the catalytic wave is advantageous for generating sufficient concentrations of the activated EPTM to compensate for the presumably sluggish kinetics of the $2H^+/2e^-$ transfer during the co-catalytic cycle. This proposal suggests that the inclusion of stronger hydrogen bond donors on the EPTM could cause greater rate enhancements.

1.7 Outline of Research Chapters

The following research chapters focus on the development of new Cr-centered molecular electrocatalysts for the reduction of CO_2 and new co-electrocatalytic systems with these Cr-centered catalysts and sulfone-based RMs. **Chapter 2** includes detailed experimental work on a terpyridine (tpy) catalyst with an N_3O ligand framework[166] based on the N_2O_2 ligand framework introduced above.[42-44] Electroanalytical data demonstrating the activity, selectivity, and overpotential of the new catalyst is reported along with kinetic data and a proposed mechanism that is compared to the previous reports of the Cr(^{tbu}dhbpy)Cl(H_2O) catalyst.

Chapters 3, **4**, and **5** all report new Cr-centered catalysts that are capable of the CO_2RR on their own as well as new RMs that enhance the activity of the catalysts on their own. Chapter 3 reports a ligand framework with *tert*-butyl groups substituted on the bpy backbone of the ligand framework which shows enhanced activity compared to the parent bpy-based catalyst. Additionally, the co-catalytic activity of both the bpy and ^{tbu}bpy catalysts with the previously reported DBTD[45, 46] and three new derivatives is reported and analyzed to gain new insights into the co-catalytic cycle.[99] Chapter 4 reports a Cr catalyst with a phenanthroline-based N_2O_2 ligand framework and compares its co-catalytic activity with two sulfone-based RMs to gain further

insight into the forces critical for the formation of key co-catalytic intermediates.[167, 168] **In Chapter 5**, the study of a phenyl-substituted phenanthroline catalyst with a benzonaphthothiophene 7,7-dioxide (BNTD) RM is discussed. **Chapter 6** includes a summary of these results along with future directions and an outlook on the field.

1.8 References

1. IPCC *IPCC, 2023: Summary for Policymakers. In: Climate Change 2023: Synthesis Report*; IPPC: Geneva, Switzerland, 2023; pp 1-34.
2. IEA *World Energy Outlook 2022*; Paris, France, 2022.
3. Can Şener, Ş. E.; Sharp, J. L.; Anctil, A., Factors impacting diverging paths of renewable energy: A review. *Renew. Sustain. Energy Rev.* **2018,** *81*, 2335-2342.
4. De Luna, P.; Hahn, C.; Higgins, D.; Jaffer, S. A.; Jaramillo, T. F.; Sargent, E. H., What would it take for renewably powered electrosynthesis to displace petrochemical processes? *Science* **2019,** *364* (6438), eaav3506.
5. Kopylovich, M. N.; Ribeiro, A. P. C.; Alegria, E. C. B. A.; Martins, N. M. R.; Martins, L. M. D. R. S.; Pombeiro, A. J. L., Chapter Three - Catalytic Oxidation of Alcohols: Recent Advances. In *Adv. Organomet. Chem.*, Pérez, P. J., Ed. Academic Press: 2015; Vol. 63, pp 91-174.
6. Guo, X.; Du, H.; Qu, F.; Li, J., Recent progress in electrocatalytic nitrogen reduction. *J. Mater. Chem. A* **2019,** *7* (8), 3531-3543.
7. Pegis, M. L.; Wise, C. F.; Martin, D. J.; Mayer, J. M., Oxygen Reduction by Homogeneous Molecular Catalysts and Electrocatalysts. *Chem. Rev.* **2018,** *118* (5), 2340-2391.
8. Francke, R.; Schille, B.; Roemelt, M., Homogeneously Catalyzed Electroreduction of Carbon Dioxide—Methods, Mechanisms, and Catalysts. *Chem. Rev.* **2018,** *118* (9), 4631-4701.
9. Sanz-Pérez, E. S.; Murdock, C. R.; Didas, S. A.; Jones, C. W., Direct Capture of CO2 from Ambient Air. *Chem. Rev.* **2016,** *116* (19), 11840-11876.
10. In *Carbon Management: Implications for R&D in the Chemical Sciences and Technology: A Workshop Report to the Chemical Sciences Roundtable*, Washington (DC), 2001.
11. Nahar, S.; Zain, M. F. M.; Kadhum, A. A. H.; Hasan, H. A.; Hasan, M. R., Advances in Photocatalytic CO_2 Reduction with Water: A Review. *Materials* **2017,** *10* (6).
12. Saha, P.; Amanullah, S.; Dey, A., Selectivity in Electrochemical CO_2 Reduction. *Acc. Chem. Res.* **2022,** *55* (2), 134-144.
13. Jiang, C.; Nichols, A. W.; Machan, C. W., A look at periodic trends in d-block molecular electrocatalysts for CO_2 reduction. *Dalton Trans.* **2019,** *48*, 9454-9468.
14. Kempler, P. A.; Nielander, A. C., Reliable reporting of Faradaic efficiencies for electrocatalysis research. *Nat. Commun.* **2023,** *14* (1), 1158.
15. Appel, A. M.; Helm, M. L., Determining the Overpotential for a Molecular Electrocatalyst. *ACS Catal.* **2014,** *4* (2), 630-633.
16. Costentin, C.; Drouet, S.; Robert, M.; Savéant, J.-M., Turnover Numbers, Turnover Frequencies, and Overpotential in Molecular Catalysis of Electrochemical Reactions. Cyclic Voltammetry and Preparative-Scale Electrolysis. *J. Am. Chem. Soc.* **2012,** *134* (27), 11235-11242.
17. Costentin, C.; Drouet, S.; Robert, M.; Savéant, J.-M., Correction to Turnover Numbers, Turnover Frequencies, and Overpotential in Molecular Catalysis of Electrochemical

Reactions. Cyclic Voltammetry and Preparative-Scale Electrolysis. *J. Am. Chem. Soc.* **2012,** *134* (48), 19949-19950.
18. Kozuch, S.; Martin, J. M. L., "Turning Over" Definitions in Catalytic Cycles. *ACS Catal.* **2012,** *2* (12), 2787-2794.
19. Wang, V. C. C.; Johnson, B. A., Interpreting the Electrocatalytic Voltammetry of Homogeneous Catalysts by the Foot of the Wave Analysis and Its Wider Implications. *ACS Catal.* **2019,** *9* (8), 7109-7123.
20. Cometto, C.; Chen, L.; Lo, P.-K.; Guo, Z.; Lau, K.-C.; Anxolabéhère-Mallart, E.; Fave, C.; Lau, T.-C.; Robert, M., Highly Selective Molecular Catalysts for the CO_2-to-CO Electrochemical Conversion at Very Low Overpotential. Contrasting Fe vs Co Quaterpyridine Complexes upon Mechanistic Studies. *ACS Catal.* **2018,** *8* (4), 3411-3417.
21. Beley, M.; Collin, J.-P.; Ruppert, R.; Sauvage, J.-P., Nickel(II)-cyclam: an extremely selective electrocatalyst for reduction of CO_2 in water. *J. Chem. Soc., Chem. Commun.* **1984,** (19), 1315-1316.
22. Beley, M.; Collin, J. P.; Ruppert, R.; Sauvage, J. P., Electrocatalytic reduction of carbon dioxide by nickel cyclam^{2+} in water: study of the factors affecting the efficiency and the selectivity of the process. *J. Am. Chem. Soc.* **1986,** *108* (24), 7461-7467.
23. Song, J.; Klein, E. L.; Neese, F.; Ye, S., The Mechanism of Homogeneous CO_2 Reduction by Ni(cyclam): Product Selectivity, Concerted Proton–Electron Transfer and C–O Bond Cleavage. *Inorg. Chem.* **2014,** *53* (14), 7500-7507.
24. Froehlich, J. D.; Kubiak, C. P., Homogeneous CO_2 Reduction by Ni(cyclam) at a Glassy Carbon Electrode. *Inorg. Chem.* **2012,** *51* (7), 3932-3934.
25. Froehlich, J. D.; Kubiak, C. P., The Homogeneous Reduction of CO_2 by [Ni(cyclam)]$^+$: Increased Catalytic Rates with the Addition of a CO Scavenger. *J. Am. Chem. Soc.* **2015,** *137* (10), 3565-3573.
26. Hawecker, J.; Lehn, J.-M.; Ziessel, R., Electrocatalytic reduction of carbon dioxide mediated by Re(bipy)(CO)$_3$Cl (bipy = 2,2′-bipyridine). *J. Chem. Soc., Chem. Commun.* **1984,** (6), 328-330.
27. Ishida, H.; Tanaka, K.; Tanaka, T., Electrochemical CO_2 reduction catalyzed by ruthenium complexes [Ru(bpy)$_2$(CO)$_2$]$^{2+}$ and [Ru(bpy)$_2$(CO)Cl]$^+$. Effect of pH on the formation of CO and HCOO. *Organometallics* **1987,** *6* (1), 181-186.
28. Benson, E. E.; Sampson, M. D.; Grice, K. A.; Smieja, J. M.; Froehlich, J. D.; Friebel, D.; Keith, J. A.; Carter, E. A.; Nilsson, A.; Kubiak, C. P., The Electronic States of Rhenium Bipyridyl Electrocatalysts for CO_2 Reduction as Revealed by X-ray Absorption Spectroscopy and Computational Quantum Chemistry. *Angew. Chem., Int. Ed.* **2013,** *52* (18), 4841-4844.
29. Ishida, H.; Fujiki, K.; Ohba, T.; Ohkubo, K.; Tanaka, K.; Terada, T.; Tanaka, T., Ligand effects of ruthenium 2,2′-bipyridine and 1,10-phenanthroline complexes on the electrochemical reduction of CO_2. *J. Chem. Soc., Dalton Trans.* **1990,** (7), 2155-2160.
30. Bourrez, M.; Molton, F.; Chardon-Noblat, S.; Deronzier, A., [Mn(bipyridyl)(CO)$_3$Br]: An Abundant Metal Carbonyl Complex as Efficient Electrocatalyst for CO_2 Reduction. *Angew. Chem. Int. Ed.* **2011,** *50* (42), 9903-9906.
31. Sampson, M. D.; Nguyen, A. D.; Grice, K. A.; Moore, C. E.; Rheingold, A. L.; Kubiak, C. P., Manganese Catalysts with Bulky Bipyridine Ligands for the Electrocatalytic Reduction of Carbon Dioxide: Eliminating Dimerization and Altering Catalysis. *J. Am. Chem. Soc.* **2014,** *136* (14), 5460-5471.
32. Machan, C. W.; Stanton, C. J., III; Vandezande, J. E.; Majetich, G. F.; Schaefer, H. F., III; Kubiak, C. P.; Agarwal, J., Electrocatalytic Reduction of Carbon Dioxide by Mn(CN)(2,2′-bipyridine)(CO)$_3$: CN Coordination Alters Mechanism. *Inorg. Chem.* **2015,** *54* (17), 8849-8856.

33. Hammouche, M.; Lexa, D.; Savéant, J. M.; Momenteau, M., Catalysis of the electrochemical reduction of carbon dioxide by iron("0") porphyrins. *J. Electroanal. Chem. Interf. Electrochem.* **1988,** *249* (1), 347-351.
34. Azcarate, I.; Costentin, C.; Robert, M.; Savéant, J.-M., Through-Space Charge Interaction Substituent Effects in Molecular Catalysis Leading to the Design of the Most Efficient Catalyst of CO_2-to-CO Electrochemical Conversion. *J. Am. Chem. Soc.* **2016,** *138* (51), 16639-16644.
35. Costentin, C.; Passard, G.; Robert, M.; Saveant, J. M., Ultraefficient homogeneous catalyst for the CO_2-to-CO electrochemical conversion. *PNAS USA* **2014,** *111* (42), 14990-4.
36. Nichols, Eva M.; Derrick, J. S.; Nistanaki, S. K.; Smith, P. T.; Chang, C. J., Positional effects of second-sphere amide pendants on electrochemical CO_2 reduction catalyzed by iron porphyrins. *Chem. Sci.* **2018,** *9* (11), 2952-2960.
37. Derrick, J. S.; Loipersberger, M.; Nistanaki, S. K.; Rothweiler, A. V.; Head-Gordon, M.; Nichols, E. M.; Chang, C. J., Templating Bicarbonate in the Second Coordination Sphere Enhances Electrochemical CO_2 Reduction Catalyzed by Iron Porphyrins. *J. Am. Chem. Soc.* **2022,** *144* (26), 11656-11663.
38. Teindl, K.; Patrick, B. O.; Nichols, E. M., Linear Free Energy Relationships and Transition State Analysis of CO_2 Reduction Catalysts Bearing Second Coordination Spheres with Tunable Acidity. *J. Am. Chem. Soc.* **2023,** *145* (31), 17176-17186.
39. Margarit, C. G.; Schnedermann, C.; Asimow, N. G.; Nocera, D. G., Carbon Dioxide Reduction by Iron Hangman Porphyrins. *Organometallics* **2019,** *38* (6), 1219-1223.
40. Tory, J.; Setterfield-Price, B.; Dryfe, R. A. W.; Hartl, F., [$M(CO)_4$(2,2′-bipyridine)] (M = Cr, Mo, W) Complexes as Efficient Catalysts for Electrochemical Reduction of CO_2 at a Gold Electrode. *ChemElectroChem.* **2015,** *2* (2), 213-217.
41. Grice, K. A.; Saucedo, C., Electrocatalytic Reduction of CO_2 by Group 6 $M(CO)_6$ Species without "Non-Innocent" Ligands. *Inorg. Chem.* **2016,** *55* (12), 6240-6246.
42. Hooe, S. L.; Dressel, J. M.; Dickie, D. A.; Machan, C. W., Highly Efficient Electrocatalytic Reduction of CO_2 to CO by a Molecular Chromium Complex. *ACS Catal.* **2020,** *10* (2), 1146-1151.
43. Moreno, J. J.; Hooe, S. L.; Machan, C. W., DFT Study on the Electrocatalytic Reduction of CO_2 to CO by a Molecular Chromium Complex. *Inorg. Chem.* **2021,** *60* (6), 3635-3650.
44. Moreno, J. J.; Hooe, S. L.; Machan, C. W., Correction to DFT Study on the Electrocatalytic Reduction of CO2 to CO by a Molecular Chromium Complex. *Inorg. Chem.* **2022**.
45. Hooe, S. L.; Moreno, J. J.; Reid, A. G.; Cook, E. N.; Machan, C. W., Mediated Inner-Sphere Electron Transfer Induces Homogeneous Reduction of CO_2 via Through-Space Electronic Conjugation**. *Angew. Chem., Int. Ed.* **2022,** *61* (1), e202109645.
46. Hooe, S. L.; Moreno, J. J.; Reid, A. G.; Cook, E. N.; Machan, C. W., Corrigendum: Mediated Inner-Sphere Electron Transfer Induces Homogeneous Reduction of CO_2 via Through-Space Electronic Conjugation. *Angew. Chem., Int. Ed.* **2022,** *61* (25), e202205139.
47. Badalyan, A.; Stahl, S. S., Cooperative electrocatalytic alcohol oxidation with electron-proton-transfer mediators. *Nature* **2016,** *535* (7612), 406-410.
48. Anson, C. W.; Stahl, S. S., Cooperative Electrocatalytic O_2 Reduction Involving Co(salophen) with p-Hydroquinone as an Electron–Proton Transfer Mediator. *J. Am. Chem. Soc.* **2017,** *139* (51), 18472-18475.
49. Kristensen, S. B.; van Mourik, T.; Pedersen, T. B.; Sørensen, J. L.; Muff, J., Simulation of electrochemical properties of naturally occurring quinones. *Sci. Rep.* **2020,** *10* (1), 13571.
50. Alcázar-Fabra, M.; Navas, P.; Brea-Calvo, G., Coenzyme Q biosynthesis and its role in the respiratory chain structure. *Biochim. Biophys. Acta - Bioenerg* **2016,** *1857* (8), 1073-1078.
51. Chen, H.; Simoska, O.; Lim, K.; Grattieri, M.; Yuan, M.; Dong, F.; Lee, Y. S.; Beaver, K.; Weliwatte, S.; Gaffney, E. M.; Minteer, S. D., Fundamentals, Applications, and Future Directions of Bioelectrocatalysis. *Chem. Rev.* **2020,** *120* (23), 12903-12993.

52. Schneider, C. R.; Shafaat, H. S., An internal electron reservoir enhances catalytic CO_2 reduction by a semisynthetic enzyme. *ChemComm* **2016,** *52* (64), 9889-9892.
53. Johnson, D. C.; Dean, D. R.; Smith, A. D.; Johnson, M. K., STRUCTURE, FUNCTION, AND FORMATION OF BIOLOGICAL IRON-SULFUR CLUSTERS. *Annu. Rev. Biochem.* **2005,** *74*, 247-81.
54. Ibrahim, I. M.; Wu, H.; Ezhov, R.; Kayanja, G. E.; Zakharov, S. D.; Du, Y.; Tao, W. A.; Pushkar, Y.; Cramer, W. A.; Puthiyaveetil, S., An evolutionarily conserved iron-sulfur cluster underlies redox sensory function of the Chloroplast Sensor Kinase. *Commun. Biol.* **2020,** *3* (1), 13.
55. Silveira, C. M.; Almeida, M. G., Small electron-transfer proteins as mediators in enzymatic electrochemical biosensors. *Anal. Bioanal. Chem.* **2013,** *405* (11), 3619-3635.
56. Nöll, T.; Nöll, G., Strategies for “wiring” redox-active proteins to electrodes and applications in biosensors, biofuel cells, and nanotechnology. *Chem. Soc. Rev.* **2011,** *40* (7), 3564-3576.
57. Heller, A.; Feldman, B., Electrochemical Glucose Sensors and Their Applications in Diabetes Management. *Chem. Rev.* **2008,** *108* (7), 2482-2505.
58. Abasıyanık, M. F.; Şenel, M., Immobilization of glucose oxidase on reagentless ferrocene-containing polythiophene derivative and its glucose sensing application. *J. Electroanal. Chem.* **2010,** *639* (1), 21-26.
59. De Wael, K.; Bashir, Q.; Van Vlierberghe, S.; Dubruel, P.; Heering, H. A.; Adriaens, A., Electrochemical determination of hydrogen peroxide with cytochrome *c* peroxidase and horse heart cytochrome *c* entrapped in a gelatin hydrogel. *Bioelectrochemistry* **2012,** *83*, 15-18.
60. Dronov, R.; Kurth, D. G.; Scheller, F. W.; Lisdat, F., Direct and Cytochrome c Mediated Electrochemistry of Bilirubin Oxidase on Gold. *Electroanalysis* **2007,** *19* (15), 1642-1646.
61. Gong, J.; Liu, W.; Du, X.; Liu, C.; Zhang, Z.; Sun, F.; Yang, L.; Xu, D.; Guo, H.; Deng, Y., Direct Conversion of Wheat Straw into Electricity with a Biomass Flow Fuel Cell Mediated by Two Redox Ion Pairs. *ChemSusChem* **2017,** *10* (3), 506-513.
62. Zu, X.; Sun, L.; Gong, J.; Liu, X.; Liu, Y.; Du, X.; Liu, W.; Chen, L.; Yi, G.; Zhang, W.; Lin, W.; Li, W.; Deng, Y., Ferric ion pair mediated biomass redox flow fuel cell and related chemical reaction kinetics study. *Chem. Eng. J.* **2018,** *348*, 476-484.
63. Lamb, A. B.; Elder, L. W., THE ELECTROMOTIVE ACTIVATION OF OXYGEN. *J. Am. Chem. Soc.* **1931,** *53* (1), 137-163.
64. Kummer, J. T.; Oei, D. G., A chemically regenerative redox fuel cell. II. *J. Appl. Electrochem.* **1985,** *15* (4), 619-629.
65. Zhao, X.; Zhu, J. Y., Efficient Conversion of Lignin to Electricity Using a Novel Direct Biomass Fuel Cell Mediated by Polyoxometalates at Low Temperatures. *ChemSusChem* **2016,** *9* (2), 197-207.
66. Bergens, S. H.; Gorman, C. B.; Palmore, G. T. R.; Whitesides, G. M., A Redox Fuel-Cell That Operates with Methane as Fuel at 120-Degrees-C. *Science* **1994,** *265* (5177), 1418-1420.
67. Gorman, C. B.; Bergens, S. H.; Whitesides, G. M., Platinum-Catalyzed Oxidations of Organic Compounds by Ferric Sulfate: Use of a Redox Fuel Cell to Mediate Complete Oxidation of Ethylene Glycol by Dioxygen at 80°C. *J. Catal.* **1996,** *158* (1), 92-96.
68. Anson, C. W.; Stahl, S. S., Mediated Fuel Cells: Soluble Redox Mediators and Their Applications to Electrochemical Reduction of O_2 and Oxidation of H_2, Alcohols, Biomass, and Complex Fuels. *Chem. Rev.* **2020,** *120* (8), 3749-3786.
69. Milton, R. D.; Cai, R.; Abdellaoui, S.; Leech, D.; De Lacey, A. L.; Pita, M.; Minteer, S. D., Bioelectrochemical Haber–Bosch Process: An Ammonia-Producing H2/N2 Fuel Cell. *Angew. Chem., Int. Ed.* **2017,** *56* (10), 2680-2683.
70. Silverstein, T. P., Marcus Theory: Thermodynamics CAN Control the Kinetics of Electron Transfer Reactions. *J. Chem. Educ.* **2012,** *89* (9), 1159-1167.

71. Piechota, E. J.; Meyer, G. J., Introduction to Electron Transfer: Theoretical Foundations and Pedagogical Examples. *J. Chem. Educ.* **2019,** *96* (11), 2450-2466.
72. Lennox, A. J. J.; Nutting, J. E.; Stahl, S. S., Selective electrochemical generation of benzylic radicals enabled by ferrocene-based electron-transfer mediators. *Chem. Sci.* **2018,** *9* (2), 356-361.
73. Zhu, L.; Xiong, P.; Mao, Z.-Y.; Wang, Y.-H.; Yan, X.; Lu, X.; Xu, H.-C., Electrocatalytic Generation of Amidyl Radicals for Olefin Hydroamidation: Use of Solvent Effects to Enable Anilide Oxidation. *Angew. Chem., Int. Ed.* **2016,** *55* (6), 2226-2229.
74. Wu, Z.-J.; Xu, H.-C., Synthesis of C3-Fluorinated Oxindoles through Reagent-Free Cross-Dehydrogenative Coupling. *Angew. Chem., Int. Ed.* **2017,** *56* (17), 4734-4738.
75. Francke, R.; Little, R. D., Redox catalysis in organic electrosynthesis: basic principles and recent developments. *Chem. Soc. Rev.* **2014,** *43* (8), 2492-2521.
76. Wang, F.; Gerken, J. B.; Bates, D. M.; Kim, Y. J.; Stahl, S. S., Electrochemical Strategy for Hydrazine Synthesis: Development and Overpotential Analysis of Methods for Oxidative N–N Coupling of an Ammonia Surrogate. *J. Am. Chem. Soc.* **2020,** *142* (28), 12349-12356.
77. Nutting, J. E.; Rafiee, M.; Stahl, S. S., Tetramethylpiperidine N-Oxyl (TEMPO), Phthalimide N-Oxyl (PINO), and Related N-Oxyl Species: Electrochemical Properties and Their Use in Electrocatalytic Reactions. *Chem. Rev.* **2018,** *118* (9), 4834-4885.
78. McCann, S. D.; Stahl, S. S., Copper-Catalyzed Aerobic Oxidations of Organic Molecules: Pathways for Two-Electron Oxidation with a Four-Electron Oxidant and a One-Electron Redox-Active Catalyst. *Acc. Chem. Res.* **2015,** *48* (6), 1756-1766.
79. Hoover, J. M.; Ryland, B. L.; Stahl, S. S., Mechanism of Copper(I)/TEMPO-Catalyzed Aerobic Alcohol Oxidation. *J. Am. Chem. Soc.* **2013,** *135* (6), 2357-2367.
80. Wang, F.; Stahl, S. S., Electrochemical Oxidation of Organic Molecules at Lower Overpotential: Accessing Broader Functional Group Compatibility with Electron−Proton Transfer Mediators. *Acc. Chem. Res.* **2020,** *53* (3), 561-574.
81. Shan, B.; Schmehl, R., Photochemical Generation of Strong One-Electron Reductants via Light-Induced Electron Transfer with Reversible Donors Followed by Cross Reaction with Sacrificial Donors. *J. Phys. Chem. A* **2014,** *118* (45), 10400-10406.
82. Tyson, E. L.; Niemeyer, Z. L.; Yoon, T. P., Redox Mediators in Visible Light Photocatalysis: Photocatalytic Radical Thiol–Ene Additions. *J. Org. Chem.* **2014,** *79* (3), 1427-1436.
83. Happ, B.; Winter, A.; Hager, M. D.; Schubert, U. S., Photogenerated avenues in macromolecules containing Re(I), Ru(II), Os(II), and Ir(III) metal complexes of pyridine-based ligands. *Chem. Soc. Rev.* **2012,** *41* (6), 2222-2255.
84. Andreiadis, E. S.; Chavarot-Kerlidou, M.; Fontecave, M.; Artero, V., Artificial Photosynthesis: From Molecular Catalysts for Light-driven Water Splitting to Photoelectrochemical Cells. *Photochem. Photobiol.* **2011,** *87* (5), 946-964.
85. Teets, T. S.; Nocera, D. G., Photocatalytic hydrogen production. *Chem. Commun.* **2011,** *47* (33), 9268-9274.
86. Sakai, K.; Ozawa, H., Homogeneous catalysis of platinum(II) complexes in photochemical hydrogen production from water. *Coord. Chem. Rev.* **2007,** *251* (21), 2753-2766.
87. Oh, Y.; Hu, X. L., Organic molecules as mediators and catalysts for photocatalytic and electrocatalytic CO_2 reduction. *Chem. Soc. Rev.* **2013,** *42* (6), 2253-2261.
88. Vasilyev, D. V.; Dyson, P. J., The Role of Organic Promoters in the Electroreduction of Carbon Dioxide. *ACS Catal.* **2021,** *11* (3), 1392-1405.
89. Koval, C. A.; Lercher, J.; Scott, S. L.; Coates, G. W.; Iglesia, E.; Bullock, R. M.; Jaramillo, T. F.; Flytzani-Stephanopoulos, M.; Resasco, D.; Tway, C. L.; Batista, V.; Chapman, K. W.; Dai, S.; Dumesic, J.; Friend, C.; Hille, R.; Johnson, K.; Nørskov, J.; Rekoske, J.; Sarkar, R.; Bradley, C.; Garrett, B.; Henderson, C.; Miranda, R.; Peden, C.; Schwartz, V.; Runkles, K.; Fellner, K.; Jenks, C.; Nelson, M.; Appel, A. M.; Bare, S.; Bartlett, B. M.; Bligaard, T.; Chandler, B. D.; Davis, R. J.; Glezakou, V.-A.; Gregoire, J.; Hille, R.;

Hock, A. S.; Kitchin, J.; Kung, H. H.; Rousseau, R.; Sadow, A. D.; Schaak, R. E.; Shaw, W. J.; Stacchiola, D. J.; Delferro, M.; Bunel, E.; Holladay, J.; Houle, F.; Jenks, C.; Krause, T.; Marshall, C.; Neale, N.; Parks, J.; Schaidle, J.; VandeLagemaat, J.; Wang, Y.; Weber, R. *Basic Research Needs for Catalysis Science to Transform Energy Technologies: Report from the U.S. Department of Energy, Office of Basic Energy Sciences Workshop May 8–10, 2017, in Gaithersburg, Maryland*; United States, 2017-05-08, 2017.

90. Galvin, C. M.; Waymouth, R. M., Electron-Rich Phenoxyl Mediators Improve Thermodynamic Performance of Electrocatalytic Alcohol Oxidation with an Iridium Pincer Complex. *J. Am. Chem. Soc.* **2020,** *142* (45), 19368-19378.
91. McLoughlin, E. A.; Armstrong, K. C.; Waymouth, R. M., Electrochemically Regenerable Hydrogen Atom Acceptors: Mediators in Electrocatalytic Alcohol Oxidation Reactions. *ACS Catal.* **2020,** *10* (19), 11654-11662.
92. Chalkley, M. J.; Del Castillo, T. J.; Matson, B. D.; Peters, J. C., Fe-Mediated Nitrogen Fixation with a Metallocene Mediator: Exploring p*K*a Effects and Demonstrating Electrocatalysis. *J. Am. Chem. Soc.* **2018,** *140* (19), 6122-6129.
93. Garrido-Barros, P.; Derosa, J.; Chalkley, M. J.; Peters, J. C., Tandem electrocatalytic N_2 fixation via proton-coupled electron transfer. *Nature* **2022,** *609* (7925), 71-76.
94. Derosa, J.; Garrido-Barros, P.; Li, M.; Peters, J. C., Use of a PCET Mediator Enables a Ni-HER Electrocatalyst to Act as a Hydride Delivery Agent. *J. Am. Chem. Soc.* **2022,** *144* (43), 20118-20125.
95. Chambers, G. M.; Wiedner, E. S.; Bullock, R. M., H_2 Oxidation Electrocatalysis Enabled by Metal-to-Metal Hydrogen Atom Transfer: A Homolytic Approach to a Heterolytic Reaction. *Angew. Chem., Int. Ed.* **2018,** *57* (41), 13523-13527.
96. Hooe, S. L.; Cook, E. N.; Reid, A. G.; Machan, C. W., Non-covalent assembly of proton donors and p-benzoquinone anions for co-electrocatalytic reduction of dioxygen. *Chem. Sci.* **2021,** *12*, 9733-9741.
97. Gerken, J. B.; Stahl, S. S., High-Potential Electrocatalytic O_2 Reduction with Nitroxyl/NO_x Mediators: Implications for Fuel Cells and Aerobic Oxidation Catalysis. *ACS Cent. Sci.* **2015,** *1* (5), 234-243.
98. Smith, P. T.; Weng, S.; Chang, C. J., An NADH-Inspired Redox Mediator Strategy to Promote Second-Sphere Electron and Proton Transfer for Cooperative Electrochemical CO_2 Reduction Catalyzed by Iron Porphyrin. *Inorg. Chem.* **2020,** *59* (13), 9270-9278.
99. Reid, A. G.; Moreno, J. J.; Hooe, S. H.; Baugh, K. R.; Thomas, I. H.; Dickie, D. A.; Machan, C. W., Inverse Potential Scaling in Co-Electrocatalytic Activity for CO_2 Reduction Through Redox Mediator Tuning and Catalyst Design. *Chem. Sci.* **2022,** *13*, 9595-9606.
100. Dey, S.; Masero, F.; Brack, E.; Fontecave, M.; Mougel, V., Electrocatalytic metal hydride generation using CPET mediators. *Nature* **2022,** *607* (7919), 499-506.
101. Walker, B. R.; Manabe, S.; Brusoe, A. T.; Sevov, C. S., Mediator-Enabled Electrocatalysis with Ligandless Copper for Anaerobic Chan–Lam Coupling Reactions. *J. Am. Chem. Soc.* **2021,** *143* (16), 6257-6265.
102. Lee, K. J.; Lodaya, K. M.; Gruninger, C. T.; Rountree, E. S.; Dempsey, J. L., Redox mediators accelerate electrochemically-driven solubility cycling of molecular transition metal complexes. *Chem. Sci.* **2020,** *11* (36), 9836-9851.
103. Ciriminna, R.; Palmisano, G.; Pagliaro, M., Electrodes Functionalized with the 2,2,6,6-Tetramethylpiperidinyloxy Radical for the Waste-Free Oxidation of Alcohols. *ChemCatChem* **2015,** *7* (4), 552-558.
104. Bobbitt, J. M.; BrüCkner, C.; Merbouh, N., Oxoammonium- and Nitroxide-Catalyzed Oxidations of Alcohols. *Org. React.* **2010**, 103-424.
105. Semmelhack, M. F.; Chou, C. S.; Cortes, D. A., Nitroxyl-mediated electrooxidation of alcohols to aldehydes and ketones. *J. Am. Chem. Soc.* **1983,** *105* (13), 4492-4494.

106. Rafiee, M.; Miles, K. C.; Stahl, S. S., Electrocatalytic Alcohol Oxidation with TEMPO and Bicyclic Nitroxyl Derivatives: Driving Force Trumps Steric Effects. *J. Am. Chem. Soc.* **2015,** *137* (46), 14751-14757.
107. Hickey, D. P.; Schiedler, D. A.; Matanovic, I.; Doan, P. V.; Atanassov, P.; Minteer, S. D.; Sigman, M. S., Predicting Electrocatalytic Properties: Modeling Structure–Activity Relationships of Nitroxyl Radicals. *J. Am. Chem. Soc.* **2015,** *137* (51), 16179-16186.
108. Speelman, A. L.; Gerken, J. B.; Heins, S. P.; Wiedner, E. S.; Stahl, S. S.; Appel, A. M., Determining overpotentials for the oxidation of alcohols by molecular electrocatalysts in non-aqueous solvents. *Energy Environ. Sci.* **2022,** *15* (10), 4015-4024.
109. Waldie, K. M.; Flajslik, K. R.; McLoughlin, E.; Chidsey, C. E. D.; Waymouth, R. M., Electrocatalytic Alcohol Oxidation with Ruthenium Transfer Hydrogenation Catalysts. *J. Am. Chem. Soc.* **2017,** *139* (2), 738-748.
110. Matson, B. D.; Peters, J. C., Fe-Mediated HER vs N_2RR: Exploring Factors That Contribute to Selectivity in $P_3^EFe(N_2)$ (E = B, Si, C) Catalyst Model Systems. *ACS Catal.* **2018,** *8* (2), 1448-1455.
111. Chalkley, M. J.; Drover, M. W.; Peters, J. C., Catalytic N_2-to-NH_3 (or -N_2H_4) Conversion by Well-Defined Molecular Coordination Complexes. *Chem. Rev.* **2020,** *120* (12), 5582-5636.
112. Chalkley, M. J.; Del Castillo, T. J.; Matson, B. D.; Roddy, J. P.; Peters, J. C., Catalytic N_2-to-NH_3 Conversion by Fe at Lower Driving Force: A Proposed Role for Metallocene-Mediated PCET. *ACS Cent. Sci.* **2017,** *3* (3), 217-223.
113. Anson, C. W.; Ghosh, S.; Hammes-Schiffer, S.; Stahl, S. S., Co(salophen)-Catalyzed Aerobic Oxidation of p-Hydroquinone: Mechanism and Implications for Aerobic Oxidation Catalysis. *J. Am. Chem. Soc.* **2016,** *138* (12), 4186-4193.
114. Nitopi, S.; Bertheussen, E.; Scott, S. B.; Liu, X.; Engstfeld, A. K.; Horch, S.; Seger, B.; Stephens, I. E. L.; Chan, K.; Hahn, C.; Nørskov, J. K.; Jaramillo, T. F.; Chorkendorff, I., Progress and Perspectives of Electrochemical CO_2 Reduction on Copper in Aqueous Electrolyte. *Chem. Rev.* **2019,** *119* (12), 7610-7672.
115. Hooe, S. L.; Rheingold, A. L.; Machan, C. W., Electrocatalytic Reduction of Dioxygen to Hydrogen Peroxide by a Molecular Manganese Complex with a Bipyridine-Containing Schiff Base Ligand. *J. Am. Chem. Soc.* **2018,** *140* (9), 3232-3241.
116. Hooe, S. L.; Machan, C. W., Dioxygen Reduction to Hydrogen Peroxide by a Molecular Mn Complex: Mechanistic Divergence between Homogeneous and Heterogeneous Reductants. *J. Am. Chem. Soc.* **2019,** *141* (10), 4379-4387.
117. Huynh, M. T.; Anson, C. W.; Cavell, A. C.; Stahl, S. S.; Hammes-Schiffer, S., Quinone 1 e^- and 2 e^-/2 H^+ Reduction Potentials: Identification and Analysis of Deviations from Systematic Scaling Relationships. *J. Am. Chem. Soc.* **2016,** *138* (49), 15903-15910.
118. Gupta, N.; Linschitz, H., Hydrogen-Bonding and Protonation Effects in Electrochemistry of Quinones in Aprotic Solvents. *J. Am. Chem. Soc.* **1997,** *119* (27), 6384-6391.
119. Costentin, C., Electrochemical Approach to the Mechanistic Study of Proton-Coupled Electron Transfer. *Chem. Rev.* **2008,** *108* (7), 2145-2179.
120. Quan, M.; Sanchez, D.; Wasylkiw, M. F.; Smith, D. K., Voltammetry of Quinones in Unbuffered Aqueous Solution: Reassessing the Roles of Proton Transfer and Hydrogen Bonding in the Aqueous Electrochemistry of Quinones. *J. Am. Chem. Soc.* **2007,** *129* (42), 12847-12856.
121. Staley, P. A.; Lopez, E. M.; Clare, L. A.; Smith, D. K., Kinetic Stabilization of Quinone Dianions via Hydrogen Bonding by Water in Aprotic Solvents. *J. Phys. Chem. C* **2015,** *119* (35), 20319-20327.
122. Evans, D. H., One-Electron and Two-Electron Transfers in Electrochemistry and Homogeneous Solution Reactions. *Chem. Rev.* **2008,** *108* (7), 2113-2144.

123. Astudillo, P. D.; Tiburcio, J.; González, F. J., The role of acids and bases on the electrochemical oxidation of hydroquinone: Hydrogen bonding interactions in acetonitrile. *J. Electroanal. Chem.* **2007,** *604* (1), 57-64.
124. Astudillo, P. D.; Valencia, D. P.; González-Fuentes, M. A.; Díaz-Sánchez, B. R.; Frontana, C.; González, F. J., Electrochemical and chemical formation of a low-barrier proton transfer complex between the quinone dianion and hydroquinone. *Electrochim. Acta* **2012,** *81*, 197-204.
125. Alligrant, T. M.; Hackett, J. C.; Alvarez, J. C., Acid/base and hydrogen bonding effects on the proton-coupled electron transfer of quinones and hydroquinones in acetonitrile: Mechanistic investigation by voltammetry, ^{1}H NMR and computation. *Electrochim. Acta* **2010,** *55* (22), 6507-6516.
126. Lam, Y. C.; Nielsen, R. J.; Gray, H. B.; Goddard, W. A., A Mn Bipyrimidine Catalyst Predicted To Reduce CO_2 at Lower Overpotential. *ACS Catal.* **2015,** *5* (4), 2521-2528.
127. Macías-Ruvalcaba, N. A.; Okumura, N.; Evans, D. H., Change in Reaction Pathway in the Reduction of 3,5-Di-*tert*-butyl-1,2-benzoquinone with Increasing Concentrations of 2,2,2-Trifluoroethanol. *J. Phys. Chem. B* **2006,** *110* (43), 22043-22047.
128. Evans, D. H.; René, A., Reinvestigation of a former concerted proton-electron transfer (CPET), the reduction of a hydrogen-bonded complex between a proton donor and the anion radical of 3,5-di-*tert*-butyl-1,2-benzoquinone. *Phys. Chem. Chem. Phys.* **2012,** *14* (14), 4844-4848.
129. Shi, R. R. S.; Tessensohn, M. E.; Lauw, S. J. L.; Foo, N. A. B. Y.; Webster, R. D., Tuning the reduction potential of quinones by controlling the effects of hydrogen bonding, protonation and proton-coupled electron transfer reactions. *ChemComm* **2019,** *55* (16), 2277-2280.
130. Cook, E. N.; Machan, C. W., Homogeneous Catalysis of Dioxygen Reduction by Molecular Mn Complexes. *ChemComm* **2022,** *58*, 11746-11761.
131. Nichols, E. M.; Chang, C. J., Urea-Based Multipoint Hydrogen-Bond Donor Additive Promotes Electrochemical CO_2 Reduction Catalyzed by Nickel Cyclam. *Organometallics* **2019,** *38* (6), 1213-1218.
132. Saveant, J. M.; Costentin, C., Elements of Molecular and Biomolecular Electrochemistry: An Electrochemical Approach to Electron Transfer Chemistry, 2nd Edition. *Elements of Molecular and Biomolecular Electrochemistry: An Electrochemical Approach to Electron Transfer Chemistry, 2nd Edition* **2019**, 1-616.
133. Agarwal, R. G.; Coste, S. C.; Groff, B. D.; Heuer, A. M.; Noh, H.; Parada, G. A.; Wise, C. F.; Nichols, E. M.; Warren, J. J.; Mayer, J. M., Free Energies of Proton-Coupled Electron Transfer Reagents and Their Applications. *Chem. Rev.* **2022,** *122* (1), 1-49.
134. Sampson, M. D.; Kubiak, C. P., Manganese Electrocatalysts with Bulky Bipyridine Ligands: Utilizing Lewis Acids To Promote Carbon Dioxide Reduction at Low Overpotentials. *J. Am. Chem. Soc.* **2016,** *138* (4), 1386-1393.
135. Li, J.; Shen, P. Z., Zujin; Tang, Ben Z., Through-Space Conjugation: A Thriving Alternative for Optoelectronic Materials. *CCS Chem.* **2019,** *1* (2), 181-196.
136. Garcia-Yoldi, I.; Miller, J. S.; Novoa, J. J., Structure and Stability of the $[TCNE]_2^{2-}$ Dimers in Dichloromethane Solution: A Computational Study. *J. Phys. Chem. A.* **2007,** *111* (32), 8020-8027.
137. Garcia-Yoldi, I.; Miller, J. S.; Novoa, J. J., $[Cyanil]_2^{2-}$ dimers possess long, two-electron ten-center ($2e^-/10c$) multicenter bonding. *Phys. Chem. Chem. Phys.* **2008,** *10* (28), 4106-4109.
138. Mota, F.; Miller, J. S.; Novoa, J. J., Comparative Analysis of the Multicenter, Long Bond in $[TCNE]^{\cdot-}$ and Phenalenyl Radical Dimers: A Unified Description of Multicenter, Long Bonds. *J. Am. Chem. Soc.* **2009,** *131* (22), 7699-7707.
139. Kertesz, M., Pancake Bonding: An Unusual Pi-Stacking Interaction. *Chem. Eur. J.* **2019,** *25* (2), 400-416.

140. Kozuch, S.; Shaik, S., How to Conceptualize Catalytic Cycles? The Energetic Span Model. *Acc. Chem. Res.* **2011,** *44* (2), 101-110.
141. Costentin, C.; Savéant, J.-M., Homogeneous Molecular Catalysis of Electrochemical Reactions: Manipulating Intrinsic and Operational Factors for Catalyst Improvement. *J. Am. Chem. Soc.* **2018,** *140* (48), 16669-16675.
142. Azcarate, I.; Costentin, C.; Robert, M.; Saveant, J. M., Through-Space Charge Interaction Substituent Effects in Molecular Catalysis Leading to the Design of the Most Efficient Catalyst of CO_2-to-CO Electrochemical Conversion. *J. Am. Chem. Soc.* **2016,** *138* (51), 16639-16644.
143. Gotico, P.; Roupnel, L.; Guillot, R.; Sircoglou, M.; Leibl, W.; Halime, Z.; Aukauloo, A., Atropisomeric Hydrogen Bonding Control for CO_2 Binding and Enhancement of Electrocatalytic Reduction at Iron Porphyrins. *Angew. Chem., Int. Ed.* **2020,** *59* (50), 22451-22455.
144. Nie, W.; Tarnopol, D. E.; McCrory, C. C. L., Enhancing a Molecular Electrocatalyst's Activity for CO_2 Reduction by Simultaneously Modulating Three Substituent Effects. *J. Am. Chem. Soc.* **2021,** *143* (10), 3764-3778.
145. Bordwell, F. G.; Bausch, M. J., Acidity-oxidation-potential (AOP) values as estimates of relative bond dissociation energies and radical stabilities in dimethyl sulfoxide solution. *J. Am. Chem. Soc.* **1986,** *108* (8), 1979-1985.
146. Bordwell, F. G.; Cheng, J. P.; Harrelson, J. A., Homolytic bond dissociation energies in solution from equilibrium acidity and electrochemical data. *J. Am. Chem. Soc.* **1988,** *110* (4), 1229-1231.
147. Wise, C. F.; Agarwal, R. G.; Mayer, J. M., Determining Proton-Coupled Standard Potentials and X–H Bond Dissociation Free Energies in Nonaqueous Solvents Using Open-Circuit Potential Measurements. *J. Am. Chem. Soc.* **2020,** *142* (24), 10681-10691.
148. Warren, J. J.; Tronic, T. A.; Mayer, J. M., Thermochemistry of Proton-Coupled Electron Transfer Reagents and its Implications. *Chem Rev* **2010,** *110* (12), 6961-7001.
149. Cuerva, J. M.; Campaña, A. G.; Justicia, J.; Rosales, A.; Oller-López, J. L.; Robles, R.; Cárdenas, D. J.; Buñuel, E.; Oltra, J. E., Water: The Ideal Hydrogen-Atom Source in Free-Radical Chemistry Mediated by TiIII and Other Single-Electron-Transfer Metals? *Angew. Chem., Int. Ed.* **2006,** *45* (33), 5522-5526.
150. Blanksby, S. J.; Ellison, G. B., Bond Dissociation Energies of Organic Molecules. *Acc. Chem. Res.* **2003,** *36* (4), 255-263.
151. Ryland, B. L.; McCann, S. D.; Brunold, T. C.; Stahl, S. S., Mechanism of Alcohol Oxidation Mediated by Copper(II) and Nitroxyl Radicals. *J. Am. Chem. Soc.* **2014,** *136* (34), 12166-12173.
152. Ruscic, B., Active Thermochemical Tables: Sequential Bond Dissociation Enthalpies of Methane, Ethane, and Methanol and the Related Thermochemistry. *J. Phys. Chem. A* **2015,** *119* (28), 7810-7837.
153. Saouma, C. T.; Mayer, J. M., Do spin state and spin density affect hydrogen atom transfer reactivity? *Chem. Sci.* **2014,** *5* (1), 21-31.
154. Shaik, S.; Hirao, H.; Kumar, D., Reactivity of High-Valent Iron–Oxo Species in Enzymes and Synthetic Reagents: A Tale of Many States. *Acc. Chem. Res.* **2007,** *40* (7), 532-542.
155. Zhu, X.-Q.; Wang, C.-H.; Liang, H., Scales of Oxidation Potentials, p*K*a, and BDE of Various Hydroquinones and Catechols in DMSO. *J. Org. Chem. Res* **2010,** *75* (21), 7240-7257.
156. Wiedner, E. S.; Chambers, M. B.; Pitman, C. L.; Bullock, R. M.; Miller, A. J. M.; Appel, A. M., Thermodynamic Hydricity of Transition Metal Hydrides. *Chem. Rev.* **2016,** *116* (15), 8655-8692.
157. Waldie, K. M.; Ostericher, A. L.; Reineke, M. H.; Sasayama, A. F.; Kubiak, C. P., Hydricity of Transition-Metal Hydrides: Thermodynamic Considerations for CO_2 Reduction. *ACS Catal.* **2018,** *8* (2), 1313-1324.

158. Wu, A.; Masland, J.; Swartz, R. D.; Kaminsky, W.; Mayer, J. M., Synthesis and Characterization of Ruthenium Bis(β-diketonato) Pyridine-Imidazole Complexes for Hydrogen Atom Transfer. *Inorg. Chem.* **2007,** *46* (26), 11190-11201.
159. Kütt, A.; Tshepelevitsh, S.; Saame, J.; Lõkov, M.; Kaljurand, I.; Selberg, S.; Leito, I., Strengths of Acids in Acetonitrile. *Eur. J. Org. Chem.* **2021,** *2021* (9), 1407-1419.
160. Burgess, S. A.; Appel, A. M.; Linehan, J. C.; Wiedner, E. S., Changing the Mechanism for CO_2 Hydrogenation Using Solvent-Dependent Thermodynamics. *Angew. Chem., Int. Ed.* **2017,** *56* (47), 15002-15005.
161. Lim, C.-H.; Ilic, S.; Alherz, A.; Worrell, B. T.; Bacon, S. S.; Hynes, J. T.; Glusac, K. D.; Musgrave, C. B., Benzimidazoles as Metal-Free and Recyclable Hydrides for CO_2 Reduction to Formate. *J. Am. Chem. Soc.* **2019,** *141* (1), 272-280.
162. Ilic, S.; Alherz, A.; Musgrave, C. B.; Glusac, K. D., Thermodynamic and kinetic hydricities of metal-free hydrides. *Chem. Soc. Rev.* **2018,** *47* (8), 2809-2836.
163. Bonin, J.; Maurin, A.; Robert, M., Molecular catalysis of the electrochemical and photochemical reduction of CO_2 with Fe and Co metal based complexes. Recent advances. *Coord. Chem. Rev.* **2017,** *334*, 184-198.
164. Costentin, C.; Drouet, S.; Robert, M.; Savéant, J.-M., A Local Proton Source Enhances CO_2 Electroreduction to CO by a Molecular Fe Catalyst. *Science* **2012,** *338* (6103), 90–94.
165. Costentin, C.; Robert, M.; Savéant, J.-M., Current Issues in Molecular Catalysis Illustrated by Iron Porphyrins as Catalysts of the CO_2-to-CO Electrochemical Conversion. *Acc. Chem. Res.* **2015,** *48* (12), 2996-3006.
166. Reid, A. G.; Hooe, S. L.; Moreno, J. J.; Dickie, D. A.; Charles, W. M., Homogeneous Electrocatalytic Reduction of CO_2 by a CrN_3O Complex: Electronic Coupling with Redox-Active Terpyridine Fragment Favors Selectivity for CO. *ChemRxiv* **2022**, 10.26434/chemrxiv-2021-lplvt-v2.
167. Reid, A. G.; Moberg, M. E.; Koellner, C. A.; Moreno, J. J.; Hooe, S. L.; Baugh, K. R.; Dickie, D. A.; Machan, C. W., Comparisons of bpy and phen Ligand Backbones in Cr-Mediated (Co-)Electrocatalytic CO_2 Reduction. *Organometallics* **2023,** *42* (11), 1139-1148.
168. Reid, A. G.; Moberg, M. E.; Koellner, C. A.; Moreno, J. J.; Hooe, S. L.; Baugh, K. R.; Dickie, D. A.; Machan, C. W., Correction to “Comparisons of bpy and phen Ligand Backbones in Cr-Mediated (Co-) Electrocatalytic CO_2 Reduction”. *Organometallics* **2024,** *43* (3), 438-438.

Chapter 2

Homogeneous Electrocatalytic Reduction of CO_2 by a CrN_3O Complex: Electronic Coupling with a Redox-Active Terpyridine Fragment Favors Selectivity for CO

Containing work originally published in:

Reid, A. G.; Hooe, S. L.; Moreno, J. J.; Dickie, D. A.; Machan, C. W., Inorganic Chemistry **2022**, *61* (43), 16963-16970.

2.1 Abstract

Electrocatalyst design and optimization strategies continue to be an active area of research interest for the applied use of renewable energy resources. The electrocatalytic conversion of carbon dioxide (CO_2) is an attractive approach in this context because of the added potential benefit of addressing its rising atmospheric concentrations. In previous experimental and computational studies, we have described the mechanism of the first molecular Cr complex capable of electrocatalytically reducing CO_2 to carbon monoxide (CO) in the presence of an added proton donor, which contained a redox-active 2,2'-bipyridine (bpy) fragment, CrN_2O_2. The high selectivity for CO in the bpy-based system was dependent on a delocalized $Cr^{II}(bpy^{\bullet-})$ active state. Subsequently, we became interested in exploring how expanding the polypyridyl ligand core would impact the selectivity and activity during electrocatalytic CO_2 reduction. Here, we report a new CrN_3O catalyst, $Cr(tpy^{tbu}pho)Cl_2$ (**1**), where 2-(2,2':6',2''-terpyridin]-6-yl)-4,6-di-*tert*-butylphenolate = $[tpy^{tbu}pho]^-$, which reduces CO_2 to CO with almost quantitative selectivity via a different mechanism than our previously reported $Cr(^{tbu}dhbpy)Cl(H_2O)$ catalyst. Computational analyses indicate that, although the stoichiometry of both reactions is identical, changes in the observed rate law are the combined result of a decrease in the intrinsic ligand charge (L_3X vs L_2X_2) and an increase in the ligand redox activity, which result in increased electronic coupling between the doubly reduced tpy fragment of the ligand and the Cr^{II} center. The strong electronic coupling enhances the rate of protonation and subsequent C–OH bond cleavage, resulting in CO_2 binding becoming the rate-determining step, which is an uncommon mechanism during protic CO_2 reduction.

2.2 Introduction

Rising concerns over increasing energy demands and global climate change have led to continued interest in the development of molecular catalysts capable of interconverting electrical and chemical energy.[1-3] Specifically, the electrocatalytic reduction of carbon dioxide (CO_2) to

carbon monoxide (CO) using renewable energy[4-6] represents a potentially valuable pathway to the synthesis of liquid fuels via the Fischer–Tropsch process,[7] in the manufacturing of acetic acid,[8] and in hydroformylation reactions.[9] In homogeneous electrocatalysis for CO_2 reduction, the Cr/Mo/W triad is underrepresented,[4-6] with a limited number of reports of systems that are electrochemically or electrocatalytically active, few of which exhibit stability during electrolysis.[10-17]

Previously, we reported the first homogeneous Cr electrocatalyst for quantitative CO_2 reduction to CO, Cr(^{tbu}dhbpy)Cl(H_2O), where 6,6'-di(3,5-di-*tert*-butyl-2-phenolate)-2,2'-bipyridine = [^{tbu}dhbpy]$^{2-}$.[18-20] We proposed a catalytic mechanism for the Cr(^{tbu}dhbpy)Cl(H_2O) catalyst whereby C–OH bond cleavage was the rate-determining step, based on mechanistic and computational studies. The noteworthy kinetic selectivity of this complex for CO was ascribed to the electronic structure of the catalytically active species: a square-planar [Cr^{II}(^{tbu}dhpy$^{\bullet}$)]$^{-}$ species (**Figure 2.1**) that exhibited antiferromagnetic coupling between a bpy-based radical anion and the Cr^{II} center (S = 3/2). On the basis of previous reports about the role of electronic coupling in driving selectivity,[21-27] we reasoned that the redox activity of our bpy-based ligand could be translated to expanded polypyridyl ligand frameworks to examine how electronic coupling between Cr and the reduced ligand frameworks impacts the catalytic performance. This was motivated by the known role of electronic coupling between 2,2':6',2''-terpyridine (tpy) fragments or 2,2':6',2'':6'',2‴-quaterpyridine (qpy) and later transition metals like Fe[23, 24, 27] or Co[27] in achieving high selectivity and activity at low overpotentials (η).

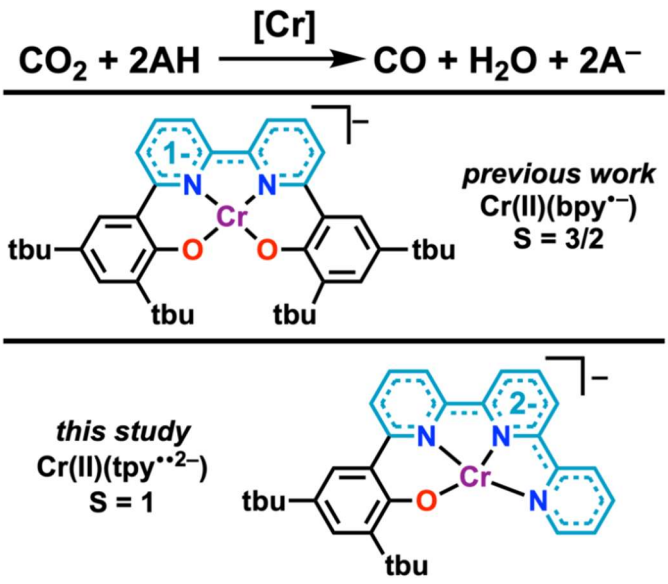

Figure 2.1. Comparison of the electronic structure of the active states for bpy- and tpy-based Cr complexes capable of mediating homogeneous electrocatalytic CO_2 reduction to CO.

Here we present a new molecular Cr catalyst, Cr(tpy^{tbu}pho)Cl_2 (**1**), where 2-(2,2':6',2''-terpyridin-6-yl)-4,6-di-*tert*-butylphenolate = [tpy^{tbu}pho]$^-$, which exhibits activity for CO_2 reduction to CO via a different mechanism relative to our initial Cr(^{tbu}dhbpy)Cl(H_2O) catalyst. Experimental and computational analyses reveal that the new electrocatalyst **1** operates with important differences in the overall mechanism, which arise from the expanded redox activity of the tpy fragment relative to bpy, achieving an active state best described as [Cr^{II}(tpy^{tbu}pho$^{2•}$)]$^-$ (**Figure 2.1**). Interestingly, these results also reveal that the charge of the supporting ligand plays an important role because the benefit of the expanded redox activity in [tpy^{tbu}pho]$^-$ appears to be balanced by the shift from an L_2X_2 coordination environment to L_3X. This study suggests that Cr electrocatalysts for CO_2 reduction can benefit from ligand design strategies that have previously been explored only for later transition metals.[23, 24, 27]

2.3 Results

The synthesis of 2-(2,2':6',2''-terpyridin-6-yl)-4,6-di-*tert*-butylphenol, [tpy^{tbu}phoH]^0, was achieved via an initial coupling of 2,6-dibromopyridine to 2,2'-bipyridine to make 6-bromo-2,2':6',2''-terpyridine.[28] Subsequent microwave-assisted Suzuki-type cross-coupling of 6-bromo-

2,2':6',2''-terpyridine with (3,5-di-*tert*-butyl-2-hydroxy-phenyl)boronic acid[18] produced [tpy^{tbu}pho(H)]^{0} in high yield. **1** was synthesized in a manner similar to that in our previous report.[18] Both [tpy^{tbu}pho(H)]^{0} and **1** were characterized via high-resolution mass spectrometry (HRMS) and elemental analysis (EA) as well as NMR and UV–vis spectroscopies (**Table S2.2**, and **Figures S2.1-S2.5**). The proposed molecular connectivity was supported by the structural data obtained from single-crystal X-ray diffraction studies (**Figure 2.2**).

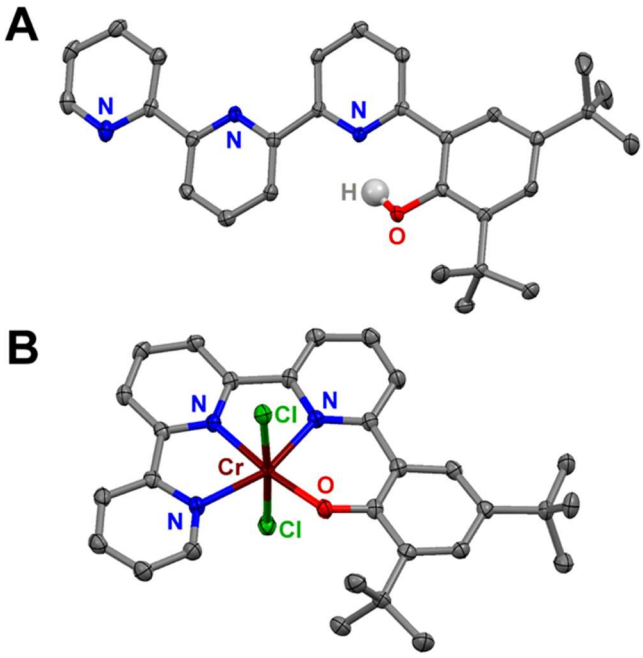

Figure 2.2. (**A**) Molecular structure of [tpy^{tbu}phoH]^{0} obtained from single-crystal X-ray diffraction studies. All non-phenol H atoms have been removed for clarity. Crystals were grown by slow cooling a saturated hexane solution of the ligand. (**B**) Molecular structure of 1 obtained from single-crystal X-ray diffraction studies. Crystals were grown from the slow evaporation of a dichloromethane/acetonitrile mixture at room temperature. H atoms and acetonitrile molecule have been omitted for clarity. Color code: blue, N; red, O; gray, C; green, Cl; maroon, Cr; white, H atoms. Thermal ellipsoids are at 50%. CCDC: 2086769 and 2086770.

Cyclic voltammetry (CV) experiments were performed on **1** in a solution of 0.1 M tetrabutylammonium hexafluorophosphate ($TBAPF_6$) in *N,N*-dimethylformamide (DMF). Under argon (Ar) saturation conditions, **1** displays three redox features at potentials more negative than the ferrocenium/ferrocene (Fc^{+}/Fc) redox couple: E_p = −1.46 V, $E_{1/2}$ = −1.64 V, and $E_{1/2}$ = −2.18 V

versus Fc^+/Fc (**Figure 2.3**, black and **Figure S2.6**), assigned as E_1^0, E_2^0, and E_3^0, respectively. A small wave is observed at $E_{1/2}$ = −1.85 V, following the second reduction, which we propose relates to equilibria involving the solvent displacement of a Cl^- ion bound to Cr. This proposal is supported by CV data obtained with tetrabutylammonium chloride (TBACl) present as a source of excess Cl^- anions (**Figures S2.7** and **S2.8**). Under Ar saturation conditions with added TBACl, only three reduction waves are observed and there is a shift toward more negative potentials for the first and second reductions of **1** relative to identical conditions in the absence of TBACl; the minor wave observed at $E_{1/2}$ = −1.85 V versus Fc^+/Fc also disappears. These data suggest that, overall, the complex undergoes three one-electron reduction events in the observed potential window, with two chloride-loss equilibria affecting the first two reductions, **Eq (2.1)-Eq (2.6)**, where L = $[tpy^{tbu}pho]^-$ and S = DMF. These assignments are supported by experiments described above, as well as density functional theory (DFT) calculations, which show that the relevant equilibria depicted in **Eq (2.1)** and **Eq (2.3)** present reaction free energies of 0.9 kcal/mol (K_{eq} = 0.22) and −0.3 kcal/mol (K_{eq} = 1.7) as written, *vide infra* (**Figure S2.9**).

$[Cr(L)Cl_2]^0 + S \rightleftharpoons [Cr(L)Cl(S)]^+ + Cl^-$		**Eq (2.1)**
$[Cr(L)Cl(S)]^+ + e^- \rightleftharpoons [Cr(L)Cl(S)]^0$	E_1^0	**Eq (2.2)**
$[Cr(L)Cl(S)]^0 + S \rightleftharpoons [Cr(L)(S)_2]^+ + Cl^-$		**Eq (2.3)**
$[Cr(L)(S)_2]^+ + e^- \rightleftharpoons [Cr(L)(S)_2]^0$	E_2^0	**Eq (2.4)**
$[Cr(L)(S)_2]^0 \rightleftharpoons [Cr(L)(S)_2]^0 + S$		**Eq (2.5)**
$[Cr(L)S]^0 + e^- \rightleftharpoons [Cr(L)S]^-$	E_3^0	**Eq (2.6)**

Upon the addition of 0.1 M phenol (PhOH) under Ar saturation conditions, minimal shifts in the first two redox features of **1** are observed, but the third redox feature displays a slight increase in current with some loss of reversibility (**Figure 2.3**, green). In the absence of an added proton donor under CO_2 saturation conditions, CV data indicate that favorable CO_2 binding occurs: the third redox feature is observed to shift positively to E_p = −2.13 V versus Fc^+/Fc (**Figure 2.3**, red). The irreversibility observed at this feature and the appearance of a second irreversible

feature at a more negative potential (both with slight current increases) is consistent with limited aprotic CO_2 reduction activity occurring after CO_2 binding.

Under CO_2 saturation conditions in the presence of 0.1 M PhOH, a slight shift to positive potentials and a large increase in current are observed, which is consistent with the electrocatalytic CO_2 reduction reaction (CO_2RR) mediated by **1** (**Figure 2.3**, blue). At 0.1 M PhOH cross-tracing is apparent by CV, which disappears with increased PhOH concentrations (**Figure S2.10**) and at higher scan rates (**Figure S2.11**). Additionally, similar CO_2RR reactivity in DMF is observed with H_2O as a proton source instead of PhOH (**Figure S2.12**).

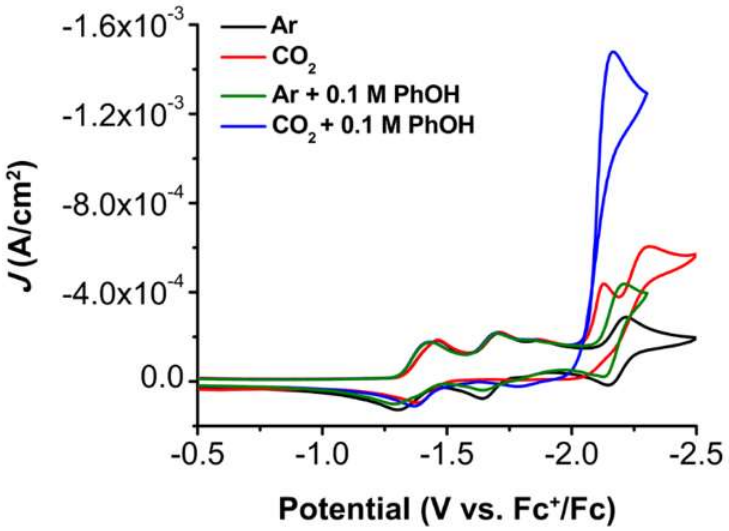

Figure 2.3. Comparison of the CVs of 1.0 mM **1** under Ar and CO_2 saturation conditions with and without 0.1 M PhOH. Conditions: 0.1 M $TBAPF_6$/DMF; glassy carbon disc working electrode, glassy carbon rod counter electrode, Ag/AgCl pseudoreference electrode; referenced to Fc^+/Fc internal standard; 100 mV/s scan rate.

Variable concentration studies imply a first-order concentration dependence of the catalytic current on **1** and CO_2, which saturates at modest concentrations when independently varied (**Figures S2.13** and **S2.14**, respectively). However, contrary to our previous report with Cr(^{tbu}dhbpy)Cl(H_2O), the catalytic current of the system with **1** is immediately saturated and does not increase with larger [PhOH] (**Figure S2.10**). This observation is distinct compared to the Cr(^{tbu}dhbpy)Cl(H_2O) system because it suggests that C–OH is no longer rate-limiting in the

catalytic mechanism with **1**. Controlled potential electrolysis (CPE) experiments were performed at −2.3 V versus Fc^+/Fc with **1** and 0.6 M PhOH under CO_2 saturation conditions (**Figure S2.16** and **Table S2.3**). These results demonstrated a 93 ± 7% Faradaic efficiency for CO (FE_{CO}) for **1** over 5 turnovers operating at an η of 260 mV with 2.66 ± 0.05% H_2 detected (**Table 2.1**). Note that turnovers have been determined to show the catalytic nature of the process representing two electron equivalents of charge passed for 1 equiv of **1** in solution and do not represent a measurement to complete loss of activity. No liquid products were detected in the post-bulk solution by ^1H NMR. The turnover frequency (TOF_{CPE}) derived from this electrolysis experiment is 1.82 s^{-1}, which is less than the TOF of 4.35 s^{-1} achieved by the bpy-based system during electrolysis.[18, 19] The stability of the current during CPE is indicative of a stable catalytic system, which is supported by characterization of the post-CPE solution by UV–vis spectroscopy (**Figure S2.17**). To assess whether catalytic material had deposited during electrolysis, the working electrode was rinsed and used to perform a control electrolysis in the absence of **1** under otherwise identical conditions; nonquantifiable amounts of CO and significant H_2 were observed (**Figure S2.18** and **Table S2.4**). A control electrolysis experiment with PhOH under CO_2 saturation conditions in the absence of **1** and a freshly polished electrode showed the same product makeup as the rinse test (**Figure S2.19**).

Additionally, a CPE experiment was performed with 2% (v/v) H_2O in DMF as the proton source instead of PhOH (**Figure S2.20** and **Table S2.5**). With H_2O as a proton source in CPE experiments, **1** maintained excellent selectivity for CO, with a FE_{CO} of 93 ± 4% over 8 turnovers with no quantifiable amount of H_2 detected and a TOF of 3.25 s^{-1} at an η of 470 mV (**Table 2.1**). A control electrolysis experiment with 2% H_2O in DMF showed no detectable CO and significant production of H_2 (**Figure S2.21**). Both TOF_{CPE} values are in good agreement with the TOF_{max} values of 4.37 and 13.7 s^{-1} calculated from CV data using the ratio of catalytic to Faradaic current

at scan rates of 100 mV/s using PhOH and H_2O as the proton donor, respectively (**Figures 2.3** and **S2.12**).

Table 2.1. Results from CPE experiments under CO_2 saturation conditions.

Trial	Conditions	Proton Donor	Potential (V vs Fc^+/Fc)	FE_{CO}	FE_{H2}	TOF_{CPE} (s^{-1})	η (V)	TON_{CO}
1	1+CO_2	0.6 M PhOH	−2.3	93 ± 7	2.66 ± 0.05	1.82	0.26	5.4
2	1+CO_2	1.0 M H_2O	−2.3	93 ± 4	–	3.25	0.47	7.5
3	CO_2[a]	0.6 M PhOH	−2.3	–	–	–	n/a	–

[a]Performed with a used working electrode from trial 1 in the absence of the Cr-based precatalyst. Turnovers correspond to moles of electrons passed in coulometry studies divided by two to account for CO formation.

2.4 Mechanistic Insight via Computational (DFT) Analyses

In order to obtain additional insight, the reaction mechanism was interrogated by means of DFT calculations. CV data guided the initial investigation of the successive reduction events that the precatalyst undergoes to form the active species. On the basis of the proposal that solution equilibria involving the chloride ligands exists, five distinct redox events were examined for the overall three-electron reduction of complex **1**. Importantly, a good correlation (R^2 = 0.94) between the experimental redox potentials and computational results was obtained, suggesting that the level of theory was appropriate for modeling of this system (see **Table S2.6** and **Figure S2.22**). Note that, in the shorthand notation used in the ensuing discussion to describe these calculations, the [tpypho]$^-$ ligand has been eliminated for clarity and the other numbers are defined as follows $^{multiplicity}_{\#bound\ DMF}\mathrm{Cr}^{charge}_{\square}$.

Unlike our previous study with the Cr(^{tbu}dhbpy)Cl(H_2O) catalyst,[18, 19] the two-electron-reduced species of Cr(tpy^{tbu}pho)Cl_2 is not reactive toward CO_2. Consistent with experimental observations, it is the third overall reduction event (exp. $E_{1/2}$ = −2.18 V vs Fc^+/Fc) that produces an overall monoanionic species capable of binding and activating CO_2. Therefore, the active species of both catalysts have analogous overall charge (1–) and formal metal oxidation states

(high-spin Cr^{II}), while differing in the number of ligand-centered reduction events (one for ^{tbu}dhbpy and two for tpy^{tbu}pho). In order to experimentally support this assignment, we synthesized a Zn complex in the same ligand framework, [Zn(tpy^{tbu}pho)][OTf] (**Figure S2.25**). The CVs of this Zn complex reveal two quasi-reversible one-electron redox features at slightly more negative potentials than the second and third redox features observed for **1** (**Figure S2.26**). In this potential range, Zn^{II} is expected to remain redox-inert, and therefore the absence of a third reduction feature for the Zn-based control complex is consistent with the proposal that two primarily ligand-based reductions occur during the precatalytic activation of **1**. The negative shift of the redox events for the Zn-based complex relative to **1** can be attributed to the absence of electronic coupling between the ligand and the d^{10} Zn^{II} center, in comparison to the high-spin d^4 Cr^{II} center.

As a consequence of this increased ligand-based redox activity, the overall spin manifold is necessarily different between the tpy- and bpy-based complexes: while *S* = 3/2 was found to be the preferential configuration for $[Cr^{II}(^{tbu}dhbpy^{\bullet})]^{-}$, the lowest-energy spin configuration for the active species for $[Cr^{II}(tpy^{tbu}pho^{2\bullet})]^{-}$ was an overall triplet (*S* = 1), with a terpyridine triplet diradical antiferromagnetically coupled to a high-spin Cr^{II} center (**Figures 2.4A** and **S2.23A**). This finding is in good agreement with previous studies of terpyridine-containing electrocatalysts.[23, 24] Notably, the pentacoordinate solvent adduct ${}^{3}_{1}\mathbf{Cr}^{-1}_{\square}$ and tetracoordinate species ${}^{3}_{0}\mathbf{Cr}^{-1}_{\square}$ of the tpy-based catalyst are almost equally stable (ΔG = 0.2 kcal/mol), the former being the lowest-energy configuration. Quintet (${}^{5}_{0}\mathbf{Cr}^{-1}_{\square}$) and septet (${}^{7}_{0}\mathbf{Cr}^{-1}_{\square}$) configurations were found at 3.0 and 6.8 kcal/mol above ${}^{3}_{1}\mathbf{Cr}^{-1}_{\square}$, respectively.

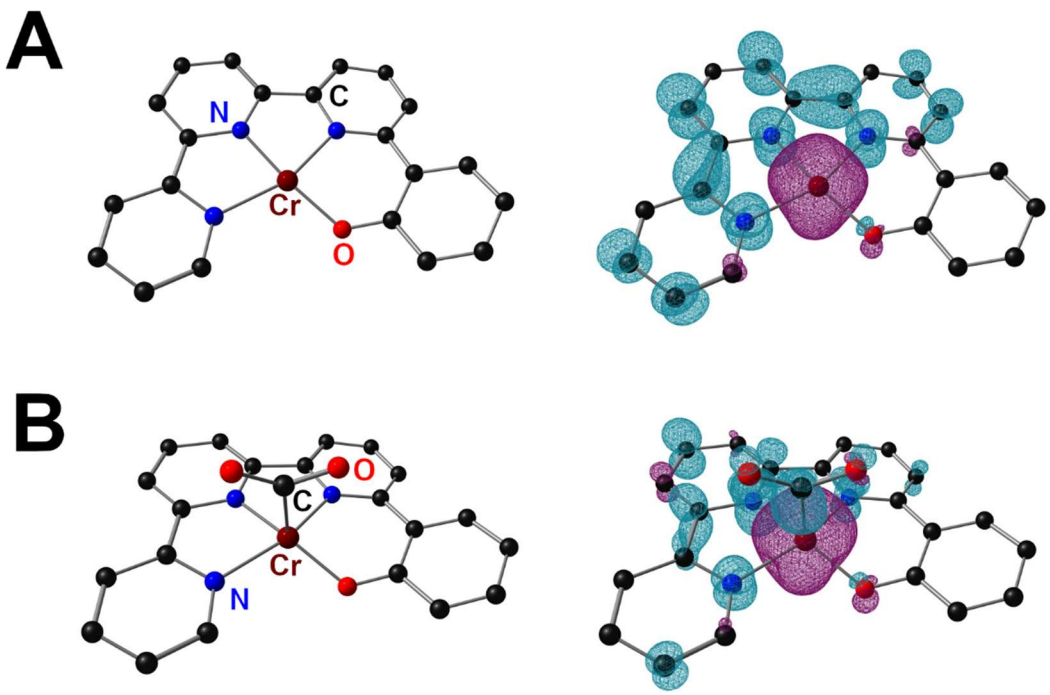

Figure 2.4. Molecular geometry and spin density plots of ${}^{3}_{0}\mathbf{Cr}^{-1}_{\square}$ (**A**) and ${}^{3}_{0}\mathbf{Cr(CO_2)}^{-1}_{\square}$ (**B**). For clarity, tbu groups and H atoms have been omitted.

From ${}^{3}_{1}\mathbf{Cr}^{-1}_{\square}$, the lowest-energy configuration for the transition state to bind CO_2 (no axial DMF; **Figures S2.23** and **S2.24**) and the corresponding adduct (**Figure 2.4B** and **S23B**) were located in the *S* = 1 surface. The barrier for this catalyst was found to be higher (${}^{3}_{0}\mathbf{TS1}^{-1}_{\square}$, +12.2 kcal/mol; **Figure 2.5**) than that located for CO_2 binding for the dhbpy counterpart (+10.0 kcal/mol). Interestingly, ${}^{3}_{0}\mathbf{TS1}^{-1}_{\square}$ presents a Cr−C bond distance of 2.35 Å, much shorter than the 2.64 Å found for the corresponding TS of the dhbpy system. This can be rationalized by analyzing the electronic structure of these species: for the dhbpy catalyst system, one of the two electrons that form the Cr−C bond is highly delocalized in a bpy-centered, metal-mixed π* orbital in the transition state geometry (see reference 19), conversely, for ${}^{3}_{0}\mathbf{TS1}^{-1}_{\square}$, both electrons have predominantly Cr−C σ-bond character (**Figure S2.24**). Furthermore, for the terpyridine-based catalyst, CO_2 binding is exergonic (${}^{3}_{0}\mathbf{Cr(CO_2)}^{-1}_{\square}$, −1.9 kcal/mol), in stark contrast to the endergonic binding

calculated previously for the dhbpy system (+4.7 kcal/mol; **Figure S2.27**) and in good agreement with the CV data for both systems. The electronic structure of the CO_2 adduct confirms partial charge transfer from the reduced ligand: $^{3}_{0}\mathbf{Cr(CO_2)}^{-1}_{\square}$ presents a singly reduced tpy fragment (**Figure 2.4B**). The barrier for the thermodynamically favorable (−15.8 kcal/mol) formation of a metal hydride was located at +20.7 kcal/mol above $^{3}_{1}\mathbf{Cr}^{-1}_{\square}$, in agreement with the observed nearly quantitative kinetic selectivity for CO (**Figure S2.27**).

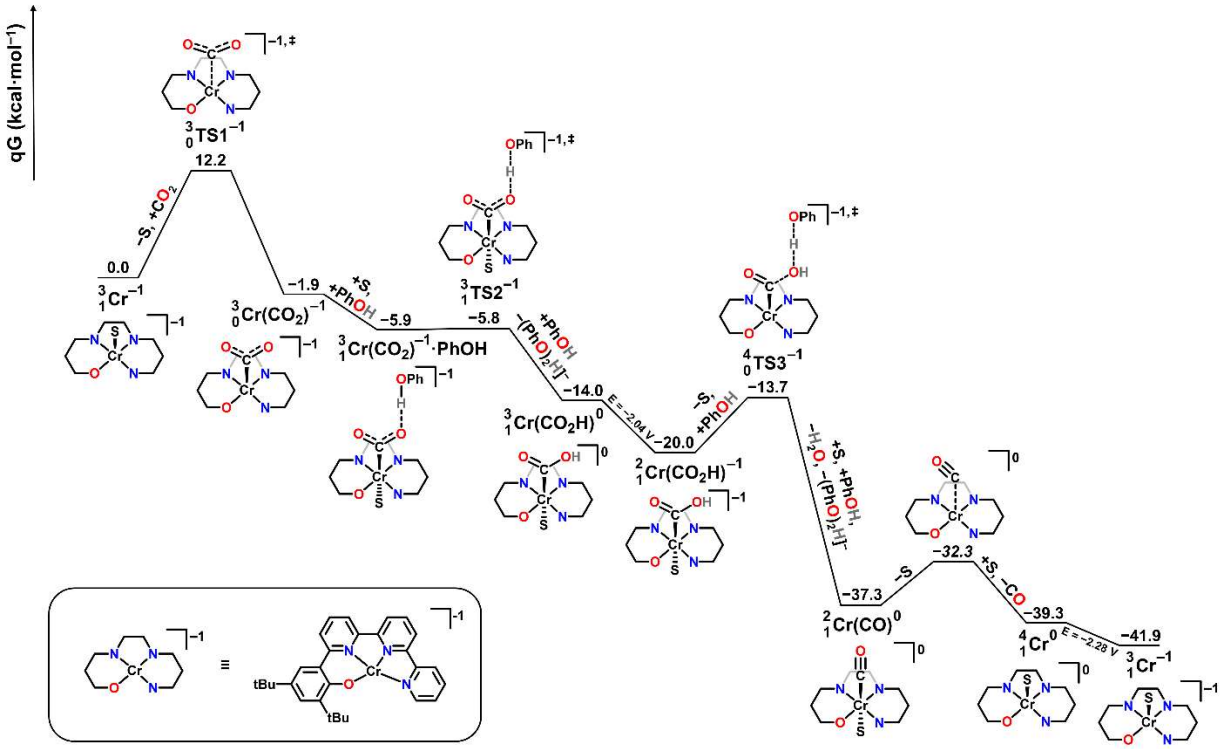

Figure 2.5. Free energy profile of the electrocatalytic CO_2RR cycle for **1**. Precatalyst reduction steps are omitted for clarity. S indicates a solvent adduct of DMF; the procedure for the estimation of the barrier for CO release is described in the SI.

PhOH favorably binds to $^{3}_{0}\mathbf{Cr(CO_2)}^{-1}_{\square}$ to give $^{3}_{1}\mathbf{Cr(CO_2)\cdot PhOH}^{-1}_{\square}$ at −5.9 kcal/mol relative to $^{3}_{1}\mathbf{Cr}^{-1}_{\square}$, from which proton transfer has a barrier of only 0.1 kcal/mol ($^{3}_{1}\mathbf{TS2}^{-1}_{\square}$; **Figure 2.6A**) and is thermodynamically favorable by 12.1 kcal/mol relative to $^{3}_{0}\mathbf{Cr(CO_2)}^{-1}_{\square}$ (PhOH homoconjugation in DMF and DMF binding to the product were taken into account[19, 29]). The

calculated reduction potential for the neutral six-coordinate hydroxycarbonyl complex $^{3}_{1}$**Cr(CO$_2$H)**$^{0}_{\square}$ is −2.12 V, leading to the doublet species $^{2}_{1}$**Cr(CO$_2$H)**$^{-1}_{\square}$ at potentials below the experimentally observed $E_{cat/2}$. The electronic structure of $^{2}_{1}$**Cr(CO$_2$H)**$^{-1}_{\square}$ is comprised of a doubly reduced, triplet diradical terpyridine and a high-spin Cr^{III} center (**Figure S2.28**). Hydrogen bonding of PhOH to $^{2}_{1}$**Cr(CO$_2$H)**$^{-1}_{\square}$ to form $^{2}_{1}$**Cr(CO$_2$H)·PhOH**$^{-1}_{\square}$ is slightly uphill (+2.3 kcal/mol). Importantly, the quartet configuration of the PhOH adduct, $^{4}_{0}$**Cr(CO$_2$H)·PhOH**$^{-1}_{\square}$, becomes isoenergetic (just 0.2 kcal/mol above $^{2}_{1}$**Cr(CO$_2$H)·PhOH**$^{-1}_{\square}$) upon DMF release, giving access to the lowest-energy C−OH bond cleavage transition state for this system ($^{4}_{0}$**TS3**$^{-1}_{\square}$; **Figure 2.6B**) at only +6.3 kcal/mol above $^{2}_{1}$**Cr(CO$_2$H)**$^{-1}_{\square}$ and free PhOH (**Figure 2.5**). By comparison the transition state for the doublet solvento species $^{2}_{1}$**TS3**$^{-1}_{\square}$ lies higher in energy at +10.6 kcal/mol above $^{2}_{1}$**Cr(CO$_2$H)**$^{-1}_{\square}$ and free PhOH. C–OH bond cleavage therefore is both thermodynamically favorable (−17.4 kcal/mol) and does not appear to be rate-limiting. Notably, this reaction barrier is much lower than the corresponding C−OH bond cleavage in the dhbpy system (+10.4 kcal/mol).

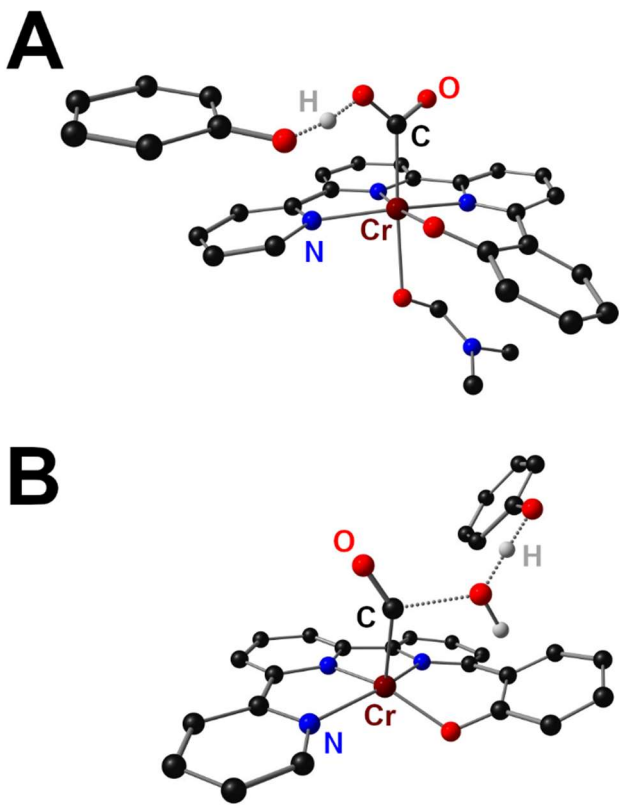

Figure 2.6. Molecular geometries of ${}^{3}_{1}$**TS2**$^{-1}_{\square}$ (**A**) and ${}^{4}_{0}$**TS3**$^{-1}_{\square}$ (**B**). For clarity, tbu groups and H atoms have been omitted.

The lowest-energy spin configuration of the metal carbonyl formed from C–OH bond cleavage is the doublet (${}^{2}_{1}$**Cr(CO)**$^{0}_{\square}$), arising from antiferromagnetically coupled electrons delocalized through the terpyridine backbone and Cr−CO bond (**Figure S2.29**), from which we propose that CO dissociation is facile and irreversible (**Figure S2.30**).[18, 19, 30, 31] It is worth noting that while doublet spin configurations are preferred for the reactants and products of the C–OH bond cleavage step, the lowest-energy transition state is a quartet. The spin change that occurs in the isoenergetic dissociation (+0.2 kcal/mol) of DMF from ${}^{2}_{1}$**Cr(CO$_2$H)·PhOH**$^{-1}_{\square}$ to generate the five-coordinate ${}^{4}_{0}$**Cr(CO$_2$H)·PhOH**$^{-1}_{\square}$ reflects the transfer of an electron from a primarily ligand-centered orbital to a molecular orbital that is distributed between the Cr and tpy fragments (compare **Figures S2.31** and **S2.32**). In the corresponding transition states for each spin

manifold, antibonding character builds up in the C–OH bond in $^{4}_{0}$**TS3**$^{-1}_{\square}$ (**Figure S2.33**), while the comparable frontier orbitals of $^{2}_{1}$**TS3**$^{-1}_{\square}$ show significant π bonding between Cr and C (**Figure S2.34**), reminiscent of the nascent carbonyl group. In other words, solvent dissociation allows electron transfer from tpy to the Cr orbitals relevant to bond cleavage, manifesting in a lower-energy pathway as these orbitals become more reactive. While this electron transfer does not manifest in a formal shift from a $Cr^{III}(tpy^{2\bullet-})$ configuration to $Cr^{II}(tpy^{\bullet-})$, it can be thought of as an intermediate scenario along this continuum.Alternate spin manifolds were considered for all intermediates and transition states but were found to be higher in energy. The relative energetic positioning of possible spin manifolds in the catalytic cycle also showed good agreement between the hybrid B3LYP functional[32-35] and the meta-GGA revised TPSS functional,[36, 37] indicating that method was appropriate for these assignments (**Table S2.7**).[38]

2.5 Discussion

It is striking that the tpy-based Cr complex **1** largely achieves comparable activity and selectivity at overpotentials similar to those of the bpy-based catalyst that we have reported previously. Unlike the bpy-based catalyst, however, complex **1** binds CO_2 in the absence of a proton donor (**Figure 2.3**, red). Computational studies relevant to CO_2 binding suggest that, in comparison to the bpy-based complex,[18, 19] at the TS geometry the electrons forming the incipient Cr–C bond are relatively more localized on the metal and σ-based, which could contribute to the relatively heightened barrier for **1** in comparison to the bpy-based complex. Indeed, this is consistent with the need for charge reorganization from the doubly reduced tpy fragment to Cr being a key component. The formation of the CO_2 adduct $[Cr(tpy^{tbu}pho^{\bullet})(\eta^1\text{-}CO_2)]^-$ is also significantly exergonic, in contrast to the endergonic formation of $[Cr(^{tbu}dhbpy)(\eta^1\text{-}CO_2)]^-$.[18, 19] This trend is consistent with differences in the operating potential: the catalytically relevant reduction

potential of complex **1** ($E_{1/2}$ = −2.18 V) is 0.23 V more negative than the bpy-based complex ($E_{1/2}$ = −1.95 V).

Facile access to the σ-basic character at Cr makes $[Cr^{II}(tpy^{tbu}pho^{2\bullet})(DMF)]^{-}$ more adept at interacting with the added proton donor PhOH than $[Cr^{II}(^{tbu}dhbpy^{\bullet})]^{-}$, which presents relatively more π-basic character. In CV studies with added PhOH under Ar saturation (**Figure 2.3**, green), a loss of reversibility occurs at the third reduction, consistent with an interaction between the Cr center and proton donor. Conversely, the bpy-based Cr catalyst exhibited no comparable activity with added PhOH.[18, 19] DFT calculations show that the difference in the transition state energy (ΔTS) between the barrier for protonation and CO_2 binding narrows across these two catalysts (ΔTS is 8.5 kcal/mol for $[Cr^{II}(tpy^{tbu}pho^{2\bullet})(DMF)]^{-}$, versus 20.2 kcal/mol for $[Cr^{II}(^{tbu}dhbpy^{\bullet})]^{-}$;[19] **Figure S2.27**), consistent with the experimentally observed reactivity trends. Further, hydride formation from $[Cr^{II}(^{tbu}dhbpy^{\bullet})]^{-}$ is exergonic (−7.2 kcal/mol), whereas comparable hydride formation from $[Cr^{II}(tpy^{tbu}pho^{2\bullet})(DMF)]^{-}$ is even more thermodynamically favored, –15.8 kcal/mol. The difference is apparent under electrocatalytic conditions: **1** produces minor amounts of H_2 (**Table 2.1**).

An additional consequence of the more negative potentials required for CO_2 binding by **1** appears to be relatively lower barriers for protonation to generate and protonate a hydroxycarbonyl intermediate (Cr–CO_2H) than those for the bpy-based analogue. Experimentally, saturation of the electrocatalytic current with an added proton donor occurs at low concentrations for **1**, whereas a kinetic rate dependence was previously assessed for the bpy-based analogue. Computations again reflect these reactivity trends, suggesting that CO_2 binding is the rate-determining step for complex **1**, as opposed to the bpy-based catalyst, where C–OH bond cleavage was determined to be the rate-determining step.

Formation of a second key diradical state in the reduced ligand occurs again in $[Cr^{II}(tpy^{tbu}pho^{2\bullet})(\eta^1\text{-}CO_2H)]^{-}$ (S = 3/2), which precedes C–OH bond cleavage. During formation of

the Cr carbonyl and H_2O coproducts, one of these ligand-based unpaired electrons is transferred to the π-back-bonding scaffold of the forming CO ligand. For $[Cr^{II}(^{tbu}dhbpy^{\bullet})(\eta^1\text{-}CO_2H)]^-$ (S = 1), a similar reaction pathway occurs; however, the barrier is relatively more significant and defines the rate of the process.[18, 19] It is noteworthy that the increased redox activity of tpy assists in diminishing the barrier of this chemical reaction step, because two charge equivalents are coupled to Cr and available for transfer rather than one. Although excellent agreement between the theory and experiment have been achieved here, we encourage the use of higher levels of theory for obtaining *a priori* predictive insight into the electronic structure of metal complexes whose spin manifolds might contain strongly coupled ligand and metal components to better assess the possibility of multiconfigurational active spaces.[39]

2.6 Conclusions

We report a new Cr-based electrocatalyst for the reduction of CO_2 to CO. Selective and stable Cr-based catalysts are underrepresented for the CO_2RR.[4-6] Indeed, there are limited overall examples of the Cr/Mo/W triad showing either electrochemical or electrocatalytic activity.[10-17] By expansion of the polypyridyl core of the ligand, the ligand must be reduced twice to initiate the catalytic cycle, producing an active state that is best described as $[Cr^{II}(tpy^{tbu}pho^{2\bullet})]^-$ (S = 1). The formation of a ligand-based diradical occurs again later in the catalytic cycle, when the intermediate prior to C–OH bond cleavage, $^{2}_{1}\mathbf{Cr(CO_2H)}^{-1}$, is generated, demonstrating that coupling between the tpy-based ligand and Cr center alters the rate-determining step of the catalytic cycle. These results suggest that the ligand design principles used to develop selective, active, and stable late-transition-metal catalysts for the CO_2RR can be applied to metals much earlier in the transition-metal series to create new categories of carbonyl ligand-free catalysts.

2.7 Supplementary Information

2.7.1 Materials and Methods

General

All chemicals and solvents (ACS or HPLC grade) were commercially available and used as received unless otherwise indicated. For all air-sensitive reactions and electrochemical experiments, HPLC-grade solvents were obtained as anhydrous and air-free from a PPT Glass Contour Solvent Purification System. Gas cylinders were obtained from Praxair (Ar as 5.0; O_2 as 4.0) and passed through activated molecular sieves prior to use. Gas mixing for variable concentration experiments was accomplished using a gas proportioning rotameter from Omega Engineering. UV-vis absorbance spectra were obtained on a Cary 60 from Agilent. An Anton-Parr Multiwave Pro SOLV, NXF-8 microwave reactor was used for microwave syntheses.

Electrochemistry

All electroanalytical experiments were performed using a Metrohm Autolab PGSTAT302N potentiostat. Glassy carbon working (⌀ = 3 mm) and non-aqueous silver/silver chloride pseudoreference electrodes behind PTFE tips were obtained from CH Instruments. The pseudoreference electrodes were obtained by depositing chloride on bare silver wire in 10% HCl at oxidizing potentials and stored in a 0.1 M tetrabutylammonium hexafluorophosphate/*N*,*N*-dimethylformamide ($TBAPF_6$/DMF) solution in the dark prior to use. The counter electrode was a glassy carbon rod (⌀ = 3 mm). All CV experiments were performed in a modified scintillation vial (20 mL volume) as a single-chamber cell with a cap modified with ports for all electrodes and a sparging needle. $TBAPF_6$ was purified by recrystallization from ethanol and dried in a vacuum oven before being stored in a desiccator. All data were referenced to an internal ferrocene standard (ferricenium/ferrocene reduction potential under stated conditions) unless otherwise specified. All voltammograms were corrected for internal resistance and obtained at scan rates of 100 mV/s unless otherwise specified. Ferrocene was purified by sublimation prior to use.

Controlled Potential Electrolysis (CPE)

Bulk electrolysis experiments were performed in a glass Pine H-cell with two compartments separated by a glass frit. A 60 mL stock solution of DMF with 0.1 M $TBAPF_6$ was prepared for each bulk electrolysis experiment. Approximately 26 mL of the stock solution was added to each half of the H-cell. One side of the H-cell contained the $Cr(tpy^{tbu}pho)Cl_2$ **1** catalyst, any additional substrate, such as PhOH or H_2O, and a glassy carbon or graphite rod working electrode. The other side of the H-cell contained approximately 0.075 M ferrocene as a sacrificial reductant along with a graphite rod counter electrode and a Ag/AgCl pseudoreference electrode. The electrolysis experiment was referenced by taking a CV of the side of the H-cell that contained the ferrocene solution. The H-cell was sealed with two septa that were connected by a piece of PTFE tubing which aided to maintain equal pressure between each half of the cell during the electrolysis. Before starting the electrolysis experiment, both sides of the H-cell were sparged with the desired gas for 20 minutes and the sealed cell was allowed to equilibrate for 1 hour. The resistance between the two halves of the H-cell was measured using the i-interrupt procedure available in the NOVA software provided by Metrohm. The electrolysis with **1** and PhOH was kept in the dark while potential was applied and during all product analysis.

CPE Product Analysis

During bulk electrolysis experiments, either 150 or 250 µL GC injections of the headspace were periodically taken for the detection and quantification of any gaseous products produced. After each bulk electrolysis experiment, the total volume of solution was measured. The total volume of the sealed H-cell was also measured to account for the total headspace volume for accurate quantification of gaseous products. A calibration curve for CO and H_2 was used to quantify gaseous products produced during electrolysis experiments in the same manner as we previously reported.[18]

Analysis of gas phase products was done by sampling electrolysis headspace through syringe injections into an Agilent 7890B GC equipped with a specialty gas split column 5 Å mol sieve/Porabond Q column (15 m length; 0.320 mm diameter; 25.0 μm film) and thermal conductivity detector with He as a carrier gas. A calibration curve for CO and H_2 was made in the H-cell with an experimental setup containing identical volumes of 0.1 M $TBAPF_6$ in DMF to those used during electrolysis. Known volumes of CO and H_2 were injected into the cell with stirring and 250 μL injections of the headspace were taken for GC injections after equilibration. The limit of detection (LOD) and limit of quantitation (LOQ) for CO and H_2 in the GC were determined from seven consecutive injections at the lowest observable concentrations of each gaseous product respectively. For CO, the LOD was determined to be 5.77 x 10^{-7} moles and the LOQ was determined to be 1.92 x 10^{-6} moles. For H_2, the LOD was determined to be 4.55 x 10^{-6} moles and the LOQ was determined to be 1.52 x 10^{-5} moles.

Calculation of Overpotential

PhOH Conditions

The calculation of overpotential for Cr(tpy^{tbu}pho)Cl_2 **1** was performed according to reported methods.[40] The following equation was used for the determination of the reaction standard potential in V with respect to the Fc^+/Fc couple:

$$E_{CO_2/CO} = -0.73\,V - 0.059(pK_a) \qquad \textbf{Eq (S2.1)}$$

The pK_a for PhOH in DMF is reported as 18.8[41]:

$$E_{CO_2/CO}(PhOH) = -1.84\,V\ vs\ Fc^+/Fc \qquad \textbf{Eq (S2.2)}$$

The $E_{cat/2}$ determined experimentally for Cr(tpy^{tbu}pho)Cl_2 **1** is –2.10 V vs Fc^+/Fc for protic CO_2 reduction (1.0 mM Cr(tpy^{tbu}pho)Cl_2 **1** and 37 mM PhOH under CO_2 saturation); the overpotential is:

$$\eta = \left|E_{cat/2} - E_{CO_2/CO}\right| = 260\,mV \qquad \textbf{Eq (S2.3)}$$

This assumes no contribution from homoconjugation of the acid. We note that the homoconjugation constant (HA_2^-) for PhOH in DMF has been reported as $\log(K_{HA_2^-})$ = 3.8.[29] Therefore, we emphasize that the described overpotential calculated above for PhOH is the lower-limit approximation, as homoconjugation is expected to alter the effective overpotential. The overpotential equation can be modified to account for homoconjugation:

$$E_{CO_2/CO} = -0.73\,V - 0.059(pK_a) - \frac{-2.303RT}{nF}\log\,(mK_{HA_2^-}) \qquad \textbf{Eq (S2.4)}$$

Where n = number of electrons (2) and m = number of proton transfers (2). The modified equation provides a value of $E^0_{CO_2/CO}$ = –1.72 V and η = 380 mV. This value does not account for the possible thermodynamic contributions of the water coordinated to the pre-catalyst, the equimolar quantities of water produced for each equivalent of CO generated, or any adventitious H_2O present in the CO_2, solvent, or electrolyte. Under CO_2 saturation, any water present can form carbonic acid, pK_a(DMF) 7.37,[42] and generate new equilibria involving CO_2 and bicarbonate. The role of carbonic acid (and the general hydration of CO_2 in non-aqueous solvent systems) in altering the overall thermodynamics combined with the effects of homoconjugation has been assessed by Matsubara.[43] Considering the role of water, Matsubara obtained a standard potential for CO_2 reduction to CO of –1.70 V versus Fc^+/Fc for PhOH in DMF with 10 mM water present (see below). Note the same value is obtained considering 10 mM water only.

For 10 mM H_2O in DMF, where AH = PhOH:[43]

$$3CO_{2(g)} + H_2O_{(sol,x)} + 2e^- \rightleftharpoons CO_{(g)} + 2HCO_{3\,(sol)}^- \qquad E^0 = -1.70\,V\ vs.\,Fc^+/Fc$$

$$CO_{2(g)} + 2AH_{(sol)} + 2e^- \rightleftharpoons CO_{(g)} + 2A^-_{(sol)} + H_2O_{(sol,x)} \qquad E^0 = -1.96\,V\ vs.\,Fc^+/Fc$$

$$CO_{2(g)} + 4AH_{(sol)} + 2e^- \rightleftharpoons CO_{(g)} + 2HA_{2\,(sol)}^- + H_2O_{(sol,x)} \qquad E^0 = -1.70\,V\ vs.\,Fc^+/Fc$$

<u>2% H_2O Conditions</u>

Matsubara has also assessed the standard potential for CO_2 reduction to CO in DMF under various concentrations of H_2O.[43] The reported value of $E^0_{CO2/CO}$ (2% H_2O) is –1.64 V vs. Fc^+/Fc

and the $E_{cat/2}$ determined experimentally for Cr(tpy^{tbu}pho)Cl_2 **1** is –2.10 V vs Fc^+/Fc for protic CO_2 reduction (1.0 mM Cr(tpy^{tbu}pho)Cl_2 **1** and 2%H_2O under CO_2 saturation); the overpotential is:

$$\eta = \left|E_{cat/2} - E_{CO_2/CO}\right| = 470\ mV \qquad \textbf{Eq (S2.5)}$$

Computational Methods

DFT calculations were performed on the Rivanna High-Performance Computing Cluster at the University of Virginia using the Gaussian 16 program, Rev B.01.[44] The hybrid functional B3LYP[32-35] and the def2-SVP basis set for all atoms[45, 46] were used for all calculations. Energies were refined by means of single point calculations with the larger def2-TZVP basis set. Unrestricted geometry optimizations were carried out without geometry constraints and dispersion effects were accounted for by using Grimme's D3 parameter set with Becke-Johnson (BJ) damping.[47] Bulk solvent effects (*N*,*N*-dimethylformamide = DMF) were included at the optimization stage with the CPCM model.[48, 49] The stationary points and their nature as minima or saddle points (TS) were characterized by vibrational analysis, which also produced enthalpy (H), entropy (S) and Gibbs energy (G) data at 298.15 K. The minima connected by a given transition state were determined by Intrinsic Reaction Coordinate (IRC) calculations or by perturbing the transition states along the TS coordinate and optimizing to the nearest minimum. Free energies were corrected to account for concentration effects and for errors associated with the harmonic oscillator approximation. Thus, according to Truhlars's quasi-harmonic approximation, all vibrational frequencies below 100 cm^{-1} were set to this value.[50] All anharmonic and concentration corrections were calculated with the Goodvibes 3.0.1 code[51]; the entropic quasi-harmonic treatment used a mixture of RRHO and Free-rotor vibrational entropies[52] and the enthalpic quasi-harmonic treatment used the RRHO treatment with an approximation term for vibrational energy.[53] The concentration corrections for all species under representative catalytic conditions were set to 1 mM, with the following exceptions: [PhOH] = 0.1 M; [CO_2] = 0.23 M; [DMF] = 12.97 M. Kohn-Sham orbital projections and spin densities were plotted with isovalues of 0.045 and 0.005, respectively. The energetic

ordering of the spin manifold predicted by the hybrid B3LYP functional was checked[38] by using single-point calculations with the meta-GGA revised TPSS functional[36, 37] with single point calculations using def2-TZVP basis set.

Determination of TOF from Preparative ElectrolysisThe integrated expression of current for a homogeneous electrocatalytic response (considering an application of steady-state conditions to the substrate) has been solved previously.[54, 55]

$$\frac{i}{FA} = \frac{n_{cat}^{\sigma}[cat]\sqrt{(k_{obs}D_{cat})}}{1 + \exp\left[\frac{F}{RT}\left(E_{app} - E_{1/2}\right)\right]}$$

where

$$k_{obs} = k_{cat}[CO_2]$$

where i is the average current (Amps) specific to the reaction product of interest, F is Faraday's constant (96485 C mol^{-1}), A is the area of the electrode (cm^2), n_{cat}^{σ} is the number of electrons in the catalytic process (2) with σ = 1 under the assumption that all electrons are delivered to the catalyst by the electrode, $[cat]$ is the concentration of the catalyst (mol cm^{-3}), k_{obs} is the apparent turnover frequency (s^{-1}), $[CO_2]$ is the concentration of CO_2 saturated in DMF (mol cm^{-3}), D_{cat} is the diffusion coefficient of the catalyst (cm^2 s^{-1}), R is the ideal gas constant (Joule mol^{-1} K^{-1}), T is the temperature (K), E_{app} is the applied potential during preparative electrolysis (V), and $E_{1/2}$ is the standard potential of the catalyst (V).

and

$$\frac{i}{A} = J = CO\ specific\ current\ density$$

Substituting and rearranging the first expression to solve for k_{obs}

$$k_{obs} = \frac{J^2\left(1 + \exp\left[\frac{F}{RT}\left(E_{app} - E_{1/2}\right)\right]\right)^2}{F^2(n_{cat}^{\sigma}[cat])^2 D_{cat}}$$

with k_{obs} in hand, the TOF can be expressed for a given potential according to the following relationship

$$TOF = \frac{k_{obs}}{1 + \exp\left[\frac{F}{RT}\left(E_{app} - E_{1/2}\right)\right]}$$

Parameters for electrocatalysis mediated by Cr(tpy^{tbu}pho)Cl_2 **1** in DMF under CO_2 saturation not found in **Table 2.1**:

- $E_{1/2}$ catalyst: −2.18 V vs Fc^+/Fc
- Temperature: 298.15 K
- $[CO_2]$: 2.3 x 10^{-4} mol cm^{-3}
- Diffusion coefficient: 3.89 x 10^{-6} cm^2 s^{-1}
- Electrode area: 2.61 cm^2 (experiment with PhOH) or 3.66 cm^2 (experiment with H_2O)

Determination of TOF_{max} from Cyclic VoltammetryThe expression for TOF_{max} for a homogeneous electrocatalytic response (considering an application of steady-state conditions to the substrate) has been solved previously.[18, 56]

$$TOF_{max} = 0.1992\frac{n_p^3}{n_{cat}^2}\frac{Fv}{RT}\left(\frac{i_{cat}}{i_p}\right)^2$$

Where n_p is the number of electrons transferred under faradaic conditions, n_{cat} is the number of electrons transferred under catalytic conditions, R is the ideal gas constant, F is Faraday's constant, *v* is the scan rate, T is temperature, i_{cat} is the catalytic current, and i_p is the Faradaic current.

Synthesis of 2-([2,2':6',2''-terpyridin]-6-yl)-4,6-di-tert-butylphenol, tpy^{tbu}pho(H)

The preparation of 6-bromo-2,2':6',2''-terpyridine was carried out as previously reported.[28] The (3,5-di-*tert*-butyl-2-hydroxy-phenyl)boronic acid was prepared as we have previously reported.[57] Subsequent microwave assisted Suzuki-type cross coupling of 6-bromo-2,2':6',2''-terpyridine with (3,5-di-*tert*-butyl-2-hydroxy-phenyl)boronic acid was done in an analogous fashion to our previous establish synthetic method.[18] To a single microwave tube was added 6-bromo-2,2':6',2''-terpyridine (1.50 g, 0.481 mmol), sodium carbonate (3.50 g, 4.19 mmol), $Pd(PPh_3)_4$ (100 mg, 0.0086 mmol), (3,5-di-*tert*-butyl-2-hydroxy-phenyl)boronic acid (2.16 g, 0.865 mmol), degassed toluene (50 mL), degassed DI water (10 mL), and degassed methanol (12 mL). The microwave was set to run for 120 minutes at 170 ºC at the highest ramp rate. After the reaction, the aqueous and organic layers were separated. The aqueous layer was washed with dichloromethane (DCM) (2x50mL) and the organic layer was washed with brine (3x50 mL). The organic layers were combined, dried over $MgSO_4$, and condensed to dryness. Addition of 50 mL of methanol induced precipitation of the tpytbupho(H) ligand as a light-yellow solid which was collected via vacuum filtration. 94% isolated yield (1.98 g). ^{1}H NMR (d_2-CD_2Cl_2, 600 MHz): δ 15.20 (s, 1H, O*H*), 8.79 (m, 1H, Ar*H*), 8.70 (m, 1H, Ar*H*), 8.54 (m, 1H, Ar*H*), 8.38 (m, 1H, Ar*H*), 8.20 (m, 1H, Ar*H*), 8.05 and 8.03 (m, 3H, Ar*H*), 7.91(m, 1H, Ar*H*), 7.77 (d, 1H, Ar*H*), 7.46 (d, 1H, Ar*H*), 7.37 (m, 1H, Ar*H*), 1.56 (s, 9H, -C(CH_3)$_3$), 1.40 (s, 9H, -C(CH_3)$_3$), ^{13}C{^{1}H} (d_2-CD_2Cl_2, 600 MHz) NMR δ 158.94 (Ar*C*), 157.38 (Ar*C*), 156.45 (Ar*C*), 156.26 (Ar*C*), 154.00 (Ar*C*), 152.95 (Ar*C*), 149.57 (Ar*C*), 140.37 (Ar*C*), 139.07 (Ar*C*), 138.68 (Ar*C*), 137.95 (Ar*C*), 137.33 (Ar*C*), 126.76 (Ar*C*), 124.43 (Ar*C*), 121.61 (Ar*C*), 121.48 (Ar*C*), 120.95 (Ar*C*), 120.23 (Ar*C*), 119.13 (Ar*C*), 118.26 (Ar*C*), 110.46 (Ar*C*), 35.70 (tbu*C*), 34.71 (tbu*C*), 31.79 (tbu*C*), 29.80 (tbu*C*). Elemental analysis for $C_{38}H_{48}N_2O_2$: calc'd: C: 79.60, H: 7.14 N: 9.60 found: C: 79.71 H: 7.30 N: 9.44. MSMS (m/z): calc'd: 438.2534 found: 238.2551

Synthesis of Cr(tpy^{tbu}pho)Cl$_2$ (1)

Metalation of tpy^{tbu}pho(H) with Cr(III) to generate Cr(tpy^{tbu}pho)Cl$_2$ **1** was achieved by stirring tpy^{tbu}pho(H) (0.250 g, 0.571 mmol) with 1.05 equivalents of chromium(II) dichloride (0.0737 g, 0.600 mmol) in tetrahydrofuran (150 mL) under an inert atmosphere overnight. Following exposure to air, the reaction mixture was filtered to collect the precipitate. The precipitate was washed with saturated aqueous ammonium chloride (25 mL). The solid was then dissolved in DCM and filtered through a PTFE syringe filter to remove any residual ammonium chloride. The solution was then condensed down. Then 20 mL of pentanes was added with sonication to collect the product as a dark red crystalline solid via vacuum filtration. 42.2% isolated yield (135 mg). Elemental analysis for $C_{29}H_{30}Cl_2CrN_3O_1$ calc'd: C 62.26, H 5.41, N 7.51; found: C 62.41, H 5.23, N 7.42. MSMS (m/z): calc'd: 505.1821 found: 505.1821. Note MS results align with data in the absence of the chloride anions and in the presence of one bound hydroxy ligand. λ_{max}: 243 nm (ε = 12900 M^{-1} cm^{-1}), 282 nm (ε = 8390 M^{-1} cm^{-1}), 350 nm (ε = 3700 M^{-1} cm^{-1}), 428 nm (ε = 1400 M^{-1} cm^{-1}).

Synthesis of [Zn(tpy^{tbu}pho)][OTf]

Metalation of tpy^{tbu}pho(H) with Zn(II) to generate [Zn(tpy^{tbu}pho)][OTf] was achieved by stirring tpy^{tbu}pho(H) (0.0490 g, 0.112 mmol) with 1.1 equivalents zinc(II) triflate (0.0448 g, 0.123 mmol) in acetonitrile at room temperature under an inert atmosphere for 24 hours. Following exposure to air, the acetonitrile was removed via reduced pressure and the solid was recrystallized with minimal acetonitrile and diethyl ether. Then, the solid was collected via filtration and dissolved in DCM and filtered through a PTFE syringe filter to remove residual Zn salt. The solution was condensed to dryness to obtain a light-yellow solid. 52% isolated yield (38 mg). Elemental analysis for $C_{30}H_{30}F_3N_3O_4SZn\cdot[CH_2Cl_2]_{1.5}$ calc'd: C 48.60, H 4.27, N 5.40; found: C 48.90, H 4.12, N 5.53. ^{1}H NMR (d_2-CD_2Cl_2, 600 MHz): δ 8.79 (d, 1H, Ar*H*), 8.39 (m, 2H, Ar*H*), 8.34 (m, 2H, Ar*H*), 8.33 (m, 2H, Ar*H*), 8.22 (m, 1H, Ar*H*), 7.93 (m, 1H, Ar*H*), 7.64 (m, 1H, Ar*H*), 7.50 (m, 1H, Ar*H*), 1.57 (s, 9H, -C(CH_3)$_3$), 1.39 (s, 9H, -C(CH_3)$_3$).

Evans' Method Characterization of 1

The spin state of the Cr(tpy^{tbu}pho)Cl_2 (**1**) catalyst was characterized as a Cr(III) species via Evans' Method.[58, 59] Three capillary inserts were made with a 50% v/v mixture of DMF and DMF-d_7. Each insert was flame sealed, and then placed in an NMR tube. Then 5.9 mg of **1** was dissolved in 2.5 mL of DMF. Approximately 0.6 mL of the solution of **1** was added to each of the three NMR tubes containing a flame sealed insert. ^{1}H NMR spectra with 64 scans were then taken using a 600 MHz Varian NMR Spectrometer. The results of this experiment, which was run in triplicate, can be seen in **Table S2.1**. The average μ_{eff} of **1** was 3.89±0.03.

X-ray Crystallography

A single crystal of tpy^{tbu}phoH or Cr(tpy^{tbu}pho)Cl_2 **1** was coated with Paratone oil and mounted on a MiTeGen MicroLoop. The X-ray intensity data were measured on a Bruker Kappa APEXII Duo system equipped with a fine-focus sealed tube (Mo K_α, λ = 0.71073 Å) and a graphite monochromator, and an Incoatec Microfocus IμS (Cu K_α, λ = 1.54178 Å) and a multi-layer mirror monochromator. The frames were integrated with the Bruker SAINT software package[60] using a narrow-frame algorithm. Data were corrected for absorption effects using the Multi-Scan method (SADABS). Each structure was solved and refined using the Bruker SHELXTL Software Package[61] within APEX3[60] and OLEX2.[62] Non-hydrogen atoms were refined anisotropically. The O-H hydrogen atom in tpy^{tbu}phoH was located in the electron density map and refined isotropically. All other hydrogen atoms in both structures were placed in geometrically calculated positions with U_{iso} = 1.2U_{equiv} of the parent atom (1.5U_{equiv} for methyl).

Table S2.1. X-ray crystallographic data for tpy^{tbu}phoH and Cr(tpy^{tbu}pho)Cl_2.

	tpy^{tbu}phoH	Cr(tpy^{tbu}pho)Cl_2
CCDC number	2086770	2086769
Formula	$C_{29}H_{31}N_3O$	$C_{31}H_{33}Cl_2CrN_4O$
FW (g/mol)	437.57	600.51
Temp (K)	100(2)	100(2)
λ (Å)	0.71073	1.54178
Size (mm)	0.060 x 0.132 x 0.352	0.037 x 0.123 x 0.129
Crystal habit	colorless rod	orange plate
Crystal system	triclinic	monoclinic
Space group	P -1	P $2_1/c$
a (Å)	7.0865(11)	11.3002(4)
b(Å)	10.0756(15)	14.6424(5)
c (Å)	17.671(3)	17.6380(7)
α (°)	82.004(5)	90
β (°)	78.474(4)	96.229(3)
γ (°)	70.496(4)	90
Volume (Å^3)	1161.8(3)	2901.19(18)
Z	2	4
Density (g/cm^3)	1.251	1.375
μ (mm^{-1})	0.076	5.182
F(000)	468	252
θ range (°)	1.18 to 27.57	3.93 to 68.34
Index ranges	-9 ≤ h ≤ 9 -13 ≤ k ≤ 12 -22 ≤ l ≤ 22	-13 ≤ h ≤ 13 -16 ≤ k ≤ 17 -21 ≤ l ≤ 20
Reflns collected	23615	34898
Independent reflns	5353 [R_{int} = 0.0833]	5321 [R_{int} = 0.1056]
Data / restraints /parameters	5353 / 0 / 308	5321 / 0 / 359
GOF on F^2	1.030	1.024
R_1 (I>2σ(I))	0.0654	0.0518
wR_2 (all data)	0.1865	0.1392

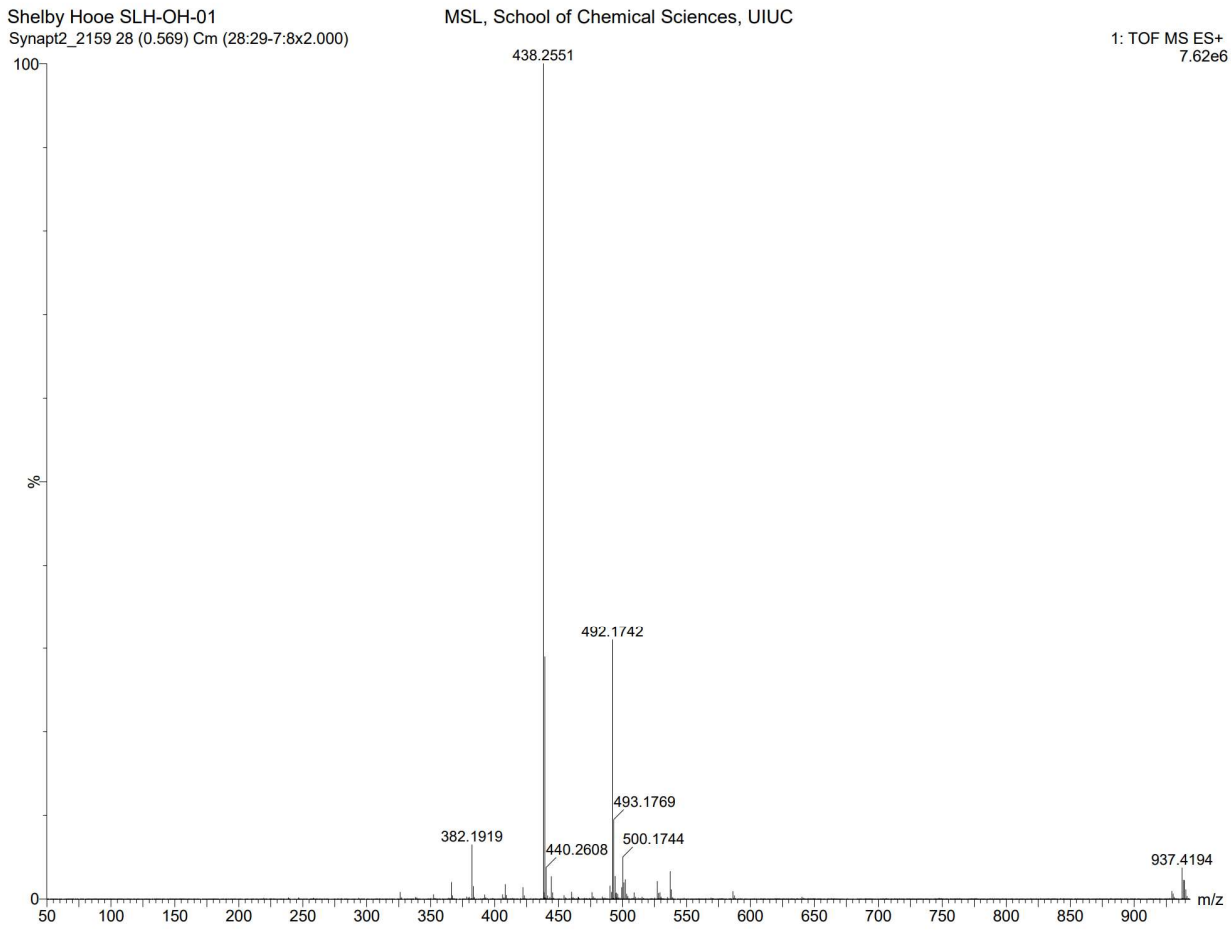

Figure S2.1. MS results for tpy^{tbu}pho(H) ligand.

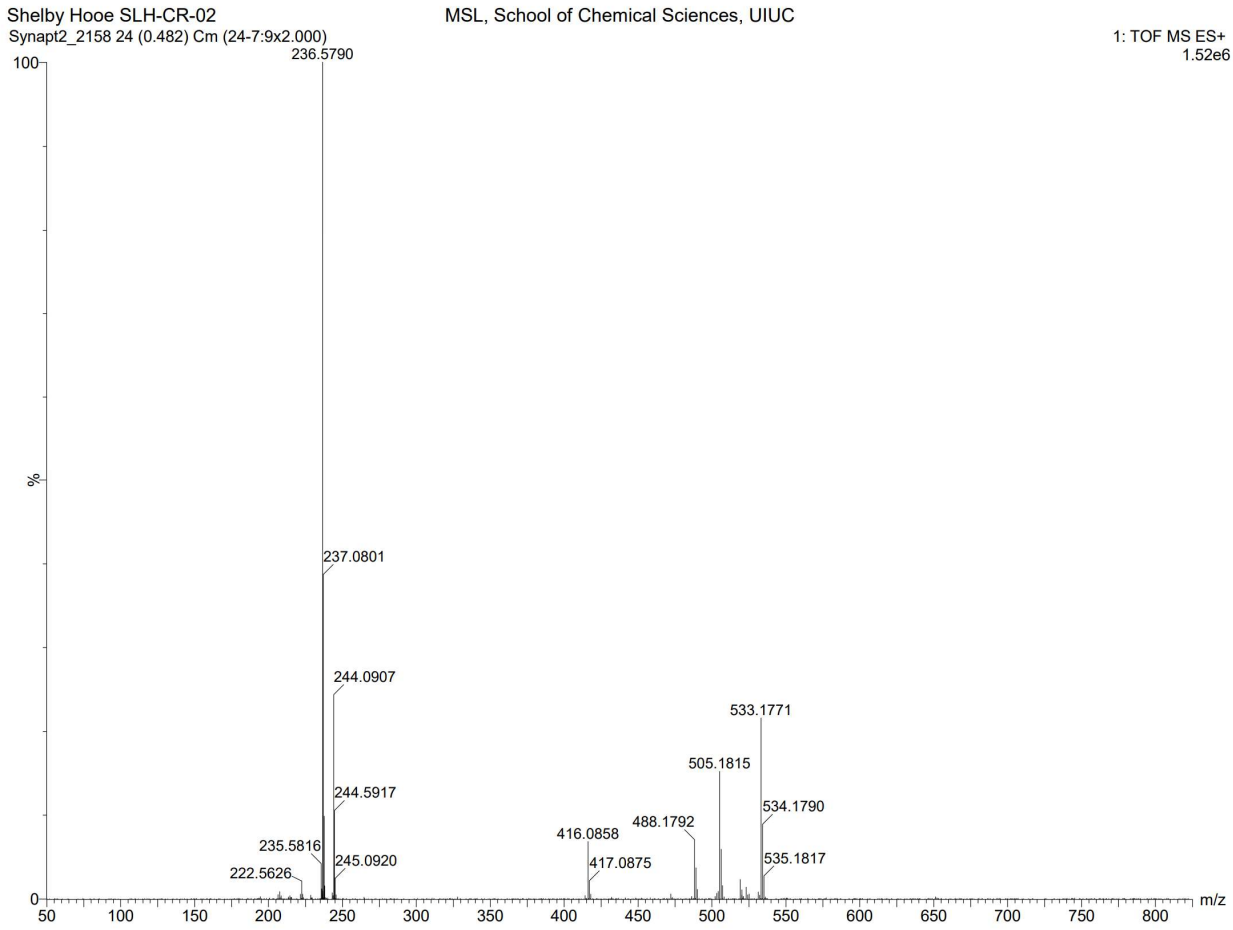

Figure S2.2. MS results for Cr(tpy^{tbu}pho)Cl_2 1.

Table S2.2. Evans' method results for Cr(tpy^{tbu}pho)Cl_2 **1** in DMF.[58, 59]

Trial	Chemical Shift (ppm)	Chemical Shift (Hz)	Total Magnetic Moment (emu mol^{-1})	Paramagnetic Moment (emu mol^{-1})	μ_{eff} (Bohr Magnetons)
1	0.111	66.6	0.00628	6.29×10^{-3}	3.87
2	0.114	68.4	0.00645	6.46×10^{-3}	3.92
3	0.112	67.2	0.00633	6.34×10^{-3}	3.89

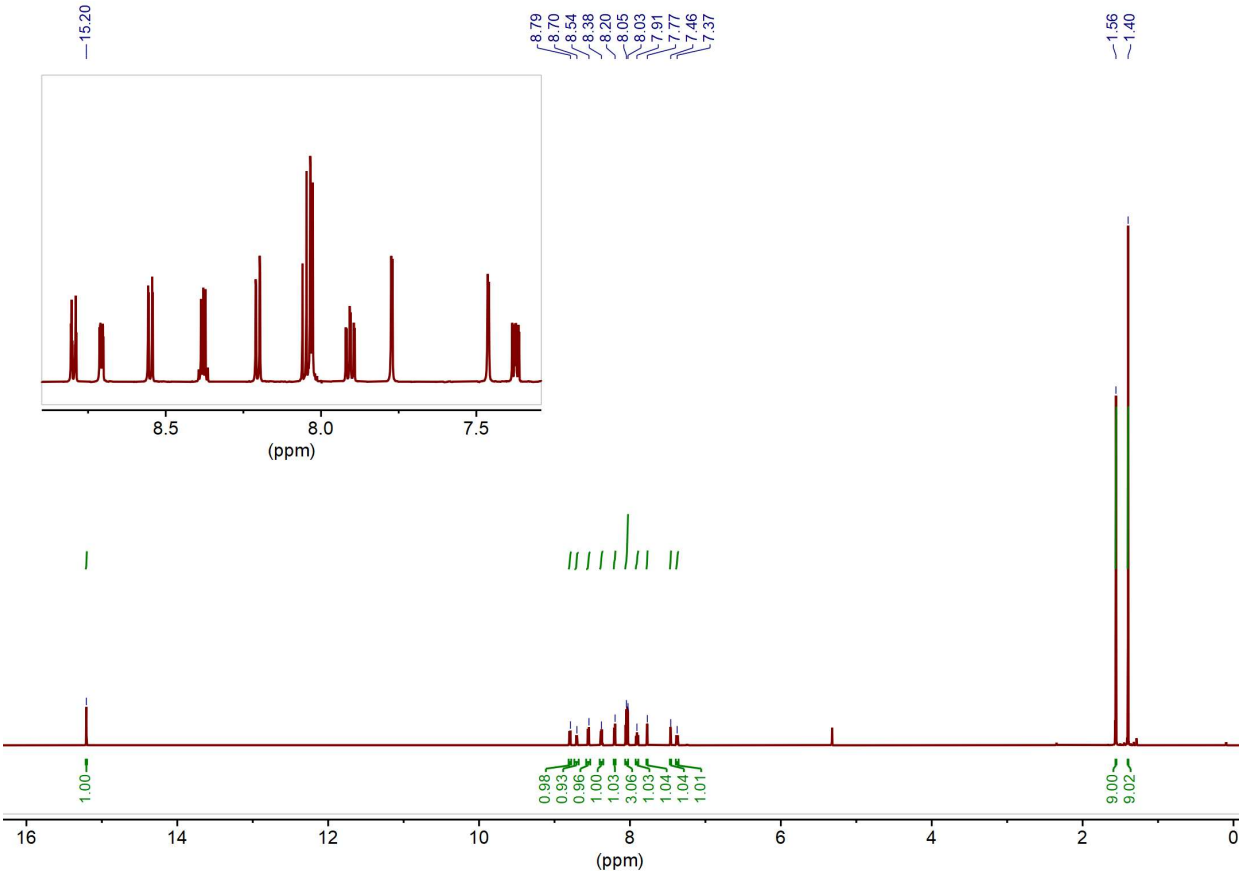

Figure S2.3. ^{1}H NMR of tpy^{tbu}phoH ligand; CD_2Cl_2; 600 MHz Varian.

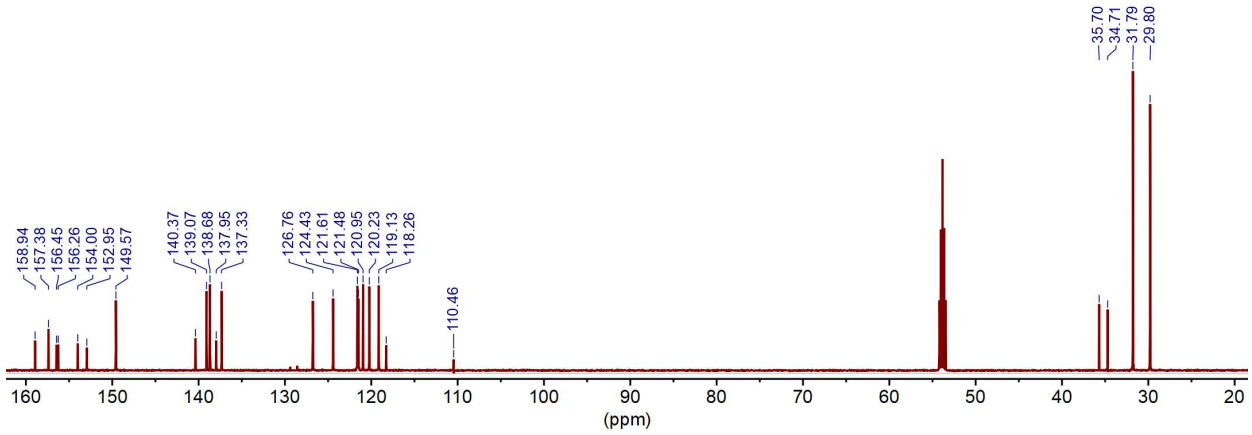

Figure S2.4. $^{13}C\{^{1}H\}$ NMR of tpy^{tbu}phoH ligand; CD_2Cl_2; 150 MHz Varian.

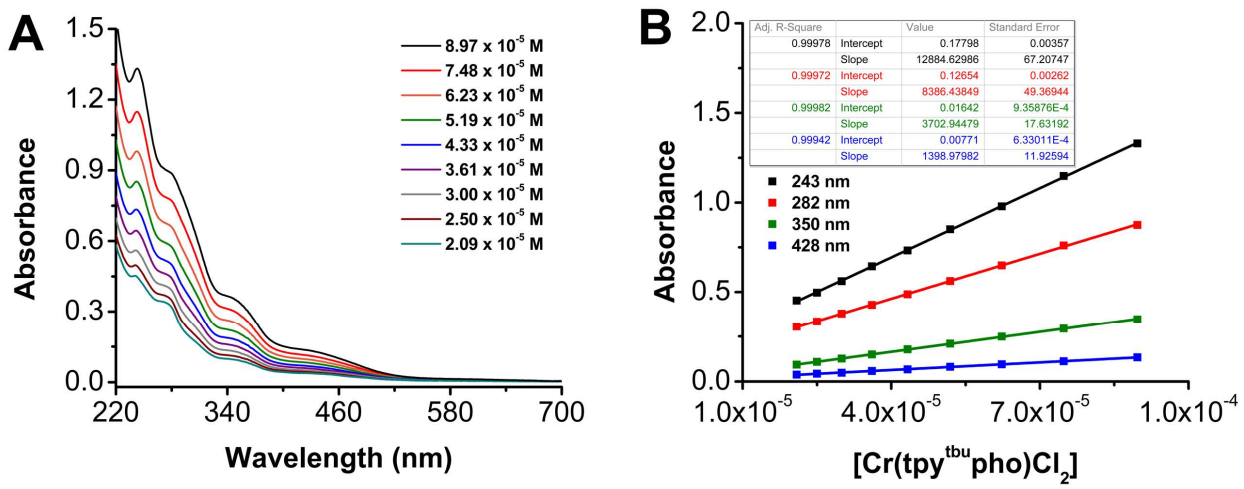

Figure S2.5. (**A**) UV-vis serial dilution absorbance data obtained from Cr(tpy^{tbu}pho)Cl$_2$ **1** in DMF solution. (**B**) Plot of absorbance versus concentration from data in (**A**) (λmax = 243 (12900 M^{-1}cm^{-1}), 282 (8390 M^{-1}cm^{-1}), 350 nm (3700 M^{-1}cm^{-1}), and 428 nm (1400 M^{-1}cm^{-1})). Conditions: varying concentration; quartz cell with 1 cm pathlength.

2.7.2 Electrochemistry

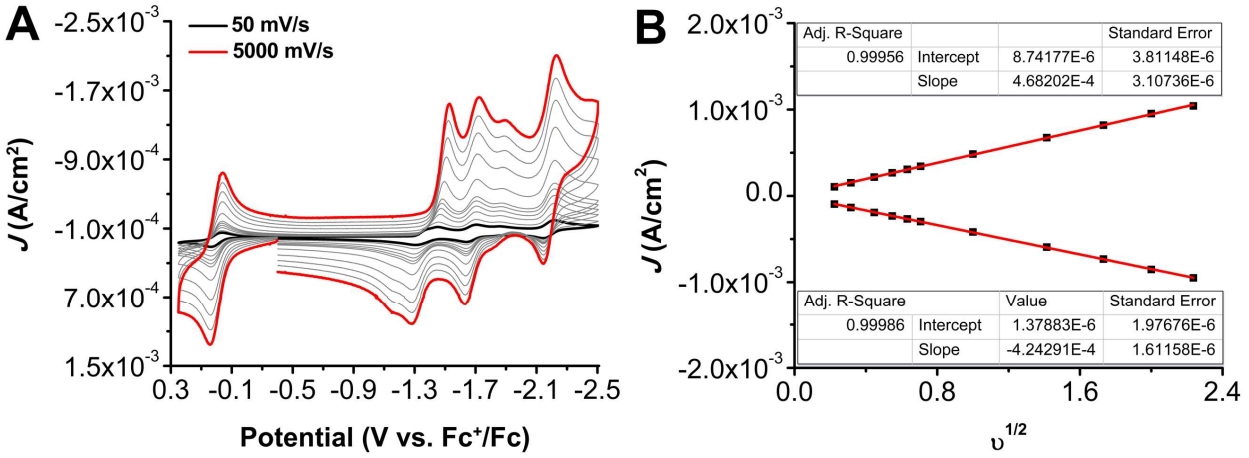

Figure S2.6. (**A**) CVs of Cr(tpy^{tbu}pho)Cl$_2$ **1** at variable scan rates ranging from 50 (black) to 5000 (red) mV/s, obtained under Ar saturation conditions. (**B**) Linear Fit of variable scan rate data from (**A**) demonstrating that Cr(tpy^{tbu}pho)Cl$_2$ **1** shows a diffusion-limited current response. The data in (**B**) was obtained from the reversible redox feature at −2.18 V vs Fc$^+$/Fc. Conditions: 1.0 mM analyte, 0.1 M TBAPF$_6$/DMF; glassy carbon working electrode, glassy carbon counter electrode, Ag/AgCl pseudoreference electrode; varied scan rate; referenced to internal ferrocene standard. Scan rates are 50, 100, 200, 300, 400, 500, 1000, 2000, 3000, 4000, and 5000 mV/s.

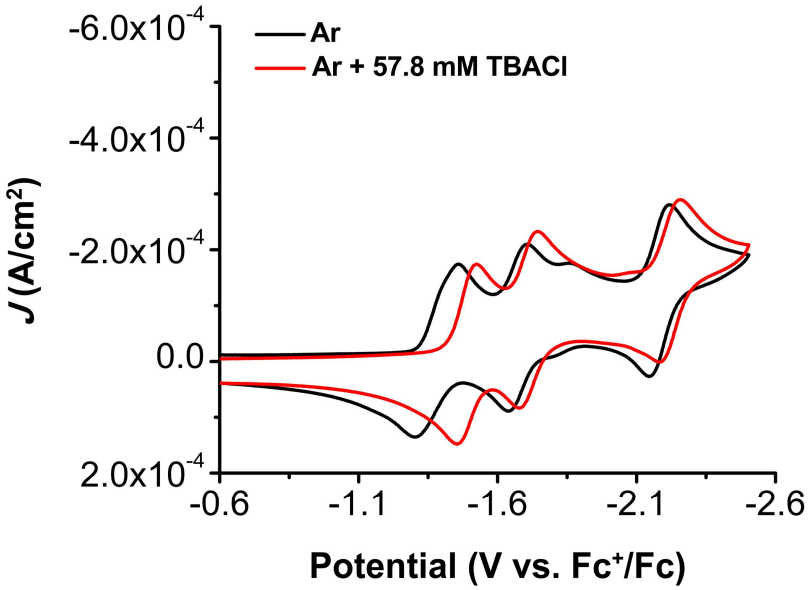

Figure S2.7. CVs of Cr(tpy^{tbu}pho)Cl_2 **1** under Ar saturation conditions examining the effect of TBACl under aprotic conditions. Conditions: 1.0 mM analyte, 0.1 M $TBAPF_6$/DMF; glassy carbon working electrode, glassy carbon counter electrode, Ag/AgCl pseudoreference electrode; 100 mV/s scan rate; referenced to internal ferrocene standard.

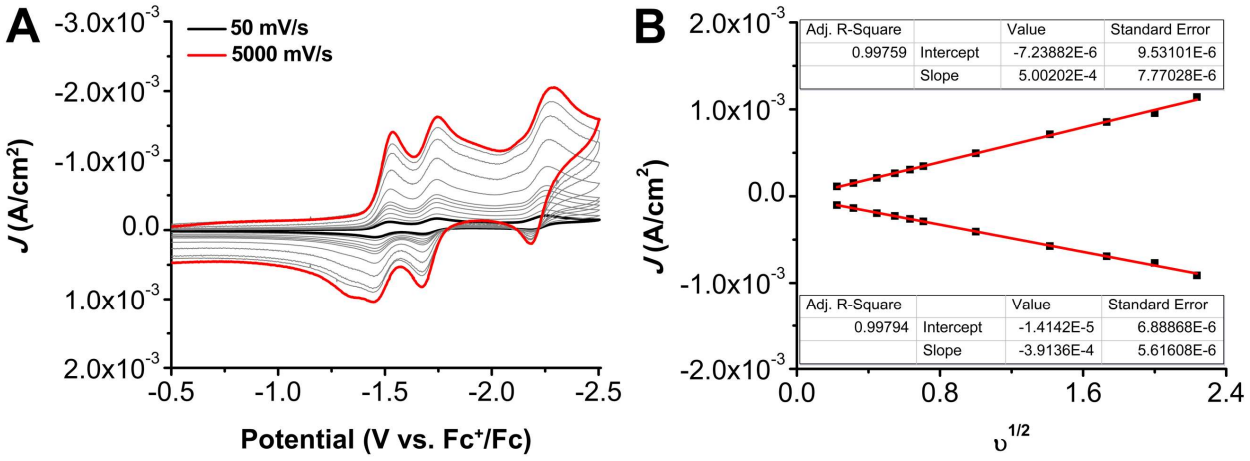

Figure S2.8. (**A**) CVs of Cr(tpy^{tbu}pho)Cl_2 **1** and 57.8 mM TBACl at variable scan rates ranging from 50 (black) to 5000 (red) mV/s, obtained under Ar saturation conditions. (**B**) Linear Fit of variable scan rate data from (**A**) demonstrating that Cr(tpy^{tbu}pho)Cl_2 **1** shows a diffusion-limited current response. The data in (**B**) was obtained from the reversible redox feature at −2.22 V vs Fc^+/Fc. Conditions: 1.0 mM analyte, 0.1 M $TBAPF_6$/DMF; glassy carbon working electrode, glassy carbon counter electrode, Ag/AgCl pseudoreference electrode; varied scan rate; referenced to internal ferrocene standard. Scan rates are 50, 100, 200, 300, 400, 500, 1000, 2000, 3000, 4000, and 5000 mV/s.

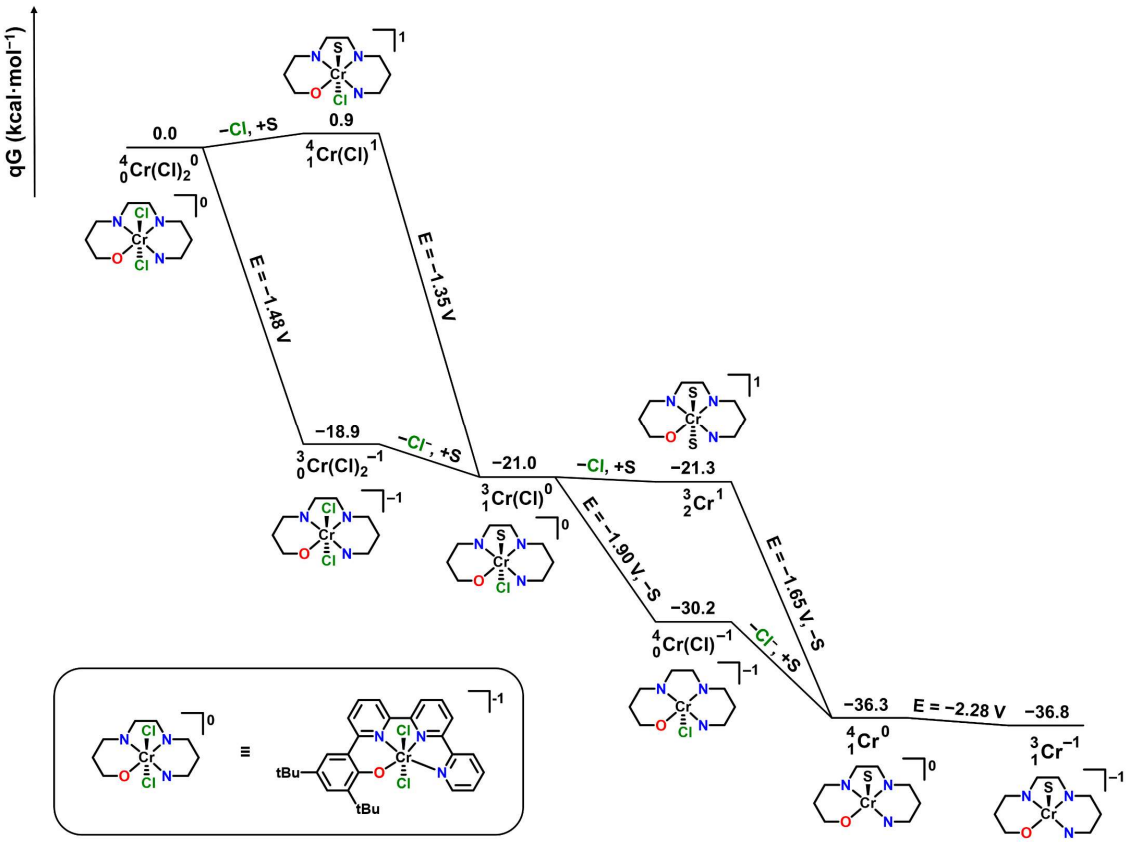

Figure S2.9. Free energy profile of the precatalyst reduction steps for **1**. S indicates a DMF solvent adduct of DMF.

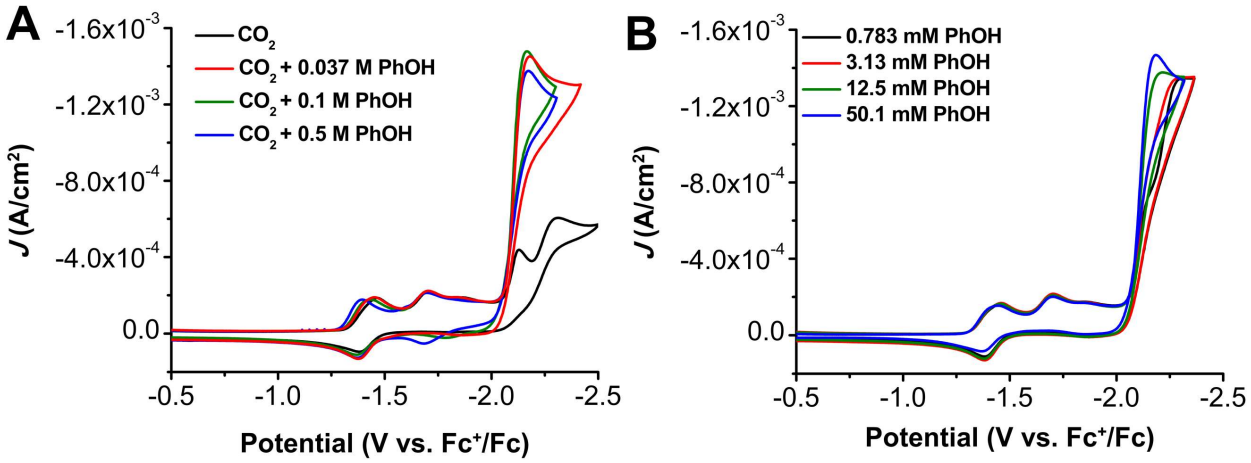

Figure S2.10. CVs of Cr(tpy^{tbu}pho)Cl$_2$ **1** obtained under CO_2 saturation conditions with varying amounts of PhOH showing no dependence on acid concentration. Conditions: 1.0 mM analyte with 0.1 M TBAPF$_6$/DMF; glassy carbon working electrode, glassy carbon counter electrode, Ag/AgCl pseudoreference electrode; 100 mV/s scan rate; referenced to internal ferrocene

standard.

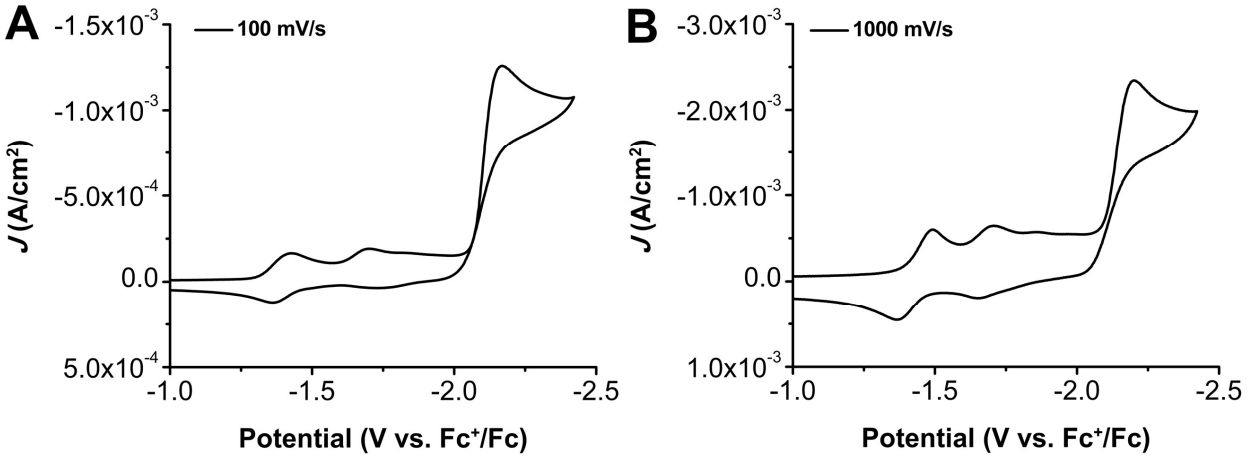

Figure S2.11. CVs of Cr(tpy^{tbu}pho)Cl_2 **1** with 0.16 M PhOH under CO_2 saturation conditions. These data are comparing the presence and absence of crossover tracing at 100 mV/s (**A**) and 1000 mV/s (**B**), respectively. Conditions: 1.0 mM analyte, 0.1 M $TBAPF_6$/DMF; glassy carbon working electrode, glassy carbon counter electrode, Ag/AgCl pseudoreference electrode; varied scan rate; referenced to internal ferrocene standard.

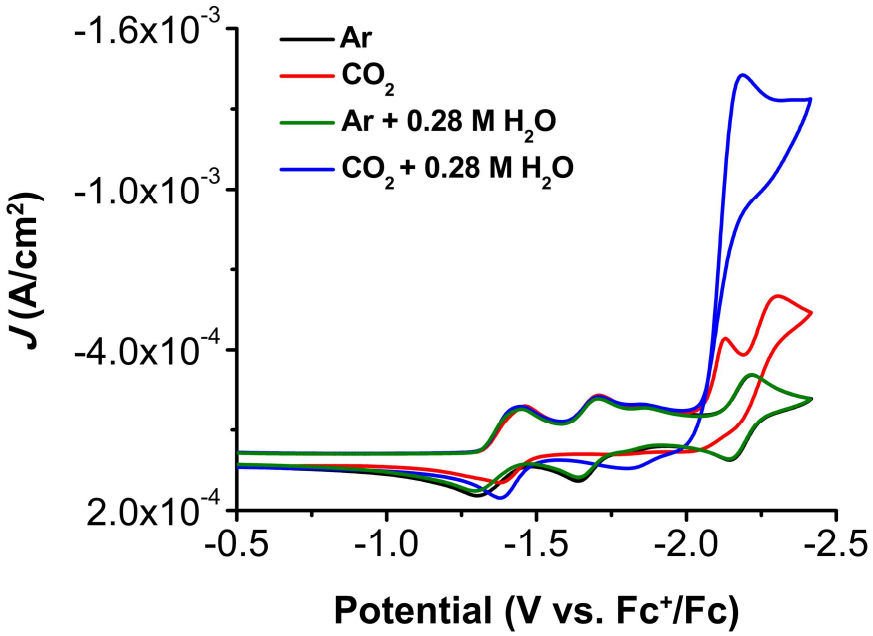

Figure S2.12. Comparison of CVs of 1.0 mM Cr(tpy^{tbu}pho)Cl_2 **1** under Ar and CO_2 saturation conditions with and without 0.28 M H_2O. Conditions: 0.1 M $TBAPF_6$/DMF; glassy carbon working electrode, glassy carbon rod counter electrode, Ag/AgCl pseudoreference electrode; referenced to Fc^+/Fc internal standard; 100 mV/s scan rate.

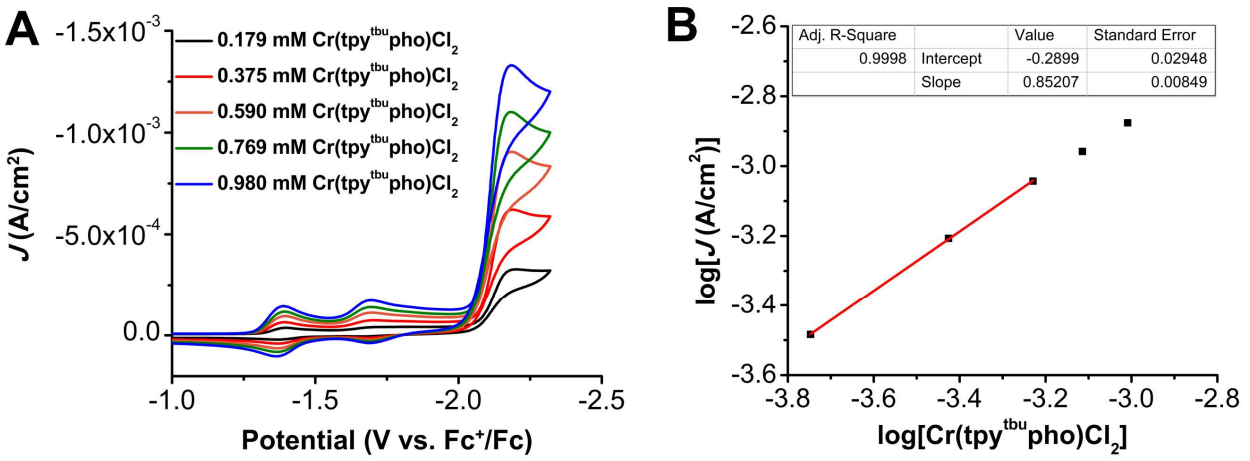

Figure S2.13. (**A**) CVs of Cr(tpy^{tbu}pho)Cl$_2$ **1** at variable concentrations, obtained under CO_2 saturation with 0.50 M PhOH. Conditions: 0.1 M TBAPF$_6$/DMF; glassy carbon working electrode, glassy carbon counter electrode, Ag/AgCl pseudoreference electrode; 100 mV/s scan rate; referenced to internal ferrocene standard. (**B**) Log-log plot from data obtained from CVs in (**A**) with only the first three points fitted due to saturation of the system at higher concentrations.

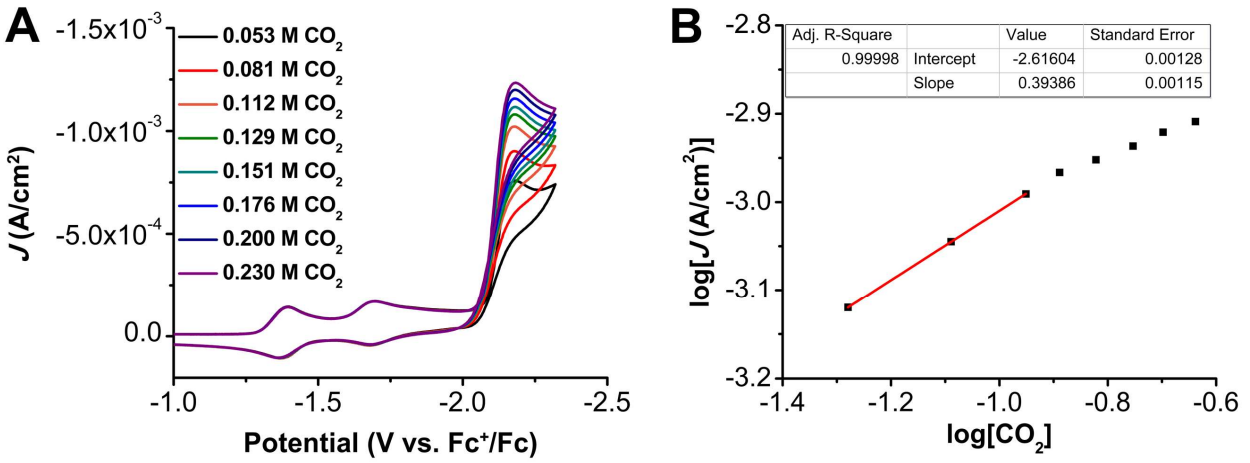

Figure S2.14. (**A**) CVs of Cr(tpy^{tbu}pho)Cl$_2$ **1** obtained under variable CO_2 concentrations with 0.50 M PhOH. Conditions: 0.1 M TBAPF$_6$/DMF; glassy carbon working electrode, glassy carbon counter electrode, Ag/AgCl pseudoreference electrode; 100 mV/s scan rate; referenced to internal ferrocene standard. (**B**) Log–log plot from data obtained from CVs in (**A**) with only the first three points fitted due to saturation of the system at higher concentrations.

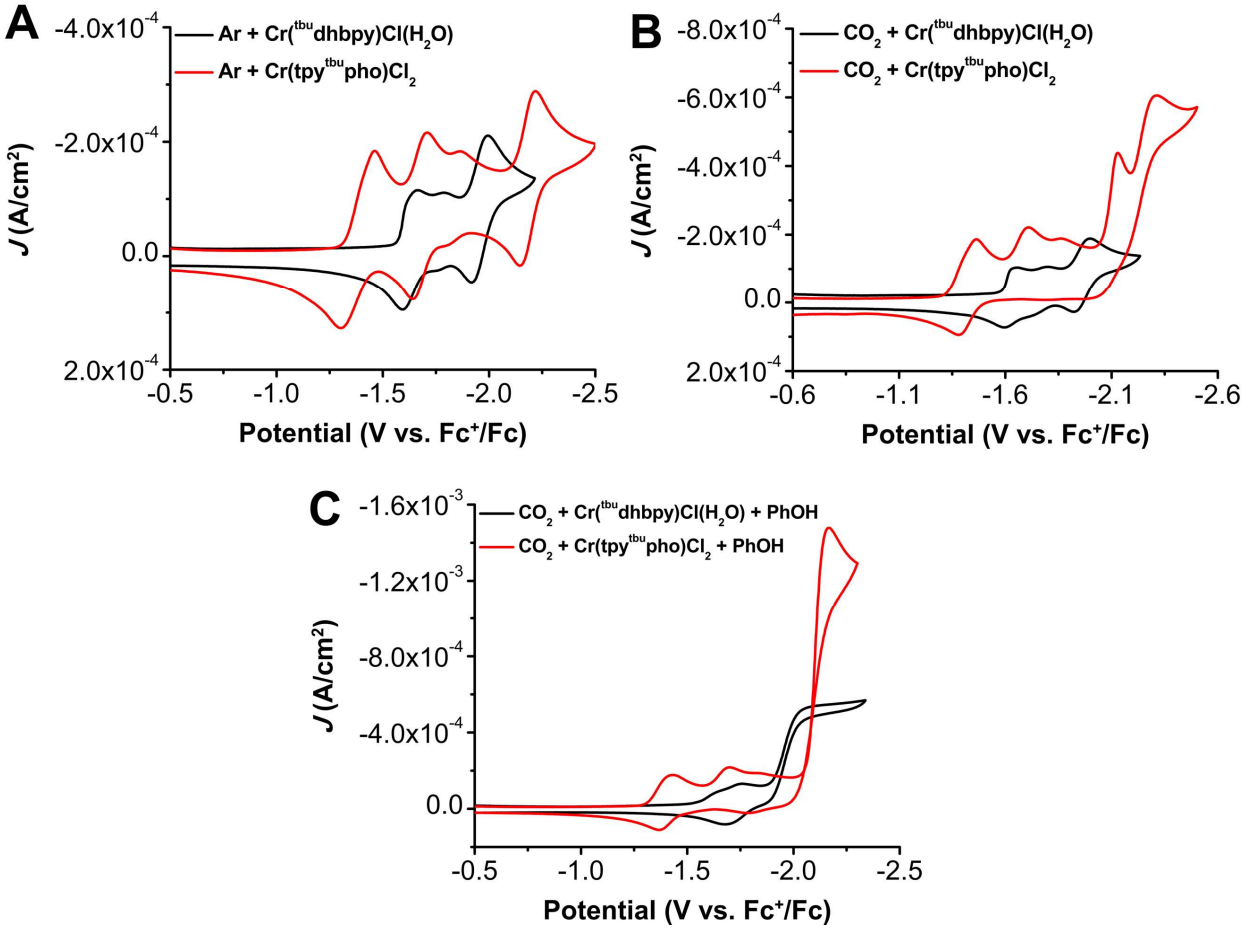

Figure S2.15. Comparison CVs of Cr(tpy^{tbu}pho)Cl$_2$ **1** and Cr(^{tbu}dhbpy)Cl(H$_2$O)[18] obtained under (**A**) Ar saturation and without (**B**) and with (**C**) 0.1 M PhOH under CO_2 saturation. Conditions: 1.0 mM catalyst with 0.1 M TBAPF$_6$/DMF; glassy carbon working electrode, glassy carbon counter electrode, Ag/AgCl pseudoreference electrode; 100 mV/s scan rate; referenced to internal ferrocene standard.

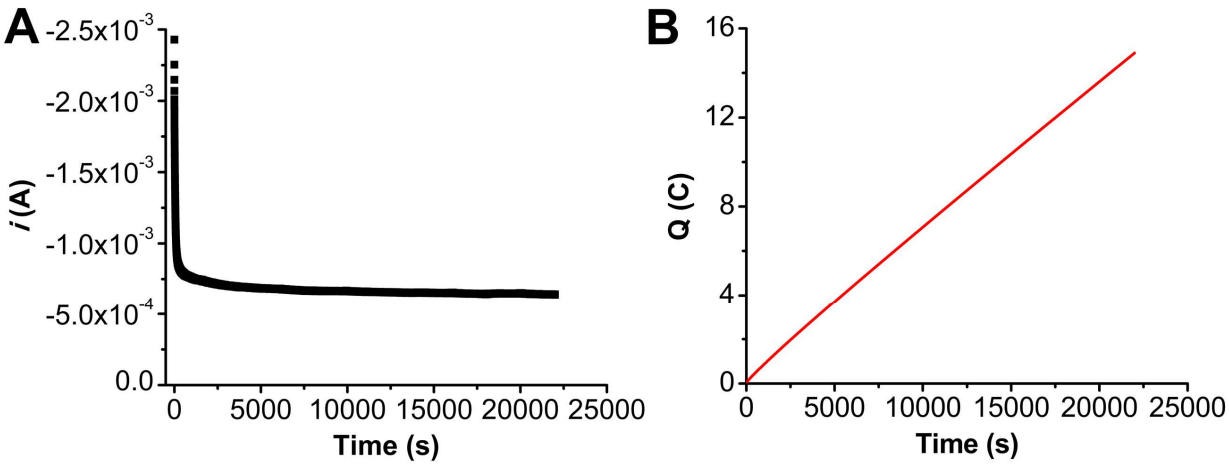

Figure S2.16. (**A**) Current versus time trace from CPE experiment with Cr(tpy^{tbu}pho)Cl_2 **1** and PhOH. (**B**) Charge passed versus time for the CPE experiment shown in (**A**). Conditions were 0.5 mM Cr(tpy^{tbu}pho)Cl_2 **1** and 0.6 M PhOH under a CO_2 atmosphere at −2.3 V vs Fc^+/Fc in 0.1 M $TBAPF_6$/DMF; working and counter electrodes were graphite rods and the reference was a nonaqueous Ag/AgCl pseudoreference electrode; 0.075 M Fc was used as sacrificial oxidant; cell was kept in the dark while applying potential and product analysis.

Table S2.3. Results from CPE experiment in **Figure S2.16**.

Time (s)	Charge (coulombs)	moles (e^-)	Moles of CO	FE_{CO}	Moles of H_2	FE_{H2}
*22000	14.9	1.54 x 10^{-4}	7.16 x 10^{-4}	92.71	2.07 x 10^{-6}	2.68
*22000	14.9	1.54 x 10^{-4}	6.56 x 10^{-4}	84.94	2.00 x 10^{-6}	2.59
*22000	14.9	1.54 x 10^{-4}	7.79 x 10^{-4}	100.87	2.08 x 10^{-6}	2.70

* indicates a triplicate series of injections carried out upon completion of electrolysis

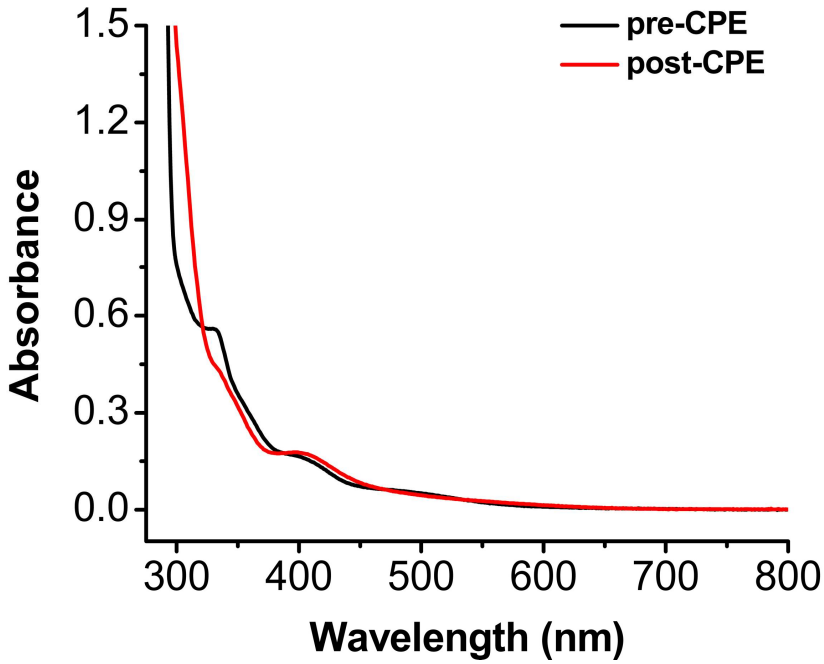

Figure S2.17. UV-vis spectrum of pre (black) and post (red) bulk CPE solution from experiment in **Figure S2.16** after dilution. Conditions: 0.1 mL CPE solution in 2.9 mL 0.1 M $TBAPF_6$/DMF; quartz cell with 1 cm pathlength.

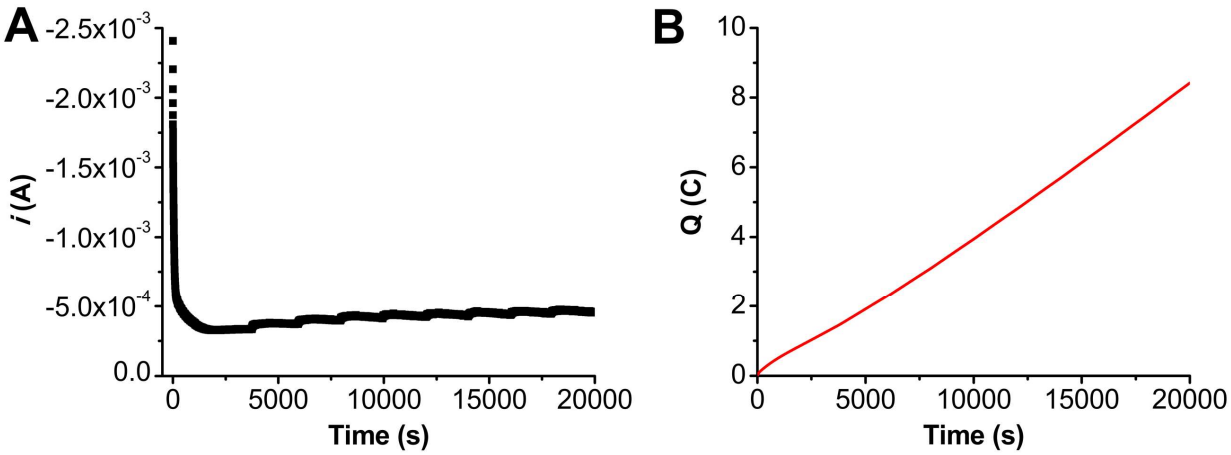

Figure S2.18. (**A**) Current versus time trace from rinse test CPE experiment. (**B**) Charge passed versus time for the CPE experiment shown in (**A**). Conditions were 0.6 M PhOH under a CO_2 atmosphere at −2.3 V vs Fc^+/Fc in 0.1 M $TBAPF_6$/DMF; working electrode was the graphite rod used in the experiment shown in **Figure S2.16** that was rinsed with DMF and not polished, counter electrode was a graphite rod, and the reference was a nonaqueous Ag/AgCl pseudoreference electrode; 0.075 M Fc was used as sacrificial oxidant.

Table S2.4. Results from CPE experiment in **Figure S2.18**.

Time (s)	Charge (coulombs)	moles (e^-)	Moles of CO
*20000	8.42	8.73×10^{-5}	<LOQ
*20000	8.42	8.73×10^{-5}	<LOQ
*20000	8.42	8.73×10^{-5}	<LOQ

* indicates a triplicate series of injections carried out upon completion of electrolysis

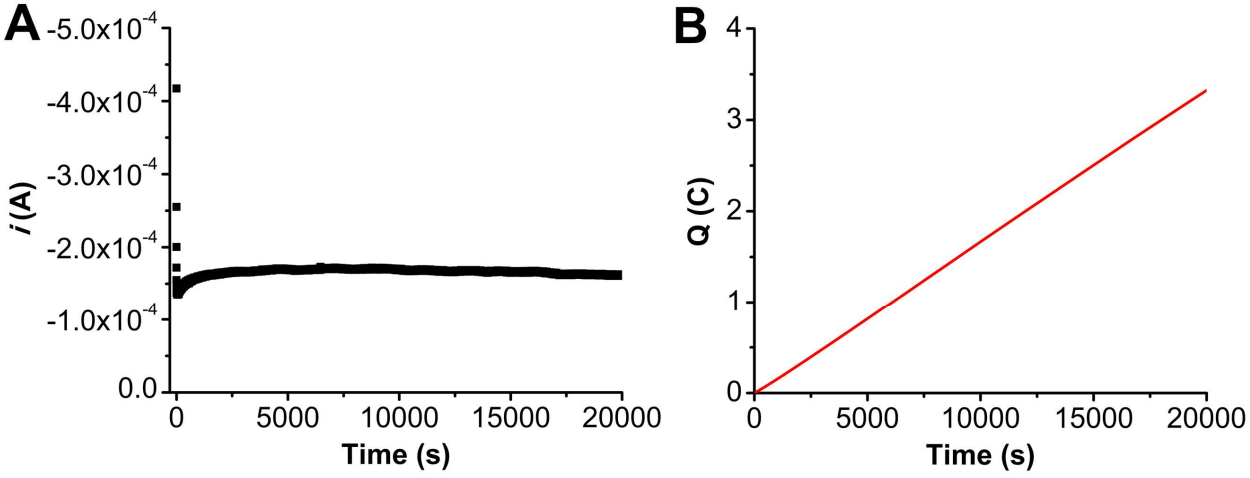

Figure S2.19. (**A**) Current versus time trace from control CPE experiment with PhOH. (**B**) Charge passed versus time for the CPE experiment shown in (**A**). Conditions were 0.6 M PhOH under a CO_2 atmosphere at −2.3 V vs Fc^+/Fc in 0.1 M $TBAPF_6$/DMF; working electrode was a glassy carbon rod, counter electrode was a graphite rod, and the reference was a nonaqueous Ag/AgCl pseudoreference electrode; 0.075 M Fc was used as sacrificial oxidant.

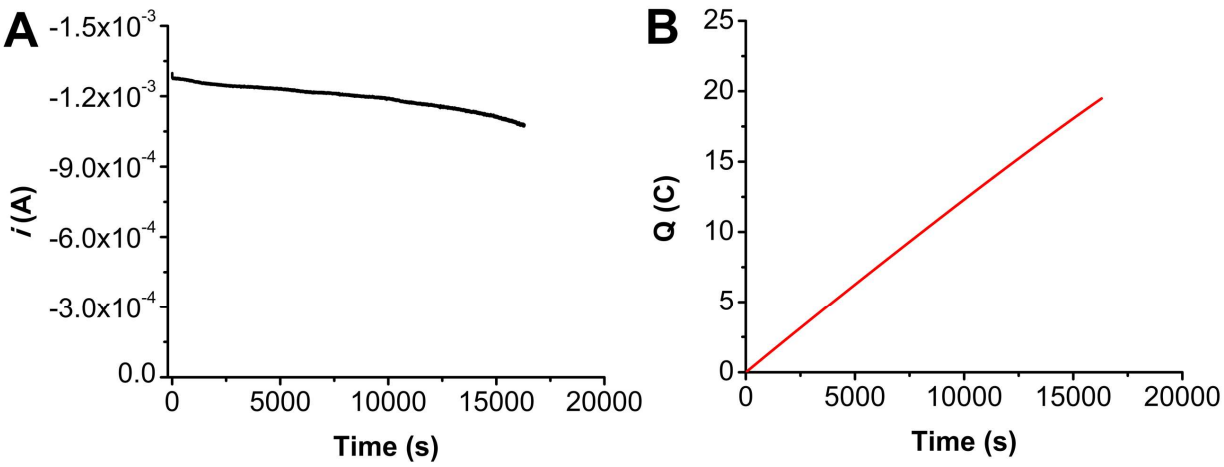

Figure S2.20. (**A**) Current versus time trace from CPE experiment with Cr(tpy^{tbu}pho)Cl_2 **1** and H_2O. (**B**) Charge passed versus time for the bulk electrolysis experiment shown in (**A**). Conditions were 0.5 mM Cr(tpy^{tbu}pho)Cl_2 **1** and 2% H_2O under a CO_2 atmosphere at −2.3 V vs Fc^+/Fc in 0.1 M $TBAPF_6$/DMF; working electrode was a glassy carbon rod, counter electrode was a graphite rod, and the reference was a nonaqueous Ag/AgCl pseudoreference electrode; 0.075 M Fc was used as sacrificial oxidant.

Table S2.5. Results from CPE experiment in **Figure S2.20**.

Time (s)	Charge (coulombs)	moles (e^-)	Moles of CO	FE_{co}
*16300	19.5	2.02 x 10^{-4}	8.85 x 10^{-5}	87.61
*16300	19.5	2.02 x 10^{-4}	9.69 x 10^{-5}	95.92
*16300	19.5	2.02 x 10^{-4}	9.60 x 10^{-5}	95.04

* indicates a triplicate series of injections carried out upon completion of electrolysis

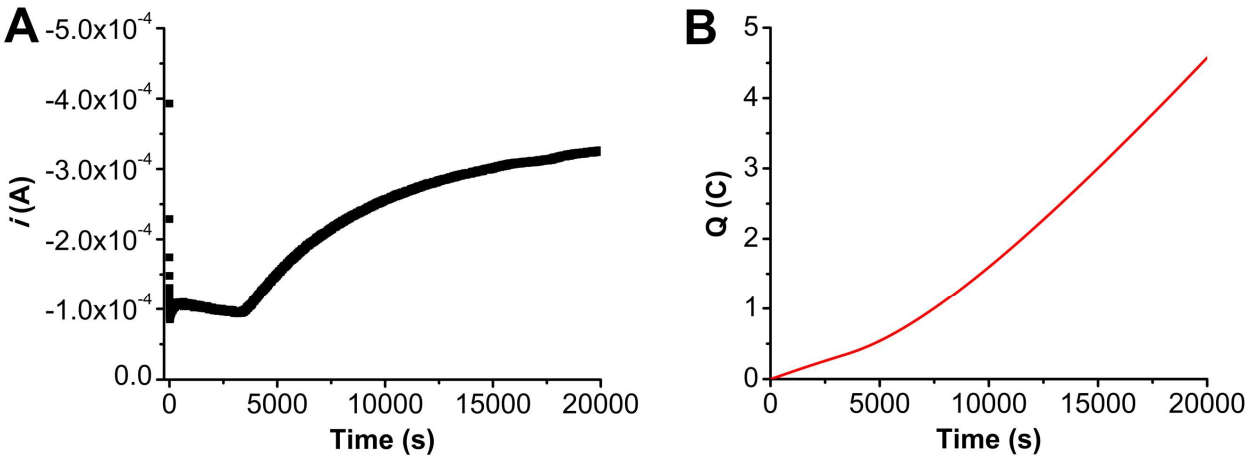

Figure S2.21. (**A**) Current versus time trace from CPE experiment with H_2O. (**B**) Charge passed versus time for the bulk electrolysis experiment shown in (**A**). Conditions were 2% H_2O under a CO_2 atmosphere at –2.3 V vs Fc^+/Fc in 0.1 M $TBAPF_6$/DMF; working electrode was a glassy carbon rod, counter electrode was a graphite rod, and the reference was a nonaqueous Ag/AgCl pseudoreference electrode; 0.075 M Fc was used as sacrificial oxidant.

2.7.3 Computational Data

Table S2.6. Experimental, calculated and calibrated redox potentials for successive redox events of precatalyst **1** (1a: $^{4}_{1}\mathbf{CrCl}^{+1}_{\square}$ to $^{3}_{1}\mathbf{CrCl}^{0}_{\square}$, 1b: $^{4}_{0}\mathbf{CrCl_2}^{0}_{\square}$ to $^{3}_{0}\mathbf{CrCl_2}^{-1}_{\square}$, 2a: $^{3}_{2}\mathbf{Cr}^{+1}_{\square}$ to $^{4}_{1}\mathbf{Cr}^{0}_{\square}$, 2b: $^{3}_{1}\mathbf{CrCl}^{0}_{\square}$ to $^{4}_{0}\mathbf{CrCl}^{-1}_{\square}$, 3: $^{4}_{1}\mathbf{Cr}^{0}_{\square}$ to $^{3}_{1}\mathbf{Cr}^{-1}_{\square}$).

Redox label	Experimental (V)	Calculated (V)	Calibrated
1a	−1.38	−1.36	−1.35
1b	−1.49	−1.53	−1.48
2a	−1.64	−1.65	−1.65
2b	−1.85	−1.77	−1.90
3	−2.18	−2.35	−2.28

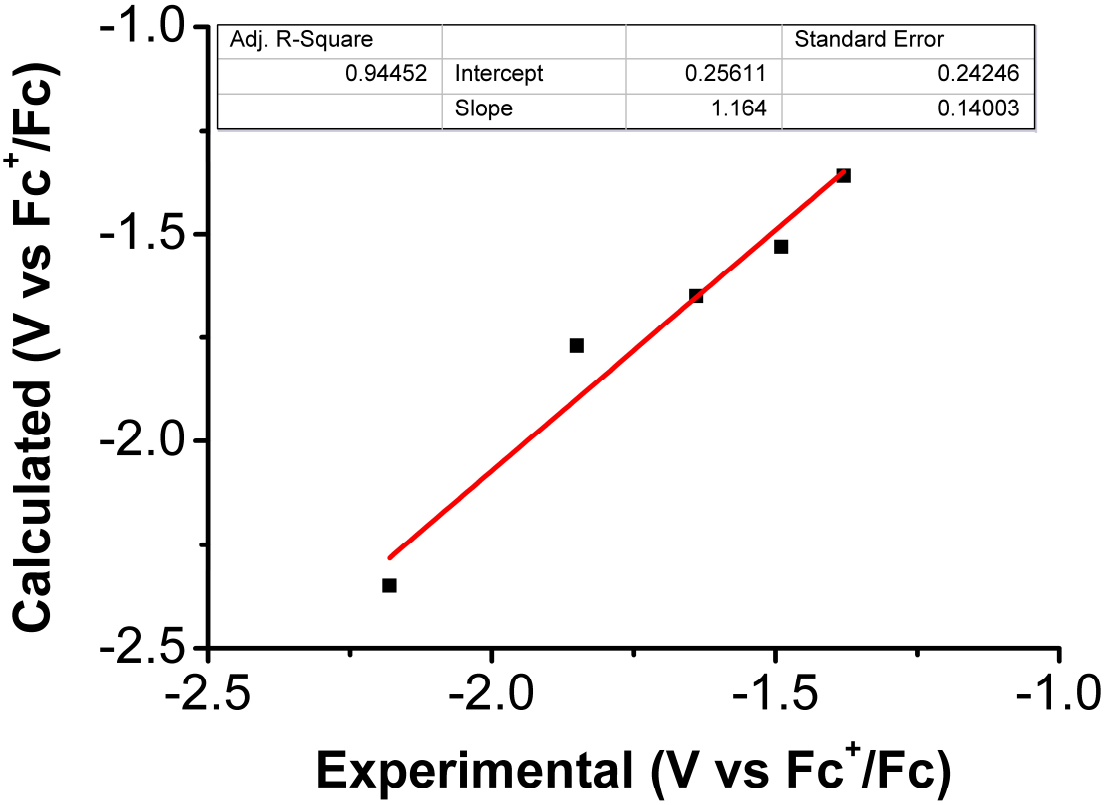

Figure S2.22. Plot of calculated versus experimental redox potentials at the triple-zeta level.

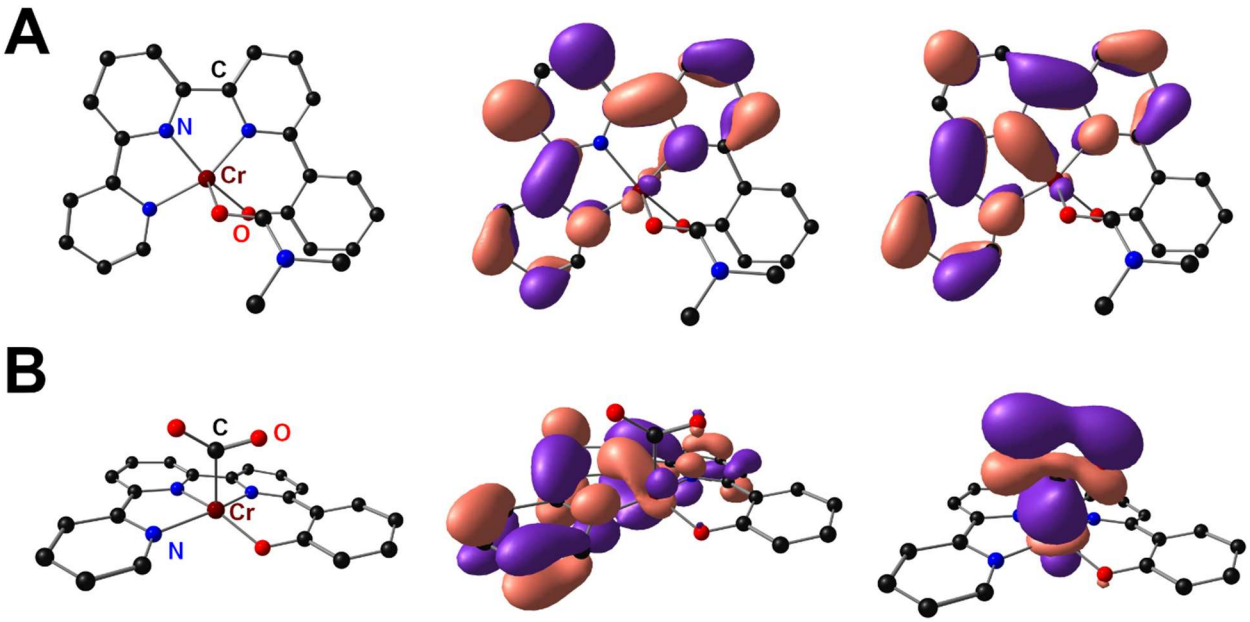

Figure S2.23. From left to right: molecular geometry, SOMO (*β*) and SOMO−1 (*β*) of $^{\mathbf{3}}_{\mathbf{1}}\mathrm{Cr}^{\mathbf{-1}}_{\square}$ (A) and $^{\mathbf{3}}_{\mathbf{0}}\mathrm{Cr(CO_2)}^{\mathbf{-1}}_{\square}$ (B). For clarity, tbu groups and H atoms have been omitted.

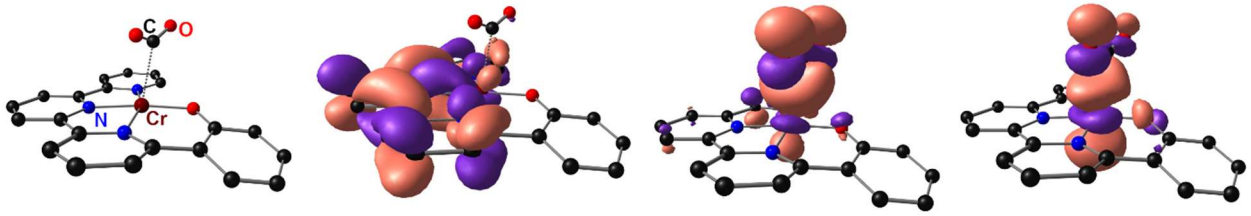

Figure S2.24. From left to right: molecular geometry, SOMO (*β*), SOMO−1 and SOMO−2 (*α*) of $^{\mathbf{3}}_{\mathbf{0}}\mathrm{TS1}^{\mathbf{-1}}_{\square}$.

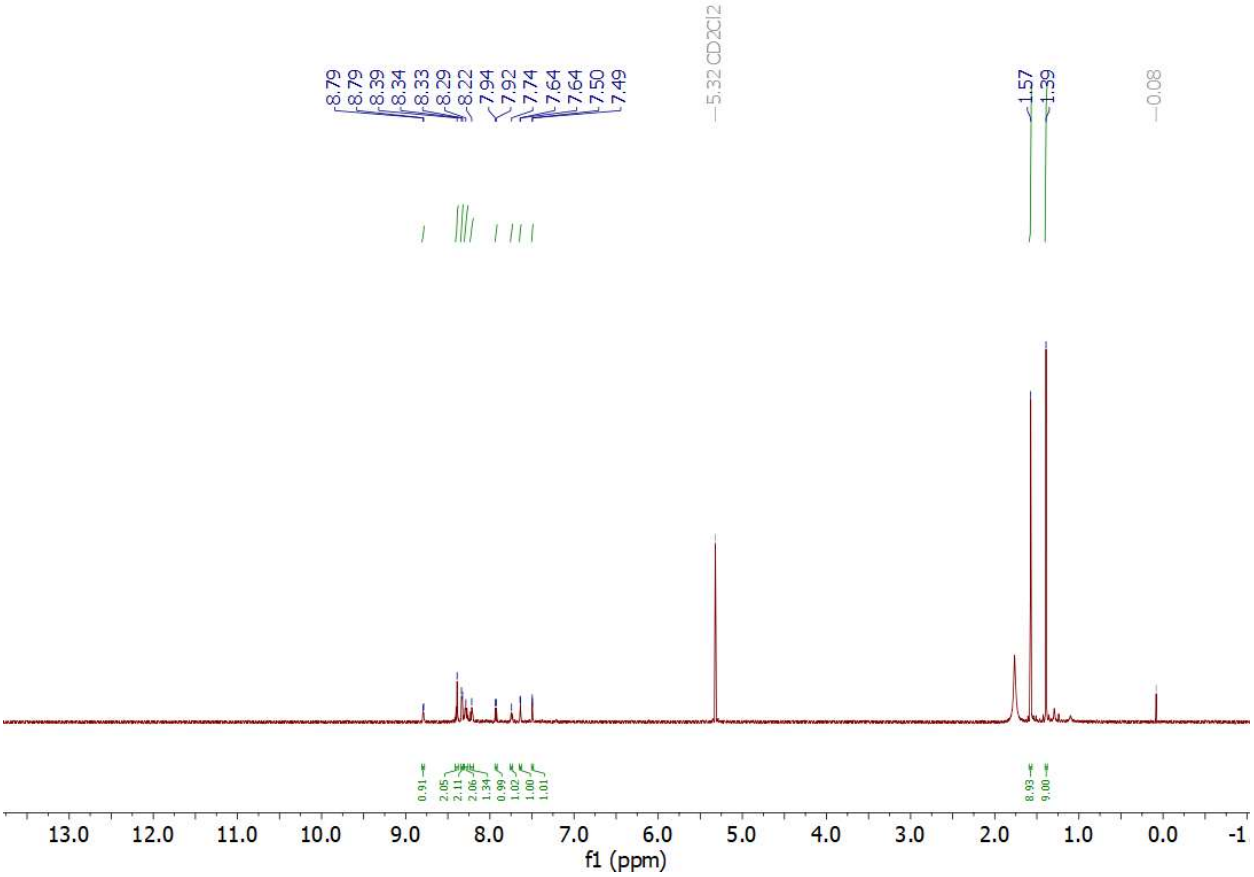

Figure S2.25. ^{1}H NMR of [Zn(tpy^{tbu}pho)][OTf]; CD_2Cl_2; 600 MHz Varian.

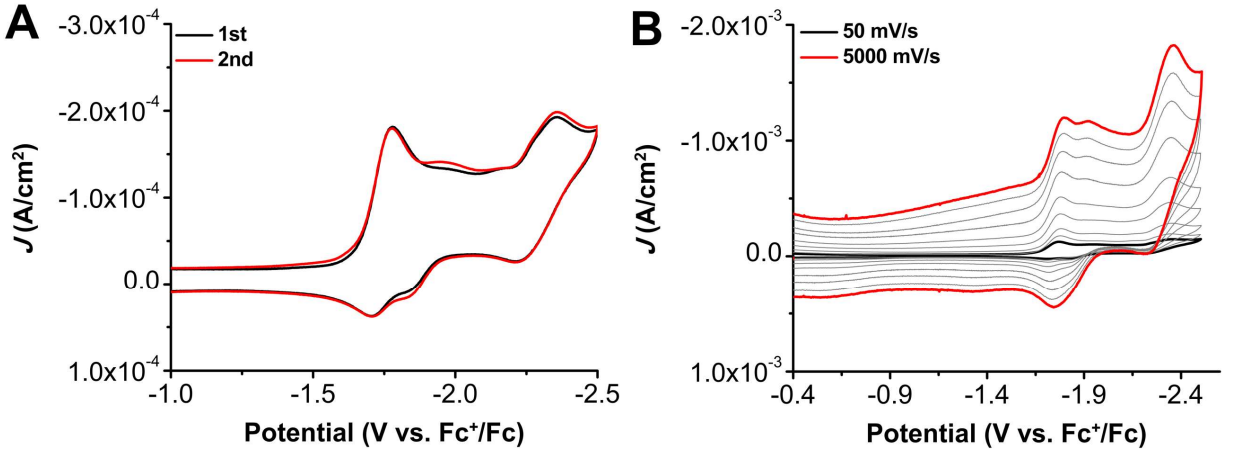

Figure S2.26. (**A**) CVs of [Zn(tpy^{tbu}pho)][OTf] showing two consecutive scans, obtained under Ar saturation conditions. (**B**) CVs of [Zn(tpy^{tbu}pho)][OTf] at variable scan rates (50 mV/s to 5000 mV/s), obtained under Ar saturation conditions. Conditions: 1.0 mM analyte, 0.1 M $TBAPF_6$/DMF; glassy carbon working electrode, glassy carbon counter electrode, Ag/AgCl pseudoreference electrode; varied scan rate; referenced to internal ferrocene standard.

The [Zn(tpy^{tbu}po)][OTf] complex has three quasi-reversible redox features at $E_{1/2}$ = –1.75 V, a minor one at $E_{1/2}$ = –1.91 V, and $E_{1/2}$ = –2.29 V vs. Fc^{+}/Fc. The minor feature at –1.91 V is ascribed to adsorption of the complex on the electrode: the redox feature grows after consecutive scans without polishing the electrode and the peak at –2.29 V becomes more irreversible as scan rate increases. Further, the electrode had to be thoroughly polished between every scan or an irreversible oxidation at –0.6 V on the return sweep appeared and increased in current over time.

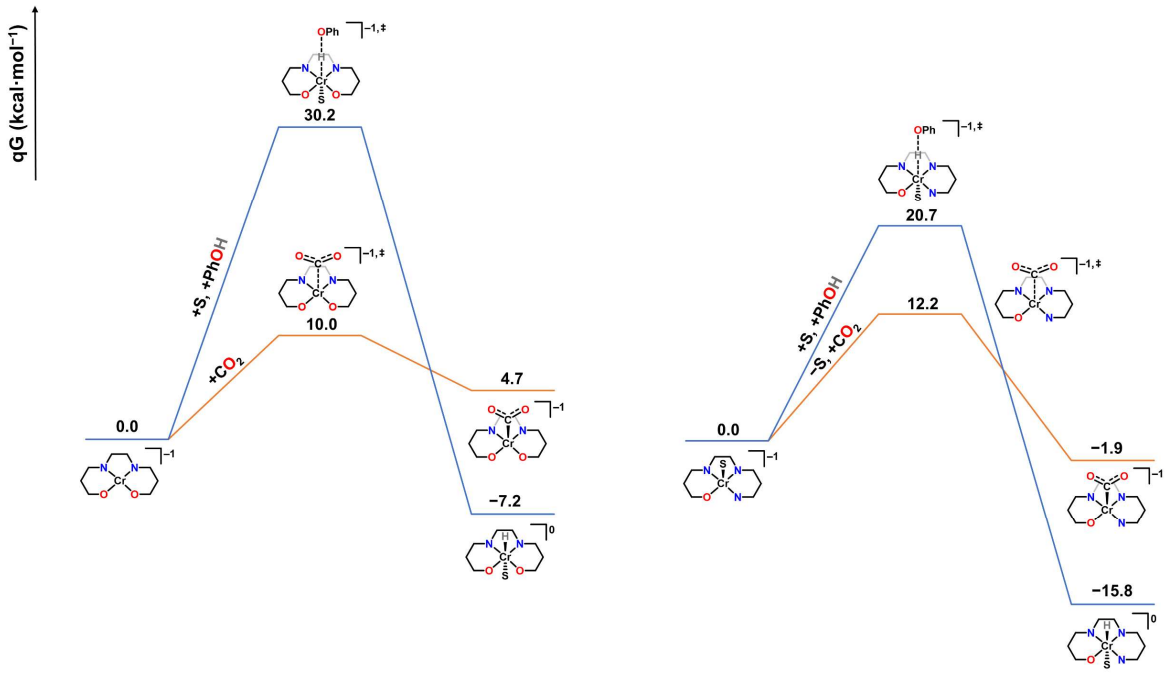

Figure S2.27. Free energy profile comparing Cr−CO_2 binding and Cr−H formation for the ^{tbu}dhbpy and tpy^{tbu}pho systems.

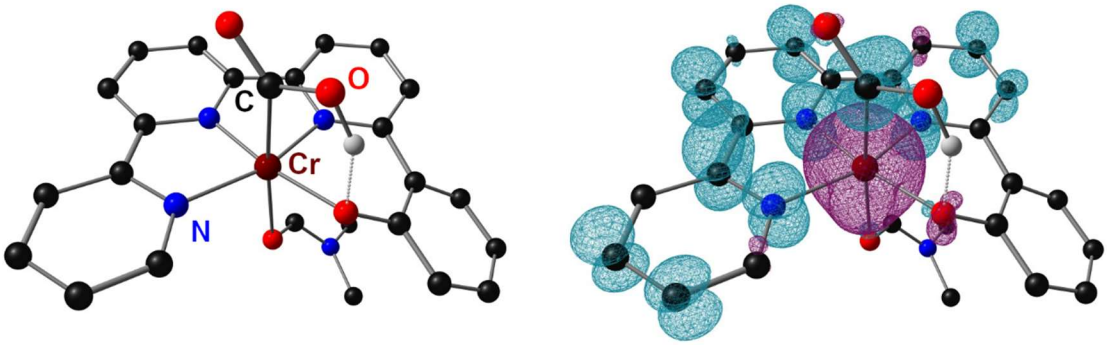

Figure S2.28. Molecular geometry and spin density plot of $^{\mathbf{2}}_{\mathbf{1}}\mathrm{Cr(CO_2H)}^{\mathbf{-1}}_{\square}$.

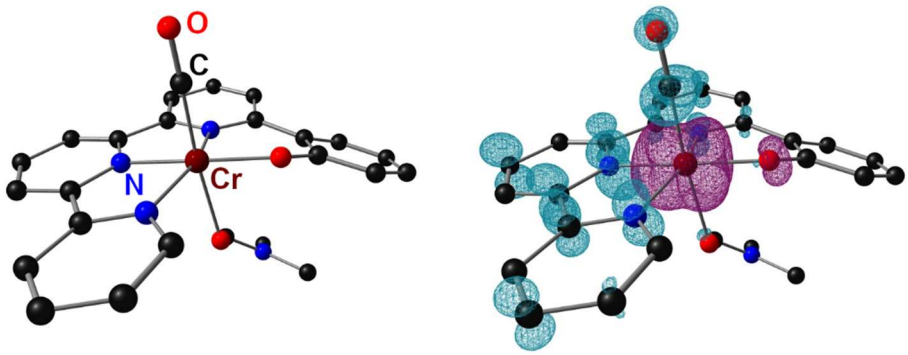

Figure S2.29. Molecular geometry and spin density plot of $^{\mathbf{2}}_{\mathbf{1}}$Cr(CO)$^{\mathbf{0}}$.

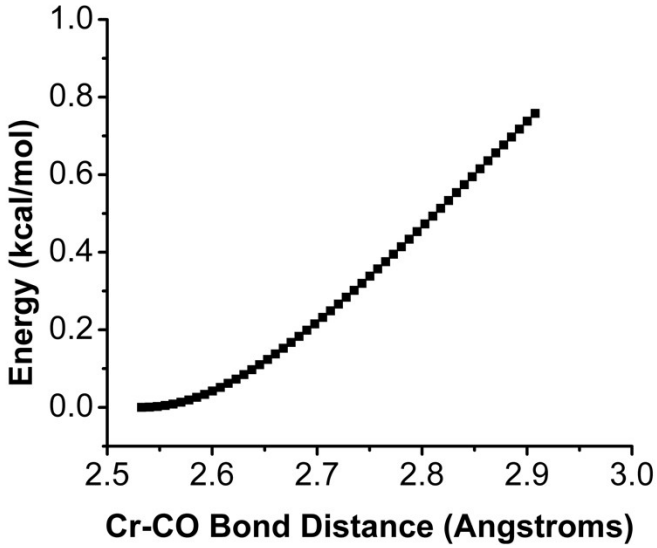

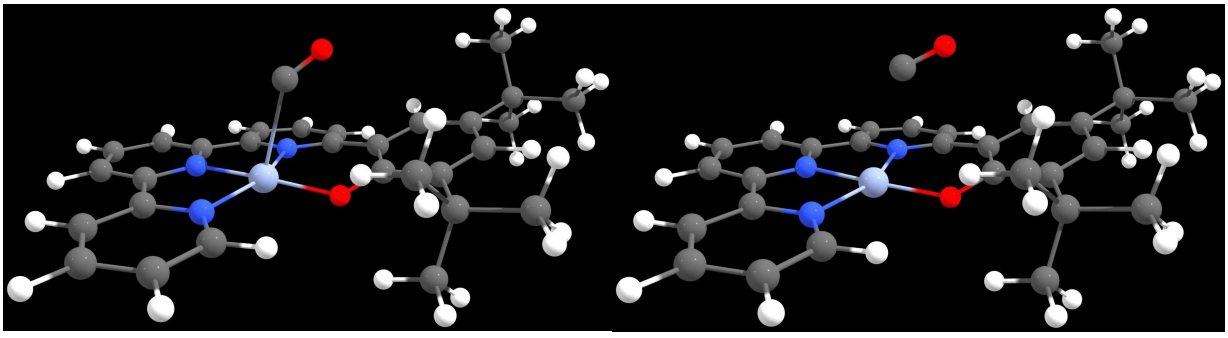

Figure S2.30. Relaxed energy scan of the elongation of the Cr–CO bond from a stable S = 3/2 adduct, $^{4}_{0}$**Cr(CO)**: $^{4}_{0}$**Cr(CO)**^{0} is 1.6 kcal/mol higher in energy than the ground state, $^{2}_{1}$**Cr(CO)**^{0} and CO release in the scan trajectory (Cr–CO 2.53 (left) to 2.91 Å (right)) occurs at a barrier of approximately 1 kcal/mol. As a conservative estimate based on these data, a value of 5 kcal/mol has been assigned to the barrier for CO release. Below: initial (left) and final (right) geometry.

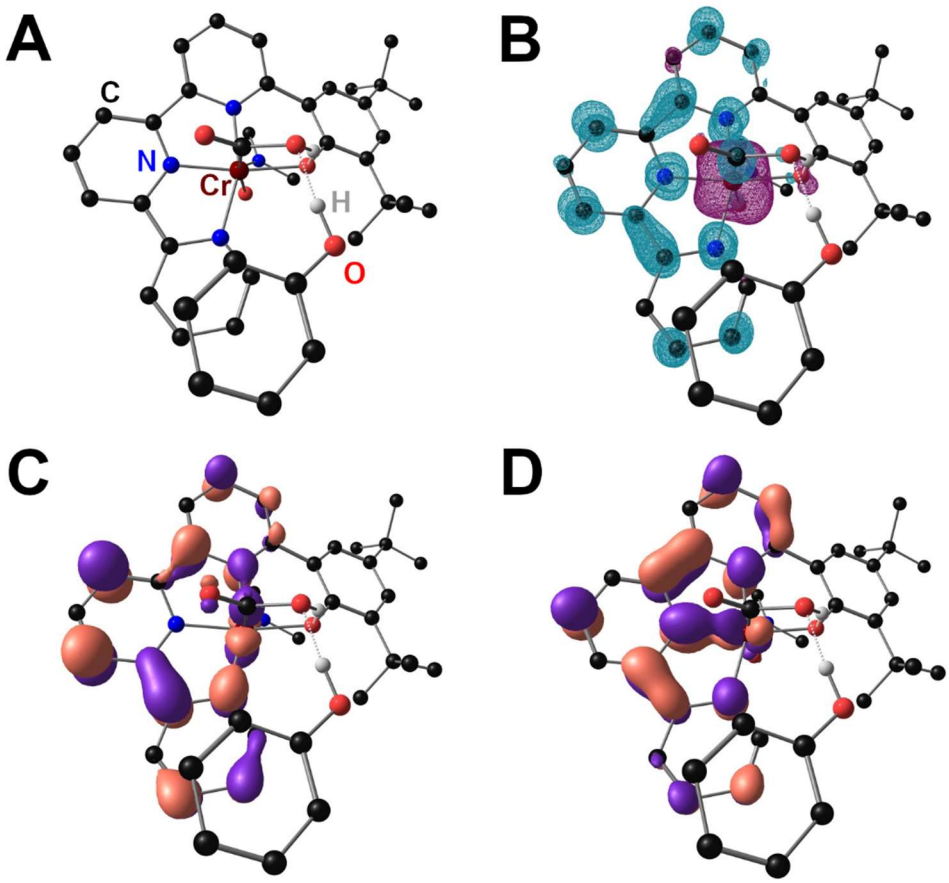

Figure S2.31. Molecular geometry (**A**), spin density (**B**) and SOMO (*β*) (**C**) and SOMO^{-1} (*β*) (**D**) of $\mathbf{^{2}_{1}}$Cr(CO$_2$H)·PhOH$^{\mathbf{-1}}$. For clarity, tbu groups and H atoms have been omitted.

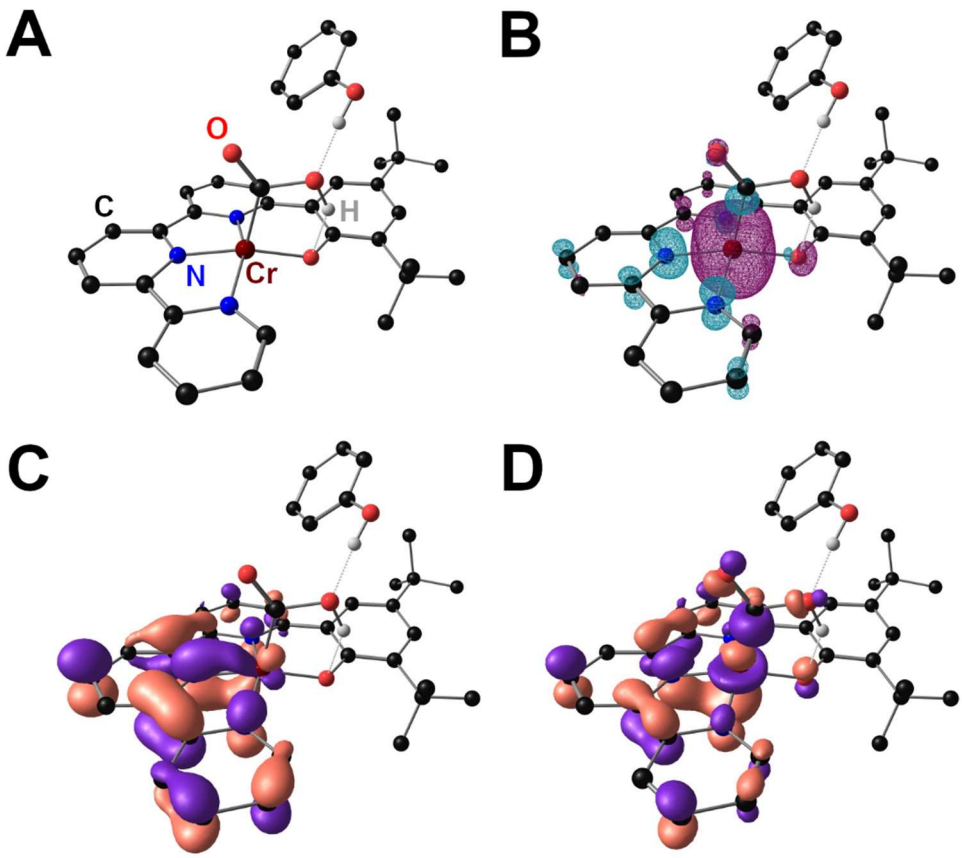

Figure S2.32. Molecular geometry (**A**), spin density (**B**) and SOMO (β) (**C**) and SOMO^{-1} (α) (**D**) of $^{\mathbf{4}}_{\mathbf{0}}$Cr(CO$_2$H)·PhOH$^{\mathbf{-1}}_{\square}$. For clarity, tbu groups and H atoms have been omitted.

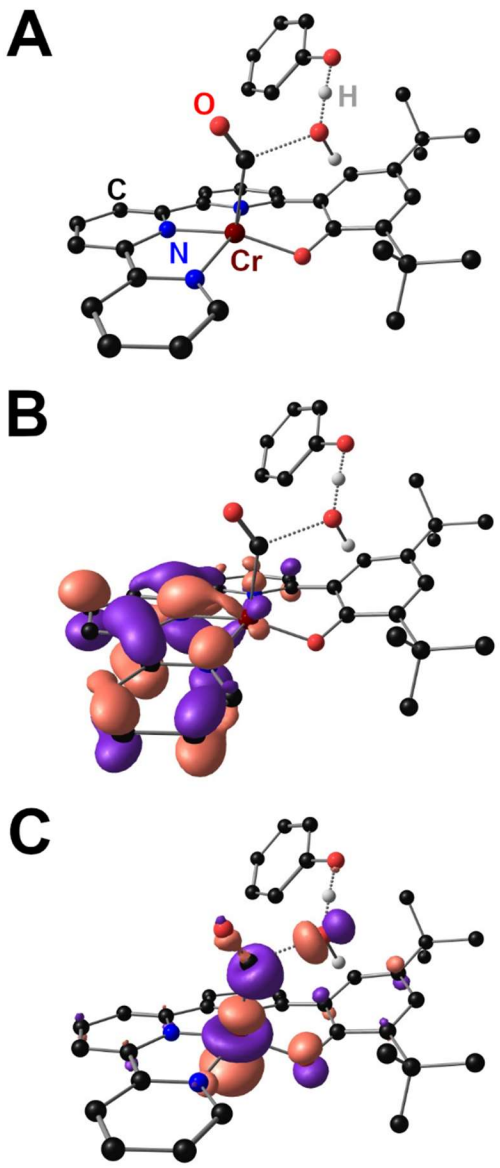

Figure S2.33. Molecular geometry (**A**), SOMO (*β*) (**B**) and SOMO−1 (*α*) (**C**) of $^{\mathbf{4}}_{\mathbf{0}}$TS3$^{\mathbf{-1}}_{\square}$. For clarity, tbu groups and H atoms have been omitted.

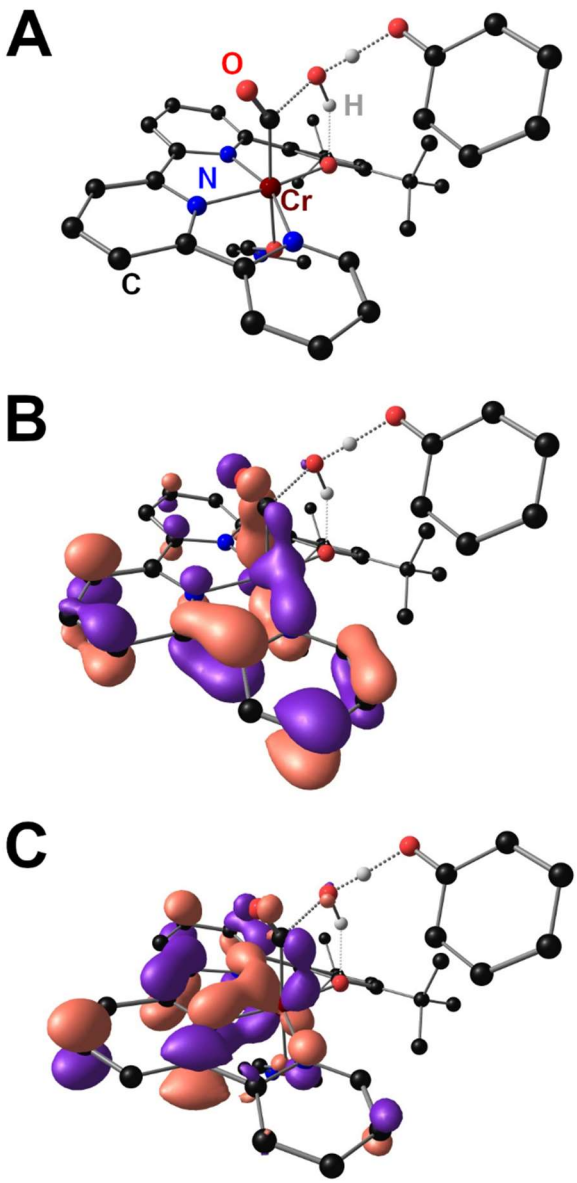

Figure S2.34. Molecular geometry (**A**), SOMO (*β*) (**B**) and SOMO−1 (*β*) (**C**) of $^{\mathbf{2}}_{\mathbf{1}}$TS3$^{\mathbf{-1}}_{\square}$. For clarity, tbu groups and H atoms have been omitted.

Table S2.7. Comparison of B3LYP and RevTPSS triple zeta SCF energies, in Hartree, relative energies in kcal/mol.

Species	B3LYP	RevTPSS	B3LYP (kcal/mol)	RevTPSS (kcal/mol)
$^{4}_{1}\mathbf{Cr}^{0}$	−2656.60194657	−2655.92742124	0.0	0.0
$^{6}_{1}\mathbf{Cr}^{0}$	−2656.59162488	−2655.91254116	6.5	9.3
$^{3}_{1}\mathbf{Cr}^{-1}$	−2656.69048036	−2656.01640600	0.0	0.0
$^{5}_{1}\mathbf{Cr}^{-1}$	−2656.68341960	−2656.00749525	4.4	5.6
$^{7}_{1}\mathbf{Cr}^{-1}$	−2656.67780096	−2655.99716419	8.0	12.1
$^{1}_{0}\mathbf{Cr}^{-1}{}_{*}$	-2407.977131	n/a	37.3	
$^{3}_{0}\mathbf{Cr}^{-1}$	−2408.03652308	−2407.43662890	0.0	0.0
$^{5}_{0}\mathbf{Cr}^{-1}$	−2408.03080006	−2407.43008860	3.6	4.1
$^{7}_{0}\mathbf{Cr}^{-1}$	−2408.02468900	−2407.41963475	7.4	10.7
$^{3}_{0}\mathbf{CrCO_2}^{-1}$	−2596.73019452	−2596.08907217	0.0	0.0
$^{5}_{0}\mathbf{CrCO_2}^{-1}$	−2596.72234300	−2596.07328357	4.9	9.9
$^{3}_{1}\mathbf{CrCO_2{\cdot}PhOH}^{-1}$	−3153.03335400	−3152.22879139	0.0	0.0
$^{5}_{1}\mathbf{CrCO_2{\cdot}PhOH}^{-1}$	−3153.02575958	−3152.21284392	4.8	10.0
$^{3}_{1}\mathbf{CrCO_2H}^{0}$	−2845.88063286	−2845.15961583	0.0	0.0
$^{5}_{1}\mathbf{CrCO_2H}^{0}$	−2845.87149601	−2845.14660783	5.7	8.2
$^{2}_{1}\mathbf{CrCO_2H}^{-1}$	−2845.97920700	−2845.25545291	0.0	0.0
$^{4}_{1}\mathbf{CrCO_2H}^{-1}$	−2845.97219387	−2845.24606945	4.4	5.9
$^{6}_{1}\mathbf{CrCO_2H}^{-1}$	−2845.96446337	−2845.23647140	9.3	11.9
$^{2}_{1}\mathbf{CrCO}^{0}$	−2769.98254100	−2769.30606300	0.0	0.0
$^{4}_{1}\mathbf{CrCO}^{0}$	−2769.96697965	−2769.28513375	9.8	13.1
$^{6}_{1}\mathbf{CrCO}^{0}$	−2769.96245460	−2769.25619377	12.6	31.3

* - spin-contaminated; (S**2 before annihilation 2.0726, after 5.8791)

2.8 References

1. DuBois, D. L., Development of Molecular Electrocatalysts for Energy Storage. *Inorg. Chem.* **2014,** *53* (8), 3935-3960.
2. Das, B.; Thapper, A.; Ott, S.; Colbran, S. B., Structural features of molecular electrocatalysts in multi-electron redox processes for renewable energy – recent advances. *Sustain. Energy Fuels* **2019,** *3* (9), 2159-2175.
3. IPCC. *Global Warming of 1.5 °C. An IPCC Special Report*; World Meterological Organization: Geneva, Switzerland, 2018.
4. Jiang, C.; Nichols, A. W.; Machan, C. W., A look at periodic trends in d-block molecular electrocatalysts for CO_2 reduction. *Dalton Trans.* **2019,** *48*, 9454-9468.
5. Francke, R.; Schille, B.; Roemelt, M., Homogeneously Catalyzed Electroreduction of Carbon Dioxide—Methods, Mechanisms, and Catalysts. *Chem. Rev.* **2018,** *118* (9), 4631-4701.
6. Kinzel, N. W.; Werlé, C.; Leitner, W., Transition Metal Complexes as Catalysts for the Electroconversion of CO_2: An Organometallic Perspective. *Angew. Chem., Int. Ed.* **2021,** *60* (21), 11628-11686.
7. West, N. M.; Miller, A. J. M.; Labinger, J. A.; Bercaw, J. E., Homogeneous syngas conversion. *Coord. Chem. Rev.* **2011,** *255* (7), 881-898.
8. Kalck, P.; Le Berre, C.; Serp, P., Recent advances in the methanol carbonylation reaction into acetic acid. *Coord. Chem. Rev.* **2020,** *402*, 213078.
9. Hood, D. M.; Johnson, R. A.; Carpenter, A. E.; Younker, J. M.; Vinyard, D. J.; Stanley, G. G., Highly active cationic cobalt(II) hydroformylation catalysts. *Science* **2020,** *367* (6477), 542-548.
10. Clark, M. L.; Grice, K. A.; Moore, C. E.; Rheingold, A. L.; Kubiak, C. P., Electrocatalytic CO_2 reduction by M(bpy-R)($CO)_4$ (M = Mo, W; R = H, *t*Bu) complexes. Electrochemical, spectroscopic, and computational studies and comparison with group 7 catalysts. *Chem. Sci.* **2014,** *5* (5), 1894-1900.
11. Ramos Sende, J. A.; Arana, C. R.; Hernandez, L.; Potts, K. T.; Keshevarz-K, M.; Abruna, H. D., Electrocatalysis of CO_2 Reduction in Aqueous Media at Electrodes Modified with Electropolymerized Films of Vinylterpyridine Complexes of Transition Metals. *Inorg. Chem.* **1995,** *34* (12), 3339-3348.
12. Pickett, C. J.; Pletcher, D., Electrochemical reduction of Group 6 metal hexacarbonyls in aprotic solvents. *J. Chem. Soc., Dalton Trans.* **1976,** (8), 749-752.
13. Maia, L. B.; Fonseca, L.; Moura, I.; Moura, J. J. G., Reduction of Carbon Dioxide by a Molybdenum-Containing Formate Dehydrogenase: A Kinetic and Mechanistic Study. *J. Am. Chem. Soc.* **2016,** *138* (28), 8834-8846.
14. Tory, J.; Setterfield-Price, B.; Dryfe, R. A. W.; Hartl, F., [$M(CO)_4$(2,2′-bipyridine)] (M = Cr, Mo, W) Complexes as Efficient Catalysts for Electrochemical Reduction of CO_2 at a Gold Electrode. *ChemElectroChem.* **2015,** *2* (2), 213-217.
15. Grice, K. A.; Saucedo, C., Electrocatalytic Reduction of CO_2 by Group 6 $M(CO)_6$ Species without “Non-Innocent” Ligands. *Inorg. Chem.* **2016,** *55* (12), 6240-6246.
16. Neri, G.; Donaldson, P. M.; Cowan, A. J., The Role of Electrode–Catalyst Interactions in Enabling Efficient CO_2 Reduction with Mo(bpy)$(CO)_4$ As Revealed by Vibrational Sum-Frequency Generation Spectroscopy. *J. Am. Chem. Soc.* **2017,** *139* (39), 13791-13797.
17. Mouchfiq, A.; Todorova, T. K.; Dey, S.; Fontecave, M.; Mougel, V., A bioinspired molybdenum–copper molecular catalyst for CO_2 electroreduction. *Chem. Sci.* **2020,** *11* (21), 5503-5510.

18. Hooe, S. L.; Dressel, J. M.; Dickie, D. A.; Machan, C. W., Highly Efficient Electrocatalytic Reduction of CO_2 to CO by a Molecular Chromium Complex. *ACS Catal.* **2020,** *10* (2), 1146-1151.
19. Moreno, J. J.; Hooe, S. L.; Machan, C. W., DFT Study on the Electrocatalytic Reduction of CO_2 to CO by a Molecular Chromium Complex. *Inorg. Chem.* **2021,** *60* (6), 3635-3650.
20. Hooe, S. L.; Moreno, J. J.; Reid, A. G.; Cook, E. N.; Machan, C. W., Mediated Inner-Sphere Electron Transfer Induces Homogeneous Reduction of CO_2 via Through-Space Electronic Conjugation**. *Angew. Chem., Int. Ed.* **2022,** *61* (1), e202109645.
21. Benson, E. E.; Sampson, M. D.; Grice, K. A.; Smieja, J. M.; Froehlich, J. D.; Friebel, D.; Keith, J. A.; Carter, E. A.; Nilsson, A.; Kubiak, C. P., The Electronic States of Rhenium Bipyridyl Electrocatalysts for CO_2 Reduction as Revealed by X-ray Absorption Spectroscopy and Computational Quantum Chemistry. *Angew. Chem., Int. Ed.* **2013,** *52* (18), 4841-4844.
22. Smieja, J. M.; Benson, E. E.; Kumar, B.; Grice, K. A.; Seu, C. S.; Miller, A. J. M.; Mayer, J. M.; Kubiak, C. P., Kinetic and structural studies, origins of selectivity, and interfacial charge transfer in the artificial photosynthesis of CO. *Proc. Natl. Acad. Sci. U.S.A.* **2012,** *109* (39), 15646-15650.
23. Derrick, J. S.; Loipersberger, M.; Chatterjee, R.; Iovan, D. A.; Smith, P. T.; Chakarawet, K.; Yano, J.; Long, J. R.; Head-Gordon, M.; Chang, C. J., Metal–Ligand Cooperativity via Exchange Coupling Promotes Iron- Catalyzed Electrochemical CO_2 Reduction at Low Overpotentials. *J. Am. Chem. Soc.* **2020,** *142* (48), 20489-20501.
24. Loipersberger, M.; Cabral, D. G. A.; Chu, D. B. K.; Head-Gordon, M., Mechanistic Insights into Co and Fe Quaterpyridine-Based CO_2 Reduction Catalysts: Metal–Ligand Orbital Interaction as the Key Driving Force for Distinct Pathways. *J. Am. Chem. Soc.* **2021,** *143* (2), 744-763.
25. Keith, J. A.; Grice, K. A.; Kubiak, C. P.; Carter, E. A., Elucidation of the Selectivity of Proton-Dependent Electrocatalytic CO_2 Reduction by fac-Re(bpy)$(CO)_3$Cl. *J. Am. Chem. Soc.* **2013,** *135* (42), 15823-15829.
26. Riplinger, C.; Sampson, M. D.; Ritzmann, A. M.; Kubiak, C. P.; Carter, E. A., Mechanistic Contrasts between Manganese and Rhenium Bipyridine Electrocatalysts for the Reduction of Carbon Dioxide. *J. Am. Chem. Soc.* **2014,** *136* (46), 16285-16298.
27. Cometto, C.; Chen, L.; Lo, P.-K.; Guo, Z.; Lau, K.-C.; Anxolabéhère-Mallart, E.; Fave, C.; Lau, T.-C.; Robert, M., Highly Selective Molecular Catalysts for the CO_2-to-CO Electrochemical Conversion at Very Low Overpotential. Contrasting Fe vs Co Quaterpyridine Complexes upon Mechanistic Studies. *ACS Catal.* **2018,** *8* (4), 3411-3417.
28. Newkome, G. R.; Hager, D. C.; Kiefer, G. E., Chemistry of heterocyclic compounds. Part 119. Synthesis of halogenated terpyridines and incorporation of the terpyridine nucleus into a polyetheral macrocycle. *J. Org. Chem.* **1986,** *51* (6), 850-853.
29. Nielsen, M. F.; Hammerich, O.; Rise, F.; Gogoll, A.; Undheim, K.; Wang, D. N.; Christensen, S. B., The Effect of Hydrogen Bonding between Methyl-Substituted Phenols and Dipolar Aprotic Solvents on the Rate Constants for. *Acta. Chem. Scan.* **1992,** *46*, 883-896.
30. Labrum, N. S.; Chen, C.-H.; Caulton, K. G., A bis-Pyrazolate Pincer on Reduced Cr Deoxygenates CO_2: Selective Capture of the Derived Oxide by Cr^{II}. *Chem. - Eur. J.* **2019,** *25* (33), 7935-7940.
31. Perrotin, P.; Shapiro, P. J.; Williams, M.; Twamley, B., In Search of a Versatile Pathway to ansa-Chromocene Complexes. Synthesis and Characterization of the Highly Unstable ansa-Chromocene Carbonyl Complex $Me_2C(C_5H_4)_2CrCO$. *Organometallics* **2007,** *26* (7), 1823-1826.
32. Becke, A. D., Density-functional thermochemistry. III. The role of exact exchange. *J. Chem. Phys.* **1993,** *98* (7), 5648-5652.

33. Vosko, S. H.; Wilk, L.; Nusair, M., Accurate spin-dependent electron liquid correlation energies for local spin density calculations: a critical analysis. *Can. J. Phys.* **1980,** *58* (8), 1200-1211.
34. Lee, C.; Yang, W.; Parr, R. G., Development of the Colle-Salvetti correlation-energy formula into a functional of the electron density. *Phys. Rev. B* **1988,** *37* (2), 785-789.
35. Stephens, P. J.; Devlin, F. J.; Chabalowski, C. F.; Frisch, M. J., Ab Initio Calculation of Vibrational Absorption and Circular Dichroism Spectra Using Density Functional Force Fields. *J. Phys. Chem.* **1994,** *98* (45), 11623-11627.
36. Perdew, J. P.; Ruzsinszky, A.; Csonka, G. I.; Constantin, L. A.; Sun, J., Workhorse Semilocal Density Functional for Condensed Matter Physics and Quantum Chemistry. *Phys. Rev. Lett.* **2009,** *103* (2), 026403.
37. Perdew, J. P.; Ruzsinszky, A.; Csonka, G. I.; Constantin, L. A.; Sun, J., Erratum: Workhorse Semilocal Density Functional for Condensed Matter Physics and Quantum Chemistry [Phys. Rev. Lett. 103, 026403 (2009)]. *Phys. Rev. Lett.* **2011,** *106* (17), 179902.
38. Neale, S. E.; Pantazis, D. A.; Macgregor, S. A., Accurate computed spin-state energetics for Co(III) complexes: implications for modelling homogeneous catalysis. *Dalton Trans.* **2020,** *49* (19), 6478-6487.
39. Keith, J. A.; Vassilev-Galindo, V.; Cheng, B.; Chmiela, S.; Gastegger, M.; Müller, K.-R.; Tkatchenko, A., Combining Machine Learning and Computational Chemistry for Predictive Insights Into Chemical Systems. *Chem. Rev.* **2021,** *121* (16), 9816-9872.
40. Pegis, M. L.; Wise, C. F.; Martin, D. J.; Mayer, J. M., Oxygen Reduction by Homogeneous Molecular Catalysts and Electrocatalysts. *Chem. Rev.* **2018,** *118* (5), 2340-2391.
41. Pegis, M. L.; Roberts, J. A. S.; Wasylenko, D. J.; Mader, E. A.; Appel, A. M.; Mayer, J. M., Standard Reduction Potentials for Oxygen and Carbon Dioxide Couples in Acetonitrile and *N,N*-Dimethylformamide. *Inorg. Chem.* **2015,** *54* (24), 11883-11888.
42. Roy, S.; Sharma, B.; Pécaut, J.; Simon, P.; Fontecave, M.; Tran, P. D.; Derat, E.; Artero, V., Molecular Cobalt Complexes with Pendant Amines for Selective Electrocatalytic Reduction of Carbon Dioxide to Formic Acid. *J. Am. Chem. Soc.* **2017,** *139* (10), 3685-3696.
43. Matsubara, Y., Unified Benchmarking of Electrocatalysts in Noninnocent Second Coordination Spheres for CO_2 Reduction. *ACS Energy Lett.* **2019,** *4* (8), 1999-2004.
44. Frisch, M. J.; Trucks, G. W.; Schlegel, H. B.; Scuseria, G. E.; Robb, M. A.; Cheeseman, J. R.; Scalmani, G.; Barone, V.; Petersson, G. A.; Nakatsuji, H.; Li, X.; Caricato, M.; Marenich, A. V.; Bloino, J.; Janesko, B. G.; Gomperts, R.; Mennucci, B.; Hratchian, H. P.; Ortiz, J. V.; Izmaylov, A. F.; Sonnenberg, J. L.; Williams; Ding, F.; Lipparini, F.; Egidi, F.; Goings, J.; Peng, B.; Petrone, A.; Henderson, T.; Ranasinghe, D.; Zakrzewski, V. G.; Gao, J.; Rega, N.; Zheng, G.; Liang, W.; Hada, M.; Ehara, M.; Toyota, K.; Fukuda, R.; Hasegawa, J.; Ishida, M.; Nakajima, T.; Honda, Y.; Kitao, O.; Nakai, H.; Vreven, T.; Throssell, K.; Montgomery Jr., J. A.; Peralta, J. E.; Ogliaro, F.; Bearpark, M. J.; Heyd, J. J.; Brothers, E. N.; Kudin, K. N.; Staroverov, V. N.; Keith, T. A.; Kobayashi, R.; Normand, J.; Raghavachari, K.; Rendell, A. P.; Burant, J. C.; Iyengar, S. S.; Tomasi, J.; Cossi, M.; Millam, J. M.; Klene, M.; Adamo, C.; Cammi, R.; Ochterski, J. W.; Martin, R. L.; Morokuma, K.; Farkas, O.; Foresman, J. B.; Fox, D. J. *Gaussian 16 Rev. B.01*, Wallingford, CT, 2016.
45. Weigend, F.; Ahlrichs, R., Balanced basis sets of split valence, triple zeta valence and quadruple zeta valence quality for H to Rn: Design and assessment of accuracy. *Phys. Chem. Chem. Phys.* **2005,** *7* (18), 3297-3305.
46. Weigend, F., Accurate Coulomb-fitting basis sets for H to Rn. *Phys. Chem. Chem. Phys.* **2006,** *8* (9), 1057-1065.
47. Grimme, S.; Antony, J.; Ehrlich, S.; Krieg, H., A consistent and accurate ab initio parametrization of density functional dispersion correction (DFT-D) for the 94 elements H-Pu. *J. Chem. Phys.* **2010,** *132* (15), 154104.

48. Cossi, M.; Rega, N.; Scalmani, G.; Barone, V., Energies, structures, and electronic properties of molecules in solution with the C-PCM solvation model. *J. Comput. Chem.* **2003,** *24* (6), 669-681.
49. Barone, V.; Cossi, M., Quantum Calculation of Molecular Energies and Energy Gradients in Solution by a Conductor Solvent Model. *J. Phys. Chem. A* **1998,** *102* (11), 1995-2001.
50. Ribeiro, R. F.; Marenich, A. V.; Cramer, C. J.; Truhlar, D. G., Use of Solution-Phase Vibrational Frequencies in Continuum Models for the Free Energy of Solvation. *J. Phys. Chem. B* **2011,** *115* (49), 14556-14562.
51. Luchini, G.; Alegre-Requena, J.; Funes-Ardoiz, I.; Rodríguez-Guerra, J.; Chen, J. T.; Paton, R. *Goodvibes v3.0.1*, 2019.
52. Grimme, S., Supramolecular Binding Thermodynamics by Dispersion-Corrected Density Functional Theory. *Chem. – Eur. J.* **2012,** *18* (32), 9955-9964.
53. Li, Y.-P.; Gomes, J.; Mallikarjun Sharada, S.; Bell, A. T.; Head-Gordon, M., Improved Force-Field Parameters for QM/MM Simulations of the Energies of Adsorption for Molecules in Zeolites and a Free Rotor Correction to the Rigid Rotor Harmonic Oscillator Model for Adsorption Enthalpies. *J. Phys. Chem. C* **2015,** *119* (4), 1840-1850.
54. Costentin, C.; Drouet, S.; Robert, M.; Savéant, J.-M., Turnover Numbers, Turnover Frequencies, and Overpotential in Molecular Catalysis of Electrochemical Reactions. Cyclic Voltammetry and Preparative-Scale Electrolysis. *J. Am. Chem. Soc.* **2012,** *134* (27), 11235-11242.
55. Costentin, C.; Drouet, S.; Robert, M.; Savéant, J.-M., Correction to Turnover Numbers, Turnover Frequencies, and Overpotential in Molecular Catalysis of Electrochemical Reactions. Cyclic Voltammetry and Preparative-Scale Electrolysis. *J. Am. Chem. Soc.* **2012,** *134* (48), 19949-19950.
56. Franco, F.; Pinto, M. F.; Royo, B.; Lloret-Fillol, J., A Highly Active N-Heterocyclic Carbene Manganese(I) Complex for Selective Electrocatalytic CO_2 Reduction to CO. *Angew. Chem., Int. Ed.* **2018,** *57* (17), 4603-4606.
57. Hooe, S. L.; Rheingold, A. L.; Machan, C. W., Electrocatalytic Reduction of Dioxygen to Hydrogen Peroxide by a Molecular Manganese Complex with a Bipyridine-Containing Schiff Base Ligand. *J. Am. Chem. Soc.* **2018,** *140* (9), 3232-3241.
58. Grant, D. H., Paramagnetic Susceptibility by NMR: The "Solvent Correction" Reexamined. *J. Chem. Educ.* **1995,** *72* (1), 39.
59. Bain, G. A.; Berry, J. F., Diamagnetic corrections and Pascal's constants. *J. Chem. Educ.* **2008,** *85* (4), 532-536.
60. Bruker *Saint; SADABS;TWINABS; APEX3*, Bruker AXS Inc.: Madison, Wisconsin, USA, 2012.
61. Sheldrick, G., SHELXT - Integrated space-group and crystal-structure determination. *Acta Cryst.* **2015,** *71* (1), 3-8.
62. Dolomanov, O. V.; Bourhis, L. J.; Gildea, R. J.; Howard, J. A. K.; Puschmann, H., OLEX2: a complete structure solution, refinement and analysis program. *J. Appl. Cryst.* **2009,** *42* (2), 339-341.

Chapter 3

Inverse Potential Scaling in Co-electrocatalytic Activity for CO_2 Reduction Through Redox Mediator Tuning and Catalyst Design

Containing work originally published in:

Reid, A. G.; Moreno, J. J.; Hooe, S. H.; Baugh, K. R.; Thomas, I. H.; Dickie, D. A.; Machan, C. W., *Chemical Science* **2022**, *13*, 9595-9606.

3.1 Abstract

Electrocatalytic CO_2 reduction is an attractive strategy to mitigate the continuous rise in atmospheric CO_2 concentrations and generate value-added chemical products. A possible strategy to increase the activity of molecular systems for these reactions is the co-catalytic use of redox mediators (RMs), which direct reducing equivalents from the electrode surface to the active site. Recently, we demonstrated that a sulfone-based RM could trigger co-electrocatalytic CO_2 reduction via an inner-sphere mechanism under aprotic conditions. Here, we provide support for inner-sphere cooperativity under protic conditions by synthetically modulating the mediator to increase activity at lower overpotentials (inverse potential scaling). Furthermore, we show that both the intrinsic and co-catalytic performance of the Cr-centered catalyst can be enhanced by ligand design. By tuning both the Cr-centered catalyst and RM appropriately, an optimized co-electrocatalytic system with quantitative selectivity for CO at an overpotential (η) of 280 mV and turnover frequency (TOF) of 194 s^{-1} is obtained, representing a three-fold increase in co-catalytic activity at 130 mV lower overpotential than our original report. Importantly, this work lays the foundation of a powerful tool for developing co-catalytic systems for homogeneous electrochemical reactions.

3.2 Introduction

The interest in electrochemical carbon dioxide (CO_2) reduction is two-fold: the association of climate change with the global rise in atmospheric CO_2 concentrations and the increasing need to transition from non-renewable fossil fuel-derived hydrocarbons as chemical feedstocks and energy sources.[1] The reduction of CO_2 to carbon monoxide (CO) could help to mitigate both of these issues through conversion of CO_2 into useful building blocks for the synthesis of chemical feedstocks and fuels while using renewable energy sources, such as sunlight and wind, as the source of electricity.[2, 3] In recent years, the focus of molecular electrocatalyst development has

shifted towards the use of abundant first-row transition metal centers to address the need for cost-effective and scalable systems.[4-8]

Nature frequently leverages co-catalytic systems during reactions involving electron transfer. For example, during cellular respiration the electron transport chain uses several redox mediators (RMs) to shuttle protons and electrons between different redox-active cofactors. The final step of this cycle involves ubiquinone shuttling electrons and protons to cytochrome *c* oxidase as a part of the overall reduction of dioxygen to water.[9] The use of RMs is necessary for enzymatic systems to transfer electron equivalents due to the limitations associated with relatively stationary active sites buried within protein superstructures that are spatially separated from redox centers in the electron transport chain.[10] Co-catalytic systems which utilize RMs have been successfully developed for homogeneous O_2 reduction, increasing the overall activity of the system and shifting the selectivity of the reaction.[11-13] In these homogeneous systems, RMs deliver redox equivalents to the catalyst active sites with greater mobility than is possible in biological systems. Parallel developments have enabled electrocatalytic N_2 reduction, where weak C–H bonds are generated in a metallocene-based RM to assist in the cleavage of inert bonds,[14] and alcohol oxidation, where RMs are utilized to facilitate hydrogen atom transfer processes that work in conjunction with the catalyst.[15-17] Additional work has focused on the use of small-molecule RMs to enhance the activation of photosensitizers,[18-23] as catalysts in electrosynthesis,[24] or to enhance the CO_2 reduction reaction on heterogeneous surfaces.[25, 26] Smith *et al.* reported the first homogeneous co-electrocatalytic system for the reduction of CO_2 using a NADH analogue as the RM and an Fe tetraarylporphyrin complex that shows enhanced catalytic activity as a combined system.[27] The NADH analogue transfers protons and electrons during the reaction, although the exact reaction sequence is currently unknown.

Recently, we reported a co-electrocatalytic system comprised of a chromium-centered catalyst, Cr(^{tbu}dhbpy)Cl(H_2O) (**1**), where the ligand precursor is (^{tbu}dhbpy($H)_2$) is 6,6'-di(3,5-di-*tert*-butyl-2-hydroxybenzene)-2,2'-bipyridine,[8, 28] and dibenzothiophene-5,5-dioxide (DBTD) as the

RM.[29] When both species are present under aprotic conditions, the co-catalytic reductive disproportionation of two equivalents of CO_2 occurs to produce CO and carbonate (CO_3^{2-}). Because neither the catalyst nor the mediator demonstrates intrinsic reactivity for CO_2 reduction under these conditions, an outer-sphere mechanism could be excluded. For clarity, the following labeling scheme will be used for Cr complexes ${}^{\text{multiplicity}}_{\#\text{ bound DMF}}\mathbf{Cr}(\mathbf{axial\ ligands})^{\text{charge}}_{\square}$ and for RM species ${}^{\text{multiplicity}}_{\square}\mathbf{RM}^{\text{charge}}_{\square}$; the ligand frameworks do not change the κ^4 coordination mode during the reaction, so it is omitted in the notation where possible for clarity. These studies suggested that that the assembly of ${}^{2}_{\square}\mathbf{DBTD}^{-1}_{\square}$ with an intermediate bis-CO_2 adduct, ${}^{4}_{0}\mathbf{Cr}(\mathbf{CO_2CO_2})^{-1}_{\square}$, through inner-sphere coordination produces a dianion, ${}^{3}_{0}\mathbf{Cr}(\mathbf{CO_2CO_2})(\mathbf{DBTD})^{-2}_{\square}$, which mediates carbon–oxygen bond cleavage. Association between the catalyst and mediator monoanions under aprotic conditions is driven by contributions from dispersive interactions, Cr–O bond formation between the metal complex and $[DBTD]^-$, and through-space electronic conjugation (TSEC, **Figure 3.1**) between the ligand backbone of the catalyst and the RM.[29] TSEC is a non-covalent interaction between cofacial aromatic rings based on the interaction of their spatially delocalized π electrons.[30]

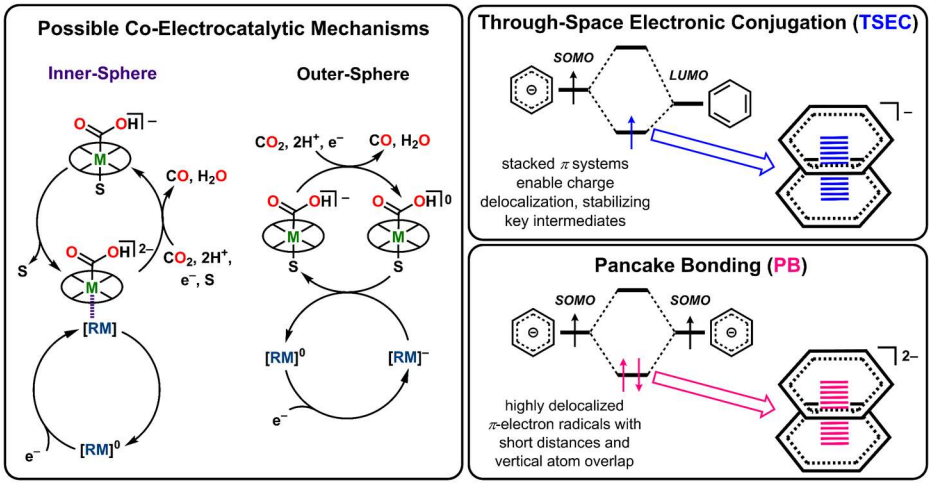

Figure 3.1. Overview of protic CO_2 reduction co-electrocatalysis, through-space electronic conjugation, and pancake bonding interactions relevant to the results presented here.

When phenol (PhOH) is added as a sacrificial proton source under co-catalytic conditions there is an increase in activity compared to when only **1** or DBTD is present.[8, 29] It was proposed that the association under protic conditions is driven in part by pancake bonding (PB, **Figure 3.1**), which is a parallel π-stacking interaction between planar aromatic moieties with significant radical character.[31-34] Under co-electrocatalytic conditions, PB favors an equilibrium solvent displacement from $^{3}_{1}\mathbf{Cr}(\mathbf{CO_2H})^{-1}$ by $^{2}\mathbf{DBTD}^{-1}$ to form the dianion $^{4}_{0}\mathbf{Cr}(\mathbf{CO_2H})(\mathbf{DBTD})^{-2}$, with contributions from chromium–sulfone coordination and dispersive interactions. In this bimolecular assembly under protic conditions, both the $[RM]^-$ and the bipyridine (bpy) fragment of the $[Cr–CO_2H]^-$ complex are formally reduced by one electron, consistent with PB. However, since the Cr catalyst itself has intrinsic CO_2 reduction activity when PhOH is present, we could not definitively discard the possibility that $[DBTD]^-$ enhanced reactivity by outer-sphere electron transfer (**Figure 3.1**). We reasoned that the strength of the interaction between the RM and Cr complex could be increased by synthetic means, since it has been noted that the strength of PB generally scales with respect to the extent of π-electron delocalization in the participating radicals and their steric protection from sigma-bonding interactions.[34]

Here, we compare the activity and overpotential (η) of two Cr catalysts with four RM architectures, to better understand and optimize the co-electrocatalytic system under protic conditions. These results suggest that extended aromatic character in the RM structure has the dual benefit of lowering its standard reduction potential while also favoring its binding to the Cr complex, resulting in inverse reaction scaling where increased activity occurs at lower overpotentials. We propose that mediator designs which extend aromatic character and match redox potential with the metal complex induce stronger interactions that improve the stability and activity of co-electrocatalysis, without requiring changes in the coordinating strength of the axial sulfone ligand.

3.3 Results

3.3.1 Electrochemistry of Cr Catalysts

The synthesis of the (^{tbu}dhbpy(H)$_2$) ligand and its subsequent metalation to generate Cr(^{tbu}dhbpy)Cl(H$_2$O) (**1**) were carried out as previously reported (**Figure S3.1**).[8] To improve the catalyst activity we synthesized a ligand framework with electron-donating *tert*-butyl groups on the bpy-backbone, 6,6′-di(3,5-di-*tert*-butyl-2-hydroxybenzene)-4,4′-di-*tert*-butyl-2,2′-bipyridine (^{tbu}dh^{tbu}bpy(H)$_2$) which allows us to probe ligand electronic effects on the catalyst and co-catalytic system (see **Section 3.7** and **Figures S3.2-S3.4**). The metalation of (^{tbu}dh^{tbu}bpy(H)$_2$) to form Cr(^{tbu}dh^{tbu}bpy)Cl(H$_2$O) (**2**) was carried out in a similar fashion to **1** and **2** was characterized by UV-vis (**Figure S3.5**), NMR (**Table S3.3**), electrospray ionization-mass spectrometry (ESI-MS), microanalysis, and single-crystal X-ray diffraction (XRD) studies (**Figure 3.2**).

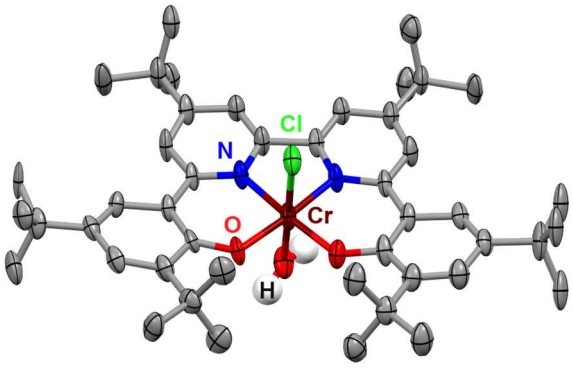

Figure 3.2. Molecular structure of Cr(^{tbu}dh^{tbu}bpy)Cl(H_2O) (**2**) obtained from single-crystal X-ray diffraction studies. Blue = N, red = O, gray = C, green = Cl, maroon = Cr, white = H atoms of bound water molecule; thermal ellipsoids at 50%; ligand H atoms and occluded diethyl ether molecules omitted for clarity; hydrogen atoms of the Cr-bound water molecule were located in the diffraction map and refined isotropically. CCDC 2150930.

Cyclic voltammetry (CV) experiments were performed on **1** and **2** in *N,N*-dimethylformamide (DMF) with 0.1 M tetrabutylammonium hexafluorophosphate ($TBAPF_6$) as the supporting electrolyte. As reported previously, **1** exhibits three redox features under argon (Ar) saturation conditions, E_p = −1.66 and −1.78 V and $E_{1/2}$ = −1.95 V versus the ferrocenium/ferrocene (Fc^+/Fc) reduction potential.[8] Complex **2** also exhibits three redox features, but due to the electron-donating quality of the *tert*-butyl groups on the bpy core of the ligand, all three are located at the more negative potentials of E_p = −1.76 and −1.87 V and $E_{1/2}$ = −2.00 V vs. Fc^+/Fc (**Figure S3.6**). The first two redox features of **1** were shown to be related to one another, previously assigned to the formation of a solvento species resulting from an equilibrium chloride displacement reaction.[8, 28] Due to the consistencies in redox potential, reversibility, and relative current intensities of these features in **2,** the same can be concluded here. As was the case with **1**, the first two reduction features coalesce at scan rates ≥2000 mV/s, which is consistent with this assignment (**Figure S3.7**).

Upon the addition of PhOH under Ar saturation conditions, **1** and **2** demonstrate only a small change in the redox features, suggestive of either hydrogen bonding interactions between the reduced complex and PhOH or increased favorability of chloride anion solvation, but not

formal protonation.[35-37] Under CO_2 saturation without PhOH, there are minimal changes to the redox features for both catalysts, meaning that aprotic CO_2 reduction is not inherent to either **1** or **2**. Variable scan rate analysis under both Ar and CO_2 saturation shows that the electron transfer reaction is diffusion-controlled for **2** at the third reduction feature, indicating a homogenous electrochemical response (**Figures S3.7** and **S3.8**) as was observed previously for **1**.[8]

The similarity of the redox activity between complexes **1** and **2** extends to catalytic behavior: **2** also catalyzes CO_2 reduction at the third redox feature ($E_{cat/2}$ = −2.00 V vs. Fc^+/Fc) in the presence of PhOH. However, **2** more than doubles the amount of current density (1.38 mA/cm^2, **Figure 3.3B**, red) under the same conditions as **1** (0.554 mA/cm^2, **Figure 3.3B**, black). This significant increase in current density comes with a shift of only 50 mV to more negative potentials, increasing the η from 110 mV to 160 mV. Complex **1** was previously found to have first-order concentration dependences with respect to electrocatalytic current for PhOH, catalyst, and CO_2.[8] Performing the same variable concentration experiments with **2** (**Figures S3.9-S3.11**) established that in this system electrocatalytic current also has first-order concentration dependences with respect to PhOH (**Figure S3.9**), catalyst (**Figure S3.10**), and CO_2 (**Figure S3.11**).

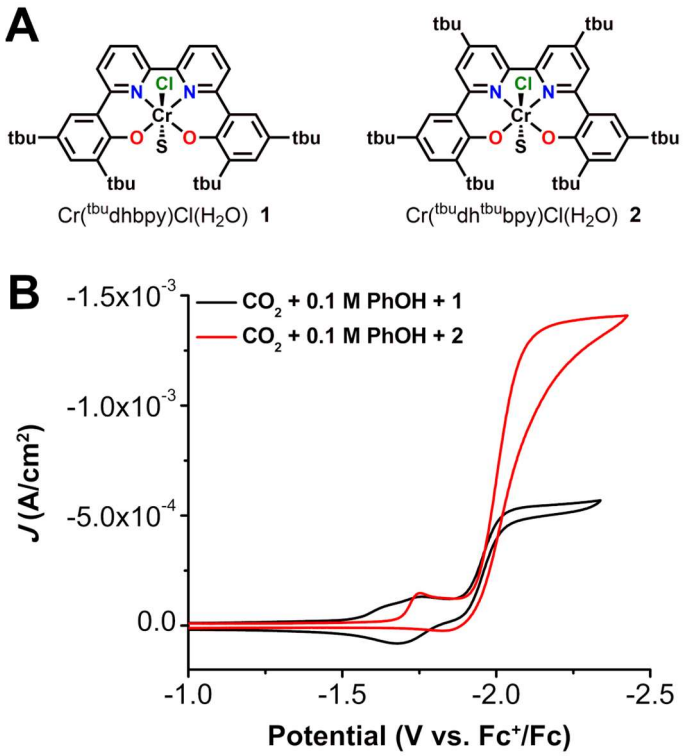

Figure 3.3. (**A**) Structures of Cr(^{tbu}dhbpy)Cl(H_2O) **1** and Cr(^{tbu}dh^{tbu}bpy)Cl(H_2O) **2**, where S is a solvent adduct of water or DMF. (**B**) Comparison of CVs for different Cr catalysts (1.0 mM) under CO_2 saturation conditions and 0.1 M PhOH. Conditions: 0.1 M $TBAPF_6$/DMF; glassy carbon disc working electrode, glassy carbon rod counter electrode, Ag/AgCl pseudoreference electrode; referenced to Fc^+/Fc internal standard; 100 mV/s scan rate.

To quantify the product selectivity and turnover frequency (TOF) of **2**, controlled potential electrolysis (CPE) was performed with added PhOH under CO_2 saturation conditions (**Figure S3.12**). Gaseous products were quantified by gas chromatography (GC, see **SI**). The results of this experiment (**Table S3.4**) show that **2** is selectively reducing CO_2 to CO under these conditions with 95 ± 8% FE_{CO} over 13.0 turnovers (turnover represents two electron equivalents of charge passed for each equivalent of **2** in solution) with a TOF_{CPE} of 9.29 s^{-1} which is in good agreement with the TOF_{max} value of 14 ± 1 s^{-1} determined by CV (**Figures S3.13-3.14** and **Table S3.5**).[38] Note that in all instances turnovers have been determined to show the catalytic nature of the process and *do not represent a measurement to complete loss of activity*.

3.3.2 Electrochemistry of Redox Mediators

To test the inner-sphere nature of the co-electrocatalytic mechanism we previously reported and further optimize the system,[29] we prepared three new aromatic sulfone derivatives to establish structure-activity relationships with Cr catalysts **1** and **2**. Triphenylothiophene-4,4-dioxide (TPTD, **Figure 3.4A**) was synthesized by previously reported methods.[39, 40] Additionally, both 2,8-dimesityldibenzothiophene-5,5-dioxide (Mes_2DBTD) and 2,8-diphenyldibenzothiophene-5,5-dioxide (Ph_2DBTD) (**Figure 3.4A**) were prepared using Pd-catalyzed cross-coupling and characterized by NMR (**Figures S3.15-S3.18**), ESI-MS, microanalysis, and XRD studies (**Figure 3.4A**). CV experiments were carried out under the same conditions as **1** and **2**, in 0.1 M $TBAPF_6$ with DMF as the solvent. Under Ar saturation conditions, DBTD displays a reversible redox feature with an $E_{1/2}$ = −2.25 V versus Fc^+/Fc corresponding to a single-electron event.[29] TPTD, Mes_2DBTD, and Ph_2DBTD also show single reversible one-electron redox features under Ar saturation conditions, but the $E_{1/2}$ values for all three are shifted to more positive potentials compared to DBTD (**Figure 3.4B**). Mes_2DBTD has the most similar redox feature to DBTD with an $E_{1/2}$ = −2.24 V versus Fc^+/Fc, while TPTD and Ph_2DBTD shift to more positive potentials with $E_{1/2}$ = −2.19 V and −2.12 V versus Fc^+/Fc, respectively.

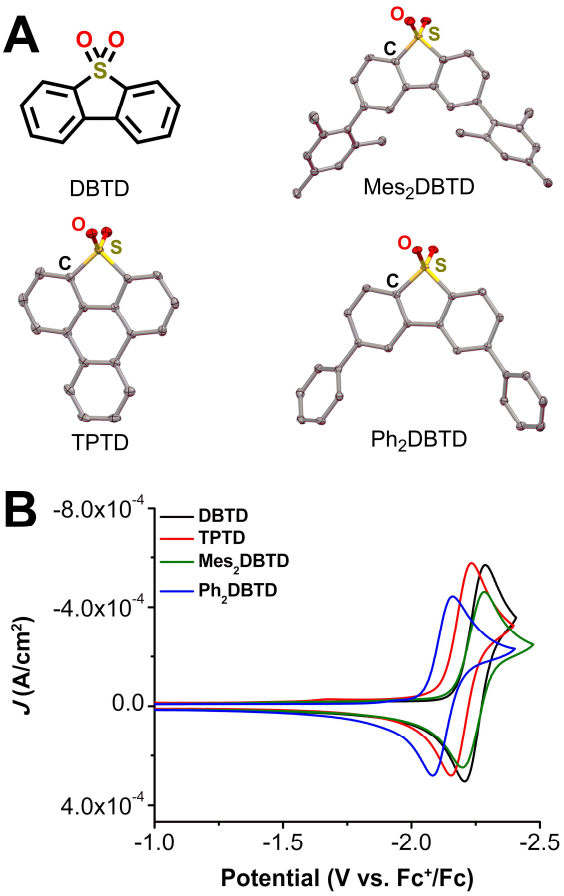

Figure 3.4. (**A**) Structures of redox mediators dibenzothiophene-5,5-dioxide (DBTD), triphenylothiophene-4,4-dioxide (TPTD), 2,8-dimesityldibenzothiophene-5,5-dioxide (Mes_2DBTD), and 2,8-diphenyldibenzothiophene-5,5-dioxide (Ph_2DBTD). TPTD, Mes_2DBTD, and Ph_2DBTD obtained from single-crystal X-ray diffraction studies. Yellow = S, red = O, gray = C; thermal ellipsoids at 50%; H atoms and occluded toluene molecules (Ph_2DBTD only) omitted for clarity. CCDC 215497-215499. (**B**) Comparison of CVs for different RMs (2.5 mM) under Ar saturation. Conditions: 0.1 M $TBAPF_6$/DMF; glassy carbon disc working electrode, glassy carbon rod counter electrode, Ag/AgCl pseudoreference electrode; referenced to Fc^+/Fc internal standard; 100 mV/s scan rate.

Control experiments performed with TPTD, Mes_2DBTD, and Ph_2DBTD demonstrate little reactivity with CO_2 or PhOH on the CV timescale, as was previously observed for analogous experiments with DBTD (**Figures S3.19-S3.21**). Variable scan rate experiments were performed for all four sulfone derivatives to calculate their diffusion coefficients (**Figures S3.22-S3.25**).[41] Unsurprisingly, the experimentally determined diffusion coefficients for these molecules scale with their molecular weight: DBTD (6.22 x 10^{-6} cm^2/s) > TPTD (3.93 x 10^{-6} cm^2/s) > Ph_2DBTD (3.68 x

10^{-6} cm^2/s) > Mes_2DBTD (3.57 x 10^{-6} cm^2/s). **3.3.3 Co-electrocatalysis Under Protic Conditions**

Since the addition of PhOH as a sacrificial proton donor led to a large increase in catalytic activity for **1**+DBTD in previous studies, we sought to see if a similar trend would be observed for **1** with the new RMs and **2** with all four RMs. Briefly, the observed trend in current density under CV conditions for all the RMs when added to a solution of **1** and PhOH can be summarized: DBTD exhibits the greatest amount of current followed by TPTD, and the use of Ph_2DBTD produces more current than Mes_2DBTD *despite having a standard reduction potential which is 120 mV more positive in its one-electron reduction potential* (**Figure 3.5A**). The addition of all four RMs causes a significant increase in current and completely irreversible waveforms. Variable concentration studies were completed for **1**, all four RMs, PhOH, and CO_2. These data show that the observed current is proportional to the concentration of **1** (**Figures S3.29**-**S3.31**), RM (**Figures S3.32**-**S3.34**), a fixed ratio of **1** and RM (**Figures S3.35**-**S3.37**), PhOH (**Figures S3.38**-**S3.40**), and CO_2 (**Figures S3.41**-**S3.43**) where RM is DBTD,[29] TPTD, Mes_2DBTD, or Ph_2DBTD.

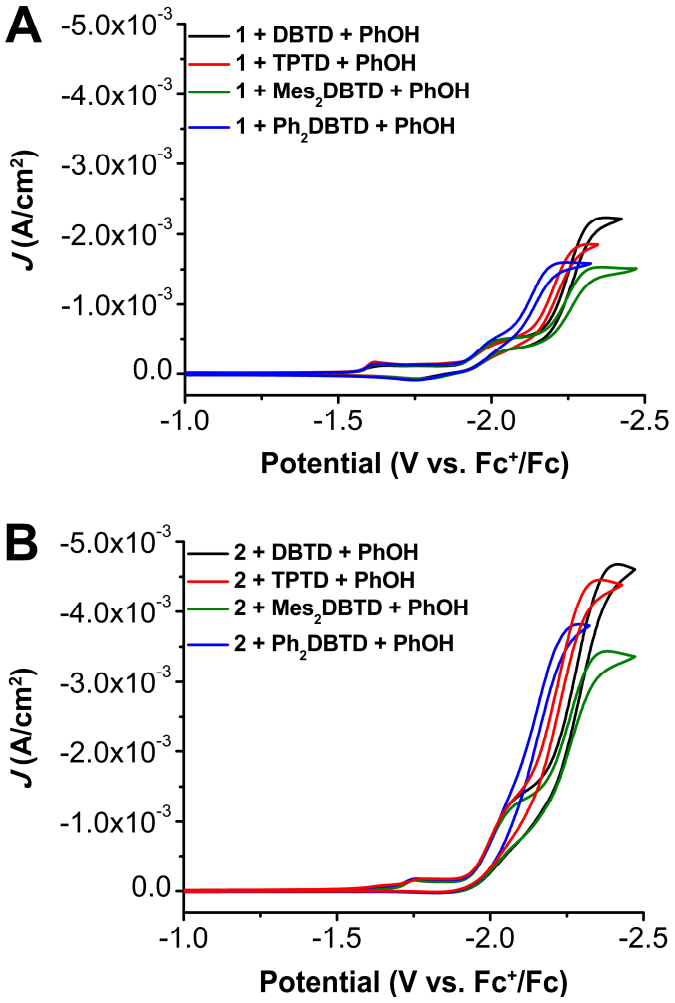

Figure 3.5. CVs of 1.0 mM Cr(^{tbu}dhbpy)Cl(H_2O) **1** (**A**) or Cr(^{tbu}dh^{tbu}bpy)Cl(H_2O) **2** (**B**) with 2.5 mM DBTD (black), TPTD (red), Mes_2DBTD (green), and Ph_2DBTD (blue) as the RM and 0.1 M PhOH under CO_2 saturation conditions. Conditions: 0.1 M $TBAPF_6$/DMF; glassy carbon disc working electrode, glassy carbon rod counter electrode, Ag/AgCl pseudoreference electrode; referenced to Fc^+/Fc internal standard; 100 mV/s scan rate.

When we compare the protic catalytic activity of **2** with all the RMs, we see a similar trend to the activity of **1** observed under comparable conditions. DBTD again shows the largest amount of current followed by TPTD under CV conditions (**Figure 3.5B**). However, for complex **2** there is a significant difference in the activity of the co-catalytic system with Ph_2DBTD relative to that with Mes_2DBTD; Ph_2DBTD again outperforms Mes_2DBTD as a RM when paired with **2** despite its more positive standard reduction potential. Since **2** is an intrinsically better catalyst than **1** under CO_2 saturation with a proton donor, we were delighted to find that co-electrocatalysis involving **2** and

the four RMs under protic conditions also reached much larger current densities than any combination involving **1**. Variable concentration experiments were also performed for **2**, all four RMs, a fixed ratio of complex **2** and all RMs, PhOH, and CO_2, demonstrating proportional increases in current with respect to each reaction component (see **Figures S3.48-S3.67**).

CPE experiments were performed in the presence of 0.12 M PhOH with **1** or **2** and across three concentrations of DBTD, TPTD, Mes_2DBTD, and Ph_2DBTD (**Figures S3.68-S3.74**). The current observed during the CPE experiments with **1** as the catalyst scaled with increasing RM concentration at the tested catalyst:RM ratios of 1:1, 1:3, and 1:5 (Ref[29] and **Figures S3.68-S3.70**). However, this did not hold true for all RM combinations with **2**. When TPTD, Mes_2DBTD, and Ph_2DBTD were used as the RM, the observed current scaled with respect to their concentration. However, when DBTD was used as the RM with **2**, saturation was observed at the 1:3 ratio with no further increase observed at the 1:5 ratio (**Figure S3.71**). Both catalysts with all mediators at all ratios tested were found to be quantitatively selective for CO (**Tables S3.7-S3.27**). However, since the 1:5 (catalyst:RM) produced the largest amount of CO on average for all the systems, we will focus the remainder of our analysis on these experiments. All combinations of the protic co-electrocatalytic systems show high activity with TOF values ranging from 64.0 to 208 s^{-1} (**Table 3.1**), *one to two orders of magnitude higher than the catalysts alone*.

As was the case for DBTD,[29] control CPE experiments for TPTD, Mes_2DBTD, and Ph_2DBTD in the presence of PhOH without catalyst (**Figures S3.75-S3.77**) show non-quantifiable amounts of CO (**Tables S3.28-S3.30**) and no H_2 production, implicating the possibility of a degradation pathway in the absence of the Cr complex. To understand the stability of DBTD during electrolysis, a control CPE of DBTD and PhOH under N_2 was performed (**Figure S3.78**). Characterization of the pre- and post-CPE solution by gas chromatography/mass spectrometry (GC/MS) with appropriate controls demonstrates a minor amount of DBTD is reduced to the corresponding sulfoxide, dibenzothiophene 5-oxide (DBTO; **Figure S3.78**). However, while

comparable analysis of the CPE solution before and after the experiment under catalytic conditions (**1**, DBTD, and PhOH under CO_2) also shows reduction of DBTD to DBTO, an additional product with a mass too high to be dibenzothiophene is detected, implying that reductive C–S bond cleavage is a possible degradation pathway (**Figure S3.79**). It is worth emphasizing that the high catalytic efficiencies observed under all measured conditions suggest that these pathways are minor contributors for all systems (**Table 3.1**). While our original report showed the appearance of aprotic CO_2 reduction with **1** and DBTD, the new systems here showed passivation of the electrode during CPE experiments, suggestive of solubility issues under these conditions.

Table 3.1. Results of CPE experiments with PhOH under CO_2 saturation conditions.

Conditions	Potential (V vs Fc^+/Fc)	FE_{CO} (%)	TOF_{CPE} (s^{-1})	η (V)	Turnovers of CO w.r.t [1 or 2]	Turnovers of CO w.r.t [RM]	i_{cat}/i_p [e]
1 + PhOH[29, a]	–2.30	111 ± 14	7.12	0.11	11.4	–	3.4
1 + DBTD + PhOH[29, b]	–2.30	102 ± 14	65.3	0.41	29	5.8	2.8
1 + TPTD + PhOH[c]	–2.25	98 ± 17	74.5	0.35	25	4.9	3.0
1 + Mes_2DBTD + PhOH[c]	–2.30	98 ± 6	64.0	0.40	19	4.7	2.6
1 + Ph_2DBTD + PhOH[c]	–2.20	100 ± 2	69.3	0.28	22	5.3	3.6
2 + PhOH[d]	–2.30	95 ± 8	9.29	0.16	13	–	8.4
2 + DBTD + PhOH[c]	–2.30	109 ± 9	163	0.41	28	6.5	5.8
2 + TPTD + PhOH[c]	–2.25	97 ± 6	208	0.35	31	8.0	6.6
2 + Mes_2DBTD + PhOH[c]	–2.30	98 ± 4	149	0.40	27	5.9	5.7
2 + Ph_2DBTD + PhOH[c]	–2.20	97 ± 5	194	0.28	35	8.8	7.1

[a] – 0.5 mM catalyst and 0.6 M PhOH; [b] – 0.5 mM catalyst, 2.5 mM RM, and 0.6 M PhOH; [c] – 0.1 mM catalyst, 0.5 mM RM, and 0.12 M PhOH; [d] – 0.1 mM catalyst and 0.12 M PhOH; [e] – scan rate = 100 mV/s.

The systems with **1** and **2** as the catalyst followed the same trend in TOF_{CPE} for CO formation when comparing across the RMs: Mes_2DBTD < DBTD < Ph_2DBTD < TPTD (**Table 3.1**). As introduced above, our proposed inner-sphere mechanism for this co-electrocatalytic reaction relies on the binding of the reduced RM to an intermediate $[Cr–CO_2H]^-$ species before the rate-determining C−OH bond cleavage step.[29] Although all RMs are reducing enough to transfer electron equivalents via an outer-sphere mechanism, the data presented in **Table 3.1** are most consistent with the predominance of an inner-sphere RM pathway: the observed co-catalytic activity does not scale with the reduction potential of the RMs or their diffusion coefficients. For a purely outer-sphere mechanism, conformity to a Marcus theory-type model would be expected, where increased electrochemical driving force would equate to an increased rate of reaction (under the assumption that the inverted region or diffusion limit are not reached under experimental conditions).[42] Instead, the two RMs with the most positive standard reduction potentials (TPTD and Ph_2DBTD) demonstrate the greatest activity. Likewise, if outer-sphere electron transfer was the primary reaction pathway, the relatively slowly diffusing Ph_2DBTD would be expected to show decreased activity compared to DBTD, however an opposite trend is observed experimentally. The relatively limited performance of the Mes_2DBTD derivative despite a similar reduction potential to DBTD suggests that sterically encumbering the dibenzothiophene-5,5-dioxide core has a kinetic effect, which is also consistent with an inner-sphere pathway causing the greatest activity enhancement. The optimized combination of **2**+Ph_2DBTD under protic conditions achieves a TOF of 194 s^{-1} at an η of 280 mV, which demonstrates a three-fold increase in activity at an η which is 130 mV lower in comparison to the previous system with **1** and DBTD.[29]

The trend in activity data derived from CPE is at first glance different than the overall current trend observed in the CV data (**Figure 3.5**). However, homogeneous current density is dependent on the diffusion coefficients of all reaction components under experimental conditions.

In an effort to account for the effect the diffusion coefficients have on the observed trend in the CV data, we have calculated the value of i_{cat}/i_p (i_{cat} = catalytic plateau current and i_p = Faradaic current) for each of the co-catalytic systems at the redox feature of the respective mediators (**Table 3.1** and **Figure S3.80**). This experimental value can be used to calculate a TOF_{max} value from CV data,[43] however, since the RMs and Cr complexes do not interact under Faradaic conditions, we are unable to use this method since diffusion coefficient and concentration are not properly normalized by the procedure. Therefore, the i_{cat}/i_p ratio can only qualitatively represent relative catalytic activity when compared across systems. The trend observed for the i_{cat}/i_p ratios is generally consistent with the TOF_{CPE}: the co-catalytic Ph_2DBTD and TPTD systems have larger activities than the other RMs.

3.4 Computational Studies

To gain insight into the assembly of RMs and catalysts, DFT calculations were done with the Gaussian 16 package at the B3LYP-D3(BJ)/def2-tzvp//B3LYP-D3(BJ)/def2-svp level of theory (see **Section 3.7** for details).[44-52] As previously reported,[29] including dispersion corrections at the optimization stage is of paramount importance due to the key role of non-covalent interactions. The free energies of formation of the dianionic ${}^{4}_{0}\mathbf{Cr}(\mathbf{CO_2H})(\mathbf{RM})^{-2}_{\square}$ assemblies for **1** and **2** summarized by **Eq (3.1)**, where ${}^{multiplicity}_{\#\ bound\ DMF}\boldsymbol{Cr}(\boldsymbol{axial\ ligands})^{charge}_{\square}$, are collected in **Table 3.2**.

$$ {}^{3}_{1}\mathbf{Cr}(\mathbf{CO_2H})^{-1}_{\square} + {}^{2}_{\square}\mathbf{RM}^{-1}_{\square} \overset{\boldsymbol{K_{RM}}}{\rightleftharpoons} {}^{4}_{0}\mathbf{Cr}(\mathbf{CO_2H})(\mathbf{RM})^{-2}_{\square} + \mathbf{DMF} \qquad \textbf{Eq (3.1)} $$

Table 3.2. Calculated free energies of $[RM]^-$ ligand displacement reaction summarized by **Eq (3.1)**, calculated free energies of activation for the rate-limiting C−OH bond cleavage step and experimental redox potentials of the RMs vs Fc^+/Fc. S = DMF.

Cr Complex	RM	ΔG Eq (3.1) (kcal/mol)	$\Delta G^{\ddagger}$ C–OH (kcal/mol)	$RM^{0/-}$ vs $Fc^{+/0}$
$[Cr(^{tbu}dhbpy)(CO_2H)S)]^-$	none	n/a	13.5	n/a
$[Cr(^{tbu}dhbpy)(CO_2H)S)]^-$	$[DBTD]^-$	−0.1	11.6	−2.25
$[Cr(^{tbu}dhbpy)(CO_2H)S)]^-$	$[Mes_2DBTD]^-$	0.5	–	−2.24
$[Cr(^{tbu}dhbpy)(CO_2H)S)]^-$	$[TPTD]^-$	−2.9	11.6	−2.19
$[Cr(^{tbu}dhbpy)(CO_2H)S)]^-$	$[Ph_2DBTD]^-$	−3.1	11.6	−2.12
$[Cr(^{tbu}dh^{tbu}bpy)(CO_2H)S)]^-$	none	n/a	12.5	n/a
$[Cr(^{tbu}dh^{tbu}bpy)(CO_2H)S)]^-$	$[DBTD]^-$	−2.3	10.7	−2.25
$[Cr(^{tbu}dh^{tbu}bpy)(CO_2H)S)]^-$	$[Mes_2DBTD]^-$	−2.0	–	−2.24
$[Cr(^{tbu}dh^{tbu}bpy)(CO_2H)S)]^-$	$[TPTD]^-$	−6.6	10.9	−2.19
$[Cr(^{tbu}dh^{tbu}bpy)(CO_2H)S)]^-$	$[Ph_2DBTD]^-$	−6.1	10.8	−2.12

Despite Coulombic repulsion, the substitution of a DMF molecule for the reduced mediator is favorable in almost all cases, reaching large free energies of reaction of −6.1 and −6.6 kcal/mol for the combination of Ph_2DBTD and TPTD with **2**. These values show good correlation with the experimental TOF values for **2**, while for **1** the trend is less pronounced (**Figure 3.6**). Indeed, while transition state energies determined for the dianionic assemblies of DBTD, TPTD, and Ph_2DBTD RMs with both complexes **1** and **2** show minimal variance with respect one another, they are uniformly lower than the comparable transition state energy of the monoanionic DMF adduct (**Table 3.2**). In other words, the solvento species for both complexes **1** and **2** lies on a higher-energy pathway than any of the co-catalytic combinations studied. Importantly, this result implies that the equilibrium represented in **Eq (3.1)** has a direct effect on catalyst speciation relevant to the observed activity.

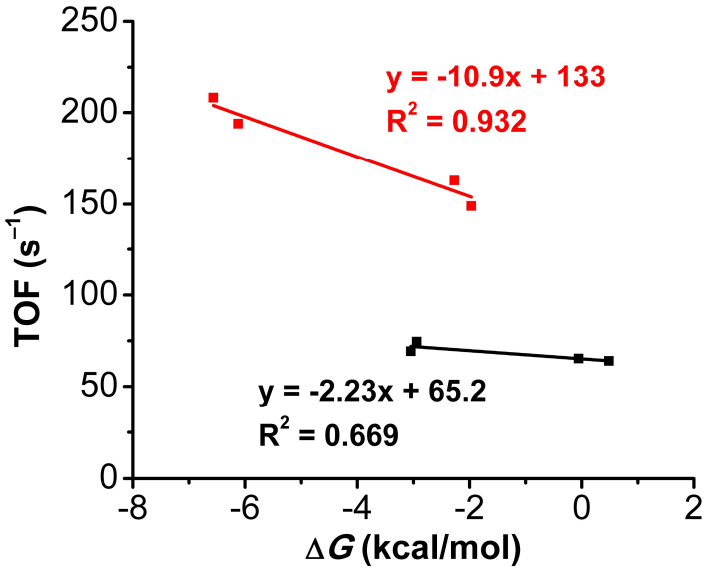

Figure 3.6. Correlation between computed DMF displacement energies and TOF.

The apparent PB interaction can be visualized in the spin density plots and Kohn-Sham (KS) orbital representations of the singly occupied molecular orbitals of the $^{4}_{0}\mathbf{Cr(CO_2H)(Ph_2DBTD)}^{-2}$ adduct (**Figure 3.7**). In addition to the favorable energetics of the association of the Ph_2DBTD and the Cr complex, these plots show antiferromagnetic coupling between Ph_2DBTD and the bpy fragment of the ligand in singly occupied orbitals of relevant symmetries. While a PB between $[RM]^-$ and $[Cr–CO_2H]^-$ requires sufficient extended aromatic character, another component of fundamental importance for any bonding interaction is that in order to be maximized, orbitals need to be close both in terms of orbital shape and energy. In other words, we propose that *the PB is maximized as the standard potential of the RM approaches that of the catalyst because the radical-containing orbitals of the reduced aromatic fragments become closer in energy*. Nuclear Independent Chemical Shift (NICS(0)) calculations on all RMs in the neutral and radical anion states indicate that the five-membered sulfone-containing ring goes from antiaromatic to aromatic upon reduction (**Tables S3.31-S3.34**). KS representations of all $^{4}_{0}\mathbf{Cr(CO_2H)(RM)}^{-2}$ adducts show that orbitals from this five-membered ring are key to the

proposed PB, interacting with the partially occupied π* orbitals of the bpy fragment in the Cr complex relevant to the co-catalytic pathway.[28, 29]

It is worth stating again, however, that with the present data the observed correlation is weak for complex **1**. This suggests that while RM redox potentials are to some extent an indirect measure of relevant orbital energies, there are additional kinetic components influenced by the steric bulk of the catalyst and the RM. This kinetic effect is seen most directly in the comparison of the experimental and computational data of DBTD and Mes_2DBTD, which despite being nearly identical in terms of redox potential have significantly different activity.

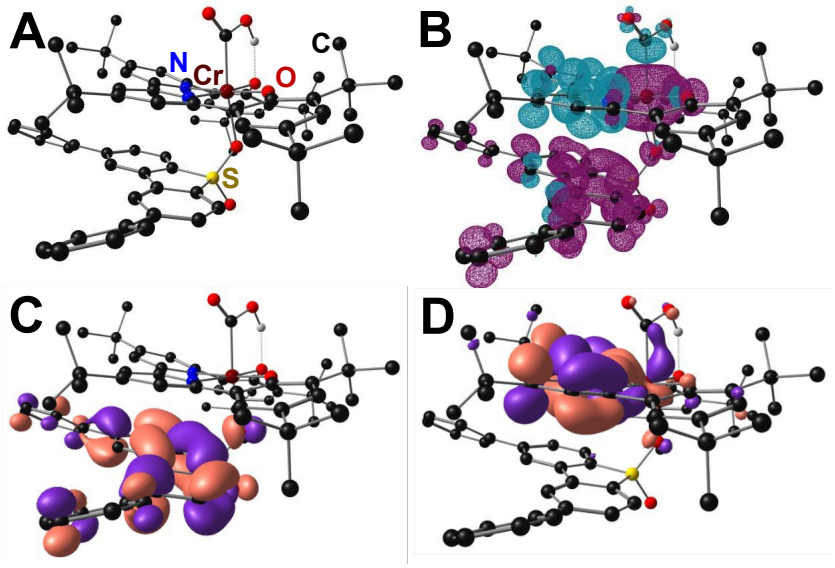

Figure 3.7. Molecular geometry of the $^{4}_{0}\mathbf{Cr(CO_2H)(Ph_2DBTD)}^{-2}$ adduct (**A**) DFT-calculated spin density (**B**) Kohn-Sham orbital projection of SOMO (**C**) and $SOMO^{-1}$ (**D**).

3.5 Discussion

Here, both the experimental and computational data indicate that the RM is operating by an inner-sphere mechanism under protic conditions (**Figure 3.8**). We propose that first, the four-coordinate neutral catalyst, ***i***, is reduced to the monoanionic Cr species ***ii***. Based on calculations previously performed on the co-electrocatalytic mechanism of **1**, CO_2 readily binds to ***ii*** to form $[Cr–CO_2]^-$ ***iii***.[8, 28, 29] With PhOH present this species is protonated, binds DMF and is then reduced

to form the monoanionic [Cr–CO_2H]$^-$ ***iv***. The one electron reduced [RM]$^-$ binds to this species to form ***v***, which we proposed to be the key intermediate, $^{4}_{0}\mathbf{Cr(CO_2H)(RM)}^{-2}$, stabilized by pancake bonding between the one-electron reduced bpy-backbone and the π-framework of the reduced RM. We propose that ***v*** is further stabilized when the π-framework of the RM is extended, due to closer energy levels of the orbitals involved in PB and greater dispersive interactions. Furthermore, extended aromatic character can protect the radical character of the RM in the reduced state, aligning with the improved performance of these mediators under electrolysis conditions. Following the addition of a second proton equivalent, the neutral RM is released along with water leaving [Cr–CO]$^-$ ***vi***, which we have previously shown is not stable.[8] This species then releases CO to form the monoanionic four-coordinate neutral Cr species ***ii***, completing the cycle.

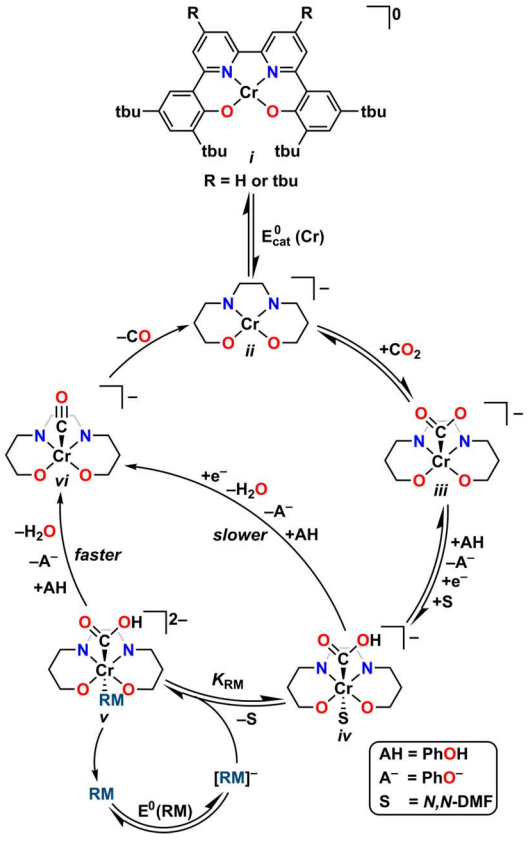

Figure 3.8. Proposed catalytic mechanism for co-electrocatalytic CO_2 reduction by Cr and RM under protic conditions where Cr is **1** or **2** and RM is DBTD, TPTD, Ph_2DBTD, or Mes_2DBTD.

Computational results show that the barrier for C–OH bond cleavage in all computed $^{4}_{0}\mathbf{Cr}(\mathbf{CO_2H})(\mathbf{RM})^{-2}_{\square}$ adducts is roughly equivalent for all possibilities and lower than the corresponding solvento species $^{4}_{0}\mathbf{Cr}(\mathbf{CO_2H})(\mathbf{DMF})^{-1}_{\square}$. This means that the equilibrium displacement of the axial solvent ligand by $[RM]^-$ dictates whether lower or higher energy catalytic pathways are accessible and will be directly reflected in the rate observed at co-catalytic potentials. Further, the minimal difference in barrier height across the $^{4}_{0}\mathbf{Cr}(\mathbf{CO_2H})(\mathbf{RM})^{-2}_{\square}$ adducts and the minimal changes in the bond between sulfone and Cr center are consistent with the proposal that changes in dispersion effects and PB are responsible for the differences in binding energy (**Table S3.35**). Both TPTD and Ph_2DBTD show increased activity compared to DBTD and Mes_2DBTD as RMs when combined with **1** or **2**, despite the more negative operating potentials of the latter pair, which is consistent with an inner-sphere process. Although the kinetic complexity of the system precludes straightforward analysis of variable concentration CV data, the proportional increase in current as the catalyst:RM ratio increased observed in CPE suggests that this equilibrium binding interaction is relevant to the catalytic rate expression. This leads to an *inverse scaling effect between RM standard potential and the observed activity*, with greater catalytic activity observed at lower reduction potentials.

Previously, the existence of inverse potential scaling relationships in molecular electrocatalysts for CO_2 reduction has been primarily explained through the kinetic stabilization of key intermediates. Initial work from Savéant and co-workers in 2016 showed that the inclusion of trimethylammonium groups on the catalyst ligand framework resulted in significant kinetic enhancements to CO production under protic conditions at low overpotentials.[6] This kinetic effect at more positive catalyst standard reduction potentials was initially proposed to be the result of coulombic stabilization of a key [Fe–CO_2] intermediate, however, a later computational study showed that the relatively long distance (3.8 Å) resulted in effective charge screening by the

implicit solvent used.[53] Energy decomposition analysis showed that both through-space and through-structure effects contribute to the stabilization of the [Fe–CO_2] intermediate, with through-structure being stronger, but both being necessary to kinetic enhancements at low applied potentials. Nichols *et al.* then reported in 2018 that when hydrogen-bond donors are properly positioned in the secondary coordination sphere, significant increases in activity occur with minor variance in the standard reduction potential of the catalyst.[54] Mechanistic experiments again indicated that this observation resulted from stabilization of the [Fe–CO_2] intermediate and not the inclusion of acidic amide protons near the catalytic active site. Subsequently, Gotico *et al*. demonstrated that using urea functional groups as multipoint hydrogen-bond donors in similar frameworks could further enhance this kinetic stabilization effect.[55] A recent report from McCrory and co-workers on a non-porphyrinic Co-based catalyst revealed a previously unobserved effect where the combination of ligand reduction potential and electrostatic effects could be manipulated to facilitate the storing of additional charge equivalents, improving catalytic activity for CO_2 reduction at lower catalyst standard potentials.[56]

Our proposed mechanism for inverse potential scaling is unique with respect to these previous examples. Unlike the use of electrostatic effects to stabilize bound CO_2 intermediates or facilitate the storage of electron equivalents in the ligand framework, dispersive interactions and PB drive the association of RM and Cr complex, surmounting the Coulombic repulsion between the two fragments. This co-catalytic assembly presents a lower barrier for the rate-limiting C–OH bond cleavage step. Importantly, this barrier is equivalent across all RMs and instead it is the favorability of the pre-equilibrium comprising the formation of the co-catalytic assembly that dictates the extent the faster mechanism contributes to the observed activity. Mediators with extended aromaticity operate at lower redox potentials, but present stronger PB and dispersive interactions with the metal catalyst, favoring the formation of the co-catalytic assembly and thus yielding enhanced reaction rates at lower overpotential.

3.6 Conclusion

These results show that by tuning properties of both catalyst and RM, an increase in activity for the co-electrocatalytic reduction of CO_2 can be achieved at lower overpotential by means of inner-sphere electron transfer. Through the addition of electron-donating groups to the bpy backbone in complex **2**, we have improved the activity of our Cr-centered catalyst for CO_2 reduction. Consistent with the proposal in our initial report of co-catalytic systems with **1**,[29] these data provide a theoretical and experimental basis for an inner-sphere mechanism under protic conditions. By tuning the stereoelectronic properties of the catalyst and the RM, we have optimized our system to decrease the overpotential while increasing the activity, contrary to what would be predicted by a classical outer-sphere Marcus-theory type model.[42] As a result, an equilibrium solvent displacement reaction can be used to access a lower energy catalytic pathway, with increased favorability driving the system to higher observed activity. Additionally, the selectivity of the parent Cr complexes is retained with all catalytically competent systems being quantitatively selective for CO. Importantly, implementing the strategies identified by this work will be a powerful tool for developing systems which improve the performance of molecular catalyst systems. We are exploring additional strategies to optimize the co-electrocatalytic response in ongoing studies.

3.7 Supporting Information

3.7.1 Materials and Methods

General

All chemicals and solvents (ACS or HPLC grade) were commercially available and used as received unless otherwise indicated. For all air-sensitive reactions and electrochemical experiments, HPLC-grade solvents were obtained as anhydrous and air-free from a PPT Glass Contour Solvent Purification System. Gas cylinders were obtained from Praxair (Ar as 5.0; CO_2 as 4.0) and passed through activated molecular sieves prior to use. Gas mixing for variable

concentration experiments was accomplished using a gas proportioning rotameter from Omega Engineering. UV-vis absorbance spectra were obtained on a Cary 60 from Agilent. An Anton-Parr Multiwave Pro SOLV, NXF-8 microwave reactor was used for microwave syntheses.

Electrochemistry

All electroanalytical experiments were performed using a Metrohm Autolab PGSTAT302N potentiostat. Glassy carbon working (⌀ = 3 mm) and non-aqueous silver/silver chloride pseudoreference electrodes behind PTFE tips were obtained from CH Instruments. The pseudoreference electrodes were obtained by depositing chloride on bare silver wire in 10% HCl at oxidizing potentials and stored in a 0.1 M tetrabutylammonium hexafluorophosphate/*N,N*-dimethylformamide (DMF) solution in the dark prior to use. The counter electrode was a glassy carbon rod (⌀ = 3 mm). All CV experiments were performed in a modified scintillation vial (20 mL volume) as a single-chamber cell with a cap modified with ports for all electrodes and a sparging needle. Tetrabutylammonium hexafluorophosphate ($TBAPF_6$) was purified by recrystallization from ethanol and dried in a vacuum oven before being stored in a desiccator. All data were referenced to an internal ferrocene standard (ferricenium/ferrocene (Fc^+/Fc) reduction potential under stated conditions) unless otherwise specified. All voltammograms were corrected for internal resistance. Ferrocene was purified by sublimation prior to use.

Controlled Potential Electrolysis (CPE)

CPE experiments were performed in a glass Pine Research Instrumentation H-cell with two compartments separated by a glass frit. A 55 mL stock solution of DMF with 0.1 M $TBAPF_6$ was prepared for each bulk electrolysis experiment. Approximately 26 mL of the stock solution was added to each half of the H-cell. One side of the H-cell contained the catalyst, any additional substrate, such as the mediator and/or PhOH, and a glassy carbon rod working electrode. The other side of the H-cell contained approximately 0.075 M ferrocene as a sacrificial reductant along with a graphite rod counter electrode and a Ag/AgCl pseudoreference electrode. The electrolysis experiment was referenced by taking a CV of the side of the H-cell that contained the ferrocene

solution. The H-cell was sealed with two septa that were connected by a piece of PTFE tubing which aided to maintain equal pressure between each half of the cell during the electrolysis. Before starting the electrolysis experiment, both sides of the H-cell were sparged with the desired gas for 20 minutes and the sealed cell was allowed to equilibrate for 1 hour. The resistance between the two halves of the H-cell was measured using the i-interrupt procedure available in the NOVA software provided by Metrohm.

The concentration of catalyst was chosen so that the concentration of product within the H-cell remained in the optimal concentration range for GC product analysis described below. The ratio of catalyst to PhOH remained the same as well as the ratios for RM described for each individual experiment.

Controlled Potential Electrolysis (CPE) Product Analysis

During CPE experiments, either 50 or 250 µL GC injections of the headspace were periodically taken for the detection and quantification of any gaseous products produced. After each CPE experiment, the total volume of solution was measured. The total volume of the sealed H-cell was also measured to account for the total headspace volume for accurate quantification of gaseous products. A calibration curve for CO and H_2 was used to quantify gaseous products produced during electrolysis experiments in the same manner as we previously reported.[8]

Analysis of gas phase products was done by sampling electrolysis headspace through syringe injections into an Agilent 7890B GC equipped with a specialty gas split column 5 Å mol sieve/Porabond Q column (15 m length; 0.320 mm diameter; 25.0 µm film) and thermal conductivity detector with He as a carrier gas. A calibration curve for CO and H_2 was made in the H-cell with an experimental setup containing identical volumes of DMF in 0.1 M $TBAPF_6$ to those used during electrolysis. Known volumes of CO and H_2 were injected into the cell with stirring and 250 µL injections of the headspace were taken for GC injections after equilibration. The limit of

detection (LOD) and limit of quantitation (LOQ) for CO and H_2 in the GC were determined from seven consecutive injections at the lowest observable concentrations of each gaseous product respectively. For CO, the LOD was determined to be 5.77 x 10^{-7} moles and the LOQ was determined to be 1.92 x 10^{-6} moles. For H_2, the LOD was determined to be 4.55 x 10^{-6} moles and the LOQ was determined to be 1.52 x 10^{-5} moles.

Gas Chromatography/Mass Spectrometry (GC/MS) Analysis of CPE Solutions

The samples for GC/MS analysis were prepared by diluting 0.1 mL of the CPE solution with 0.9 mL of dichloromethane (DCM). 1 µL of these solutions were injected by a 7693A ALS into a 7890B GC equipped with an ultra inert column (30 m length; 0.25 mm diameter; 0.25 µm film) and 5977B MSD.

Calculation of Overpotential for CO_2 Reduction with PhOH Present (Adapted)

The calculation of overpotential for all catalysts was performed according to reported methods.[57] The following equation was used for the determination of the reaction standard potential in V with respect to the Fc^+/Fc couple:

$$E_{CO2/CO} = -0.73\,V - 0.059(pK_a) \qquad \textbf{Eq (S3.1)}$$

The pK_a for PhOH in DMF is reported as 18.8:[58]

$$E_{CO2/CO}(PhOH) = -1.84\,V\ vs\ Fc^+/Fc \qquad \textbf{Eq (S3.2)}$$

The $E_{cat/2}$ determined experimentally for Cr(^{tbu}dhbpy)Cl(H_2O) and Cr(^{tbu}dh^{tbu}bpy)Cl(H_2O) is –1.95 V[8] and –2.00 V vs Fc^+/Fc, respectively. For protic CO_2 reduction (1.0 mM catalyst and 0.1 M PhOH under CO_2 saturation); the overpotential is:

$$\eta = \left|E_{cat/2} - E_{CO2/CO}\right| \qquad \textbf{Eq (S3.3)}$$

Cr(^{tbu}dhbpy)Cl(H_2O)	η = 110 mV
Cr(^{tbu}dh^{tbu}bpy)Cl(H_2O)	η = 160 mV

This assumes no contribution from homoconjugation of the acid. We note that the homoconjugation constant (HA_2^-) for PhOH in DMF has been reported as $\log(K_{HA_2^-})$ = 3.8.[59]

Therefore, we emphasize that the described overpotential calculated above for PhOH is the lower-limit approximation, as homoconjugation is expected to alter the effective overpotential. The overpotential equation can be modified to account for homoconjugation:

$$E_{CO2/CO} = -0.73\,V - 0.059(pK_a) - \frac{-2.303RT}{nF}\log\left(mK_{HA_2^-}\right) \qquad \textbf{Eq (S3.4)}$$

Where n = number of electrons (2) and m = number of proton transfers (2). The modified equation provides $E^0_{CO2/CO}$ = −1.72 V and the following η values:

Cr(^{tbu}dhbpy)Cl(H_2O)	η = 230 mV
Cr(^{tbu}dh^{tbu}bpy)Cl(H_2O)	η = 280 mV

This value does not account for the possible thermodynamic contributions of the water coordinated to the pre-catalyst, the equimolar quantities of water produced for each equivalent of CO generated, or any adventitious H_2O present in the CO_2, solvent, or electrolyte. Under CO_2 saturation, any water present can form carbonic acid, pK_a(DMF) 7.37,[60] and generate new equilibria involving CO_2 and bicarbonate. The role of carbonic acid (and the general hydration of CO_2 in non-aqueous solvent systems) in altering the overall thermodynamics combined with the effects of homoconjugation has been assessed by Matsubara.[61] Considering the role of water, Matsubara obtained a standard potential for CO_2 reduction to CO of −1.70 V versus Fc^+/Fc for PhOH in DMF with 10 mM water present (see below). Note the same value is obtained considering 10 mM water only.

For 10 mM H_2O in DMF, where AH = PhOH:[61]

$$3CO_{2(g)} + H_2O_{(sol,x)} + 2e^- \rightleftharpoons CO_{(g)} + 2HCO_{3\,(sol)}^- \qquad E^0 = -1.70\,V\ vs.\,Fc^+/Fc$$
$$CO_{2(g)} + 2AH_{(sol)} + 2e^- \rightleftharpoons CO_{(g)} + 2A^-_{(sol)} + H_2O_{(sol,x)} \qquad E^0 = -1.96\,V\ vs.\,Fc^+/Fc$$
$$CO_{2(g)} + 4AH_{(sol)} + 2e^- \rightleftharpoons CO_{(g)} + 2HA_{2\,(sol)}^- + H_2O_{(sol,x)} \qquad E^0 = -1.70\,V\ vs.\,Fc^+/Fc$$

Determination of TOF_{max} from Cyclic Voltammetry

The expression for TOF_{max} for a homogeneous electrocatalytic response (considering an application of steady-state conditions to the substrate) has been solved previously.[8, 62]

$$TOF_{max} = 0.1992 \frac{n_p^3}{n_{cat}^2} \frac{Fv}{RT} \left(\frac{i_{cat}}{i_p}\right)^2 \quad \textbf{Eq (S3.5)}$$

Where $n_p^{\square}$ is the number of electrons transferred under faradaic conditions, $n_{cat}^{\square}$ is the number of electrons transferred under catalytic conditions, R is the ideal gas constant, F is Faraday's constant, *v* is the scan rate, T is temperature, $i_{cat}^{\square}$ is the catalytic current, and $i_p^{\square}$is the Faradaic current.

Determination of TOF from Preparative Electrolysis

The integrated expression of current for a homogeneous electrocatalytic response (considering an application of steady-state conditions to the substrate) has been solved previously:[38, 63]

$$\frac{i}{FA} = \frac{n_{cat}^{\sigma}[cat]\sqrt{(k_{obs}D_{cat})}}{1 + \exp\left[\frac{F}{RT}\left(E_{app} - E_{1/2}\right)\right]} \text{ where}$$

$$k_{obs} = k_{cat}[CO_2]$$

where i is the average current (Amps) specific to the reaction product of interest, F is Faraday's constant (96485 C mol^{-1}), A is the area of the electrode (cm^2), n_{cat}^{σ} is the number of electrons in the catalytic process (2) with σ = 1 under the assumption that all electrons are delivered to the catalyst by the electrode electrode[5] (σ = 0.5 corresponds to homogeneous electron transfer occurring between catalyst molecules in solution; used here for co-electrocatalytic conditions), $[cat]$ is the concentration of the catalyst (mol cm^{-3}), k_{obs} is the apparent turnover frequency (s^{-1}), $[CO_2]$ is the concentration of CO_2 saturated in DMF (mol cm^{-3}), D_{cat} is the diffusion coefficient of the catalyst (cm^2 s^{-1}), R is the ideal gas constant (Joule mol^{-1} K^{-1}), T is the temperature (K), E_{app} is the applied potential during preparative electrolysis (V), and $E_{1/2}$ is the standard potential of the catalyst (V).

and

$$\frac{i}{A} = J = CO\ specific\ current\ density$$

Substituting and rearranging the first expression to solve for k_{obs}

$$k_{obs} = \frac{J^2\left(1 + \exp\left[\frac{F}{RT}\left(E_{app} - E_{1/2}\right)\right]\right)^2}{F^2(n_{cat}^{\sigma}[cat])^2 D_{cat}}$$

with k_{obs} in hand, the TOF can be expressed for a given potential according to the following relationship

$$TOF = \frac{k_{obs}}{1 + \exp\left[\frac{F}{RT}\left(E_{app} - E_{1/2}\right)\right]}$$

Parameters for CPE experiments reported here not found in **Table 3.1**.

- $E_{1/2}$ catalyst:
  - −1.95 V vs Fc^+/Fc for Cr(^{tbu}dhbpy)Cl(H_2O) **1**
  - −2.00 V vs Fc^+/Fc for Cr(^{tbu}dh^{tbu}bpy)Cl(H_2O) **2**
- Temperature: 298.15 K
- $[CO_2]$: 2.3 x 10^{-4} mol cm^{-3}
- Diffusion coefficient:
  - 2.0 x 10^{-6} cm^2 s^{-1} for Cr(^{tbu}dhbpy)Cl(H_2O) **1**
  - 2.3 x 10^{-6} cm^2 s^{-1} for Cr(^{tbu}dh^{tbu}bpy)Cl(H_2O) **2**
- Electrode area: 3.93 cm^2

Calculation of Diffusion Coefficients

The calculation of the diffusion coefficient for each redox mediator was performed by reported methods.[41] Cyclic voltammetry (CV) experiments were done with a solution of 2.5 mM RM in 0.1 M $TBAPF_6$/DMF under Ar saturation conditions. The scan rate of these CVs was varied from 25 mV/s to 5000 mV/s (**Figures S22-S25**). The increase in current observed as the scan rate increases can be represented by the following equation where i_p is the peak current, n is the number of electrons, A is the area of the electrode, D is the diffusion coefficient, C is the concentration of analyte, and v is the scan rate:

$$i_p = (2.69 \times 10^5) n^{3/2} A C D^{1/2} v^{1/2}$$

By plotting the current density as a function of $v^{1/2}$ (**Figures S22-S24**), the slope can be used to find D for each RM.

$$D_{cat} = \frac{(\text{slope})^2}{n^3 C^2 (2.69 \times 10^5)^2}$$

Calculation of i_{cat}/i_p for Co-electrocatalytic Systems

A common technique for evaluating diffusion, electrode surface area, and concentration independent observed rate constants (k_{obs}) for a two-electron catalytic process is to determine i_{cat}/i_p for a catalytic system, where i_{cat} is the catalytic plateau current and i_p is the one-electron peak in the absence of substrate.[43] Due to the complex nature of the co-catalytic systems we present here, we are unable to calculate k_{obs} by this method. However, these ratios still offer an insightful measure into the relative current increase under catalytic conditions between systems that are sensitive to the diffusion coefficient of both co-catalysts.

To calculate the values of i_p and i_{cat} for all systems, the capacitive current must be subtracted from the measured current at either the peak or the plateau. To determine the potential to find the capacitive, peak, catalytic, and co-catalytic plateau currents, the first derivative was taken of the forward trace for CVs obtained with **1** or **2**, RM, and PhOH under Ar (i_p) and under CO_2 (i_{cat}). Where the first derivative is equal to zero there is a plateau in the CV trace. The current in the CV at the same potential corresponding to a value of zero in the first derivative was used (**Figure S3.80A**). However, due to close overlap of features in the co-catalytic trace under CO_2, the local minima corresponding to the inflection point of the curve were used to determine an effective current plateau (**Figure S3.80B**). All CV data used had a scan rate = 100 mV/s.

Computational Methods

Geometry optimizations were performed without geometry constraints at the DFT level with the Gaussian 16 program, Rev B.01,[44] employing the hybrid functional B3LYP[45-48] and the def2-SVP basis set was used for all atoms.[49, 50] Dispersion and bulk solvent effects (*N*,*N*-dimethylformamide = DMF; ε = 37.219) were accounted for at the optimization stage, by using Grimme's D3 parameter set with Becke-Johnson (BJ) damping[51, 52] and the CPCM continuum model,[64]

respectively. The stationary points and their nature as minima (no imaginary frequencies) were characterized by vibrational analysis using the IGRRHO approach as implemented by default in the software package, which also produced enthalpy (H), entropy (S) and Gibbs energy (G) data at 298.15 K. The minima connected by a given transition state were determined by perturbing the transition states along the TS coordinate and optimizing to the nearest minimum. Free energies were corrected (ΔG_{qh}) to account for concentration effects and for errors associated with the harmonic oscillator approximation. Thus, according to Truhlars's quasi-harmonic approximation for vibrational entropy and enthalpy, all vibrational frequencies below 100 cm^{-1} were set to this value.[65] These anharmonic and concentration corrections were calculated with the Goodvibes code.[66] Concentrations were set at 0.001 M for metal complexes, 0.005 for RM and RM^{-}, and 12.92 M for DMF. Energies were refined by means of single point calculations with the larger def2-TZVP basis set. The stability of the wavefunction and spin contamination were studied at the double- and triple-zeta levels of theory. Nucleus-Independent Chemical Shift (NICS)[67] values were computed for the mediators by computing magnetic shielding tensors of ghost atoms placed at the centroid of each ring using the Gauge Independent Atomic Orbital (GIAO)[68-71] method at the B3LYP-D3BJ/def2-TZVP level of theory with the ORCA 5.0 program.[72]

Kohn-Sham orbital projections and spin densities were plotted in ChemCraft with contour values of 0.030 and 0.0025, respectively. The color scheme used for atoms is C = black, O = red, N = blue, H = grey, S = yellow and Cr = maroon. For added clarity, select figures were generated with truncated structures and omitted H atoms as indicated in the respective captions; all calculations were performed using the complete structural model. The labelling scheme for minima is $^{\text{multiplicity}}_{\#\text{ bound DMF}}\mathbf{Cr}(\boldsymbol{axial\ ligands})^{\text{charge}}$ and $^{\text{multiplicity}}\mathbf{RM}^{\text{charge}}$ for RM species; the $[^{tbu}dhbpy]^{2-}$ or $[^{tbu}dh^{tbu}bpy]^{2-}$ ligand framework is a common feature of all Cr species and does not change its coordination mode during the reaction, so it is omitted in the notation where possible for clarity.

Single crystal X-ray diffraction

A single crystal of each sample was coated with Paratone oil and mounted on a MiTeGen MicroLoop. The X-ray intensity data were measured on a Bruker Kappa APEXII Duo system equipped with an Incoatec Microfocus IμS (Cu K_α, λ = 1.54178 Å) and a multi-layer mirror monochromator, and a fine-focus sealed tube (Mo K_α, λ = 0.71073 Å) and a graphite monochromator or Bruker D8 Venture Kappa four-circle diffractometer system equipped with an Incoatec IμS 3.0 micro-focus sealed X-ray tube (Mo Kα, λ = 0.71073 Å) and a HELIOS double bounce multilayer mirror monochromator.

The frames were integrated with the bruker SAINT software package[73] using a narrow-frame algorithm. Data were corrected for absorption effects using the Multi-Scan method (SADABS or TWINABS).[74] Each structure was solved and refined using the Bruker SHELXTL Software Package[74] within APEX3[73] and OLEX2.[75] Non-hydrogen atoms were refined anisotropically. The O-H hydrogen atoms were located in the electron density map and refined isotropically. All other hydrogen atoms were placed in geometrically calculated positions with U_{iso} = 1.2U_{equiv} of the parent atom (U_{iso} = 1.5U_{equiv} for methyl).

Both polymorphs of ^{tbu}dhbpy$(H)_2$ were twinned. For polymorph 1, a two-domain twin was identified using CELL_NOW.[76] Starting with 767 reflections, 620 reflections were fit to the first domain, and 539 to the second domain (132 exclusively), with 15 unindexed reflection remaining. The twin domain was oriented at a 179.8º rotation about the reciprocal axis 0.000 0.001 1.000. The twin law was -0.998 -0.004 0.001 / 0.004 -1.002 0.001 / -0.642 -0.366 1.000. It was refined on on HKLF5 data, with the BASF for the twin domain refining to 0.33031. For polymorph 2, a three-domain twin was identified using CELL_NOW.[76] Starting with 1469 reflections, 1084 reflections were fit to the first domain, 1073 to the second domain (246 exclusively), and 189 to the third domain (43 exclusively) with 96 unindexed reflection remaining. The second domain was oriented at a 179.9º rotation about the reciprocal axis 0.000 0.000 1.000. The twin law was -0.999 0.002

0.004 / 0.000 -1.001 -0.002 / 0.539 0.999 1.000. The third domain was oriented at a 179.7º rotation about the real axis 1.000 -0.411 -0.412 and its twin law was -0.039 -0.398 -0.398 / -0.553 -0.768 0.234 / -1.956 0.796 -0.193. It was refined on HKLF5 data, with the BASF for the twin domains refining to 0.47711 and 0.02195. For **2**, one *tert*-butyl group was found to be disordered across two positions. The relative occupancy of the positions was freely refined, with constraints on the anisotropic displacement parameters of the disordered atoms. Chloroform and hexane solvent located in the crystal lattice was severely disordered and could not be adequately modeled with or without restraints. Thus, the structure factors were modified using the PLATON SQUEEZE[77] technique, in order to produce a "solvate-free" structure factor set. PLATON reported a total electron density of 326 e^- and total solvent accessible volume of 1276 $Å^3$.

Table S3.1. Crystallographic data for ^{tbu}dhbpy(H)$_2$, ^{tbu}dh^{tbu}bpy(H)$_2$, and Cr(^{tbu}dh^{tbu}bpy)Cl(H$_2$O) **2**.

	^{tbu}dhbpy(H)$_2$ polymorph 1	^{tbu}dhbpy(H)$_2$ polymorph 2	^{tbu}dh^{tbu}bpy(H)$_2$	Cr(^{tbu}dh^{tbu}bpy)Cl(H$_2$O) **2**
CCDC number	1984949	1984950	2150929	2150930
Formula	$C_{38}H_{48}N_2O_2$	$C_{38}H_{48}N_2O_2$	$C_{46}H_{64}N_2O_2$	$C_{99}H_{139}Cl_5Cr_2N_6O_6$
FW (g/mol)	564.78	564.78	676.99	1790.40
Temp (K)	100(2)	100(2)	100(2)	100(2)
λ (Å)	1.54178	0.71073	0.71073	1.54178
Size (mm)	0.051 x 0.067 x 0.157	0.077 x 0.091 x 0.589	0.164 x 0.222 x 0.362	0.048 x 0.048 x 0.059
Crystal habit	yellow plate	yellow plate	yellow block	orange plate
Crystal system	triclinic	triclinic	monoclinic	triclinic
Space group	P -1	P -1	I 2/m	P -1
a (Å)	10.0611(10)	6.142(2)	13.809(3)	15.1726(10)
b(Å)	11.5414(11)	9.094(3)	8.7376(17)	19.0611(13)
c (Å)	15.8166(15)	15.431(5)	17.190(5)	20.9243(15)
α (°)	77.316(7)	106.415(5)	90	84.198(5)
β (°)	74.707(7)	93.806(5)	99.585(5)	81.186(5)
γ (°)	65.801(7)	97.936(6)	90	73.704(5)
Volume (Å^3)	1602.9(3)	813.8(5)	2045.1(8)	5729.0(7)
Z	2	1	2	2
Density (g/cm^3)	1.170	1.152	1.099	1.038
μ (mm^{-1})	0.549	0.070	0.066	2.990
F(000)	612	306	740	1912
θ range (°)	2.92 to 68.33	2.36 to 25.26	1.76 to 29.63	2.14 to 50.63
Index ranges	-11 ≤ h ≤ 12 -13 ≤ k ≤ 13 0 ≤ l ≤ 19	-7 ≤ h ≤ 7 -10 ≤ k ≤ 10 0 ≤ l ≤ 18	-19 ≤ h ≤ 19 -12 ≤ k ≤ 12 -23 ≤ l ≤ 23	-15 ≤ h<=15 -19 ≤ k ≤ 19 -20 ≤ l ≤ 20
Data / restraints /parameters	5760 / 0 / 400	3031 / 0 / 202	3058 / 0 / 149	11907 / 0 / 1104
GOF on F^2	1.068	1.047	1.023	0.996
R_1 (I>2σ(I))	0.0738	0.0815	0.0450	0.0996
wR_2 (all data)	0.2099	0.2350	0.1281	0.3073

Table S3.2. Crystallographic data for TPTD, Mes_2DBTD, and Ph_2DBTD.

	TPTD	Mes_2DBTD	Ph_2DBTD
CCDC number	2154597	2154599	2154598
Formula	$C_{18}H_{10}O_2S$	$C_{30}H_{28}O_2S$	$C_{31}H_{24}O_2S$
FW (g/mol)	290.32	452.58	460.56
Temp (K)	100.00	100.00	100.00
λ (Å)	0.71073	0.71073	0.71073
Size (mm)	0.438 × 0.164 × 0.068	0.375 × 0.095 × 0.043	0.233 × 0.064 × 0.039
Crystal habit	colorless plate	colorless rod	colorless needle
Crystal system	monoclinic	orthorhombic	orthorhombic
Space group	$P2_1/c$	$Pca2_1$	Pbcn
a (Å)	7.0219(4)	19.7648(12)	15.4383(16)
b(Å)	20.7503(10)	7.4276(4)	20.371(2)
c (Å)	17.2210(10)	16.1962(9)	7.3501(7)
α (°)	90	90	90
β (°)	91.096(2)	90	90
γ (°)	90	90	90
Volume ($Å^3$)	2508.8(2)	2377.7(2)	2311.6(4)
Z	8	4	4
Density (g/cm^3)	1.537	1.264	1.323
μ (mm^{-1})	0.258	0.161	0.168
F(000)	1200.0	960.0	968.0
θ range (°)	2.562 to 28.294	2.061 to 26.377	1.999 to 28.296
Index ranges	$9 \le h \le 9$ $-22 \le k \le 27$ $-22 \le l \le 22$	$-24 \le h \le 24$ $-9 \le k \le 7$ $-20 \le l \le 20$	$-20 \le h \le 20$ $-27 \le k \le 27$ $-9 \le l \le 7$
Data / restraints /parameters	6229/0/379	4845/1/305	2870/0/157
GOF on F^2	1.208	1.104	1.095
R_1 ($I>2\sigma(I)$)	0.0773	0.0754	0.0530
wR_2 (all data)	0.1738	0.1936	0.1153

3.7.2 Synthesis and Characterization

Synthesis of 6,6'-Di(3,5-di-tert-butyl-2-hydroxybenzene)-2,2'-bipyridine, ^{tbu}dhbpy(H)$_2$

The synthesis of ^{tbu}dhbpy(H)$_2$ was carried out as previously reported.[8]

Synthesis of Cr(^{tbu}dhbpy)Cl(H_2O) (1)

The metalation of ^{tbu}dhbpy(H)$_2$ to generate Cr(^{tbu}dhbpy)Cl(H_2O) (**1**) was carried out as previously reported[8] with one modification: the resulting product was further purified by dissolving in dichloromethane (DCM) and passing through a PTFE syringe filter to remove excess starting metal salt.

Synthesis of 6,6'-Di(3,5-di-tert-butyl-2-hydroxybenzene)-4,4'-di-tert-butyl-2,2'-bipyridine, $^{tbu}dh^{tbu}bpy(H)_2$

The starting materials for this reaction, dichloro-4,4′-di-*tert*-butyl-2,2′-bipyridine[78, 79] and (3,5-di-*tert*-butyl-2-hydroxy-phenyl)boronic acid[8], were all prepared by previously reported methods.

Two microwave tubes were each charged with 6,6′-dichloro-4,4′-di-*tert*-butyl-2,2′-bipyridine (0.755 g, 2.24 mmol), unpurified (3,5-di-*tert*-butyl-2-hydroxy-phenyl)boronic acid (1.96 g, 38.2 mmol), sodium carbonate (1.76 g, 16.6 mmol), $Pd(PPh_3)_4$ (0.04 g, 0.03 mmol), and degassed toluene (30 mL), water (12 mL), and methanol (8 mL). The microwave conditions were set to heat the reaction mixture to 170 °C as fast as possible and then held at that temperature for 140 minutes. After cooling, the two tubes were combined, and aqueous and organic fractions were separated and extracted. The organic layer was washed with brine (3 x 50 mL) and the aqueous layer was extracted with dichloromethane (4 x 75 mL). All organic fractions were combined and dried over $MgSO_4$ before removing the solvent via reduced pressure leaving a bright yellow oil. Methanol was added to the flask to dissolve excess boronic acid still present and a yellow solid crashed out of solution. Finally, the solution was filtered and the solid collected on the frit was washed with additional methanol leaving a bright yellow solid with an isolated yield of 30.5% (0.922 g). ^{1}H NMR (CD_2Cl_2, 600 MHz): δ 14.60 (s, 2H, O*H*), 8.22 (d, 2H, Ar*H*), 7.98 (d, 2H, Ar*H*), 7.74 (d, 2H, Ar*H*), 7.44 (d, 2H, Ar*H*), 1.51 (s, 18H, −C(CH_3)$_3$), 1.50 (s, 18H, −C(CH_3)$_3$), 1.40 (s, 18H, −C(CH_3)$_3$). ^{13}C{^{1}H} NMR (CD_2Cl_2, 150 MHz): δ 163.7 (Ar*C*), 159.0 (Ar*C*), 157.0 (Ar*C*), 152.2 (Ar*C*), 140.5 (Ar*C*), 126.56 (Ar*C*), 121.5 (Ar*C*), 119.0 (Ar*C*), 117.7 (Ar*C*), 116.8 (Ar*C*), 110.5 (Ar*C*), 35.9 (tbu*C*), 35.7 (tbu*C*), 34.7 (tbu*C*), 31.8 (tbu*C*), 30.7 (tbu*C*), 29.8 (tbu*C*). Elemental Analysis for $C_{46}H_{64}N_2O_2$ calc'd: C 81.61, H 9.53, N 4.14; found: C 81.10, H 9.79, N 4.15.

Synthesis of Cr($^{tbu}dh^{tbu}bpy$)Cl(H_2O) (2)

Metalation of $^{tbu}dh^{tbu}bpy(H)_2$ with Cr(III) to generate Cr($^{tbu}dh^{tbu}bpy$)Cl(H_2O) (**3**) was achieved by stirring $^{tbu}dh^{tbu}bpy(H)_2$ (0.295 g, 0.436 mmol) and 1.05 equivalents of chromium(II) dichloride (0.0562 g, 0.458 mmol) in tetrahydrofuran (60 mL) at room temperature under an inert

atmosphere for seven days. After exposing the reaction to air, the THF was removed under reduced pressure. The solid was then dissolved in DCM and washed with brine (3 x 50 mL) and saturated ammonium chloride (6 x 50 mL). The organic layer was then dried over $MgSO_4$ and condensed under reduced pressure. The resulting solid was dissolved in minimal DCM and passed through a PTFE syringe filter. Finally, the DCM was removed, and the resulting solid was collected in a frit using pentanes to give a bright red solid. 54.5% isolated yield (0.185 g). Elemental analysis for $C_{46}H_{64}ClCrN_2O_3 \cdot CH_2Cl_2$ calc'd: C 65.23, H 7.69, N 3.24; found: C 65.36, H 7.64, N 3.69. ESI-MS (m/z): [Cr(^{tbu}dh^{tbu}bpy)]–Cl–H_2O+CH_3OH calc'd: 458.4479 found: 758.4084.

Synthesis of Triphenylothiophene 4,4-dioxide, TPTD

The synthesis of triphenylothiophene 4,4-dioxide (TPTD) was carried out following a previously reported method.[39, 40]

Synthesis of 2,8-Dimesityldibenzothiophene 5,5-dioxide, Mes$_2$DBTD

2,8-dibromodibenzothiophene 5,5-dioxide was prepared by a previously reported method.[80, 81] Three microwave tubes were each filled with 2,8-dibromodibenzothiophene 5,5-dioxide (0.503 g, 1.35 mmol), (2,4,6-trimethylphenyl)boronic acid (0.553 g, 3.37 mmol), sodium carbonate (3.77 g, 35.7 mmol), $Pd(PPh_3)_4$ (0.124 g, 0.108 mmol), and degassed toluene (30 mL), water (12 mL), and methanol (8 mL). The microwave conditions were set to heat the reaction mixture to 170 °C as fast as possible and then held at that temperature for 200 minutes. After cooling, the three tubes were combined, and the toluene layer was set aside. The aqueous layer was extracted with dichloromethane (6 x 100 mL). All organic fractions were combined and dried over $MgSO_4$ before removing the solvent via reduced pressure leaving a white solid. The solid was first recrystallized by methanol and then a second recrystallization was done using minimal hot ethyl acetate and methanol to give a fluffy white solid. 51.9% isolated yield (0.949 g). ^{1}H NMR (CD_2Cl_2, 600 MHz): δ 7.88 (dd, 2H, Ar*H*), 7.57 (dd, 2H, Ar*H*), 7.34 (dd, 2H, Ar*H*), 6.96 (s, 4H, Ar*H*), 2.31 (s, 6H, −CH_3), 2.02 (s, 6H, −CH_3). ^{13}C{^{1}H} NMR (CD_2Cl_2, 150 MHz): δ 148.4 (Ar*C*), 138.2 (Ar*C*), 137.5 (Ar*C*), 137.0 (Ar*C*), 135.9 (Ar*C*), 132.7 (Ar*C*), 132.3 (Ar*C*), 128.9 (Ar*C*), 123.5 (Ar*C*), 122.6 (Ar*C*), 21.3

(Me*C*), 21.0 (Me*C*). Elemental Analysis for $C_{30}H_{28}O_2S\cdot[C_4H_8O_2]_{1/3}$ calc'd: C 78.08, H 6.41, N 0.00; found: C 78.14, H 6.29, N 0.02. ESI-MS (m/z): calc'd: 452.1010; found 452.1803.

Synthesis of 2,8-Diphenyldibenzothiophene 5,5-dioxide, Ph_2DBTD

2,8-Dibromodibenzothiophene 5,5-dioxide (1.00 g, 2.67 mmol), phenylboronic acid (0.750 g, 6.15 mmol), K_3PO_4 (0.57 g, 2.7 mmol), $Pd(PPh_3)_4$ (0.15 g, 0.13 mmol), and 1,4-dioxane (100 mL) were added to a 250 mL pressure flask with a stir bar in an inert atmosphere glovebox. The reaction was stirred at 130 °C under inert atmosphere for 3 days. After cooling to room temperature, the reaction was exposed to air. The reaction was then diluted with brine (75 mL) and the dioxane layer was separated. The aqueous layer was then extracted with DCM (5 x 75 mL) and all organic layers were dried over $MgSO_4$. Silica was added to the flask (15 g) and the solvent was removed to dryness under reduced pressure. The dry loaded sample was then separated by column chromatography with hexanes and DCM as eluent. Solvent mixture was initially 50% hexanes and 50% DCM and gradually adjusted to 100% DCM. The third fraction was collected and solvent was removed to yield an off-white solid with an isolated yield of 0.288 g, 29.2% yield. ^{1}H NMR (CD_2Cl_2, 600 MHz): δ 8.74 (s, 1H, Ar*H*), 8.06 (d, 1H, Ar*H*), 7.97 (dd, 1H, Ar*H*), 7.91 (d, 2H, Ar*H*), 7.57 (t, 2H, Ar*H*) 7.50 (t, 1H, Ar*H*). ^{13}C{^{1}H} NMR (CD_2Cl_2, 150 MHz): δ 147.8 (Ar*C*), 139.8 (Ar*C*), 137.4 (Ar*C*), 132.8 (Ar*C*), 130.0 (Ar*C*), 129.7 (Ar*C*), 129.4 (Ar*C*), 127.9 (Ar*C*), 122.8 (Ar*C*), 121.0 (Ar*C*). Elemental Analysis for $C_{24}H_{16}O_2S$ calcd: C 78.27, H 4.38, N 0.00; found: C 77.67, H 4.38, N 0.01. ESI-MS (m/z): calcd: 368.0871; found 368.0872.

Evans' Method Characterization of 2

The spin state of the Cr(^{tbu}dh^{tbu}bpy)Cl(H_2O) (**2**) catalyst was characterized as a Cr(III) species via Evans' Method.[82, 83] Three capillary inserts were made with a 50% v/v mixture of DMF and DMF-d_7. Each insert was flame sealed, and then placed in an NMR tube. Then 8.3 mg of **2** was dissolved in 3 mL of DMF. Approximately 0.6 mL of the solution of **2** was added to each of the three NMR tubes containing a flame sealed insert. ^{1}H NMR spectra with 64 scans were then taken

using a 600 MHz Varian NMR Spectrometer. The results of this experiment, which was run in triplicate, can be seen in **Table S3.3**. The average μ_{eff} of **2** was 3.86±0.10.

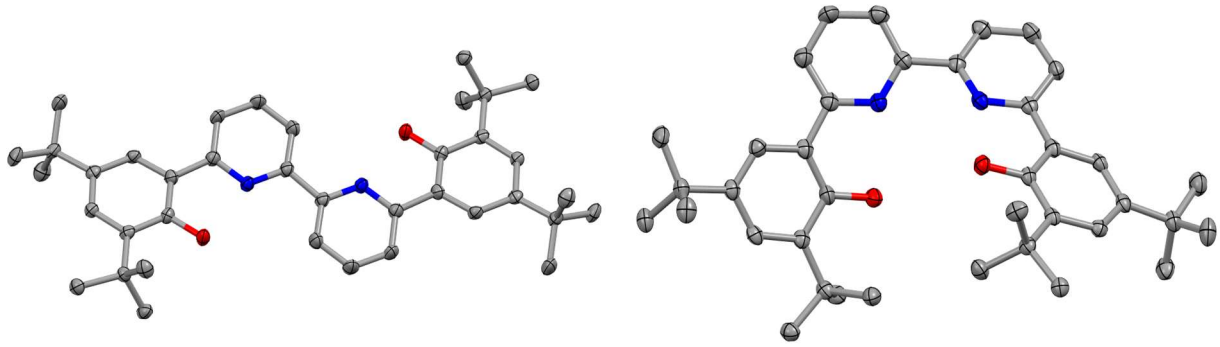

Figure S3.1. The two polymorphs of single crystal structures of ^{tbu}dhbpy(H)$_2$ ligandobtained from X-ray diffraction studies. Blue = N, red = O, gray = C; thermal ellipsoids at 50%; H atoms omitted for clarity. CCDC 1984950 (left) and 1984949 (right).

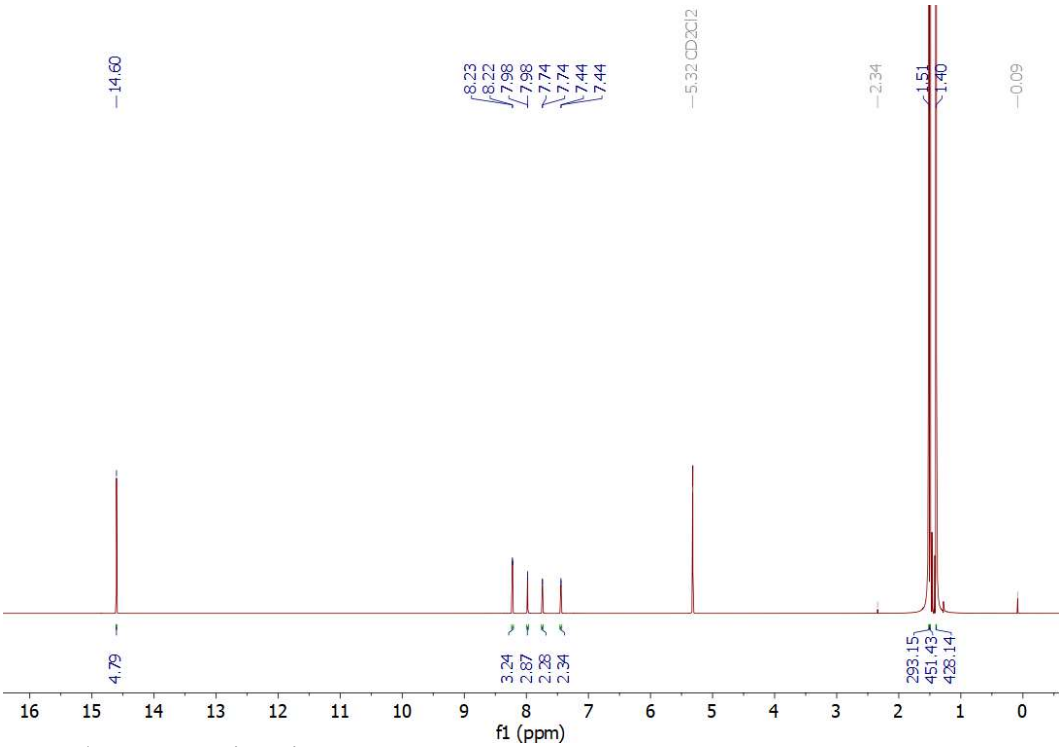

Figure S3.2. ^{1}H NMR of ^{tbu}dh^{tbu}bpy(H)$_2$ ligand; CD_2Cl_2; 600 MHz.

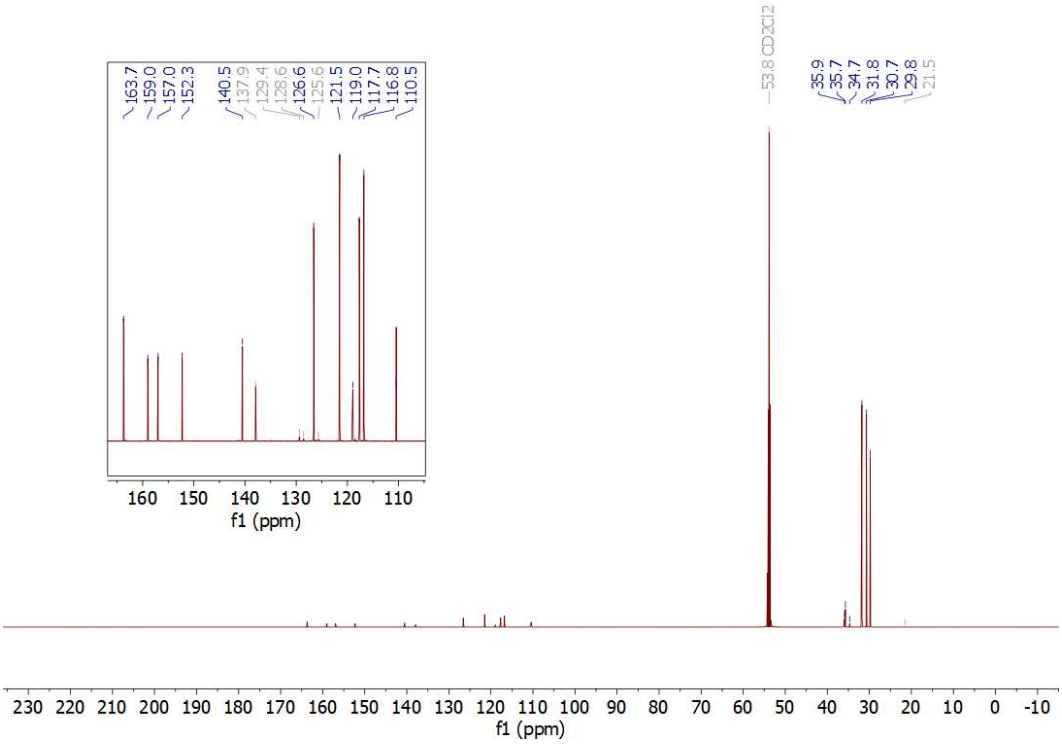

Figure S3.3. $^{13}C\{^{1}H\}$

NMR of $^{tbu}dh^{tbu}bpy(H)_2$ ligand; CD_2Cl_2; 150 MHz.

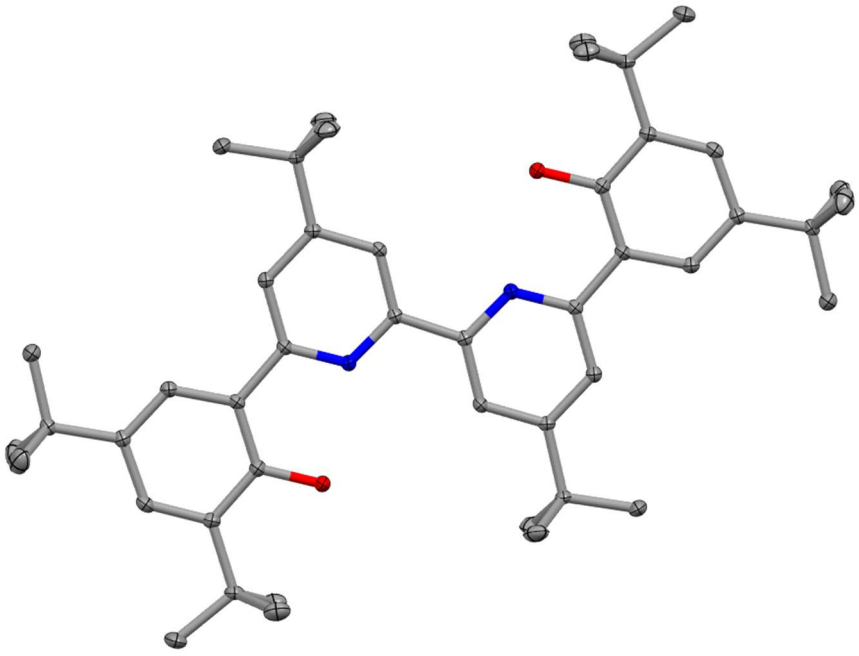

Figure S3.4. Single crystal structures of $^{tbu}dh^{tbu}bpy(H)_2$ ligand obtained from single-crystal X-ray diffraction studies. Blue = N, red = O, gray = C; thermal ellipsoids at 50%; H atoms omitted for clarity. CCDC 2150929.

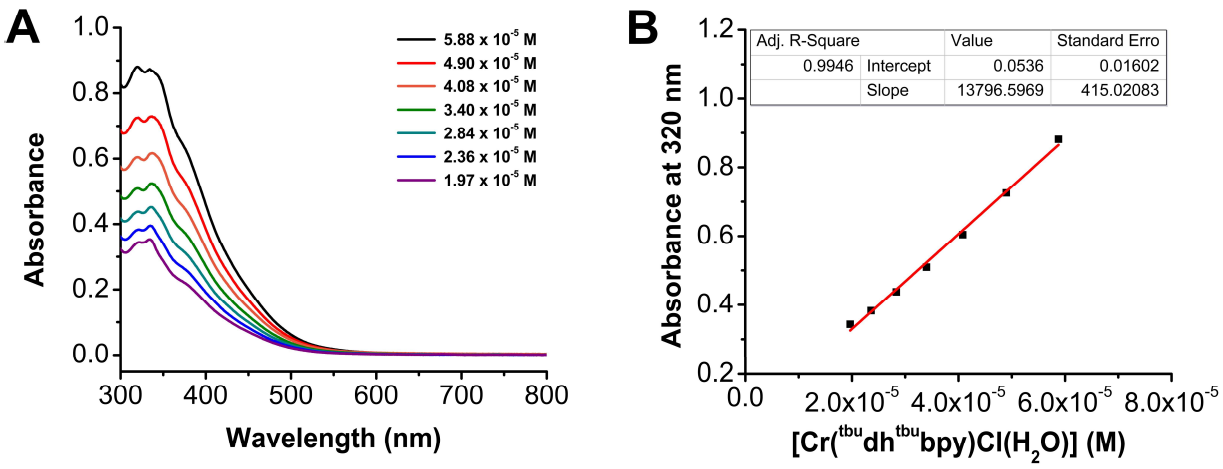

Figure S3.5. (**A**) UV-vis serial dilution absorbance data obtained from Cr(^{tbu}dh^{tbu}bpy)Cl(H_2O) **2** in a DMF solution. Conditions: varying concentration; quartz cell with 1 cm pathlength. (**B**) Plot of absorbance versus concentration (M) for Cr(^{tbu}dh^{tbu}bpy)Cl(H_2O) **2** in DMF at 320 nm (13800 M^{-1} cm^{-1}); R^2 = 0.995. All: λ_{max} = 333 nm (13300 M^{-1} cm^{-1}) and 383 nm (9780 M^{-1} cm^{-1}).

Table S3.3. Evans' method results for Cr(^{tbu}dh^{tbu}bpy)Cl(H_2O) (**2**) in DMF.[82, 83]

Trial	Chemical Shift (ppm)	Chemical Shift (Hz)	Total Magnetic Moment (emu mol^{-1})	Paramagnetic Moment (emu mol^{-1})	μ_{eff} (Bohr Magnetons)
1	0.0805	48.3	0.00542	5.96 x 10^{-3}	3.77
2	0.0896	53.8	0.00603	6.57 x 10^{-3}	3.96
3	0.0803	48.2	0.00541	5.94 x 10^{-3}	3.76

3.7.3 Electrochemistry of **2**

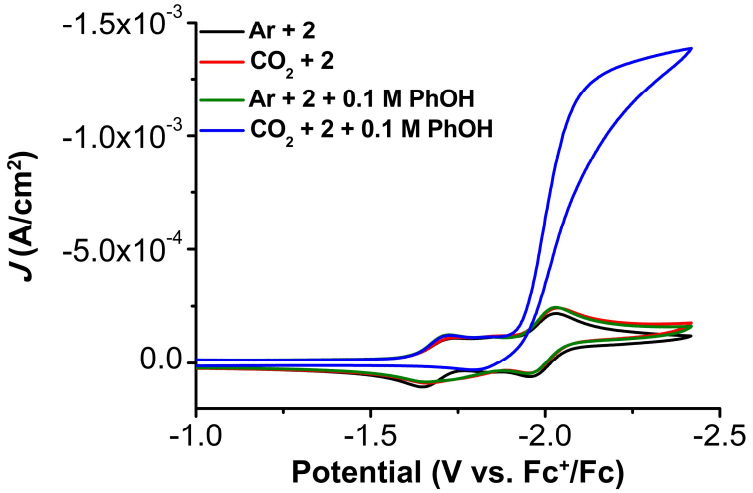

Figure S3.6. Comparison of CVs of 1.0 mM Cr(^{tbu}dh^{tbu}bpy)Cl(H_2O) **2** under Ar and CO_2 saturation conditions with and without 0.1 M PhOH. Conditions: 0.1 M $TBAPF_6$/DMF; glassy carbon working electrode, glassy carbon rod counter electrode, Ag/AgCl pseudoreference electrode; referenced to Fc^+/Fc internal standard; 100 mV/s scan rate.

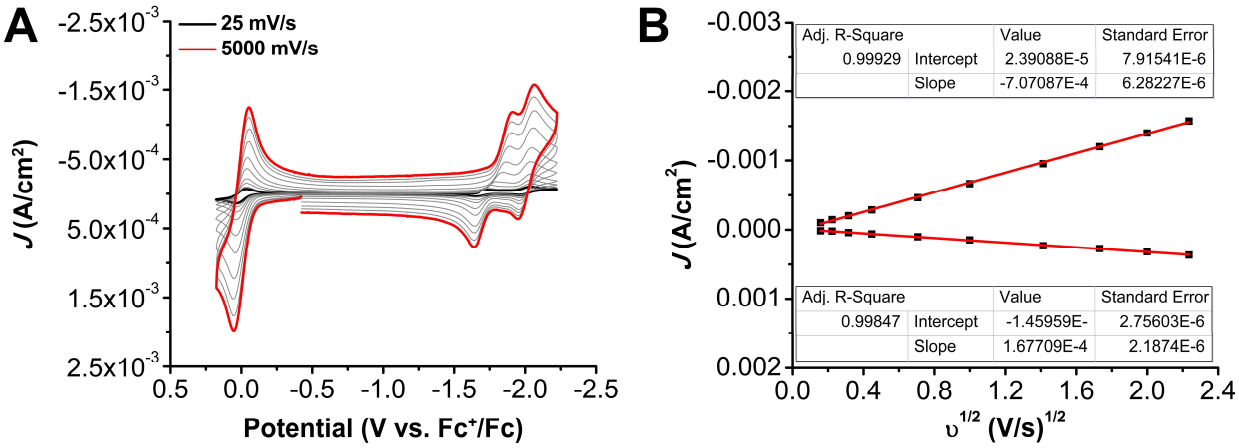

Figure S3.7. (**A**) CVs of Cr(^{tbu}dh^{tbu}bpy)Cl(H_2O) **2** at variable scan rates ranging from 25 (black) to 5000 (red) mV/s, obtained under Ar saturation conditions. (**B**) Linear Fit of variable scan rate data from (**A**) demonstrating that Cr(^{tbu}dh^{tbu}bpy)Cl(H_2O) **2** shows a diffusion-limited current response. The data in (**B**) was obtained from the reversible redox feature at −2.00 V vs Fc^+/Fc. Conditions:

1.0 mM **2**, 0.1 M $TBAPF_6$/DMF; glassy carbon working electrode, glassy carbon counter electrode, Ag/AgCl pseudoreference electrode; varied scan rate; referenced to internal ferrocene standard.

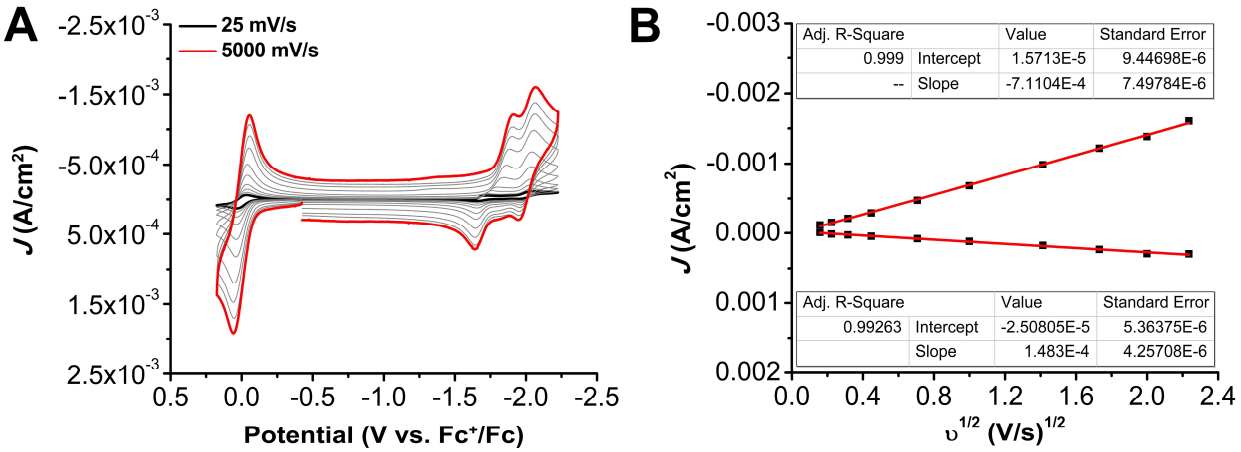

Figure S3.8. (**A**) CVs of Cr(^{tbu}dh^{tbu}bpy)Cl(H_2O) **2** at variable scan rates ranging from 25 (black) to 5000 (red) mV/s, obtained under CO_2 saturation conditions. (**B**) Linear Fit of variable scan rate data from (**A**) demonstrating that Cr(^{tbu}dh^{tbu}bpy)Cl(H_2O) **2** shows a diffusion-limited current response. The data in (**B**) was obtained from the reversible redox feature at −2.00 V vs Fc^+/Fc. Conditions: 1.0 mM **2**, 0.1 M $TBAPF_6$/DMF; glassy carbon working electrode, glassy carbon counter electrode, Ag/AgCl pseudoreference electrode; varied scan rate; referenced to internal ferrocene standard.

For all variable concentration studies without the presence of RMs (Figures S3.9-S3.11) analysis was adapted from Sathrum and Kubiak J. Phys. Chem. Lett. 2011, *2*, 2372.[84] F is Faraday's constant, A is the electrode area, [Q] is the substrate concentration, k_{cat} is the catalytic rate, D is the diffusion constant of the catalyst, [cat] is the concentration of the catalyst, and n_{cat} is the number of electrons involved in the catalytic process.

$$\boldsymbol{i_{cat} = n_{cat}FA[cat](Dk_{cat}[Q]^{y})^{\frac{1}{2}}}$$

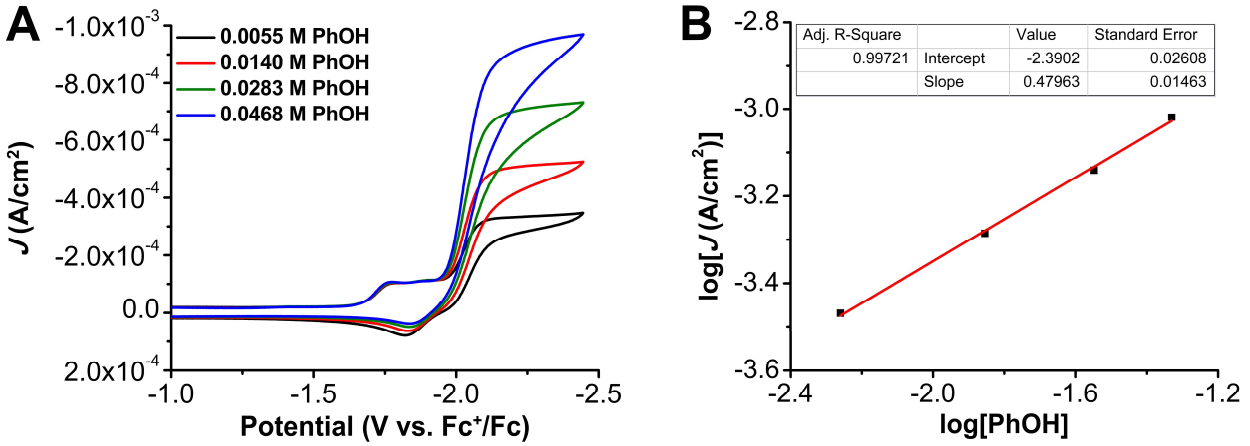

Figure S3.9. (**A**) CVs of 1.0 mM Cr(^{tbu}dh^{tbu}bpy)Cl(H_2O) **2**, obtained under CO_2 saturation conditions with variable PhOH concentration. Conditions: 1.0 mM **2**, 0.1 M $TBAPF_6$/DMF; glassy carbon working electrode, glassy carbon counter electrode, Ag/AgCl pseudoreference electrode; 100 mV/s scan rate; referenced to internal ferrocene standard. (**B**) Log-log plot from data obtained from CVs in **A** at −2.36 V vs. Fc^+/Fc.

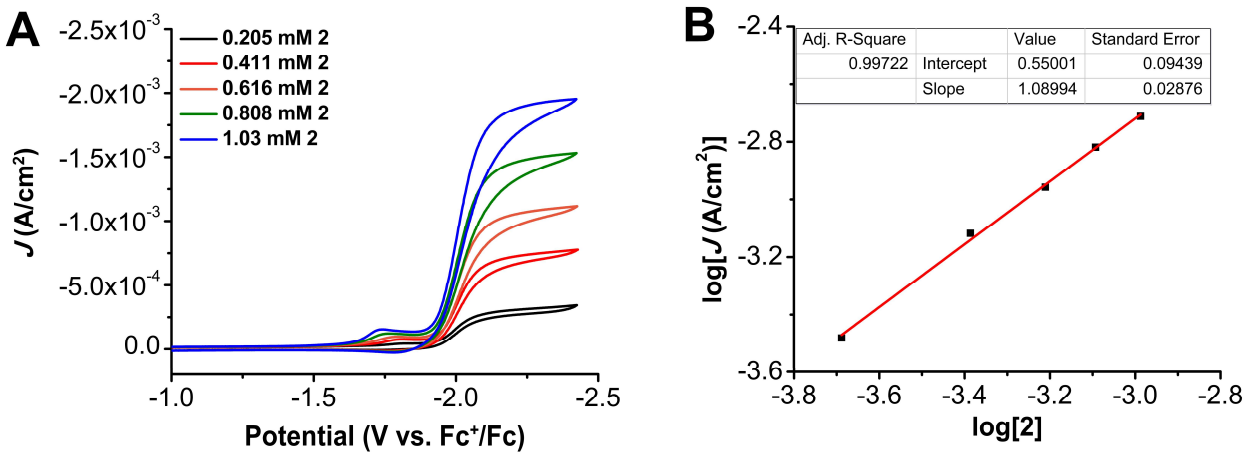

Figure S3.10. (**A**) CVs of Cr(^{tbu}dh^{tbu}bpy)Cl(H_2O) **2** at variable concentrations, obtained under CO_2 saturation with 0.325 M PhOH. Conditions: 0.1 M $TBAPF_6$/DMF; glassy carbon working electrode, glassy carbon counter electrode, Ag/AgCl pseudoreference electrode; 100 mV/s scan rate; referenced to internal ferrocene standard. (**B**) Log-log plot from data obtained from CVs in **A** at −2.36 V vs. Fc^+/Fc.

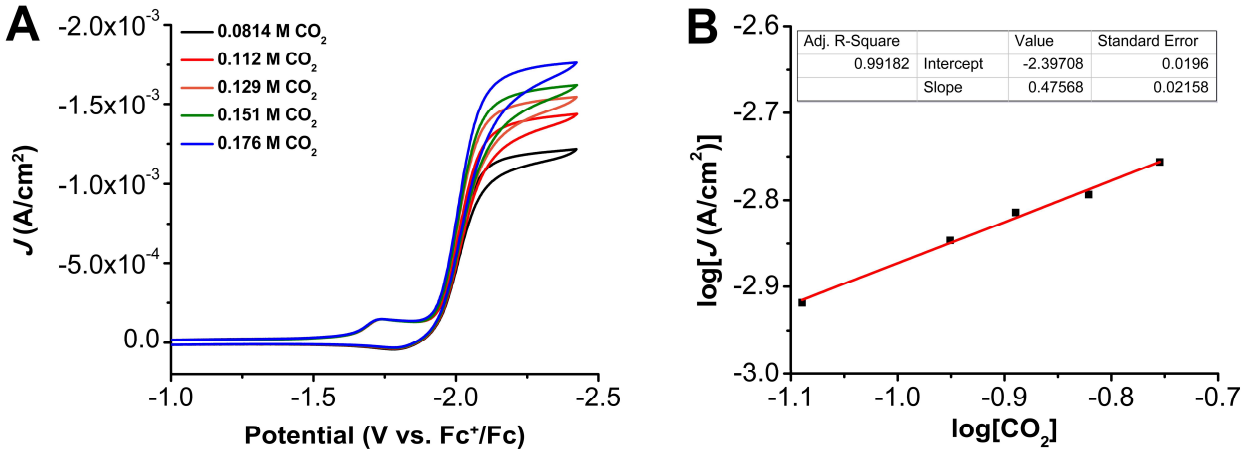

Figure S3.11. (**A**) CVs of 1.0 mM Cr(^{tbu}dh^{tbu}bpy)Cl(H_2O) **2** obtained under variable CO_2 concentration with 0.325 M PhOH. Conditions: 0.1 M $TBAPF_6$/DMF; glassy carbon working electrode, glassy carbon counter electrode, Ag/AgCl pseudoreference electrode; 100 mV/s scan rate; referenced to internal ferrocene standard. (**B**) Log–log plot from data obtained from CVs in **A** at −2.36 V vs. Fc^+/Fc.

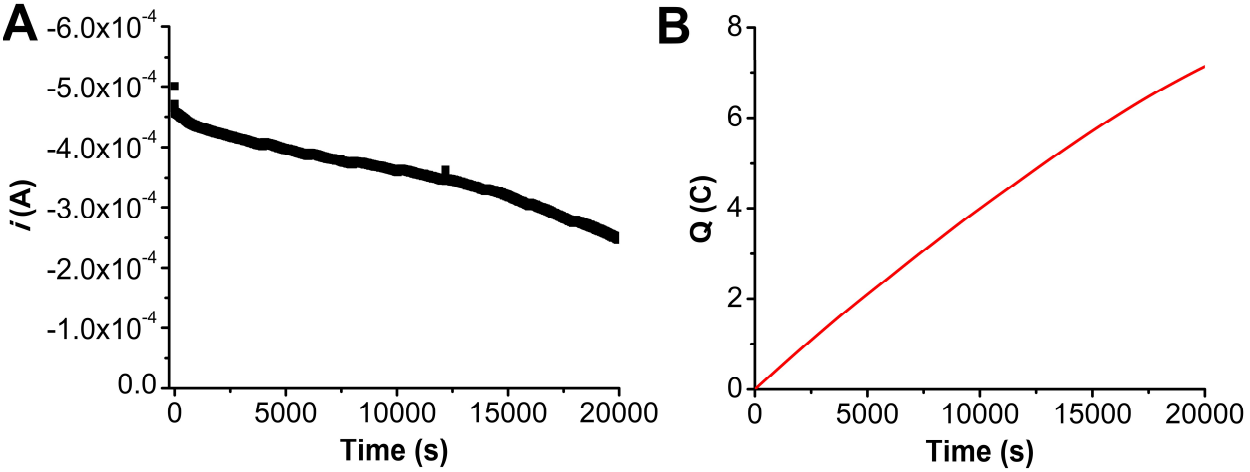

Figure S3.12. (**A**) Current versus time trace from CPE experiment for **2**+PhOH. (**B**) Charge passed versus time for the CPE experiment shown in **A**. Conditions were 0.1 mM Cr(^{tbu}dh^{tbu}bpy)Cl(H_2O) **2** and 0.12 M PhOH under a CO_2 atmosphere at −2.30 V vs Fc^+/Fc in 0.1 M $TBAPF_6$/DMF; working electrode was a glassy carbon rod, counter electrode was a graphite rod, and the reference was a nonaqueous Ag/AgCl pseudoreference electrode; 0.075 M Fc was used as sacrificial oxidant.

Table S3.4. Results from CPE experiment in Figure S3.12, **2** + PhOH.

Time (s)	Charge (coulombs)	moles (e^-)	Moles of CO	FE_{CO}
17914	6.58	6.82×10^{-5}	3.64×10^{-5}	106.8
20000*	7.14	7.40×10^{-5}	3.53×10^{-5}	95.34
20000*	7.14	7.40×10^{-5}	3.16×10^{-5}	85.34
20000*	7.14	7.40×10^{-5}	3.39×10^{-5}	91.68

* indicates a triplicate series of injections carried out upon completion of electrolysis.

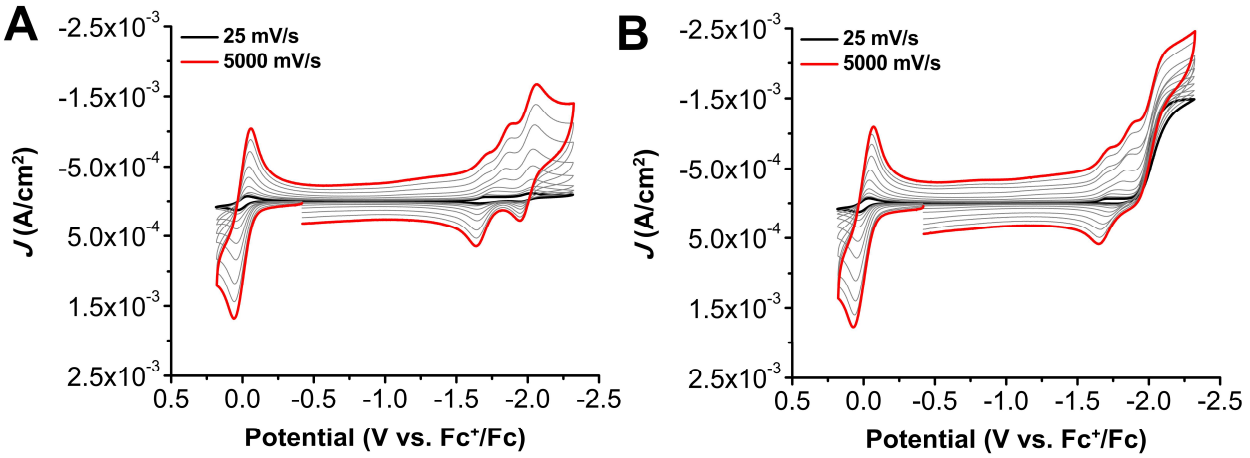

Figure S3.13. CVs of Cr(^{tbu}dh^{tbu}bpy)Cl(H_2O) **2** with 0.1 M PhOH at variable scan rates ranging from 25 (black) to 5000 (red) mV/s, obtained under Ar (**A**) and CO_2 (**B**) saturation conditions. Conditions: 1.0 mM 2, 0.1 M $TBAPF_6$/DMF; glassy carbon working electrode, glassy carbon counter electrode, Ag/AgCl pseudoreference electrode; varied scan rate; referenced to internal ferrocene standard.

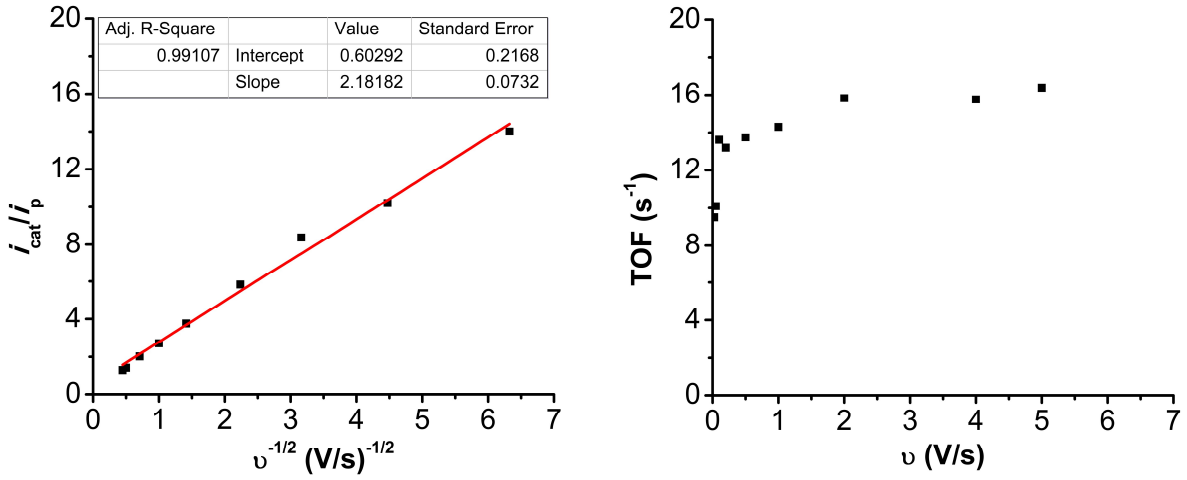

Figure S3.14. Plots of (**A**) i_{cat}/i_p versus the inverse of the square root of the scan rate and (**B**) TOF versus scan rate for Cr(^{tbu}dh^{tbu}bpy)Cl(H_2O) **2**, with 0.1 M PhOH from data in Figure S3.13.

Table S3.5. TOF values determined from the i_{cat}/i_p method with variable scan rates in Figure S3.13 and S3.14.

Scan Rate (V/s)	TOF (s^{-1})
0.025	9.50
0.05	10.1
0.1	13.6
0.2	13.2
0.5	13.7
1	14.3
2	15.8
4	15.8
5	16.4

3.7.4 Characterization of RMs

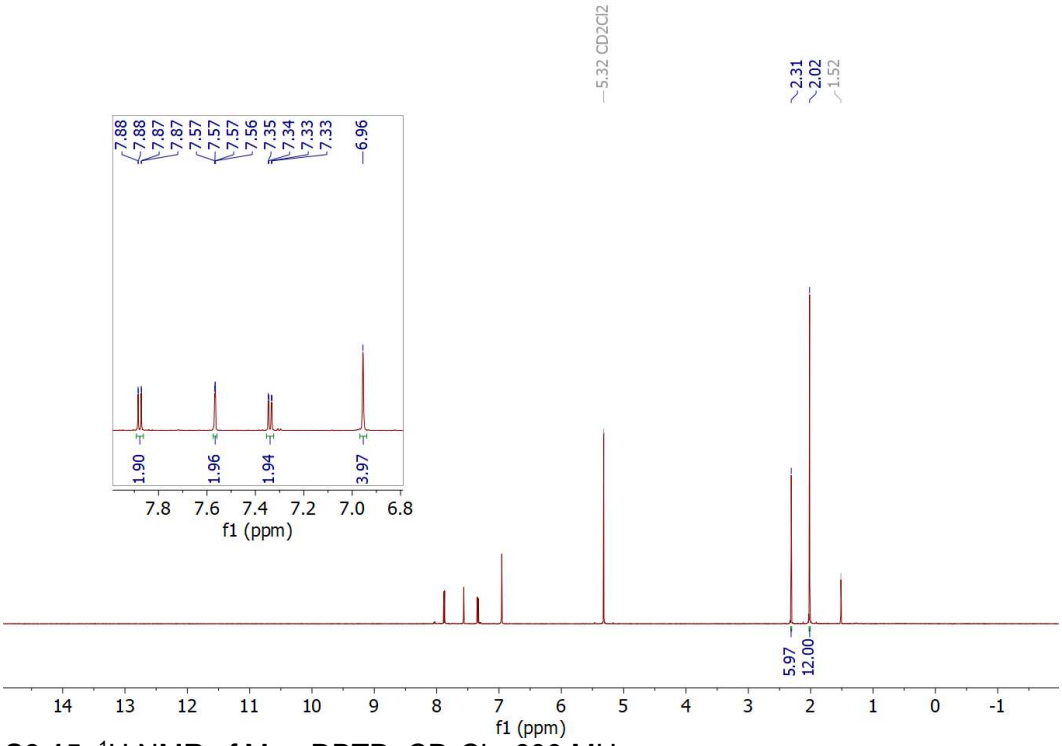

Figure S3.15. ^{1}H NMR of Mes_2DBTD; CD_2Cl_2; 600 MHz.

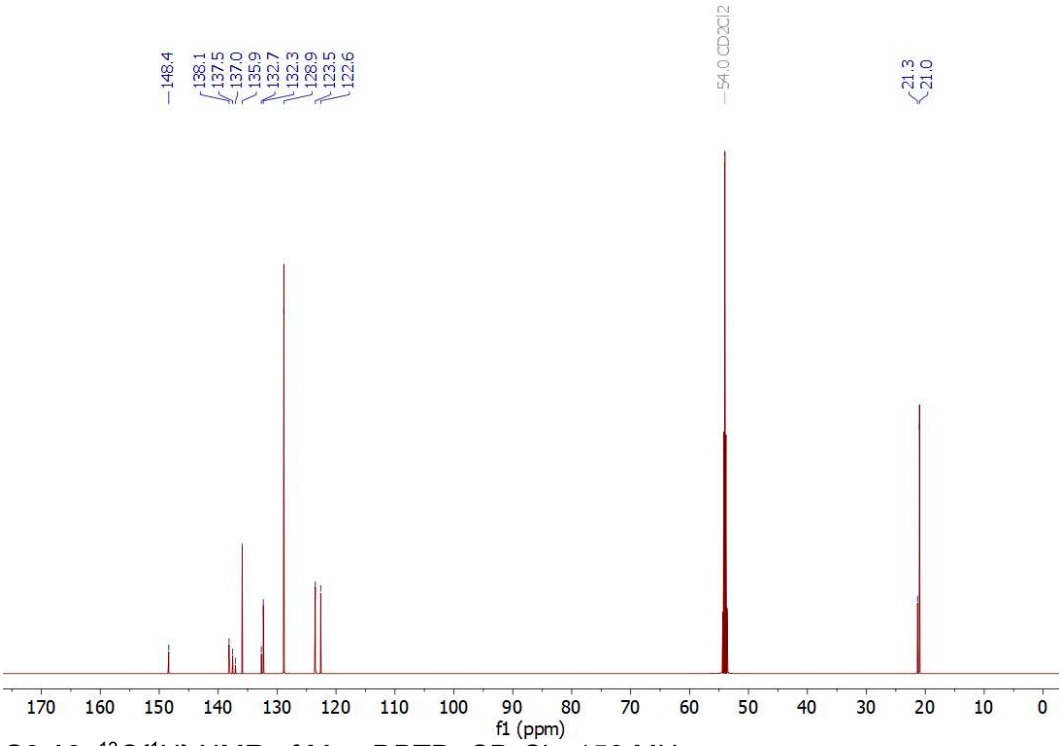

Figure S3.16. $^{13}C\{^{1}H\}$ NMR of Mes_2DBTD; CD_2Cl_2; 150 MHz.

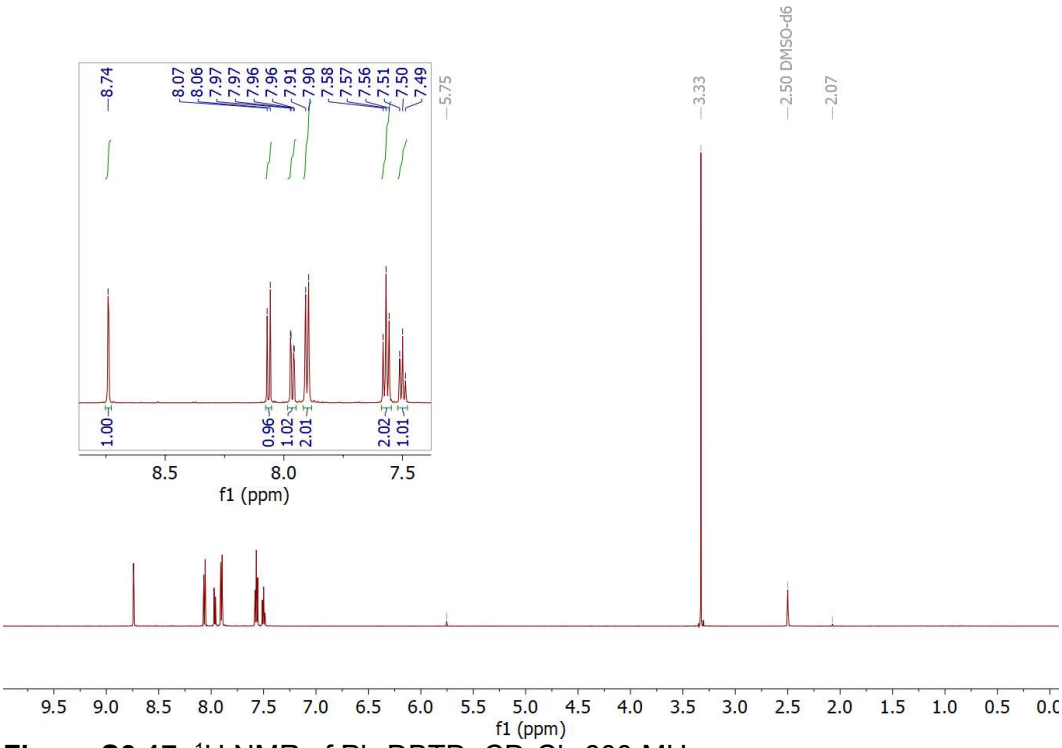

Figure S3.17. ^{1}H NMR of Ph_2DBTD; CD_2Cl_2; 600 MHz.

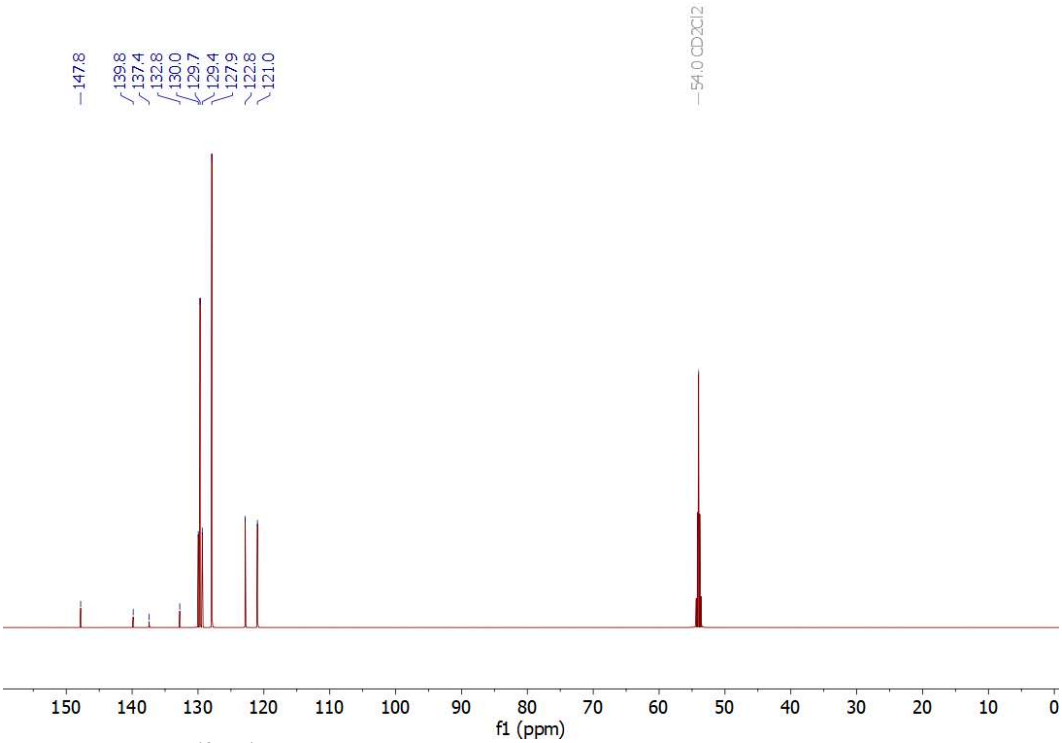

Figure S3.18. $^{13}C\{^{1}H\}$ NMR of Ph_2DBTD; CD_2Cl_2; 150 MHz.

3.7.5 Electrochemistry of RMs

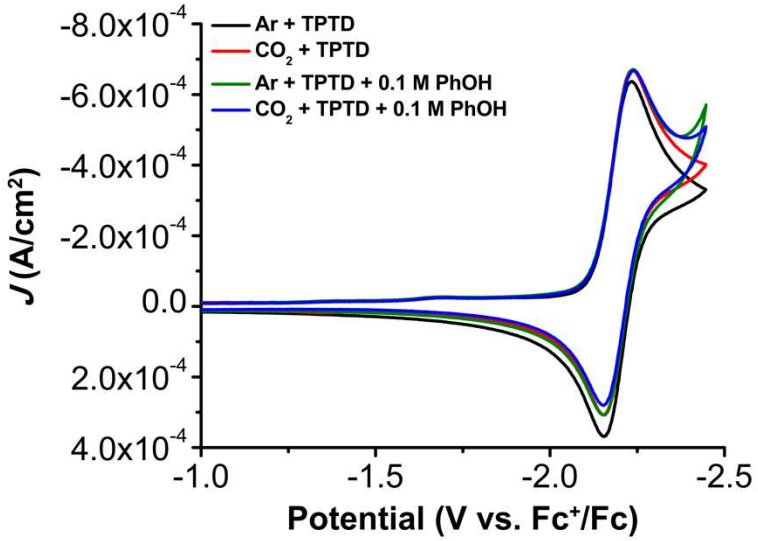

Figure S3.19. CVs of 2.5 mM TPTD both with and without 0.1 M PhOH obtained under Ar and CO_2 saturation conditions. Conditions: 0.1 M $TBAPF_6$/DMF; glassy carbon working electrode, glassy carbon rod counter electrode, Ag/AgCl pseudoreference electrode; referenced to Fc^+/Fc internal standard; 100 mV/s scan rate.

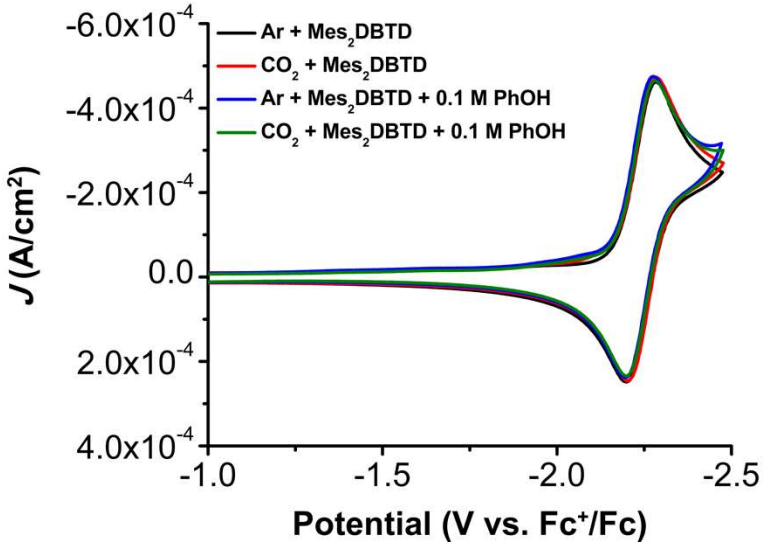

Figure S3.20. CVs of 2.5 mM Mes_2DBTD both with and without 0.1 M PhOH obtained under Ar and CO_2 saturation conditions. Conditions: 0.1 M $TBAPF_6$/DMF; glassy carbon working electrode, glassy carbon rod counter electrode, Ag/AgCl pseudoreference electrode; referenced to Fc^+/Fc internal standard; 100 mV/s scan rate.

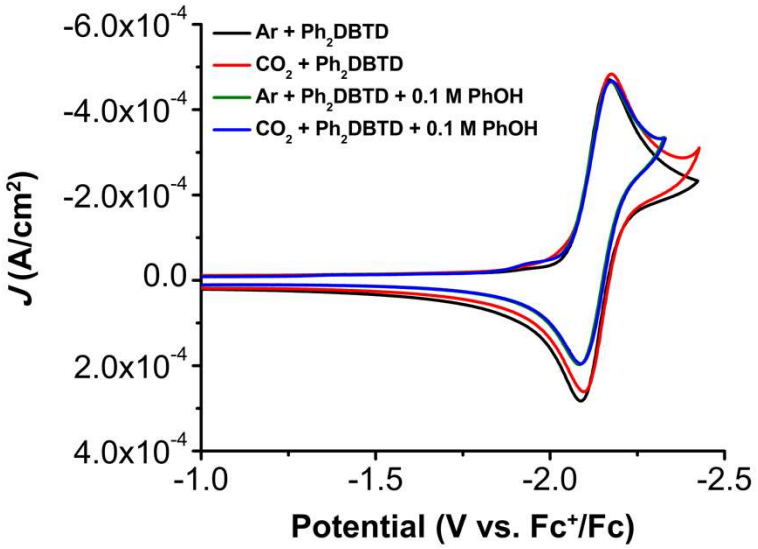

Figure S3.21. CVs of 2.5 mM Ph_2DBTD both with and without 0.1 M PhOH obtained under Ar and CO_2 saturation conditions. Conditions: 0.1 M $TBAPF_6$/DMF; glassy carbon working electrode, glassy carbon rod counter electrode, Ag/AgCl pseudoreference electrode; referenced to Fc^+/Fc internal standard; 100 mV/s scan rate.

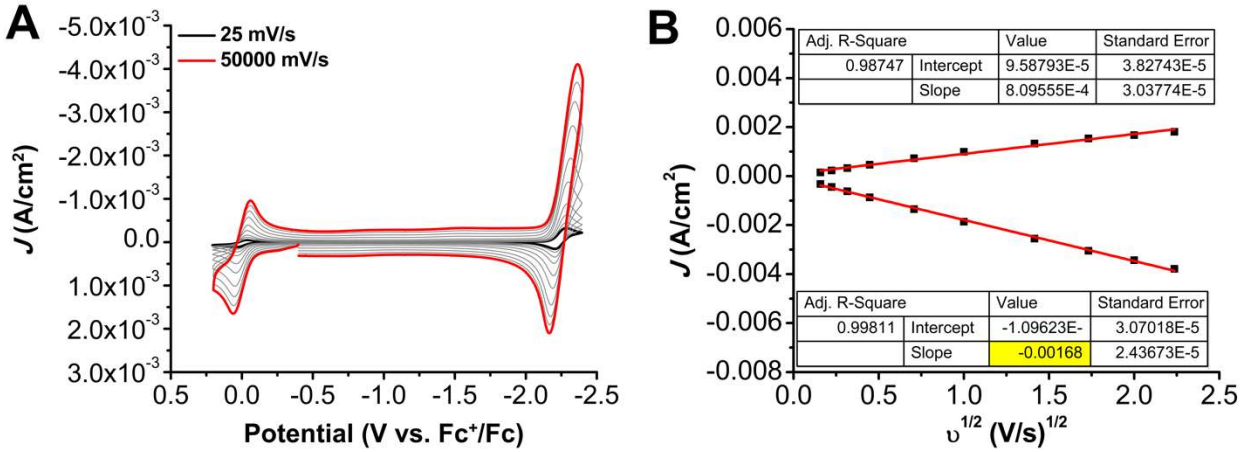

Figure S3.22. (**A**) CVs of 2.5 mM DBTD at variable scan rates ranging from 25 (black) to 5000 (red) mV/s, obtained under Ar saturation conditions. (**B**) Linear Fit of variable scan rate data from **A** demonstrating that DBTD shows a diffusion-limited current response. The slope highlighted in yellow was used to calculate the diffusion coefficient in Table S3.6. The data in **B** was obtained from the reversible redox feature at −2.25 V vs Fc^+/Fc. Conditions: 0.1 M $TBAPF_6$/DMF; glassy carbon working electrode, glassy carbon counter electrode, Ag/AgCl pseudoreference electrode; varied scan rate; referenced to internal ferrocene standard.

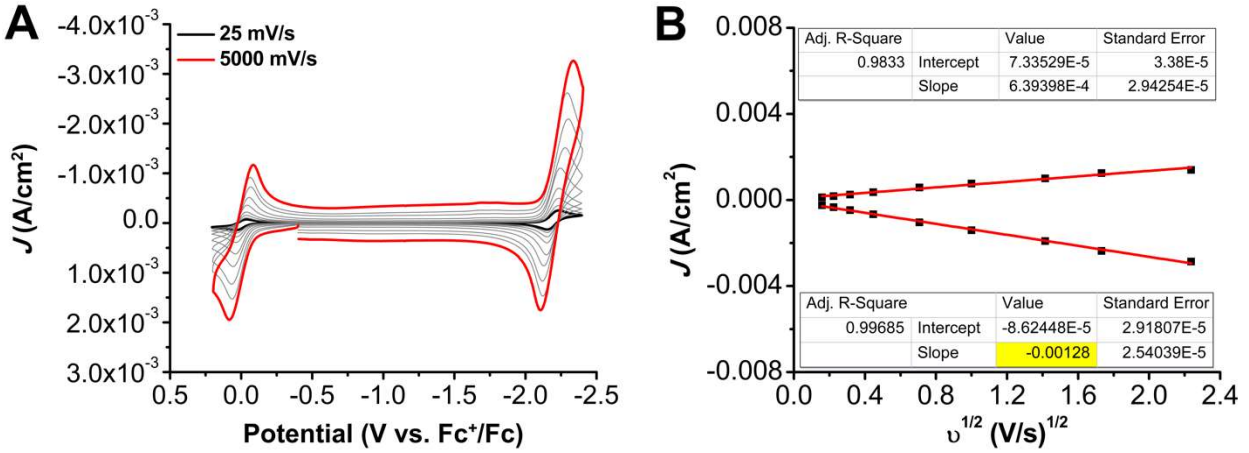

Figure S3.23. (**A**) CVs of 2.4 mM TPTD at variable scan rates ranging from 25 (black) to 5000 (red) mV/s, obtained under Ar saturation conditions. (**B**) Linear Fit of variable scan rate data from **A** demonstrating that DBTD shows a diffusion-limited current response. The slope highlighted in yellow was used to calculate the diffusion coefficient in Table S3.6. The data in **B** was obtained from the reversible redox feature at −2.19 V vs Fc^+/Fc. Conditions: 0.1 M $TBAPF_6$/DMF; glassy carbon working electrode, glassy carbon counter electrode, Ag/AgCl pseudoreference electrode; varied scan rate; referenced to internal ferrocene standard.

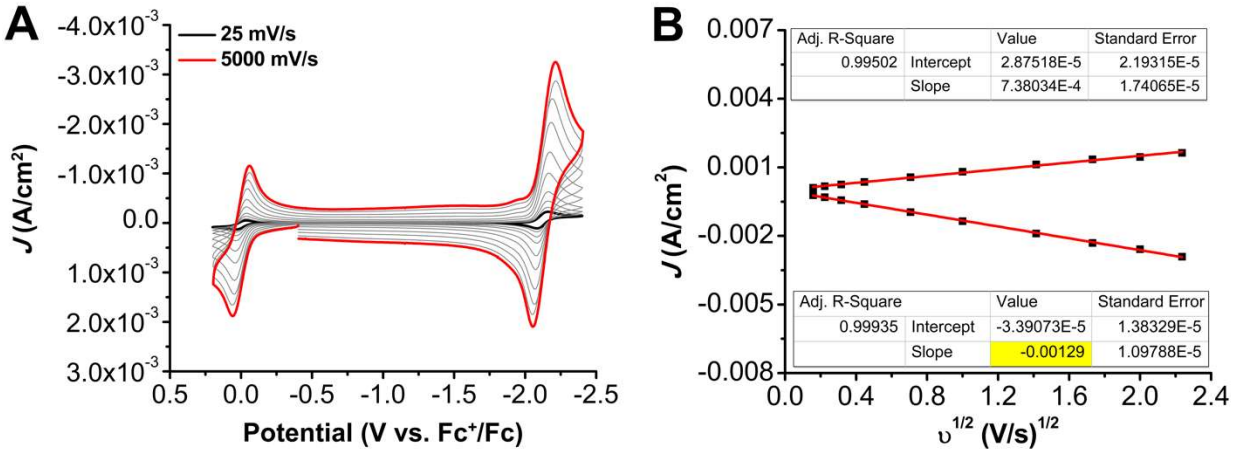

Figure S3.24. (**A**) CVs of 2.5 mM Ph_2DBTD at variable scan rates ranging from 25 (black) to 5000 (red) mV/s, obtained under Ar saturation conditions. (**B**) Linear Fit of variable scan rate data from **A** demonstrating that DBTD shows a diffusion-limited current response. The slope highlighted in yellow was used to calculate the diffusion coefficient in Table S3.6. The data in **B** was obtained from the reversible redox feature at −2.12 V vs Fc^+/Fc. Conditions: 0.1 M $TBAPF_6$/DMF; glassy carbon working electrode, glassy carbon counter electrode, Ag/AgCl pseudoreference electrode; varied scan rate; referenced to internal ferrocene standard.

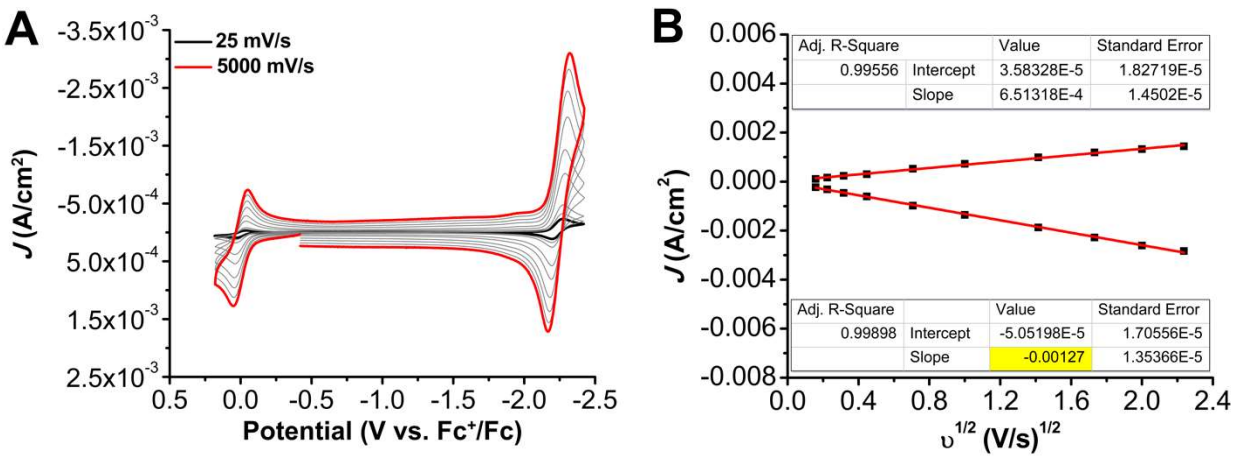

Figure S3.25. (**A**) CVs of 2.5 mM Mes_2DBTD at variable scan rates ranging from 25 (black) to 5000 (red) mV/s, obtained under Ar saturation conditions. (**B**) Linear Fit of variable scan rate data from **A** demonstrating that DBTD shows a diffusion-limited current response. The slope highlighted in yellow was used to calculate the diffusion coefficient in Table S3.6. The data in **B** was obtained from the reversible redox feature at −2.24 V vs Fc^+/Fc. Conditions: 0.1 M $TBAPF_6$/DMF; glassy carbon working electrode, glassy carbon counter electrode, Ag/AgCl pseudoreference electrode; varied scan rate; referenced to internal ferrocene standard.

Table S3.6. Results of Diffusion Coefficient Calculations

	Number of electrons	**Concentration (mM)**	**Slope**	**Diffusion Coefficient (cm^2/s)**
DBTD	1	2.50	−0.00168	6.22×10^{-6}
TPTD	1	2.40	−0.00128	3.93×10^{-6}
Ph_2DBTD	1	2.50	−0.00129	3.68×10^{-6}
Mes_2DBTD	1	2.50	-0.00127	3.57×10^{-6}

3.7.6 Cyclic Voltammetry Under Protic Conditions

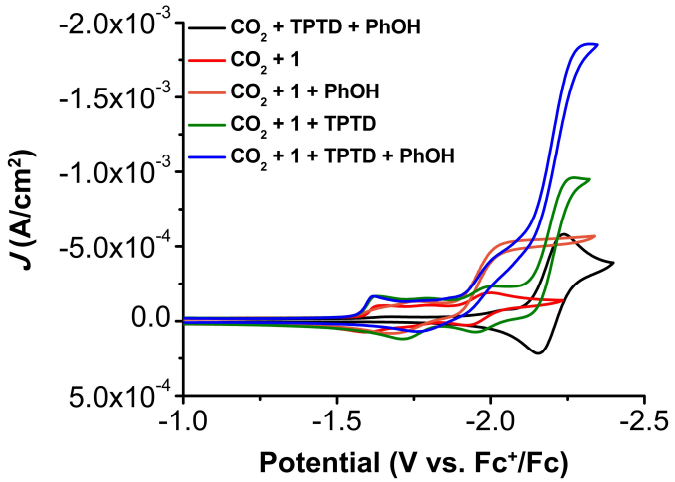

Figure S3.26. Comparison of CVs of 1.0 mM Cr(^{tbu}dhbpy)Cl(H_2O) **1** with and without 2.5 mM TPTD and 0.1 M PhOH under CO_2 saturation conditions. Conditions: 0.1 M $TBAPF_6$/DMF; glassy carbon working electrode, glassy carbon rod counter electrode, Ag/AgCl pseudoreference electrode; referenced to Fc^+/Fc internal standard; 100 mV/s scan rate.

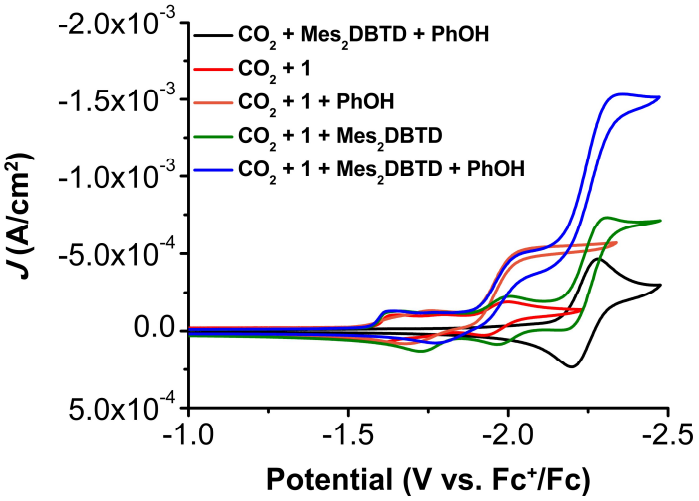

Figure S3.27. Comparison of CVs of 1.0 mM Cr(^{tbu}dhbpy)Cl(H_2O) **1** with and without 2.5 mM Mes_2DBTD and 0.1 M PhOH under CO_2 saturation conditions. Conditions: 0.1 M $TBAPF_6$/DMF; glassy carbon working electrode, glassy carbon rod counter electrode, Ag/AgCl pseudoreference electrode; referenced to Fc^+/Fc internal standard; 100 mV/s scan rate.

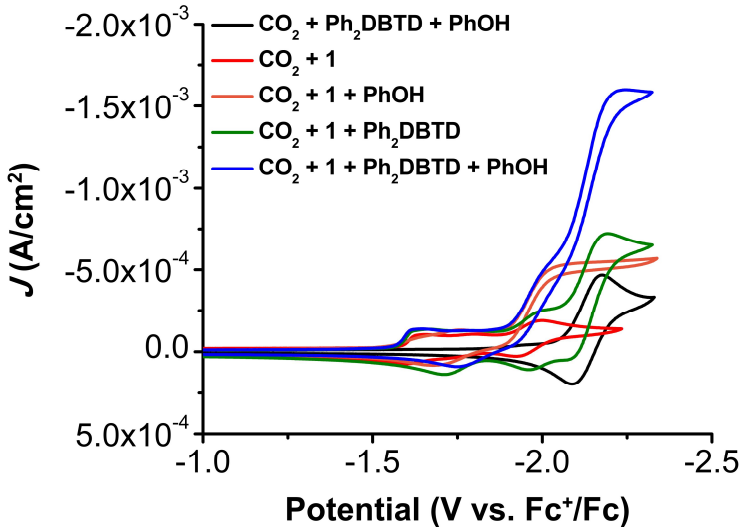

Figure S3.28. Comparison of CVs of 1.0 mM Cr(^{tbu}dhbpy)Cl(H_2O) **1** with and without 2.5 mM Ph_2DBTD and 0.1 M PhOH under CO_2 saturation conditions. Conditions: 0.1 M $TBAPF_6$/DMF; glassy carbon working electrode, glassy carbon rod counter electrode, Ag/AgCl pseudoreference electrode; referenced to Fc^+/Fc internal standard; 100 mV/s scan rate.

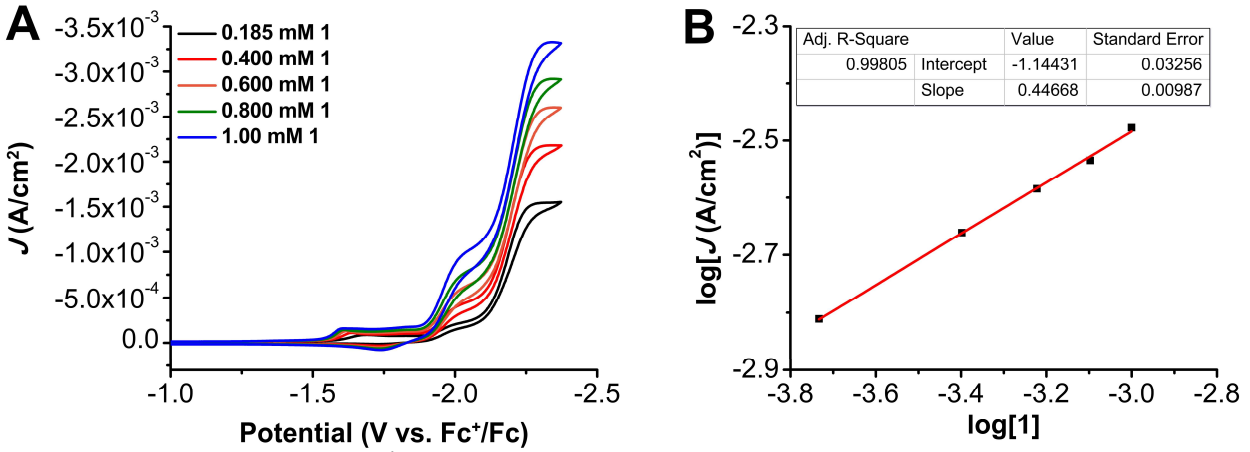

Figure S3.29. (**A**) CVs of Cr(^{tbu}dhbpy)Cl(H_2O) **1** at variable concentrations, obtained under CO_2 saturation with 2.5 mM TPTD and 0.325 M PhOH. Conditions: 0.1 M $TBAPF_6$/DMF; glassy carbon working electrode, glassy carbon counter electrode, Ag/AgCl pseudoreference electrode; 100 mV/s scan rate; referenced to internal ferrocene standard. (**B**) Log-log plot from data obtained from CVs in **A** at −2.34 V vs. Fc^+/Fc.

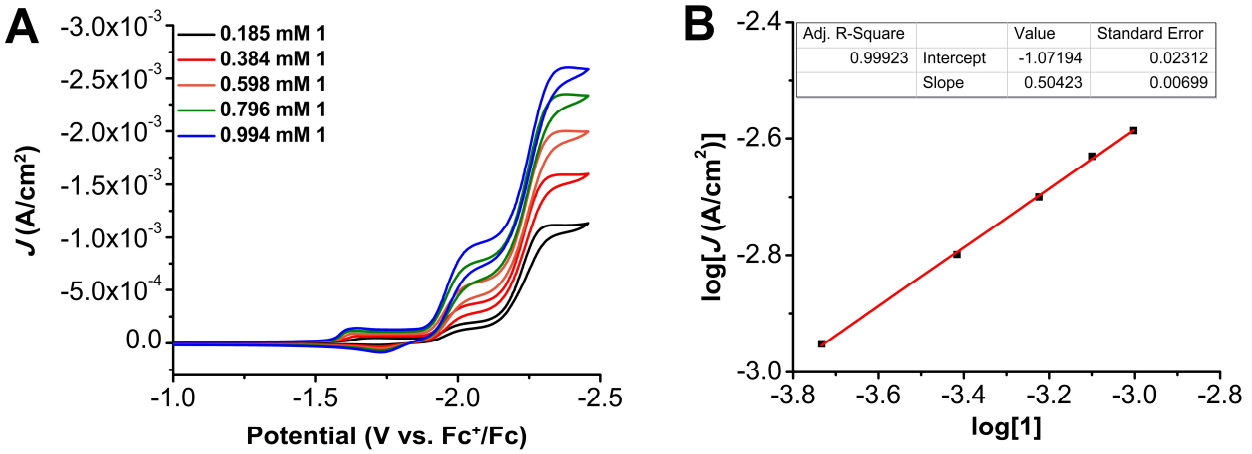

Figure S3.30. (**A**) CVs of Cr(^{tbu}dhbpy)Cl(H_2O) **1** at variable concentrations, obtained under CO_2 saturation with 2.5 mM Mes_2DBTD and 0.325 M PhOH. Conditions: 0.1 M $TBAPF_6$/DMF; glassy carbon working electrode, glassy carbon counter electrode, Ag/AgCl pseudoreference electrode; 100 mV/s scan rate; referenced to internal ferrocene standard. (**B**) Log-log plot from data obtained from CVs in **A** at −2.36 V vs. Fc^+/Fc.

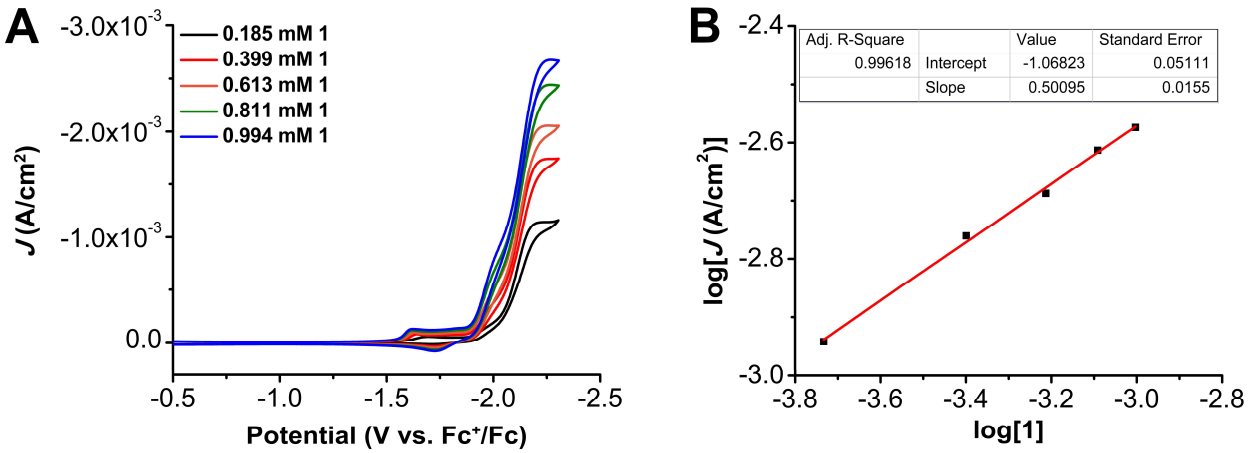

Figure S3.31. (**A**) CVs of Cr(^{tbu}dhbpy)Cl(H_2O) **1** at variable concentrations, obtained under CO_2 saturation with 2.5 mM Ph_2DBTD and 0.325 M PhOH. Conditions: 0.1 M $TBAPF_6$/DMF; glassy carbon working electrode, glassy carbon counter electrode, Ag/AgCl pseudoreference electrode; 100 mV/s scan rate; referenced to internal ferrocene standard. (**B**) Log-log plot from data obtained from CVs in **A** at −2.25 V vs. Fc^+/Fc.

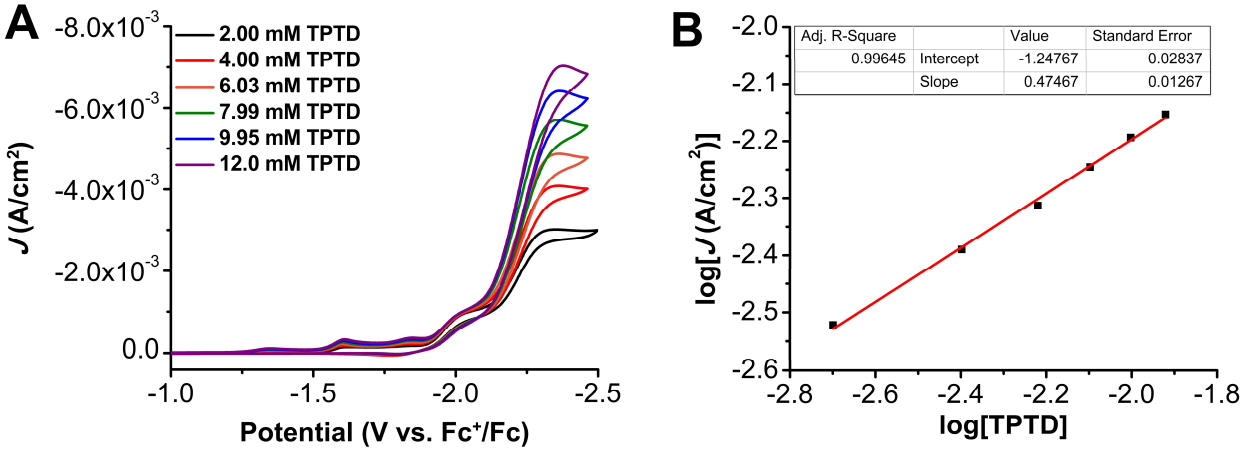

Figure S3.32. (**A**) CVs of 1.0 mM Cr(^{tbu}dhbpy)Cl(H_2O) **1** with 0.325 M PhOH at variable TPTD concentrations, obtained under CO_2 saturation. Conditions: 0.1 M $TBAPF_6$/DMF; glassy carbon working electrode, glassy carbon counter electrode, Ag/AgCl pseudoreference electrode; 100 mV/s scan rate; referenced to internal ferrocene standard. (**B**) Log-log plot from data obtained from CVs in **A** at −2.38 V vs. Fc^+/Fc.

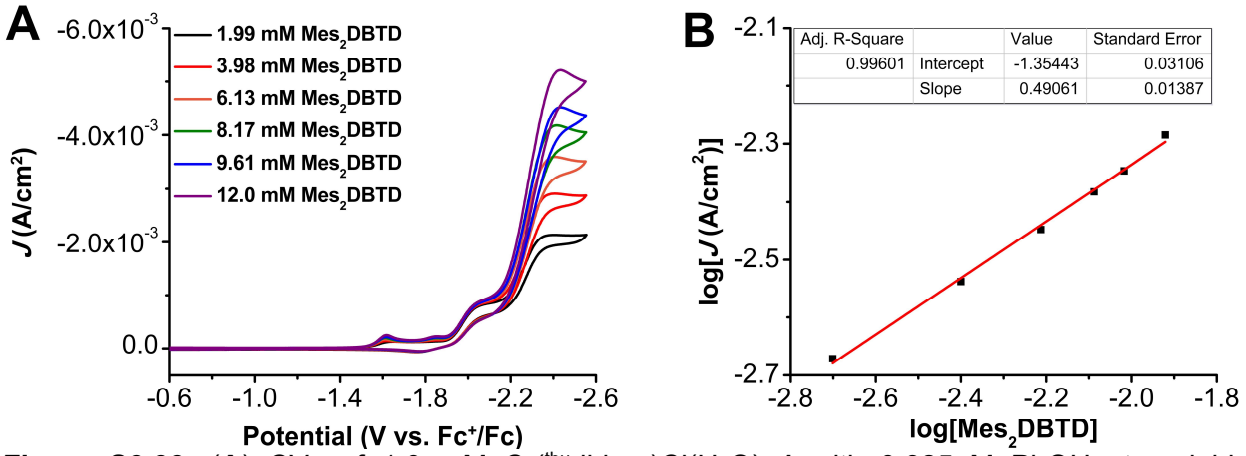

Figure S3.33. (**A**) CVs of 1.0 mM Cr(^{tbu}dhbpy)Cl(H_2O) **1** with 0.325 M PhOH at variable Mes_2DBTD concentrations, obtained under CO_2 saturation. Conditions: 0.1 M $TBAPF_6$/DMF; glassy carbon working electrode, glassy carbon counter electrode, Ag/AgCl pseudoreference electrode; 100 mV/s scan rate; referenced to internal ferrocene standard. (**B**) Log-log plot from data obtained from CVs in **A** at −2.43 V vs. Fc^+/Fc.

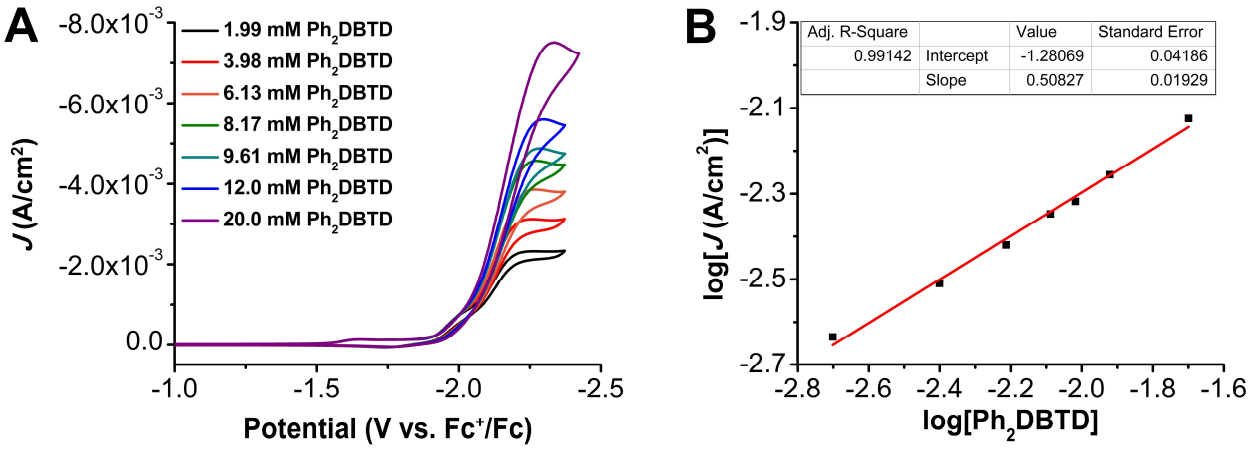

Figure S3.34. (**A**) CVs of 1.0 mM Cr(^{tbu}dhbpy)Cl(H_2O) **1** with 0.325 M PhOH at variable Ph_2DBTD concentrations, obtained under CO_2 saturation. Conditions: 0.1 M $TBAPF_6$/DMF; glassy carbon working electrode, glassy carbon counter electrode, Ag/AgCl pseudoreference electrode; 100 mV/s scan rate; referenced to internal ferrocene standard. (**B**) Log-log plot from data obtained from CVs in **A** at −2.33 V vs. Fc^+/Fc.

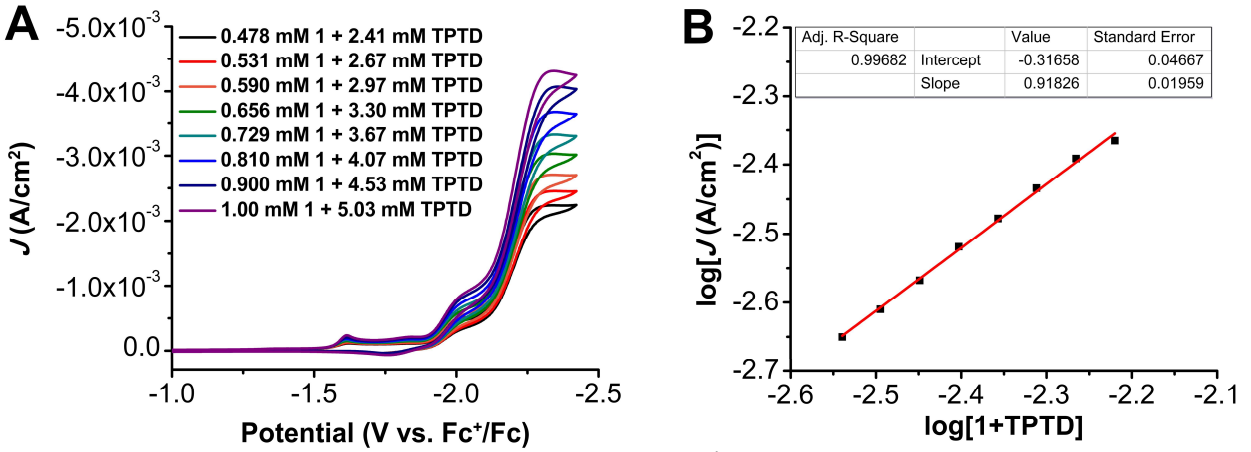

Figure S3.35. (**A**) CVs where the concentrations of Cr(^{tbu}dhbpy)Cl(H_2O) **1** and TPTD were varied at a fixed 1:5 ratio of **1**:TPTD with 0.325 M PhOH under CO_2 saturation conditions. Conditions: 0.1 M $TBAPF_6$/DMF; glassy carbon working electrode, glassy carbon counter electrode, Ag/AgCl pseudoreference electrode; 100 mV/s scan rate; referenced to internal ferrocene standard. (**B**) Log-log plot from data obtained from CVs in **A** at −2.34 V vs. Fc^+/Fc.

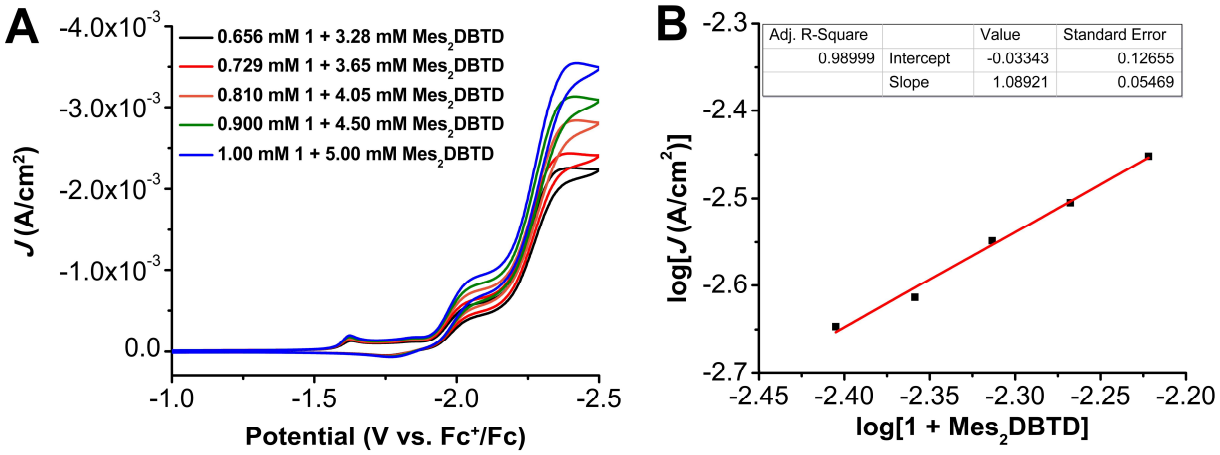

Figure S3.36. (**A**) CVs where the concentrations of Cr(^{tbu}dhbpy)Cl(H_2O) **1** and Mes_2DBTD were varied at a fixed 1:5 ratio of **1**:Mes_2DBTD with 0.325 M PhOH under CO_2 saturation conditions. Conditions: 0.1 M $TBAPF_6$/DMF; glassy carbon working electrode, glassy carbon counter electrode, Ag/AgCl pseudoreference electrode; 100 mV/s scan rate; referenced to internal ferrocene standard. (**B**) Log-log plot from data obtained from CVs in **A** at −2.40 V vs. Fc^+/Fc.

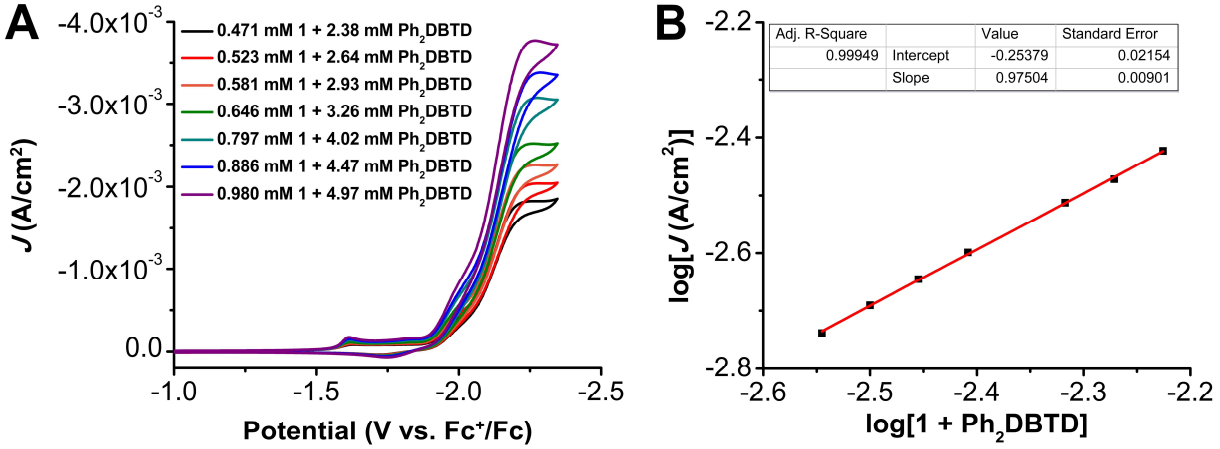

Figure S3.37. (**A**) CVs where the concentrations of Cr(^{tbu}dhbpy)Cl(H_2O) **1** and Ph_2DBTD were varied at a fixed 1:5 ratio of **1**:Ph_2DBTD with 0.325 M PhOH under CO_2 saturation conditions. Conditions: 0.1 M $TBAPF_6$/DMF; glassy carbon working electrode, glassy carbon counter electrode, Ag/AgCl pseudoreference electrode; 100 mV/s scan rate; referenced to internal ferrocene standard. (**B**) Log-log plot from data obtained from CVs in **A** at −2.27 V vs. Fc^+/Fc.

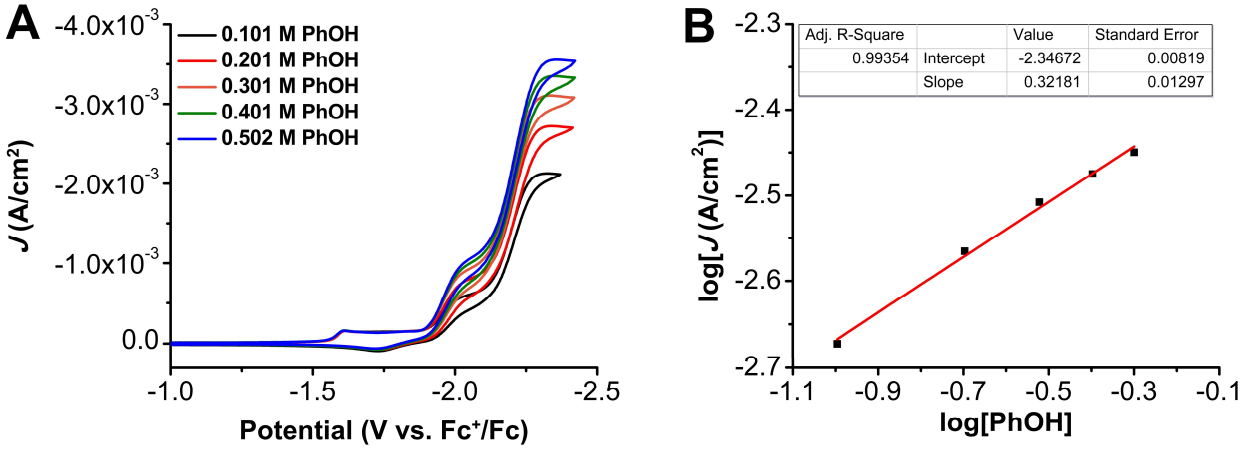

Figure S3.38. (**A**) CVs of PhOH at variable concentrations, obtained under CO_2 saturation with 1.0 mM Cr(^{tbu}dhbpy)Cl(H_2O) **1** and 2.5 mM TPTD. Conditions: 0.1 M $TBAPF_6$/DMF; glassy carbon working electrode, glassy carbon counter electrode, Ag/AgCl pseudoreference electrode; 100 mV/s scan rate; referenced to internal ferrocene standard. (**B**) Log-log plot from data obtained from CVs in **A** at −2.34 V vs. Fc^+/Fc.

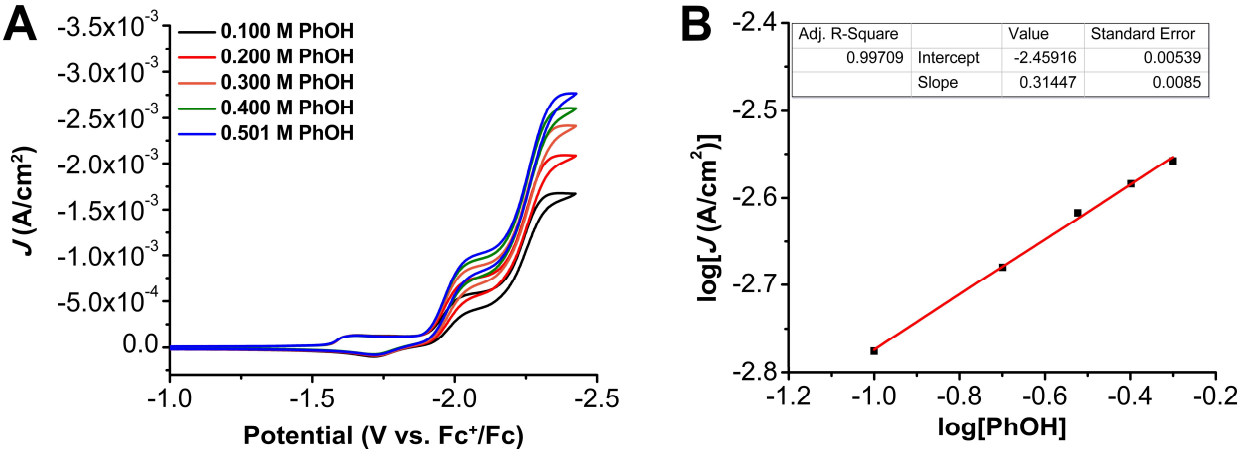

Figure S3.39. (**A**) CVs of PhOH at variable concentrations, obtained under CO_2 saturation with 1.0 mM Cr(^{tbu}dhbpy)Cl(H_2O) **1** and 2.5 mM Mes_2DBTD. Conditions: 0.1 M $TBAPF_6$/DMF; glassy carbon working electrode, glassy carbon counter electrode, Ag/AgCl pseudoreference electrode; 100 mV/s scan rate; referenced to internal ferrocene standard. (**B**) Log-log plot from data obtained from CVs in **A** at −2.40 V vs. Fc^+/Fc.

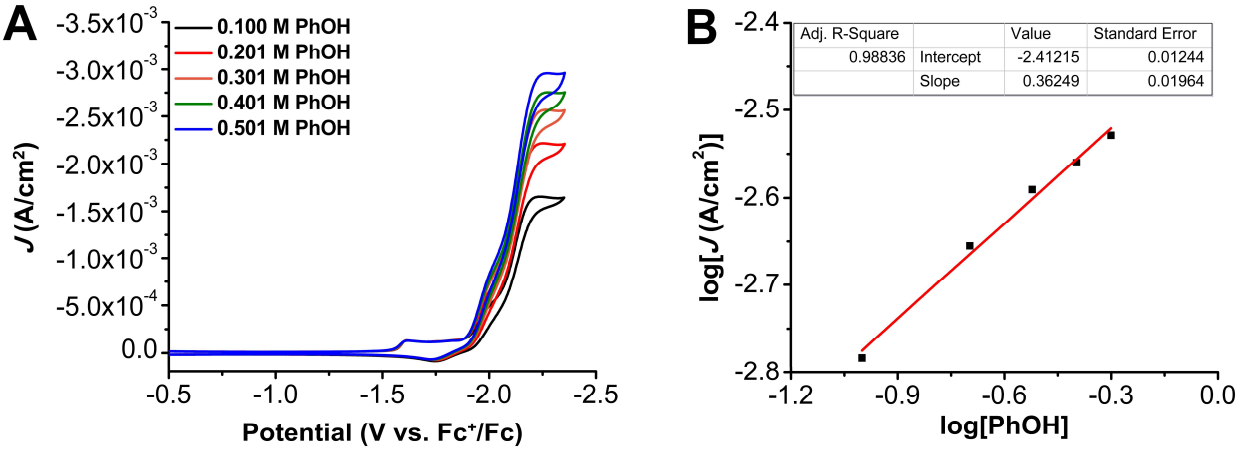

Figure S3.40. (**A**) CVs of PhOH at variable concentrations, obtained under CO_2 saturation with 1.0 mM Cr(^{tbu}dhbpy)Cl(H_2O) **1** and 2.5 mM Ph_2DBTD. Conditions: 0.1 M $TBAPF_6$/DMF; glassy carbon working electrode, glassy carbon counter electrode, Ag/AgCl pseudoreference electrode; 100 mV/s scan rate; referenced to internal ferrocene standard. (**B**) Log-log plot from data obtained from CVs in **A** at −2.27 V vs. Fc^+/Fc.

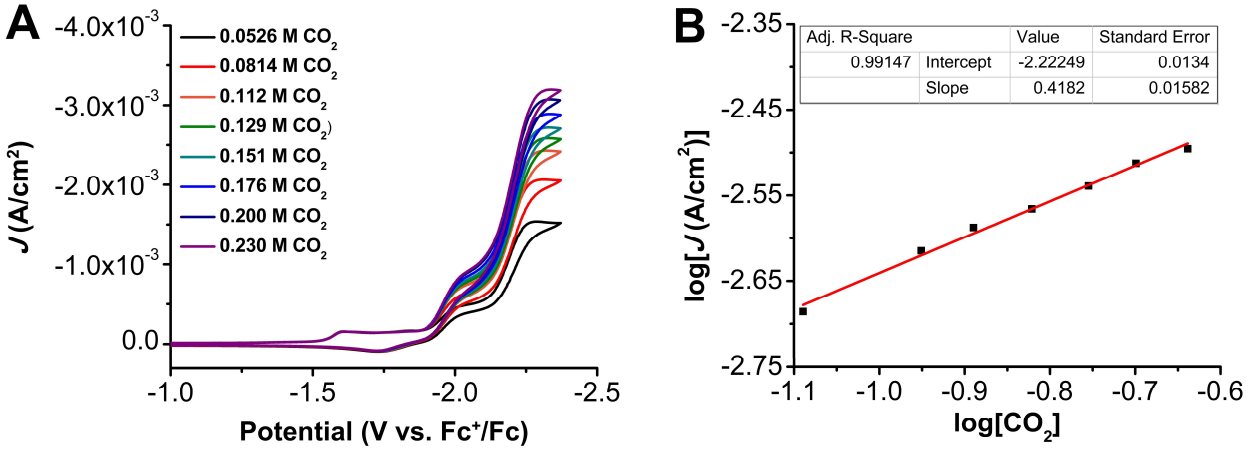

Figure S3.41. (**A**) CVs of 1.0 mM Cr(^{tbu}dhbpy)Cl(H_2O) **1**, 2.5 mM TPTD, 0.325 M PhOH at varied CO_2 concentrations. Conditions: 0.1 M $TBAPF_6$/DMF; glassy carbon working electrode, glassy carbon counter electrode, Ag/AgCl pseudoreference electrode; 100 mV/s scan rate; referenced to internal ferrocene standard. (**B**) Log-log plot from data obtained from CVs in **A** at −2.29 V vs. Fc^+/Fc.

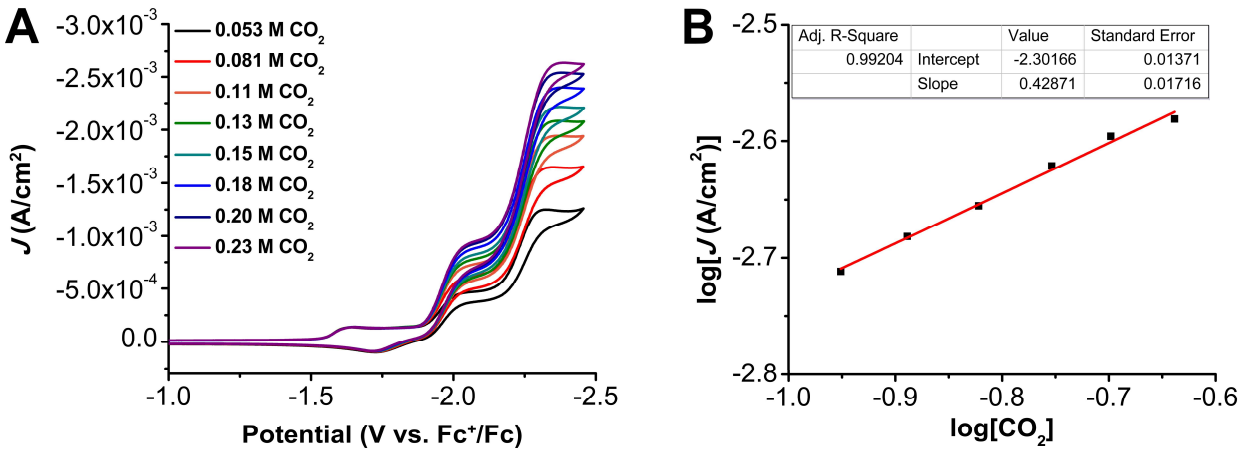

Figure S3.42. (**A**) CVs of 1.0 mM Cr(^{tbu}dhbpy)Cl(H_2O) **1**, 2.5 mM Mes_2DBTD, 0.325 M PhOH at varied CO_2 concentrations. Conditions: 0.1 M $TBAPF_6$/DMF; glassy carbon working electrode, glassy carbon counter electrode, Ag/AgCl pseudoreference electrode; 100 mV/s scan rate; referenced to internal ferrocene standard. (**B**) Log-log plot from data obtained from CVs in **A** at −2.36 V vs. Fc^+/Fc.

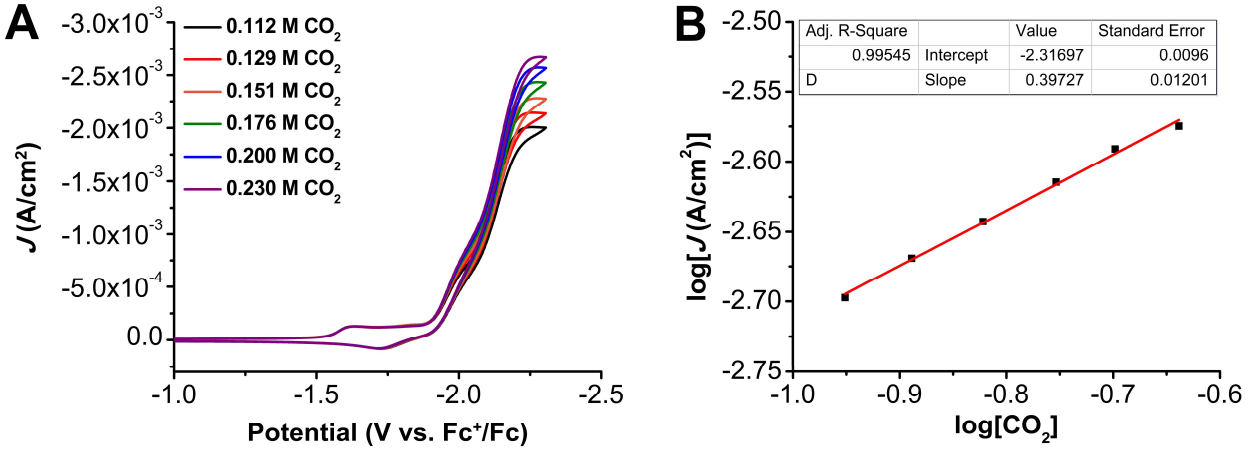

Figure S3.43. (**A**) CVs of 1.0 mM Cr(^{tbu}dhbpy)Cl(H_2O) **1**, 2.5 mM Ph_2DBTD, 0.325 M PhOH at varied CO_2 concentrations. Conditions: 0.1 M $TBAPF_6$/DMF; glassy carbon working electrode, glassy carbon counter electrode, Ag/AgCl pseudoreference electrode; 100 mV/s scan rate; referenced to internal ferrocene standard. (**B**) Log-log plot from data obtained from CVs in **A** at −2.26 V vs. Fc^+/Fc.

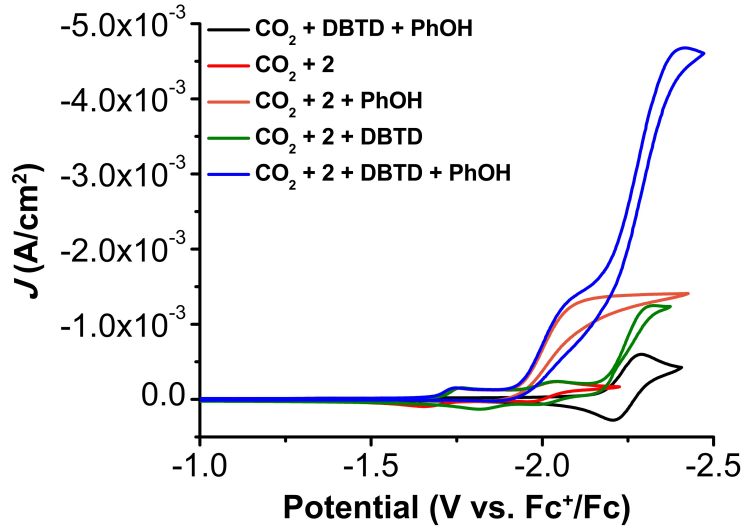

Figure S3.44. Comparison of CVs of 1.0 mM Cr(^{tbu}dh^{tbu}bpy)Cl(H_2O) **2** with and without 2.5 mM DBTD and 0.1 M PhOH under CO_2 saturation conditions. Conditions: 0.1 M $TBAPF_6$/DMF; glassy carbon working electrode, glassy carbon rod counter electrode, Ag/AgCl pseudoreference electrode; referenced to Fc^+/Fc internal standard; 100 mV/s scan rate.

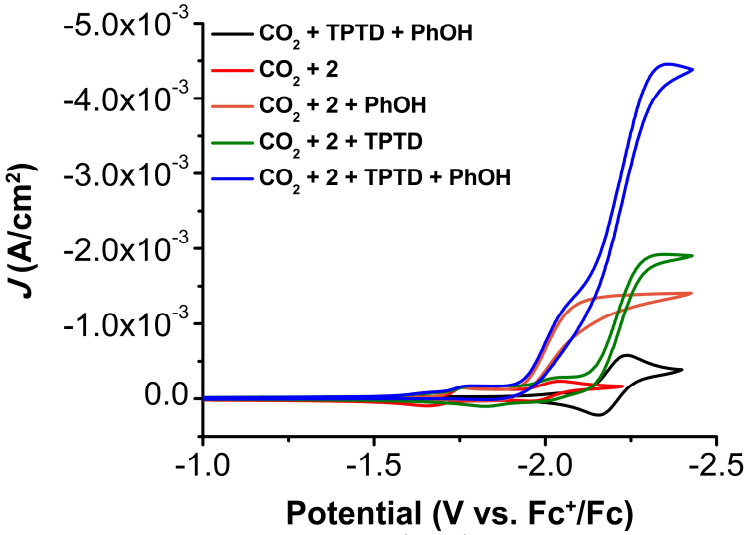

Figure S3.45. Comparison of CVs of 1.0 mM Cr(^{tbu}dh^{tbu}bpy)Cl(H_2O) **2** with and without 2.5 mM TPTD and 0.1 M PhOH under CO_2 saturation conditions. Conditions: 0.1 M $TBAPF_6$/DMF; glassy carbon working electrode, glassy carbon rod counter electrode, Ag/AgCl pseudoreference electrode; referenced to Fc^+/Fc internal standard; 100 mV/s scan rate.

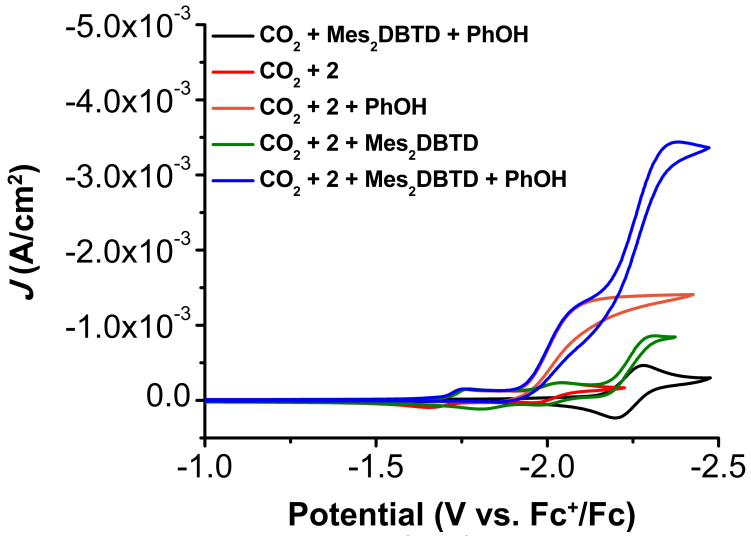

Figure S3.46. Comparison of CVs of 1.0 mM Cr(^{tbu}dh^{tbu}bpy)Cl(H_2O) **2** with and without 2.5 mM Mes_2DBTD and 0.1 M PhOH under CO_2 saturation conditions. Conditions: 0.1 M $TBAPF_6$/DMF; glassy carbon working electrode, glassy carbon rod counter electrode, Ag/AgCl pseudoreference electrode; referenced to Fc^+/Fc internal standard; 100 mV/s scan rate.

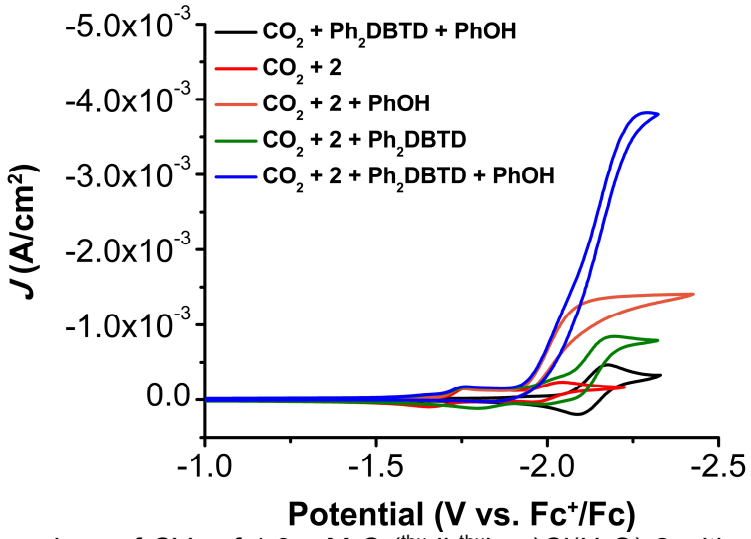

Figure S3.47. Comparison of CVs of 1.0 mM Cr(^{tbu}dh^{tbu}bpy)Cl(H_2O) **2** with and without 2.5 mM Ph_2DBTD and 0.1 M PhOH under CO_2 saturation conditions. Conditions: 0.1 M $TBAPF_6$/DMF; glassy carbon working electrode, glassy carbon rod counter electrode, Ag/AgCl pseudoreference electrode; referenced to Fc^+/Fc internal standard; 100 mV/s scan rate.

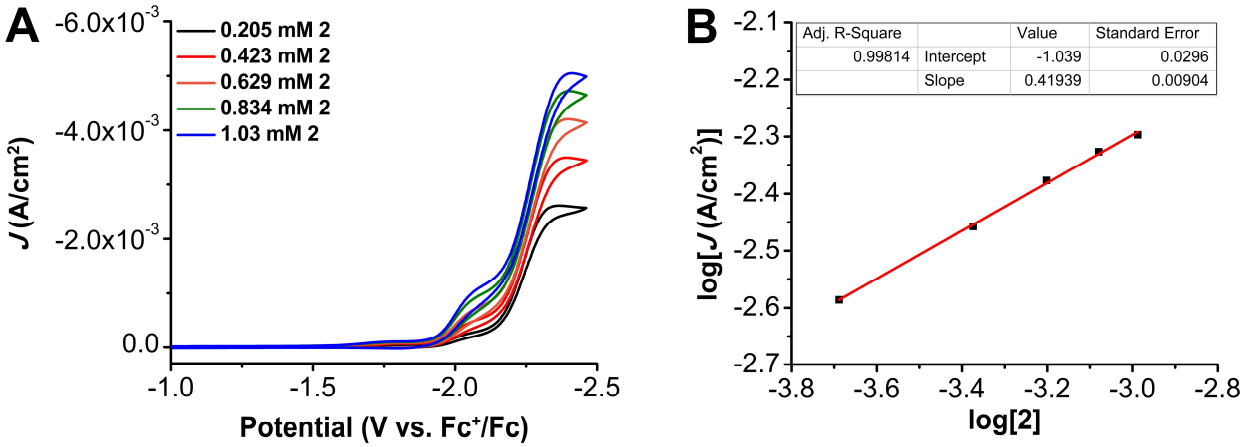

Figure S3.48. (**A**) CVs of Cr(^{tbu}dh^{tbu}bpy)Cl(H_2O) **2** at variable concentrations, obtained under CO_2 saturation with 2.5 mM DBTD and 0.325 M PhOH. Conditions: 0.1 M $TBAPF_6$/DMF; glassy carbon working electrode, glassy carbon counter electrode, Ag/AgCl pseudoreference electrode; 100 mV/s scan rate; referenced to internal ferrocene standard. (**B**) Log-log plot from data obtained from CVs in **A** at −2.41 V vs. Fc^+/Fc.

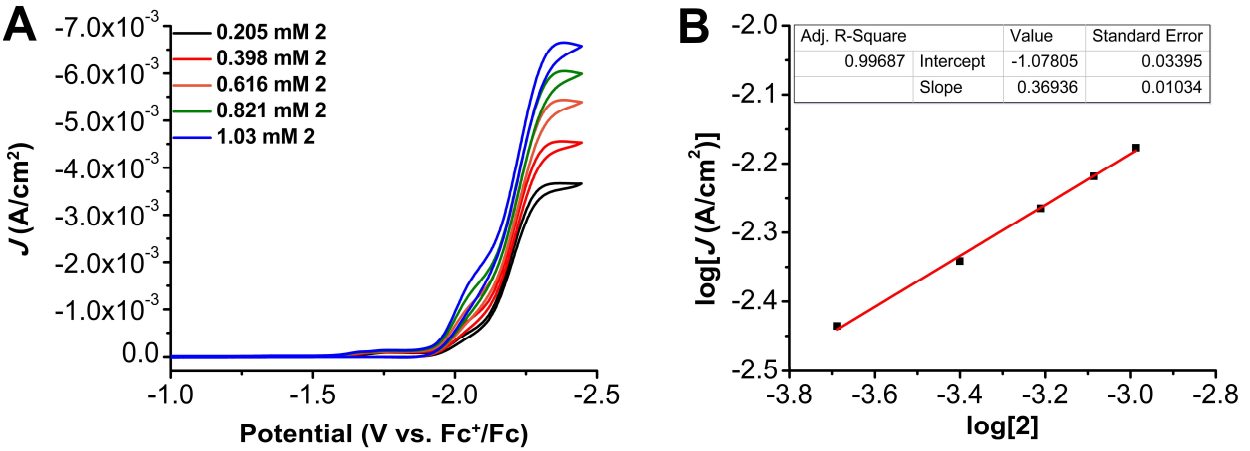

Figure S3.49. (**A**) CVs of Cr(^{tbu}dh^{tbu}bpy)Cl(H_2O) **2** at variable concentrations, obtained under CO_2 saturation with 2.5 mM TPTD and 0.325 M PhOH. Conditions: 0.1 M $TBAPF_6$/DMF; glassy carbon working electrode, glassy carbon counter electrode, Ag/AgCl pseudoreference electrode; 100 mV/s scan rate; referenced to internal ferrocene standard. (**B**) Log-log plot from data obtained from CVs in **A** at −2.38 V vs. Fc^+/Fc.

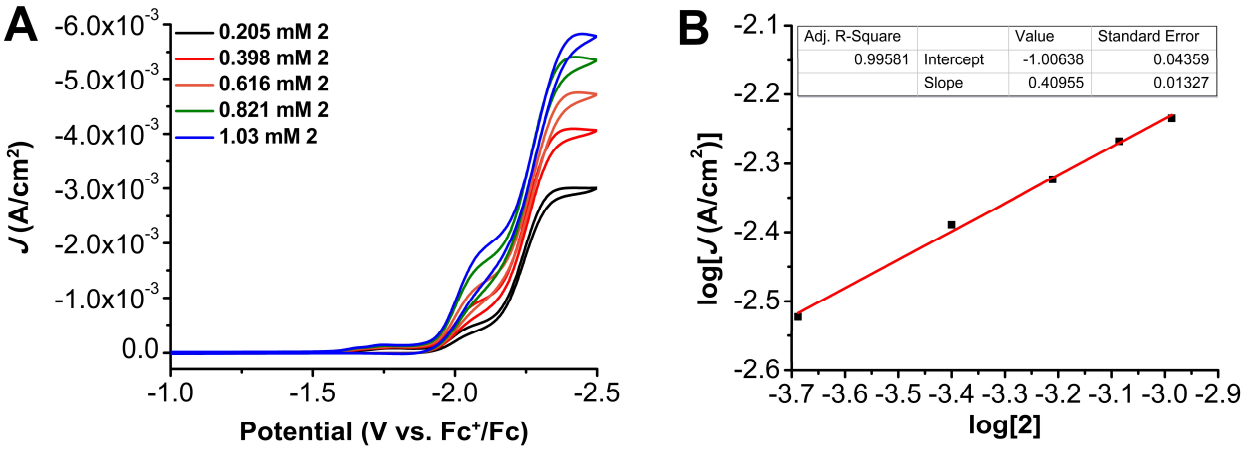

Figure S3.50. (**A**) CVs of Cr(^{tbu}dh^{tbu}bpy)Cl(H_2O) **2** at variable concentrations, obtained under CO_2 saturation with 2.5 mM Mes_2DBTD and 0.325 M PhOH. Conditions: 0.1 M $TBAPF_6$/DMF; glassy carbon working electrode, glassy carbon counter electrode, Ag/AgCl pseudoreference electrode; 100 mV/s scan rate; referenced to internal ferrocene standard. (**B**) Log-log plot from data obtained from CVs in **A** at −2.45 V vs. Fc^+/Fc.

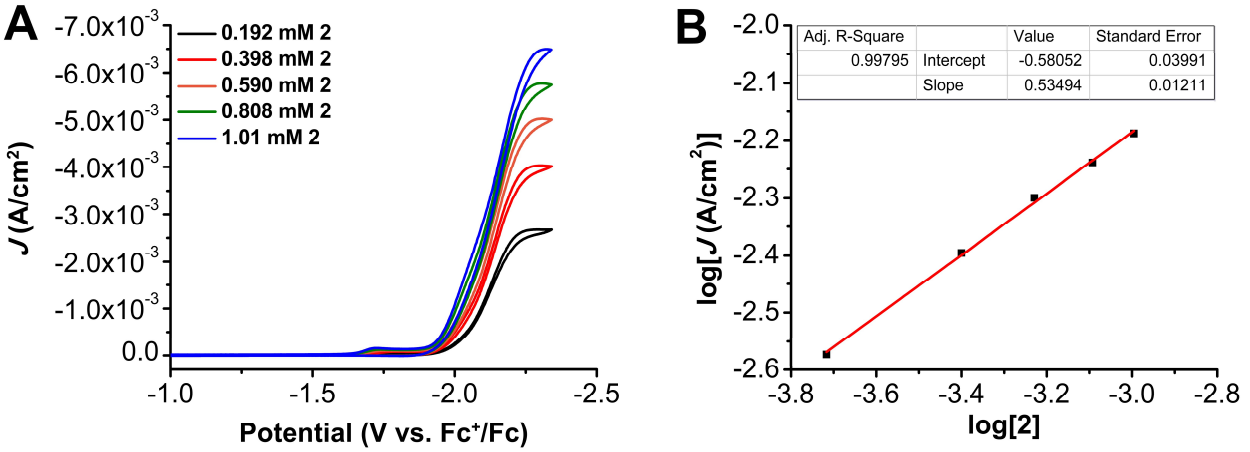

Figure S3.51. (**A**) CVs of Cr(^{tbu}dh^{tbu}bpy)Cl(H_2O) **2** at variable concentrations, obtained under CO_2 saturation with 2.5 mM Ph_2DBTD and 0.325 M PhOH. Conditions: 0.1 M $TBAPF_6$/DMF; glassy carbon working electrode, glassy carbon counter electrode, Ag/AgCl pseudoreference electrode; 100 mV/s scan rate; referenced to internal ferrocene standard. (**B**) Log-log plot from data obtained from CVs in **A** at −2.32 V vs. Fc^+/Fc.

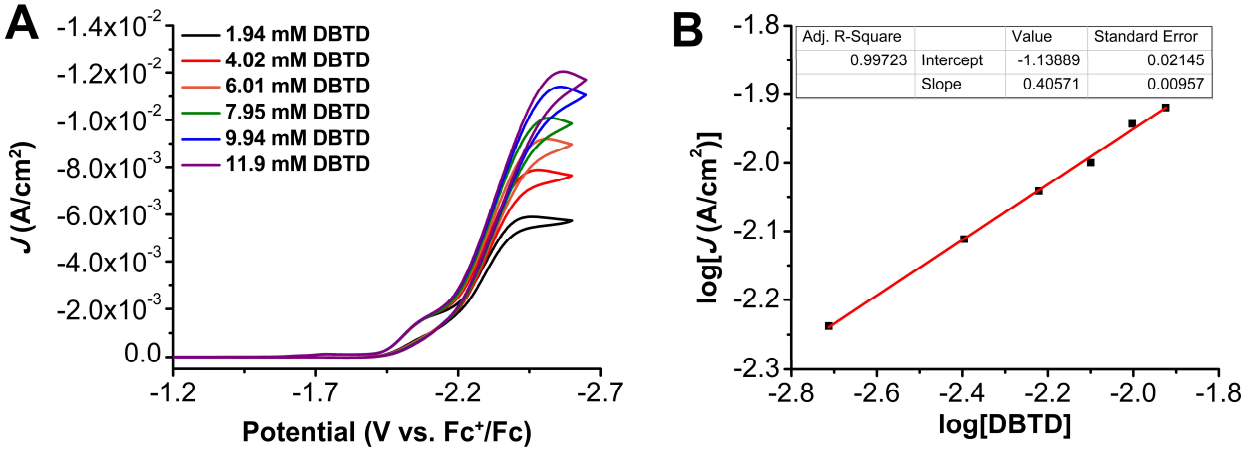

Figure S3.52. (**A**) CVs of 1.0 mM Cr(^{tbu}dh^{tbu}bpy)Cl(H_2O) **2** with 0.325 M PhOH at variable DBTD concentrations, obtained under CO_2 saturation. Conditions: 0.1 M $TBAPF_6$/DMF; glassy carbon working electrode, glassy carbon counter electrode, Ag/AgCl pseudoreference electrode; 100 mV/s scan rate; referenced to internal ferrocene standard. (**B**) Log-log plot from data obtained from CVs in **A** at −2.56 V vs. Fc^+/Fc.

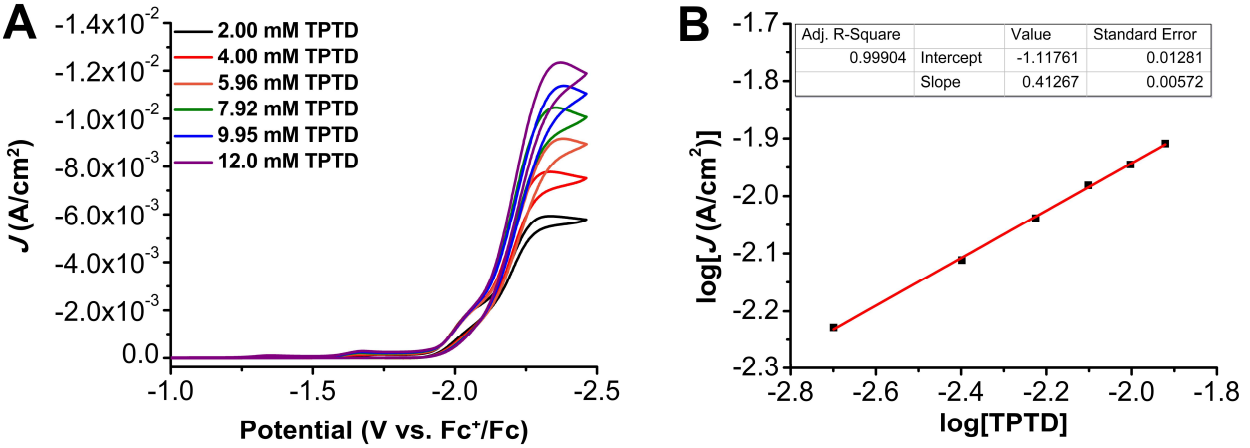

Figure S3.53. (**A**) CVs of 1.0 mM Cr(^{tbu}dh^{tbu}bpy)Cl(H_2O) **2** with 0.325 M PhOH at variable TPTD concentrations, obtained under CO_2 saturation. Conditions: 0.1 M $TBAPF_6$/DMF; glassy carbon working electrode, glassy carbon counter electrode, Ag/AgCl pseudoreference electrode; 100 mV/s scan rate; referenced to internal ferrocene standard. (**B**) Log-log plot from data obtained from CVs in **A** at −2.37 V vs. Fc^+/Fc.

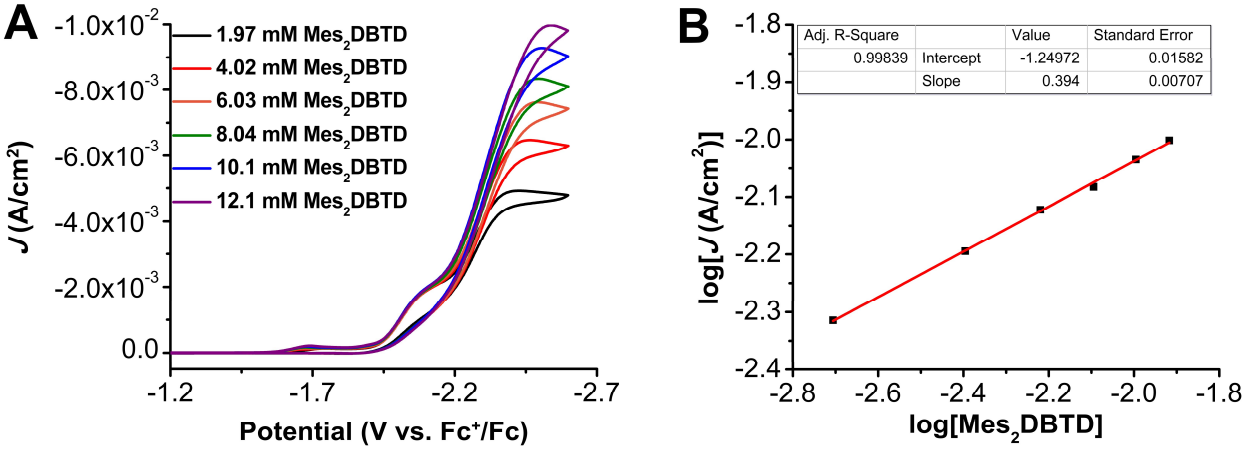

Figure S3.54. (**A**) CVs of 1.0 mM Cr(^{tbu}dh^{tbu}bpy)Cl(H_2O) **2** with 0.325 M PhOH at variable Mes_2DBTD concentrations, obtained under CO_2 saturation. Conditions: 0.1 M $TBAPF_6$/DMF; glassy carbon working electrode, glassy carbon counter electrode, Ag/AgCl pseudoreference electrode; 100 mV/s scan rate; referenced to internal ferrocene standard. (**B**) Log-log plot from data obtained from CVs in **A** at −2.54 V vs. Fc^+/Fc.

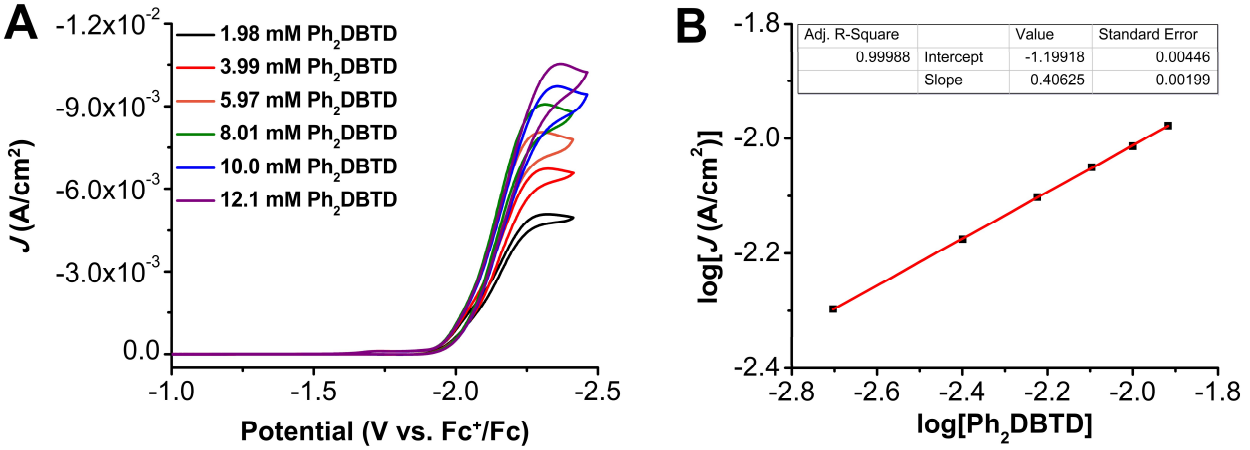

Figure S3.55. (**A**) CVs of 1.0 mM Cr(^{tbu}dh^{tbu}bpy)Cl(H_2O) **2** with 0.325 M PhOH at variable Ph_2DBTD concentrations, obtained under CO_2 saturation. Conditions: 0.1 M $TBAPF_6$/DMF; glassy carbon working electrode, glassy carbon counter electrode, Ag/AgCl pseudoreference electrode; 100 mV/s scan rate; referenced to internal ferrocene standard. (**B**) Log-log plot from data obtained from CVs in **A** at −2.37 V vs. Fc^+/Fc.

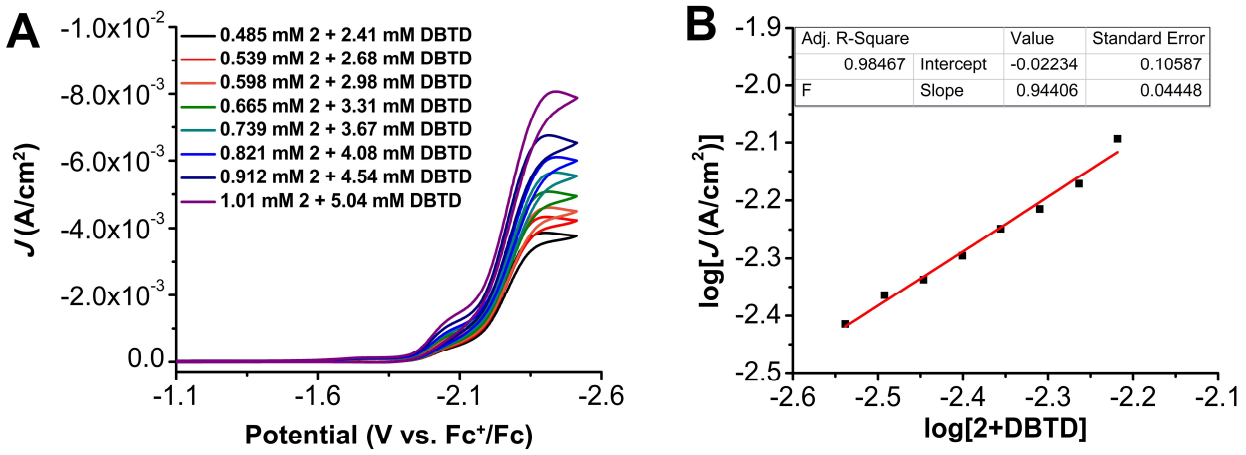

Figure S3.56. (**A**) CVs where the concentrations of Cr(^{tbu}dh^{tbu}bpy)Cl(H_2O) **2** and DBTD were varied at a fixed 1:5 ratio of **1**:DBTD with 0.325 M PhOH under CO_2 saturation conditions. Conditions: 0.1 M $TBAPF_6$/DMF; glassy carbon working electrode, glassy carbon counter electrode, Ag/AgCl pseudoreference electrode; 100 mV/s scan rate; referenced to internal ferrocene standard. (**B**) Log-log plot from data obtained from CVs in **A** at −2.43 V vs. Fc^+/Fc.

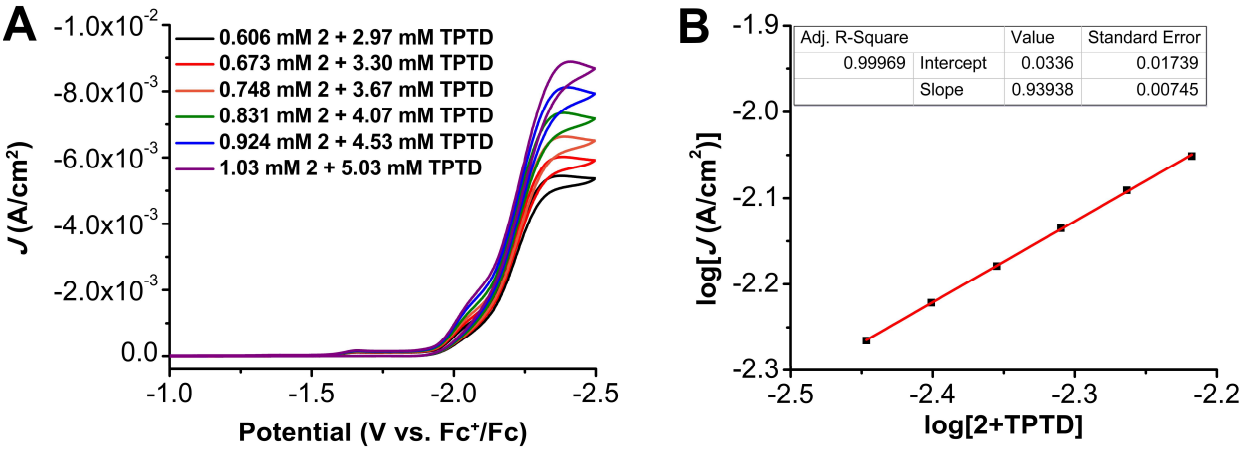

Figure S3.57. (**A**) CVs where the concentrations of Cr(^{tbu}dh^{tbu}bpy)Cl(H_2O) **2** and TPTD were varied at a fixed 1:5 ratio of **1**:TPTD with 0.325 M PhOH under CO_2 saturation conditions. Conditions: 0.1 M $TBAPF_6$/DMF; glassy carbon working electrode, glassy carbon counter electrode, Ag/AgCl pseudoreference electrode; 100 mV/s scan rate; referenced to internal ferrocene standard. (**B**) Log-log plot from data obtained from CVs in **A** at −2.41 V vs. Fc^+/Fc.

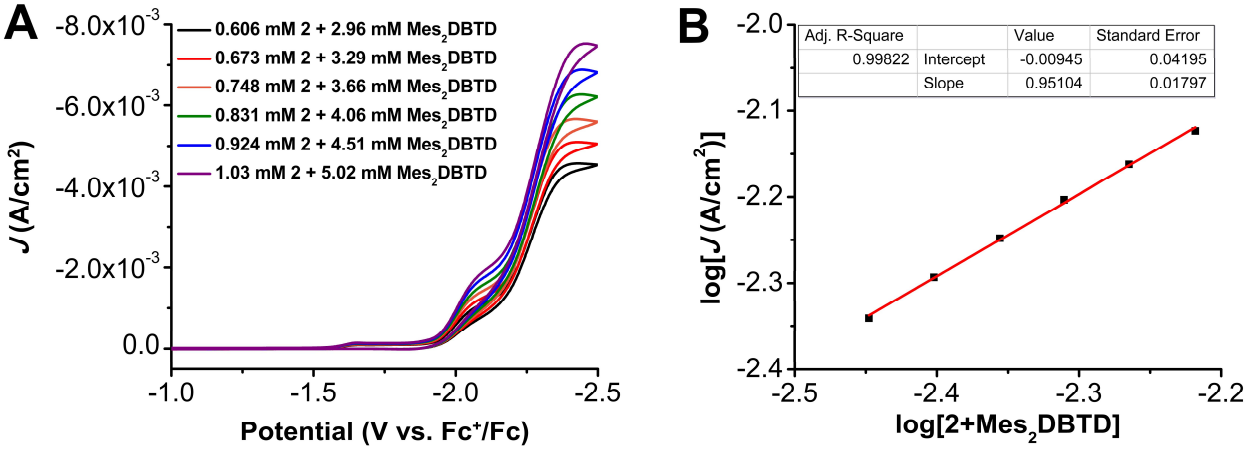

Figure S3.58. (**A**) CVs where the concentrations of Cr(^{tbu}dh^{tbu}bpy)Cl(H_2O) **2** and Mes_2DBTD were varied at a fixed 1:5 ratio of **1**:Mes_2DBTD with 0.325 M PhOH under CO_2 saturation conditions. Conditions: 0.1 M $TBAPF_6$/DMF; glassy carbon working electrode, glassy carbon counter electrode, Ag/AgCl pseudoreference electrode; 100 mV/s scan rate; referenced to internal ferrocene standard. (**B**) Log-log plot from data obtained from CVs in **A** at −2.45 V vs. Fc^+/Fc.

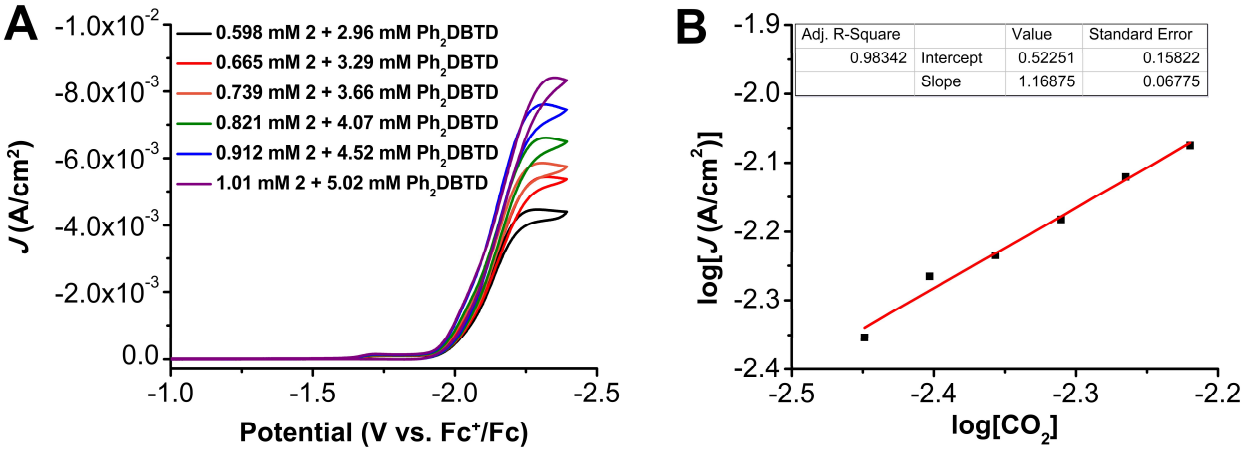

Figure S3.59. (**A**) CVs where the concentrations of Cr(^{tbu}dh^{tbu}bpy)Cl(H_2O) **2** and Ph_2DBTD were varied at a fixed 1:5 ratio of **1**:Ph_2DBTD with 0.325 M PhOH under CO_2 saturation conditions. Conditions: 0.1 M $TBAPF_6$/DMF; glassy carbon working electrode, glassy carbon counter electrode, Ag/AgCl pseudoreference electrode; 100 mV/s scan rate; referenced to internal ferrocene standard. (**B**) Log-log plot from data obtained from CVs in **A** at −2.35 V vs. Fc^+/Fc.

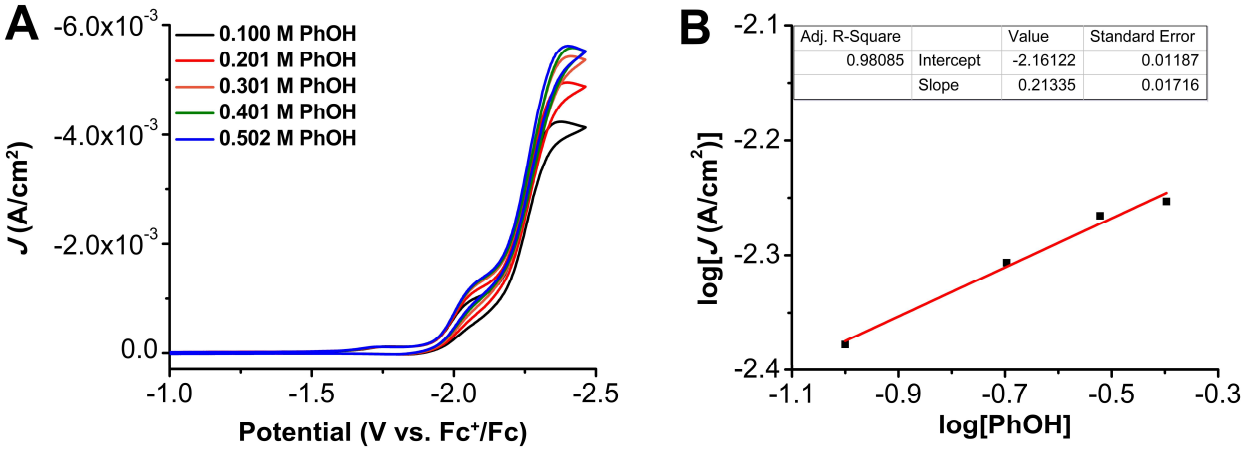

Figure S3.60. (**A**) CVs of PhOH at variable concentrations, obtained under CO_2 saturation with 1.0 mM Cr(^{tbu}dh^{tbu}bpy)Cl(H_2O) **2** and 2.5 mM DBTD. Conditions: 0.1 M $TBAPF_6$/DMF; glassy carbon working electrode, glassy carbon counter electrode, Ag/AgCl pseudoreference electrode; 100 mV/s scan rate; referenced to internal ferrocene standard. (**B**) Log-log plot from data obtained from CVs in **A** at −2.42 V vs. Fc^+/Fc.

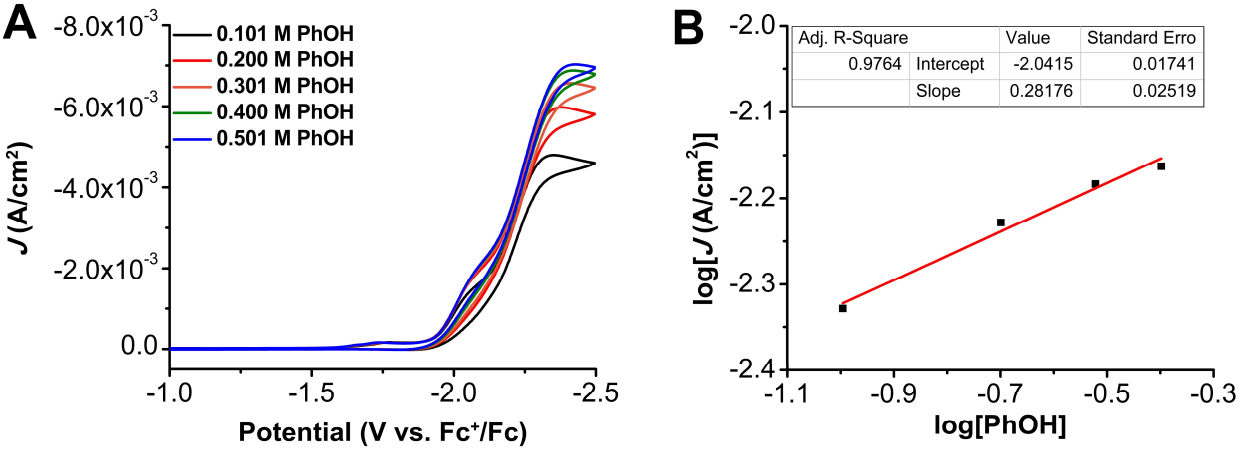

Figure S3.61. (**A**) CVs of PhOH at variable concentrations, obtained under CO_2 saturation with 1.0 mM Cr(^{tbu}dh^{tbu}bpy)Cl(H_2O) **2** and 2.5 mM TPTD. Conditions: 0.1 M $TBAPF_6$/DMF; glassy carbon working electrode, glassy carbon counter electrode, Ag/AgCl pseudoreference electrode; 100 mV/s scan rate; referenced to internal ferrocene standard. (**B**) Log-log plot from data obtained from CVs in **A** at −2.43 V vs. Fc^+/Fc.

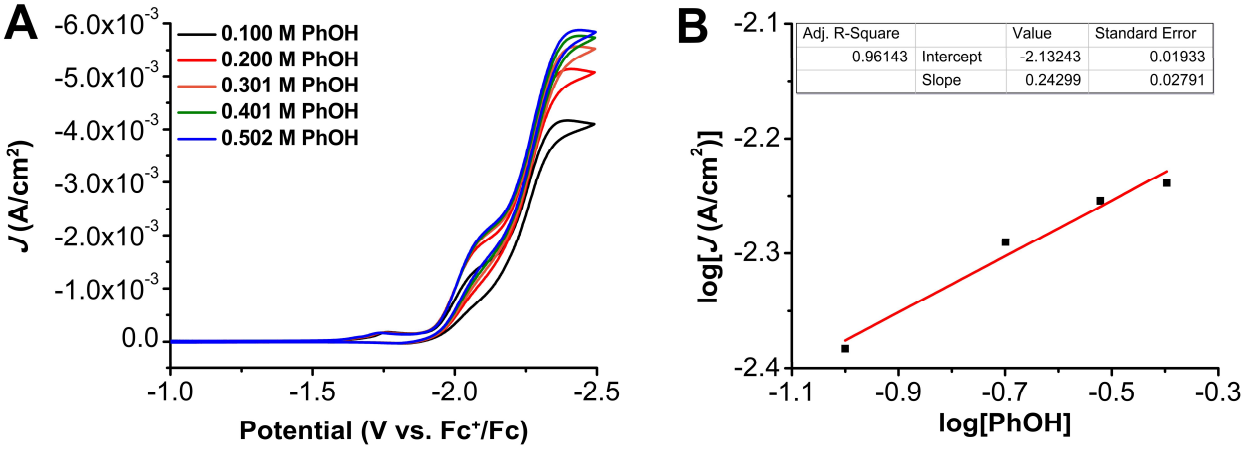

Figure S3.62. (**A**) CVs of PhOH at variable concentrations, obtained under CO_2 saturation with 1.0 mM Cr(^{tbu}dh^{tbu}bpy)Cl(H_2O) **2** and 2.5 mM Mes_2DBTD. Conditions: 0.1 M $TBAPF_6$/DMF; glassy carbon working electrode, glassy carbon counter electrode, Ag/AgCl pseudoreference electrode; 100 mV/s scan rate; referenced to internal ferrocene standard. (**B**) Log-log plot from data obtained from CVs in **A** at −2.44 V vs. Fc^+/Fc.

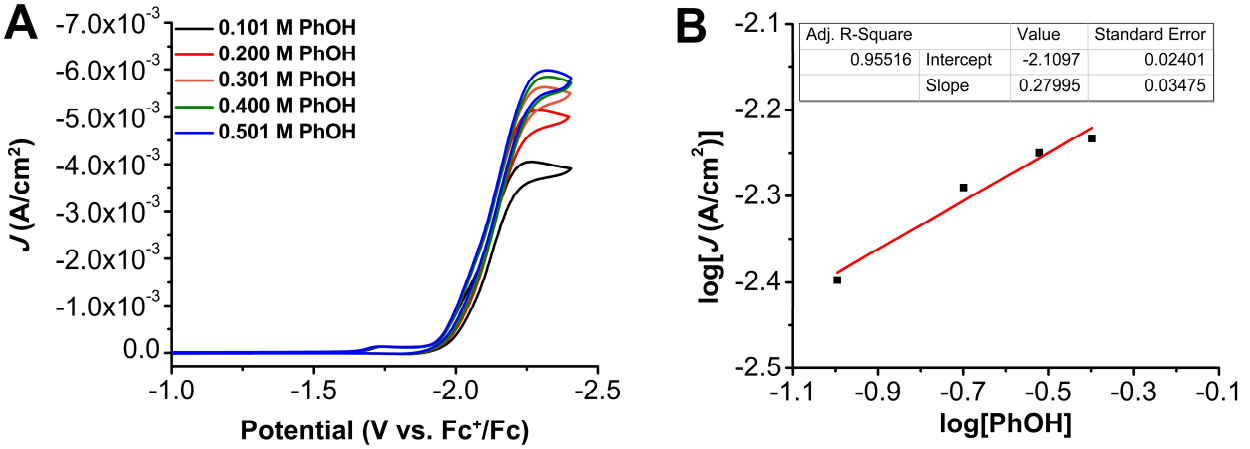

Figure S3.63. (**A**) CVs of PhOH at variable concentrations, obtained under CO_2 saturation with 1.0 mM Cr(^{tbu}dh^{tbu}bpy)Cl(H_2O) **2** and 2.5 mM Ph_2DBTD. Conditions: 0.1 M $TBAPF_6$/DMF; glassy carbon working electrode, glassy carbon counter electrode, Ag/AgCl pseudoreference electrode; 100 mV/s scan rate; referenced to internal ferrocene standard. (**B**) Log-log plot from data obtained from CVs in **A** at −2.32 V vs. Fc^+/Fc.

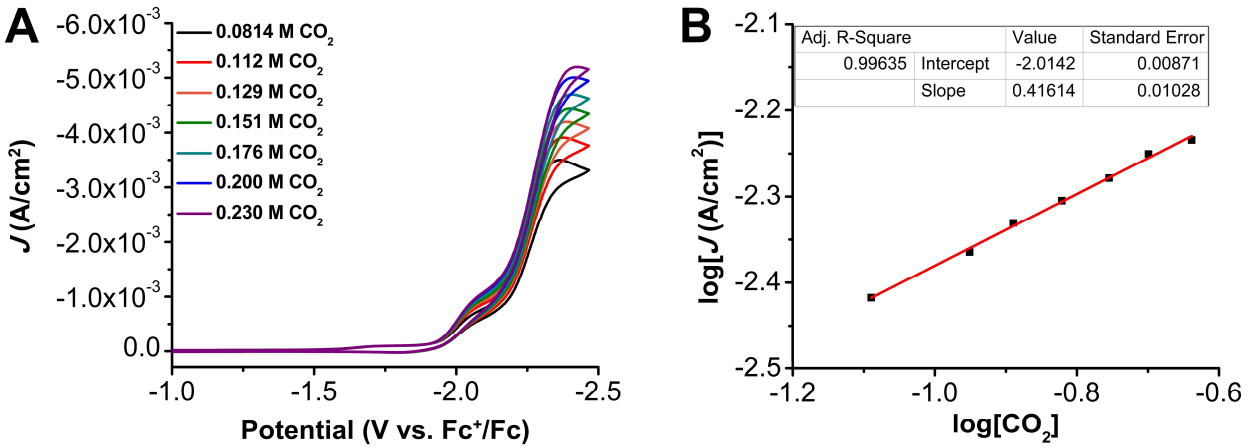

Figure S3.64. (**A**) CVs of 1.0 mM Cr(^{tbu}dh^{tbu}bpy)Cl(H_2O) **2**, 2.5 mM DBTD, 0.325 M PhOH at varied CO_2 concentrations. Conditions: 0.1 M $TBAPF_6$/DMF; glassy carbon working electrode, glassy carbon counter electrode, Ag/AgCl pseudoreference electrode; 100 mV/s scan rate; referenced to internal ferrocene standard. (**B**) Log-log plot from data obtained from CVs in **A** at −2.42 V vs. Fc^+/Fc.

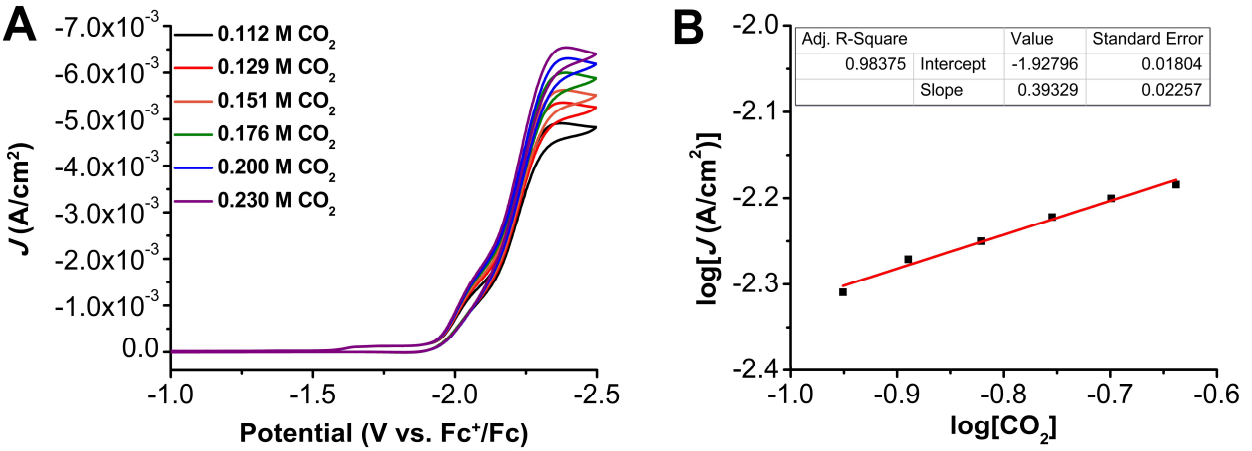

Figure S3.65. (**A**) CVs of 1.0 mM Cr(^{tbu}dh^{tbu}bpy)Cl(H_2O) **2**, 2.5 mM TPTD, 0.325 M PhOH at varied CO_2 concentrations. Conditions: 0.1 M $TBAPF_6$/DMF; glassy carbon working electrode, glassy carbon counter electrode, Ag/AgCl pseudoreference electrode; 100 mV/s scan rate; referenced to internal ferrocene standard. (**B**) Log-log plot from data obtained from CVs in **A** at −2.39 V vs. Fc^+/Fc.

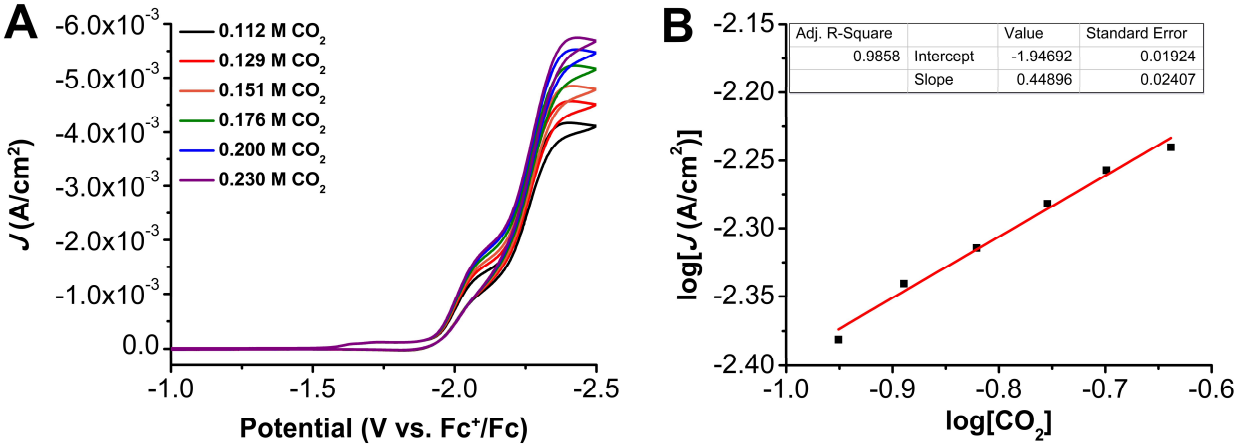

Figure S3.66. (**A**) CVs of 1.0 mM Cr(^{tbu}dh^{tbu}bpy)Cl(H_2O) **2**, 2.5 mM Mes_2DBTD, 0.325 M PhOH at varied CO_2 concentrations. Conditions: 0.1 M $TBAPF_6$/DMF; glassy carbon working electrode, glassy carbon counter electrode, Ag/AgCl pseudoreference electrode; 100 mV/s scan rate; referenced to internal ferrocene standard. (**B**) Log-log plot from data obtained from CVs in **A** at −2.43 V vs. Fc^+/Fc.

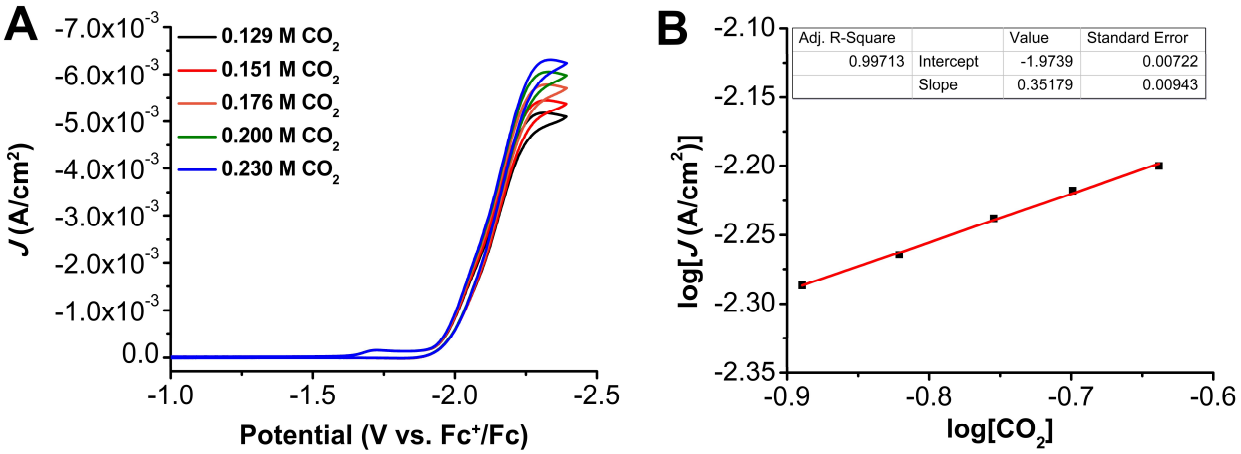

Figure S3.67. (**A**) CVs of 1.0 mM Cr(^{tbu}dh^{tbu}bpy)Cl(H_2O) **2**, 2.5 mM Ph_2DBTD, 0.325 M PhOH at varied CO_2 concentrations. Conditions: 0.1 M $TBAPF_6$/DMF; glassy carbon working electrode, glassy carbon counter electrode, Ag/AgCl pseudoreference electrode; 100 mV/s scan rate; referenced to internal ferrocene standard. (**B**) Log-log plot from data obtained from CVs in **A** at −2.33 V vs. Fc^+/Fc.

3.7.7 Controlled Potential Electrolysis Experiments (Protic Conditons)

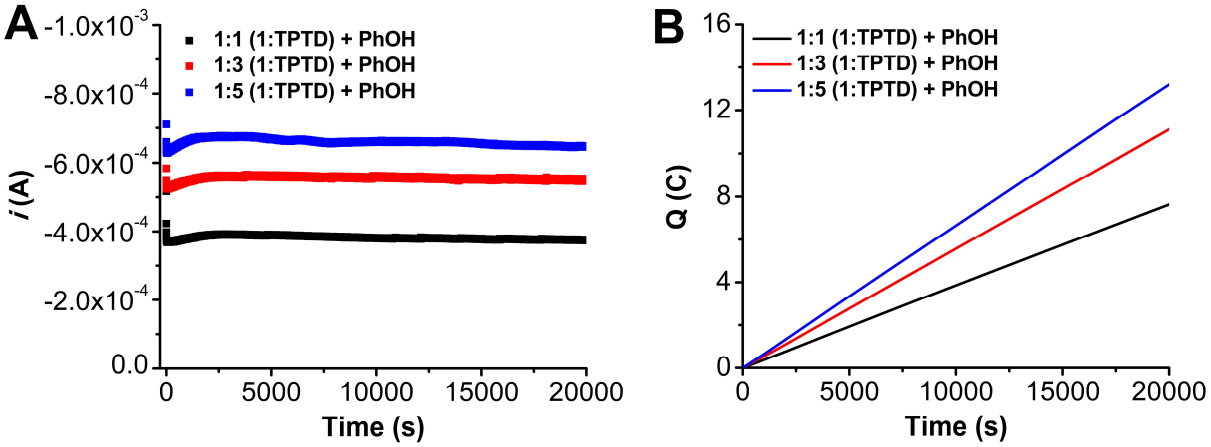

Figure S3.68. (**A**) Current versus time trace from CPE experiments of **1**+TPTD+PhOH. (**B**) Charge passed versus time for the CPE experiments shown in **A**. Conditions were 0.1 mM Cr(^{tbu}dhbpy)Cl(H_2O) **1**, 0.12 M PhOH, and either 0.1, 0.3, or 0.5 (blue) mM TPTD under a CO_2 atmosphere at −2.25 V vs Fc^+/Fc in 0.1 M $TBAPF_6$/DMF; working electrode was a glassy carbon rod, counter electrode was a graphite rod, and the reference was a nonaqueous Ag/AgCl pseudoreference electrode; 0.075 M Fc was used as sacrificial oxidant.

Table S3.7. Results from CPE experiment in Figure S3.68, 1:1 (**1**:TPTD) + PhOH (black).

Time (s)	Charge (coulombs)	moles (e^-)	Moles of CO	FE_{CO}
10828	4.17	4.32 x 10^{-5}	2.02 x 10^{-5}	93.5
12125	4.66	4.83 x 10^{-5}	2.70 x 10^{-5}	111.9
20000*	7.63	7.91 x 10^{-5}	4.50 x 10^{-5}	113.8
20000*	7.63	7.91 x 10^{-5}	4.19 x 10^{-5}	105.9
20000*	7.63	7.91 x 10^{-5}	4.15 x 10^{-5}	104.8

* indicates a triplicate series of injections carried out upon completion of electrolysis

Table S3.8. Results from CPE experiment in Figure S3.68, 1:3 (**1**:TPTD) + PhOH (black).

Time (s)	Charge (coulombs)	moles (e^-)	Moles of CO	FE_{CO}
20000*	11.1	1.15 x 10^{-4}	6.00 x 10^{-5}	104.3
20000*	11.1	1.15 x 10^{-4}	5.97 x 10^{-5}	103.7
20000*	11.1	1.15 x 10^{-4}	5.72 x 10^{-5}	99.3

* indicates a triplicate series of injections carried out upon completion of electrolysis

Table S3.9. Results from CPE experiment in Figure S3.68, 1:5 (**1**:TPTD) + PhOH (blue).

Time (s)	Charge (coulombs)	moles (e^-)	Moles of CO	FE_{CO}
15932	10.6	1.09×10^{-4}	6.34×10^{-5}	115.9
17894	11.8	1.23×10^{-4}	7.47×10^{-5}	121.9
20000*	13.2	1.37×10^{-4}	5.83×10^{-5}	85.2
20000*	13.2	1.37×10^{-4}	5.84×10^{-5}	85.4
20000*	13.2	1.37×10^{-4}	5.76×10^{-5}	84.3

* indicates a triplicate series of injections carried out upon completion of electrolysis

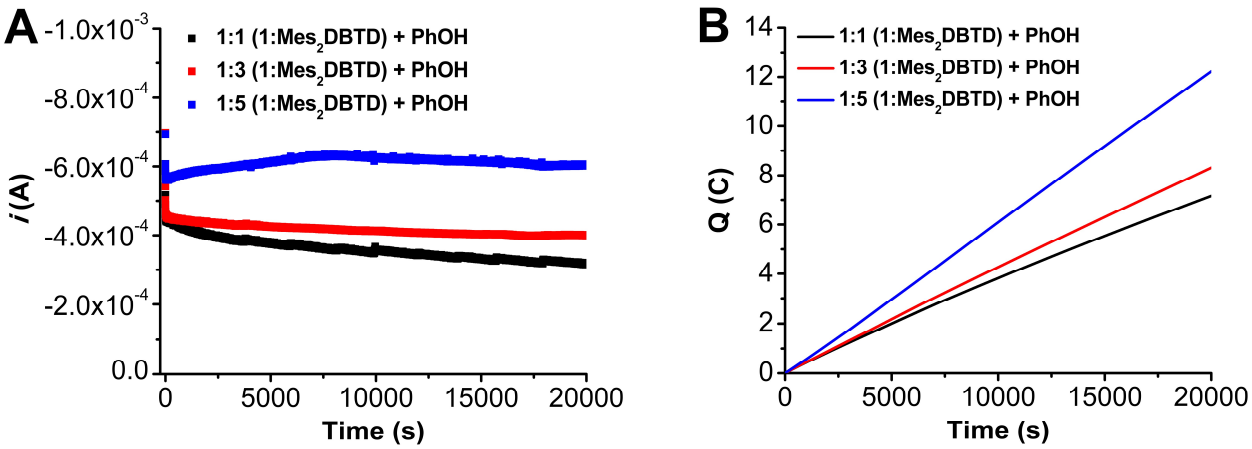

Figure S3.69. (**A**) Current versus time trace from CPE experiments with **1**+Mes_2DBTD+PhOH. (**B**) Charge passed versus time for the CPE experiments shown in **A**. Conditions were 0.1 mM Cr(^{tbu}dhbpy)Cl(H_2O) **1**, 0.12 M PhOH, and either 0.1, 0.3 (red), or 0.5 (blue) mM Mes_2DBTD under a CO_2 atmosphere at −2.25 V vs Fc^+/Fc in 0.1 M $TBAPF_6$/DMF; working electrode was a glassy carbon rod, counter electrode was a graphite rod, and the reference was a nonaqueous Ag/AgCl pseudoreference electrode; 0.075 M Fc was used as sacrificial oxidant.

Table S3.10. Results from CPE experiment in Figure S3.69, 1:1 (**1**:Mes_2DBTD) + PhOH (red).

Time (s)	Charge (coulombs)	moles (e^-)	Moles of CO	FE_{CO}
5895	2.33	2.42×10^{-5}	1.10×10^{-5}	90.7
8147	3.16	3.28×10^{-5}	1.59×10^{-5}	97.2
9925	3.80	3.93×10^{-5}	2.11×10^{-5}	107.3
12005	4.52	4.69×10^{-5}	2.37×10^{-5}	101.1
13897	5.17	5.36×10^{-5}	2.53×10^{-5}	94.3
15696	5.77	5.98×10^{-5}	2.91×10^{-5}	97.2
20001*	7.16	7.42×10^{-5}	3.33×10^{-5}	89.7
20001*	7.16	7.42×10^{-5}	3.45×10^{-5}	92.8
20001*	7.16	7.42×10^{-5}	3.47×10^{-5}	93.4

* indicates a triplicate series of injections carried out upon completion of electrolysis

Table S3.11. Results from CPE experiment in Figure S3.69, 1:3 (1:Mes_2DBTD) + PhOH (red).

Time (s)	Charge (coulombs)	moles (e^-)	Moles of CO	FE_{CO}
16050	6.73	6.73×10^{-5}	3.42×10^{-5}	98.1
18000	7.51	7.78×10^{-5}	4.31×10^{-5}	110.8
20000*	8.31	8.61×10^{-5}	4.35×10^{-5}	101.1
20000*	8.31	8.61×10^{-5}	4.76×10^{-5}	110.5
20000*	8.31	8.61×10^{-5}	4.41×10^{-5}	102.4

* indicates a triplicate series of injections carried out upon completion of electrolysis

Table S3.12. Results from CPE experiment in Figure S3.69, 1:5 (**1**:Mes_2DBTD) + PhOH (blue).

Time (s)	Charge (coulombs)	moles (e^-)	Moles of CO	FE_{CO}
20000*	12.2	1.27×10^{-4}	6.78×10^{-5}	107.1
20000*	12.2	1.27×10^{-4}	5.85×10^{-5}	92.3
20000*	12.2	1.27×10^{-4}	6.05×10^{-5}	95.5

* indicates a triplicate series of injections carried out upon completion of electrolysis

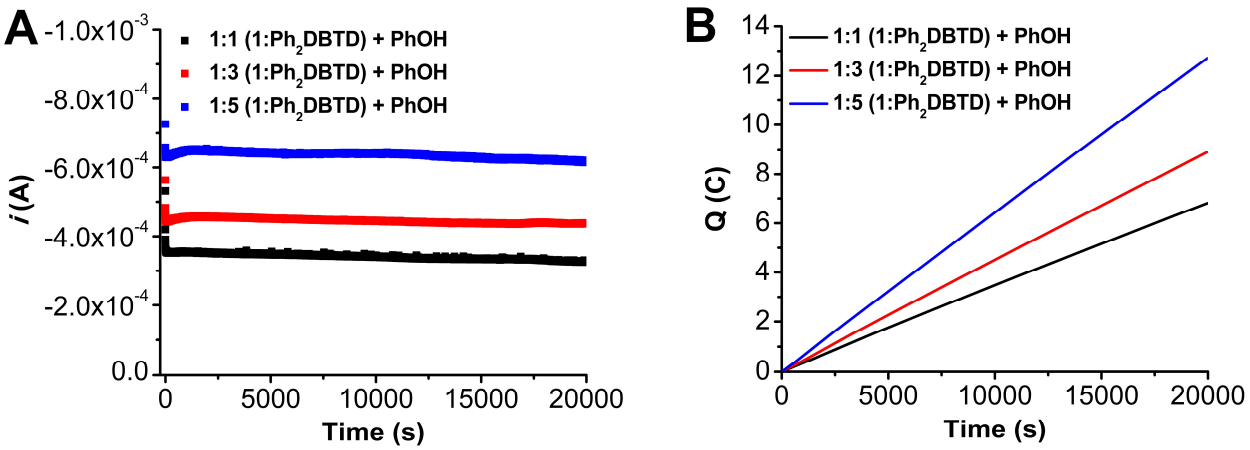

Figure S3.70. (**A**) Current versus time trace from CPE experiments with **1**+Ph_2DBTD+PhOH. (**B**) Charge passed versus time for the CPE experiments shown in **A**. Conditions were 0.1 mM Cr(^{tbu}dhbpy)Cl(H_2O) **1**, 0.12 M PhOH, and either 0.1 (black), 0.3 (red), or 0.5 (blue) mM Ph_2DBTD under a CO_2 atmosphere at −2.20 V vs Fc^+/Fc in 0.1 M $TBAPF_6$/DMF; working electrode was a glassy carbon rod, counter electrode was a graphite rod, and the reference was a nonaqueous Ag/AgCl pseudoreference electrode; 0.075 M Fc was used as sacrificial oxidant.

Table S3.13. Results from CPE experiment in Figure S3.70, 1:1 (**1**:Ph_2DBTD) + PhOH (black).

Time (s)	Charge (coulombs)	moles (e^-)	Moles of CO	FE_{CO}
20000*	6.8	7.07×10^{-5}	3.73×10^{-5}	105.4
20000*	6.8	7.07×10^{-5}	3.62×10^{-5}	102.4
20000*	6.8	7.07×10^{-5}	3.47×10^{-5}	98.3

* indicates a triplicate series of injections carried out upon completion of electrolysis

Table S3.14. Results from CPE experiment in Figure S3.70, 1:3 (**1**:Ph_2DBTD) + PhOH (red).

Time (s)	Charge (coulombs)	moles (e^-)	Moles of CO	FE_{CO}
20000*	8.9	9.23×10^{-5}	4.48×10^{-5}	97.2
20000*	8.9	9.23×10^{-5}	4.65×10^{-5}	100.8
20000*	8.9	9.23×10^{-5}	4.78×10^{-5}	103.5

* indicates a triplicate series of injections carried out upon completion of electrolysis

Table S3.15. Results from CPE experiment in Figure S3.70, 1:5 (**1**:Ph_2DBTD) + PhOH (blue).

Time (s)	Charge (coulombs)	moles (e^-)	Moles of CO	FE_{CO}
20000*	12.7	1.32×10^{-4}	7.28×10^{-5}	110.4
20000*	12.7	1.32×10^{-4}	6.76×10^{-5}	102.6
20000*	12.7	1.32×10^{-4}	6.45×10^{-5}	97.9

* indicates a triplicate series of injections carried out upon completion of electrolysis

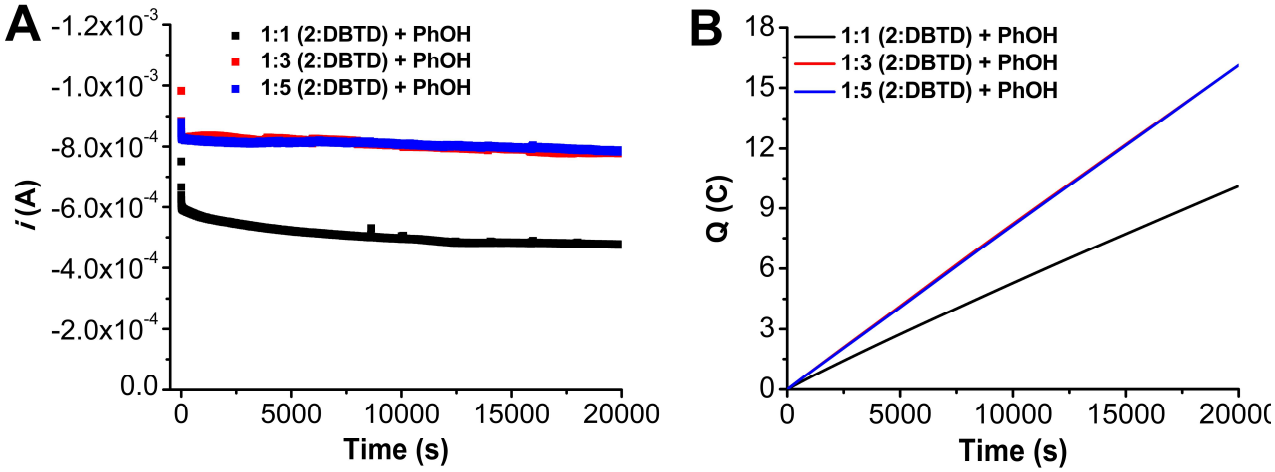

Figure S3.71. (**A**) Current versus time trace from CPE experiments with **2**+DBTD+PhOH. (**B**) Charge passed versus time for the CPE experiments shown in **A**. Conditions were 0.1 mM Cr(^{tbu}dh^{tbu}bpy)Cl(H_2O) **2**, 0.12 M PhOH, and either 0.1 (black), 0.3 (red), or 0.5 (blue) mM DBTD under a CO_2 atmosphere at −2.30 V vs Fc^+/Fc in 0.1 M $TBAPF_6$/DMF; working electrode was a glassy carbon rod, counter electrode was a graphite rod, and the reference was a nonaqueous Ag/AgCl pseudoreference electrode; 0.075 M Fc was used as sacrificial oxidant.

Table S3.16. Results from CPE experiment in Figure S3.71, 1:1 (**2**:DBTD) + PhOH (black).

Time (s)	Charge (coulombs)	moles (e^-)	Moles of CO	FE_{CO}
20000*	10.1	1.05×10^{-4}	5.25×10^{-5}	100.1
20000*	10.1	1.05×10^{-4}	5.64×10^{-5}	107.7
20000*	10.1	1.05×10^{-4}	5.35×10^{-5}	102.1

* indicates a triplicate series of injections carried out upon completion of electrolysis

Table S3.17. Results from CPE experiment in Figure S3.71, 1:3 (**2**:DBTD) + PhOH (red).

Time (s)	Charge (coulombs)	moles (e^-)	Moles of CO	FE_{co}
20000*	16.2	1.68×10^{-4}	8.22×10^{-5}	98.1
20000*	16.2	1.68×10^{-4}	8.25×10^{-5}	98.4
20000*	16.2	1.68×10^{-4}	8.41×10^{-5}	100.4

* indicates a triplicate series of injections carried out upon completion of electrolysis

Table S3.18. Results from CPE experiment in Figure S3.71, 1:5 (**2**:DBTD) + PhOH (blue).

Time (s)	Charge (coulombs)	moles (e^-)	Moles of CO	FE_{co}
3758	3.07	3.18×10^{-5}	1.34×10^{-5}	84.4
5893	4.81	4.98×10^{-5}	2.74×10^{-5}	110.0
7873	6.42	6.65×10^{-5}	3.88×10^{-5}	116.9
11924	9.70	1.00×10^{-4}	5.93×10^{-5}	118.1
13648	11.1	1.15×10^{-4}	6.74×10^{-5}	117.4
15918	12.9	1.34×10^{-4}	7.46×10^{-5}	111.6
17982	14.5	1.51×10^{-4}	8.37×10^{-5}	111.2
20000*	16.1	1.67×10^{-4}	9.32×10^{-5}	111.6
20000*	16.1	1.67×10^{-4}	9.20×10^{-5}	110.1
20000*	16.1	1.67×10^{-4}	8.61×10^{-5}	103.1

* indicates a triplicate series of injections carried out upon completion of electrolysis

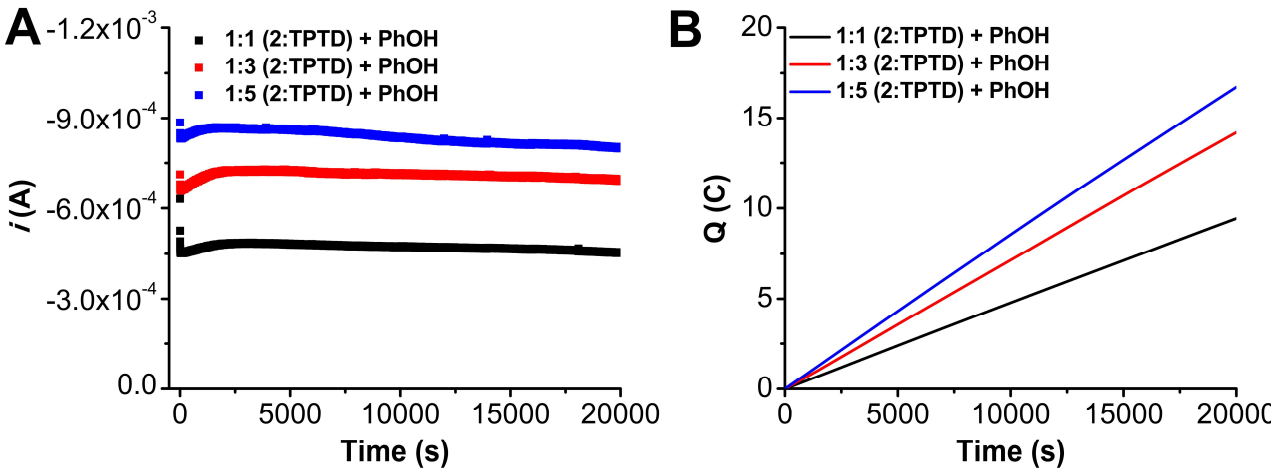

Figure S3.72. (**A**) Current versus time trace from CPE experiments with **2**+TPTD+PhOH. (**B**) Charge passed versus time for the CPE experiments shown in **A**. Conditions were 0.1 mM Cr(^{tbu}dh^{tbu}bpy)Cl(H_2O) **2**, 0.12 M PhOH, and either 0.1 (black), 0.3 (red), or 0.5 (blue) mM TPTD under a CO_2 atmosphere at −2.25 V vs Fc^+/Fc in 0.1 M $TBAPF_6$/DMF; working electrode was a glassy carbon rod, counter electrode was a graphite rod, and the reference was a nonaqueous Ag/AgCl pseudoreference electrode; 0.075 M Fc was used as sacrificial oxidant.

Table S3.19. Results from CPE experiment in Figure S3.72, 1:1 (**2**:TPTD) + PhOH (black).

Time (s)	Charge (coulombs)	moles (e^-)	Moles of CO	FE_{CO}
20000*	9.43	9.78×10^{-5}	4.99×10^{-5}	102.1
20000*	9.43	9.78×10^{-5}	4.99×10^{-5}	102.0
20000*	9.43	9.78×10^{-5}	4.54×10^{-5}	92.8

* indicates a triplicate series of injections carried out upon completion of electrolysis

Table S3.20. Results from CPE experiment in Figure S3.72, 1:3 (**2**:TPTD) + PhOH (red).

Time (s)	Charge (coulombs)	moles (e^-)	Moles of CO	FE_{CO}
5783	4.13	4.28×10^{-5}	2.11×10^{-5}	98.5
7901	5.65	5.85×10^{-5}	2.99×10^{-5}	102.2
20000*	14.2	1.47×10^{-4}	8.01×10^{-5}	108.9
20000*	14.2	1.47×10^{-4}	7.96×10^{-5}	108.2
20000*	14.2	1.47×10^{-4}	7.65×10^{-5}	104.0

* indicates a triplicate series of injections carried out upon completion of electrolysis

Table S3.21. Results from CPE experiment in Figure S3.72, 1:5 (**2**:TPTD) + PhOH (blue).

Time (s)	Charge (coulombs)	moles (e^-)	Moles of CO	FE_{co}
5976	5.14	5.33×10^{-5}	2.39×10^{-5}	89.6
7970	6.85	7.09×10^{-5}	3.29×10^{-5}	92.6
9975	8.53	8.84×10^{-5}	4.39×10^{-5}	99.3
11992	10.2	1.06×10^{-4}	5.84×10^{-5}	110.4
13938	11.8	1.22×10^{-4}	6.04×10^{-5}	98.8
15938	13.4	1.39×10^{-4}	7.35×10^{-5}	105.6
17858	15.0	1.55×10^{-4}	7.59×10^{-5}	97.7
20000*	16.7	1.73×10^{-4}	7.96×10^{-5}	91.9
20000*	16.7	1.73×10^{-4}	8.40×10^{-5}	97.0
20000*	16.7	1.73×10^{-4}	7.86×10^{-5}	90.7

* indicates a triplicate series of injections carried out upon completion of electrolysis

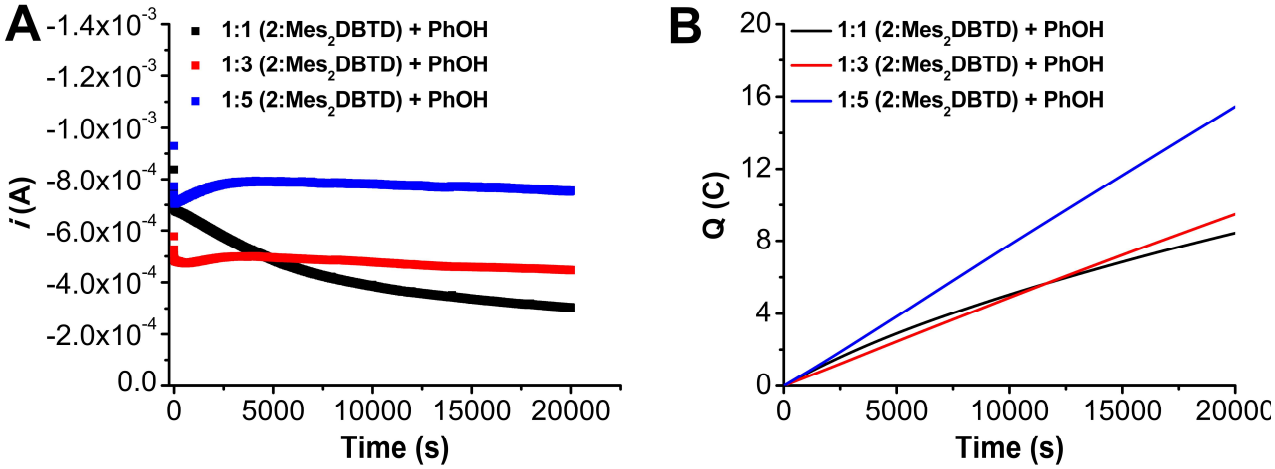

Figure S3.73. (**A**) Current versus time trace from CPE experiments with **2**+Mes_2DBTD+PhOH. (**B**) Charge passed versus time for the CPE experiments shown in **A**. Conditions were 0.1 mM Cr(^{tbu}dh^{tbu}bpy)Cl(H_2O) **2**, 0.12 M PhOH, and either 0.1 (black), 0.3 (red), or 0.5 (blue) mM Mes_2DBTD under a CO_2 atmosphere at −2.30 V vs Fc^+/Fc in 0.1 M $TBAPF_6$/DMF; working electrode was a glassy carbon rod, counter electrode was a graphite rod, and the reference was a nonaqueous Ag/AgCl pseudoreference electrode; 0.075 M Fc was used as sacrificial oxidant.

Table S3.22. Results from CPE experiment in Figure S3.73, 1:1 (**2**:Mes_2DBTD) + PhOH (black).

Time (s)	Charge (coulombs)	moles (e^-)	Moles of CO	FE_{CO}
11926	5.76	5.97×10^{-5}	2.82×10^{-5}	94.6
13952	6.48	6.72×10^{-5}	3.54×10^{-5}	105.5
15926	7.15	7.41×10^{-5}	3.79×10^{-5}	102.2
17896	7.78	8.07×10^{-5}	4.12×10^{-5}	102.1
20000*	8.44	8.74×10^{-5}	4.56×10^{-5}	104.3
20000*	8.44	8.74×10^{-5}	5.06×10^{-5}	115.7
20000*	8.44	8.74×10^{-5}	4.64×10^{-5}	106.1

* indicates a triplicate series of injections carried out upon completion of electrolysis

Table S3.23. Results from CPE experiment in Figure S3.73, 1:3 (**2**:Mes_2DBTD) + PhOH (red).

Time (s)	Charge (coulombs)	moles (e^-)	Moles of CO	FE_{CO}
9923	4.85	5.02×10^{-5}	2.31×10^{-5}	91.8
11855	5.76	5.97×10^{-5}	3.07×10^{-5}	102.7
14146	6.82	7.07×10^{-5}	3.94×10^{-5}	111.4
15810	7.59	7.86×10^{-5}	4.17×10^{-5}	105.9
17805	8.50	8.80×10^{-5}	4.39×10^{-5}	99.6
20000*	9.48	9.83×10^{-5}	5.20×10^{-5}	105.8
20000*	9.48	9.83×10^{-5}	5.54×10^{-5}	112.7
20000*	9.48	9.83×10^{-5}	5.44×10^{-5}	110.8

* indicates a triplicate series of injections carried out upon completion of electrolysis

Table S3.24. Results from CPE experiment in Figure S3.73, 1:5 (**2**:Mes_2DBTD) + PhOH (blue).

Time (s)	Charge (coulombs)	moles (e^-)	Moles of CO	FE_{co}
13925	10.8	1.12×10^{-4}	5.78×10^{-5}	103.2
15940	12.4	1.28×10^{-4}	6.01×10^{-5}	93.9
18120	14.0	1.45×10^{-4}	6.98×10^{-5}	96.1
20000*	15.5	1.60×10^{-4}	7.69×10^{-5}	96.0
20000*	15.5	1.60×10^{-4}	7.92×10^{-5}	99.0
20000*	15.5	1.60×10^{-4}	7.54×10^{-5}	94.1

* indicates a triplicate series of injections carried out upon completion of electrolysis

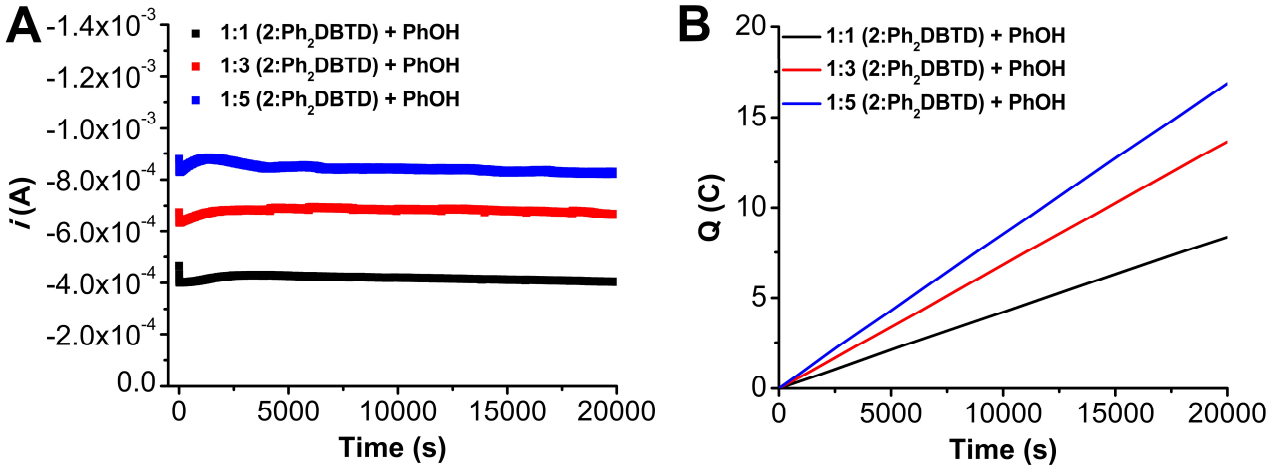

Figure S3.74. (**A**) Current versus time trace from CPE experiments with **2**+Ph_2DBTD+PhOH. (**B**) Charge passed versus time for the CPE experiments shown in **A**. Conditions were 0.1 mM Cr(^{tbu}dh^{tbu}bpy)Cl(H_2O) **2**, 0.12 M PhOH, and either 0.1 (black), 0.3 (red), or 0.5 (blue) mM Ph_2DBTD under a CO_2 atmosphere at −2.20 V vs Fc^+/Fc in 0.1 M $TBAPF_6$/DMF; working electrode was a glassy carbon rod, counter electrode was a graphite rod, and the reference was a nonaqueous Ag/AgCl pseudoreference electrode; 0.075 M Fc was used as sacrificial oxidant.

Table S3.25. Results from CPE experiment in Figure S3.74, 1:1 (**2**:Ph_2DBTD) + PhOH (black).

Time (s)	Charge (coulombs)	moles (e^-)	Moles of CO	FE_{CO}
7888	3.33	3.64×10^{-5}	1.71×10^{-5}	99.0
9711	4.10	4.25×10^{-5}	2.26×10^{-5}	106.4
20000*	8.35	8.65×10^{-5}	4.94×10^{-5}	114.3
20000*	8.35	8.65×10^{-5}	5.11×10^{-5}	118.1
20000*	8.35	8.65×10^{-5}	4.88×10^{-5}	112.8

* indicates a triplicate series of injections carried out upon completion of electrolysis

Table S3.26. Results from CPE experiment in Figure S3.74, 1:3 (**2**:Ph_2DBTD) + PhOH (red).

Time (s)	Charge (coulombs)	moles (e^-)	Moles of CO	FE_{CO}
20000*	13.6	1.41×10^{-4}	6.83×10^{-5}	96.7
20000*	13.6	1.41×10^{-4}	6.76×10^{-5}	95.7
20000*	13.6	1.41×10^{-4}	7.14×10^{-5}	101.0

* indicates a triplicate series of injections carried out upon completion of electrolysis

Table S3.27. Results from CPE experiment in Figure S3.74, 1:5 (**2**:Ph_2DBTD) + PhOH (blue).

Time (s)	Charge (coulombs)	moles (e^-)	Moles of CO	FE_{CO}
20000*	16.8	1.75×10^{-4}	8.30×10^{-5}	95.0
20000*	16.8	1.75×10^{-4}	8.09×10^{-5}	92.6
20000*	16.8	1.75×10^{-4}	9.10×10^{-5}	104.1

* indicates a triplicate series of injections carried out upon completion of electrolysis

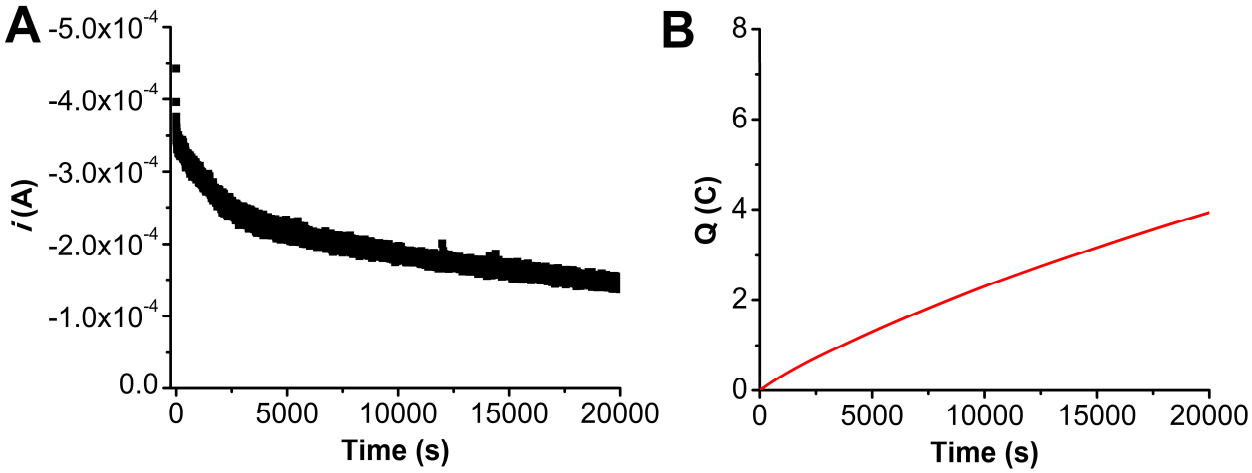

Figure S3.75. (**A**) Current versus time trace from CPE experiment with TPTD+PhOH. (**B**) Charge passed versus time for the CPE experiment shown in **A**. Conditions were 0.5 mM TPTD and 0.12 M PhOH under a CO_2 atmosphere at −2.25 V vs Fc^+/Fc in 0.1 M $TBAPF_6$/DMF; working electrode was a glassy carbon rod, counter electrode was a graphite rod, and the reference was a nonaqueous Ag/AgCl pseudoreference electrode; 0.075 M Fc was used as sacrificial oxidant.

Table S3.28. Results from CPE experiment in Figure S3.75, Ph_2DBTD + PhOH.

Time (s)	Charge (coulombs)	moles (e^-)	Moles of CO
20000*	3.94	4.08 x 10^{-5}	< LOQ
20000*	3.94	4.08 x 10^{-5}	< LOQ
20000*	3.94	4.08 x 10^{-5}	< LOQ

* indicates a triplicate series of injections carried out upon completion of electrolysis

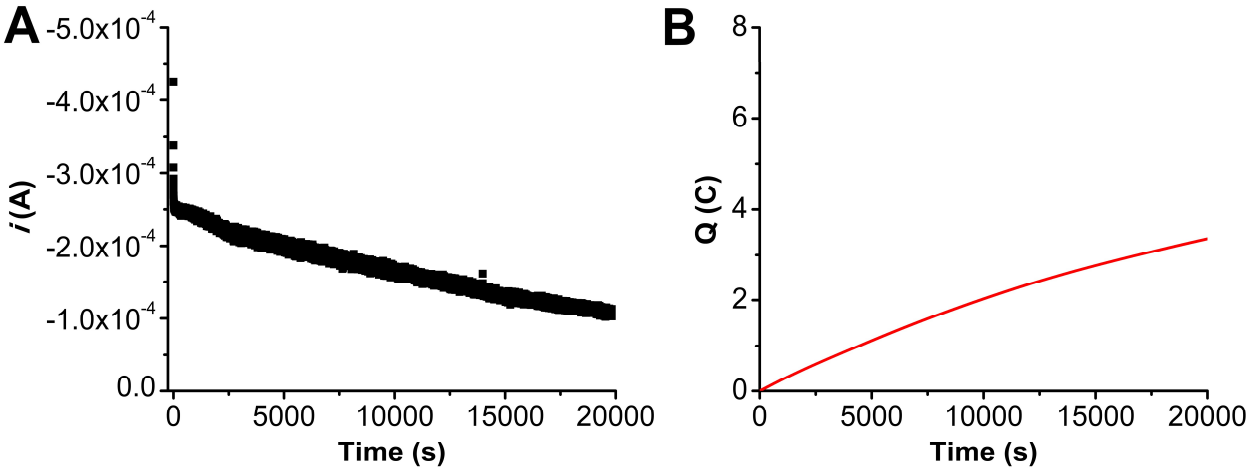

Figure S3.76. (**A**) Current versus time trace from CPE experiment with Mes_2DBTD+PhOH. (**B**) Charge passed versus time for the CPE experiment shown in **A**. Conditions were 0.5 mM Mes_2DBTD and 0.12 M PhOH under a CO_2 atmosphere at −2.30 V vs Fc^+/Fc in 0.1 M $TBAPF_6$/DMF; working electrode was a glassy carbon rod, counter electrode was a graphite rod, and the reference was a nonaqueous Ag/AgCl pseudoreference electrode; 0.075 M Fc was used as sacrificial oxidant.

Table S3.29. Results from CPE experiment in Figure S3.76, Mes_2DBTD + PhOH.

Time (s)	Charge (coulombs)	moles (e^-)	Moles of CO
20000*	3.35	3.48 x 10^{-5}	< LOQ
20000*	3.35	3.48 x 10^{-5}	< LOQ
20000*	3.35	3.48 x 10^{-5}	< LOQ

* indicates a triplicate series of injections carried out upon completion of electrolysis

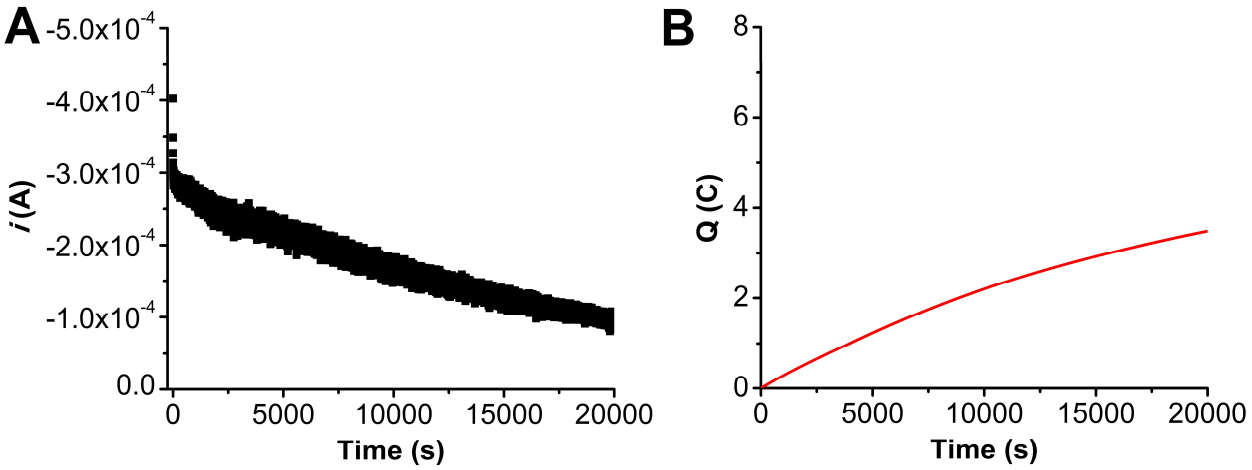

Figure S3.77. (**A**) Current versus time trace from CPE experiment with Ph_2DBTD+PhOH. (**B**) Charge passed versus time for the CPE experiment shown in **A**. Conditions were 0.5 mM Ph_2DBTD and 0.12 M PhOH under a CO_2 atmosphere at −2.20 V vs Fc^+/Fc in 0.1 M $TBAPF_6$/DMF; working electrode was a glassy carbon rod, counter electrode was a graphite rod, and the reference was a nonaqueous Ag/AgCl pseudoreference electrode; 0.075 M Fc was used as sacrificial oxidant.

Table S3.30. Results from CPE experiment in Figure S3.77, Mes_2DBTD + PhOH.

Time (s)	Charge (coulombs)	moles (e^-)	Moles of CO
20000*	3.48	3.61 x 10^{-5}	< LOQ
20000*	3.48	3.61 x 10^{-5}	< LOQ
20000*	3.48	3.61 x 10^{-5}	< LOQ

* indicates a triplicate series of injections carried out upon completion of electrolysis

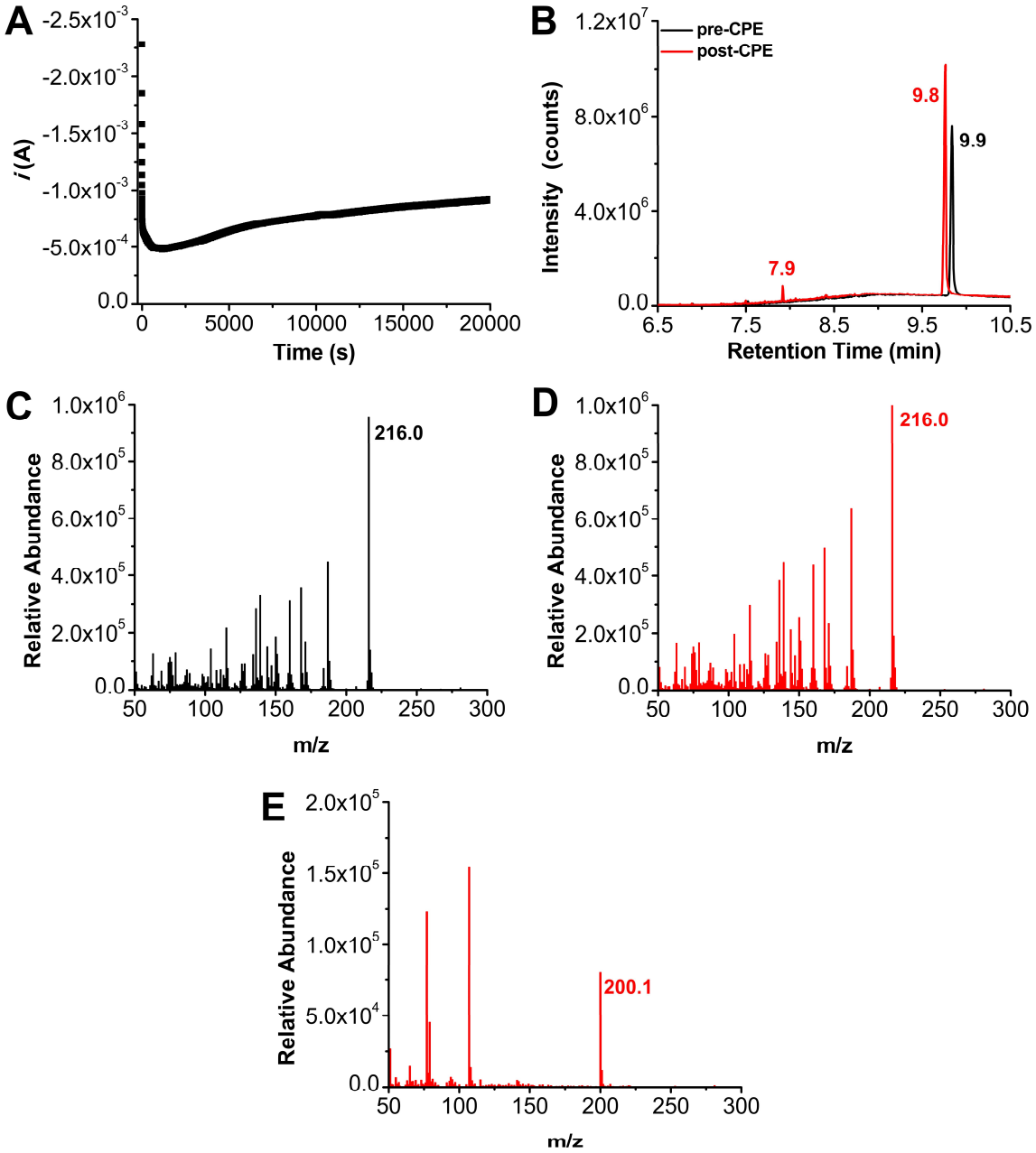

Figure S3.78. (**A**) Current versus time trace of control CPE experiment with DBTD and PhOH under N_2. (**B**) Gas chromatograph of the pre- and post-CPE solution. The mass spectrum for the peak at 9.9 min in the pre-CPE sample (**C**) and 9.8 min for the post-CPE sample (**D**) corresponds to DBTD. The MS spectrum of the peak at 7.9 min in the post-CPE sample corresponds to dibenzothiophene 5-oxide (**E**). Conditions for (**A**) were 5 mM DBTD and 0.1 M PhOH under a N_2 atmosphere at −2.30 V vs Fc^+/Fc in 0.1 M $TBAPF_6$/DMF; working and counter electrodes were carbon cloth and the reference was a nonaqueous Ag/AgCl pseudoreference electrode; 0.075 M Fc was used as sacrificial oxidant.

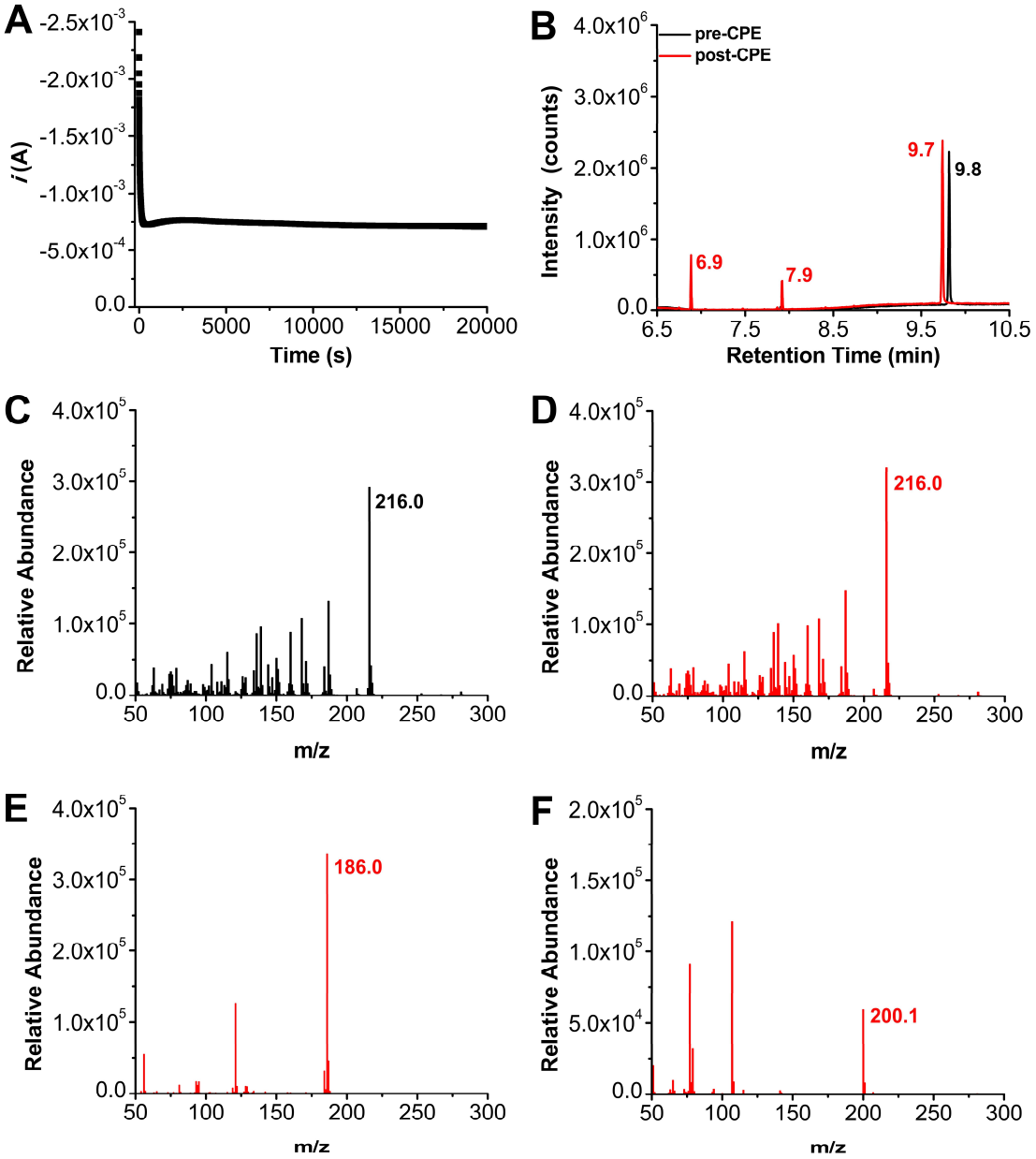

Figure S3.79. (**A**) Current versus time trace of control CPE experiment with **1**, DBTD, and PhOH under CO_2. (**B**) Gas chromatograph of the pre- and post-CPE solution. The mass spectrum for the peak at 9.8 min in the pre-CPE sample (**C**) and 9.7 min for the post-CPE sample (**D**) corresponds to DBTD. The MS spectrum of the peak at 6.9 min in the post-CPE sample likely corresponds to [1,1′-biphenyl]-2-thiol (**E**). The MS spectrum of the peak at 7.9 min in the post-CPE sample corresponds to dibenzothiophene 5-oxide (**F**). Conditions for (**A**) were 0.5 mM Cr(^{tbu}dhbpy)Cl(H_2O) **1**, 2.5 mM DBTD and 0.6 M PhOH under a N_2 atmosphere at −2.30 V vs Fc^+/Fc in 0.1 M $TBAPF_6$/DMF; working and counter electrodes were graphite rods, and the reference was a nonaqueous Ag/AgCl pseudoreference electrode; 0.075 M Fc was used as sacrificial oxidant.

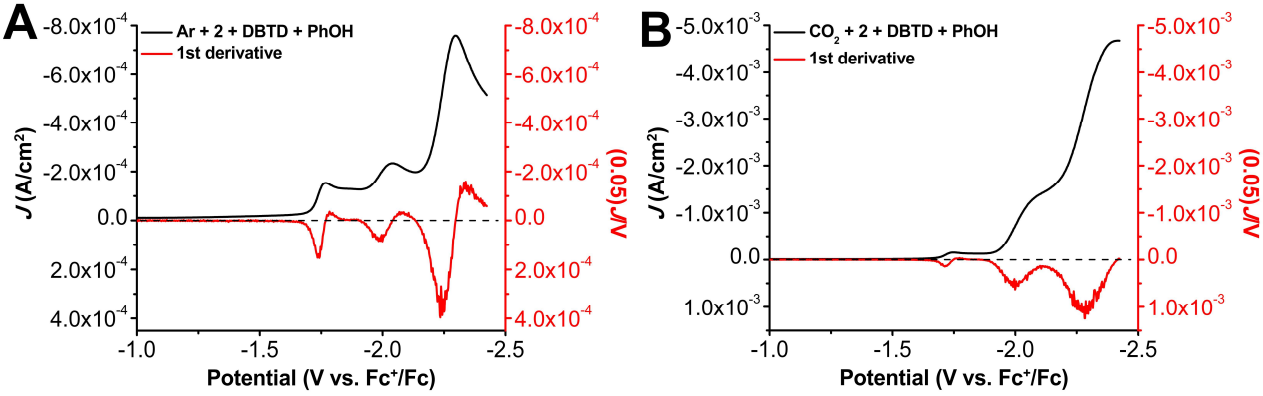

Figure S3.80. Example forward CV trace and first derivative plot used in i_{cat}/i_p calculationsfor 1.0 mM Cr(^{tbu}dh^{tbu}bpy)Cl(H_2O) **2** with 2.5 mM DBTD and 0.1 M PhOH under Ar (**A**) and CO_2 (**B**).

3.7.8 Computational Studies

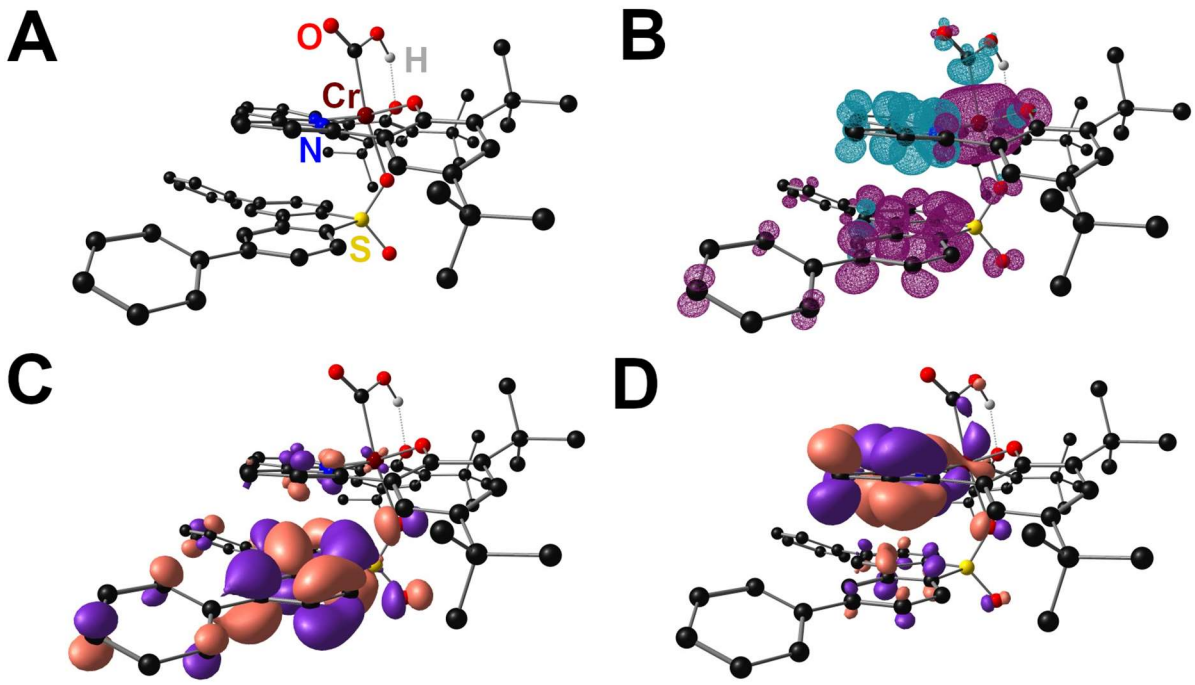

Figure S3.81. Molecular geometry of the $^{4}_{0}\mathbf{Cr(CO_2H)(Ph_2DBTD)}^{-2}$ adduct (**A**) DFT calculated spin density (**B**) Kohn-Sham orbital projection of SOMO (**C**) and SOMO^{-1} (**D**). Where Cr = Cr(^{tbu}dhbpy).

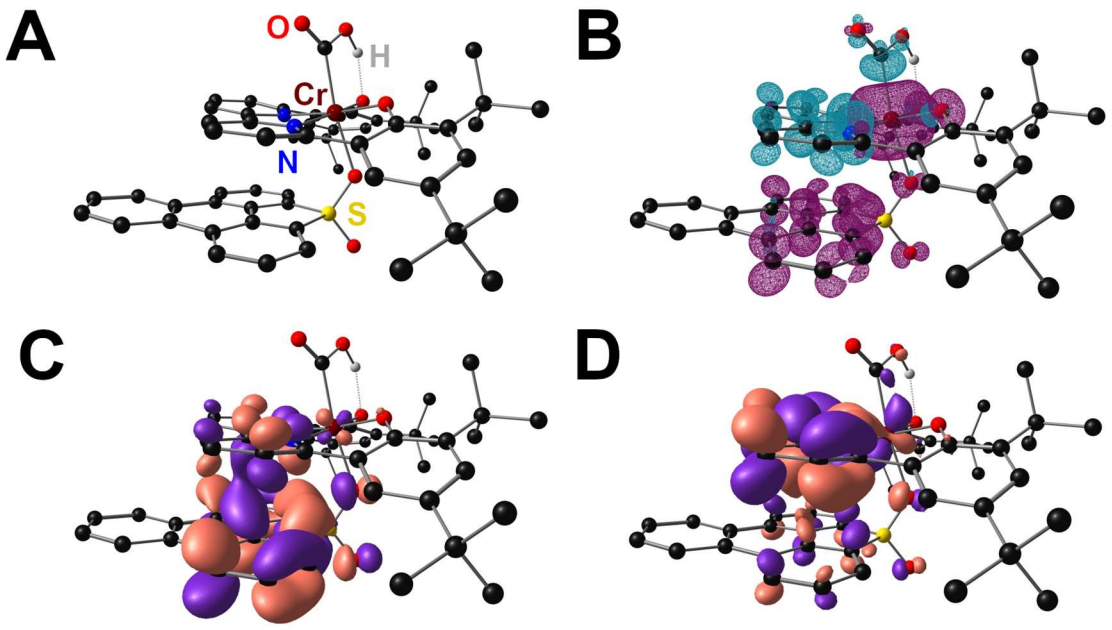

Figure S3.82. Molecular geometry of the ${}^{4}_{0}\mathbf{Cr(CO_2H)(TPTD)}^{-2}$ adduct (**A**) DFT calculated spin density (**B**) Kohn-Sham orbital projection of SOMO (**C**) and SOMO^{-1} (**D**). Where Cr = Cr(^{tbu}dhbpy).

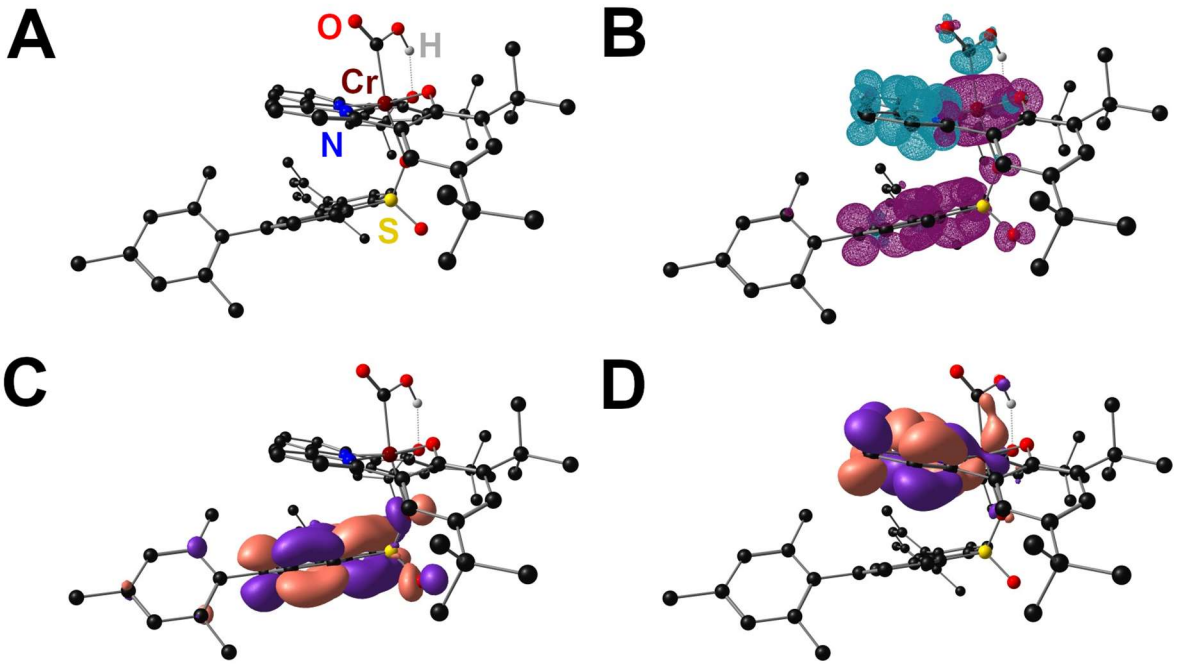

Figure S3.83. Molecular geometry of the ${}^{4}_{0}\mathbf{Cr(CO_2H)(Mes_2DBTD)}^{-2}$ adduct (**A**) DFT calculated spin density (**B**) Kohn-Sham orbital projection of SOMO (**C**) and SOMO^{-1} (**D**). Where Cr = Cr(^{tbu}dhbpy).

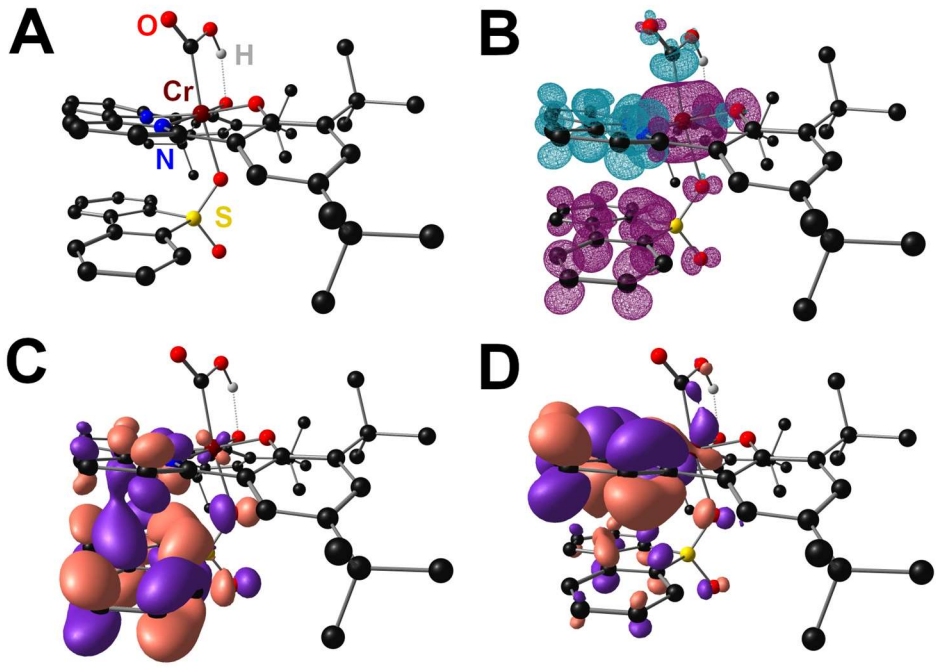

Figure S3.84. Molecular geometry of the ${}^{4}_{0}\mathbf{Cr(CO_2H)(DBTD)}^{-2}$ adduct (**A**) DFT calculated spin density (**B**) Kohn-Sham orbital projection of SOMO (**C**) and SOMO^{-1} (**D**). Where Cr = Cr(^{tbu}dhbpy).

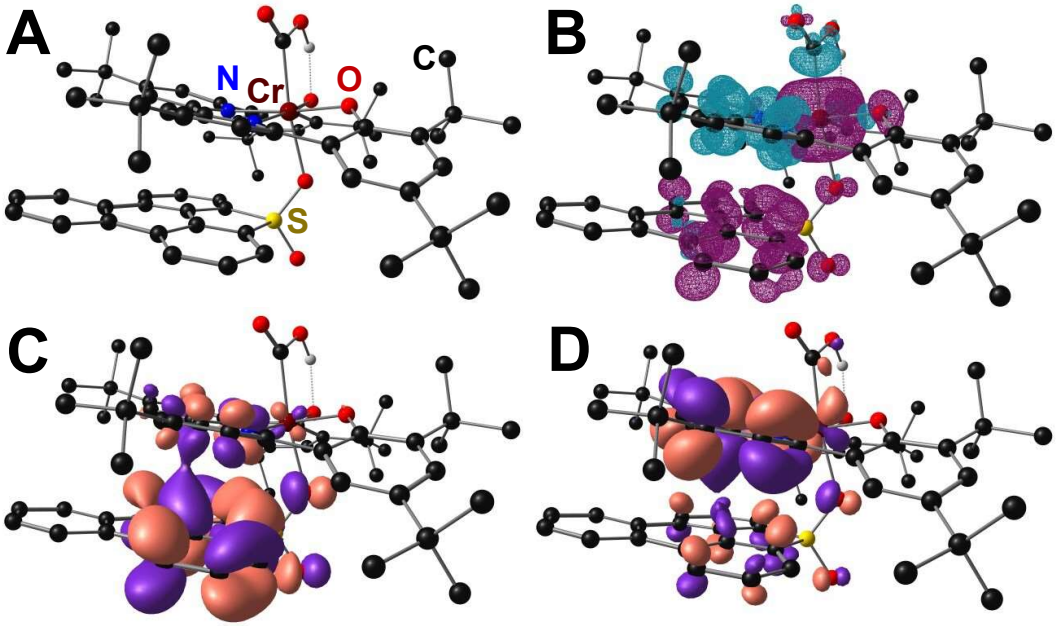

Figure S3.85. Molecular geometry of the ${}^{4}_{0}\mathbf{Cr(CO_2H)(TPTD)}^{-2}$ adduct (**A**) DFT calculated spin density (**B**) Kohn-Sham orbital projection of SOMO (**C**) and SOMO^{-1} (**D**). Where Cr = Cr(^{tbu}dh^{tbu}bpy).

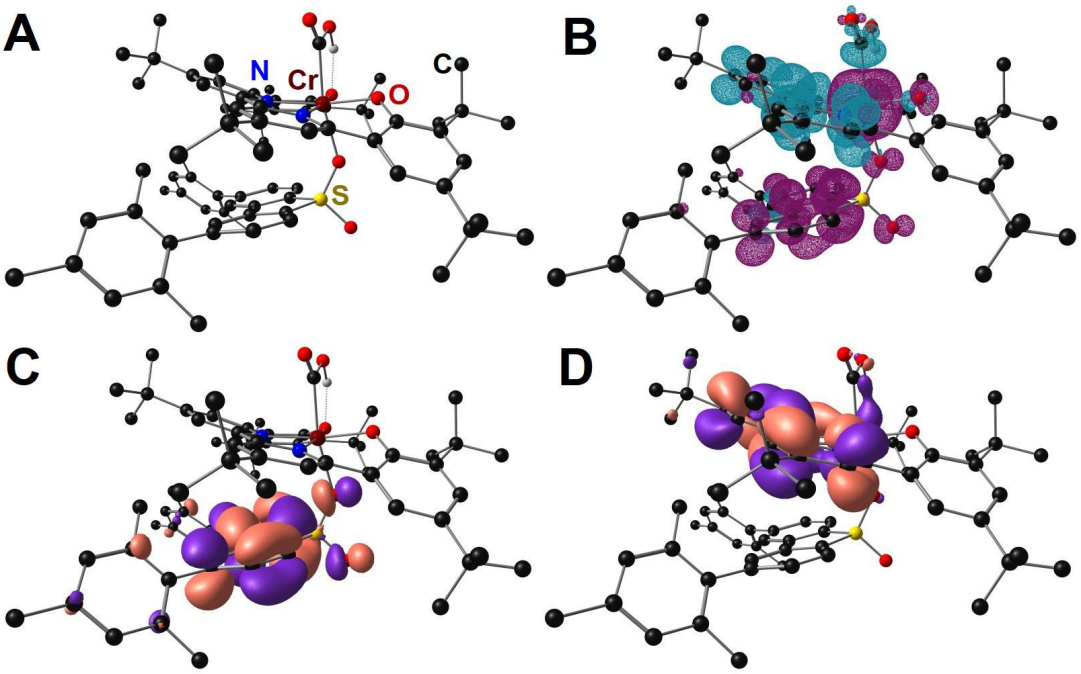

Figure S3.86. Molecular geometry of the $^{4}_{0}\mathbf{Cr(CO_2H)(Mes_2DBTD)}^{-2}$ adduct (**A**) DFT calculated spin density (**B**) Kohn-Sham orbital projection of SOMO (**C**) and SOMO^{-1} (**D**). Where Cr = Cr(^{tbu}dh^{tbu}bpy).

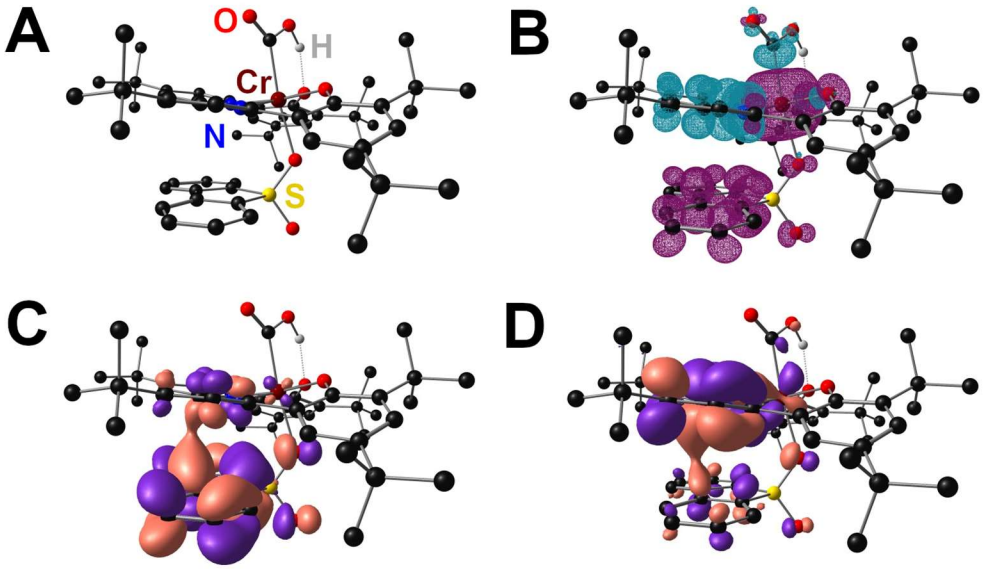

Figure S3.87. Molecular geometry of the $^{4}_{0}\mathbf{Cr(CO_2H)(DBTD)}^{-2}$ adduct (**A**) DFT calculated spin density (**B**) Kohn-Sham orbital projection of SOMO (**C**) and SOMO^{-1} (**D**). Where Cr = Cr(^{tbu}dh^{tbu}bpy).

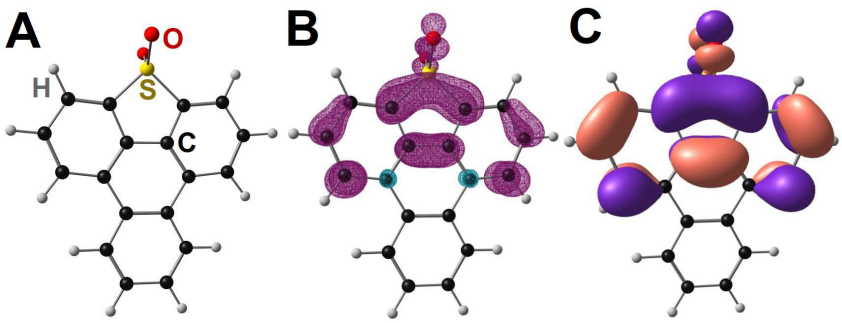

Figure S3.88. Molecular geometry of the $^{2}_{\square}\mathbf{TPTD}^{-1}_{\square}$ adduct(**A**) DFT calculated spin density (**B**) Kohn-Sham orbital projection of SOMO (**C**).

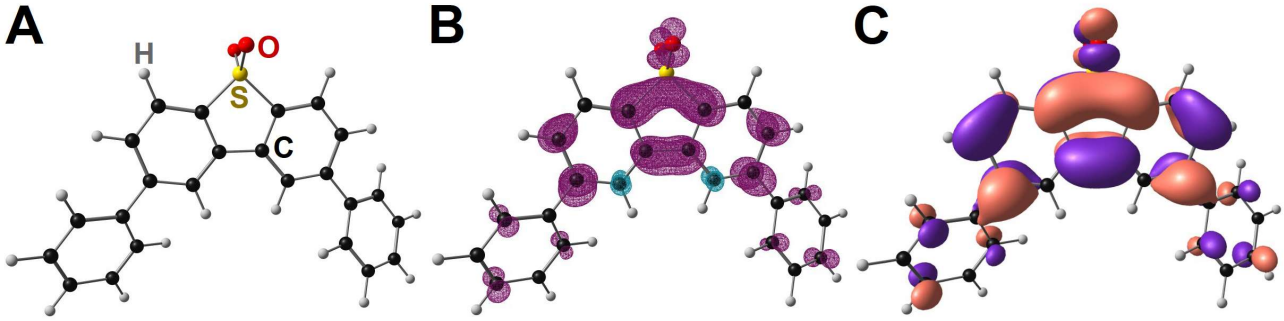

Figure S3.89. Molecular geometry of the $^{2}_{\square}\mathbf{Ph_2DBTD}^{-1}_{\square}$ adduct (**A**) DFT calculated spin density (**B**) Kohn-Sham orbital projection of SOMO (**C**).

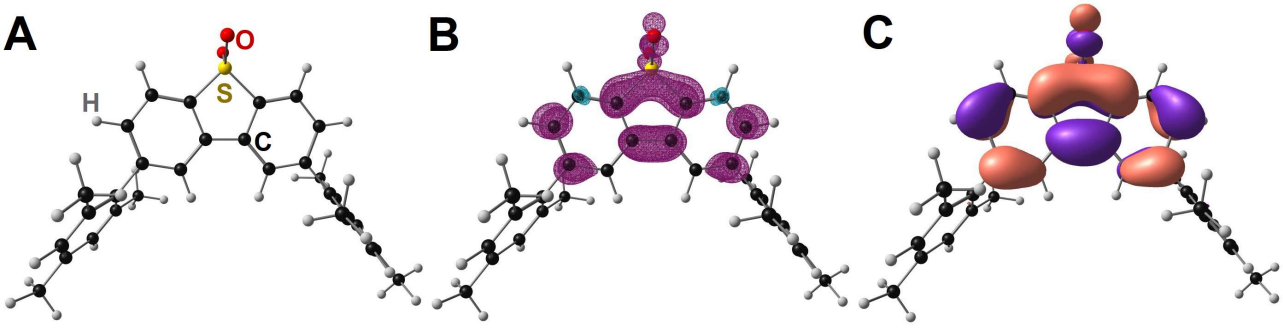

Figure S3.90. Molecular geometry of the $^{2}_{\square}\mathbf{Mes_2DBTD}^{-1}_{\square}$ adduct (**A**) DFT calculated spin density (**B**) Kohn-Sham orbital projection of SOMO (**C**).

Table S3.31. Calculated NICS(0) values for DBTD.

Ring	$[RM]^0$ NICS(0)	$[RM]^-$ NICS(0)	ΔNICS(0)
A	+2.913	–6.703	–9.616
B	–6.916	–1.709	+5.207

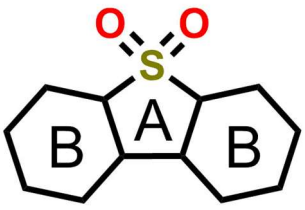

Table S3.32. Calculated NICS(0) values for TPTD.

Ring	$[RM]^0$ NICS(0)	$[RM]^-$ NICS(0)	ΔNICS(0)
A	+4.084	–9.162	–13.246
B	–7.820	–1.190	+6.630
C	–1.836	–1.339	+0.497
D	–7.554	–9.010	+1.456

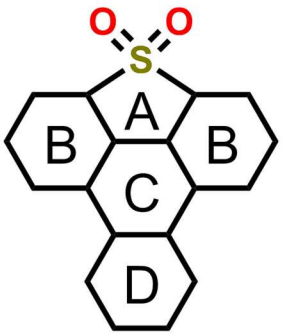

Table S3.33. Calculated NICS(0) values for Ph_2DBTD.

Ring	$[RM]^0$ NICS(0)	$[RM]^-$ NICS(0)	ΔNICS(0)
A	+2.798	–5.583	–8.381
B	–6.181	–2.214	+3.967
C	–7.177	–5.980	+1.197

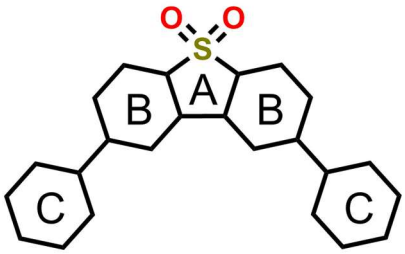

Table S3.34. Calculated NICS(0) values for Mes_2DBTD.

Ring	$[RM]^0$ NICS(0)	$[RM]^-$ NICS(0)	ΔNICS(0)
A	+3.041	–6.074	–9.115
B	–6.462	–1.403	+5.059
C	–7.299	–7.283	+0.016

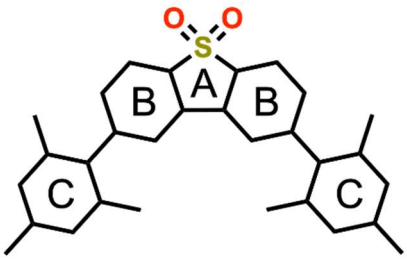

Table S3.35. Calculated centroid–centroid distances (benzene rings of the dibenzothiophene core to the bpy ligand of the Cr complex) and Cr–sulfone bond distances for all $[Cr(L)(CO_2H)(RM)]^{2-}$ adducts. Where L is $[^{tbu}dhbpy]^{2-}$ or $[^{tbu}dh^{tbu}bpy]^{2-}$ and S=3/2.

Cr Complex	Centroid–Centroid Distances (Å)	Cr–Sulfone Distance (Å)
$[Cr(^{tbu}dhbpy)(CO_2H)(DBTD)]^{2-}$	3.329 3.287	2.189
$[Cr(^{tbu}dhbpy)(CO_2H)(Mes_2DBTD)]^{2-}$	4.678 3.889	2.164
$[Cr(^{tbu}dhbpy)(CO_2H)(TPTD)]^{2-}$	3.252 3.229	2.195
$[Cr(^{tbu}dhbpy)(CO_2H)(Ph_2DBTD)]^{2-}$	3.326 3.278	2.187
$[Cr(^{tbu}dh^{tbu}bpy)(CO_2H)(DBTD)]^{2-}$	3.361 3.316	2.185
$[Cr(^{tbu}dh^{tbu}bpy)(CO_2H)(Mes_2DBTD)]^{2-}$	4.852 3.862	2.165
$[Cr(^{tbu}dh^{tbu}bpy)(CO_2H)(TPTD)]^{2-}$	3.314 3.285	2.188
$[Cr(^{tbu}dh^{tbu}bpy)(CO_2H)(Ph_2DBTD)]^{2-}$	3.465 3.649	2.184

3.7.9 Analysis of Electrochemical CO_2 Reduction Under Aprotic Conditions

Previously we observed that the addition of DBTD to a solution of **1** under CO_2 saturation conditions lead to the appearance of an aprotic catalytic feature that is not intrinsic to either component.[29] The addition of TPTD (**Figure S3.91**) to a solution of **1** and CO_2 leads to the appearance of an irreversible redox feature at the $E_{1/2}$ of TPTD (−2.19 V vs. Fc^+/Fc), although the increase is less than that observed for DBTD. Despite a 120 mV difference in standard potential, Mes_2DBTD and Ph_2DBTD RMs demonstrate roughly the same increase in the observed current density and some retention of the return oxidation feature of the RM. This suggests an excess of the RM radical anion is being generated with respect to its rate of interaction with complex **1**, and as a result, on the return CV sweep the radical anion is still present for re-oxidation, leading to the observed quasi-reversibility. When we compare these data with the aprotic CV data for all four RMs with **2**, we see a deviation from the trend described for **1** above: the addition of all RMs lead to a completely irreversible wave (**Figure S3.91**). Notably, TPTD shows a significant increase in current density over DBTD when added to a solution of **2** under CO_2 saturation conditions

(**Figure S3.91B**, red). Variable concentration studies were completed for all systems that produce an electrochemically irreversible system under aprotic conditions: the observed current density is proportional to the concentration of all reaction components (**Figures S92-S108**).

CPE experiments were then performed to assess reaction efficiency under aprotic conditions. Unlike the results for **1**+DBTD, all new systems reported here (**1** with the new RMs and **2** with all RMs) demonstrated insignificant catalytic properties under tested electrolysis conditions. The CPE experiments for **1** with Mes_2DBTD and TPTD as the RM and **2** with all four RMs led to a rapid loss of activity: following an initial stable period, current quickly diminishes (**Figures S109-S114**), with no amount of CO detected above limit of quantification (LOQ, see **SI**). Initial stability followed by rapid loss of activity suggests molecular adsorption to the electrode, resulting in a passivation of the electrode surface.[85] Comparing these results with control CPE experiments of **1**,[29] **2**, DBTD,[29] TPTD, Mes_2DBTD, and Ph_2DBTD individually under aprotic conditions (**Figures S115**-**S118**) also showed either no CO or the presence of non-quantifiable amounts of CO (**Tables S3.42-S3.44**). A similar phenomenon is observed when Ph_2DBTD is used as the RM with **1** (**Figure S3.119**), but in this case the system has a FE_{CO} = 26±2% (**Table S3.45**) and ^{1}H NMR of the post-bulk solution shows the appearance of carbonate (CO_3^{2-}), but no other carbon-containing products (**Figure S3.120**). Although CV data indicates that some of these combinations should result in aprotic catalytic activity, these combinations are not stable under the tested electrolysis conditions.

3.7.10 Cyclic Voltammetry Under Aprotic Conditions

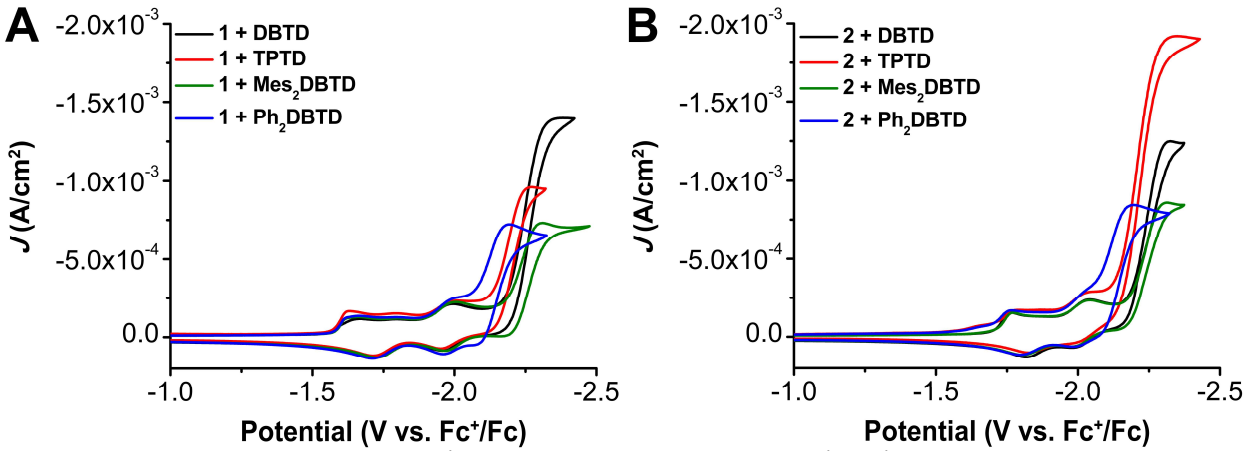

Figure S3.91. CVs of 1.0 mM Cr(^{tbu}dhbpy)Cl(H_2O) **1** (**A**) or Cr(^{tbu}dh^{tbu}bpy)Cl(H_2O) **2** (**B**) with 2.5 mM DBTD (black), TPTD (red), Mes_2DBTD (green), and Ph_2DBTD (blue) as the RM under CO_2 saturation conditions. Conditions: 0.1 M $TBAPF_6$/DMF; glassy carbon working electrode, glassy carbon rod counter electrode, Ag/AgCl pseudoreference electrode; referenced to Fc^+/Fc internal standard; 100 mV/s scan rate.

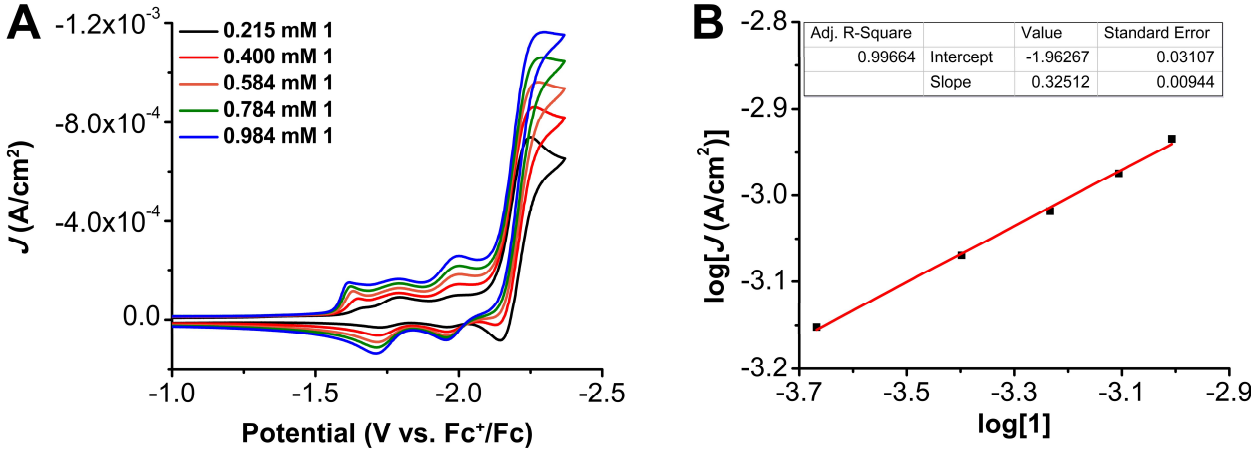

Figure S3.92. (**A**) CVs of Cr(^{tbu}dhbpy)Cl(H_2O) **1** at variable concentrations, obtained under CO_2 saturation with 2.5 mM TPTD. Conditions: 0.1 M $TBAPF_6$/DMF; glassy carbon working electrode, glassy carbon counter electrode, Ag/AgCl pseudoreference electrode; 100 mV/s scan rate; referenced to internal ferrocene standard. (**B**) Log-log plot from data obtained from CVs in **A** at −2.29 V vs. Fc^+/Fc.

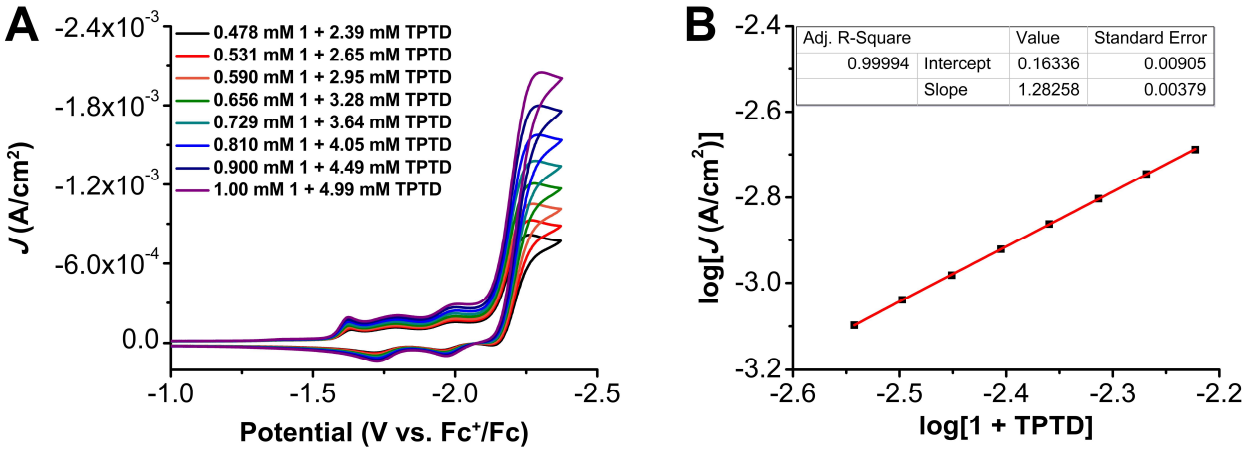

Figure S3.93. (**A**) CVs where the concentrations of Cr(^{tbu}dhbpy)Cl(H_2O) **1** and TPTD were varied at a fixed 1:5 ratio of **1**:TPTD under CO_2 saturation conditions. Conditions: 0.1 M $TBAPF_6$/DMF; glassy carbon working electrode, glassy carbon counter electrode, Ag/AgCl pseudoreference electrode; 100 mV/s scan rate; referenced to internal ferrocene standard. (B) Log-log plot from data obtained from CVs in A at −2.30 V vs. Fc^+/Fc.

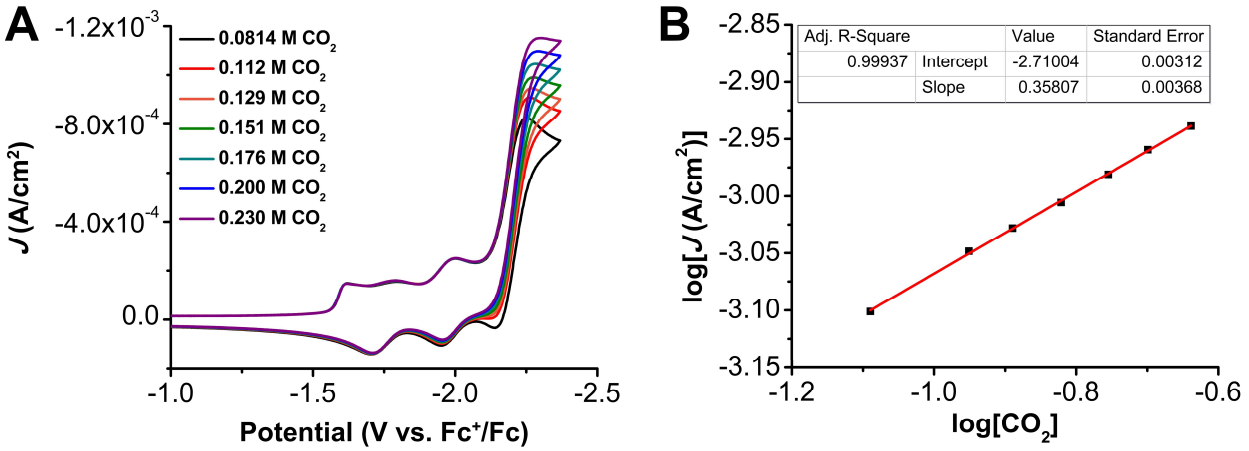

Figure S3.94. (**A**) CVs of 1.0 mM Cr(^{tbu}dhbpy)Cl(H_2O) **1** and 2.5 mM TPTD at varied CO_2 concentrations. Conditions: 0.1 M $TBAPF_6$/DMF; glassy carbon working electrode, glassy carbon counter electrode, Ag/AgCl pseudoreference electrode; 100 mV/s scan rate; referenced to internal ferrocene standard. (**B**) Log-log plot from data obtained from CVs in **A** at −2.29 V vs. Fc^+/Fc.

The variable concentration experiment for TPTD with fixed concentrations of **1** and CO_2 could not be completed. The co-catalytic effect quickly reached saturation and the irreversible redox feature became obscured by unbound TPTD in solution.

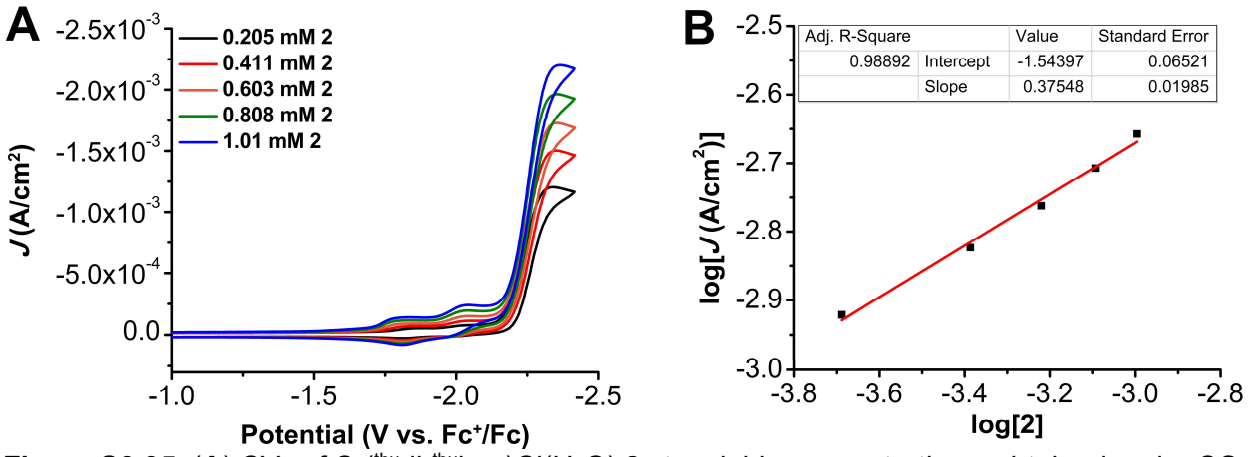

Figure S3.95. (**A**) CVs of Cr(^{tbu}dh^{tbu}bpy)Cl(H_2O) **2** at variable concentrations, obtained under CO_2 saturation with 2.5 mM DBTD. Conditions: 0.1 M $TBAPF_6$/DMF; glassy carbon working electrode, glassy carbon counter electrode, Ag/AgCl pseudoreference electrode; 100 mV/s scan rate; referenced to internal ferrocene standard. (**B**) Log-log plot from data obtained from CVs in **A** at −2.36 V vs. Fc^+/Fc.

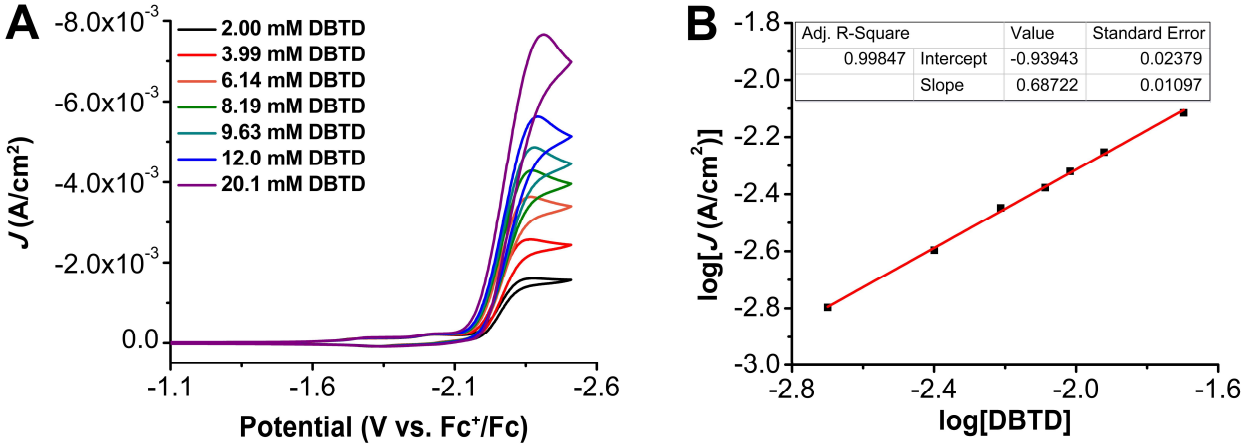

Figure S3.96. (**A**) CVs of 1.0 mM Cr(^{tbu}dh^{tbu}bpy)Cl(H_2O) **2** at variable DBTD concentrations, obtained under CO_2 saturation. Conditions: 0.1 M $TBAPF_6$/DMF; glassy carbon working electrode, glassy carbon counter electrode, Ag/AgCl pseudoreference electrode; 100 mV/s scan rate; referenced to internal ferrocene standard. (**B**) Log-log plot from data obtained from CVs in **A** at −2.41 V vs. Fc^+/Fc.

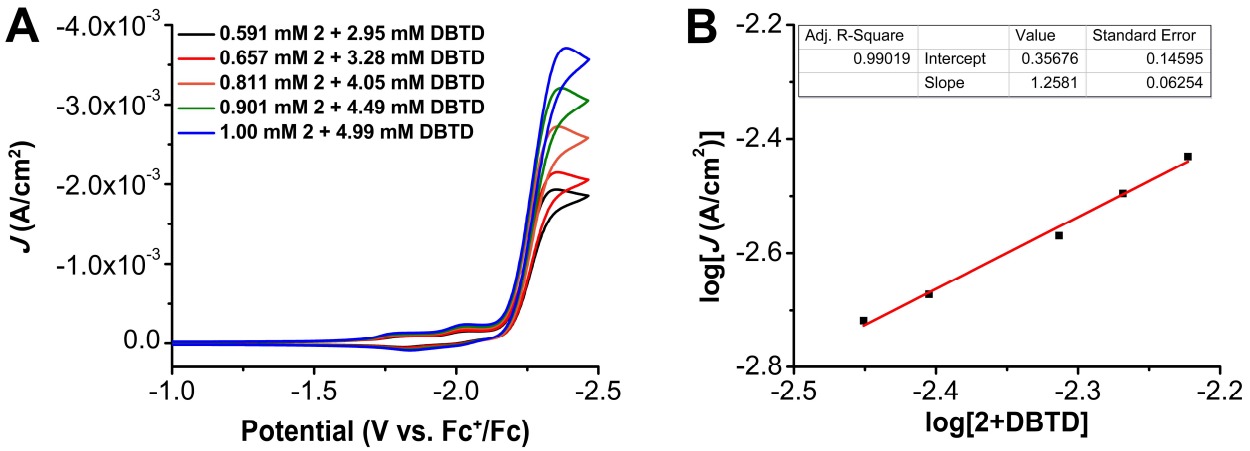

Figure S3.97. (**A**) CVs where the concentrations of Cr(^{tbu}dh^{tbu}bpy)Cl(H_2O) **2** and DBTD were varied at a fixed 1:5 ratio of **1**:DBTD under CO_2 saturation conditions. Conditions: 0.1 M $TBAPF_6$/DMF; glassy carbon working electrode, glassy carbon counter electrode, Ag/AgCl pseudoreference electrode; 100 mV/s scan rate; referenced to internal ferrocene standard. (**B**) Log-log plot from data obtained from CVs in **A** at −2.38 V vs. Fc^+/Fc.

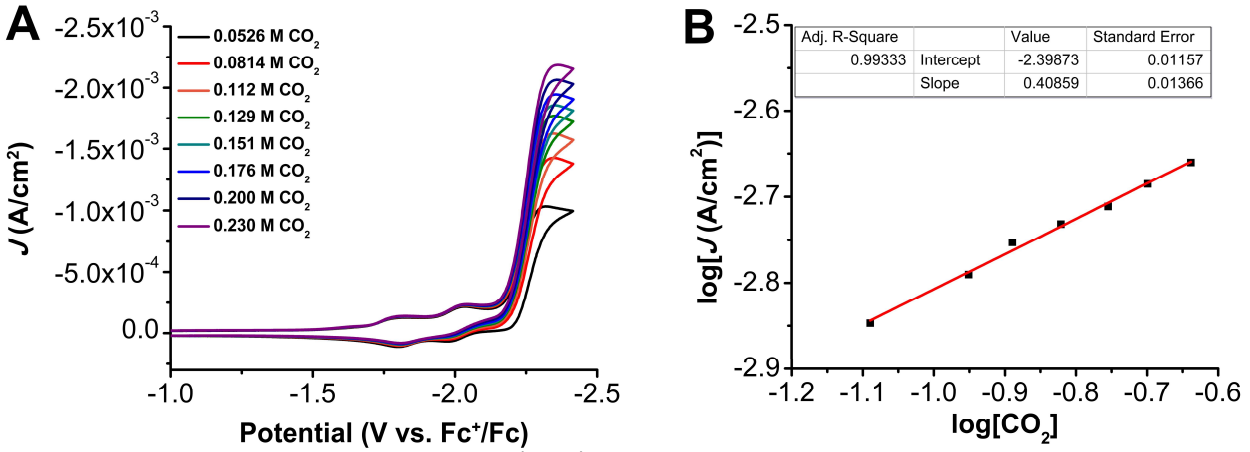

Figure S3.98. (**A**) CVs of 1.0 mM Cr(^{tbu}dh^{tbu}bpy)Cl(H_2O) **2** and 2.5 mM DBTD at varied CO_2 concentrations. Conditions: 0.1 M $TBAPF_6$/DMF; glassy carbon working electrode, glassy carbon counter electrode, Ag/AgCl pseudoreference electrode; 100 mV/s scan rate; referenced to internal ferrocene standard. (**B**) Log-log plot from data obtained from CVs in **A** at −2.36 V vs. Fc^+/Fc.

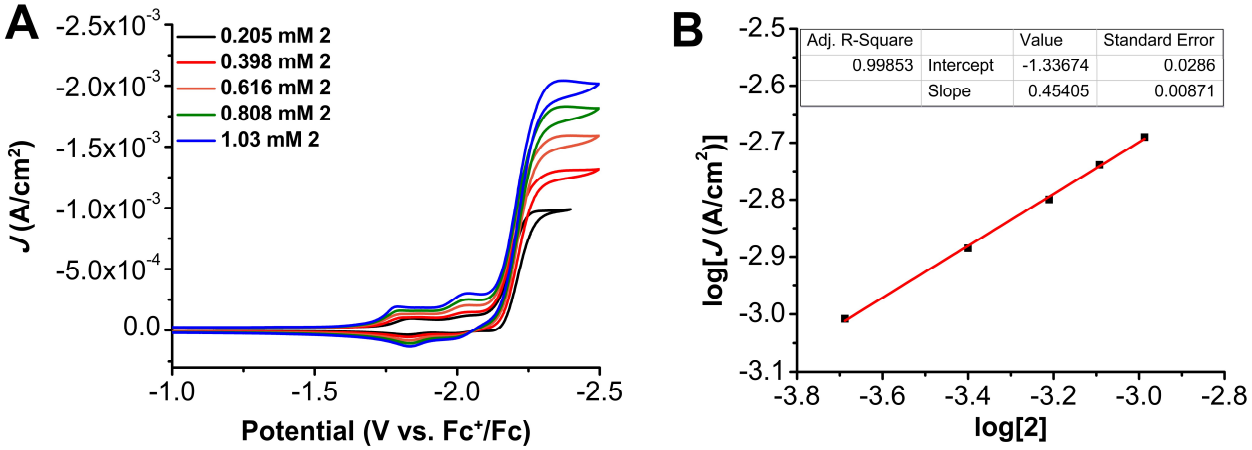

Figure S3.99. (**A**) CVs of Cr(^{tbu}dh^{tbu}bpy)Cl(H_2O) **2** at variable concentrations, obtained under CO_2 saturation with 2.5 mM TPTD. Conditions: 0.1 M $TBAPF_6$/DMF; glassy carbon working electrode, glassy carbon counter electrode, Ag/AgCl pseudoreference electrode; 100 mV/s scan rate; referenced to internal ferrocene standard. (**B**) Log-log plot from data obtained from CVs in **A** at −2.36 V vs. Fc^+/Fc.

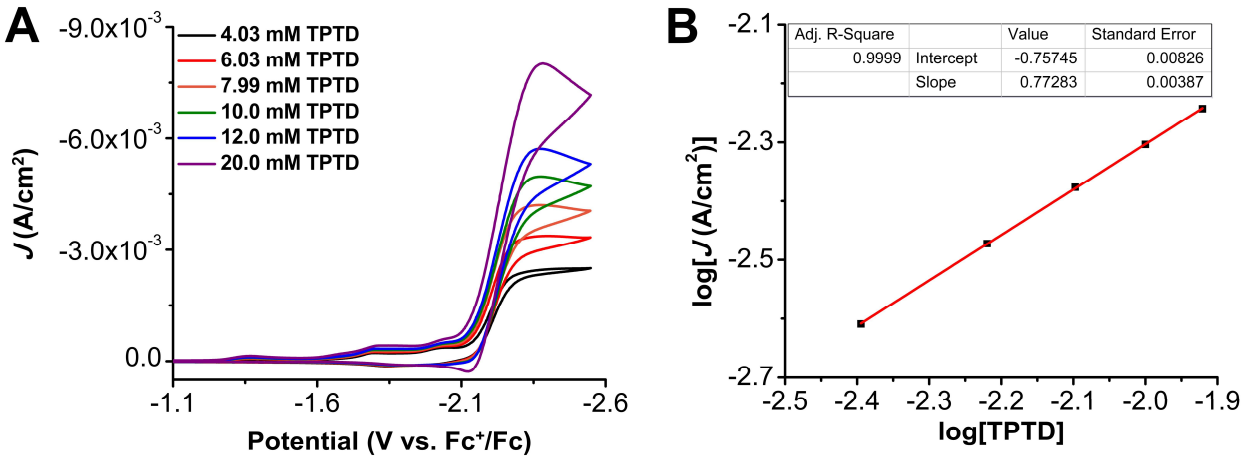

Figure S3.100. (**A**) CVs of 1.0 mM Cr(^{tbu}dh^{tbu}bpy)Cl(H_2O) **2** at variable TPTD concentrations, obtained under CO_2 saturation.Conditions: 0.1 M $TBAPF_6$/DMF; glassy carbon working electrode, glassy carbon counter electrode, Ag/AgCl pseudoreference electrode; 100 mV/s scan rate; referenced to internal ferrocene standard. (**B**) Log-log plot from data obtained from CVs in **A** at −2.38 V vs. Fc^+/Fc.

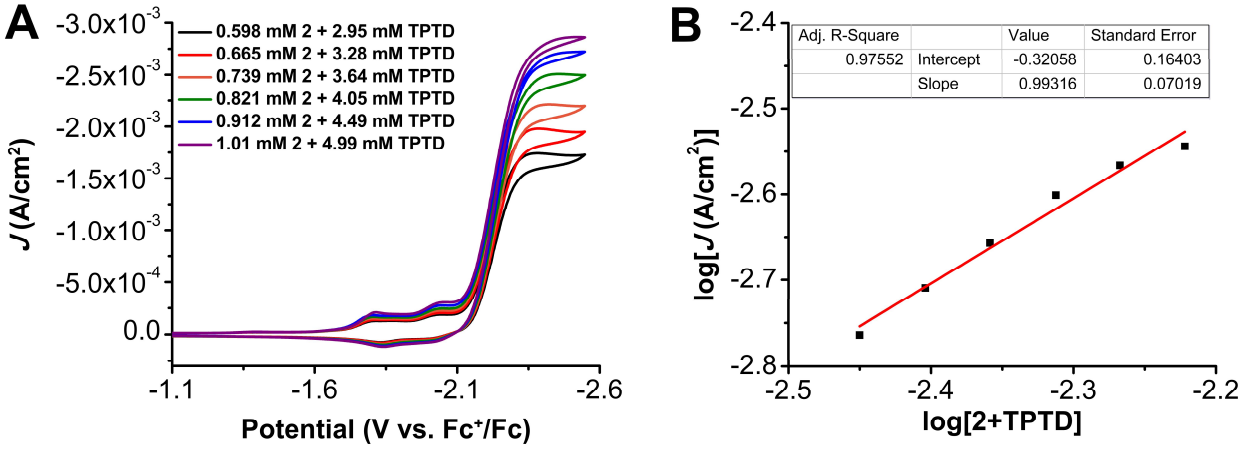

Figure S3.101. (**A**) CVs where the concentrations of Cr(^{tbu}dh^{tbu}bpy)Cl(H_2O) **2** and TPTD were varied at a fixed 1:5 ratio of **1**:TPTD under CO_2 saturation conditions. Conditions: 0.1 M $TBAPF_6$/DMF; glassy carbon working electrode, glassy carbon counter electrode, Ag/AgCl pseudoreference electrode; 100 mV/s scan rate; referenced to internal ferrocene standard. (**B**) Log-log plot from data obtained from CVs in **A** at −2.48 V vs. Fc^+/Fc.

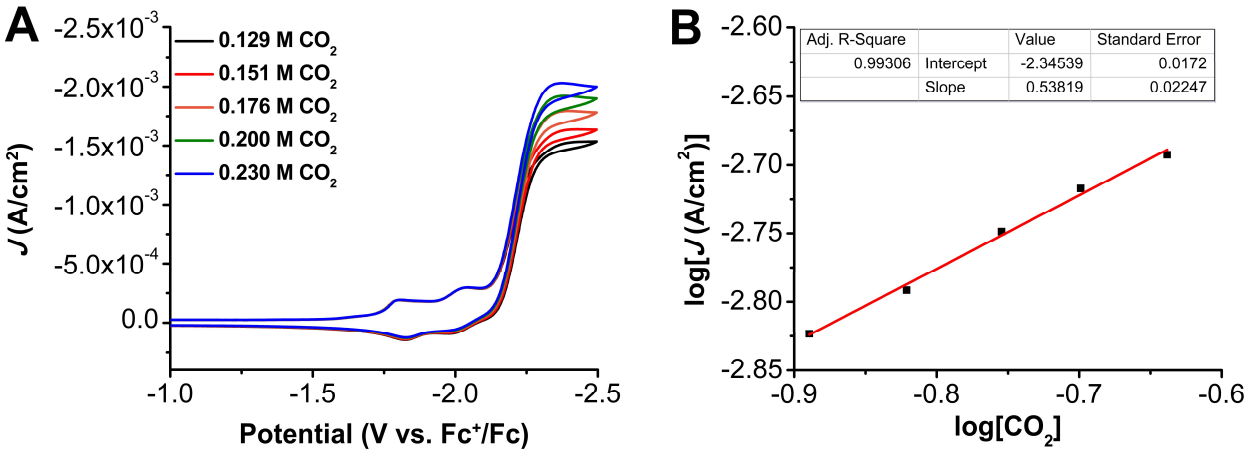

Figure S3.102. (**A**) CVs of 1.0 mM Cr(^{tbu}dh^{tbu}bpy)Cl(H_2O) **2** and 2.5 mM TPTD at varied CO_2 concentrations. Conditions: 0.1 M $TBAPF_6$/DMF; glassy carbon working electrode, glassy carbon counter electrode, Ag/AgCl pseudoreference electrode; 100 mV/s scan rate; referenced to internal ferrocene standard. (**B**) Log-log plot from data obtained from CVs in **A** at −2.37 V vs. Fc^+/Fc.

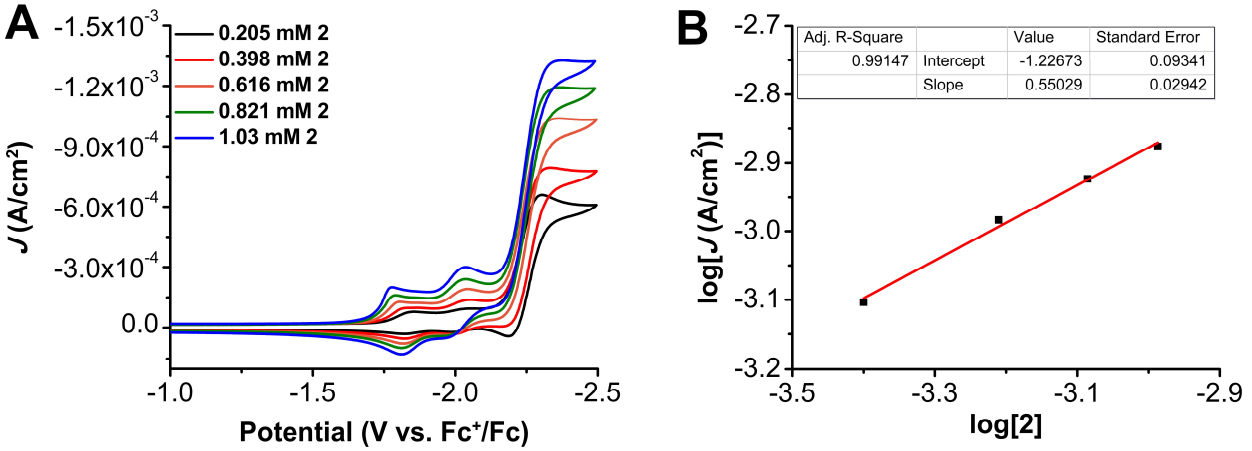

Figure S3.103. (**A**) CVs of Cr(^{tbu}dh^{tbu}bpy)Cl(H_2O) **2** at variable concentrations, obtained under CO_2 saturation with 2.5 mM Mes_2DBTD. Conditions: 0.1 M $TBAPF_6$/DMF; glassy carbon working electrode, glassy carbon counter electrode, Ag/AgCl pseudoreference electrode; 100 mV/s scan rate; referenced to internal ferrocene standard. (**B**) Log-log plot from data obtained from CVs in **A** at −2.37 V vs. Fc^+/Fc.

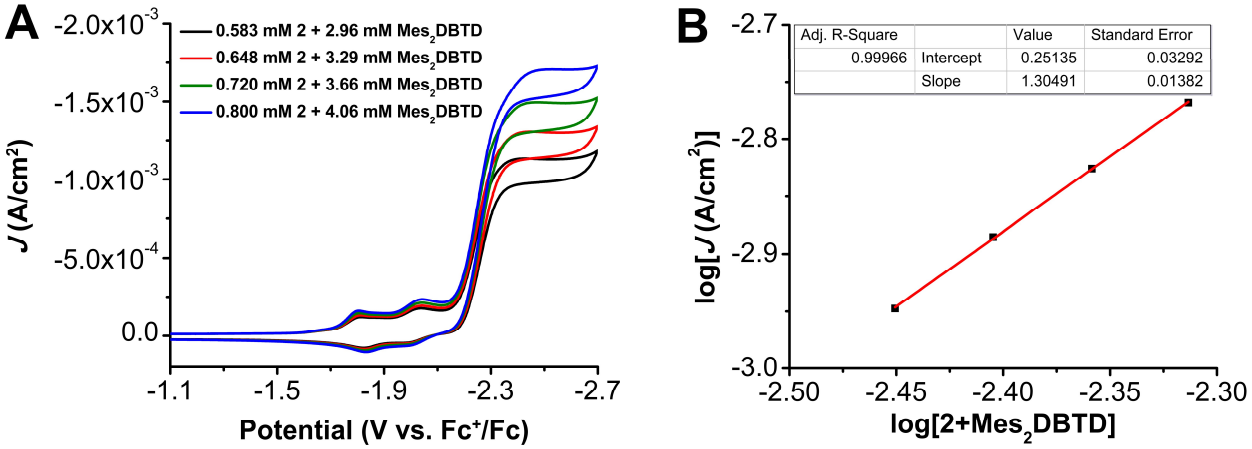

Figure S3.104. (**A**) CVs where the concentrations of Cr(^{tbu}dh^{tbu}bpy)Cl(H_2O) **2** and Mes_2DBTD were varied at a fixed 1:5 ratio of **1**:Mes_2DBTD under CO_2 saturation conditions. Conditions: 0.1 M $TBAPF_6$/DMF; glassy carbon working electrode, glassy carbon counter electrode, Ag/AgCl pseudoreference electrode; 100 mV/s scan rate; referenced to internal ferrocene standard. (**B**) Log-log plot from data obtained from CVs in **A** at −2.50 V vs. Fc^+/Fc.

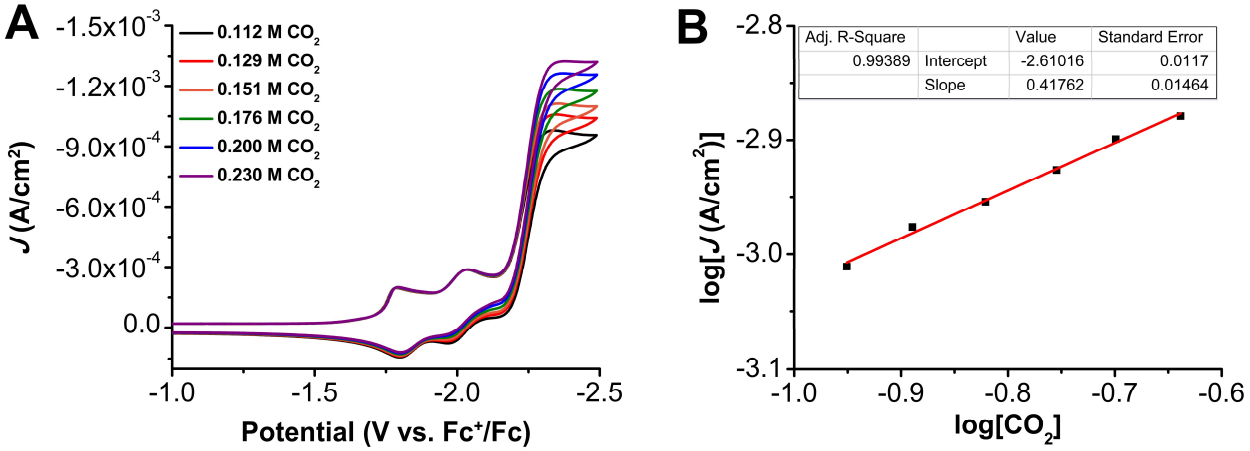

Figure S3.105. (**A**) CVs of 1.0 mM Cr(^{tbu}dh^{tbu}bpy)Cl(H_2O) **2** and 2.5 mM Mes_2DBTD at varied CO_2 concentrations. Conditions: 0.1 M $TBAPF_6$/DMF; glassy carbon working electrode, glassy carbon counter electrode, Ag/AgCl pseudoreference electrode; 100 mV/s scan rate; referenced to internal ferrocene standard. (**B**) Log-log plot from data obtained from CVs in **A** at −2.37 V vs. Fc^+/Fc.

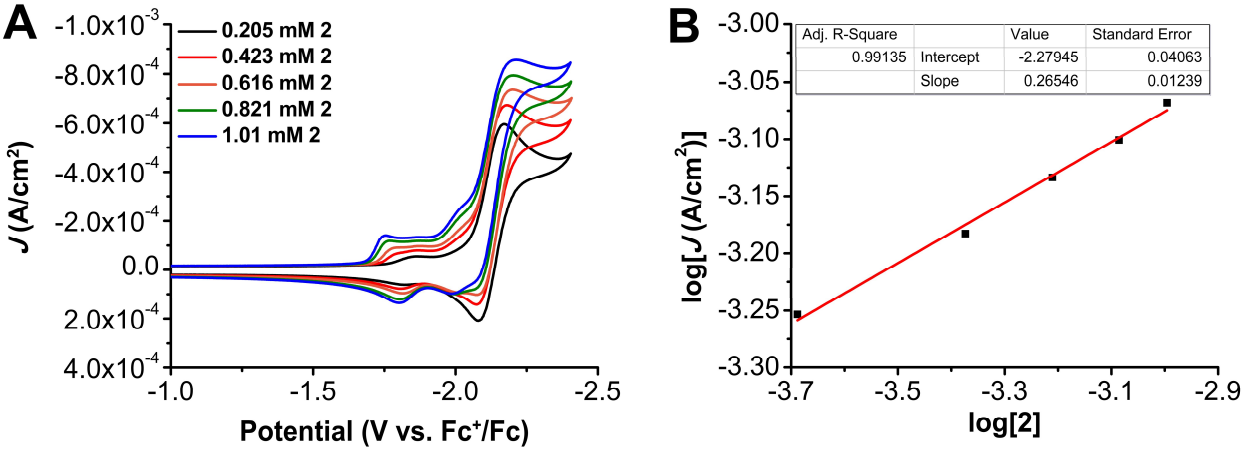

Figure S3.106. (**A**) CVs of Cr(^{tbu}dh^{tbu}bpy)Cl(H_2O) **2** at variable concentrations, obtained under CO_2 saturation with 2.5 mM Ph_2DBTD. Conditions: 0.1 M $TBAPF_6$/DMF; glassy carbon working electrode, glassy carbon counter electrode, Ag/AgCl pseudoreference electrode; 100 mV/s scan rate; referenced to internal ferrocene standard. (**B**) Log-log plot from data obtained from CVs in **A** at −2.21 V vs. Fc^+/Fc.

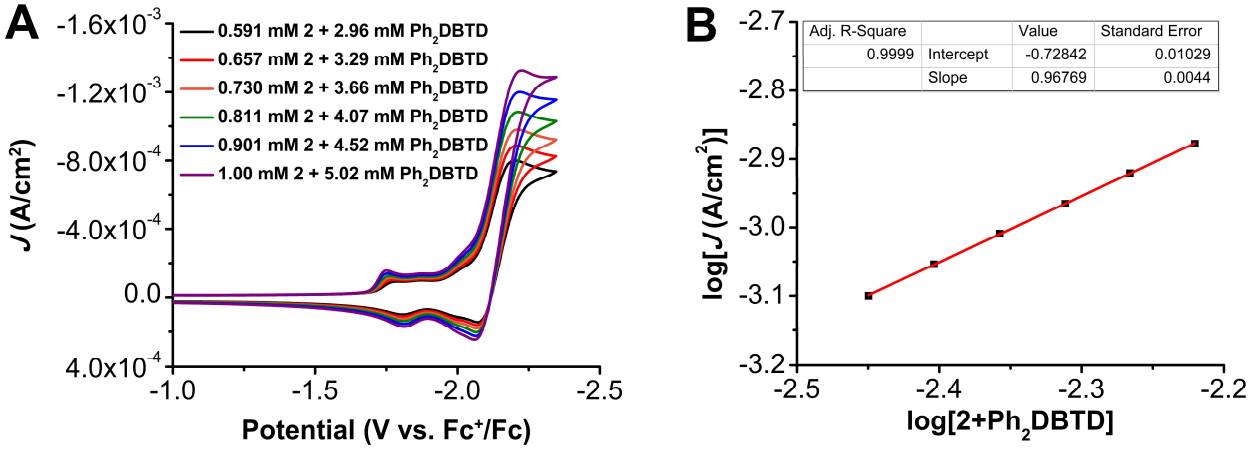

Figure S3.107. (**A**) CVs where the concentrations of Cr(^{tbu}dh^{tbu}bpy)Cl(H_2O) **2** and Ph_2DBTD were varied at a fixed 1:5 ratio of **1**:Ph_2DBTD under CO_2 saturation conditions. Conditions: 0.1 M $TBAPF_6$/DMF; glassy carbon working electrode, glassy carbon counter electrode, Ag/AgCl pseudoreference electrode; 100 mV/s scan rate; referenced to internal ferrocene standard. (**B**) Log-log plot from data obtained from CVs in **A** at −2.22 V vs. Fc^+/Fc.

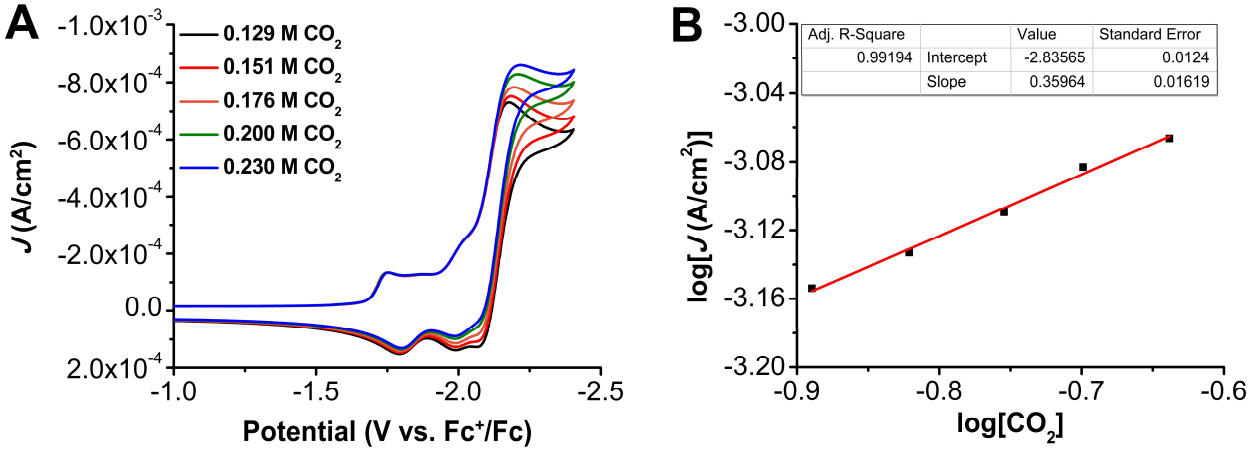

Figure S3.108. (**A**) CVs of 1.0 mM Cr(^{tbu}dh^{tbu}bpy)Cl(H_2O) **2** and 2.5 mM Ph_2DBTD at varied CO_2 concentrations. Conditions: 0.1 M $TBAPF_6$/DMF; glassy carbon working electrode, glassy carbon counter electrode, Ag/AgCl pseudoreference electrode; 100 mV/s scan rate; referenced to internal ferrocene standard. (**B**) Log-log plot from data obtained from CVs in **A** at −2. 22V vs. Fc^+/Fc.

As was the case for **1** with TPTD, the variable RM experiment for Mes_2DBTD and Ph_2DBTD was not able to be performed. The co-catalytic effect quickly reached saturation and the irreversible redox feature became obscured by unbound RM in solution.

3.7.11 Controlled Potential Electrolysis Experiments (Aprotic Conditions)

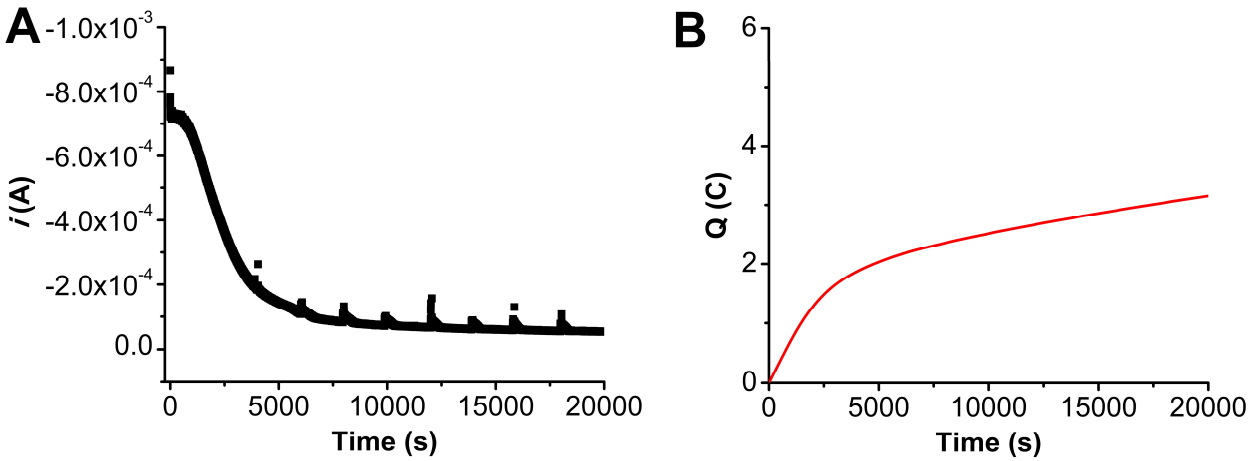

Figure S3.109. (**A**) Current versus time trace from CPE experiment with **1**+Mes_2DBTD. (**B**) Charge passed versus time for the CPE experiment shown in **A**. Conditions were 0.5 mM Cr(^{tbu}dhbpy)Cl(H_2O) **1** and 2.5 mM Mes_2DBTD under a CO_2 atmosphere at −2.30 V vs Fc^+/Fc in 0.1 M $TBAPF_6$/DMF; working electrode was a glassy carbon rod, counter electrode was a graphite rod, and the reference was a nonaqueous Ag/AgCl pseudoreference electrode; 0.075 M Fc was used as sacrificial oxidant.

Table S3.36. Results from CPE experiment in Figure S3.109, 1:5 (**1**:Mes_2DBTD).

Time (s)	Charge (coulombs)	moles (e^-)	Moles of CO
20000*	3.15	3.27 x 10^{-5}	< LOQ
20000*	3.15	3.27 x 10^{-5}	< LOQ
20000*	3.15	3.27 x 10^{-5}	< LOQ

* indicates a triplicate series of injections carried out upon completion of electrolysis

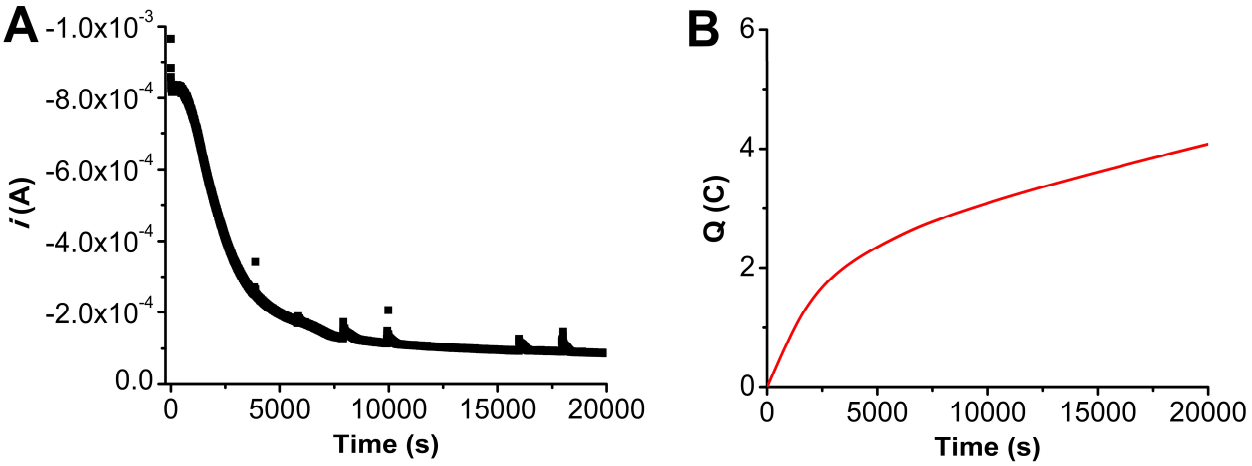

Figure S3.110. (**A**) Current versus time trace from CPE experiment with **1**+TPTD. (**B**) Charge passed versus time for the CPE experiment shown in **A**. Conditions were 0.5 mM Cr(^{tbu}dhbpy)Cl(H_2O) 1 and 2.5 mM TPTD under a CO_2 atmosphere at −2.25 V vs Fc^+/Fc in 0.1 M $TBAPF_6$/DMF; working electrode was a glassy carbon rod, counter electrode was a graphite rod, and the reference was a nonaqueous Ag/AgCl pseudoreference electrode; 0.075 M Fc was used as sacrificial oxidant.

Table S3.37. Results from CPE experiment in Figure S3.110, 1:5 (**1**:TPTD).

Time (s)	Charge (coulombs)	moles (e^-)	Moles of CO
20000*	4.08	4.23×10^{-5}	< LOQ
20000*	4.08	4.23×10^{-5}	< LOQ
20000*	4.08	4.23×10^{-5}	< LOQ

* indicates a triplicate series of injections carried out upon completion of electrolysis

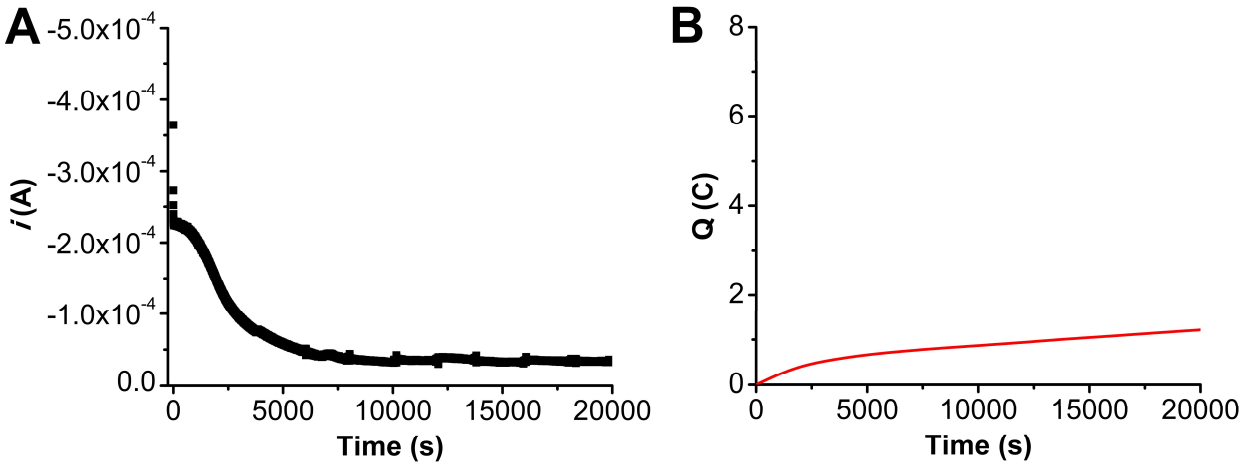

Figure S3.111. (**A**) Current versus time trace from CPE experiment with **2**+DBTD. (**B**) Charge passed versus time for the CPE experiment shown in **A**. Conditions were 0.1 mM Cr(^{tbu}dh^{tbu}bpy)Cl(H_2O) **2** and 0.5 mM DBTD under a CO_2 atmosphere at −2.30 V vs Fc^+/Fc in 0.1 M $TBAPF_6$/DMF; working electrode was a glassy carbon rod, counter electrode was a graphite rod, and the reference was a nonaqueous Ag/AgCl pseudoreference electrode; 0.075 M Fc was used as sacrificial oxidant.

Table S3.38. Results from CPE experiment in Figure S3.111, 1:5 (**2**:DBTD).

Time (s)	Charge (coulombs)	moles (e^-)	Moles of CO
20000*	1.22	1.26 x 10^{-5}	< LOQ
20000*	1.22	1.26 x 10^{-5}	< LOQ
20000*	1.22	1.26 x 10^{-5}	< LOQ

* indicates a triplicate series of injections carried out upon completion of electrolysis

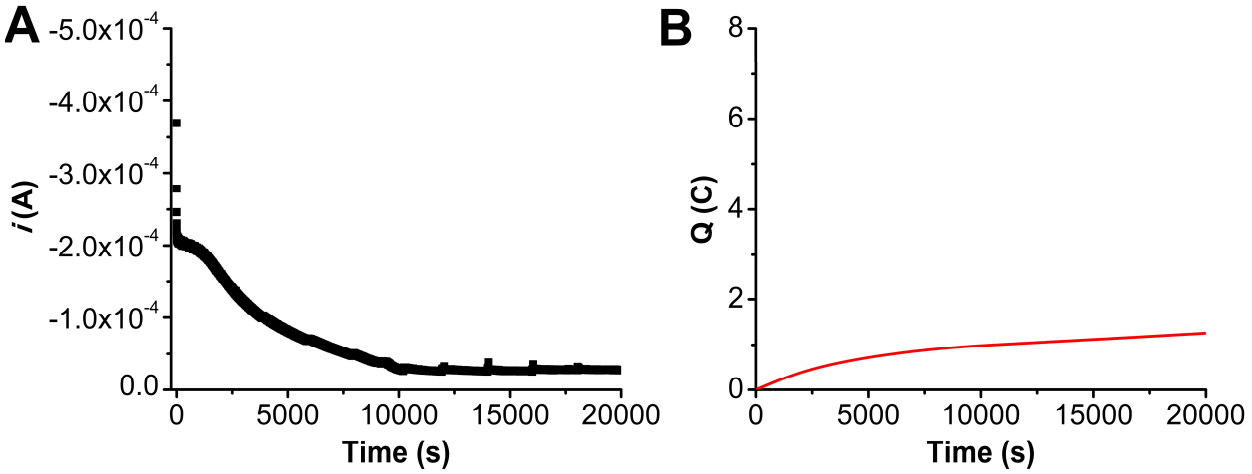

Figure S3.112. (**A**) Current versus time trace from CPE experiment with **2**+TPTD. (**B**) Charge passed versus time for the CPE experiment shown in **A**. Conditions were 0.1 mM Cr(^{tbu}dh^{tbu}bpy)Cl(H_2O) **2** and 0.5 mM TPTD under a CO_2 atmosphere at −2.25 V vs Fc^+/Fc in 0.1 M $TBAPF_6$/DMF; working electrode was a glassy carbon rod, counter electrode was a graphite rod, and the reference was a nonaqueous Ag/AgCl pseudoreference electrode; 0.075 M Fc was used as sacrificial oxidant.

Table S3.39. Results from CPE experiment in Figure S3.112, 1:5 (**2**:TPTD).

Time (s)	Charge (coulombs)	moles (e^-)	Moles of CO
20000*	1.26	1.30 x 10^{-5}	< LOQ
20000*	1.26	1.30 x 10^{-5}	< LOQ
20000*	1.26	1.30 x 10^{-5}	< LOQ

* indicates a triplicate series of injections carried out upon completion of electrolysis

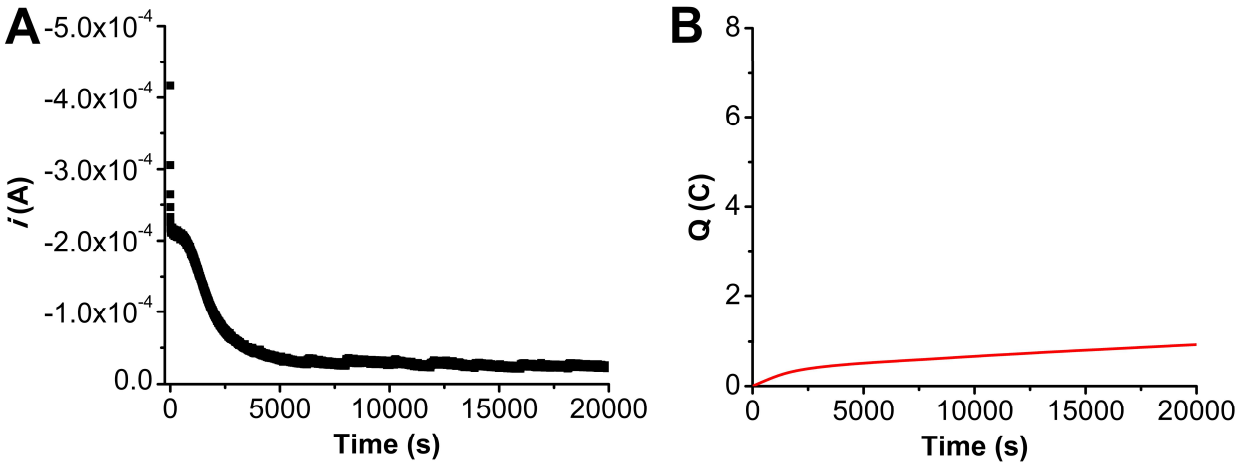

Figure S3.113. (**A**) Current versus time trace from CPE experiment with **2**+Mes_2DBTD. (**B**) Charge passed versus time for the CPE experiment shown in **A**. Conditions were 0.1 mM Cr(^{tbu}dh^{tbu}bpy)Cl(H_2O) **2** and 0.5 mM Mes_2DBTD under a CO_2 atmosphere at −2.30 V vs Fc^+/Fc in 0.1 M $TBAPF_6$/DMF; working electrode was a glassy carbon rod, counter electrode was a graphite rod, and the reference was a nonaqueous Ag/AgCl pseudoreference electrode; 0.075 M Fc was used as sacrificial oxidant.

Table S3.40. Results from CPE experiment in Figure S3.1, 1:5 (**2**:Mes_2DBTD).

Time (s)	Charge (coulombs)	moles (e^-)	Moles of CO
20000*	0.912	9.46 x 10^{-6}	< LOQ
20000*	0.912	9.46 x 10^{-6}	< LOQ
20000*	0.912	9.46 x 10^{-6}	< LOQ

* indicates a triplicate series of injections carried out upon completion of electrolysis

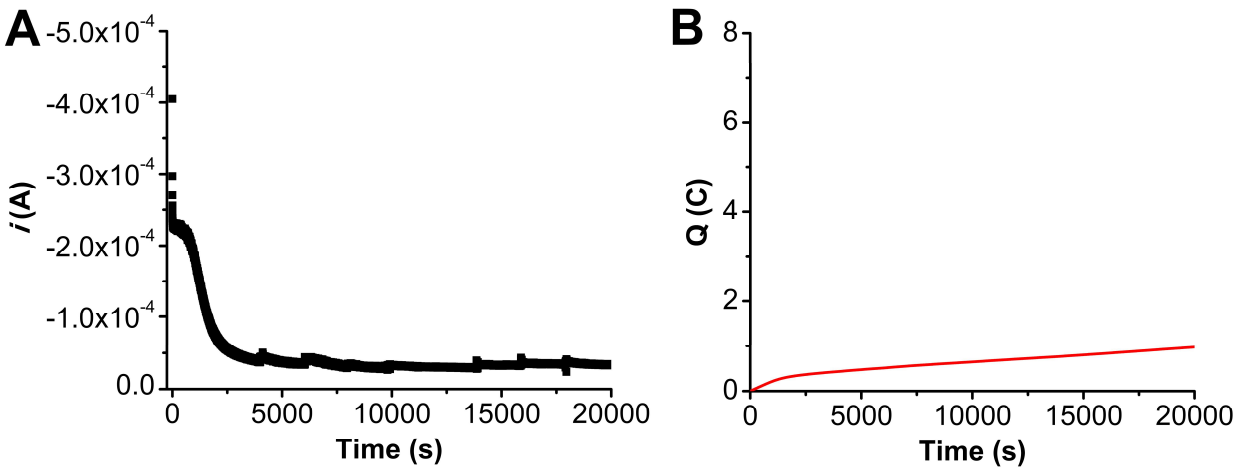

Figure S3.114. (**A**) Current versus time trace from CPE experiment with **2**+Ph_2DBTD. (**B**) Charge passed versus time for the CPE experiment shown in **A**. Conditions were 0.1 mM Cr(^{tbu}dh^{tbu}bpy)Cl(H_2O) **2** and 0.5 mM Ph_2DBTD under a CO_2 atmosphere at −2.20 V vs Fc^+/Fc in 0.1 M TBAPF_6/DMF; working electrode was a glassy carbon rod, counter electrode was a graphite rod, and the reference was a nonaqueous Ag/AgCl pseudoreference electrode; 0.075 M Fc was used as sacrificial oxidant.

Table S3.41. Results from CPE experiment in Figure S3.114, 1:5 (**2**:Ph_2DBTD).

Time (s)	Charge (coulombs)	moles (e^-)	Moles of CO
20000*	0.975	1.01 x 10^{-5}	< LOQ
20000*	0.975	1.01 x 10^{-5}	< LOQ
20000*	0.975	1.01 x 10^{-5}	< LOQ

* indicates a triplicate series of injections carried out upon completion of electrolysis

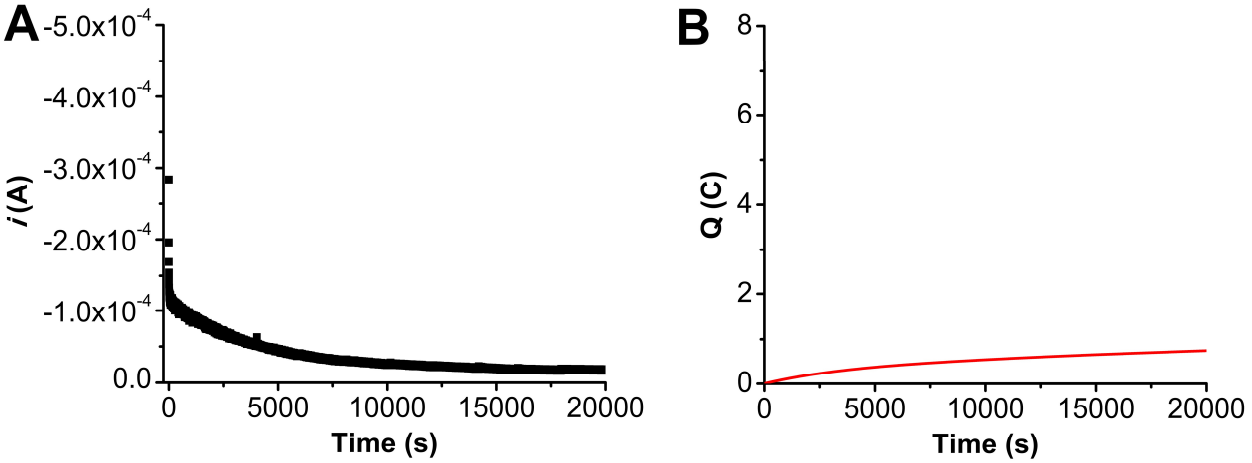

Figure S3.115. (**A**) Current versus time trace from CPE experiment with **2** under aprotic conditions. (**B**) Charge passed versus time for the CPE experiment shown in **A**. Conditions were 0.1 mM Cr(^{tbu}dh^{tbu}bpy)Cl(H_2O) **2** under a CO_2 atmosphere at −2.30 V vs Fc^+/Fc in 0.1 M $TBAPF_6$/DMF; working electrode was a glassy carbon rod, counter electrode was a graphite rod, and the reference was a nonaqueous Ag/AgCl pseudoreference electrode; 0.075 M Fc was used as sacrificial oxidant.

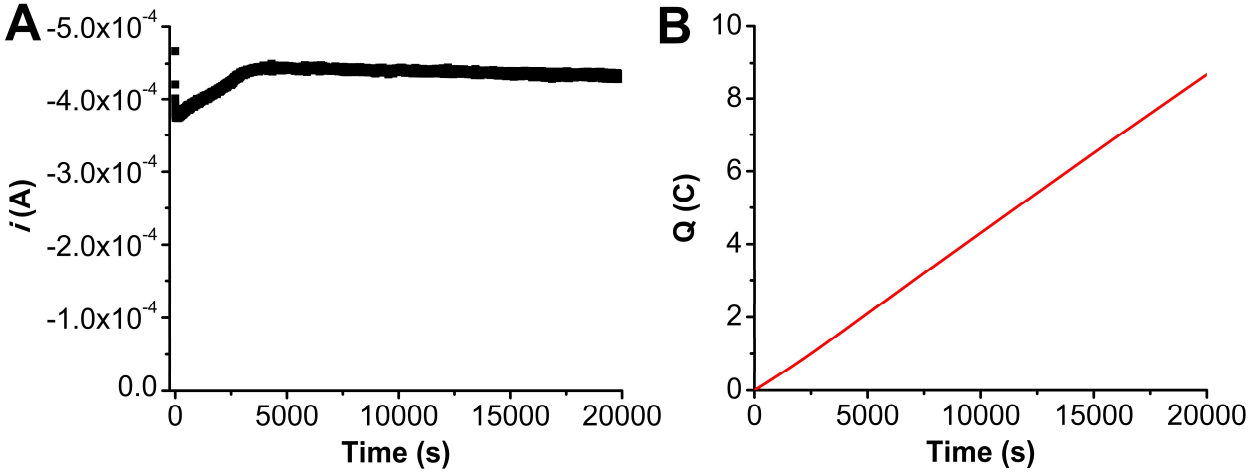

Figure S3.116. (**A**) Current versus time trace from CPE experiment with TPTD under aprotic conditions. (**B**) Charge passed versus time for the CPE experiment shown in **A**. Conditions were 2.5 mM TPTD under a CO_2 atmosphere at −2.25 V vs Fc^+/Fc in 0.1 M $TBAPF_6$/DMF; working electrode was a glassy carbon rod, counter electrode was a graphite rod, and the reference was a nonaqueous Ag/AgCl pseudoreference electrode; 0.075 M Fc was used as sacrificial oxidant.

Table S3.42. Results from CPE experiment in Figure S3.116, 2.5 mM TPTD.

Time (s)	Charge (coulombs)	moles (e^-)	Moles of CO
20000*	8.67	8.98 x 10^{-5}	< LOQ
20000*	8.67	8.98 x 10^{-5}	< LOQ
20000*	8.67	8.98 x 10^{-5}	< LOQ

* indicates a triplicate series of injections carried out upon completion of electrolysis

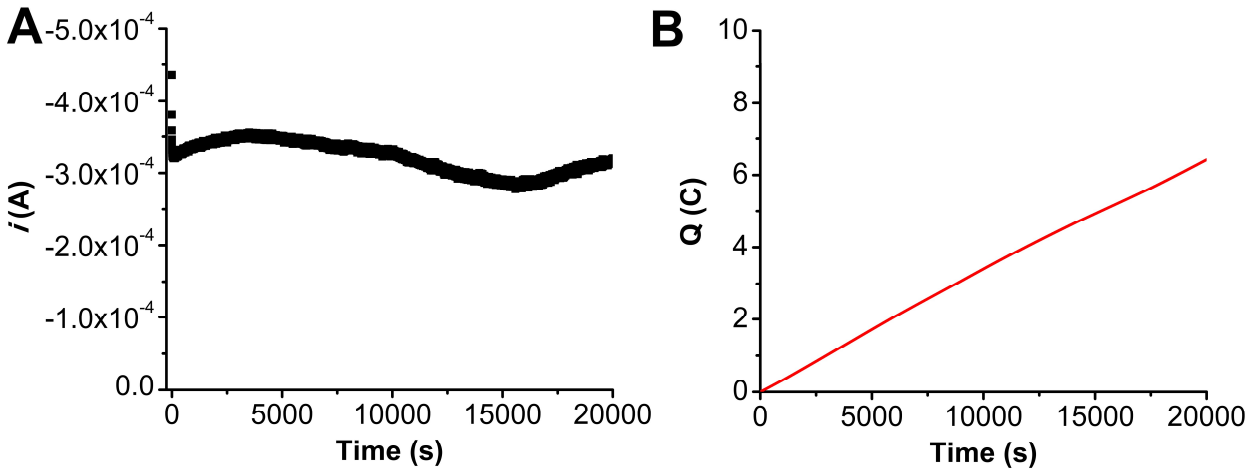

Figure S3.117. (**A**) Current versus time trace from CPE experiment with Mes_2DBTD under aprotic conditions. (**B**) Charge passed versus time for the CPE experiment shown in **A**. Conditions were 2.5 mM Mes_2DBTD under a CO_2 atmosphere at −2.30 V vs Fc^+/Fc in 0.1 M $TBAPF_6$/DMF; working electrode was a glassy carbon rod, counter electrode was a graphite rod, and the reference was a nonaqueous Ag/AgCl pseudoreference electrode; 0.075 M Fc was used as sacrificial oxidant.

Table S3.43. Results from CPE experiment in Figure S3.117, 2.5 mM Mes_2DBTD.

Time (s)	Charge (coulombs)	moles (e^-)	Moles of CO
20000*	6.42	6.65 x 10^{-5}	< LOQ
20000*	6.42	6.65 x 10^{-5}	< LOQ
20000*	6.42	6.65 x 10^{-5}	< LOQ

* indicates a triplicate series of injections carried out upon completion of electrolysis

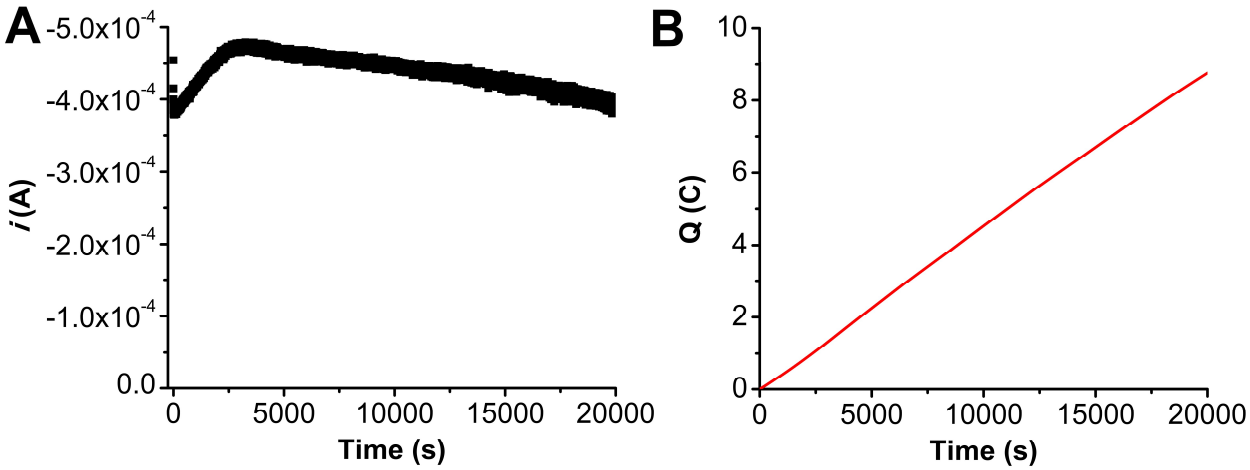

Figure S3.118. (**A**) Current versus time trace from CPE experiment with Ph_2DBTD under aprotic conditions. (**B**) Charge passed versus time for the CPE experiment shown in **A**. Conditions were 2.5 mM Ph_2DBTD under a CO_2 atmosphere at −2.20 V vs Fc^+/Fc in 0.1 M $TBAPF_6$/DMF; working electrode was a glassy carbon rod, counter electrode was a graphite rod, and the reference was a nonaqueous Ag/AgCl pseudoreference electrode; 0.075 M Fc was used as sacrificial oxidant.

Table S3.44. Results from CPE experiment in Figure S3.118, 2.5 mM Ph_2DBTD.

Time (s)	Charge (coulombs)	moles (e^-)	Moles of CO
20000*	8.76	9.08×10^{-5}	< LOQ
20000*	8.76	9.08×10^{-5}	< LOQ
20000*	8.76	9.08×10^{-5}	< LOQ

* indicates a triplicate series of injections carried out upon completion of electrolysis

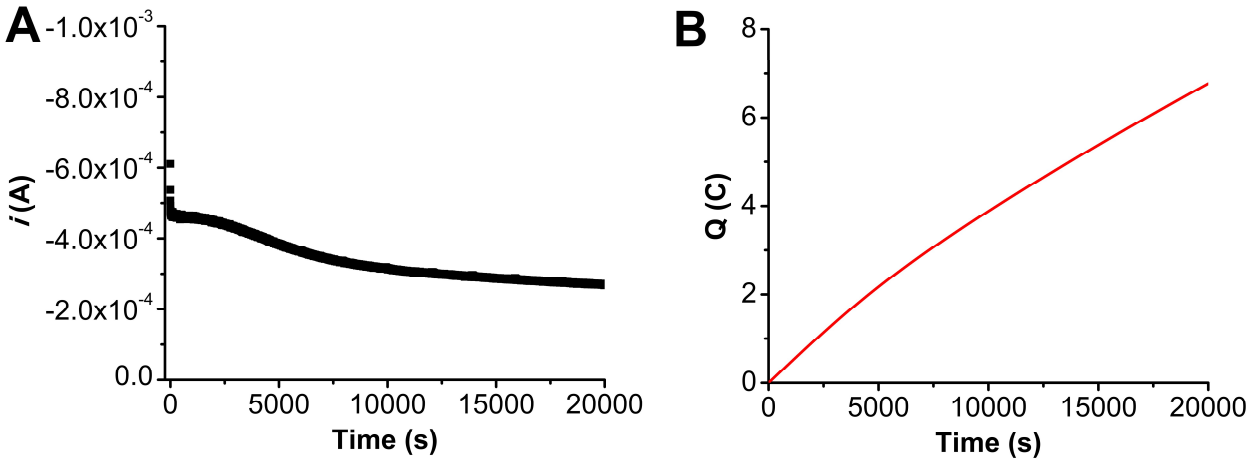

Figure S3.119. (**A**) Current versus time trace from CPE experiment with **1**+Ph_2DBTD.(**B**) Charge passed versus time for the CPE experiment shown in **A**. Conditions were 0.5 mM Cr(^{tbu}dhbpy)Cl(H_2O) **1** and 2.5 mM Ph_2DBTD under a CO_2 atmosphere at −2.20 V vs Fc^+/Fc in 0.1 M $TBAPF_6$/DMF; working electrode was a glassy carbon rod, counter electrode was a graphite rod, and the reference was a nonaqueous Ag/AgCl pseudoreference electrode; 0.075 M Fc was used as sacrificial oxidant.

Table S3.45. Results from CPE experiment in Figure S3.119, 1:5 (**1**:Ph_2DBTD).

Time (s)	Charge (coulombs)	moles (e^-)	Moles of CO	FE_{CO}
20000*	6.77	7.02×10^{-5}	8.46×10^{-6}	24.1
20000*	6.77	7.02×10^{-5}	8.99×10^{-6}	25.6
20000*	6.77	7.02×10^{-5}	1.02×10^{-5}	29.2

* indicates a triplicate series of injections carried out upon completion of electrolysis

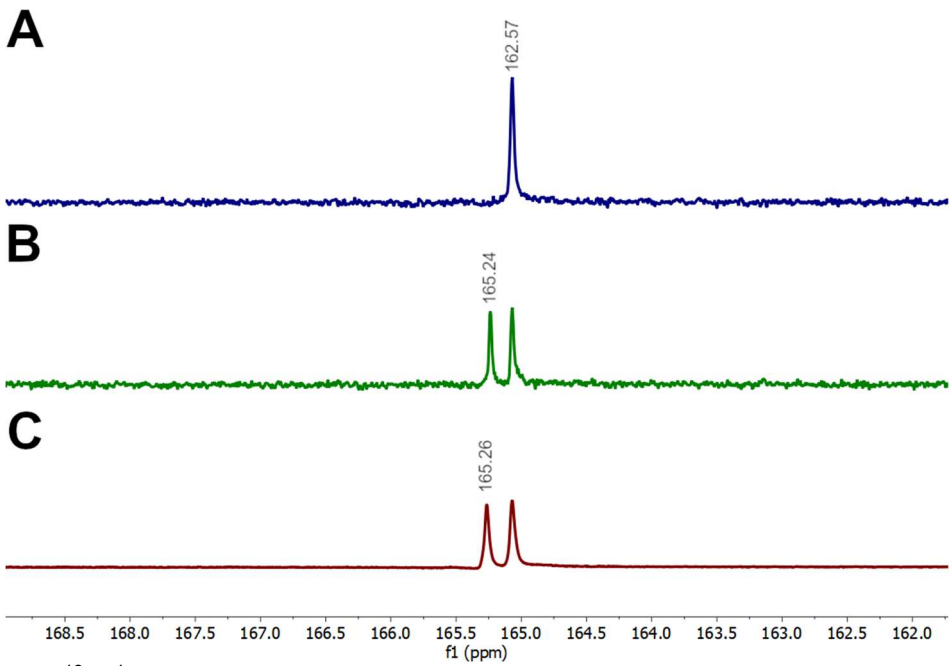

Figure S3.120. $^{13}C\{^{1}H\}$ NMRs in CD_2Cl_2 for product analysis of CPE solution with **1**+Ph_2DBTD. (**A**) $^{13}C\{^{1}H\}$ NMR in CD_2Cl_2 of DMF. (**B**) $^{13}C\{^{1}H\}$ NMR in CD_2Cl_2 and DMF from prepared sample of $TBA^{+}[HCO_3]^{-}$ that was synthesized according to reported procedures.[86] (**C**) $^{13}C\{^{1}H\}$ NMR in CD_2Cl_2 from the post electrolysis solution of Cr(^{tbu}dhbpy)Cl(H_2O) **1** and Ph_2DBTD in DMF under a CO_2 atmosphere at −2.20 V vs. Fc^{+}/Fc (Figure S3.119).

Table S3.46. Summary of Results from CPE experiments under aprotic conditions (Figures S109-S115, S119 and Tables S3.36-S3.41, S3.45).

Conditions	Potential (V vs Fc^{+}/Fc)	FE_{CO} (%)	TOF_{CPE} s^{-1}	η (V)	Turnovers of CO w.r.t [**1** or **2**]	Turnovers of CO w.r.t [RM]
1[29,a]	−2.30	0	–	0.11	–	–
1 + DBTD[29,a]	−2.30	91±10	36.8	0.69	16	3.1
1 + TPTD[a]	−2.25	0	–	0.63	–	–
1 + Mes_2DBTD[a]	−2.30	0	–	0.68	–	–
1 + Ph_2DBTD[a]	−2.20	26±2	0.1	0.58	0.68	0.14
2[b]	−2.30	0	–	0.16	–	–
2 + DBTD[b]	−2.30	0	–	0.69	–	–
2 + TPTD[b]	−2.25	0	–	0.63	–	–
2 + Mes_2DBTD[b]	−2.30	0	–	0.68	–	–
2 + Ph_2DBTD[b]	−2.20	0	–	0.58	–	–

[a] – 0.5 mM Cr(^{tbu}dhbpy)Cl(H_2O) **1** and 2.5 mM RM
[b] – 0.1 mM Cr(^{tbu}dh^{tbu}bpy)Cl(H_2O) **2** and 0.5 mM RM

Table S3.47. Comparison of experimental and calculated reduction potentials for RMs.[28]

Redox Mediator	Calculated Potential (V vs Fc^{+}/Fc)	Experimental Potential (V vs Fc^{+}/Fc)
$DBTD^{0/-}$	–2.26	–2.25
$TPTD^{0/-}$	–2.24	–2.19
$Mes_2DBTD^{0/-}$	–2.29	–2.24
$Ph_2DBTD^{0/-}$	–2.14	–2.12

3.8 References

1. De Luna, P.; Hahn, C.; Higgins, D.; Jaffer, S. A.; Jaramillo, T. F.; Sargent, E. H., What would it take for renewably powered electrosynthesis to displace petrochemical processes? *Science* **2019,** *364* (6438), eaav3506.
2. Aresta, M.; Dibenedetto, A.; Angelini, A., Catalysis for the Valorization of Exhaust Carbon: from CO_2 to Chemicals, Materials, and Fuels. Technological Use of CO_2. *Chem. Rev.* **2014,** *114* (3), 1709-1742.
3. Senftle, T. P.; Carter, E. A., The Holy Grail: Chemistry Enabling an Economically Viable CO2 Capture, Utilization, and Storage Strategy. *Acc. Chem. Res.* **2017,** *50* (3), 472-475.
4. Froehlich, J. D.; Kubiak, C. P., Homogeneous CO_2 Reduction by Ni(cyclam) at a Glassy Carbon Electrode. *Iorg. Chem.* **2012,** *51* (7), 3932-3934.
5. Cometto, C.; Chen, L.; Lo, P.-K.; Guo, Z.; Lau, K.-C.; Anxolabéhère-Mallart, E.; Fave, C.; Lau, T.-C.; Robert, M., Highly Selective Molecular Catalysts for the CO_2-to-CO Electrochemical Conversion at Very Low Overpotential. Contrasting Fe vs Co Quaterpyridine Complexes upon Mechanistic Studies. *ACS Catal.* **2018,** *8* (4), 3411-3417.
6. Azcarate, I.; Costentin, C.; Robert, M.; Savéant, J.-M., Through-Space Charge Interaction Substituent Effects in Molecular Catalysis Leading to the Design of the Most Efficient Catalyst of CO_2-to-CO Electrochemical Conversion. *J. Am. Chem. Soc.* **2016,** *138* (51), 16639-16644.
7. Sampson, M. D.; Nguyen, A. D.; Grice, K. A.; Moore, C. E.; Rheingold, A. L.; Kubiak, C. P., Manganese Catalysts with Bulky Bipyridine Ligands for the Electrocatalytic Reduction of Carbon Dioxide: Eliminating Dimerization and Altering Catalysis. *J. Am. Chem. Soc.* **2014,** *136* (14), 5460-5471.
8. Hooe, S. L.; Dressel, J. M.; Dickie, D. A.; Machan, C. W., Highly Efficient Electrocatalytic Reduction of CO_2 to CO by a Molecular Chromium Complex. *ACS Catal.* **2020,** *10* (2), 1146-1151.
9. Babcock, G. T.; Wikström, M., Oxygen activation and the conservation of energy in cell respiration. *Nature* **1992,** *356* (6367), 301-309.
10. Chen, H.; Simoska, O.; Lim, K.; Grattieri, M.; Yuan, M.; Dong, F.; Lee, Y. S.; Beaver, K.; Weliwatte, S.; Gaffney, E. M.; Minteer, S. D., Fundamentals, Applications, and Future Directions of Bioelectrocatalysis. *Chem. Rev.* **2020,** *120* (23), 12903-12993.
11. Anson, C. W.; Ghosh, S.; Hammes-Schiffer, S.; Stahl, S. S., Co(salophen)-Catalyzed Aerobic Oxidation of p-Hydroquinone: Mechanism and Implications for Aerobic Oxidation Catalysis. *J. Am. Chem. Soc.* **2016,** *138* (12), 4186-4193.
12. Anson, C. W.; Stahl, S. S., Cooperative Electrocatalytic O_2 Reduction Involving Co(salophen) with p-Hydroquinone as an Electron–Proton Transfer Mediator. *J. Am. Chem. Soc.* **2017,** *139* (51), 18472-18475.
13. Hooe, S. L.; Cook, E. N.; Reid, A. G.; Machan, C. W., Non-covalent assembly of proton donors and p-benzoquinone anions for co-electrocatalytic reduction of dioxygen. *Chem. Sci.* **2021,** *12* (28), 9733-9741.
14. Chalkley, M. J.; Del Castillo, T. J.; Matson, B. D.; Peters, J. C., Fe-Mediated Nitrogen Fixation with a Metallocene Mediator: Exploring p*K*a Effects and Demonstrating Electrocatalysis. *J. Am. Chem. Soc.* **2018,** *140* (19), 6122-6129.
15. McLoughlin, E. A.; Armstrong, K. C.; Waymouth, R. M., Electrochemically Regenerable Hydrogen Atom Acceptors: Mediators in Electrocatalytic Alcohol Oxidation Reactions. *ACS Catal.* **2020,** *10* (19), 11654-11662.
16. Galvin, C. M.; Waymouth, R. M., Electron-Rich Phenoxyl Mediators Improve Thermodynamic Performance of Electrocatalytic Alcohol Oxidation with an Iridium Pincer Complex. *J. Am. Chem. Soc.* **2020,** *142* (45), 19368-19378.

17. Badalyan, A.; Stahl, S. S., Cooperative electrocatalytic alcohol oxidation with electron-proton-transfer mediators. *Nature* **2016,** *535* (7612), 406-410.
18. Shan, B.; Schmehl, R., Photochemical Generation of Strong One-Electron Reductants via Light-Induced Electron Transfer with Reversible Donors Followed by Cross Reaction with Sacrificial Donors. *J. Phys. Chem. A* **2014,** *118* (45), 10400-10406.
19. Tyson, E. L.; Niemeyer, Z. L.; Yoon, T. P., Redox Mediators in Visible Light Photocatalysis: Photocatalytic Radical Thiol–Ene Additions. *J. Org. Chem.* **2014,** *79* (3), 1427-1436.
20. Happ, B.; Winter, A.; Hager, M. D.; Schubert, U. S., Photogenerated avenues in macromolecules containing Re(I), Ru(II), Os(II), and Ir(III) metal complexes of pyridine-based ligands. *Chem. Soc. Rev.* **2012,** *41* (6), 2222-2255.
21. Andreiadis, E. S.; Chavarot-Kerlidou, M.; Fontecave, M.; Artero, V., Artificial Photosynthesis: From Molecular Catalysts for Light-driven Water Splitting to Photoelectrochemical Cells. *Photochem. Photobiol.* **2011,** *87* (5), 946-964.
22. Teets, T. S.; Nocera, D. G., Photocatalytic hydrogen production. *Chem. Commun.* **2011,** *47* (33), 9268-9274.
23. Sakai, K.; Ozawa, H., Homogeneous catalysis of platinum(II) complexes in photochemical hydrogen production from water. *Coord. Chem. Rev.* **2007,** *251* (21), 2753-2766.
24. Francke, R.; Little, R. D., Redox catalysis in organic electrosynthesis: basic principles and recent developments. *Chem. Soc. Rev.* **2014,** *43* (8), 2492-2521.
25. Oh, Y.; Hu, X. L., Organic molecules as mediators and catalysts for photocatalytic and electrocatalytic CO_2 reduction. *Chem. Soc. Rev.* **2013,** *42* (6), 2253-2261.
26. Vasilyev, D. V.; Dyson, P. J., The Role of Organic Promoters in the Electroreduction of Carbon Dioxide. *ACS Catal.* **2021,** *11* (3), 1392-1405.
27. Smith, P. T.; Weng, S.; Chang, C. J., An NADH-Inspired Redox Mediator Strategy to Promote Second-Sphere Electron and Proton Transfer for Cooperative Electrochemical CO_2 Reduction Catalyzed by Iron Porphyrin. *Inorg. Chem.* **2020,** *59* (13), 9270-9278.
28. Moreno, J. J.; Hooe, S. L.; Machan, C. W., DFT Study on the Electrocatalytic Reduction of CO_2 to CO by a Molecular Chromium Complex. *Inorg. Chem.* **2021,** *60* (6), 3635-3650.
29. Hooe, S. L.; Moreno, J. J.; Reid, A. G.; Cook, E. N.; Machan, C. W., Mediated Inner-Sphere Electron Transfer Induces Homogeneous Reduction of CO_2 via Through-Space Electronic Conjugation**. *Angew. Chem., Int. Ed.* **2022,** *61* (1), e202109645.
30. Li, J.; Shen, P. Z., Zujin; Tang, Ben Z., Through-Space Conjugation: A Thriving Alternative for Optoelectronic Materials. *CCS Chem.* **2019,** *1* (2), 181-196.
31. Garcia-Yoldi, I.; Miller, J. S.; Novoa, J. J., Structure and Stability of the $[TCNE]_2^{2-}$ Dimers in Dichloromethane Solution: A Computational Study. *J. Phys. Chem. A.* **2007,** *111* (32), 8020-8027.
32. Garcia-Yoldi, I.; Miller, J. S.; Novoa, J. J., $[Cyanil]_2^{2-}$ dimers possess long, two-electron ten-center ($2e^-/10c$) multicenter bonding. *Phys. Chem. Chem. Phys.* **2008,** *10* (28), 4106-4109.
33. Mota, F.; Miller, J. S.; Novoa, J. J., Comparative Analysis of the Multicenter, Long Bond in $[TCNE]^{\cdot-}$ and Phenalenyl Radical Dimers: A Unified Description of Multicenter, Long Bonds. *J. Am. Chem. Soc.* **2009,** *131* (22), 7699-7707.
34. Kertesz, M., Pancake Bonding: An Unusual Pi-Stacking Interaction. *Chem. Eur. J.* **2019,** *25* (2), 400-416.
35. Hooe, S. L.; Rheingold, A. L.; Machan, C. W., Electrocatalytic Reduction of Dioxygen to Hydrogen Peroxide by a Molecular Manganese Complex with a Bipyridine-Containing Schiff Base Ligand. *J. Am. Chem. Soc.* **2018,** *140* (9), 3232-3241.
36. Nichols, A. W.; Chatterjee, S.; Sabat, M.; Machan, C. W., Electrocatalytic Reduction of CO_2 to Formate by an Iron Schiff Base Complex. *Inorg. Chem.* **2018,** *57* (4), 2111-2121.
37. Hooe, S. L.; Machan, C. W., Dioxygen Reduction to Hydrogen Peroxide by a Molecular Mn Complex: Mechanistic Divergence between Homogeneous and Heterogeneous Reductants. *J. Am. Chem. Soc.* **2019,** *141* (10), 4379-4387.

38. Costentin, C.; Drouet, S.; Robert, M.; Savéant, J.-M., Turnover Numbers, Turnover Frequencies, and Overpotential in Molecular Catalysis of Electrochemical Reactions. Cyclic Voltammetry and Preparative-Scale Electrolysis. *J. Am. Chem. Soc.* **2012,** *134* (27), 11235-11242.
39. Chintala, S. M.; Petroff II, J. T.; Barnes, A.; McCulla, R. D., Photodeoxygenation of phenanthro[4,5-bcd]thiophene S-oxide, triphenyleno[1,12-bcd]thiophene S-oxide and perylo[1,12-bcd]thiophene S-oxide. *J. Sulphur Chem.* **2019,** *40* (5), 503-515.
40. Klemm, L. H.; Lawrence, R. F., The insertion and extrusion of heterosulfur bridges. X. Conversions in the triphenylene-triphenylo[4,5-bcd] thiophene system. *J. Heterocycl. Chem.* **1979,** *16* (3), 599-601.
41. Baur, J. E., Chapter 19 Diffusion Coefficients. In *Handbook of Electrochemistry*, Zoski, C. G., Ed. Elsevier: 2007; pp 829-848.
42. Piechota, E. J.; Meyer, G. J., Introduction to Electron Transfer: Theoretical Foundations and Pedagogical Examples. *J. Chem. Educ.* **2019,** *96* (11), 2450-2466.
43. Elgrishi, N.; McCarthy, B. D.; Rountree, E. S.; Dempsey, J. L., Reaction Pathways of Hydrogen-Evolving Electrocatalysts: Electrochemical and Spectroscopic Studies of Proton-Coupled Electron Transfer Processes. *ACS Catal.* **2016,** *6* (6), 3644-3659.
44. Frisch, M. J.; Trucks, G. W.; Schlegel, H. B.; Scuseria, G. E.; Robb, M. A.; Cheeseman, J. R.; Scalmani, G.; Barone, V.; Petersson, G. A.; Nakatsuji, H.; Li, X.; Caricato, M.; Marenich, A. V.; Bloino, J.; Janesko, B. G.; Gomperts, R.; Mennucci, B.; Hratchian, H. P.; Ortiz, J. V.; Izmaylov, A. F.; Sonnenberg, J. L.; Williams; Ding, F.; Lipparini, F.; Egidi, F.; Goings, J.; Peng, B.; Petrone, A.; Henderson, T.; Ranasinghe, D.; Zakrzewski, V. G.; Gao, J.; Rega, N.; Zheng, G.; Liang, W.; Hada, M.; Ehara, M.; Toyota, K.; Fukuda, R.; Hasegawa, J.; Ishida, M.; Nakajima, T.; Honda, Y.; Kitao, O.; Nakai, H.; Vreven, T.; Throssell, K.; Montgomery Jr., J. A.; Peralta, J. E.; Ogliaro, F.; Bearpark, M. J.; Heyd, J. J.; Brothers, E. N.; Kudin, K. N.; Staroverov, V. N.; Keith, T. A.; Kobayashi, R.; Normand, J.; Raghavachari, K.; Rendell, A. P.; Burant, J. C.; Iyengar, S. S.; Tomasi, J.; Cossi, M.; Millam, J. M.; Klene, M.; Adamo, C.; Cammi, R.; Ochterski, J. W.; Martin, R. L.; Morokuma, K.; Farkas, O.; Foresman, J. B.; Fox, D. J. *Gaussian 16 Rev. B.01*, Wallingford, CT, 2016.
45. Becke, A. D., Density-functional thermochemistry. III. The role of exact exchange. *J. Chem. Phys.* **1993,** *98* (7), 5648-5652.
46. Lee, C.; Yang, W.; Parr, R. G., Development of the Colle-Salvetti correlation-energy formula into a functional of the electron density. *Phys. Rev. B* **1988,** *37* (2), 785-789.
47. Vosko, S. H.; Wilk, L.; Nusair, M., Accurate spin-dependent electron liquid correlation energies for local spin density calculations: a critical analysis. *Can. J. Phys.* **1980,** *58* (8), 1200-1211.
48. Stephens, P. J.; Devlin, F. J.; Chabalowski, C. F.; Frisch, M. J., Ab Initio Calculation of Vibrational Absorption and Circular Dichroism Spectra Using Density Functional Force Fields. *J. Phys. Chem.* **1994,** *98* (45), 11623-11627.
49. Weigend, F.; Ahlrichs, R., Balanced basis sets of split valence, triple zeta valence and quadruple zeta valence quality for H to Rn: Design and assessment of accuracy. *Phys. Chem. Chem. Phys.* **2005,** *7* (18), 3297-3305.
50. Weigend, F., Accurate Coulomb-fitting basis sets for H to Rn. *Phys. Chem. Chem. Phys.* **2006,** *8* (9), 1057-1065.
51. Grimme, S.; Antony, J.; Ehrlich, S.; Krieg, H., A consistent and accurate ab initio parametrization of density functional dispersion correction (DFT-D) for the 94 elements H-Pu. *J. Chem. Phys.* **2010,** *132* (15), 154104.
52. Grimme, S.; Ehrlich, S.; Goerigk, L., Effect of the damping function in dispersion corrected density functional theory. *J. Comput. Chem.* **2011,** *32* (7), 1456-1465.

53. Mao, Y.; Loipersberger, M.; Kron, K. J.; Derrick, J. S.; Chang, C. J.; Sharada, S. M.; Head-Gordon, M., Consistent inclusion of continuum solvation in energy decomposition analysis: theory and application to molecular CO_2 reduction catalysts. *Chem. Sci.* **2021,** *12* (4), 1398-1414.
54. Nichols, Eva M.; Derrick, J. S.; Nistanaki, S. K.; Smith, P. T.; Chang, C. J., Positional effects of second-sphere amide pendants on electrochemical CO_2 reduction catalyzed by iron porphyrins. *Chem. Sci.* **2018,** *9* (11), 2952-2960.
55. Gotico, P.; Boitrel, B.; Guillot, R.; Sircoglou, M.; Quaranta, A.; Halime, Z.; Leibl, W.; Aukauloo, A., Second-Sphere Biomimetic Multipoint Hydrogen-Bonding Patterns to Boost CO_2 Reduction of Iron Porphyrins. *Angew. Chem., Int. Ed.* **2019,** *58* (14), 4504-4509.
56. Nie, W.; Tarnopol, D. E.; McCrory, C. C. L., Enhancing a Molecular Electrocatalyst's Activity for CO_2 Reduction by Simultaneously Modulating Three Substituent Effects. *J. Am. Chem. Soc.* **2021,** *143* (10), 3764-3778.
57. Pegis, M. L.; Wise, C. F.; Martin, D. J.; Mayer, J. M., Oxygen Reduction by Homogeneous Molecular Catalysts and Electrocatalysts. *Chem. Rev.* **2018,** *118* (5), 2340-2391.
58. Pegis, M. L.; Roberts, J. A. S.; Wasylenko, D. J.; Mader, E. A.; Appel, A. M.; Mayer, J. M., Standard Reduction Potentials for Oxygen and Carbon Dioxide Couples in Acetonitrile and *N,N*-Dimethylformamide. *Inorg. Chem.* **2015,** *54* (24), 11883-11888.
59. Nielsen, M. F.; Hammerich, O.; Rise, F.; Gogoll, A.; Undheim, K.; Wang, D. N.; Christensen, S. B., The Effect of Hydrogen Bonding between Methyl-Substituted Phenols and Dipolar Aprotic Solvents on the Rate Constants for. *Acta. Chem. Scan.* **1992,** *46*, 883-896.
60. Roy, S.; Sharma, B.; Pécaut, J.; Simon, P.; Fontecave, M.; Tran, P. D.; Derat, E.; Artero, V., Molecular Cobalt Complexes with Pendant Amines for Selective Electrocatalytic Reduction of Carbon Dioxide to Formic Acid. *J. Am. Chem. Soc.* **2017,** *139* (10), 3685-3696.
61. Matsubara, Y., Unified Benchmarking of Electrocatalysts in Noninnocent Second Coordination Spheres for CO_2 Reduction. *ACS Energy Lett.* **2019,** *4* (8), 1999-2004.
62. Franco, F.; Pinto, M. F.; Royo, B.; Lloret-Fillol, J., A Highly Active N-Heterocyclic Carbene Manganese(I) Complex for Selective Electrocatalytic CO_2 Reduction to CO. *Angew. Chem., Int. Ed.* **2018,** *57* (17), 4603-4606.
63. Costentin, C.; Drouet, S.; Robert, M.; Savéant, J.-M., Correction to Turnover Numbers, Turnover Frequencies, and Overpotential in Molecular Catalysis of Electrochemical Reactions. Cyclic Voltammetry and Preparative-Scale Electrolysis. *J. Am. Chem. Soc.* **2012,** *134* (48), 19949-19950.
64. Barone, V.; Cossi, M., Quantum Calculation of Molecular Energies and Energy Gradients in Solution by a Conductor Solvent Model. *J. Phys. Chem. A* **1998,** *102* (11), 1995-2001.
65. Ribeiro, R. F.; Marenich, A. V.; Cramer, C. J.; Truhlar, D. G., Use of Solution-Phase Vibrational Frequencies in Continuum Models for the Free Energy of Solvation. *J. Phys. Chem. B* **2011,** *115* (49), 14556-14562.
66. Luchini, G.; Alegre-Requena, J.; Funes-Ardoiz, I.; Rodríguez-Guerra, J.; Chen, J. T.; Paton, R. *Goodvibes v3.0.1*, 2019.
67. Schleyer, P. v. R.; Maerker, C.; Dransfeld, A.; Jiao, H.; van Eikema Hommes, N. J. R., Nucleus-Independent Chemical Shifts: A Simple and Efficient Aromaticity Probe. *J. Am. Chem. Soc.* **1996,** *118* (26), 6317-6318.
68. McWeeny, R., Perturbation Theory for the Fock-Dirac Density Matrix. *Physical Review* **1962,** *126* (3), 1028-1034.
69. Cheeseman, J. R.; Trucks, G. W.; Keith, T. A.; Frisch, M. J., A comparison of models for calculating nuclear magnetic resonance shielding tensors. *The Journal of Chemical Physics* **1996,** *104* (14), 5497-5509.
70. Ditchfield, R., Self-consistent perturbation theory of diamagnetism. *Molecular Physics* **1974,** *27* (4), 789-807.

71. Wolinski, K.; Hinton, J. F.; Pulay, P., Efficient implementation of the gauge-independent atomic orbital method for NMR chemical shift calculations. *J. Am. Chem. Soc.* **1990,** *112* (23), 8251-8260.
72. Neese, F., Software update: The ORCA program system—Version 5.0. *WIREs Computational Molecular Science* **2022,** *n/a* (n/a), e1606.
73. Bruker *Saint; SADABS;TWINABS; APEX3*, Bruker AXS Inc.: Madison, Wisconsin, USA, 2012.
74. Sheldrick, G., SHELXT - Integrated space-group and crystal-structure determination. *Acta Cryst.* **2015,** *71* (1), 3-8.
75. Dolomanov, O. V.; Bourhis, L. J.; Gildea, R. J.; Howard, J. A. K.; Puschmann, H., OLEX2: a complete structure solution, refinement and analysis program. *J. Appl. Cryst.* **2009,** *42* (2), 339-341.
76. Sheldrick, G. M. *Cell_now*, version 2008/4; Georg-August-Universität Göttingen: Göttingen, Germany, 2008.
77. Spek, A., PLATON SQUEEZE: a tool for the calculation of the disordered solvent contribution to the calculated structure factors. *Acta Crystallogr. Sect C: Struct. Chem.* **2015,** *71* (1), 9-18.
78. Lewis, F. W.; Harwood, L. M.; Hudson, M. J.; Distler, P.; John, J.; Stamberg, K.; Núñez, A.; Galán, H.; Espartero, A. G., Synthesis and Evaluation of Lipophilic BTBP Ligands for An/Ln Separation in Nuclear Waste Treatment: The Effect of Alkyl Substitution on Extraction Properties and Implications for Ligand Design. *Eur. J. Org. Chem.* **2012,** *2012* (8), 1509-1519.
79. Fujita, K.-i.; Wada, T.; Shiraishi, T., Reversible Interconversion between 2,5-Dimethylpyrazine and 2,5-Dimethylpiperazine by Iridium-Catalyzed Hydrogenation/Dehydrogenation for Efficient Hydrogen Storage. *Angew. Chem., Int. Ed.* **2017,** *56* (36), 10886-10889.
80. Gilman, H.; Nobis, J. F., Rearrangement with 4-Iododibenzothiophene in Amination by Sodamide. *J. Am. Chem. Soc.* **1945,** *67* (9), 1479-1480.
81. Yang, W.; Hou, Q.; Liu, C.; Niu, Y.; Huang, J.; Yang, R.; Cao, Y., Improvement of color purity in blue-emitting polyfluorene by copolymerization with dibenzothiophene. *J. Mater. Chem.* **2003,** *13* (6), 1351-1355.
82. Grant, D. H., Paramagnetic Susceptibility by NMR: The "Solvent Correction" Reexamined. *J. Chem. Educ.* **1995,** *72* (1), 39.
83. Bain, G. A.; Berry, J. F., Diamagnetic corrections and Pascal's constants. *J. Chem. Educ.* **2008,** *85* (4), 532-536.
84. Sathrum, A. J.; Kubiak, C. P., Kinetics and Limiting Current Densities of Homogeneous and Heterogeneous Electrocatalysts. *J. Phys. Chem. Lett.* **2011,** *2* (18), 2372-2379.
85. Lee, K. J.; McCarthy, B. D.; Dempsey, J. L., On decomposition, degradation, and voltammetric deviation: the electrochemist's field guide to identifying precatalyst transformation. *Chem. Soc. Rev.* **2019,** *48* (11), 2927-2945.
86. Cheng, S. C.; Blaine, C. A.; Hill, M. G.; Mann, K. R., Electrochemical and IR Spectroelectrochemical Studies of the Electrocatalytic Reduction of Carbon Dioxide by $[Ir_2(dimen)_4]^{2+}$ (dimen = 1,8-Diisocyanomenthane). *Inorg. Chem.* **1996,** *35* (26), 7704-7708.

Chapter 4

Comparisons of bpy and phen Ligand Backbones in Cr-Mediated (Co-)Electrocatalytic CO_2 Reduction

Containing work originally published in:

Reid, A. G.; Moberg, M. E.; Koellner, C. A.; Moreno, J. J.; Hooe, S. L.; Baugh, K. R.; Dickie, D. A.; Machan, C. W., *Organometallics* **2023,** *42* (11), 1139-1148.

4.1 Abstract

Due to the rise in atmospheric carbon dioxide (CO_2) concentrations, there is a need for the development of new strategies to enhance the selectivity and activity of the electrocatalytic conversion of CO_2 to value-added products. The incorporation of redox mediators (RMs) as co-catalysts to enhance the transfer of redox equivalents during catalysis has been gaining more attention in recent years across a variety of small molecule transformations. We have shown that using Cr-centered complexes with sulfone-based RMs leads to an enhancement of CO_2 reduction electrocatalysis under protic conditions via an inner-sphere mechanism. In these co-catalytic systems, an oxygen atom of the reduced RM binds to the Cr center to form a key intermediate stabilized by pancake bonding between the reduced aromatic components of the catalyst ligand backbone and the RM. This interaction facilitates the transfer of an electron and accesses a more kinetically favorable reaction pathway. Here, we show that expanding the aromatic character of the ligand backbone of the catalyst as well as the RM can cause a greater enhancement of co-electrocatalytic activity. These results suggest that further activity improvements can be achieved by focusing on the kinetic and thermodynamic parameters which control association between the catalyst and RM.

4.2 Introduction

Since the industrial revolution, the amount of accumulated carbon dioxide (CO_2) pollution in the atmosphere has been estimated to be 1.5 trillion tons, and this increase is the leading contributor to the current global climate crisis.[1] Electrocatalytic reduction of CO_2 to value-added chemical products could be used to both reduce current emissions and atmospheric concentrations. If earth-abundant transition metals and renewable energy sources, like wind or solar, are used to drive the electrochemical reduction of CO_2 to carbon monoxide (CO), the production of chemical feedstocks and fuels could be decoupled from petrochemical sources and feasibly scaled.[2] While earth-abundant transition metal complexes have been studied across a

range of metal centers for the reduction of CO_2,[3-6] the use of chromium (Cr)-centered homogeneous catalysts remains relatively underdeveloped with, to our knowledge, only three known catalysts reported by our group being active for the reduction of CO_2 to CO.[7-9]

There is growing interest in the use of redox mediators (RMs) to improve catalytic small molecule conversion processes.[10] Previous examples of using RMs have increased the activity of the catalytic system and/or shifted reaction selectivity by facilitating electron transfer, avoiding high energy intermediates, or avoiding competitive pathways.[9-23] While these examples are inspired by relatively static biological systems, such as the electron transport chain[24] and iron-sulfur clusters,[25-27] RMs are free to interact directly with molecular active sites, enabling the use of molecular design principles to consider kinetic aspects of the catalyst and mediator interaction, in addition to considering the thermodynamic positioning of redox processes in a manner analogous to the biological systems.[28] When the transfer of electrons from RMs to an active site is linked to a proton transfer event, these co-catalysts have been referred to as electron-proton transfer mediators (EPTMs).[13, 14] To our knowledge, only two examples of CO_2 reduction with a RM that can be regenerated by the electrode have been reported outside of our group.[20, 21] The system reported by Smith *et al.* relies on a NADH-inspired EPTM that works to enhance the transfer of an electron and proton to an iron porphyrin catalyst in order to increase the activity of the system.[20] More recently, Dey *et al.* demonstrated that the selectivity of the classic $Mn(bpy)(CO)_3Cl$ catalyst can be shifted from CO to formic acid by using an iron-sulfur cluster EPTM which promotes the formation of a M–H species at modest reducing potentials.[21]

Both of these previous reports rely on proton-coupled electron transfer reaction steps, where hydrogen atom equivalents are delivered to the metal center or metal-bound substrate.[20, 21] Our group has reported a series of systems with sulfone-containing RMs and Cr-centered catalysts that increase the rate of catalysis through an inner-sphere electron transfer mechanism *sensu stricto*, where the RM coordinates to the catalyst active site and transfers an electron

equivalent to the metal center directly.[9, 11, 12] In a recent study, we proposed that this co-catalyst assembly is stabilized by pancake bonding (PB) between the RM and bipyridine (bpy) ligand backbone under protic conditions.[9] A PB interaction occurs when highly delocalized π-radicals in aromatic systems are positioned within short distances of one another such that vertical atom overlap can occur, creating a pathway for electron transfer.[29] We observed that as the reduction potential of our catalyst and RM are shifted closer to each other, the resulting PB is more favorable (**Figure 4.1**). Since all catalyst-RM adducts were found to have comparable calculated barriers for the proposed rate-determining step, it is the favorability of their association which dictates the observed activity.

However, these studies also showed the effects of the steric profile of the catalyst in the case where *tert*-butyl groups were appended to the 4,4′ positions of the bipyridine-based ligand backbone. When the DBTD RM was modified at the 2,8 positions to tune its reduction potential and aromatic character, steric clash with these *tert*-butyl groups was introduced, resulting in a decrease of vertical atom-atom overlap (**Figure 4.1**). Consequently, energetically well-matched molecular orbitals were kinetically prevented from forming optimal interactions, lowering the quality of the PB interaction. Therefore, we were interested in exploring alternative catalyst ligand structures to address this limitation and explore how it was balanced with dispersion interactions. Our hypothesis was that increased aromatic character in the ligand backbone could better isolate the role of PB strength in co-electrocatalytic activity from other stereochemical forces.

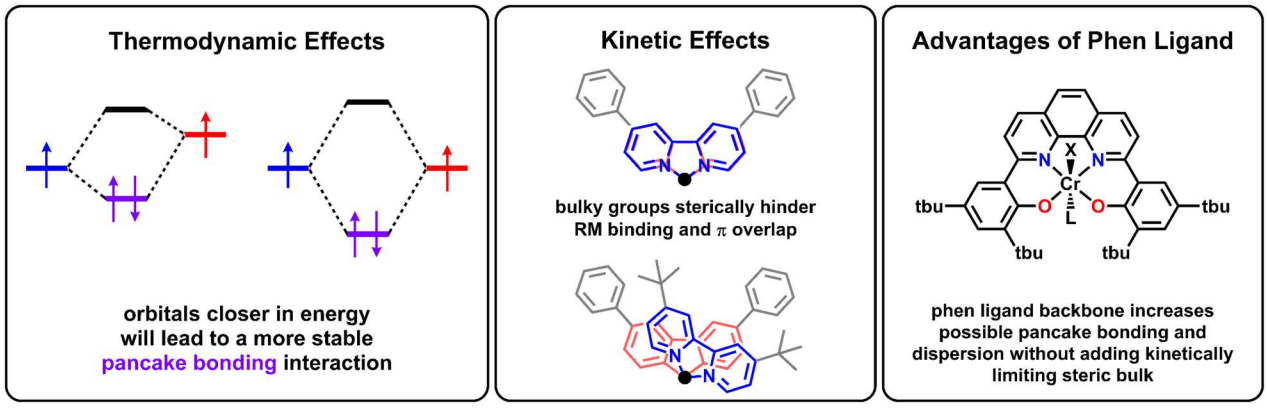

Figure 4.1. Overview of thermodynamic and kinetic effects which play a role in pancake bonding between Cr catalyst and sulfone RM and the advantages of the new phen ligand framework presented in this work. The two other components which also contribute to the association of the catalyst and RM are dispersion interactions and Cr–O bond formation; X = Cl, L = H_2O or DMF.

Here, we report a new catalyst for the reduction of CO_2 to CO with a phenanthroline (phen)-based backbone inspired by our previous ligand frameworks. Additionally, we analyze this catalyst with two sulfone-based RMs and compare the trends in activity against our previously reported Cr catalysts with bipyridine- and *tert*-butyl-substituted bipyridine backbones.[9] This new phenanthroline-based catalyst demonstrates that by considering the thermodynamic and kinetic aspects of pancake bond formation (vertical atom-atom overlap and steric hindrance) between the Cr complex and RM, significant enhancements in co-electrocatalytic rate can be achieved. Interestingly, we find there to be a compensatory relationship with the other contributors to the formation of the co-catalytic assembly: Cr-sulfone bond formation and dispersion interactions.**4.3 Results**

4.3.1. Electrochemistry of Cr Catalysts

The synthesis of the (^{tbu}dhphen)$(H)_2$) ligand (**Figure S4.2**) was carried out as previously reported.[30] The comparable metalation of the (^{tbu}dhphen$(H)_2$) ligand to make Cr(^{tbu}dhphen)Cl(H_2O) (**2**) used a modified literature procedure and **2** was characterized by UV-vis (**Figure S4.3**), NMR (**Table S4.2**), electrospray ionization-mass spectrometry (ESI-MS), microanalysis, and single-crystal X-ray diffraction (XRD) studies (**Figure 4.2**).

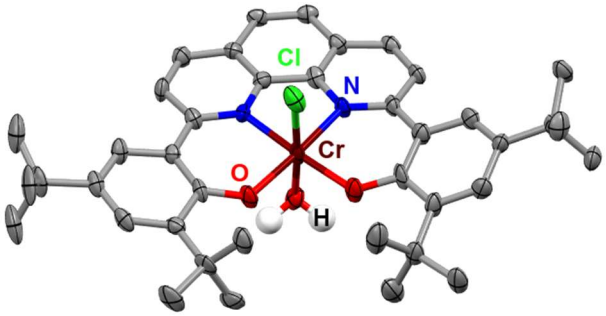

Figure 4.2. Molecular structure of Cr(^{tbu}dhphen)Cl(H_2O) (**2**) obtained from single-crystal X-ray diffraction studies. Blue = N, red = O, gray = C, green = Cl, maroon = Cr, white = H atoms of bound water molecule; thermal ellipsoids at 50%; ligand H atoms and solvent molecules omitted for clarity; only one of two chemically equivalent by crystallographically distinct molecules in the asymmetric unit is shown. CCDC 2221536.

Cyclic voltammetry (CV) experiments were performed on **2** in *N,N*-dimethylformamide (DMF) with 0.1 M tetrabutylammonium hexafluorophosphate ($TBAPF_6$) as the supporting electrolyte like was done previously for Cr(^{tbu}dhbpy)Cl(H_2O) (**1**) (structures shown in **Figure 4.3**). Under argon (Ar) saturation conditions, both catalysts exhibit three redox features and those for **2** (E_p = –1.67 and –1.79 V and $E_{1/2}$ = –1.96 V versus ferrocenium/ferrocene (Fc^+/Fc), **Figure 4.4**) are approximately 10 mV more negative than those for **1** (E_p = –1.66 and –1.78 and $E_{1/2}$ = –1.95 V vs. Fc^+/Fc).[7] Due to the similarity in redox potentials, as well as the observed reversibility and relative current densities of these waves, we propose similar assignments to those previously reported for **1**.[7, 9, 31] For complex **2**, the first two redox features are chemically related and coalesce at scan rates ≥2000 mV/s, consistent with their assignment to the end-states of a solvent displacement equilibrium involving the axial chloride ligand (**Figure S4.4** and **S4.5**). Overall, these two chemically related features correspond to a single-electron reduction of the starting complex **2**. Similar to complex **1**, the third feature observed for **2** at $E_{1/2}$ = –1.96 V vs. Fc^+/Fc represents the formal addition of a second electron overall. The addition of PhOH under Ar saturation leads to only a slight change in the observed redox features (**Figure 4.4A**, green), indicating a lack of intrinsic activity for hydride formation or hydrogen evolution.[32-34] Additionally, the redox features for **2** remain unchanged under CO_2 saturation in the absence of added proton donor (**Figure 4.4A**,

red), demonstrating the absence of aprotic CO_2 reduction activity. The electrochemistry of the Cr(^{tbu}dh^{tbu}bpy)Cl(H_2O) (**3**) catalyst is very similar to that of **1** and **2**. However, due to the electron donating character of the *tert*-butyl groups substituted on the bpy backbone, all of the redox events are shifted to more negative potentials.[9]

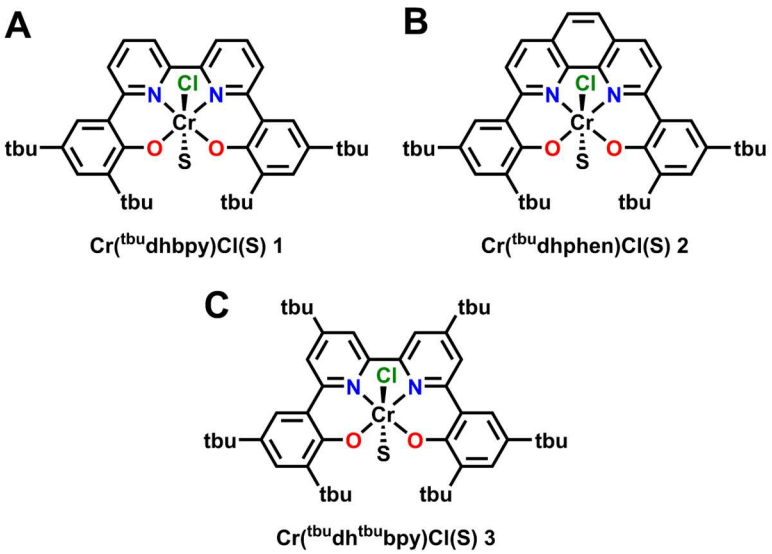

Figure 4.3. Structures of Cr catalysts discussed in this paper where S is either a H_2O or DMF solvent molecule.

The addition of 0.6 M PhOH under CO_2 saturation conditions leads to a large increase in current density and loss of reversibility at the third redox feature ($E_{cat/2}$ = –1.96 V vs. Fc^+/Fc), consistent with the electrocatalytic reduction of CO_2 (**Figure 4.4A**, blue). Notably, there is not a significant difference between this increase in current density for **2** and that observed for **1** under otherwise identical conditions (**Figure 4.4B**). We attribute this similarity in part to minimal difference in catalyst standard reduction potential ($E_{1/2}$ = –1.95 V for **1**; $E_{1/2}$ = –1.96 V for **2** vs Fc^+/Fc). Complex **3** exhibits greater catalytic activity at a more negative standard reduction potential of $E_{1/2}$ = –2.00 V vs Fc+/Fc, reflecting the contributions of the electron-donating *tert*-butyl groups. The catalytic activity of complexes **1** and **3** were previously found to have a first-order concentration dependences with respect to catalyst, PhOH, and CO_2.[7, 9] Comparable electroanalytical CV experiments with variable concentrations of **2**, PhOH, and CO_2 revealed that

the rate of catalysis is likewise first-order with respect to all three components (**Figures S4.6-S4.8**). Interestingly, the saturation of catalytic current with respect to [PhOH] occurred at 0.6 M for **2**, while the response saturated at 0.45 M for **1**.[7] Saturation of catalytic current density for complex **3** occurred at [PhOH] of 0.40 M.[9]

Table 4.1. Results of CPE experiments with PhOH under CO_2 saturation conditions.

Conditions	Potential (V vs Fc^+/Fc)	FE_{CO} (%)	TOF_{CPE} (s^{-1})	η (V)	Turnovers of CO w.r.t [1 or 2]	Turnovers of CO w.r.t [RM]	i_{cat}/i_p[g]
1 + PhOH[11, 12a]	–2.30	111 ± 14	7.12	0.11	11.4	–	7.2
1 + DBTD + PhOH[11, 12b]	–2.30	102 ± 14	65.3	0.41	29	5.8	4.6
1 + Ph_2DBTD + PhOH[9c]	–2.20	100 ± 2	69.3	0.28	22	5.3	4.8
2 + PhOH[d]	–2.30	101 ± 3	4.90	0.12	5.21	–	8.3
2 + DBTD + PhOH[e]	–2.30	94 ± 7	56.3	0.41	13.7	2.7	3.4
2 + Ph_2DBTD + PhOH[e]	–2.20	102 ± 3	126	0.28	7.08	1.4	15
3 + PhOH[9f]	–2.30	95 ± 8	9.29	0.16	13	–	8.4
3 + DBTD + PhOH[9c]	–2.30	109 ± 9	163	0.41	28	6.5	5.8
3 + Ph_2DBTD + PhOH[9c]	–2.20	97 ± 5	194	0.28	35	8.8	7.1

[a] – 0.5 mM catalyst and 0.6 M PhOH; [b] – 0.5 mM catalyst, 2.5 mM RM, and 0.6 M PhOH; [c] – 0.1 mM catalyst, 0.5 mM RM, and 0.12 M PhOH; [d] – 0.5 mM catalyst and 1.0 M PhOH; [e] – 0.1 mM catalyst, 0.5 mM RM, and 1.0 M PhOH; [f]– 0.1 mM catalyst and 0.12 M PhOH; [g] – 1.0 mM catalyst and 0.5 M PhOH, scan rate = 100 mV/s.

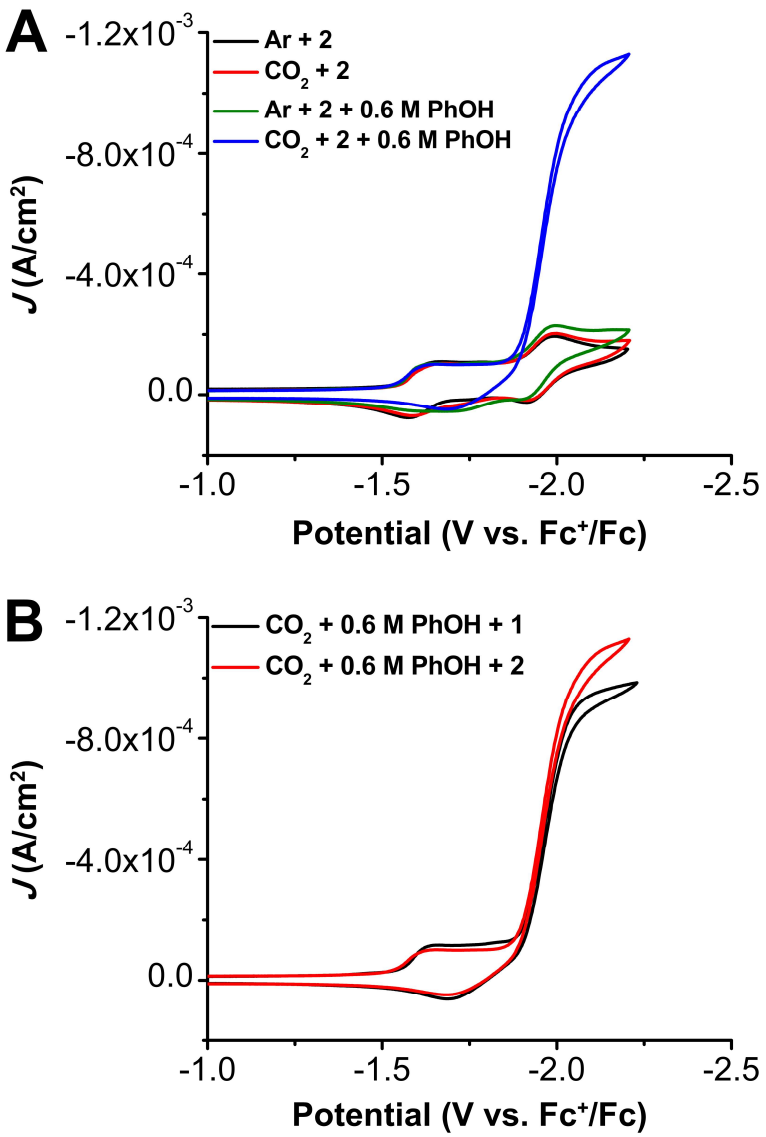

Figure 4.4. (**A**) Comparison CVs of Cr(^{tbu}dhphen)Cl(H_2O) **2** under Ar and CO_2 saturation conditions with and without 0.6 M PhOH. (**B**) Comparison CVs of Cr(^{tbu}dhbpy)Cl(H_2O) **1** and Cr(^{tbu}dhphen)Cl(H_2O) **2** under CO_2 saturation with 0.6 M PhOH. Conditions: 1.0 mM catalyst, 0.1 M $TBAPF_6$/DMF; glassy carbon working electrode, glassy carbon rod counter electrode, Ag/AgCl pseudoreference electrode; referenced to Fc^+/Fc internal standard; 100 mV/s scan rate.

To compare the activity and selectivity of **1** and **2**, controlled potential electrolysis (CPE) was performed at an applied potential of –2.3 V vs Fc^+/Fc under CO_2 saturation with added PhOH, with analysis of gaseous product formation by gas chromatography (GC). Initially, 0.6 M added PhOH was used with **2** to compare the activity and selectivity of the two catalysts, based on previously reported results for **1**.[7, 11, 12] Under these conditions, **2** is selective for the reduction of

CO_2 to CO with a Faradaic efficiency (FE_{CO}) of 94 ±1 1% over 4.6 turnovers (**Figure S4.9** and **Table S4.3**). Note that turnovers have been calculated to show the catalytic nature of the process and do not represent a measurement to the full loss of activity. Based on the observed current density in the CPE experiment, the turnover frequency (TOF_{CPE}) was estimated to be 4.57 s^{-1} with 0.6 M PhOH. Since **2** was shown to have a higher PhOH saturation (**Figure S4.7**) than **1** in initial CV studies,[7] we performed a second CPE experiment under the same conditions, but with 1.0 M PhOH as the proton source (**Figure S4.10** and **Table S4.4**). The results of this experiment showed no change in product selectivity (FE_{CO} = 101 ± 3%, **Table 4.1**) and only a minor increase in activity with a TOF_{CPE} of 4.90 s^{-1}. The electrode from this experiment was rinsed and the CPE experiment was repeated under analogous conditions in the absence of **2**, where the formation of a nonquantifiable amount of CO and significant H_2 was observed (**Figure S4.11** and **Table S4.5**). These results are in good agreement with our previously reported PhOH control CPE experiments and are consistent with a homogeneous catalytic process.[11, 12] The TOF_{CPE} values obtained for both **1** and **2** are lower than that observed for catalyst **3**, 9.29 s^{-1}, which also showed selective Faradaic efficiency for CO (FE_{CO} = 95 ± 8%, **Table 4.1**).[9]

4.3.2 Co-Electrocatalysis Under Protic Conditions

We have previously established that the combination of Cr complexes with a bpy-based ligand backbone and aromatic sulfone-based RMs results in a co-electrocatalytic system and increased activity for the reduction of CO_2 under protic conditions.[9, 11, 12] For comparison with the phen-based system reported here, we analyzed the trends in activity when dibenzothiophene-5,5-dioxide (DBTD) and 2,8-diphenyldibenzothiophene-5,5-dioxide (Ph_2DBTD) are used as the RM (**Figure 4.5A**).[9, 11, 12] Since the standard reduction potential of both RMs is more negative than that of the catalyst, the reduction potential of the mediator controls the co-electrocatalytic operating potential.[9, 11, 12] DBTD and Ph_2DBTD have $E_{1/2}$ values of –2.25 V and –2.12 V vs Fc^+/Fc, respectively (**Figure S4.12**). Notably, previous studies comparing co-catalytic systems with these

RMs have demonstrated inverse potential scaling with respect to activity: Ph_2DBTD showed the highest catalytic activity at the lowest overpotential with complex **3**.[9] **Figure 4.5** shows that the inclusion of both RMs results in an increase in the observed CV current density for complex **2** as well; however, the relative increase upon RM inclusion is different between **1** and **2**. The co-catalytic systems with **1** as the catalyst demonstrate more of an increase in current density when DBTD is the RM compared to the system with Ph_2DBTD (**Figure 4.5B**). For complex **2**, the opposite trend is observed, with Ph_2DBTD as the RM there is a larger increase in current density (**Figure 4.5C**), suggesting that the association between **2** and Ph_2DBTD is more favorable. Variable concentration experiments were performed for **2**, RM, PhOH, and CO_2. These data show that the observed current density is proportional to the concentration of **2** (**Figures S4.15** and **S4.16**), RM (**Figures S4.17** and **S4.18**), a fixed ratio of **2** and RM (**Figures S4.19** and **S4.20**), PhOH (**Figures S4.21** and **S4.22**), and CO_2 (**Figures S4.23** and **S4.24**) where RM is DBTD or Ph_2DBTD. The complexity of the overall co-catalytic system, with overlapping chemical and catalytic components, precludes us from making definitive rate dependence assignments from these data.

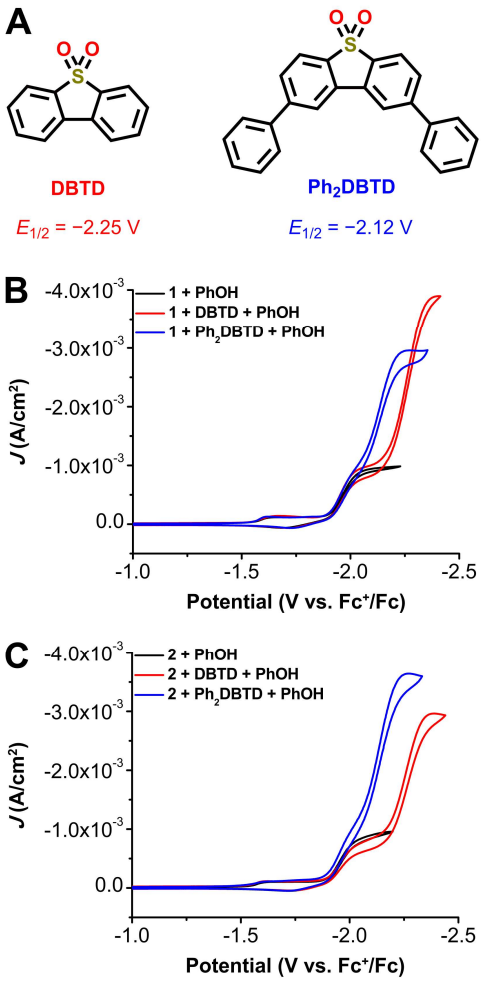

Figure 4.5. The structures of DBTD and Ph_2DBTD (**A**). CVs of 1.0 mM Cr(^{tbu}dhbpy)Cl(H_2O) **1** (**B**) or Cr(^{tbu}dhphen)Cl(H_2O) **2** (**C**) in the absence (black) and presence of 2.5 mM DBTD (red) or Ph_2DBTD (blue) as the RM and 0.5 M PhOH under CO_2 saturation conditions. Conditions: 0.1 M $TBAPF_6$/DMF; glassy carbon working electrode, glassy carbon rod counter electrode, Ag/AgCl pseudoreference electrode; referenced to Fc^+/Fc internal standard; 100 mV/s scan rate.

CPE experiments were performed to determine selectivity and activity of the co-electrocatalytic systems under protic conditions (**Figures S4.25** and **S4.26**). All CPE with the RMs were performed with a 1:5 ratio of catalyst:RM in order to compare to our previous systems.[9, 11, 12] As has previously been the case, all systems remain quantitatively selective for the formation of CO with no H_2 production observed (**Tables S4.6** and **S4.7**; **Table 4.1**).[9, 11, 12] Complexes **1**, **2**, and **3** show an increase in catalytic activity of one to two orders of magnitude when a RM is added to the system and all catalysts show the same relative trend in activity with the two RMs presented here: Ph_2DBTD is the more active co-catalyst than DBTD (**Table 4.1**). While the trend is the same

for both complex **1** and **2**, there is a distinct difference in the relative increases when comparing systems. For the systems with **1**, the TOF_{CPE} values are relatively similar to one another, despite the 130 mV difference in RM reduction potential. However, the TOF_{CPE} value more than doubles when switching the RM from DBTD to Ph_2DBTD with **2** as the catalyst (**Table 4.1**). This observed increase in activity with a decrease in the co-electrocatalytic overpotential conforms to the inverse potential scaling relationship we have observed previously.[9] In this inverse scaling relationship, the favorability of mediator association to access a lower energy reaction pathway increases as the difference in redox potential between the two components decreases. The TOF_{CPE} values for the systems with **3** are still all higher than those for **2** due to the intrinsically higher activity of complex **3**.[9] However, the difference between the systems with **2** and **3** as the catalyst and Ph_2DBTD as the RM do not scale based on the difference in inherent catalyst activity, consistent with a difference in the extent of the RM interaction between catalysts, *vide infra*. Previous CPE controls with the RMs on their own showed non-quantifiable amounts of CO and significant H_2 produced under comparable conditions.[9, 11, 12] We note that the observed CV current densities cannot be directly compared: while these current plateaus do directly relate to electrocatalytic activity, the diffusion-limited Faradaic current of the pre-catalyst system cannot be properly accounted for. In this case, the RMs do not interact with the Cr complexes in the absence of CO_2, preventing a rigorous analytical comparison. However, an approximate accounting of this component can be achieved through a modified i_{cat}/i_p (i_{cat} = catalytic plateau current and i_p = Faradaic current) ratio where the co-electrocatalytic current becomes i_{cat} and the current of the RM is i_p, as previously described (**Table 4.1**).[9] The trend in the i_{cat}/i_p ratios is the same as the trend in TOF_{CPE} values for the respective co-catalytic systems of each complex.

4.3.3 Computational Studies

To complement mechanistic experiments, DFT calculations were performed with the Gaussian 16 package at the B3LYP-D3(BJ)/def2-tzvp//B3LYP-D3(BJ)/def2-svp level of theory

previously identified as suitable for modeling these systems.[35-43] All species are abbreviated as follows: ${}^{multiplicity}_{\#\ bound\ DMF}\boldsymbol{Cr}(\boldsymbol{axial\ ligands})^{charge}$. Calculating the reduction potential which produces the catalytically relevant ${}^{4}_{1}\boldsymbol{Cr}^{-1}$ according to previous methods produced a value of –2.09 V vs Fc^+/Fc, in good agreement with the experimental value of –1.96 V vs Fc^+/Fc. Based on previous results and those presented here, it is proposed that the active catalyst species is a four-coordinate complex formulated as [Cr(^{tbu}dhbpy)]$^-$ (generated from **1**) or [Cr(^{tbu}dhphen)]$^-$ (generated from **2**). A comparison of the CO_2 binding reaction to generate [Cr(^{tbu}dhphen)(CO_2)]$^-$ and [Cr(^{tbu}dhbpy)(CO_2)]$^-$ from these two species shows a minimal difference in the reaction barrier ($\Delta\Delta G^{‡}$ = 0.3 kcal/mol), but it was found to be less endergonic ($\Delta\Delta G$ = −1.1 kcal/mol) for **2** (**Table 4.2**).

Table 4.2. Calculated activation and reaction free energies for CO_2 binding by [Cr(^{tbu}dhbpy)]$^-$ and [Cr(^{tbu}dhphen)]$^-$.

Cr Complex	$\Delta G^{‡}$ Cr–CO_2 (kcal/mol)	ΔG Cr–CO_2 (kcal/mol)
[Cr(^{tbu}dhbpy)(CO_2)]$^-$	10.4	4.6
[Cr(^{tbu}dhphen)(CO_2)]$^-$	10.7	3.5

A comparison of the barrier for C–OH bond cleavage induced by protonation, which has previously been assessed to be the turnover frequency determining transition state (TDTS) for the bpy-based catalytic cycle,[31, 44] found that the barrier for the phen-based complex was again approximately isoergic with the bpy complex ($\Delta\Delta G^{‡}$ = 0.2 kcal/mol, **Table 4.3**). For both the bpy- and phen-based complex these species are proposed to be six-coordinate, with DMF bound to the axial position opposite to the $[CO_2H]^-$ fragment. The equilibrium displacement of this axial DMF ligand by the reduced $[RM]^-$, K_{RM}, was also evaluated. We have previously shown that the favorability of this equilibrium can dictate the extent to which the catalytic response reflects the faster co-catalytic cycle over the relatively slower intrinsic one.[9] The free energies of formation of

the proposed dianionic $^{4}_{0}\mathbf{Cr(CO_2H)(RM)}^{-2}_{\square}$ assembly generated by the reaction described in **Eq (4.1)** for all known Cr-based systems are found in **Table 4.3**.

$$^{3}_{1}\mathbf{Cr(CO_2H)}^{-1}_{\square}{}_{\square} + {}^{2}_{\square}\mathbf{RM}^{-1}_{\square} \overset{K_{RM}}{\rightleftharpoons} {}^{4}_{0}\mathbf{Cr(CO_2H)(RM)}^{-2}_{\square} + \mathbf{DMF} \qquad \textbf{Eq (4.1)}$$

Table 4.3. Calculated free energies of [RM]$^-$ ligand displacement reaction summarized by **Eq (4.1)**, calculated free energies of activation for the rate-limiting C−OH bond cleavage step and CO_2 binding.

Cr Complex	ΔG **Eq (4.1)** (kcal/mol)	$\Delta G^{‡}$ C–OH (kcal/mol)	Ref
[**1a**(CO_2H)(S)]$^-$	n/a	13.5	9
[**1a**(CO_2H)(DBTD)]$^{2-}$	−0.1	11.6	9
[**1a**(CO_2H)(Ph_2DBTD)]$^{2-}$	–3.1	11.6	9
[**2a**(CO_2H)(S)]$^-$	n/a	13.7	this work
[**2a**(CO_2H)(DBTD)]$^{2-}$	−1.8	10.4	this work
[**2a**(CO_2H)(Ph_2DBTD)]$^{2-}$	–5.6	11.9	this work
[**3a**(CO_2H)S)]$^-$	n/a	12.5	9
[**3a**(CO_2H)(DBTD)]$^{2-}$	−2.3	10.7	9
[**3a**(CO_2H)(Ph_2DBTD)]$^{2-}$	−6.1	10.8	9

[a]S = DMF, [Cr(^{tbu}dhbpy)]$^-$ = **1a**, [Cr(^{tbu}dhphen)]$^-$ = **2a**, and [Cr(^{tbu}dh^{tbu}bpy)]$^-$ = **3a**.

Interestingly, although for the bpy-based system the displacement of DMF by [DBTD]$^-$ is approximately isoergic (ΔG = –0.1 kcal/mol), the formation of the same adduct with the phen-based derivative is exoergic by –1.8 kcal/mol. This value is comparable to that which we have previously obtained for complex **3** of –2.3 kcal/mol at the same level of theory.[9] This trend aligns with stronger interactions corresponding to closer energies of π* systems, but we emphasize that greater dispersive interactions are also likely to contribute. The barrier for the proposed TDTS of the phen-based derivative of 10.4 kcal/mol is lower than that determined for the bpy-based of 11.6 kcal/mol. This barrier for the phen-based complex in the co-catalytic cycle again shows greater similarity with the barrier of 10.7 kcal/mol obtained for the more active catalyst, **3**.[9]

The minimal difference in the barriers for CO_2 binding calculated for the phen- and bpy-based compounds implies an analogous electronic structure. Indeed, an assessment of the frontier KS orbitals and spin density of [Cr(^{tbu}dhphen)]$^-$ is consistent with the previous proposal of a *S*=3/2 ground state comprised of a Cr(II) center antiferromagnetically paired with a ligand-based radical anion (**Figure 4.6**).[31, 44] Further, the distribution of added electron density in the ligands of [Cr(^{tbu}dhbpy)]$^-$ and [Cr(^{tbu}dhphen)]$^-$ shows insignificant differences, despite the additional six-membered ring in the backbone of [Cr(^{tbu}dhphen)]$^-$. In the transition state for CO_2 binding, **TS^{CO2}**, a molecular orbital with significant π* phen character contributes one of the two electrons necessary for the incipient Cr–CO_2 bond (**Figure S4.28**), analogous to what was found in computational studies on the bpy-based compound. Similar to the bpy-based compound, the bending of the CO_2 molecule in this transition state for the phen-based complex is asymmetric relative to the Cr–C bond vector, but only a single Cr−C σ bonding interaction is implied.

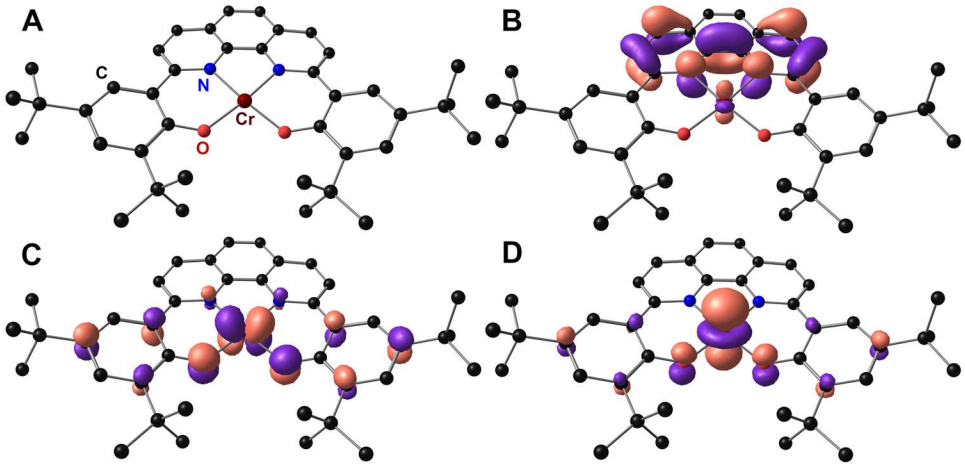

Figure 4.6. Molecular geometry of $^{4}_{0}\mathbf{Cr}^{-1}$ with H atoms omitted for clarity (**A**) Kohn-Sham orbital projection of SOMO (**B**), SOMO^{-1} (**C**), and SOMO^{-2} (**D**).

Unsurprisingly, the minor electronic structure differences found between the phen-based and bpy-based monoanionic active species and their respective transition states for CO_2 binding were also reflected in the respective TSs for the rate-determining step. Following protonation and

reduction of the CO_2 adduct, association of the proton donor is expected to produce $^{3}_{1}\mathbf{Cr(CO_2H)} \bullet (\mathbf{PhOH})^{-1}_{\square}$, prior to C–OH bond cleavage. Analysis of the spin density and KS orbitals contributing to this interaction show that the redox activity of the phen-backbone again plays an analogous role to bpy in relaying an electron to the Cr center, with only trivial differences in delocalization. Examination of $\mathbf{TS}^{\mathrm{CO2H}}_{\square}$ shows transfer of electron density from the partially populated π* orbital into the Cr center as proton transfer occurs.

The key differences between the phen- and bpy-based complexes appear to be primarily in the co-electrocatalytic cycle when Ph_2DBTD is included as the RM. In addition to the free energies of formation of the $^{4}_{0}\mathbf{Cr(CO_2H)(RM)}^{-2}_{\square}$ assembly, the quality of the pancake bonding interaction can be assessed by analyzing the vertical atom-atom overlap and distances between the ligand backbone and RM. PB is characterized as stronger than van der Waals interactions when the distances between the atoms are shorter and the vertical overlap between individual atoms is better, since orbital interactions can be maximized.[29] There is no clear difference in the atom-atom overlap between all of the assemblies with **1** and **2** as catalyst and DBTD and Ph_2DBTD as the RM (**Figure 4.8** and **Figures S4.39-S4.42**). However, the centroid–centroid distances between the phen backbone of **2** and Ph_2DBTD are overall shorter (3.238, 3.200, 3.253 Å) than any of the other intermediates (**Table S4.8**), implying a relatively stronger contribution from PB to the favorable binding energy. Although in $^{4}_{0}\mathbf{Cr(CO_2H)(DBTD)}^{-2}_{\square}$ both **1** and **2** have shorter distances between the central five-membered rings, the centroid–centroid distances for the two six-membered rings are longer (**Table S4.8**). Since PB is also characterized by highly delocalized π electrons, increased distances for portions of the π-framework sharing the radical electron density will decrease the contribution of PB to the interaction energy. Since the electron delocalization and KS orbital composition in the phen and bpy fragments remains similar in the

co-catalyst adducts, the data also imply that the relative contribution of dispersion interactions is increased for the phen backbone (**2**) relative to the bpy (**1**): $[DBTD]^-$ binding as summarized by **Eq (4.1)** is 1.7 kcal/mol more favorable than for the bpy analogue (**1**), which increases to be 2.5 kcal/mol more favorable for $[Ph_2DBTD]^-$.

4.3.4 Proposed Mechanism

Based on these results, we can propose that complex **2** follows the same intrinsic and co-catalytic cycles as complexes **1** and **3** (**Figure 4.7**).[7, 9, 11, 12, 31, 44] To initiate the intrinsic catalytic cycle, a four-coordinate neutral Cr species derived from complex **2** is reduced to a monoanionic four-coordinate species (*i*). This monoanionic species is best described as high-spin Cr(II) antiferromagnetically paired with a phen-centered radical anion, ($phen^{\bullet-}$). This species then readily binds CO_2 to form $[Cr–CO_2]^-$ (*ii*) which can then go on to be protonated by PhOH while binding DMF, before a favorable one-electron reduction generates $[Cr–CO_2H]^-$ (*iii*). Without a RM present (but at the potentials where the redox mediator is reduced), the catalyst can proceed via **Pathway A**, where protonation followed by reduction once again occurs to release H_2O and leave $[Cr–CO]^-$ (*v*). This intermediate is not stable and will readily release CO to form *i* and close the catalytic cycle.[7] When a RM is present, the singly reduced $[RM]^-$ will displace the DMF molecule in *iii* to give (*iv*) $^{4}_{0}\mathbf{Cr}(\mathbf{CO_2H})(\mathbf{RM})^{-2}$ defined by K_{RM} as discussed above. This step allows for the reaction to proceed via **Pathway B**, where *iv* is protonated and water is released to give $[Cr–CO]^-$ (*v*). Since both catalysts are active for the reduction of CO_2 to CO with or without the presence of the RM at the tested conditions, it is reasonable to assume both **Pathway A** and **Pathway B** are being accessed at the same time. *Therefore, the observed TOF values will represent a combination of catalytic and co-catalytic pathways.*

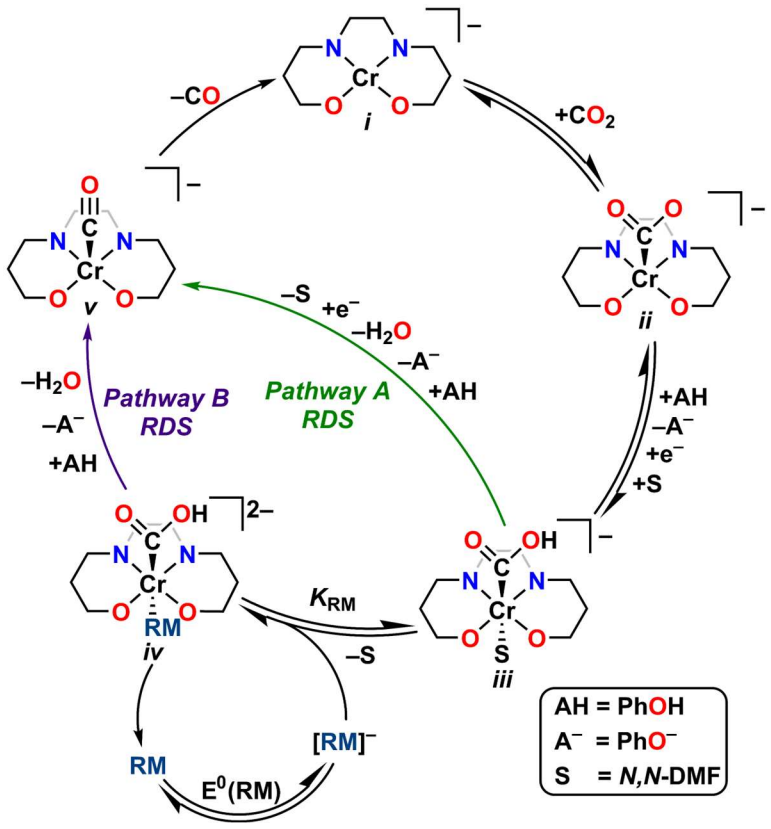

Figure 4.7. Proposed catalytic mechanism for electrocatalytic CO_2 reduction by Cr and co-electrocatalytic reduction of CO_2 by Cr and RM where Cr **1** or **2** and RM is DBTD or Ph_2DBTD. Initial reduction step to form *i* from catalyst as synthesized omitted for clarity.

4.4 Discussion

As was the case with **1** and **3** previously,[9] the experimental and computational results for **2** indicate an inner-sphere electron transfer mechanism under co-electrocatalytic conditions. In this mechanism, the reduced RM binds to the Cr center to give $^{4}_{0}\mathbf{Cr(CO_2H)(RM)}^{-2}$ prior to the rate-determining step, C–OH bond cleavage. Although the absolute TOF_{CPE} values determined for **1** with DBTD and PhOH present are approximately 10 s^{-1} faster than **2** under the same co-electrocatalytic conditions, the enhancements under co-catalytic conditions correspond to 9-fold and 11-fold increases from the intrinsic activities determined for these catalysts, respectively. In other words, the co-catalytic enhancement for **2** is greater with DBTD than it is for **1**, consistent with the greater K_{RM} (1.7 kcal/mol more favorable ΔG).

The significant difference between **1** and **2** with Ph_2DBTD as the RM can likewise be rationalized using the difference in the thermodynamics of the equilibrium binding step in **Eq (4.1)**. The difference in calculated ΔG **Eq (4.1)** values (**Table 4.3**) increases to favor **2** by 2.5 kcal/mol without a significant change in reaction barrier, suggesting that K_{RM} is one of the primary determinants in the observed increase in experimental TOF_{CPE} values (**Table 4.1**). As described above, increased binding favorability reflects both a greater contribution of the PB interaction to stabilizing the RM-bound intermediate $^{4}_{0}\mathbf{Cr}(\mathbf{CO_2H})(\mathbf{RM})^{-2}$, as well as increased dispersion interactions.[9] Here, two components are likely to contribute to the difference between **1** to **2**: the slightly more negative reduction potential of **2**, which better matches the RM reduction potential, and the increased aromatic character of the phen backbone, which should act to protect its radical character, as well as improve the magnitude of the PB and dispersion interactions. Since the computational data do not show significant delocalization of electron density into the additional six-membered ring of the phen backbone during key reaction steps, it is also clear that dispersion effects and steric protection are playing an increased role in stabilizing adduct formation.

Finally, we can compare the results described with complex **2** to those obtained with complex **3** (**Figure 4.3C**).[9] The reduction potential of **3** is 40 mV closer to Ph_2DBTD than **2**, but the activity only increases by a factor of 21 from the intrinsic response (ratio of catalytic and co-catalytic TOF values),[9] in comparison to a factor of 26 for **2** (**Table 4.1**). Notably, the calculated structures of the $^{4}_{0}\mathbf{Cr}(\mathbf{CO_2H})(\mathbf{RM})^{-2}$ intermediate for **2** and **3** where RM is Ph_2DBTD show a clear steric hindrance effect on the binding interaction (**Figure 4.8**). In the structure with **2** as the catalyst, there is very good vertical atom-atom overlap between the five and six member rings of Ph_2DBTD and the phen backbone, maximizing orbital interactions for the pancake bond. For complex **3**, which has a di-*tert*-butyl-substituted bpy backbone, steric hindrance prevents an optimal interaction and causes Ph_2DBTD to be rotated to a position with poor vertical atom-atom overlap. This rotation and decrease in overlap will limit the strength of the PB interaction between

3 and Ph_2DBTD for purely steric reasons. However, the $\Delta\Delta G$ for **Eq (4.1)** favors the association of complex **3** by about 0.5 kcal/mol relative to complex **2** (**Table 4.3**). This suggests that any relative decrease in the quality of the PB based on steric clash is compensated to some degree by contributions from dispersion. Further, because of the more reducing Cr potential for **3**, the barrier for $\Delta\Delta G^{\ddagger}$ C–OH is favored by 1.1 kcal/mol with respect to **2** following the association of $[Ph_2DBTD]^{-}$, which is reflected in the experimental observation of increased TOF_{CPE} for **3**. The relative uniformity of the $\Delta G^{\ddagger}$ C–OH barrier decrease upon RM association for all complexes – and its independence from the thermodynamics of **Eq (4.1)** – also indicates that the nature of Cr-sulfone bond formation in the axial position plays a key role.

However, the performance of **3** relative to **1** and **2** with Ph_2DBTD appears to be significantly *underperforming* in its potential co-electrocatalytic activity, which we propose is the consequence of the sterically controlled kinetic limitations on the association of the RM and Cr complex, prior to a formal bonding interaction. Interestingly, based on these data it also appears that PB and dispersion interactions have a compensatory relationship with respect to the favorability of Cr–RM adduct formation.

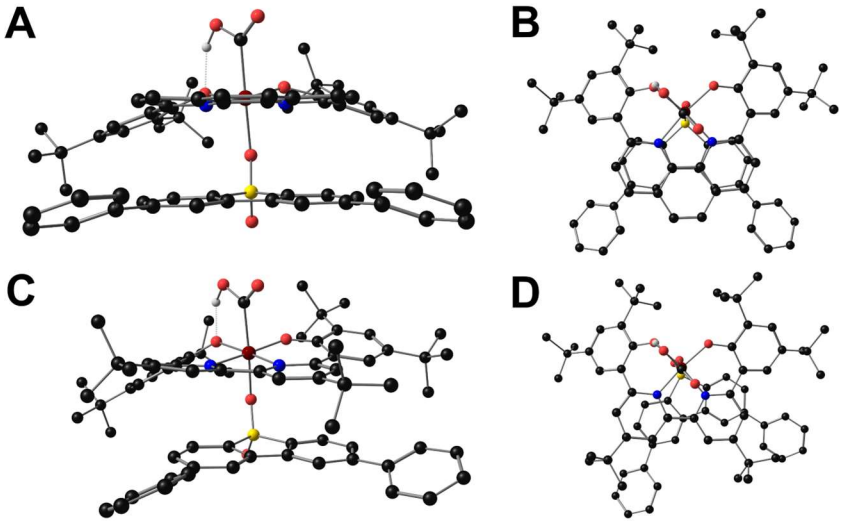

Figure 4.8. Molecular geometry of $^{4}_{0}\mathbf{Cr(CO_2H)(Ph_2DBTD)}^{-2}$ where Cr is the phen based complex **2** (**A** and **B**) or the *tert*-butyl substituted bpy complex **3** (**C** and **D**) with select H atoms removed for clarity.

4.5 Conclusion

Our previous reports demonstrate that increasing the PB interaction present in a key RM-bound intermediate by more closely matching the reduction potential of catalyst and RM can increase activity. However, the evidence presented here demonstrates that dispersion interactions can compensate for ideal orbital overlap between the π frameworks to some degree and that steric hindrance of the Cr-center also plays a significant role in controlling the rate of association between the RM and the Cr complex during co-electrocatalysis. Indeed, the increased aromatic character of the phen-backbone produces noteworthy co-catalytic enhancements, with a minimal change in catalyst reduction potential. In order to improve these systems in the future, these results indicate that we must identify catalysts and RMs that have closely matched reduction potentials and isolate new derivatives which maximize the planarity of the RM and catalyst backbone.

4.6 Supplementary Information

4.6.1 Materials and Methods

General

All chemicals and solvents (ACS or HPLC grade) were commercially available and used as received unless otherwise indicated. For all air-sensitive reactions and electrochemical experiments, HPLC-grade solvents were obtained as anhydrous and air-free from a PPT Glass Contour Solvent Purification System. Gas cylinders were obtained from Praxair (Ar as 5.0; CO_2 as 4.0) and passed through activated molecular sieves prior to use. Gas mixing for variable concentration experiments was accomplished using a gas proportioning rotameter from Omega Engineering. UV-vis absorbance spectra were obtained on a Cary 60 from Agilent. An Anton-Parr Multiwave Pro SOLV, NXF-8 microwave reactor was used for microwave syntheses.

Electrochemistry

All electroanalytical experiments were performed using a Metrohm Autolab PGSTAT302N potentiostat. Glassy carbon disc working electrodes (⌀ = 3 mm) and non-aqueous silver/silver chloride pseudoreference electrodes behind PTFE tips were obtained from CH Instruments. The pseudoreference electrodes were obtained by depositing chloride on bare silver wire in 10% HCl at oxidizing potentials and stored in a 0.1 M tetrabutylammonium hexafluorophosphate/*N*,*N*-dimethylformamide ($TBAPF_6$/DMF) solution in the dark prior to use. The counter electrode was a glassy carbon rod (⌀ = 3 mm). All CV experiments were performed in a modified scintillation vial (20 mL volume) as a single-chamber cell with a cap modified with ports for all electrodes and a sparging needle. $TBAPF_6$ was purified by recrystallization from ethanol and dried in a vacuum oven before being stored in a desiccator. All data were referenced to an internal ferrocene standard (ferricenium/ferrocene (Fc^+/Fc) reduction potential under stated conditions) unless otherwise specified. All voltammograms were corrected for internal resistance. Ferrocene was purified by sublimation prior to use.

Controlled Potential Electrolysis (CPE)

CPE experiments were performed in a glass Pine Research Instrumentation H-cell with two compartments separated by a glass frit. A 55 mL stock solution of DMF with 0.1 M $TBAPF_6$ was prepared for each bulk electrolysis experiment. Approximately 26 mL of the stock solution was added to each half of the H-cell. One side of the H-cell contained the catalyst, any additional substrate, such as the mediator and/or PhOH, and a glassy carbon rod working electrode. The other side of the H-cell contained approximately 0.075 M ferrocene as a sacrificial reductant along with a graphite rod counter electrode and a Ag/AgCl pseudoreference electrode. The electrolysis experiment was referenced by taking a CV of the side of the H-cell that contained the ferrocene solution. The H-cell was sealed with two septa that were connected by a piece of PTFE tubing which aided to maintain equal pressure between each half of the cell during the electrolysis.

Before starting the electrolysis experiment, both sides of the H-cell were sparged with the desired gas for 20 minutes and the sealed cell was allowed to equilibrate for 1 hour. The resistance between the two halves of the H-cell was measured using the i-interrupt procedure available in the NOVA software provided by Metrohm. This measured resistance value was then used to correct for resistance using the iR compensation tool in the NOVA software for potentiostatic experiments.

CPE Product Analysis

During CPE experiments, 250 µL GC injections of the headspace were periodically taken for the detection and quantification of any gaseous products produced. After each CPE experiment, the total volume of solution was measured. The total volume of the sealed H-cell was also measured to account for the total headspace volume for accurate quantification of gaseous products. A calibration curve for CO and H_2 was used to quantify gaseous products produced during electrolysis experiments in the same manner as we previously reported.[7]

Analysis of gas phase products was done by sampling electrolysis headspace through syringe injections into an Agilent 7890B GC equipped with a specialty gas split column 5 Å mol sieve/Porabond Q column (15 m length; 0.320 mm diameter; 25.0 µm film) and thermal conductivity detector with He as a carrier gas. A calibration curve for CO and H_2 was made in the H-cell with an experimental setup containing identical volumes of DMF in 0.1 M $TBAPF_6$ to those used during electrolysis. Known volumes of CO and H_2 were injected into the cell with stirring and 250 µL injections of the headspace were taken for GC injections after equilibration. The limit of detection (LOD) and limit of quantitation (LOQ) for CO and H_2 in the GC were determined from seven consecutive injections at the lowest observable concentrations of each gaseous product respectively. For CO, the LOD was determined to be 5.77×10^{-7} moles and the LOQ was determined to be 1.92×10^{-6} moles. For H_2, the LOD was determined to be 4.55×10^{-6} moles and the LOQ was determined to be 1.52×10^{-5} moles.

Calculation of Overpotential for CO_2 Reduction with PhOH Present (Adapted)

The calculation of overpotential for all catalysts was performed according to reported methods.[45] The following equation was used for the determination of the reaction standard potential in V with respect to the Fc^+/Fc couple:

$$E_{CO2/CO} = -0.73\,V - 0.059(pK_a) \quad \textbf{Eq (S4.1)}$$

The pK_a for PhOH in DMF is reported as 18.8:[46]

$$E_{CO2/CO}(PhOH) = -1.84\,V\ vs\ Fc^+/Fc \quad \textbf{Eq (S4.2)}$$

The $E_{cat/2}$ determined experimentally for Cr(^{tbu}dhbpy)Cl(H_2O) and Cr(^{tbu}dhphen)Cl(H_2O) is –1.95 V[7] and –1.96 V vs Fc^+/Fc, respectively. For protic CO_2 reduction (1.0 mM catalyst and 0.1 M PhOH under CO_2 saturation); the overpotential is:

$$\eta = \left|E_{cat/2} - E_{CO2/CO}\right| \quad \textbf{Eq (S4.3)}$$

Cr(^{tbu}dhbpy)Cl(H_2O) η = 110 mV
Cr(^{tbu}dhphen)Cl(H_2O) η = 120 mV

This assumes no contribution from homoconjugation of the acid. We note that the homoconjugation constant (HA_2^-) for PhOH in DMF has been reported as $\log(K_{HA_2^-})$ = 3.8.[47] Therefore, we emphasize that the described overpotential calculated above for PhOH is the lower-limit approximation, as homoconjugation is expected to alter the effective overpotential. The overpotential equation can be modified to account for homoconjugation:

$$E_{CO\ /CO} = -0.73\,V - 0.059(pK_a) - \frac{-2.303RT}{nF}\log\left(mK_{HA_2^-}\right) \quad \textbf{Eq (S4.4)}$$

Where n = number of electrons (2) and m = number of proton transfers (2). The modified equation provides $E^0_{CO2/CO}$ = −1.72 V and the following η values:

Cr(^{tbu}dhbpy)Cl(H_2O)	η = 230 mV
Cr(^{tbu}dhphen)Cl(H_2O)	η = 240 mV

This value does not account for the possible thermodynamic contributions of the water coordinated to the pre-catalyst, the equimolar quantities of water produced for each equivalent of CO generated, or any adventitious H_2O present in the CO_2, solvent, or electrolyte. Under CO_2 saturation, any water present can form carbonic acid, pK_a(DMF) 7.37,[48] and generate new equilibria involving CO_2 and bicarbonate. The role of carbonic acid (and the general hydration of CO_2 in non-aqueous solvent systems) in altering the overall thermodynamics combined with the effects of homoconjugation has been assessed by Matsubara.[49] Considering the role of water, Matsubara obtained a standard potential for CO_2 reduction to CO of −1.70 V versus Fc^+/Fc for PhOH in DMF with 10 mM water present (see below). Note the same value is obtained considering 10 mM water only.

For 10 mM H_2O in DMF, where AH = PhOH:[49]

$3CO_{2(g)} + H_2O_{(sol,x)} + 2e^- \rightleftharpoons CO_{(g)} + 2HCO_{3\,(sol)}^-$	$E^0 = -1.70\,V\ vs.\,Fc^+/Fc$
$CO_{2(g)} + 2AH_{(sol)} + 2e^- \rightleftharpoons CO_{(g)} + 2A^-{}_{(sol)} + H_2O_{(sol,x)}$	$E^0 = -1.96\,V\ vs.\,Fc^+/Fc$
$CO_{2(g)} + 4AH_{(sol)} + 2e^- \rightleftharpoons CO_{(g)} + 2HA_{2\,(sol)}^- + H_2O_{(sol,x)}$	$E^0 = -1.70\,V\ vs.\,Fc^+/Fc$

Determination of TOF from Preparative Electrolysis

The integrated expression of current for a homogeneous electrocatalytic response (considering an application of steady-state conditions to the substrate) has been solved previously:[50, 51]

$$\frac{i}{FA} = \frac{n_{cat}^{\sigma}[cat]\sqrt{(k_{obs}D_{cat})}}{1 + \exp\left[\frac{F}{RT}\left(E_{app} - E_{\frac{1}{2}}\right)\right]}$$

where

$$k_{obs} = k_{cat}[CO_2]$$

and i is the average current (Amps) specific to the reaction product of interest, F is Faraday's constant (96485 C mol^{-1}), A is the area of the electrode (cm^2), n_{cat}^{σ} is the number of electrons in the catalytic process (2) with σ = 1 under the assumption that all electrons are delivered to the catalyst by the electrode electrode[4] (σ = 0.5 corresponds to homogeneous electron transfer occurring between catalyst molecules in solution; used here for co-electrocatalytic conditions), $[cat]$ is the concentration of the catalyst (mol cm^{-3}), k_{obs} is the apparent turnover frequency (s^{-1}), $[CO_2]$ is the concentration of CO_2 saturated in DMF (mol cm^{-3}), D_{cat} is the diffusion coefficient of the catalyst (cm^2 s^{-1}), R is the ideal gas constant (Joule mol^{-1} K^{-1}), T is the temperature (K), E_{app} is the applied potential during preparative electrolysis (V), and $E_{1/2}$ is the standard potential of the catalyst (V).

$$\frac{i}{A} = J = CO\ specific\ current\ density$$

Substituting and rearranging the first expression to solve for k_{obs}

$$k_{obs} = \frac{J^2\left(1 + \exp\left[\frac{F}{RT}\left(E_{app} - E_{1/2}\right)\right]\right)^2}{F^2(n_{cat}^{\sigma}[cat])^2 D_{cat}}$$

with k_{obs} in hand, the TOF can be expressed for a given potential according to the following relationship

$$TOF = \frac{k_{obs}}{1 + \exp\left[\frac{F}{RT}\left(E_{app} - E_{1/2}\right)\right]}$$

Parameters for CPE experiments reported here not found in **Table 4.1**.

- $E_{1/2}$ catalyst:
  - −1.95 V vs Fc$^+$/Fc for Cr(^{tbu}dhbpy)Cl(H$_2$O) **1**
  - −1.96 V vs Fc$^+$/Fc for Cr(^{tbu}dhphen)Cl(H$_2$O) **2**
- Temperature: 298.15 K
- [CO_2]: 2.3 x 10^{-4} mol cm^{-3}
- Diffusion coefficient:
  - 2.0 x 10^{-6} cm^2 s^{-1} for Cr(^{tbu}dhbpy)Cl(H$_2$O) **1**
  - 1.6 x 10^{-6} cm^2 s^{-1} for Cr(^{tbu}dhphen)Cl(H$_2$O) **2**
- Electrode area: 3.93 cm^2, 2.51 cm^2, 2.85 cm^2, or 3.11 cm^2

Calculation of Diffusion Coefficients

The calculation of the diffusion coefficient for the Cr(^{tbu}dhphen)Cl(H_2O) **2** catalyst was performed by reported methods.[52] Cyclic voltammetry (CV) experiments were done with a solution of 1.0 mM catalyst in 0.1 M $TBAPF_6$/DMF under Ar saturation conditions. The scan rate of these CVs was varied from 25 mV/s to 5000 mV/s (**Figure S4.4**). The increase in current observed as the scan rate increases can be represented by the following equation where i_p is the peak current, n is the number of electrons, A is the area of the electrode, D is the diffusion coefficient, C is the concentration of analyte, and v is the scan rate:

$$i_p = (2.69 \times 10^5) n^{3/2} A C D^{1/2} v^{1/2}$$

By plotting the current density as a function of $v^{1/2}$ (**Figure S4.4**), the slope can be used to find D for each RM.

$$D_{cat} = \frac{(\text{slope})^2}{n^3 C^2 (2.69 \times 10^5)^2}$$

Calculation of i_{cat}/i_p for Co-electrocatalytic Systems

A common technique for evaluating diffusion, electrode surface area, and concentration independent observed rate constants (k_{obs}) for a two-electron catalytic process is to determine i_{cat}/i_p for a catalytic system, where i_{cat} is the catalytic plateau current and i_p is the one-electron peak in the absence of substrate.[53] Due to the complex nature of the co-catalytic systems we present here, we are unable to calculate k_{obs} by this method. However, these ratios still offer an insightful measure into the relative current increase under catalytic conditions between systems that are sensitive to the diffusion coefficient of both co-catalysts.

To calculate the values of i_p and i_{cat} for all systems, the capacitive current must be subtracted from the measured current at either the peak or the plateau. To determine the potential to find the

capacitive, peak, catalytic, and co-catalytic plateau currents, the first derivative was taken of the forward trace for CVs obtained with **1** or **2**, RM, and PhOH under Ar (i_p) and under CO_2 (i_{cat}). Where the first derivative is equal to zero there is a plateau in the CV trace. The current in the CV at the same potential corresponding to a value of zero in the first derivative was used (**Figure S4.1A**). However, due to close overlap of features in the co-catalytic trace under CO_2, the local minima corresponding to the inflection point of the curve were used to determine an effective current plateau (**Figure S4.1B**). All CV data used had a scan rate = 100 mV/s and 1.0 mM catalyst with 0.5 M PhOH.

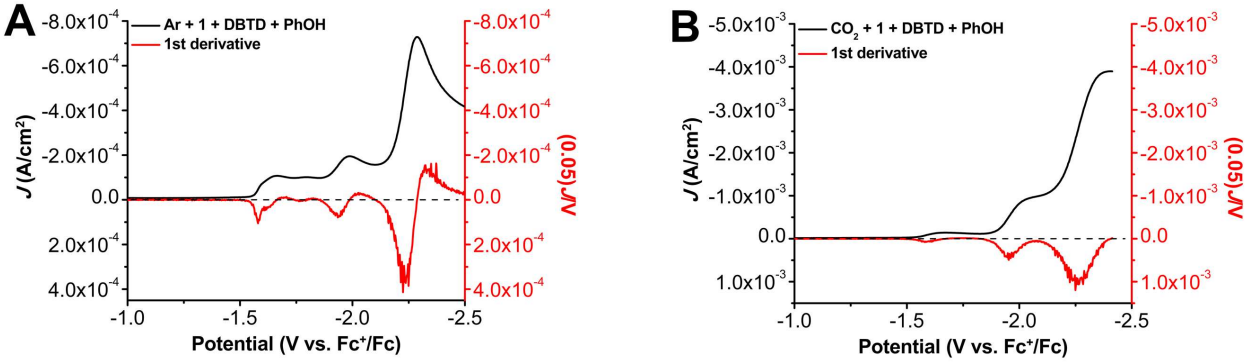

Figure S4.1. Example forward CV trace and first derivative plot used in i_{cat}/i_p calculations for 1.0 mM Cr(^{tbu}dh^{tbu}bpy)Cl(H_2O) **2** with 2.5 mM DBTD and 0.1 M PhOH under Ar (**A**) and CO_2 (**B**).

Computational Methods

Geometry optimizations were performed without geometry constraints at the DFT level with the Gaussian 16 program, Rev B.01,[35] employing the hybrid functional B3LYP[36-39] and the def2-SVP basis set was used for all atoms.[40, 41] Dispersion and bulk solvent effects (*N*,*N*-dimethylformamide = DMF; ε = 37.219) were accounted for at the optimization stage, by using Grimme's D3 parameter set with Becke-Johnson (BJ) damping[42, 43] and the CPCM continuum model,[54] respectively. The stationary points and their nature as minima (no imaginary frequencies) were characterized by vibrational analysis using the IGRRHO approach as implemented by default in the software package, which also produced enthalpy (H), entropy (S) and Gibbs energy (G) data at 298.15 K. The minima connected by a given transition state were determined by perturbing the

transition states along the TS coordinate and optimizing to the nearest minimum. Free energies were corrected (ΔG_{qh}) to account for concentration effects and for errors associated with the harmonic oscillator approximation. Thus, according to Truhlars's quasi-harmonic approximation for vibrational entropy and enthalpy, all vibrational frequencies below 100 cm^{-1} were set to this value.[55] These anharmonic and concentration corrections were calculated with the Goodvibes code.[56] Concentrations were set at 0.001 M for metal complexes, 0.005 for RM and RM^{-}, and 12.92 M for DMF. Energies were refined by means of single point calculations with the larger def2-TZVP basis set. The stability of the wavefunction and spin contamination were studied at the double- and triple-zeta levels of theory. Kohn-Sham orbital projections and spin densities were plotted with isovalues of 0.045 and 0.005, respectively.***Single Crystal X-ray Diffraction***

A single crystal of ^{tbu}dhphen$(H)_2$ or Cr(^{tbu}dhphen)Cl(H_2O) (**2**) was coated with Paratone oil and mounted on a MiTeGen MicroLoop. The X-ray intensity data were measured on a Bruker Kappa APEXII Duo diffractometer using either a fine-focus sealed tube (Mo K_α, λ = 0.71073 Å) and a graphite monochromator for ^{tbu}dhphen$(H)_2$ or an Incoatec Microfocus IμS (Cu K_α, λ = 1.54178 Å) and a multi-layer mirror monochromator for Cr(^{tbu}dhphen)Cl(H_2O) (**2**). The frames were integrated with the Bruker SAINT software package[57] using a narrow-frame algorithm. Data were corrected for absorption effects using the Multi-Scan method (SADABS or TWINABS).[58] Each structure was solved and refined using the Bruker SHELXTL Software Package[58] within APEX3[58] and OLEX2.[59] Non-hydrogen atoms were refined anisotropically. The O–H hydrogen atoms of ^{tbu}dhphen$(H)_2$ were located in the electron density map and refined isotropically. All other hydrogen atoms were placed in geometrically calculated positions with U_{iso} = 1.2U_{equiv} of the parent atom (1.5U_{equiv} for methyl).

For ^{tbu}dhphen$(H)_2$, a two-domain twin was identified using CELL_NOW.[60] Starting with 2104 reflections, 1588 reflections were fit to the first domain, 1493 to the second domain (515 exclusively), with 1 unindexed reflection remaining. The twin domain was oriented at a 180.0º

rotation about the reciprocal axis 0.001 0.002 1.000. The twin law was -1.000 0.000 0.001 / -0.002 -1.001 0.005 / -0.652 -0.406 1.001. The structure was refined on HKLF5 data with the BASF for the twin domains refined to 0.42813. The crystal of Cr(^{tbu}dhphen)Cl(H_2O) (2) was also twinned. The TWINROTMAT feature of Platon[61] was used to identify the two-fold rotation around the (0 1 0) axis. The resulting twin law was -1.000 0.000 0.000 / 0.571 1.000 0.471 / 0.000 0.000 -1.000, and the BASF refined to BASF 0.03137.

Table S4.1. Crystallographic data for ^{tbu}dhphen($H)_2$ and Cr(^{tbu}dhphen)Cl(H_2O) (**2**).

	^{tbu}dhphen($H)_2$	**Cr(^{tbu}dhphen)Cl(H_2O) (2)**
CCDC number	2221535	2221536
Formula	$C_{40}H_{48}N_2O_2$	$C_{41}H_{50}Cl_3CrN_2O_3$
FW (g/mol)	588.80	777.18
Temp (K)	100(2)	100(2)
λ (Å)	0.71073	1.54178
Size (mm)	0.118 x 0.220 x 0.297	0.053 x 0.068 x 0.146
Crystal habit	yellow block	red plate
Crystal system	triclinic	triclinic
Space group	P -1	P -1
a (Å)	9.9720(19)	12.9910(11)
b(Å)	11.526(2)	15.9195(10)
c (Å)	16.336(3)	20.9104(15)
α (°)	77.658(5)	104.786(5)
β (°)	75.462(5)	103.430(6)
γ (°)	68.975(5)	99.273(6)
Volume ($Å^3$)	1680.5(5)	3953.7(5)
Z	2	4
Density (g/cm^3)	1.164	1.306
μ (mm^{-1})	0.071	4.552
F(000)	636	1636
θ range (°)	1.30 to 29.61	2.28 to 59.38
Index ranges	-13 ≤ h ≤ 13 -15 ≤ k ≤ 16 0 ≤ l ≤ 22	-14 ≤ h ≤ 14 -17 ≤ k ≤ 16 -22 ≤ l ≤ 23
Data / restraints /parameters	9432 / 0 / 418	11352 / 0 / 928
GOF on F^2	1.032	1.042
R_1 (I>2σ(I))	0.0523	0.1122
wR_2 (all data)	0.1349	0.3376

4.6.2 Synthesis and Characterization

Synthesis of 6,6'-Di(3,5-di-tert-butyl-2-hydroxybenzene)-1,10-phenanthroline, ^{tbu}dhphen(H)$_2$

The synthesis of ^{tbu}dhphen(H)$_2$ was carried out as previously reported.[30]

Synthesis of Cr(^{tbu}dhphen)Cl(H$_2$O) (2)

Metalation of ^{tbu}dhphen(H)$_2$ with Cr(III) to generate Cr(^{tbu}dhphen)Cl(H$_2$O) (**2**) was achieved by stirring ^{tbu}dhphen(H)$_2$ (0.450 g, 0.764 mmol) and 1.05 equivalents of chromium(II) dichloride (0.0986 g, 0.802 mmol) in tetrahydrofuran (100 mL) at room temperature under an inert atmosphere for five days. After exposing the reaction to air, the solution was filtered to collect a minor amount of unreacted ligand and the filtrate was concentrated to dryness. The solid was then dissolved in DCM and washed with brine (3 x 50 mL) and saturated ammonium chloride (6 x 50 mL). The organic layer was then condensed under reduced pressure and the resulting solid was washed with deionized water (200 mL) and boiling hexanes (300 mL). 72.3% isolated yield (0.382 g). Elemental analysis for $C_{40}H_{48}ClCrN_2O_3$ calc'd: C 69.40, H 6.99, N 4.05; found: C 69.39, H 7.40, N 4.03. ESI-MS (m/z): [Cr(^{tbu}dhphen)]–Cl–H$_2$O calc'd: 638.2964 found: 638.2963.

Synthesis of 2,8-Diphenyldibenzothiophene-5,5-dioxide, Ph$_2$DBTD

The synthesis of Ph$_2$DBTD was carried out as previously reported.[9]

Evans' Method Characterization of 2

The spin state of the Cr(^{tbu}dhphen)Cl(H$_2$O) (**2**) catalyst was characterized as a Cr(III) species via Evans' Method.[62, 63] Three capillary inserts were made with a 50% v/v mixture of DMF and DMF-d_7. Each insert was flame sealed, and then placed in an NMR tube. Then 8.8 mg of **2** was dissolved in 3 mL of DMF. Approximately 0.6 mL of the solution of **2** was added to each of the three NMR tubes containing a flame sealed insert. ^{1}H NMR spectra with 64 scans were then taken using a 600 MHz Varian NMR Spectrometer. The results of this experiment, which was run in triplicate, can be seen in **Table S4.2**. The average μ_{eff} of **2** was 3.83±0.02.

Table S4.2. Evans' method results for Cr(^{tbu}dhphen)Cl(H_2O) (**2**) in DMF.[62, 63]

Trial	Chemical Shift (ppm)	Chemical Shift (Hz)	Total Magnetic Moment (emu mol^{-1})	Paramagnetic Moment (emu mol^{-1})	μ_{eff} (Bohr Magnetons)
1	0.098	58.8	0.00552	5.98 x 10^{-3}	3.78
2	0.100	60.0	0.00563	6.09 x 10^{-3}	3.81
3	0.102	61.2	0.00575	6.21 x 10^{-3}	3.85

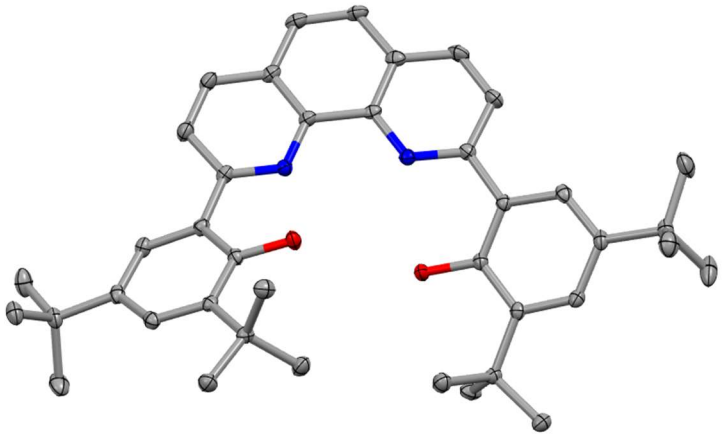

Figure S4.2. The single crystal structure of ^{tbu}dhphen$(H)_2$ ligand obtained from X-ray diffraction studies. Blue = N, red = O, gray = C; thermal ellipsoids at 50%; H atoms omitted for clarity. CCDC 2221535.

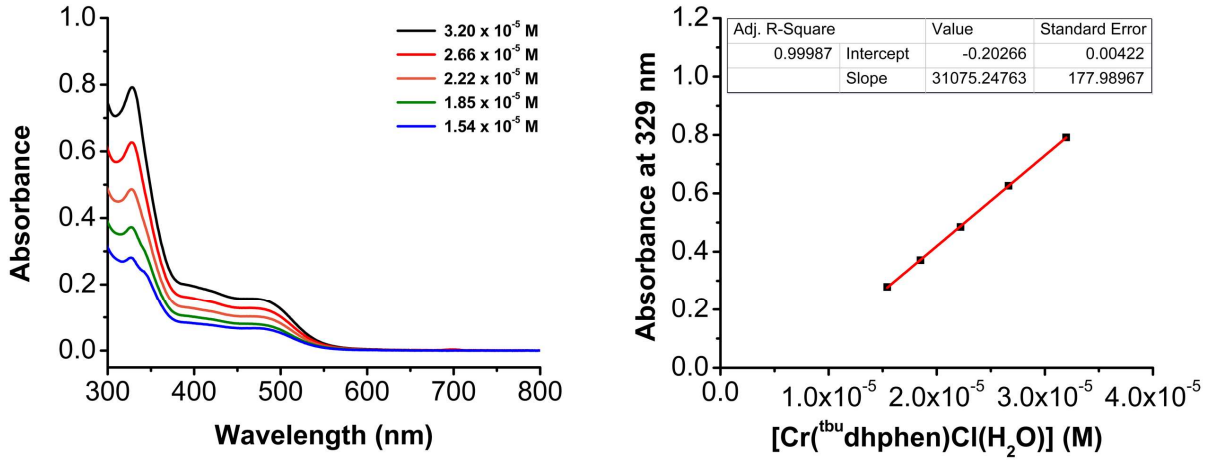

Figure S4.3. (**A**) UV-vis serial dilution absorbance data obtained from Cr(^{tbu}dhphen)Cl(H_2O) **2** in a DMF solution. Conditions: varying concentration of **2**; quartz cell with 1 cm pathlength. (**B**) Plot of absorbance versus concentration (M) for Cr(^{tbu}dhphen)Cl(H_2O) **2** in DMF at 329 nm (31100 M^{-1} cm^{-1}); R^2 = 0.999. All: λ_{max} = 416 nm (6430 M^{-1} cm^{-1}) and 494 nm (4900 M^{-1} cm^{-1}).

4.6.3 Electrochemistry of 2

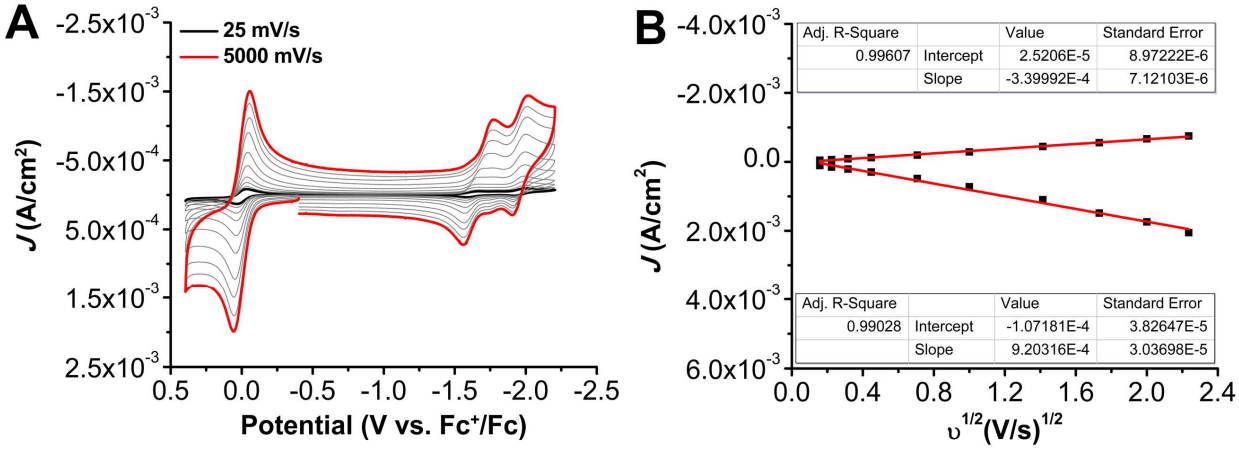

Figure S4.4. (**A**) CVs of Cr(^{tbu}dhphen)Cl(H_2O) **2** at variable scan rates ranging from 25 (black) to 5000 (red) mV/s, obtained under Ar saturation conditions. (**B**) Linear Fit of variable scan rate data from (**A**) demonstrating that Cr(^{tbu}dhphen)Cl(H_2O) **2** shows a diffusion-limited current response. The data in (**B**) was obtained from the reversible redox feature at −1.96 V vs Fc^+/Fc. Conditions: 1.0 mM **2**, 0.1 M $TBAPF_6$/DMF; glassy carbon working electrode, glassy carbon counter electrode, Ag/AgCl pseudoreference electrode; varied scan rate; referenced to internal ferrocene standard.

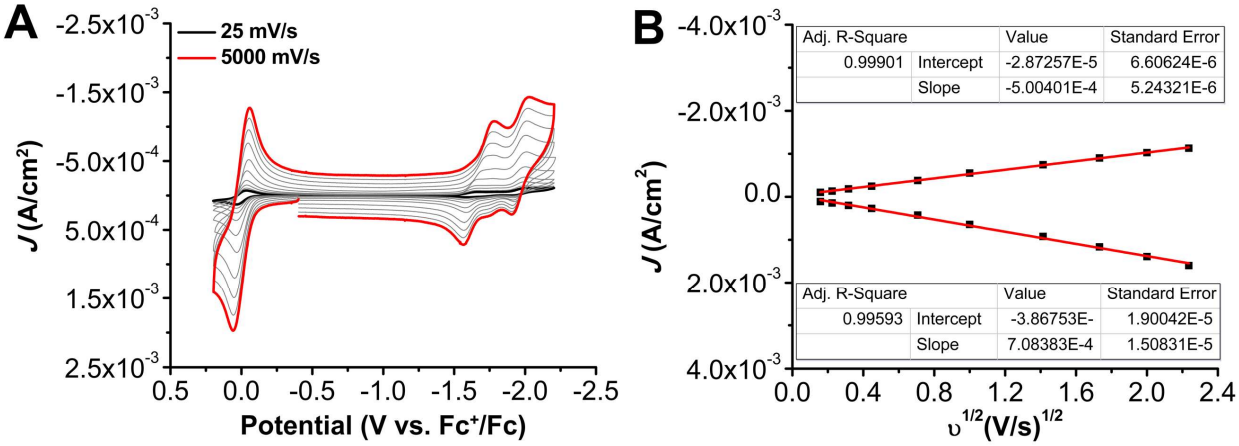

Figure S4.5. (**A**) CVs of Cr(^{tbu}dhphen)Cl(H_2O) **2** at variable scan rates ranging from 25 (black) to 5000 (red) mV/s, obtained under CO_2 saturation conditions. (**B**) Linear Fit of variable scan rate data from (**A**) demonstrating that Cr(^{tbu}dhphen)Cl(H_2O) **2** shows a diffusion-limited current response. The data in (**B**) was obtained from the reversible redox feature at −1.96 V vs Fc^+/Fc. Conditions: 1.0 mM **2**, 0.1 M $TBAPF_6$/DMF; glassy carbon working electrode, glassy carbon counter electrode, Ag/AgCl pseudoreference electrode; varied scan rate; referenced to internal ferrocene standard.

At high scan rates in **Figures S4.4** and **S4.5**, the first two reduction features condense into a single feature, consistent with outcompeting a solvent-displacement equilibrium as summarized below, where L = dhphen^{2-} and S = solvent and E_1^0 and E_2^0 are the first and second reduction features observed at 100 mV/s.

$$[Cr(L)Cl] + e^- \rightleftharpoons [Cr(L)Cl]^- \qquad E_1^0$$
$$[Cr(L)Cl]^0 + S \rightleftharpoons [Cr(L)(S)]^+ + Cl^-$$
$$[Cr(L)(S)]^+ + e^- \rightleftharpoons [Cr(L)(S)]^0 \qquad E_2^0$$

For all variable concentration studies without the presence of RMs (**Figures S4.6-S4.8**) analysis was adapted from Sathrum and Kubiak J. Phys. Chem. Lett. 2011, *2*, 2372.[64] F is Faraday's constant, A is the electrode area, [Q] is the substrate concentration, k_{cat} is the catalytic rate, D is the diffusion constant of the catalyst, [cat] is the concentration of the catalyst, and n_{cat} is the number of electrons involved in the catalytic process.

$$\boldsymbol{i_{cat} = n_{cat}FA[cat](Dk_{cat}[Q]^y)^{1/2}}$$

For the variable PhOH and CO_2 concentration experiments in **Figures S4.7** and **S4.8**, only points outside of the saturation range were included in the linear fits.

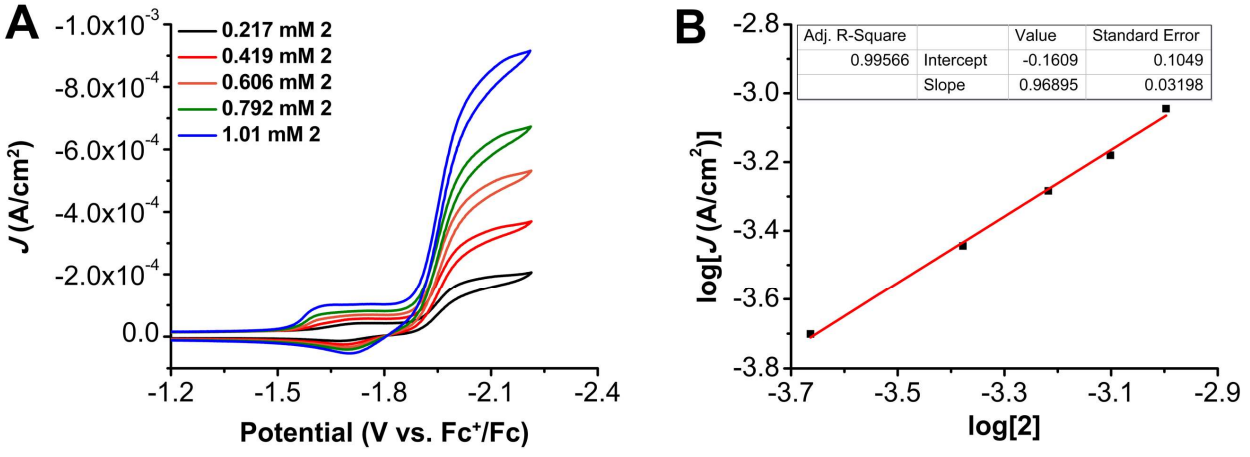

Figure S4.6. (**A**) CVs of Cr(^{tbu}dhphen)Cl(H_2O) **2** at variable concentrations, obtained under CO_2 saturation with 0.325 M PhOH. Conditions: 0.1 M $TBAPF_6$/DMF; glassy carbon working electrode, glassy carbon counter electrode, Ag/AgCl pseudoreference electrode; 100 mV/s scan rate; referenced to internal ferrocene standard. (**B**) Log-log plot from data obtained from CVs in **A** at −2.17 V vs. Fc^+/Fc.

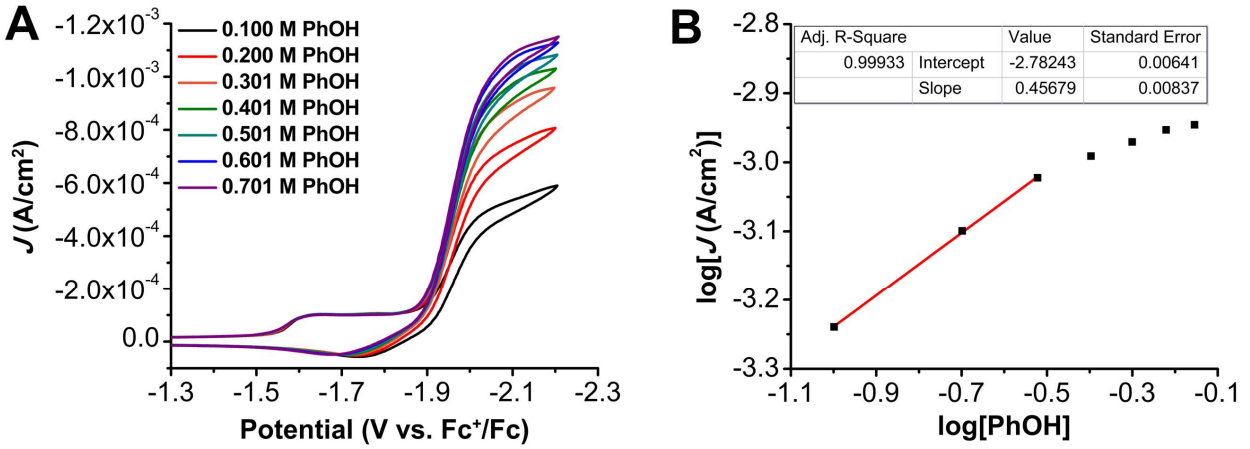

Figure S4.7. (**A**) CVs of 1.0 mM Cr(^{tbu}dhphen)Cl(H_2O) **2**, obtained under CO_2 saturation conditions with variable PhOH concentration.Conditions: 1.0 mM **2**, 0.1 M $TBAPF_6$/DMF; glassy carbon working electrode, glassy carbon counter electrode, Ag/AgCl pseudoreference electrode; 100 mV/s scan rate; referenced to internal ferrocene standard. (**B**) Log-log plot from data obtained from CVs in **A** at −2.17 V vs. Fc^+/Fc.

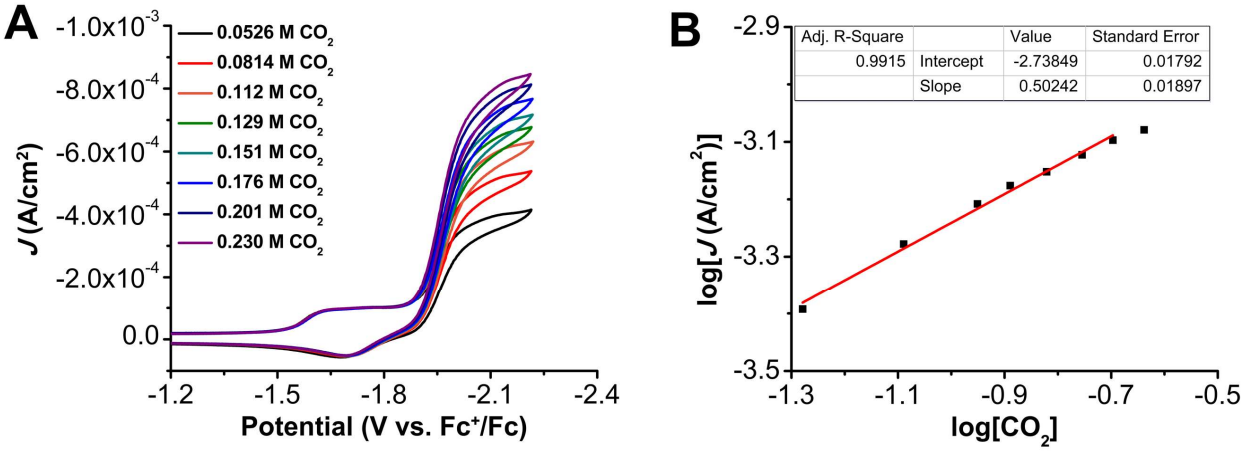

Figure S4.8. (**A**) CVs of 1.0 mM Cr(^{tbu}dhphen)Cl(H_2O) **2** obtained under variable CO_2 concentration with 0.325 M PhOH. Conditions: 0.1 M $TBAPF_6$/DMF; glassy carbon working electrode, glassy carbon counter electrode, Ag/AgCl pseudoreference electrode; 100 mV/s scan rate; referenced to internal ferrocene standard. (**B**) Log–log plot from data obtained from CVs in **A** at −2.17 V vs. Fc^+/Fc.

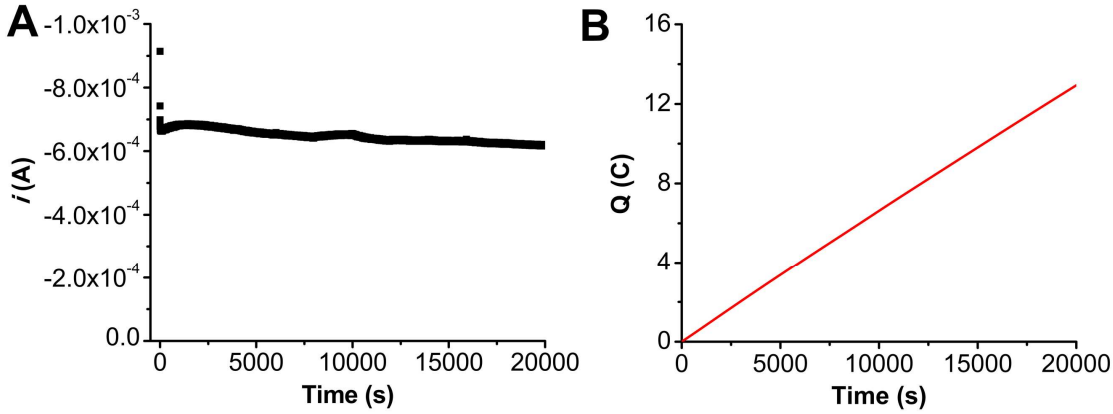

Figure S4.9. (**A**) Current versus time trace from CPE experiment for **2**+PhOH. (**B**) Charge passed versus time for the CPE experiment shown in **A**. Conditions were 0.5 mM Cr(^{tbu}dhphen)Cl(H_2O) **2** and 0.6 M PhOH under a CO_2 atmosphere at −2.30 V vs Fc^+/Fc in 0.1 M $TBAPF_6$/DMF; working electrode was a glassy carbon rod, counter electrode was a graphite rod, and the reference was a nonaqueous Ag/AgCl pseudoreference electrode; 0.075 M Fc was used as sacrificial oxidant.

Table S4.3. Results from CPE experiment in **Figure S4.9**, **2** + 0.6 M PhOH.

Time (s)	Charge (coulombs)	moles (e^-)	Moles of CO	FE_{CO}
20000*	12.9	1.34 x 10^{-4}	5.83 x 10^{-5}	87.02
20000*	12.9	1.34 x 10^{-4}	5.75 x 10^{-5}	85.76
20000*	12.9	1.34 x 10^{-4}	7.35 x 10^{-5}	109.6

*indicates a triplicate series of injections carried out upon completion of electrolysis in **Figure S4.9**.

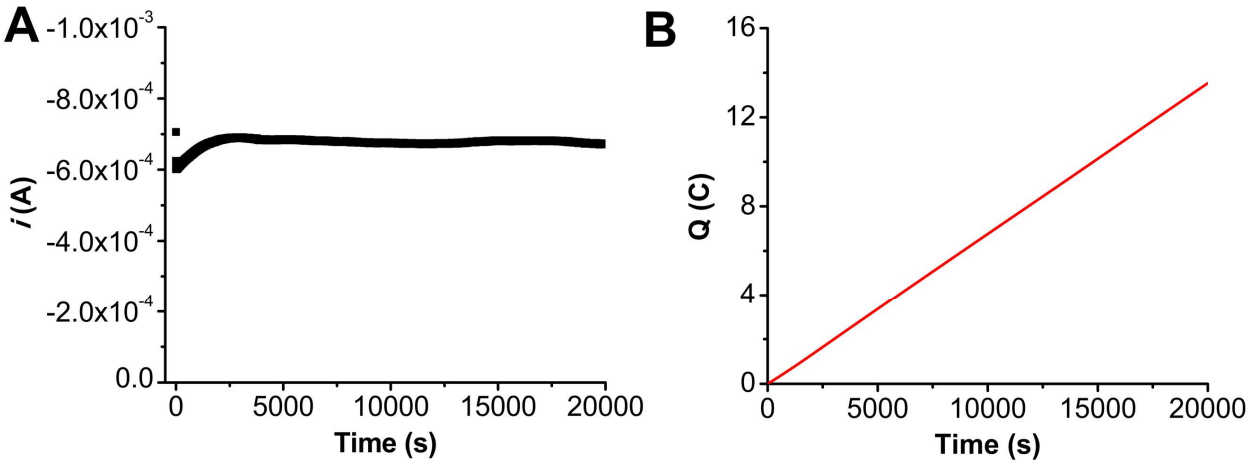

Figure S4.10. (**A**) Current versus time trace from CPE experiment for **2**+PhOH.(**B**) Charge passed versus time for the CPE experiment shown in **A**. Conditions were 0.5 mM Cr(^{tbu}dhphen)Cl(H_2O) **2** and 1.0 M PhOH under a CO_2 atmosphere at −2.30 V vs Fc^+/Fc in 0.1 M $TBAPF_6$/DMF; working electrode was a glassy carbon rod, counter electrode was a graphite rod, and the reference was a nonaqueous Ag/AgCl pseudoreference electrode; 0.075 M Fc was used as sacrificial oxidant.

Table S4.4. Results from CPE experiment in **Figure S4.10**, **2** + 1.0 M PhOH.

Time (s)	Charge (coulombs)	moles (e^-)	Moles of CO	FE_{CO}
20000*	13.5	1.40×10^{-4}	6.72×10^{-5}	95.80
20000*	13.5	1.40×10^{-4}	7.21×10^{-5}	102.7
20000*	13.5	1.40×10^{-4}	6.35×10^{-5}	90.48

* indicates a triplicate series of injections carried out upon completion of electrolysis in **Figure S4.10**.

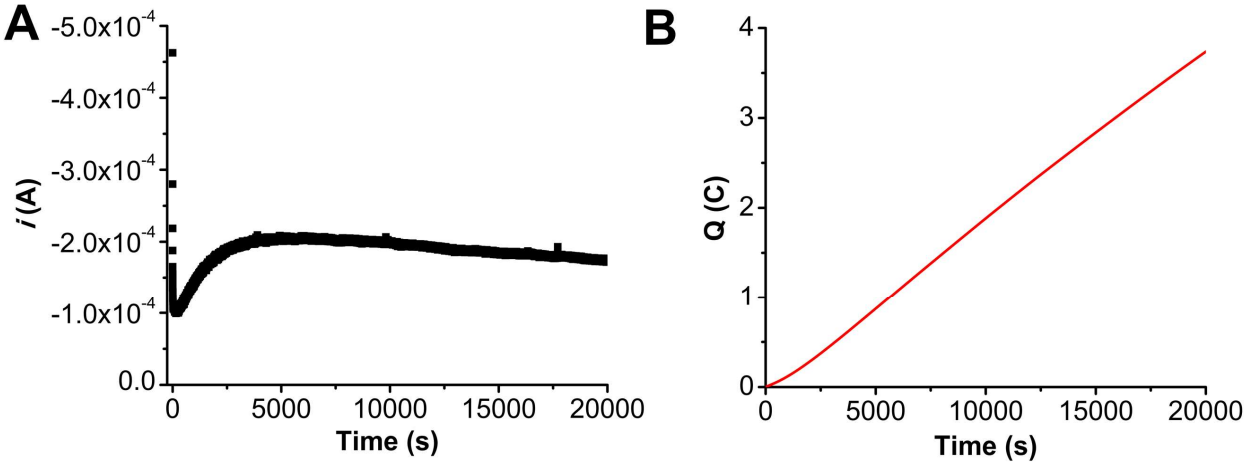

Figure S4.11. (**A**) Current versus time trace from rinse test CPE experiment. (**B**) Charge passed versus time for the CPE experiment shown in (**A**). Conditions were 1.0 M PhOH under a CO_2 atmosphere at −2.3 V vs Fc^+/Fc in 0.1 M $TBAPF_6$/DMF; working electrode was the graphite rod used in the experiment shown in **Figure S4.10** that was rinsed with DMF and not polished, counter electrode was a graphite rod, and the reference was a nonaqueous Ag/AgCl pseudoreference electrode; 0.075 M Fc was used as sacrificial oxidant.

Table S4.5. Results from CPE experiment in **Figure S4.11**.

Time (s)	Charge (coulombs)	moles (e^-)	Moles of CO	Moles of H_2
*20000	3.74	3.87×10^{-5}	<LOQ	8.17×10^{-6}
*20000	3.74	3.87×10^{-5}	<LOQ	9.33×10^{-6}
*20000	3.74	3.87×10^{-5}	<LOQ	8.50×10^{-6}

* indicates a triplicate series of injections carried out upon completion of electrolysis in **Figure S4.11**.

4.6.4 Electrochemistry with Redox Mediators

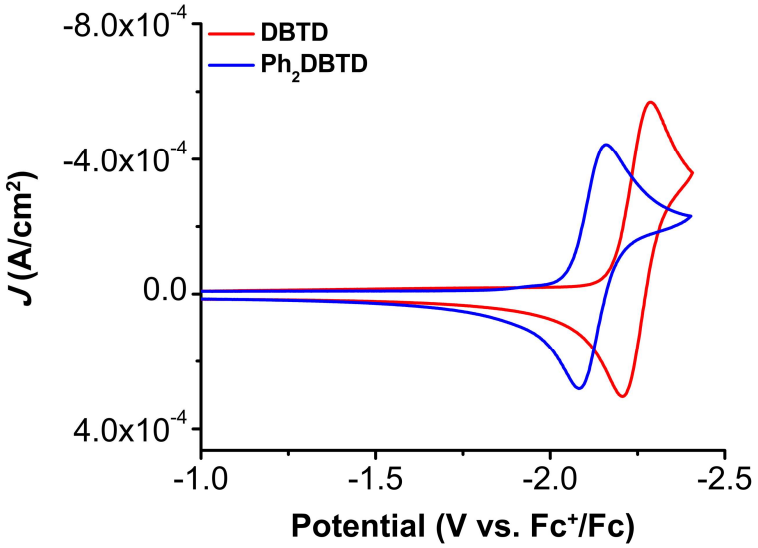

Figure S4.12. CVs of 2.5 mM DBTD and Ph_2DBTD obtained under Ar saturation conditions. Conditions: 0.1 M $TBAPF_6$/DMF; glassy carbon working electrode, glassy carbon rod counter electrode, Ag/AgCl pseudoreference electrode; referenced to Fc^+/Fc internal standard; 100 mV/s scan rate.

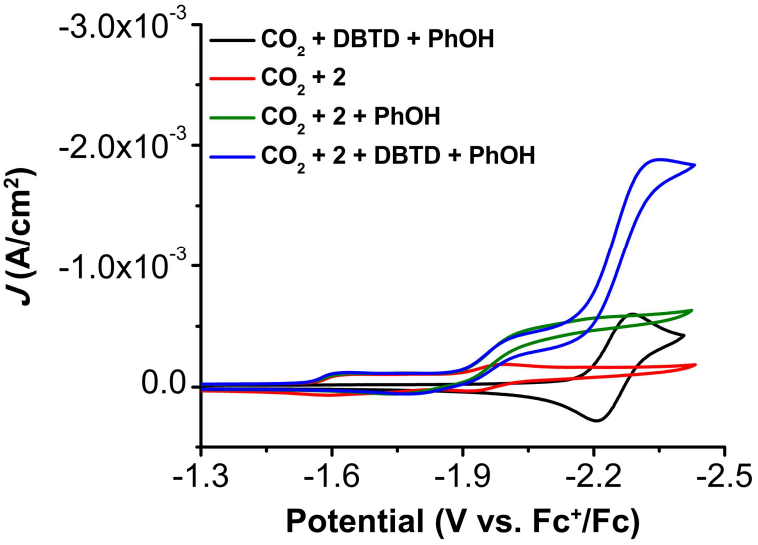

Figure S4.13. Comparison of CVs of 1.0 mM Cr(^{tbu}dhphen)Cl(H_2O) **2** with and without 2.5 mM DBTD and 0.1 M PhOH under CO_2 saturation conditions. Conditions: 0.1 M $TBAPF_6$/DMF; glassy carbon working electrode, glassy carbon rod counter electrode, Ag/AgCl pseudoreference electrode; referenced to Fc^+/Fc internal standard; 100 mV/s scan rate.

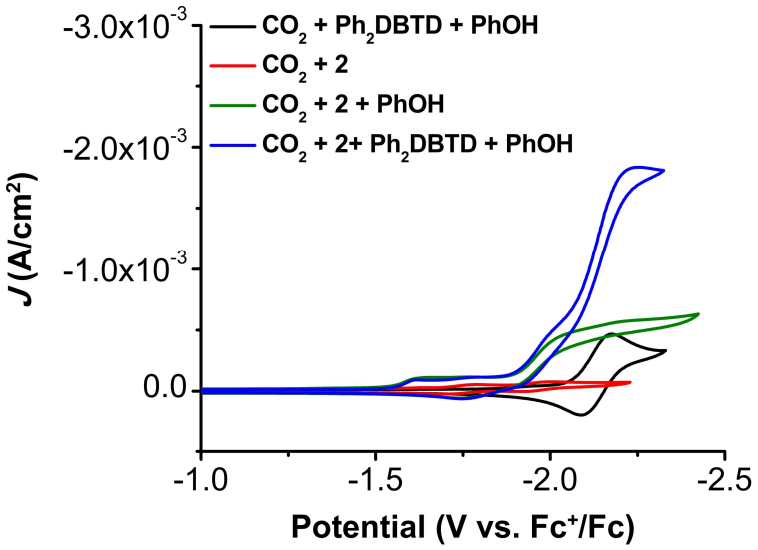

Figure S4.14. Comparison of CVs of 1.0 mM Cr(^{tbu}dhphen)Cl(H_2O) **2** with and without 2.5 mM Ph_2DBTD and 0.1 M PhOH under CO_2 saturation conditions.Conditions: 0.1 M $TBAPF_6$/DMF; glassy carbon working electrode, glassy carbon rod counter electrode, Ag/AgCl pseudoreference electrode; referenced to Fc^+/Fc internal standard; 100 mV/s scan rate.

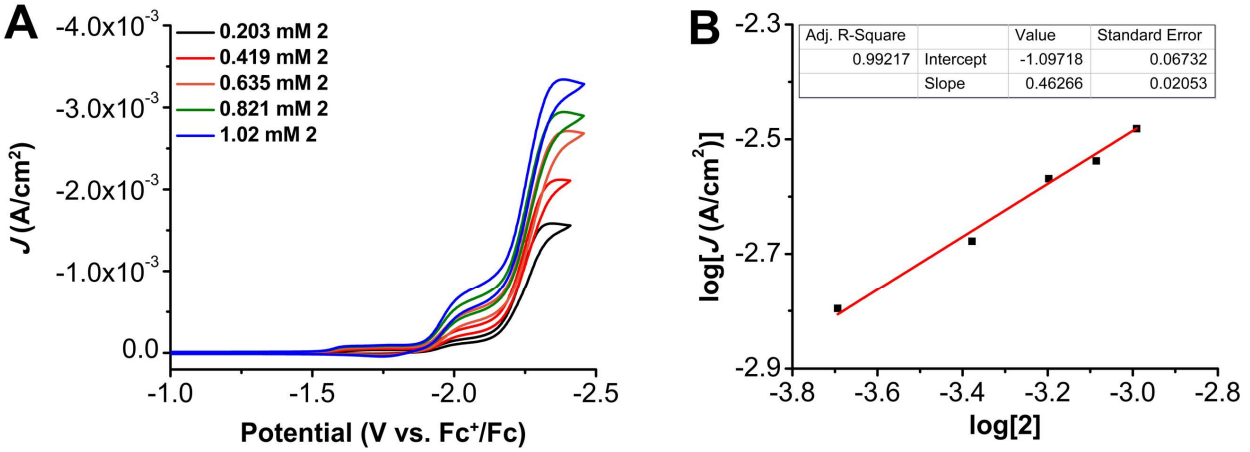

Figure S4.15. (**A**) CVs of Cr(^{tbu}dhphen)Cl(H_2O) **2** at variable concentrations, obtained under CO_2 saturation with 2.5 mM DBTD and 0.325 M PhOH. Conditions: 0.1 M $TBAPF_6$/DMF; glassy carbon working electrode, glassy carbon counter electrode, Ag/AgCl pseudoreference electrode; 100 mV/s scan rate; referenced to internal ferrocene standard. (**B**) Log-log plot from data obtained from CVs in **A** at −2.42 V vs. Fc^+/Fc.

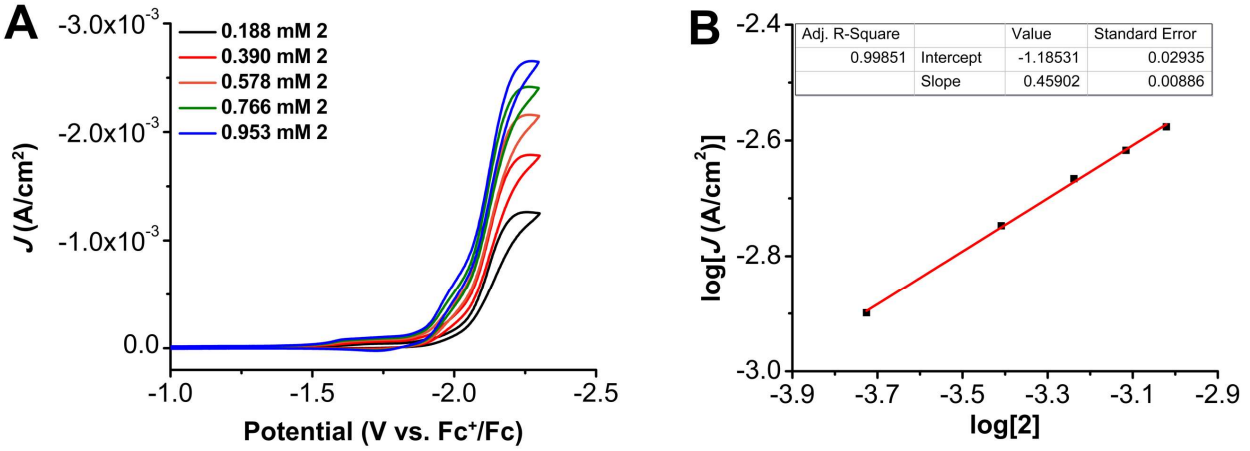

Figure S4.16. (**A**) CVs of Cr(^{tbu}dhphen)Cl(H_2O) **2** at variable concentrations, obtained under CO_2 saturation with 2.5 mM Ph_2DBTD and 0.325 M PhOH. Conditions: 0.1 M $TBAPF_6$/DMF; glassy carbon working electrode, glassy carbon counter electrode, Ag/AgCl pseudoreference electrode; 100 mV/s scan rate; referenced to internal ferrocene standard. (**B**) Log-log plot from data obtained from CVs in **A** at −2.25 V vs. Fc^+/Fc.

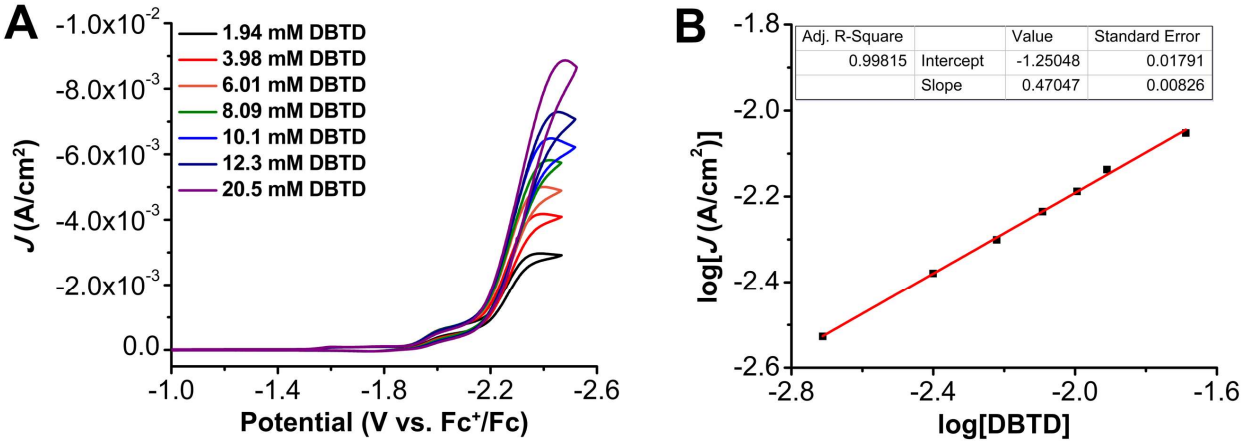

Figure S4.17. (**A**) CVs of 1.0 mM Cr(^{tbu}dhphen)Cl(H_2O) **2** with 0.325 M PhOH at variable DBTD concentrations, obtained under CO_2 saturation. Conditions: 0.1 M $TBAPF_6$/DMF; glassy carbon working electrode, glassy carbon counter electrode, Ag/AgCl pseudoreference electrode; 100 mV/s scan rate; referenced to internal ferrocene standard. (**B**) Log-log plot from data obtained from CVs in **A** at −2.46 V vs. Fc^+/Fc.

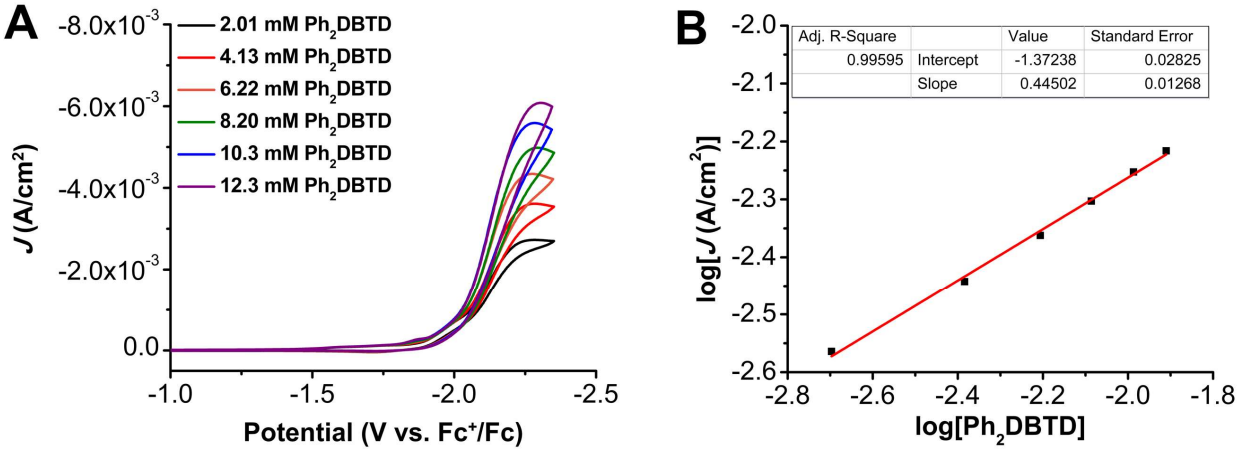

Figure S4.18. (**A**) CVs of 1.0 mM Cr(^{tbu}dhphen)Cl(H_2O) **2** with 0.325 M PhOH at variable Ph_2DBTD concentrations, obtained under CO_2 saturation. Conditions: 0.1 M $TBAPF_6$/DMF; glassy carbon working electrode, glassy carbon counter electrode, Ag/AgCl pseudoreference electrode; 100 mV/s scan rate; referenced to internal ferrocene standard. (**B**) Log-log plot from data obtained from CVs in **A** at −2.29 V vs. Fc^+/Fc.

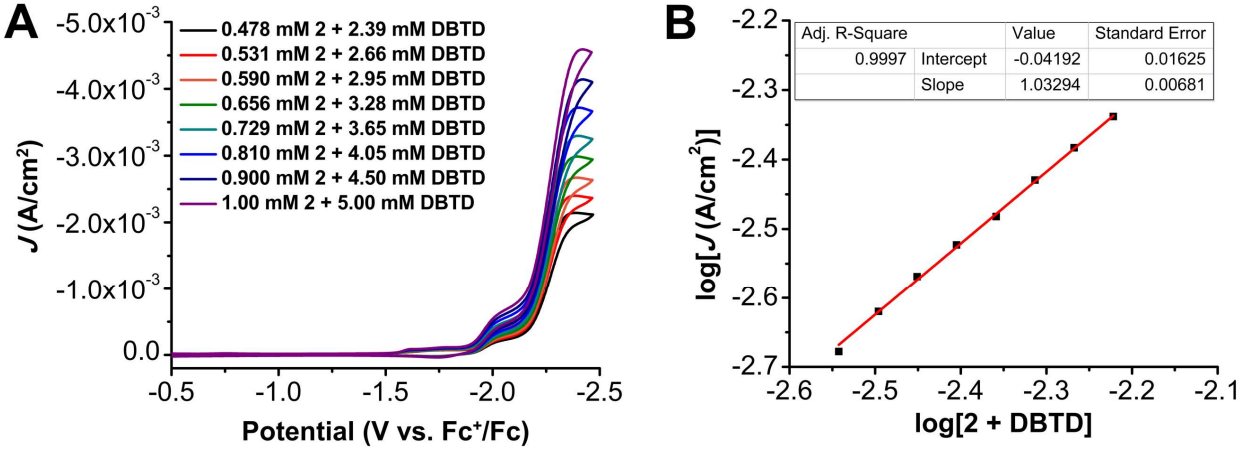

Figure S4.19. (**A**) CVs where the concentrations of Cr(^{tbu}dhphen)Cl(H_2O) **2** and DBTD were varied at a fixed 1:5 ratio of **2**:DBTD with 0.325 M PhOH under CO_2 saturation conditions. Conditions: 0.1 M $TBAPF_6$/DMF; glassy carbon working electrode, glassy carbon counter electrode, Ag/AgCl pseudoreference electrode; 100 mV/s scan rate; referenced to internal ferrocene standard. (**B**) Log-log plot from data obtained from CVs in **A** at −2.39 V vs. Fc^+/Fc.

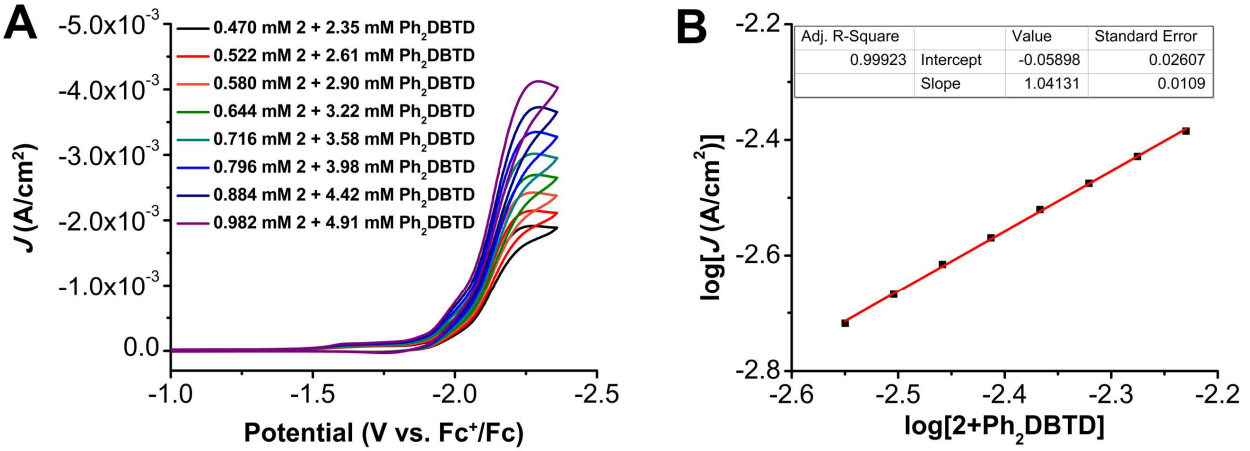

Figure S4.20. (**A**) CVs where the concentrations of Cr(^{tbu}dhphen)Cl(H_2O) **2** and Ph_2DBTD were varied at a fixed 1:5 ratio of **2**: Ph_2DBTD with 0.325 M PhOH under CO_2 saturation conditions. Conditions: 0.1 M $TBAPF_6$/DMF; glassy carbon working electrode, glassy carbon counter electrode, Ag/AgCl pseudoreference electrode; 100 mV/s scan rate; referenced to internal ferrocene standard. (**B**) Log-log plot from data obtained from CVs in **A** at −2.29 V vs. Fc^+/Fc.

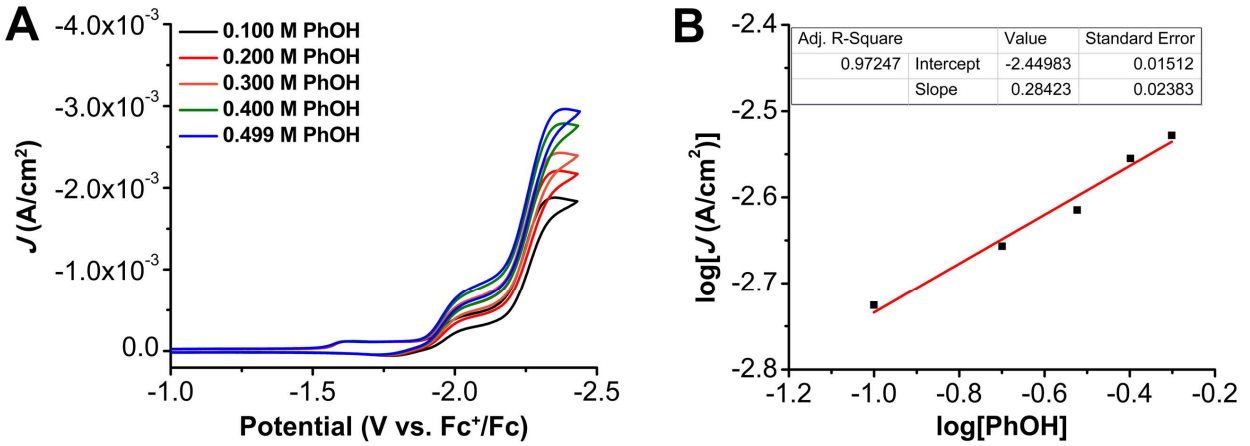

Figure S4.21. (**A**) CVs of PhOH at variable concentrations, obtained under CO_2 saturation with 1.0 mM Cr(^{tbu}dhphen)Cl(H_2O) **2** and 2.5 mM DBTD. Conditions: 0.1 M $TBAPF_6$/DMF; glassy carbon working electrode, glassy carbon counter electrode, Ag/AgCl pseudoreference electrode; 100 mV/s scan rate; referenced to internal ferrocene standard. (**B**) Log-log plot from data obtained from CVs in **A** at −2.39 V vs. Fc^+/Fc.

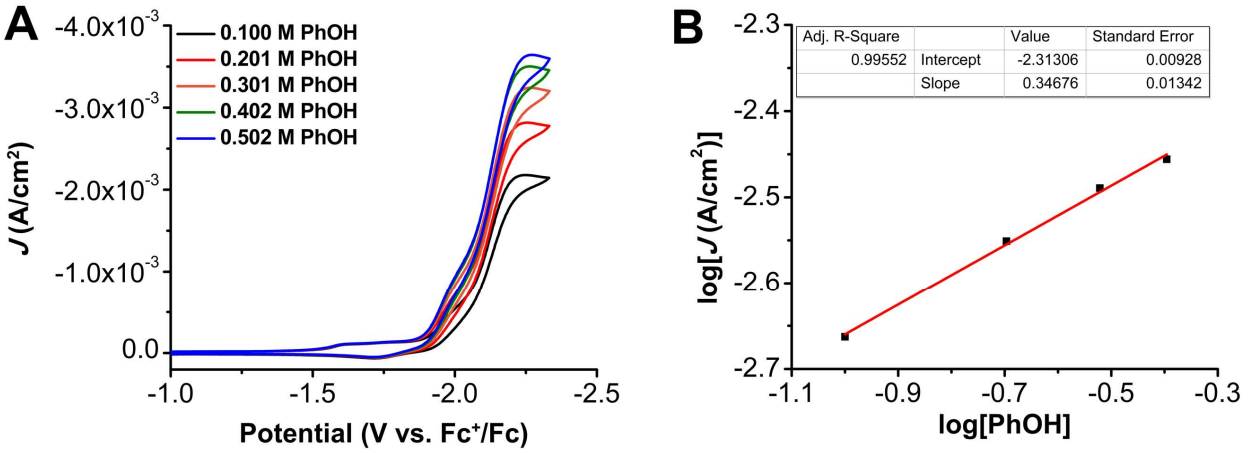

Figure S4.22. (**A**) CVs of PhOH at variable concentrations, obtained under CO_2 saturation with 1.0 mM Cr(^{tbu}dhphen)Cl(H_2O) **2** and 2.5 mM Ph_2DBTD. Conditions: 0.1 M $TBAPF_6$/DMF; glassy carbon working electrode, glassy carbon counter electrode, Ag/AgCl pseudoreference electrode; 100 mV/s scan rate; referenced to internal ferrocene standard. (**B**) Log-log plot from data obtained from CVs in **A** at −2.27 V vs. Fc^+/Fc.

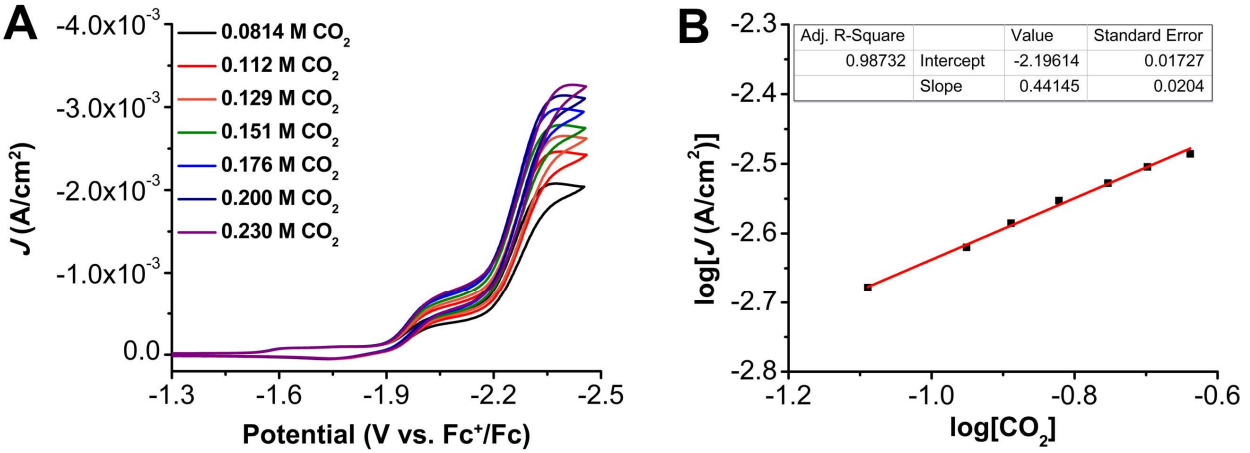

Figure S4.23. (**A**) CVs of 1.0 mM Cr(^{tbu}dhphen)Cl(H_2O) **2**, 2.5 mM DBTD, 0.325 M PhOH at varied CO_2 concentrations. Conditions: 0.1 M $TBAPF_6$/DMF; glassy carbon working electrode, glassy carbon counter electrode, Ag/AgCl pseudoreference electrode; 100 mV/s scan rate; referenced to internal ferrocene standard. (**B**) Log-log plot from data obtained from CVs in **A** at −2.42 V vs. Fc^+/Fc.

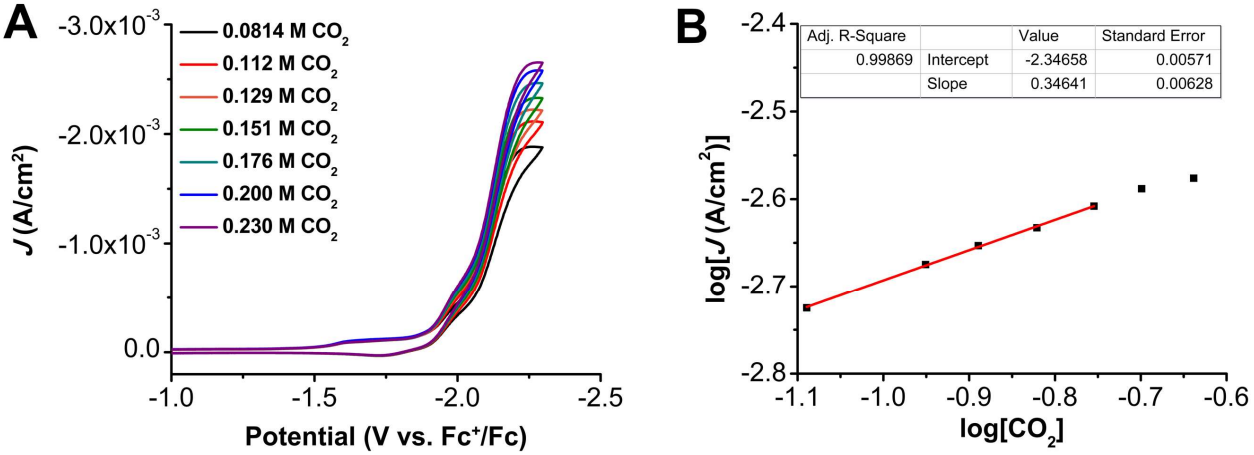

Figure S4.24. (**A**) CVs of 1.0 mM Cr(^{tbu}dhphen)Cl(H_2O) **2**, 2.5 mM Ph_2DBTD, 0.325 M PhOH at varied CO_2 concentrations. Conditions: 0.1 M $TBAPF_6$/DMF; glassy carbon working electrode, glassy carbon counter electrode, Ag/AgCl pseudoreference electrode; 100 mV/s scan rate; referenced to internal ferrocene standard. (**B**) Log-log plot from data obtained from CVs in **A** at −2.25 V vs. Fc^+/Fc.

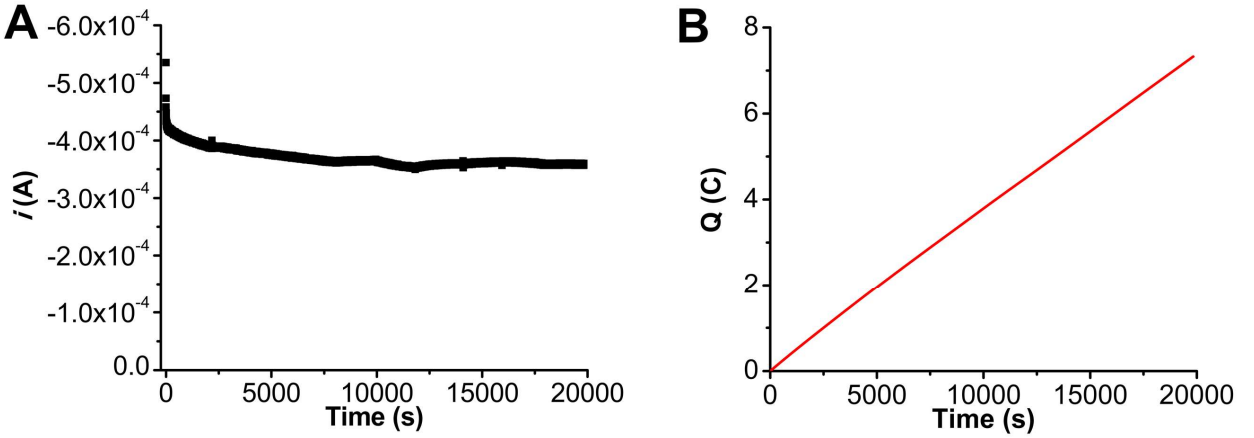

Figure S4.25. (**A**) Current versus time trace from CPE experiment for **2**+DBTD+PhOH.(**B**) Charge passed versus time for the CPE experiment shown in **A**. Conditions were 0.1 mM Cr(^{tbu}dhphen)Cl(H_2O) **2**, 0.5 mM DBTD, and 0.12 M PhOH under a CO_2 atmosphere at −2.30 V vs Fc^+/Fc in 0.1 M $TBAPF_6$/DMF; working electrode was a glassy carbon rod, counter electrode was a graphite rod, and the reference was a nonaqueous Ag/AgCl pseudoreference electrode; 0.075 M Fc was used as sacrificial oxidant.

Table S4.6. Results from CPE experiment in **Figure S4.25**, **2** + DBTD + PhOH.

Time (s)	Charge (coulombs)	moles (e^-)	Moles of CO	FE_{CO}
20000*	7.33	7.59×10^{-5}	3.22×10^{-5}	84.80
20000*	7.33	7.59×10^{-5}	3.87×10^{-5}	102.0
20000*	7.33	7.59×10^{-5}	3.60×10^{-5}	94.85

* indicates a triplicate series of injections carried out upon completion of electrolysis in **Figure S4.25**.

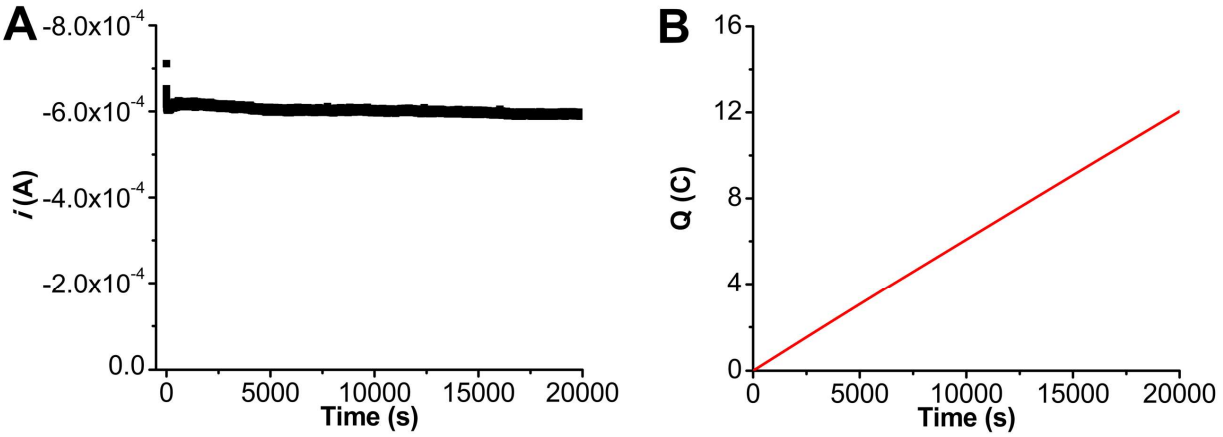

Figure S4.26. (**A**) Current versus time trace from CPE experiment for **2**+Ph_2DBTD+PhOH. (**B**) Charge passed versus time for the CPE experiment shown in **A**. Conditions were 0.1 mM Cr(^{tbu}dhphen)Cl(H_2O) **2**, 0.5 mM Ph_2DBTD, and 0.12 M PhOH under a CO_2 atmosphere at −2.20 V vs Fc^+/Fc in 0.1 M $TBAPF_6$/DMF; working electrode was a glassy carbon rod, counter electrode was a graphite rod, and the reference was a nonaqueous Ag/AgCl pseudoreference electrode; 0.075 M Fc was used as sacrificial oxidant.

Table S4.7. Results from CPE experiment in **Figure S4.26**, **2** + Ph_2DBTD + PhOH.

Time (s)	Charge (coulombs)	moles (e^-)	Moles of CO	FE_{CO}
19999*	12.0	1.25×10^{-4}	6.11×10^{-5}	97.78
19999*	12.0	1.25×10^{-4}	6.52×10^{-5}	104.5
19999*	12.0	1.25×10^{-4}	6.41×10^{-5}	102.3

* indicates a triplicate series of injections carried out upon completion of electrolysis in **Figure S4.26**.

4.6.5 Computational Data

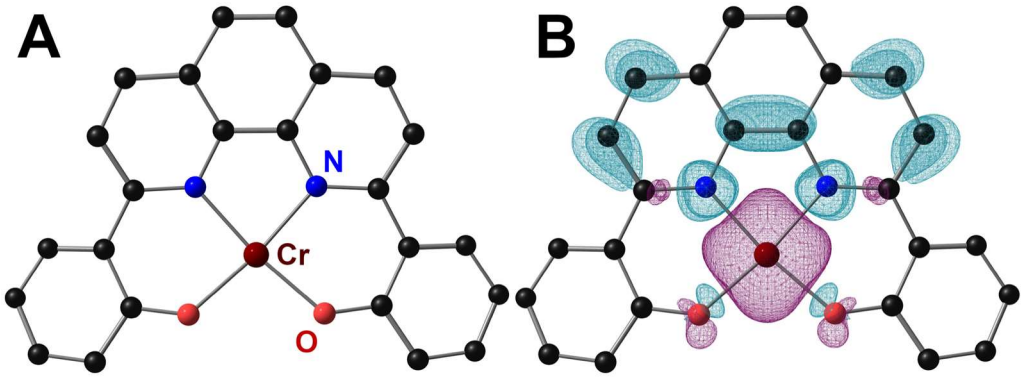

Figure S4.27. Molecular geometry of $^{4}_{0}\mathbf{Cr}^{-1}$ for phen-based complex with H atoms and tbu moieties omitted for clarity (**A**) and SCF spin density (**B**).

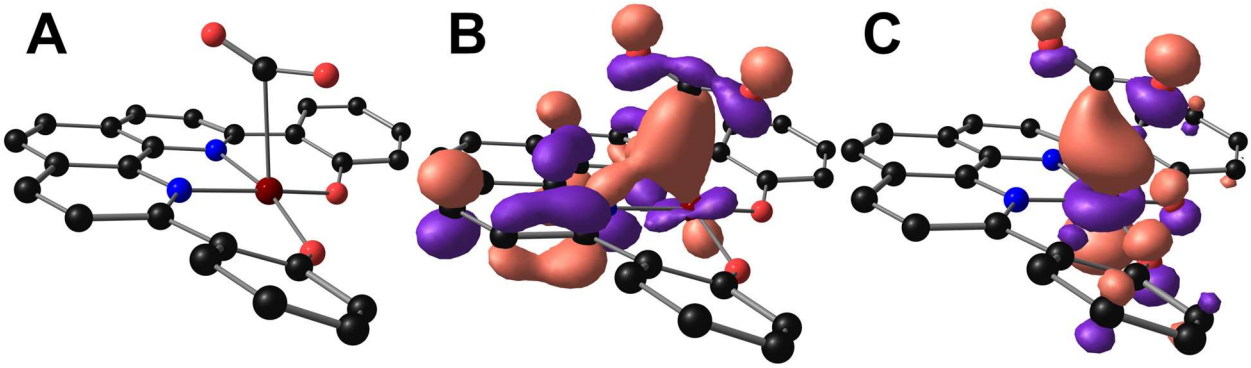

Figure S4.28. Molecular geometry of $\mathbf{TS}^{\mathbf{CO2}}$ for phen-based complex with H atoms and tbu groups omitted for clarity (**A**), Kohn-Sham orbital projection of SOMO (**B**) and SOMO^{-2} (**C**).

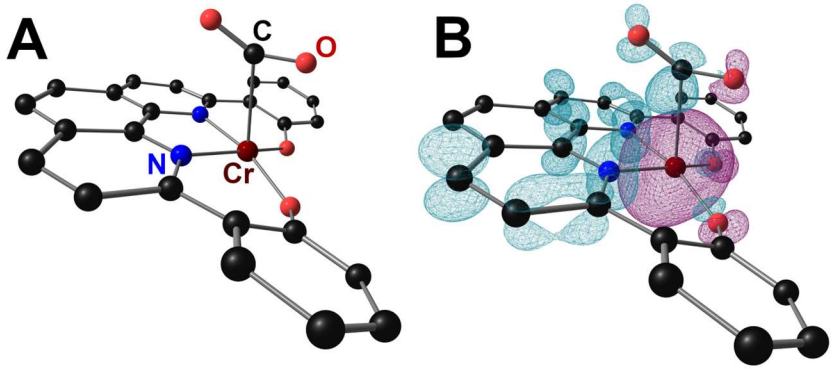

Figure S4.29. Molecular geometry of $\mathbf{TS}^{\mathbf{CO2}}$ for phen-based complex with H atoms and tbu groups omitted for clarity (**A**) and SCF spin density (**B**).

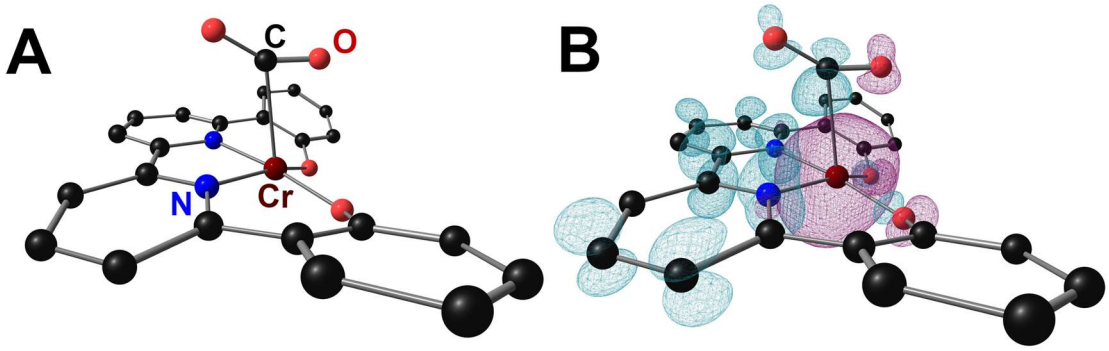

Figure S4.30. Molecular geometry of $\mathbf{TS}^{\mathbf{CO2}}_{\square}$ for bpy-based complex **1** with H atoms and tbu groups omitted for clarity (**A**) and SCF spin density (**B**).

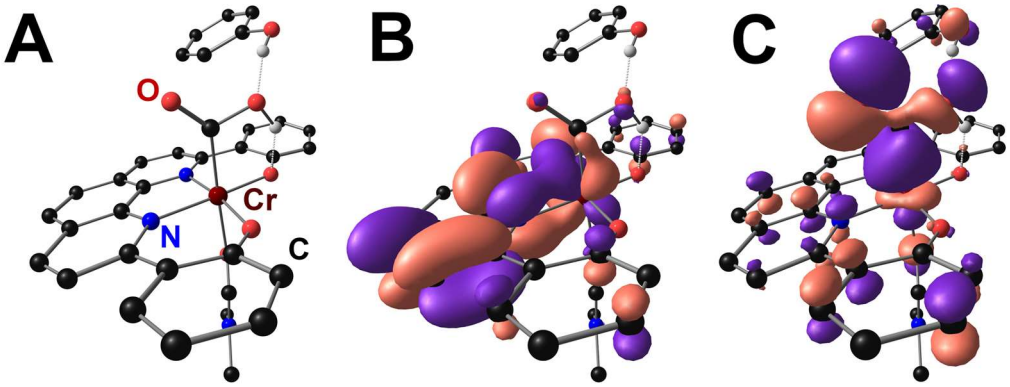

Figure S4.31. Molecular geometry of ${}^{3}_{1}\mathbf{Cr}(\mathbf{CO_2H}) \bullet (\mathbf{PhOH})^{-1}_{\square}$ for phen-based complex with select H atoms and all tbu groups omitted for clarity (**A**) with HOMO (**B**) and HOMO-4 (**C**) KS orbital projections.

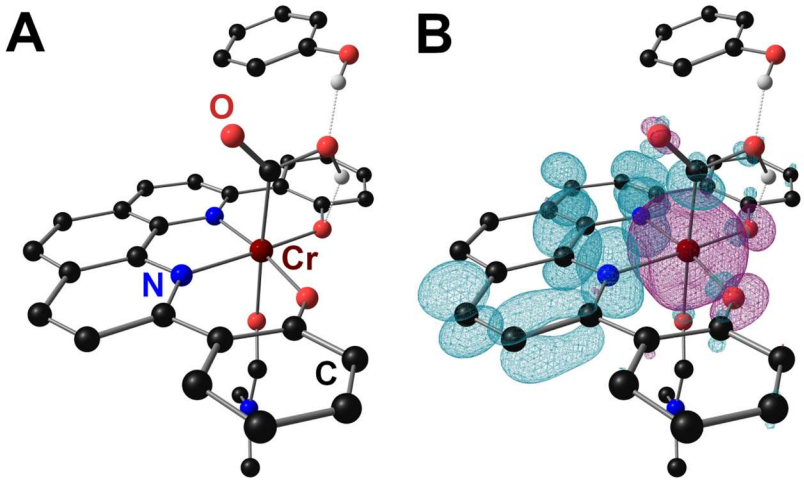

Figure S4.32. Molecular geometry of ${}^{3}_{1}\mathbf{Cr}(\mathbf{CO_2H}) \bullet (\mathbf{PhOH})^{-1}_{\square}$ for phen-based complex with select H atoms and all tbu moieties omitted for clarity (**A**) and SCF spin density (**B**).

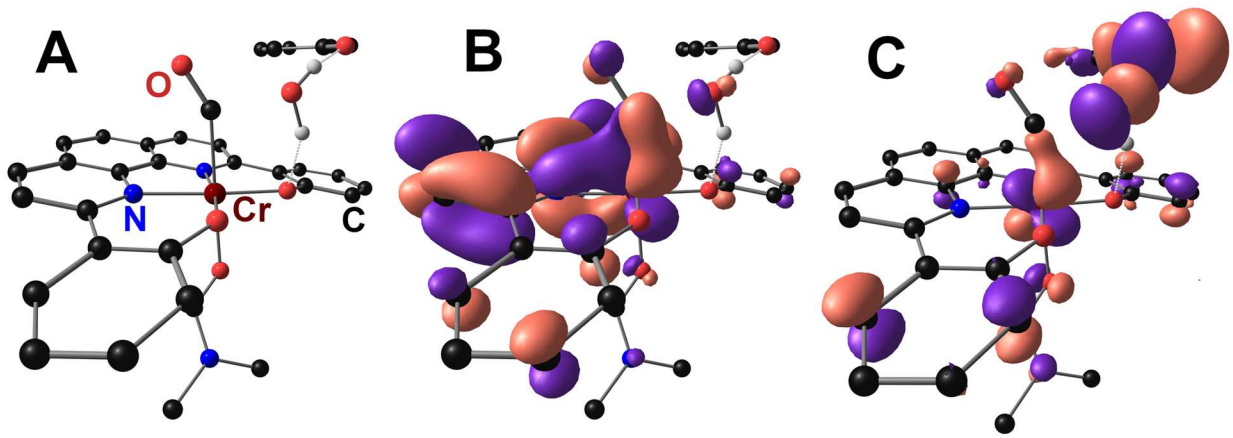

Figure S4.33. Molecular geometry of $\mathbf{TS}^{\mathbf{CO2H}}_{\square}$ for phen-based complex with select H atoms and all tbu groups omitted for clarity (**A**) with HOMO (**B**) and HOMO-4 (**C**) KS orbital projections.

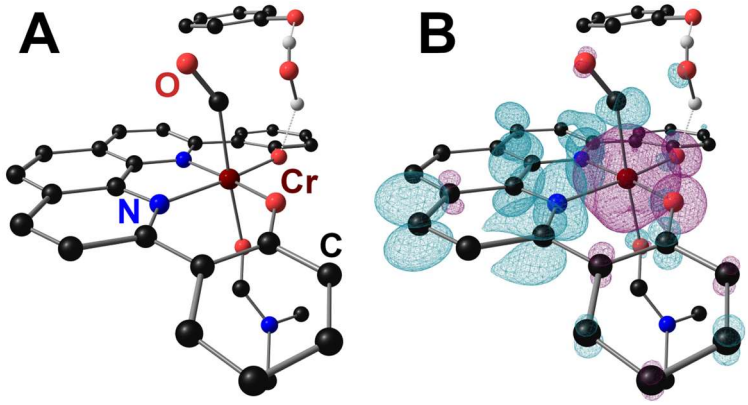

Figure S4.34. Molecular geometry of $\mathbf{TS}^{\mathbf{CO2H}}_{\square}$ for phen-based complex with select H atoms and all tbu groups omitted for clarity (**A**) with SCF spin density (**B**).

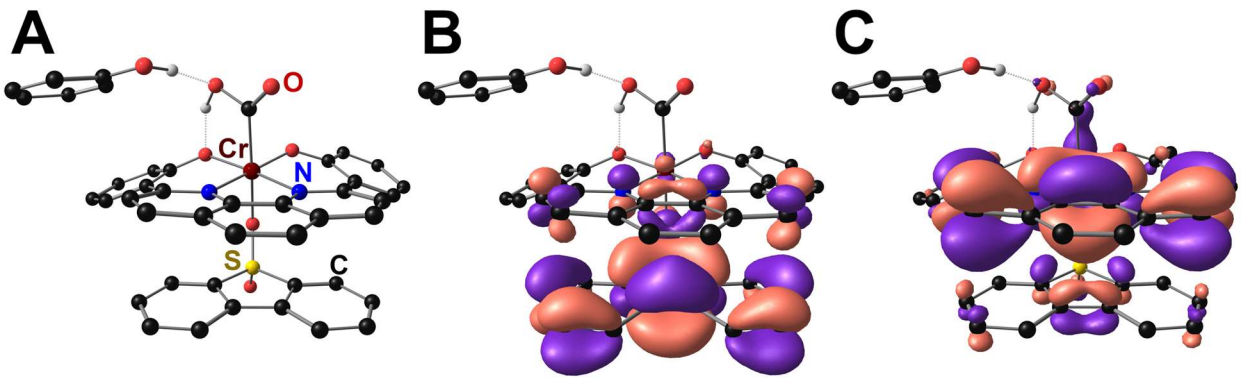

Figure S4.35. Molecular geometry of $^{\mathbf{4}}_{\mathbf{0}}\mathbf{Cr(CO_2H)(DBTD)} \bullet \mathbf{(PhOH)}^{\mathbf{-2}}_{\square}$ with select H atoms and all tbu moieties omitted for clarity (**A**) with SOMO-alpha (**B**) and HOMO-beta (**C**) KS orbital projections.

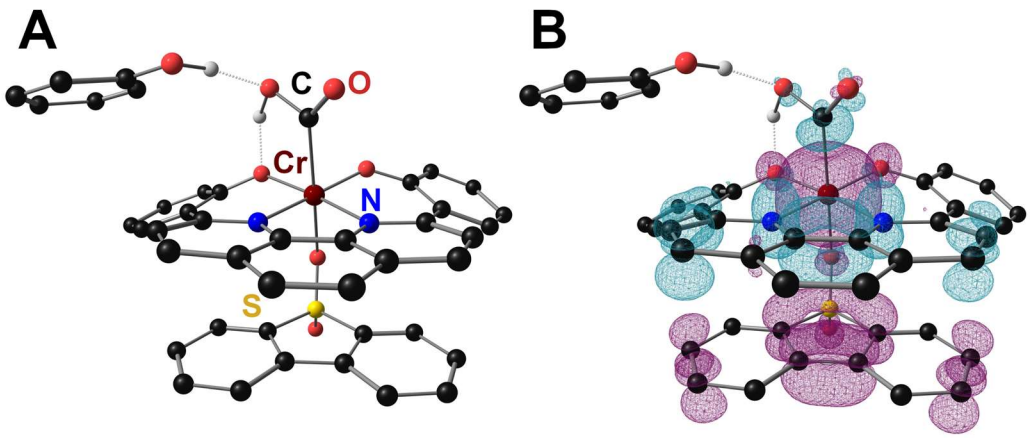

Figure S4.36. Molecular geometry of $^{4}_{0}\mathbf{Cr(CO_2H)(DBTD)} \bullet \mathbf{(PhOH)}^{-2}_{\square}$ with select H atoms and all tbu moieties omitted for clarity (**A**) and SCF spin density (**B**).

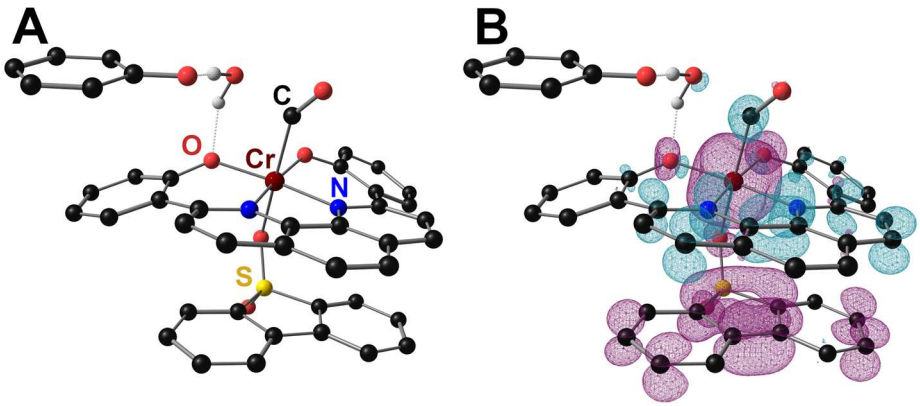

Figure S4.37. Molecular geometry of $\mathbf{TS}^{\mathbf{CO2H}}_{\mathbf{DBTD}}$ for phen-based complex with select H atoms and all tbu groups omitted for clarity (**A**) and SCF spin density (**B**).

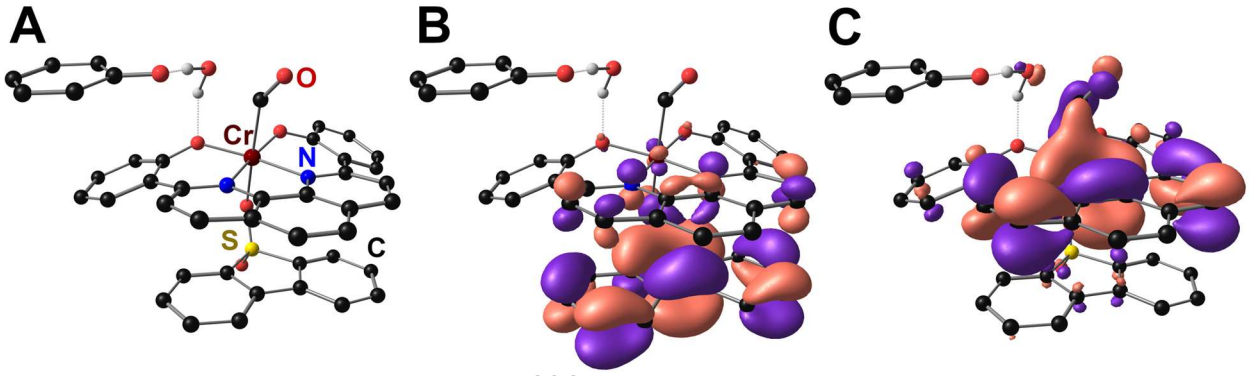

Figure S4.38. Molecular geometry of $\mathbf{TS}^{\mathbf{CO2H}}_{\mathbf{DBTD}}$ with select H atoms and all tbu moieties omitted for clarity (**A**) with SOMO-alpha (**B**) and HOMO-beta (**C**) KS orbital projections.

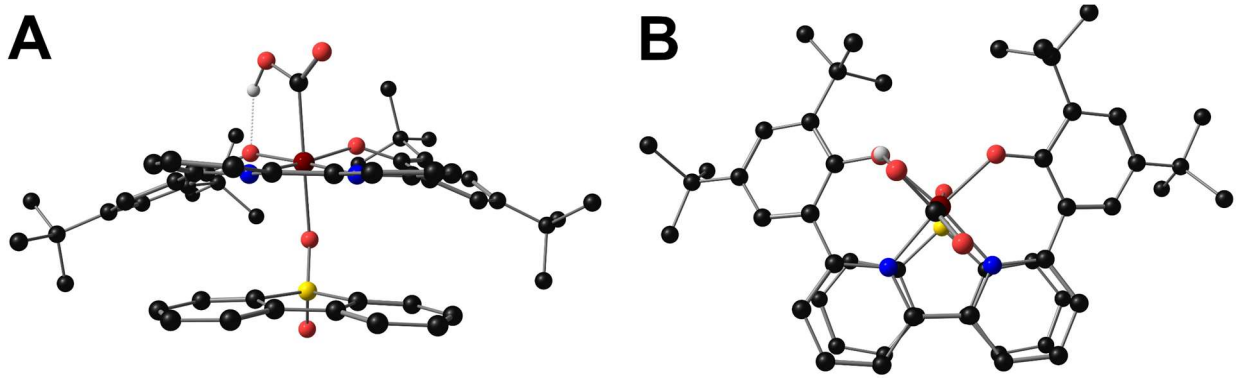

Figure S4.39. Molecular geometry of $^{4}_{0}\mathbf{Cr(CO_2H)(DBTD)}^{-2}$ for the bpy-based complex viewed from the side (**A**) and top (**B**).

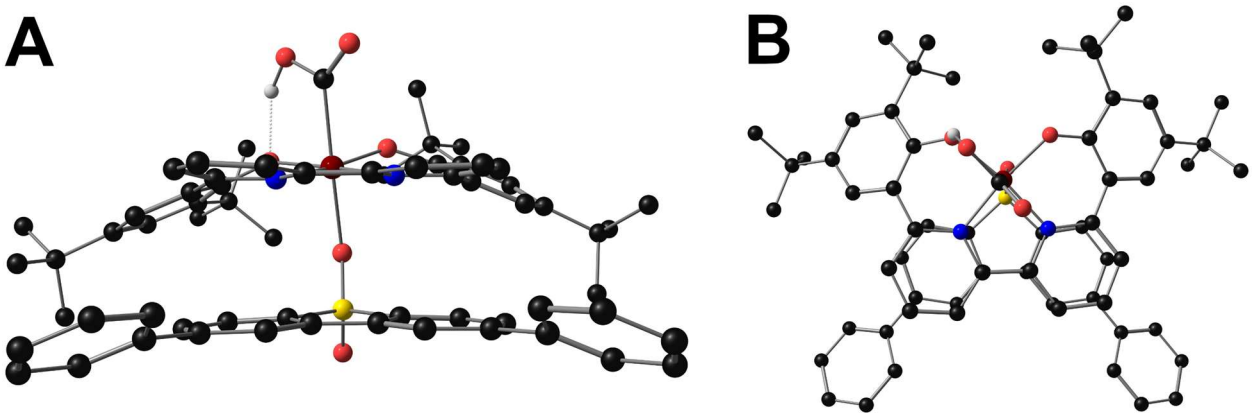

Figure S4.40. Molecular geometry of $^{4}_{0}\mathbf{Cr(CO_2H)(Ph_2DBTD)}^{-2}$ for the bpy-based complex viewed from the side (**A**) and top (**B**).

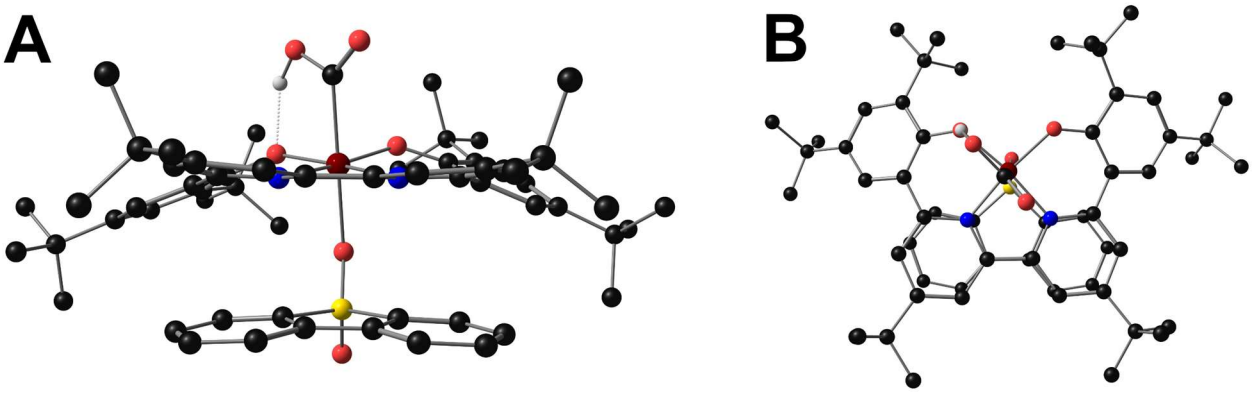

Figure S4.41. Molecular geometry of $^{4}_{0}\mathbf{Cr(CO_2H)(DBTD)}^{-2}$ for the phen-based complex viewed from the side (**A**) and top (**B**).

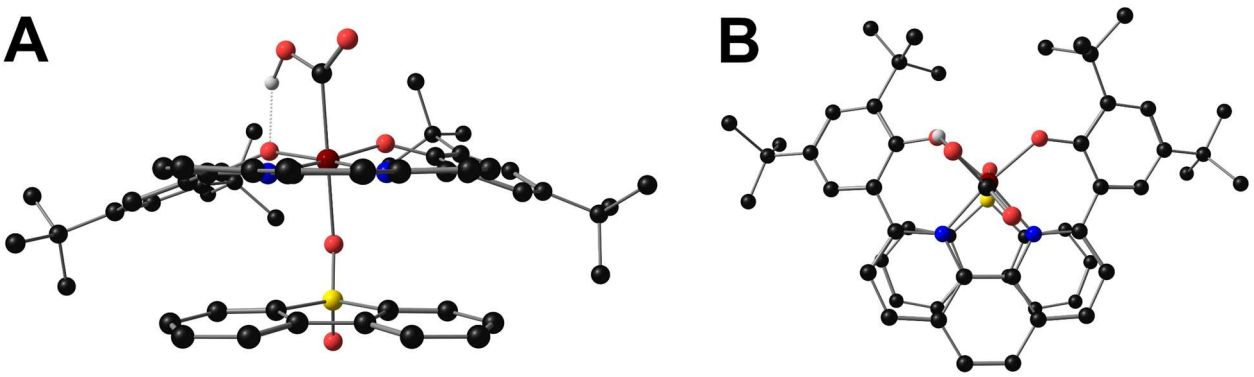

Figure S4.42. Molecular geometry of $^{\mathbf{4}}_{\mathbf{0}}\mathbf{Cr(CO_2H)(DBTD)}^{\mathbf{-2}}_{\square}$ for the *tert*-butyl substituted bpy-based complex viewed from the side (**A**) and top (**B**).

Table S4.8. Summary of calculated centroid-centroid distances for key RM bound intermediates found in **Figure 8** and **Figures S4.39-S4.42**.

Cr Complex	C_1•••C_4 (Å)	C_2•••C_5 (Å)	C_3•••C_6 (Å)
[Cr(^{tbu}dhbpy)(CO_2H)(DBTD)]$^{2-}$	3.287	3.191	3.329
[Cr(^{tbu}dhbpy)(CO_2H)(Ph_2DBTD)]$^{2-}$	3.278	3.221	3.326
[Cr(^{tbu}dhphen)(CO_2H)(DBTD)]$^{2-}$	3.259	3.183	3.266
[Cr(^{tbu}dhphen)(CO_2H)(Ph_2DBTD)]$^{2-}$	3.238	3.200	3.253
[Cr(^{tbu}dh^{tbu}bpy)(CO_2H)(DBTD)]$^{2-}$	3.316	3.169	3.361
[Cr(^{tbu}dh^{tbu}bpy)(CO_2H)(Ph_2DBTD)]$^{2-}$	3.649	3.348	3.465

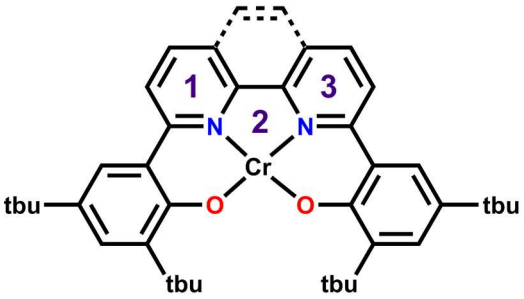

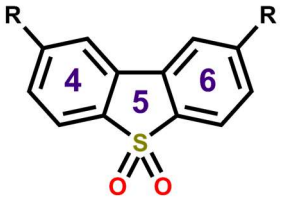

R = H or Ph

4.7 References

1. Carbon dioxide now more than 50% higher than pre-industrial levels. https://www.noaa.gov/news-release/carbon-dioxide-now-more-than-50-higher-than-pre-industrial-levels.
2. De Luna, P.; Hahn, C.; Higgins, D.; Jaffer, S. A.; Jaramillo, T. F.; Sargent, E. H., What would it take for renewably powered electrosynthesis to displace petrochemical processes? *Science* **2019,** *364* (6438), eaav3506.
3. Azcarate, I.; Costentin, C.; Robert, M.; Saveant, J. M., Through-Space Charge Interaction Substituent Effects in Molecular Catalysis Leading to the Design of the Most Efficient Catalyst of CO_2-to-CO Electrochemical Conversion. *J. Am. Chem. Soc.* **2016,** *138* (51), 16639-16644.
4. Cometto, C.; Chen, L.; Lo, P.-K.; Guo, Z.; Lau, K.-C.; Anxolabéhère-Mallart, E.; Fave, C.; Lau, T.-C.; Robert, M., Highly Selective Molecular Catalysts for the CO_2-to-CO Electrochemical Conversion at Very Low Overpotential. Contrasting Fe vs Co Quaterpyridine Complexes upon Mechanistic Studies. *ACS Catal.* **2018,** *8* (4), 3411-3417.
5. Froehlich, J. D.; Kubiak, C. P., Homogeneous CO_2 Reduction by Ni(cyclam) at a Glassy Carbon Electrode. *Iorg. Chem.* **2012,** *51* (7), 3932-3934.
6. Sampson, M. D.; Nguyen, A. D.; Grice, K. A.; Moore, C. E.; Rheingold, A. L.; Kubiak, C. P., Manganese Catalysts with Bulky Bipyridine Ligands for the Electrocatalytic Reduction of Carbon Dioxide: Eliminating Dimerization and Altering Catalysis. *J. Am. Chem. Soc.* **2014,** *136* (14), 5460-5471.
7. Hooe, S. L.; Dressel, J. M.; Dickie, D. A.; Machan, C. W., Highly Efficient Electrocatalytic Reduction of CO_2 to CO by a Molecular Chromium Complex. *ACS Catal.* **2020,** *10* (2), 1146-1151.
8. Reid, A. G.; Hooe, S. L.; Moreno, J. J.; Dickie, D. A.; Machan, C. W., Homogeneous Electrocatalytic Reduction of CO_2 by a CrN_3O Complex: Electronic Coupling with a Redox-Active Terpyridine Fragment Favors Selectivity for CO. *Inorg. Chem.* **2022,** *61* (43), 16963-16970.
9. Reid, A. G.; Moreno, J. J.; Hooe, S. H.; Baugh, K. R.; Thomas, I. H.; Dickie, D. A.; Machan, C. W., Inverse Potential Scaling in Co-Electrocatalytic Activity for CO_2 Reduction Through Redox Mediator Tuning and Catalyst Design. *Chem. Sci.* **2022,** *13*, 9595-9606.
10. Reid, A. G.; Machan, C. W., Redox Mediators in Homogeneous Co-electrocatalysis. *J. Am. Chem. Soc.* **2023,** *145* (4), 2013-2027.
11. Hooe, S. L.; Moreno, J. J.; Reid, A. G.; Cook, E. N.; Machan, C. W., Mediated Inner-Sphere Electron Transfer Induces Homogeneous Reduction of CO_2 via Through-Space Electronic Conjugation**. *Angew. Chem., Int. Ed.* **2022,** *61* (1), e202109645.
12. Hooe, S. L.; Moreno, J. J.; Reid, A. G.; Cook, E. N.; Machan, C. W., Corrigendum: Mediated Inner-Sphere Electron Transfer Induces Homogeneous Reduction of CO_2 via Through-Space Electronic Conjugation. *Angew. Chem., Int. Ed.* **2022,** *61* (25), e202205139.
13. Anson, C. W.; Stahl, S. S., Cooperative Electrocatalytic O_2 Reduction Involving Co(salophen) with p-Hydroquinone as an Electron–Proton Transfer Mediator. *J. Am. Chem. Soc.* **2017,** *139* (51), 18472-18475.
14. Badalyan, A.; Stahl, S. S., Cooperative electrocatalytic alcohol oxidation with electron-proton-transfer mediators. *Nature* **2016,** *535* (7612), 406-410.
15. Chalkley, M. J.; Del Castillo, T. J.; Matson, B. D.; Peters, J. C., Fe-Mediated Nitrogen Fixation with a Metallocene Mediator: Exploring p*K*a Effects and Demonstrating Electrocatalysis. *J. Am. Chem. Soc.* **2018,** *140* (19), 6122-6129.

16. Galvin, C. M.; Waymouth, R. M., Electron-Rich Phenoxyl Mediators Improve Thermodynamic Performance of Electrocatalytic Alcohol Oxidation with an Iridium Pincer Complex. *J. Am. Chem. Soc.* **2020,** *142* (45), 19368-19378.
17. Garrido-Barros, P.; Derosa, J.; Chalkley, M. J.; Peters, J. C., Tandem electrocatalytic N_2 fixation via proton-coupled electron transfer. *Nature* **2022,** *609* (7925), 71-76.
18. Hooe, S. L.; Cook, E. N.; Reid, A. G.; Machan, C. W., Non-covalent assembly of proton donors and p-benzoquinone anions for co-electrocatalytic reduction of dioxygen. *Chem. Sci.* **2021,** *12*, 9733-9741.
19. McLoughlin, E. A.; Armstrong, K. C.; Waymouth, R. M., Electrochemically Regenerable Hydrogen Atom Acceptors: Mediators in Electrocatalytic Alcohol Oxidation Reactions. *ACS Catal.* **2020,** *10* (19), 11654-11662.
20. Smith, P. T.; Weng, S.; Chang, C. J., An NADH-Inspired Redox Mediator Strategy to Promote Second-Sphere Electron and Proton Transfer for Cooperative Electrochemical CO_2 Reduction Catalyzed by Iron Porphyrin. *Inorg. Chem.* **2020,** *59* (13), 9270-9278.
21. Dey, S.; Masero, F.; Brack, E.; Fontecave, M.; Mougel, V., Electrocatalytic metal hydride generation using CPET mediators. *Nature* **2022,** *607* (7919), 499-506.
22. Chambers, G. M.; Wiedner, E. S.; Bullock, R. M., H_2 Oxidation Electrocatalysis Enabled by Metal-to-Metal Hydrogen Atom Transfer: A Homolytic Approach to a Heterolytic Reaction. *Angew. Chem., Int. Ed.* **2018,** *57* (41), 13523-13527.
23. Gerken, J. B.; Stahl, S. S., High-Potential Electrocatalytic O_2 Reduction with Nitroxyl/NO_x Mediators: Implications for Fuel Cells and Aerobic Oxidation Catalysis. *ACS Cent. Sci.* **2015,** *1* (5), 234-243.
24. Alcázar-Fabra, M.; Navas, P.; Brea-Calvo, G., Coenzyme Q biosynthesis and its role in the respiratory chain structure. *Biochim. Biophys. Acta - Bioenerg* **2016,** *1857* (8), 1073-1078.
25. Schneider, C. R.; Shafaat, H. S., An internal electron reservoir enhances catalytic CO_2 reduction by a semisynthetic enzyme. *ChemComm* **2016,** *52* (64), 9889-9892.
26. Johnson, D. C.; Dean, D. R.; Smith, A. D.; Johnson, M. K., STRUCTURE, FUNCTION, AND FORMATION OF BIOLOGICAL IRON-SULFUR CLUSTERS. *Annu. Rev. Biochem.* **2005,** *74*, 247-81.
27. Ibrahim, I. M.; Wu, H.; Ezhov, R.; Kayanja, G. E.; Zakharov, S. D.; Du, Y.; Tao, W. A.; Pushkar, Y.; Cramer, W. A.; Puthiyaveetil, S., An evolutionarily conserved iron-sulfur cluster underlies redox sensory function of the Chloroplast Sensor Kinase. *Commun. Biol.* **2020,** *3* (1), 13.
28. Chen, H.; Simoska, O.; Lim, K.; Grattieri, M.; Yuan, M.; Dong, F.; Lee, Y. S.; Beaver, K.; Weliwatte, S.; Gaffney, E. M.; Minteer, S. D., Fundamentals, Applications, and Future Directions of Bioelectrocatalysis. *Chem. Rev.* **2020,** *120* (23), 12903-12993.
29. Kertesz, M., Pancake Bonding: An Unusual Pi-Stacking Interaction. *Chem. Eur. J.* **2019,** *25* (2), 400-416.
30. Popowski, Y.; Moreno, J. J.; Nichols, A. W.; Hooe, S. L.; Bouchey, C. J.; Rath, N. P.; Machan, C. W.; Tolman, W. B., Mechanistic insight into initiation and regioselectivity in the copolymerization of epoxides and anhydrides by Al complexes. *Chem. Comm.* **2020,** *56* (90), 14027-14030.
31. Moreno, J. J.; Hooe, S. L.; Machan, C. W., DFT Study on the Electrocatalytic Reduction of CO_2 to CO by a Molecular Chromium Complex. *Inorg. Chem.* **2021,** *60* (6), 3635-3650.
32. Hooe, S. L.; Rheingold, A. L.; Machan, C. W., Electrocatalytic Reduction of Dioxygen to Hydrogen Peroxide by a Molecular Manganese Complex with a Bipyridine-Containing Schiff Base Ligand. *J. Am. Chem. Soc.* **2018,** *140* (9), 3232-3241.
33. Nichols, A. W.; Chatterjee, S.; Sabat, M.; Machan, C. W., Electrocatalytic Reduction of CO_2 to Formate by an Iron Schiff Base Complex. *Inorg. Chem.* **2018,** *57* (4), 2111-2121.

34. Hooe, S. L.; Machan, C. W., Dioxygen Reduction to Hydrogen Peroxide by a Molecular Mn Complex: Mechanistic Divergence between Homogeneous and Heterogeneous Reductants. *J. Am. Chem. Soc.* **2019,** *141* (10), 4379-4387.
35. Frisch, M. J.; Trucks, G. W.; Schlegel, H. B.; Scuseria, G. E.; Robb, M. A.; Cheeseman, J. R.; Scalmani, G.; Barone, V.; Petersson, G. A.; Nakatsuji, H.; Li, X.; Caricato, M.; Marenich, A. V.; Bloino, J.; Janesko, B. G.; Gomperts, R.; Mennucci, B.; Hratchian, H. P.; Ortiz, J. V.; Izmaylov, A. F.; Sonnenberg, J. L.; Williams; Ding, F.; Lipparini, F.; Egidi, F.; Goings, J.; Peng, B.; Petrone, A.; Henderson, T.; Ranasinghe, D.; Zakrzewski, V. G.; Gao, J.; Rega, N.; Zheng, G.; Liang, W.; Hada, M.; Ehara, M.; Toyota, K.; Fukuda, R.; Hasegawa, J.; Ishida, M.; Nakajima, T.; Honda, Y.; Kitao, O.; Nakai, H.; Vreven, T.; Throssell, K.; Montgomery Jr., J. A.; Peralta, J. E.; Ogliaro, F.; Bearpark, M. J.; Heyd, J. J.; Brothers, E. N.; Kudin, K. N.; Staroverov, V. N.; Keith, T. A.; Kobayashi, R.; Normand, J.; Raghavachari, K.; Rendell, A. P.; Burant, J. C.; Iyengar, S. S.; Tomasi, J.; Cossi, M.; Millam, J. M.; Klene, M.; Adamo, C.; Cammi, R.; Ochterski, J. W.; Martin, R. L.; Morokuma, K.; Farkas, O.; Foresman, J. B.; Fox, D. J. *Gaussian 16 Rev. B.01*, Wallingford, CT, 2016.
36. Becke, A. D., Density-functional thermochemistry. III. The role of exact exchange. *J. Chem. Phys.* **1993,** *98* (7), 5648-5652.
37. Lee, C.; Yang, W.; Parr, R. G., Development of the Colle-Salvetti correlation-energy formula into a functional of the electron density. *Phys. Rev. B* **1988,** *37* (2), 785-789.
38. Vosko, S. H.; Wilk, L.; Nusair, M., Accurate spin-dependent electron liquid correlation energies for local spin density calculations: a critical analysis. *Can. J. Phys.* **1980,** *58* (8), 1200-1211.
39. Stephens, P. J.; Devlin, F. J.; Chabalowski, C. F.; Frisch, M. J., Ab Initio Calculation of Vibrational Absorption and Circular Dichroism Spectra Using Density Functional Force Fields. *J. Phys. Chem.* **1994,** *98* (45), 11623-11627.
40. Weigend, F.; Ahlrichs, R., Balanced basis sets of split valence, triple zeta valence and quadruple zeta valence quality for H to Rn: Design and assessment of accuracy. *Phys. Chem. Chem. Phys.* **2005,** *7* (18), 3297-3305.
41. Weigend, F., Accurate Coulomb-fitting basis sets for H to Rn. *Phys. Chem. Chem. Phys.* **2006,** *8* (9), 1057-1065.
42. Grimme, S.; Antony, J.; Ehrlich, S.; Krieg, H., A consistent and accurate ab initio parametrization of density functional dispersion correction (DFT-D) for the 94 elements H-Pu. *J. Chem. Phys.* **2010,** *132* (15), 154104.
43. Grimme, S.; Ehrlich, S.; Goerigk, L., Effect of the damping function in dispersion corrected density functional theory. *J. Comput. Chem.* **2011,** *32* (7), 1456-1465.
44. Moreno, J. J.; Hooe, S. L.; Machan, C. W., Correction to DFT Study on the Electrocatalytic Reduction of CO2 to CO by a Molecular Chromium Complex. *Inorg. Chem.* **2022**.
45. Pegis, M. L.; Wise, C. F.; Martin, D. J.; Mayer, J. M., Oxygen Reduction by Homogeneous Molecular Catalysts and Electrocatalysts. *Chem. Rev.* **2018,** *118* (5), 2340-2391.
46. Pegis, M. L.; Roberts, J. A. S.; Wasylenko, D. J.; Mader, E. A.; Appel, A. M.; Mayer, J. M., Standard Reduction Potentials for Oxygen and Carbon Dioxide Couples in Acetonitrile and *N,N*-Dimethylformamide. *Inorg. Chem.* **2015,** *54* (24), 11883-11888.
47. Nielsen, M. F.; Hammerich, O.; Rise, F.; Gogoll, A.; Undheim, K.; Wang, D. N.; Christensen, S. B., The Effect of Hydrogen Bonding between Methyl-Substituted Phenols and Dipolar Aprotic Solvents on the Rate Constants for. *Acta. Chem. Scan.* **1992,** *46*, 883-896.
48. Roy, S.; Sharma, B.; Pécaut, J.; Simon, P.; Fontecave, M.; Tran, P. D.; Derat, E.; Artero, V., Molecular Cobalt Complexes with Pendant Amines for Selective Electrocatalytic Reduction of Carbon Dioxide to Formic Acid. *J. Am. Chem. Soc.* **2017,** *139* (10), 3685-3696.

49. Matsubara, Y., Unified Benchmarking of Electrocatalysts in Noninnocent Second Coordination Spheres for CO_2 Reduction. *ACS Energy Lett.* **2019,** *4* (8), 1999-2004.
50. Costentin, C.; Drouet, S.; Robert, M.; Savéant, J.-M., Turnover Numbers, Turnover Frequencies, and Overpotential in Molecular Catalysis of Electrochemical Reactions. Cyclic Voltammetry and Preparative-Scale Electrolysis. *J. Am. Chem. Soc.* **2012,** *134* (27), 11235-11242.
51. Costentin, C.; Drouet, S.; Robert, M.; Savéant, J.-M., Correction to Turnover Numbers, Turnover Frequencies, and Overpotential in Molecular Catalysis of Electrochemical Reactions. Cyclic Voltammetry and Preparative-Scale Electrolysis. *J. Am. Chem. Soc.* **2012,** *134* (48), 19949-19950.
52. Baur, J. E., Chapter 19 Diffusion Coefficients. In *Handbook of Electrochemistry*, Zoski, C. G., Ed. Elsevier: 2007; pp 829-848.
53. Elgrishi, N.; McCarthy, B. D.; Rountree, E. S.; Dempsey, J. L., Reaction Pathways of Hydrogen-Evolving Electrocatalysts: Electrochemical and Spectroscopic Studies of Proton-Coupled Electron Transfer Processes. *ACS Catal.* **2016,** *6* (6), 3644-3659.
54. Barone, V.; Cossi, M., Quantum Calculation of Molecular Energies and Energy Gradients in Solution by a Conductor Solvent Model. *J. Phys. Chem. A* **1998,** *102* (11), 1995-2001.
55. Ribeiro, R. F.; Marenich, A. V.; Cramer, C. J.; Truhlar, D. G., Use of Solution-Phase Vibrational Frequencies in Continuum Models for the Free Energy of Solvation. *J. Phys. Chem. B* **2011,** *115* (49), 14556-14562.
56. Luchini, G.; Alegre-Requena, J.; Funes-Ardoiz, I.; Rodríguez-Guerra, J.; Chen, J. T.; Paton, R. *Goodvibes v3.0.1*, 2019.
57. Bruker *Saint; SADABS;TWINABS; APEX3*, Bruker AXS Inc.: Madison, Wisconsin, USA, 2012.
58. Sheldrick, G., SHELXT - Integrated space-group and crystal-structure determination. *Acta Cryst.* **2015,** *71* (1), 3-8.
59. Dolomanov, O. V.; Bourhis, L. J.; Gildea, R. J.; Howard, J. A. K.; Puschmann, H., OLEX2: a complete structure solution, refinement and analysis program. *J. Appl. Cryst.* **2009,** *42* (2), 339-341.
60. Sheldrick, G. M. *Cell_now*, version 2008/4; Georg-August-Universität Göttingen: Göttingen, Germany, 2008.
61. Spek, A., Structure validation in chemical crystallography. *Acta Cryst.* **2009,** *65* (2), 148-155.
62. Grant, D. H., Paramagnetic Susceptibility by NMR: The "Solvent Correction" Reexamined. *J. Chem. Educ.* **1995,** *72* (1), 39.
63. Bain, G. A.; Berry, J. F., Diamagnetic corrections and Pascal's constants. *J. Chem. Educ.* **2008,** *85* (4), 532-536.
64. Sathrum, A. J.; Kubiak, C. P., Kinetics and Limiting Current Densities of Homogeneous and Heterogeneous Electrocatalysts. *J. Phys. Chem. Lett.* **2011,** *2* (18), 2372-2379.

Chapter 5

Improving Co-Electrocatalytic Carbon Dioxide Reduction by Optimizing the Relative Potentials of Redox Mediatory and Catalyst

This chapter contains material for upcoming publications and has been incorporated with consent of all current contributing authors. These authors include Ethan A. Zelenke, Megan E. Moberg, Diane A. Dickie, and Charles W. Machan

5.1 Abstract

The effects of fixing redox mediator (RM) reduction potential relative to a series of Cr-centered complexes capable of the reduction of CO_2 to CO is disclosed. The greatest co-electrocatalytic activity enhancement is observed when the reduction potential of catalyst and RM are identical, inferring that controlling the speciation of the Cr complex relative to RM activation is essential for improving catalytic performance. In all cases, the potential where co-catalytic activity is observed matches the reduction potential of the RM, regardless of the relative reduction potential of the Cr complex.

5.2 Introduction

As the global energy demand continues to grow, so have anthropogenic emissions of carbon dioxide (CO_2), with a corresponding increasing severity of associated climate change effects.[1, 2] One possibility for mitigating these negative effects is through the development of electrocatalytic systems capable of the carbon dioxide reduction reaction (CO_2RR), which can use renewable electricity to produce useful carbon-containing products.[3, 4] The study of molecular catalysts for the CO_2RR provides fundamental understanding of how the catalytic active sites can be tuned through mechanistic study. While molecular catalysts for CO_2 reduction have been studied for decades,[5-13] the incorporation of redox mediators (RMs) to assist in the transfer of electrons (often with protons) to catalyst active sites is a growing area of interest in the field.[14] While examples of RMs used with catalysts for the reduction of CO_2 are currently limited,[15-20] a few additional examples exist for the electrocatalytic conversion of a variety of small molecules.[20-31]

Previously, the co-electrocatalytic reduction of CO_2 with Cr-centered catalysts derived from dianionic N_2O_2 ligand frameworks and sulfone-based RMs has been studied.[16-18] Initial studies used Cr(^{tbu}dhbpy)Cl(H_2O) as the catalyst and dibenzothiophene 5,5-dioxide (DBTD;

Figure 1) as the RM, where CO_2 was reduced to carbon monoxide (CO) under both aprotic and protic conditions.[16] It was proposed that the DBTD RM operates via an inner-sphere electron transfer mechanism, where the reduced RM, $[RM]^-$, binds to the intermediate resting state of the intrinsic catalytic cycle, $[Cr–CO_2H]^-$. This binding occurs via an equilibrium displacement of an axial solvent molecule, the favorability of which is due to three forces: Cr–O bond formation, dispersion interactions, and through-space electronic conjugation (specifically pancake bonding (PB) under protic conditions). A PB interaction is defined by two highly delocalized π-based radicals with short vertical distance and high atom-atom overlap, differentiating it from weaker π-π stacking interactions.[32-35] The resulting $[RM–Cr–CO_2H]^{2-}$ adduct has a lower barrier for the rate-determining step of the reaction (C–OH bond cleavage), so the favorability of this pre-equilibrium step controls the observed activity. After this initial report, additional studies interrogated the role of ligand and RM aromaticity on favoring the co-catalytic mechanism of the CO_2RR by comparing the experimentally observed activity of catalysts Cr(^{tbu}dhphen)Cl(H_2O) (**2**) and Cr(^{tbu}dh^{tbu}bpy)Cl(H_2O) (**3**) (**Figure 1**) with a series of DBTD-derived RMs.[17, 18] From these results, it was proposed that the PB interaction of the key intermediate of the co-catalytic cycle could be strengthened when the reduction potential of the RM is closer to that of the catalyst and when there is less steric clash between RM and catalyst, since these changes should favor vertical atom-atom overlap.

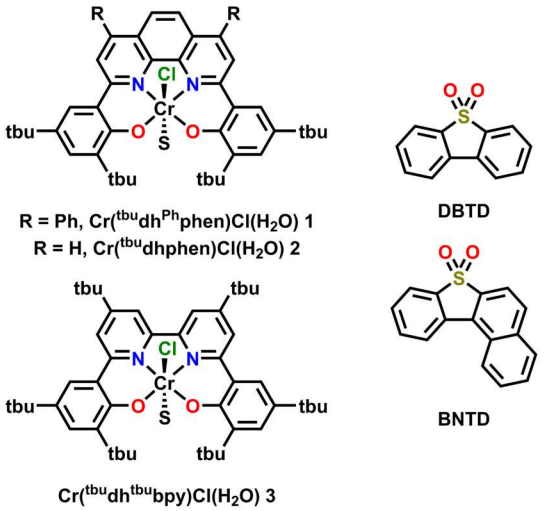

Figure 5.1. Structures of Cr catalysts and RMs discussed here.

Here, the relative position of Cr catalytic potential is varied with respect to RM potential, demonstrating that co-electrocatalytic activity is pinned to the RM potential under all conditions, even when the catalyst is formally reduced at more negative potentials. A new Cr-centered catalyst with phenyl groups substituted to the ligand phenanthroline backbone, Cr(^{tbu}dh^{Ph}phen)Cl(H_2O) (**1**) is reported, as well as a new RM, benzonaphthothiophene-7,7-dioxide (BNTD), which is tested with complexes **1**, **2**, and **3** (**Figure 5.1**). Interestingly, these studies suggest that the optimal co-electrocatalytic response occurs when the RM and Cr catalyst are potential matched, implying that tuning relative concentrations in the reaction-diffusion layer offers additional reaction control.

5.3 Results

A di-phenyl substituted phenanthroline ligand framework, 6,6′-di(3,5-di-*tert*-butyl-2-hydroxybenzene)-4,7-di-phenyl-1,10-phenanthroline (^{tbu}dh^{Ph}phen(H_2)) was synthesized from 2,9-dichloro-4,7-diphenyl-1,10-phenanthroline using Pd-catalyzed cross-coupling methods. Subsequent metalation to make Cr(^{tbu}dh^{Ph}phen)Cl(H_2O) (**1**) used a modified literature procedure

and was characterized by UV-vis (**Figure S5.3**), NMR (**Table S5.2**), electrospray ionization-mass spectrometry, and microanalysis.

5.3.1 Electrochemistry of Cr Catalysts

Cyclic voltammetry (CV) experiments were performed on **1** in *N,N*-dimethylformamide (DMF) with 0.1 M tetrabutylammonium hexafluorophosphate ($TBAPF_6$) as the supporting electrolyte. Under argon (Ar) saturation conditions, **1** exhibits three redox features ($E_{1/2}$ = –1.55 and –1.93 V and E_p = –1.70 V versus ferrocenium/ferrocene (Fc^+/Fc)); minimal changes are observed under CO_2 saturation conditions (**Figure S5.6A**). This redox response is similar to what was previously observed for Cr-centered catalysts with structurally related N_2O_2 ligand frameworks[17, 18, 36]: the first two redox features relate to a chloride-loss equilibrium through solvent displacement and the molecule is reduced by two electrons overall by –1.93 V vs Fc^+/Fc.

Upon the addition of phenol (PhOH) under Ar saturation, only minor changes are observed (**Figure S5.6A**). However, under CO_2 saturation with PhOH present, there is an increase in current density with complete loss of reversibility at the third reduction feature, indicating electrocatalytic reduction of CO_2. When comparing the catalytic CV current density of **1** with that of **2** and **3**, the relative current increase is consistent with a normal scaling relationship: as the $E_{cat/2}$ of the catalyst becomes more negative the catalytic current density increases (**Figure S5.6B**). The catalytic activity of **2** and **3** were previously found to be first-order with respect to catalyst, PhOH, and CO_2.[17, 18] When comparable variable concentration CV experiments were performed for **1**, the system was found to be first-order with respect to **1** (**Figure S5.9**), but mixed-order kinetics were observed for both PhOH (**Figure S5.10**) and CO_2 (**Figure S5.11**) concentrations. This is attributed to the decreased intrinsic activity of **1**, with a corresponding saturation of the current response at relatively low substrate concentrations.

Controlled potential electrolysis (CPE) was performed with **1** and 0.8 M PhOH under CO_2 saturation at an applied potential of –2.1 V vs. Fc^+/Fc in order to determine the selectivity and turnover frequency (TOF_{CPE}) of the catalyst (**Figure S5.12**). A 91±3% Faradaic efficiency for CO (FE_{CO}) at an overpotential of 90 mV with 6 ± 2% H_2 detected (**Table S5.3**) and a TOF_{CPE} of 0.24 s^{-1} was observed (**Table 5.1**). The measured TOF_{CPE} for **1** is much lower than that of **2** and **3**, in agreement with the observed CV current density trends and a normal Tafel scaling relationship based on the $E_{cat/2}$ of the catalysts.[5] It is important to note that the CPE experiments with **1** were performed at more positive potentials than other catalysts due to the increase in competitive hydrogen evolution reaction (HER) by the electrode at more negative potentials, which is attributed to its low intrinsic activity.

5.3.2 Co-catalytic Activity

To examine how the relative position of the RM reduction potential with respect to the reduction potentials of **1**, **2,** and **3** impacts co-electrocatalysis, it was necessary to prepare a new RM, benzonaphthothiophene-7,7-dioxide (BNTD; **Figures 5.2**, **S5.4**, and **S5.5**). Under Ar saturation, BNTD displays a single reversible redox feature with an $E_{1/2}$ = –1.96 V vs. Fc^+/Fc, corresponding to a single-electron reduction that remains unchanged upon the addition of PhOH and CO_2 (**Figure S5.15**). The $E_{1/2}$ of BNTD is more negative than the $E_{cat/2}$ of complex **1**, equal to that of complex **2**, and more positive than that of complex **3**, enabling a systematic study of the relationship between $E_{cat/2}$ and the RM $E_{1/2}$. Additionally, since BNTD is a similar size and shape to other tested derivates,[17, 18] changes in should be due primarily to electronic and not steric effects.

Figure 5.2. Molecular structure of BNTD obtained from single-crystal X-ray diffraction studies.Yellow = S, red = O, gray = C; thermal ellipsoids at 50%; H atoms omitted for clarity.

CV experiments with all three Cr complexes including BNTD as the RM led to the appearance of co-catalytic behavior with enhanced activity relative to their intrinsic activity (**Figure S5.17**). Interestingly, the observed $E_{co\text{-}cat/2}$ for all Cr complexes with BNTD is the same as the $E_{1/2}$ of BNTD, including **3**, even though BNTD is reduced at potentials approximately 40 mV more positive than the $E_{cat/2}$ of **3** (–2.00 V vs Fc+/Fc; **Figure 5.3**). *This demonstrates for the first time that the reducing power of the RM does not need to exceed that of the catalytically active Cr species for a co-catalytic response*. Variable concentration CV experiments demonstrate that there is a proportional increase in current density with respect to concentration of catalyst (**Figures S5.19**, **S5.25**, **S5.31**, and **S5.37**), RM (**Figures S5.20**, **S5.26**, **S5.32**, and **S5.38**), a fixed ratio of catalyst to RM (**Figures S5.21**, **S5.27**, **S5.33**, and **S5.39**), PhOH (**Figures S5.22**, **S5.28**, **S5.34**, and **S5.40**), and CO_2 (**Figures S5.23**, **S5.29**, **S5.35**, and **S5.41**). However, the complexity of the co-catalytic system precludes formal rate law assignments from these data.

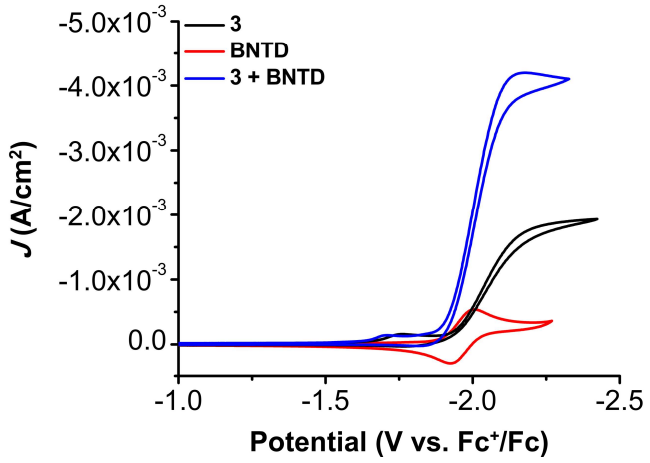

Figure 5.3. (**A**) CVs of Cr(^{tbu}dh^{tbu}bpy)Cl(H_2O) **3** and 2.5 mM BNTD alone and together under CO_2 saturation conditions with 0.5 M PhOH demonstrating the shift in catalytic potential. Conditions: 1.0 mM catalyst, 2.5 mM RM, 0.1 M $TBAPF_6$/DMF; glassy carbon disc working electrode, glassy carbon rod counter electrode, Ag/AgCl pseudoreference electrode; referenced to Fc^+/Fc internal standard; 100 mV/s scan rate.

CPE experiments were performed to determine the product selectivity and activity for CO_2 reduction with PhOH present for all three catalysts with the BNTD RM. For **1** with BNTD and 1.0 M PhOH at an applied potential of –2.20 V, the system has a FE_{CO} of 97 ± 2% with non-quantifiable H_2 detected and TOF_{CPE} of 34.0 s^{-1}, a 142-fold increase relative to its intrinsic activity (**Table 5.1**; **Figure S5.43**). As has been the case with previous studies,[16-18] under these conditions the standard reduction potential of BNTD is more negative than that of **1**. Comparable experiments with **2**, which has the same standard reduction potential as BNTD of –1.96 V vs Fc^+/Fc, show an increased TOF_{CPE} of this system is 328 s^{-1}, *the largest activity we have reported for a co-catalytic system thus far,* despite being only a 67-fold improvement over the intrinsic activity of **2**. Finally, under the same conditions the TOF_{CPE} of **3** with BNTD was determined to be 63.4 s^{-1} (**Table 5.1**), a 7-fold enhancement relative to its intrinsic activity. Although the reduction potentials of the Cr complexes shift relative to that of BNTD, quantitative selectivity is observed in all cases.

Table 5.1. Results of CPE Experiments with PhOH under CO_2 Saturation Conditions

Conditions	Potential (V vs. Fc^+/Fc)	FE_{CO} (%)	FE_{H2} (%)	TOF_{CPE} (s^{-1})	η (V)
1 + PhOH[a]	–2.10	91 ± 3	6 ± 2	0.24	0.09
1 + DBTD + PhOH[b]	–2.30	77 ± 2	18 ± 1	27.4	0.41
1 + BNTD + PhOH[b]	–2.20	97 ± 2	NQ	34.0	0.12
2 + PhOH[18c]	–2.30	101 ± 3	–	4.90	0.12
2 + DBTD + PhOH[18b]	–2.30	94 ± 7	–	56.3	0.41
2 + BNTD + PhOH[b]	–2.20	103 ± 5	–	328	0.12
3 + PhOH[17d]	–2.30	95 ± 8	–	9.29	0.16
3 + DBTD + PhOH[17e]	–2.30	109 ± 9	–	163	0.41
3 + BNTD + PhOH[e]	–2.20	100 ± 2	–	63.4	0.12

[a]0.5 mM catalyst and 0.8 M PhOH; [b]0.1 mM catalyst, 0.5 mM RM, and 1.0 M PhOH; [c] 0.5 mM catalyst and 1.0 M PhOH; [d]0.1 mM catalyst and 0.12 M PhOH; [e]0.1 mM catalyst, 0.5 mM RM, and 0.12 M PhOH; NQ = non-quantifiable

5.4 Discussion and Conclusions

In previous studies, it was proposed that closely matching the reduction potential of the catalyst with the RM resulted in more favorable association during the catalytic cycle and therefore an increase in the observed TOF_{CPE}. This hypothesis was based on the assignment of an inner-sphere electron transfer mechanism during co-catalysis, wherein the reduced RM binds to the Cr center prior to the rate-determining step of the reaction, C–OH bond cleavage.[17, 18] Previous computational results revealed that the barrier of the rate-determining step is lower overall for the RM-bound species, $[Cr(CO_2H)RM]^{2-}$, compared to $[Cr(CO_2H)S]^-$ (S = DMF), but that this barrier is not significantly different when comparing co-catalyst assemblies with the same metal complex and different RMs. Thus, the favorability of the equilibrium binding reaction between the Cr complex and RM directly impacted the observed TOF. Reasoning that the reduction potentials were an approximation of the relevant orbital energies, it was posited that closer energy differences would result in a stronger binding interaction and consequently a more favorable

equilibrium correlating to greater TOFs. This is again supported by the observed trend when comparing DBTD ($E_{1/2}$ = –2.25 V vs Fc^+/Fc) and BNTD ($E_{1/2}$ = –1.96 V vs Fc^+/Fc) as the RM.

The results presented here suggest that once the equilibrium binding interaction is favorable enough, the relative composition of the reaction-diffusion layer also becomes important. That is, if the RM is generated at positive enough potentials, the co-catalytic cycle must compete less with the intrinsic catalytic cycle of the Cr complexes. Indeed, co-catalytic activity peaks with the combination of **2** and BNTD, where both active species are generated at an identical reduction potential. However, it is also clear from the results with complex **3** that even minor concentrations of the reduced catalyst are sufficient for co-catalysis to occur, given the general favorability of RM association and the corresponding rate enhancement. Using the Nernst equation, at 40 mV positive of the standard reduction potential it can be estimated that approximately 17.4% of **3** in the reaction-diffusion layer has been reduced to its active form, consistent with the reduced co-catalytic enhancement observed. Smith *et al*. made a similar observation in their original report, proposing that a minimal potential difference offered the best enhancement for co-electrocatalysis.[15] In that previous study, the requirement for the RM to transfer $2e^-/2H^+$ for co-catalysis introduced a kinetic penalty, which was compounded by the high intrinsic activity of the catalyst, leading to greater competition between the intrinsic and co-catalytic pathways.[14]

It is striking that the $E_{1/2}$ of BNTD becomes the $E_{co\text{-}cat/2}$ potential in all cases, regardless of the relative position of the Cr-based redox potential. This clearly demonstrates that the co-catalytic benefit can be thought of as increasing the inventory of available electrons for catalytic CO_2 conversion: the Cr complex becomes effectively over-reduced once the RM is activated, enhancing TOFs and, in the event that equilibrium binding is sufficiently favorable, forming as the only catalytic species in solution with minimal concentrations of activated catalyst. Going forward, these results suggest that effective co-catalyst design strategies must begin to incorporate an

understanding of relative speciation to achieve the highest activities, in addition to leveraging components of molecular design.

5.5 Supplementary Information

5.5.1 Materials and Methods

General

All chemicals and solvents (ACS or HPLC grade) were commercially available and used as received unless otherwise indicated. For all air-sensitive reactions and electrochemical experiments, HPLC-grade solvents were obtained as anhydrous and air-free from a PPT Glass Contour Solvent Purification System. Gas cylinders were obtained from Praxair (Ar as 5.0; CO_2 as 4.0) and passed through activated molecular sieves prior to use. Gas mixing for variable concentration experiments was accomplished using a gas proportioning rotameter from Omega Engineering. UV-vis absorbance spectra were obtained on a Cary 60 from Agilent. An Anton-Parr Multiwave Pro SOLV, NXF-8 microwave reactor was used for microwave syntheses.

Electrochemistry

All electroanalytical experiments were performed using a Metrohm Autolab PGSTAT302N or a Biologic SP-50 potentiostat. Glassy carbon disc working electrodes (⌀ = 3 mm) and non-aqueous silver/silver chloride pseudoreference electrodes behind PTFE tips were obtained from CH Instruments. The pseudoreference electrodes were obtained by depositing chloride on bare silver wire in 10% HCl at oxidizing potentials and stored in a 0.1 M tetrabutylammonium hexafluorophosphate/*N*,*N*-dimethylformamide ($TBAPF_6$/DMF) solution in the dark prior to use. The counter electrode was a glassy carbon rod (⌀ = 3 mm). All CV experiments were performed in a modified scintillation vial (20 mL volume) as a single-chamber cell with a cap modified with ports for all electrodes and a sparging needle. $TBAPF_6$ was purified by recrystallization from ethanol and dried in a vacuum oven before being stored in a desiccator. All data were referenced

to an internal ferrocene standard (ferricenium/ferrocene (Fc^+/Fc) reduction potential under stated conditions) unless otherwise specified. All voltammograms were corrected for internal resistance. Ferrocene was purified by sublimation prior to use.

Controlled Potential Electrolysis (CPE)

CPE experiments were performed in a glass Pine Research Instrumentation H-cell with two compartments separated by a glass frit. A 55 mL stock solution of DMF with 0.1 M $TBAPF_6$ was prepared for each bulk electrolysis experiment. Approximately 26 mL of the stock solution was added to each half of the H-cell. One side of the H-cell contained the catalyst, any additional substrate, such as the mediator and/or PhOH, and a glassy carbon rod working electrode. The other side of the H-cell contained approximately 0.075 M ferrocene as a sacrificial reductant along with a graphite rod counter electrode and a Ag/AgCl pseudoreference electrode. The electrolysis experiment was referenced by taking a CV of the side of the H-cell that contained the ferrocene solution. The H-cell was sealed with two septa that were connected by a piece of PTFE tubing which aided to maintain equal pressure between each half of the cell during the electrolysis. Before starting the electrolysis experiment, both sides of the H-cell were sparged with the desired gas for 20 minutes and the sealed cell was allowed to equilibrate for 1 hour. The resistance between the two halves of the H-cell was measured using the i-interrupt procedure available in the NOVA software provided by Metrohm. This measured resistance value was then used to correct for resistance using the iR compensation tool in the NOVA software for potentiostatic experiments.

CPE Product Analysis

During CPE experiments, 250 µL GC injections of the headspace were periodically taken for the detection and quantification of any gaseous products produced. After each CPE experiment, the total volume of solution was measured. The total volume of the sealed H-cell was also measured

to account for the total headspace volume for accurate quantification of gaseous products. A calibration curve for CO and H_2 was used to quantify gaseous products produced during electrolysis experiments in the same manner as we previously reported.[36]

Analysis of gas phase products was done by sampling electrolysis headspace through syringe injections into an Agilent 7890B GC equipped with a specialty gas split column 5 Å mol sieve/Porabond Q column (15 m length; 0.320 mm diameter; 25.0 μm film) and thermal conductivity detector with He as a carrier gas. A calibration curve for CO and H_2 was made in the H-cell with an experimental setup containing identical volumes of DMF in 0.1 M $TBAPF_6$ to those used during electrolysis. Known volumes of CO and H_2 were injected into the cell with stirring and 250 μL injections of the headspace were taken for GC injections after equilibration. The limit of detection (LOD) and limit of quantitation (LOQ) for CO and H_2 in the GC were determined from seven consecutive injections at the lowest observable concentrations of each gaseous product respectively. For CO, the LOD was determined to be 5.77 x 10^{-7} moles and the LOQ was determined to be 1.92 x 10^{-6} moles. For H_2, the LOD was determined to be 4.55 x 10^{-6} moles and the LOQ was determined to be 1.52 x 10^{-5} moles.

Calculation of Overpotential for CO_2 Reduction with PhOH Present (Adapted)

The calculation of overpotential for all catalysts was performed according to reported methods.[37] The following equation was used for the determination of the reaction standard potential in V with respect to the Fc^+/Fc couple:

$$E_{CO\ /CO} = -0.73\ V - 0.059(pK_a) \qquad \textbf{Eq (S5.1)}$$

The pK_a for PhOH in DMF is reported as 18.8:[38]

$$E_{CO2/CO}(PhOH) = -1.84\ V\ vs\ Fc^+/Fc \qquad \textbf{Eq (S5.2)}$$

The $E_{cat/2}$ determined experimentally for Cr(^{tbu}dh^{Ph}phen)Cl(H_2O), Cr(^{tbu}dhphen)Cl(H_2O), and Cr(^{tbu}dh^{tbu}bpy)Cl(H_2O) is –1.93 V, –1.96 V[18], and –2.00 V[17] vs Fc^+/Fc, respectively. For protic CO_2 reduction (1.0 mM catalyst and 0.1 M PhOH under CO_2 saturation); the overpotential is:

$$\eta = \left|E_{cat/2} - E_{CO2/CO}\right| \qquad \textbf{Eq (S5.3)}$$

Cr(^{tbu}dh^{Ph}phen)Cl(H_2O) **1**	η = 90 mV
Cr(^{tbu}dhphen)Cl(H_2O) **2**	η = 120 mV
Cr(^{tbu}dh^{tbu}bpy)Cl(H_2O) **3**	η = 160 mV

This assumes no contribution from homoconjugation of the acid. We note that the homoconjugation constant (HA_2^-) for PhOH in DMF has been reported as $\log(K_{HA_2^-})$ = 3.8.[39] Therefore, we emphasize that the described overpotential calculated above for PhOH is the lower-limit approximation, as homoconjugation is expected to alter the effective overpotential. The overpotential equation can be modified to account for homoconjugation:

$$E_{CO2/CO} = -0.73\ V - 0.059(pK_a) - \frac{-2.303RT}{nF}\log\left(mK_{HA_2^-}\right) \qquad \textbf{Eq (S5.4)}$$

Where n = number of electrons (2) and m = number of proton transfers (2). The modified equation provides $E^0_{CO2/CO}$ = −1.72 V and the following η values:

Cr(^{tbu}dh^{Ph}phen)Cl(H_2O) **1**	η = 210 mV
Cr(^{tbu}dhphen)Cl(H_2O) **2**	η = 240 mV
Cr(^{tbu}dh^{tbu}bpy)Cl(H_2O) **3**	η = 280 mV

This value does not account for the possible thermodynamic contributions of the water coordinated to the pre-catalyst, the equimolar quantities of water produced for each equivalent of CO generated, or any adventitious H_2O present in the CO_2, solvent, or electrolyte. Under CO_2 saturation, any water present can form carbonic acid, pK_a(DMF) 7.37,[40] and generate new equilibria involving CO_2 and bicarbonate. The role of carbonic acid (and the general hydration of CO_2 in non-aqueous solvent systems) in altering the overall thermodynamics combined with the

effects of homoconjugation has been assessed by Matsubara.[41] Considering the role of water, Matsubara obtained a standard potential for CO_2 reduction to CO of −1.70 V versus Fc^+/Fc for PhOH in *N,N*-DMF with 10 mM water present (see below). Note the same value is obtained considering 10 mM water only.

For 10 mM H_2O in DMF, where AH = PhOH:[41]

$$3CO_{2(g)} + H_2O_{(sol,x)} + 2e^- \rightleftharpoons CO_{(g)} + 2HCO_{3\,(sol)}^- \qquad E^0 = -1.70\,V\ vs.\,Fc^+/Fc$$

$$CO_{2(g)} + 2AH_{(sol)} + 2e^- \rightleftharpoons CO_{(g)} + 2A^-{}_{(sol)} + H_2O_{(sol,x)} \qquad E^0 = -1.96\,V\ vs.\,Fc^+/Fc$$

$$CO_{2(g)} + 4AH_{(sol)} + 2e^- \rightleftharpoons CO_{(g)} + 2HA_{2\,(sol)}^- + H_2O_{(sol,x)} \qquad E^0 = -1.70\,V\ vs.\,Fc^+/Fc$$

Determination of TOF from Preparative Electrolysis

The integrated expression of current for a homogeneous electrocatalytic response (considering an application of steady-state conditions to the substrate) has been solved previously:[42, 43]

$$\frac{i}{FA} = \frac{n_{cat}^{\sigma}[cat]\sqrt{(k_{obs}D_{cat})}}{1 + \exp\left[\frac{F}{RT}\left(E_{app} - E_{\frac{1}{2}}\right)\right]}$$

where

$$k_{obs} = k_{cat}[CO_2]$$

and i is the average current (Amps) specific to the reaction product of interest, F is Faraday's constant (96485 C mol^{-1}), A is the area of the electrode (cm^2), n_{cat}^{σ} is the number of electrons in the catalytic process (2) with σ = 1 under the assumption that all electrons are delivered to the catalyst by the electrode[6] (σ = 0.5 corresponds to homogeneous electron transfer occurring between catalyst molecules in solution; used here for co-electrocatalytic conditions), $[cat]$ is the concentration of the catalyst (mol cm^{-3}), k_{obs} is the apparent turnover frequency (s^{-1}), $[CO_2]$ is the

concentration of CO_2 saturated in DMF (mol cm^{-3}), D_{cat} is the diffusion coefficient of the catalyst (cm^2 s^{-1}), R is the ideal gas constant (Joule mol^{-1} K^{-1}), T is the temperature (K), E_{app} is the applied potential during preparative electrolysis (V), and $E_{1/2}$ is the standard potential of the catalyst (V).

$$\frac{i}{A} = J = CO\ specific\ current\ density$$

Substituting and rearranging the first expression to solve for k_{obs}

$$k_{obs} = \frac{J^2\left(1 + \exp\left[\frac{F}{RT}\left(E_{app} - E_{1/2}\right)\right]\right)^2}{F^2(n_{cat}^{\sigma}[cat])^2 D_{cat}}$$

with k_{obs} in hand, the TOF can be expressed for a given potential according to the following relationship

$$TOF = \frac{k_{obs}}{1 + \exp\left[\frac{F}{RT}\left(E_{app} - E_{1/2}\right)\right]}$$

Parameters for CPE experiments reported here not found in **Table 5.1**.

- $E_{1/2}$ catalyst:
  - −1.93 V vs Fc$^+$/Fc for Cr(^{tbu}dh^{Ph}phen)Cl(H$_2$O) **1**
  - −1.96 V vs Fc$^+$/Fc for Cr(^{tbu}dhphen)Cl(H$_2$O) **2**
  - –2.00 V vs Fc$^+$/Fc for Cr(^{tbu}dh^{tbu}bpy)Cl(H$_2$O) **3**
- Temperature: 298.15 K
- [CO_2]: 2.3 x 10^{-4} mol cm^{-3}
- Diffusion coefficient:
  - 2.21 x 10^{-6} cm^2 s^{-1} for Cr(^{tbu}dh^{Ph}phen)Cl(H$_2$O) **1**
  - 1.60 x 10^{-6} cm^2 s^{-1} for Cr(^{tbu}dhphen)Cl(H$_2$O) **2**[18]
  - 2.18 x 10^{-6} cm^2 s^{-1} for Cr(^{tbu}dh^{tbu}bpy)Cl(H$_2$O) **3**[17]
- Electrode area: 3.65 cm^2 or 2.48 cm^2

Calculation of Diffusion Coefficient

The calculation of the diffusion coefficient for the Cr(^{tbu}dh^{Ph}phen)Cl(H_2O) **1** catalyst was performed by reported methods.[44] Cyclic voltammetry (CV) experiments were done with a solution of 1.0 mM catalyst in 0.1 M $TBAPF_6$/DMF under Ar saturation conditions. The scan rate of these CVs was varied from 25 mV/s to 5000 mV/s (**Figure S5.7**). The increase in current observed as the scan rate increases can be represented by the following equation where i_p is the peak current, n is the number of electrons, A is the area of the electrode, D is the diffusion coefficient, C is the concentration of analyte, and v is the scan rate:

$$i_p = (2.69 \times 10^5) n^{3/2} A C D^{1/2} v^{1/2}$$

By plotting the current density as a function of $v^{1/2}$ for the reversible reduction (**Figure S5.7**), the slope can be used to find D for each molecule.

$$D_{cat} = \frac{(\text{slope})^2}{n^3 C^2 (2.69 \times 10^5)^2}$$

Calculation of Active Species at a Given Potential

The calculation of the percent of Cr(^{tbu}dh^{tbu}bpy)Cl(H_2O) **3** reduced at a given potential can be achieved by rearranging the Nernst equation where E is the experimental potential (–1.96 V), E^0 is the standard reduction potential of the catalyst (–2.00 V), R is the ideal gas constant (Joule mol^{-1} K^{-1}), T is the temperature (K), n is the number of electrons, F is Faraday's constant (96485 C mol^{-1}), $[A]$ is the concentration of catalyst, and $[B]$ is the concentration of reduced catalyst:

$$E = E^0 - 2.303 \frac{RT}{nF} \log_{10}\left(\frac{[B]}{[A]}\right)$$

$$E^0 - E = 2.303 \frac{RT}{nF} \log_{10}\left(\frac{[B]}{[A]}\right)$$

$$\frac{E^0 - E}{2.303\frac{RT}{nF}} = \log_{10}\left(\frac{[B]}{[A]}\right)$$

$$\frac{E^0 - E}{2.303\frac{RT}{nF}} = \log_{10}\left(\frac{[B]}{[A]}\right)$$

$$10^{\frac{E^0 - E}{2.303\frac{RT}{nF}}} = \frac{[B]}{[A]}$$

$$if\ \frac{[B]}{[A]} = 0.211, then\ \frac{[B]}{[A]} = \frac{211}{1000}$$

$$and\ \%[B]\ in\ solution = \frac{211}{1211} \bullet 100 = 17.4\%$$

Single Crystal X-ray Diffraction

A single crystal of BNTD was coated with Paratone oil and mounted on a MiTeGen MicroLoop. The X-ray intensity data were measured on a Bruker D8 Venture Kappa four-circle diffractometer system equipped with an Incoatec IμS 3.0 micro-focus sealed X-ray tube (Mo Kα, λ = 0.71073 Å) and a HELIOS double bounce multilayer mirror monochromator.The frames were integrated with the Bruker SAINT software package[45] using a narrow-frame algorithm. Data were corrected for absorption effects using the Multi-Scan method (SADABS).[46] The structure was solved and refined using the Bruker SHELXTL Software Package[47] within APEX4[45] and OLEX2.[48] Non-hydrogen atoms were refined anisotropically. Hydrogen atoms were placed in geometrically calculated positions and were refined isotropically with U_{iso} = 1.2U_{equiv} of the parent atom.

Table S5.1. Crystallographic data for BNTD

	BNTD
Formula	$C_{16}H_{10}O_2S$
FW (g/mol)	266.30
Temp (K)	100(2)
λ (Å)	0.71073
Size (mm)	0.081 x 0.127 x 0.158
Crystal habit	yellow plate
Crystal system	triclinic
Space group	P -1
a (Å)	7.6112(4)
b(Å)	8.5345(5)
c (Å)	9.9571(6)
α (°)	111.229(2)
β (°)	102.154(2)
γ (°)	93.290(2)
Volume (Å^3)	583.02(6)
Z	2
Density (g/cm^3)	1.517
μ (mm^{-1})	0.270
F(000)	276
θ range (°)	2.27 to 27.48
Index ranges	-8 ≤ h ≤ 9 -11 ≤ k ≤ 11 -12 ≤ l ≤ 12
Data / restraints /parameters	2657 / 0 / 172
GOF on F^2	1.075
R_1 (I>2σ(I))	0.0399
wR_2 (all data)	0.1089

5.5.2 Synthesis and Characterization

Synthesis of 6,6'-Di(3,5-di-tert-butyl-2-hydroxybenzene)-4,7-di-phenyl-1,10-phenanthroline, $^{tbu}dh^{Ph}phen(H)_2$

The synthesis of the 2,9-dichloro-4,7-diphenyl-1,10-phenanthroline starting material was adapted from a previously reported procedure[49] using a 4,7-diphenyl-1,10-phenenthroline starting material. The (3,5-di-*tert*-butyl-2-hydroxy-phenyl)boronic acid starting material was synthesized as previously reported.[36]

A microwave tube was charged with 2,9-dichloro-4,7-diphenyl-1,10-phenanthroline (0.500 g, 1.25 mmol), (3,5-di-*tert*-butyl-2-hydroxy-phenyl)boronic acid (0.935 g, 3.74 mmol), sodium carbonate (0.924 g, 8.72 mmol), $Pd(PPh_3)_4$ (0.072 g, 0.062 mmol), degassed toluene (30 mL), water (12 mL), and methanol (8 mL). The microwave conditions were set to heat the reaction mixture to 170 °C as fast as possible and then held at that temperature for 200 minutes. After the reaction cooled, the reaction layers were separated. The organic layer was extracted with brine (1 x 50 mL) and the aqueous layer was extracted with dichloromethane (3 x 50 mL). All organic fractions were combined and dried over $MgSO_4$ before removing the solvent via reduced pressure leaving an orange solid. Methanol was added to the flask and the mixture was filtered leaving a bright orange solid with an isolated yield of 39.2% (0.362 g). ^{1}H NMR (CD_2Cl_2, 600 MHz): δ 14.69 (s, 2H, O*H*), 8.23 (s, 2H, Ar*H*), 7.88 (d, 2H, Ar*H*), 7.82 (s, 2H, Ar*H*), 7.59 (m, 10 H, Ar*H*), 7.53 (d, 2H, Ar*H*), 1.58 (s, 18H, −C$(CH_3)_3$), 1.40 (s, 18H, −C$(CH_3)_3$). ^{13}C{^{1}H} NMR (CD_2Cl_2, 100 MHz): δ 159.4 (Ar*C*), 157.5 (Ar*C*), 150.8 (Ar*C*), 143.3 (Ar*C*), 140.9 (Ar*C*), 138.6 (Ar*C*), 138.3 (Ar*C*), 130.3 (Ar*C*), 129.3 (Ar*C*), 127.6 (Ar*C*), 126.2 (Ar*C*), 124.1 (Ar*C*), 122.7 (Ar*C*), 122.2 (Ar*C*), 119.6 (Ar*C*), 36.0 (tbu*C*), 34.9 (tbu*C*), 32.0 (tbu*C*), 30.3 (tbu*C*). ESI-MS (m/z): [^{tbu}dh^{Ph}phen$(H)_2$] calc'd: 740.4342 found: 740.4342.

Synthesis of Cr(^{tbu}dh^{Ph}phen)Cl(H_2O) (1)

Metalation of ^{tbu}dh^{Ph}phen$(H)_2$ with Cr(III) to generate Cr(^{tbu}dh^{Ph}phen)Cl(H_2O) (**1**) was achieved by stirring ^{tbu}dh^{Ph}phen$(H)_2$ (0.190 g, 0.256 mmol) and 1.05 equivalents of chromium (II) dichloride (0.0331 g, 0.269 mmol) in tetrahydrofuran (75 mL) at room temperature under an inert atmosphere for 3 days. After exposing the reaction to air, the THF was removed under reduced pressure. Methanol was added to the flask to precipitate unreacted ligand and metal salt which was collected via filtration. The methanol was then removed under reduced pressure and the resulting red solid was dissolved in dichloromethane and extracted with brine (3 x 75 mL) and saturated ammonium chloride (5 x 100 mL). The organic layer was then dried over $MgSO_4$ and

condensed under reduced pressure to leave a dark red crystalline solid. Water was added to the roundbottom and sonicated for several minutes to suspend the solid material. This solid was collected via vacuum filtration and was washed with 200 mL of hot pentanes for a 75.8% isolated yield (0.164 g). Elemental analysis for $C_{52}H_{56}ClCrN_2O_3$•0.5(CH_2Cl_2) calc'd: C 71.10, H 6.48, N 3.16; found: C 71.45, H 6.54, N 3.22. ESI-MS (m/z): [Cr(^{tbu}dh^{Ph}phen)]–Cl–H_2O calc'd: 790.3590 found: 790.3582.

Synthesis of Cr(^{tbu}dhphen)Cl(H_2O) (2)

The synthesis of Cr(^{tbu}dhphen)Cl(H_2O) was carried out as previously reported.[18]

Synthesis of Cr(^{tbu}dh^{tbu}bpy)Cl(H_2O) (3)

The synthesis of Cr(^{tbu}dh^{tbu}bpy)Cl(H_2O) was carried out as previously reported.[17]

Synthesis of Benzonaphthothiophene 7,7-dioxide, BNTD

Benzonaphthothiophene (0.581 g, 2.48 mmol) was suspended in acetic acid (25 mL). While stirring at room temperature, 30% hydrogen peroxide (19 mL) was added dropwise to the mixture. The flask was then refluxed overnight and the precipitate changed from white to light yellow. After cooling the reaction to room temperature, the precipitate was collected via filtration and washed with water and diethyl ether for a 47.5% isolated yield (0.313 g). ^{1}H NMR (DMSO-d_6, 600 MHz): δ 8.96 (d, 1H, Ar*H*), 8.79 (d, 1H, Ar*H*), 8.30 (d, 1H, Ar*H*), 8.21 (d, 1H, Ar*H*), 8.09 (d, 1H, Ar*H*), 8.02 (d, 1H, Ar*H*), 7.88 (m, 2H, Ar*H*), 7.81 (t, 1H, Ar*H*), 7.73 (t, 1H, Ar*H*). ^{13}C{^{1}H} NMR (DMSO-d_6, 150 MHz): δ 137.4 (Ar*C*), 136.4 (Ar*C*), 135.3 (Ar*C*), 134.8 (Ar*C*), 132.7 (Ar*C*), 131.3 (Ar*C*), 130.4 (Ar*C*), 130.0 (Ar*C*), 129.6 (Ar*C*), 128.9 (Ar*C*), 128.0 (Ar*C*), 127.2 (Ar*C*), 126.1 (Ar*C*), 125.2 (Ar*C*), 122.4 (Ar*C*), 116.8 (Ar*C*). Elemental analysis for $C_{16}H_{10}O_2S$ calc'd: C 72.16, H 3.79, N 0.00; found: C 71.91, H 3.62, N 0.01. ESI-MS (m/z): [BNTD] calc'd: 266.0402 found: 266.0401.

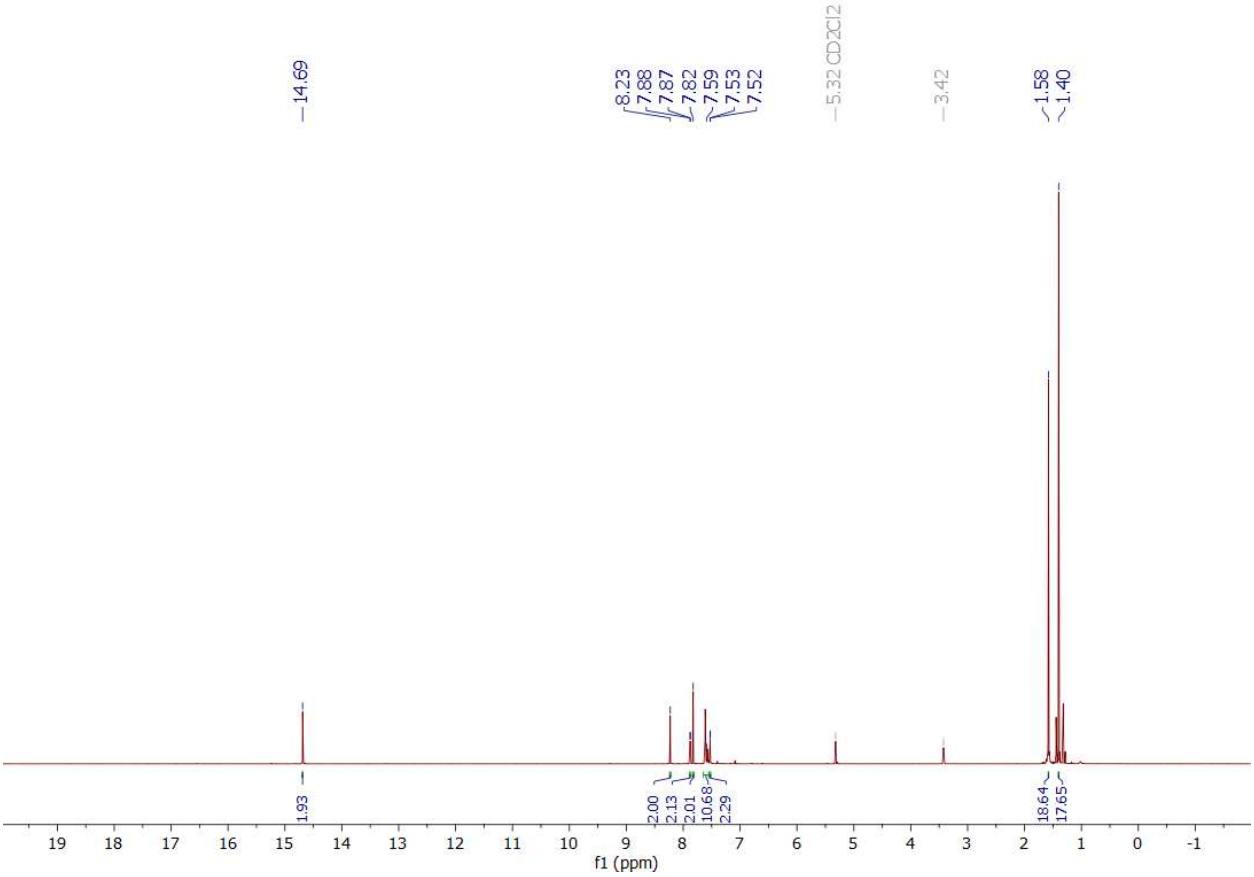

Figure S5.1. ^{1}H NMR of $^{tbu}dh^{Ph}phen(H)_2$ ligand; CD_2Cl_2; 600 MHz.

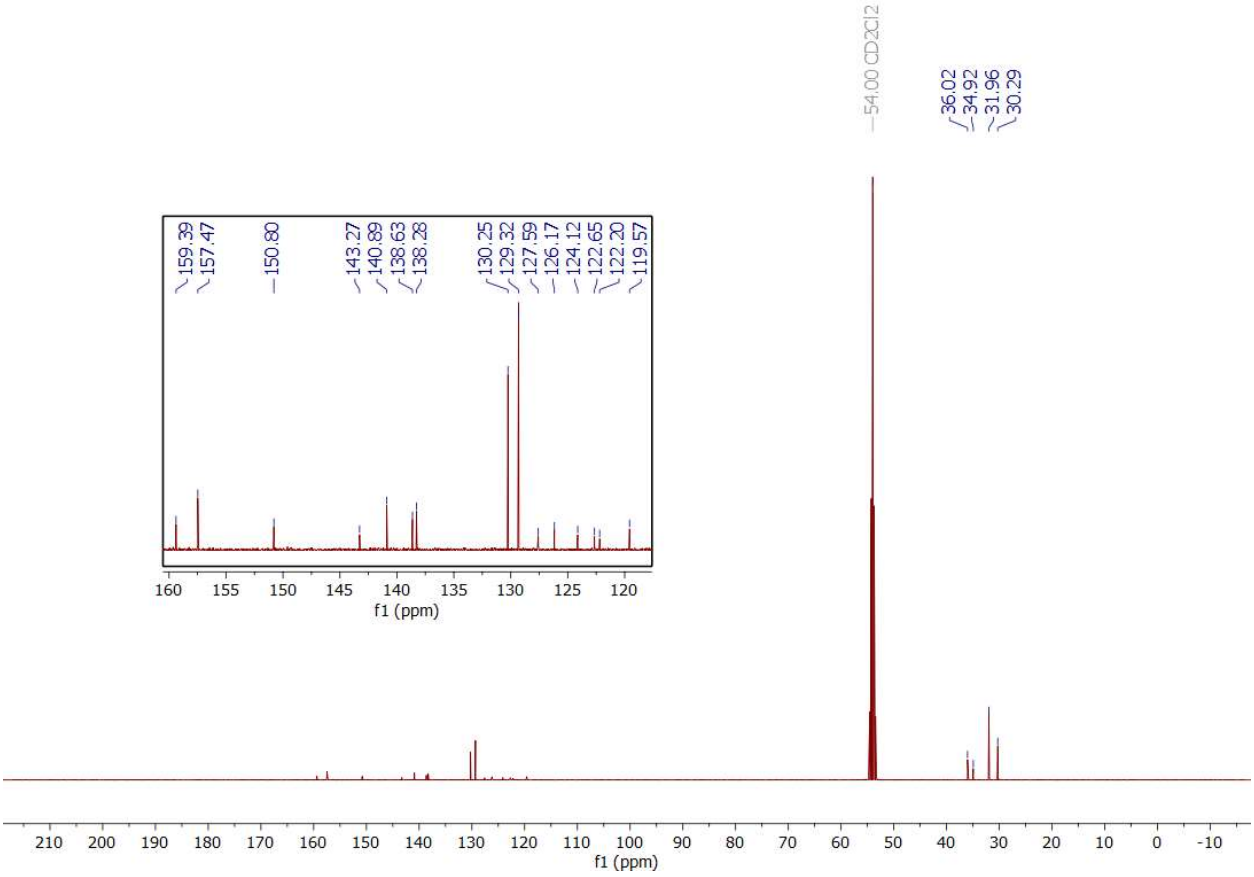

Figure S5.2. ^{13}C {^{1}H} NMR of $^{tbu}dh^{Ph}phen(H)_2$ ligand; CD_2Cl_2; 100 MHz.

Evans' Method Characterization of 1

The spin state of the Cr($^{tbu}dh^{Ph}$phen)Cl(H_2O) (**1**) catalyst was characterized as a Cr(III) species via Evans' Method.[50, 51]Three capillary inserts were made with a 50% v/v mixture of DMF and DMF-d_7. Each insert was flame sealed, and then placed in an NMR tube. Then 6.5 mg of **1** was dissolved in 3 mL of DMF. Approximately 0.6 mL of the solution of **1** was added to each of the three NMR tubes containing a flame sealed insert. ^{1}H NMR spectra with 64 scans were then taken using a 600 MHz Varian NMR Spectrometer. The results of this experiment, which was run in triplicate, can be seen in **Table S5.2**. The average μ_{eff} of 1 was 4.2±0.1.

Table S5.2. Evans' method results for Cr(^{tbu}dh^{Ph}phen)Cl(H_2O) (**1**) in DMF.[50, 51]

Trial	Chemical Shift (ppm)	Chemical Shift (Hz)	Total Magnetic Moment (emu mol^{-1})	Paramagnetic Moment (emu mol^{-1})	μ_{eff} (Bohr Magnetons)
1	0.08	32.0	0.00744	7.98×10^{-3}	4.36
2	0.08	32.0	0.00744	7.98×10^{-3}	4.36
3	0.07	28.0	0.00651	7.05×10^{-3}	4.10

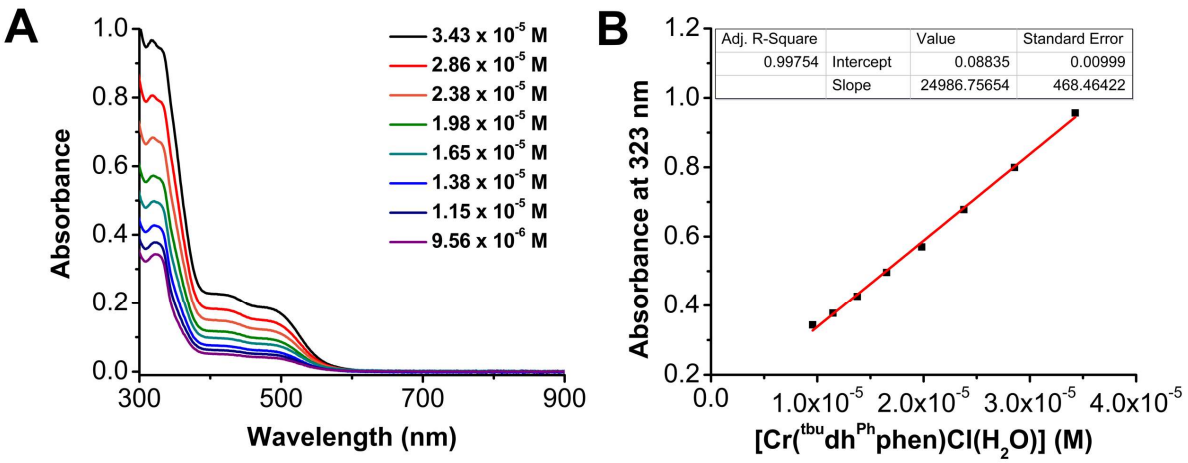

Figure S5.3. (**A**) UV-vis serial dilution absorbance data obtained from Cr(^{tbu}dh^{Ph}phen)Cl(H_2O) **1** in a DMF solution. Conditions: varying concentration of **1**; quartz cell with 1 cm pathlength. (**B**) Plot of absorbance versus concentration (M) for Cr(^{tbu}dh^{Ph}phen)Cl(H_2O) **1** in DMF at 323 nm (25000 M^{-1} cm^{-1}); R^2 = 0.997. All: λ_{max} = 425 nm (7040 M^{-1} cm^{-1}) and 490 nm (5860 M^{-1} cm^{-1}).

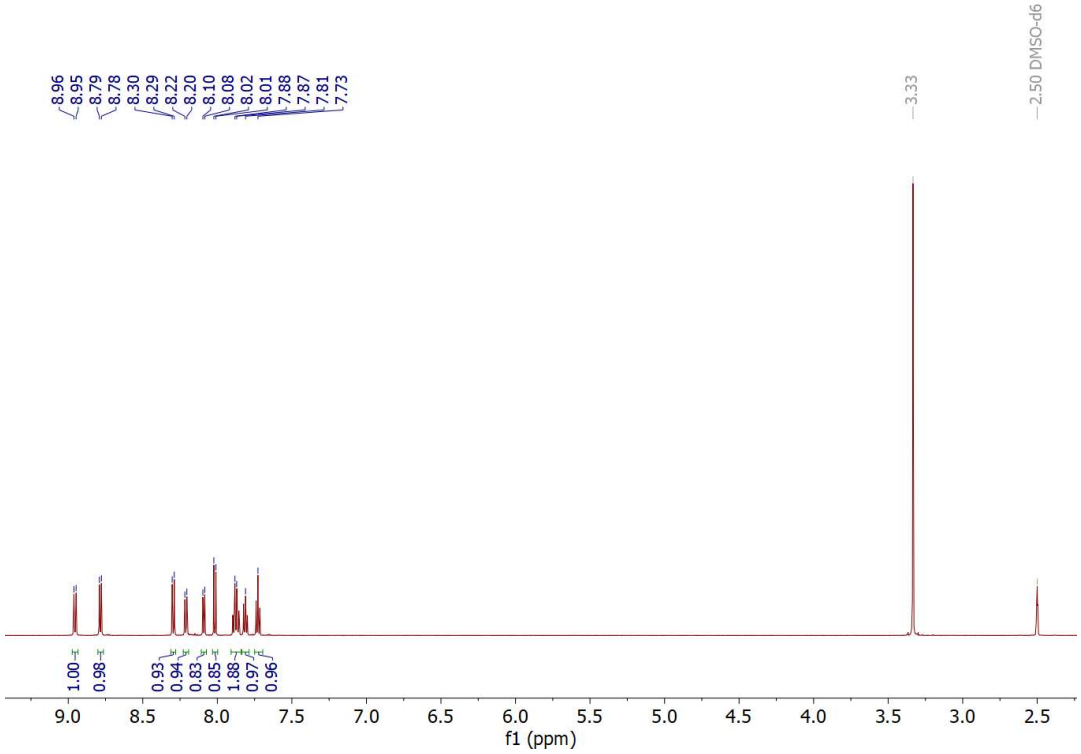

Figure S5.4. ^{1}H NMR of BNTD; DMSO-d_6; 600 MHz.

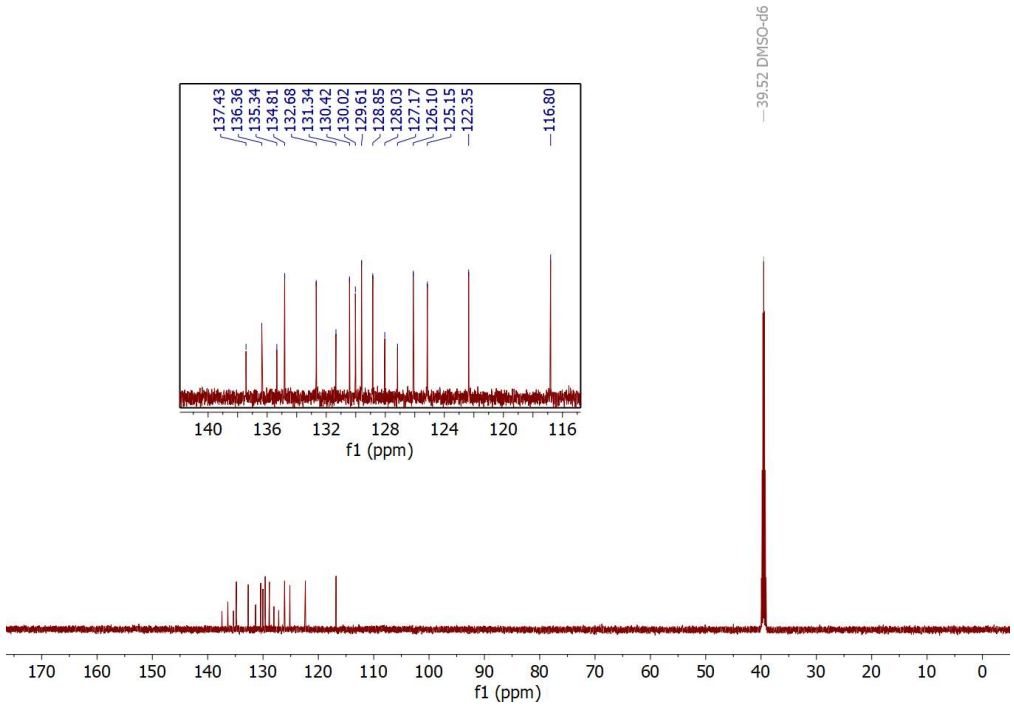

Figure S5.5. ^{13}C {^{1}H} NMR of BNTD; DMSO-d_6; 150 MHz.

5.5.3 Electrochemistry of **1**

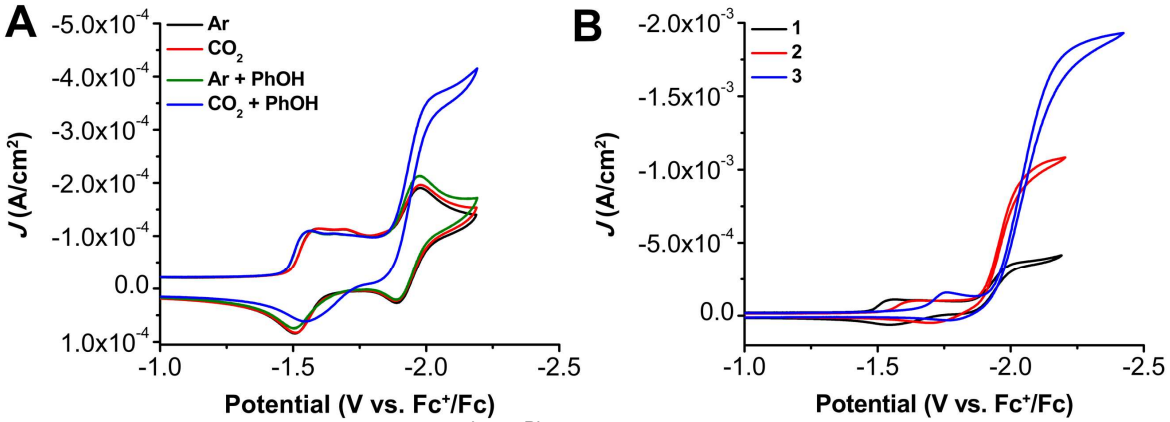

Figure S5.6. (**A**) CVs of 1.0 mM Cr(^{tbu}dh^{Ph}phen)Cl(H_2O) **1** with and without 0.5 M PhOH under Ar and CO_2 saturation conditions. (**B**) CVs of Cr(^{tbu}dh^{Ph}phen)Cl(H_2O) **1**, Cr(^{tbu}dhphen)Cl(H_2O) **2**, and Cr(^{tbu}dh^{tbu}bpy)Cl(H_2O) **3** with 0.5 M PhOH under CO_2 saturation conditions.Conditions: 0.1 M $TBAPF_6$/DMF; glassy carbon disc working electrode, glassy carbon rod counter electrode, Ag/AgCl pseudoreference electrode; referenced to Fc^+/Fc internal standard; 100 mV/s scan rate.

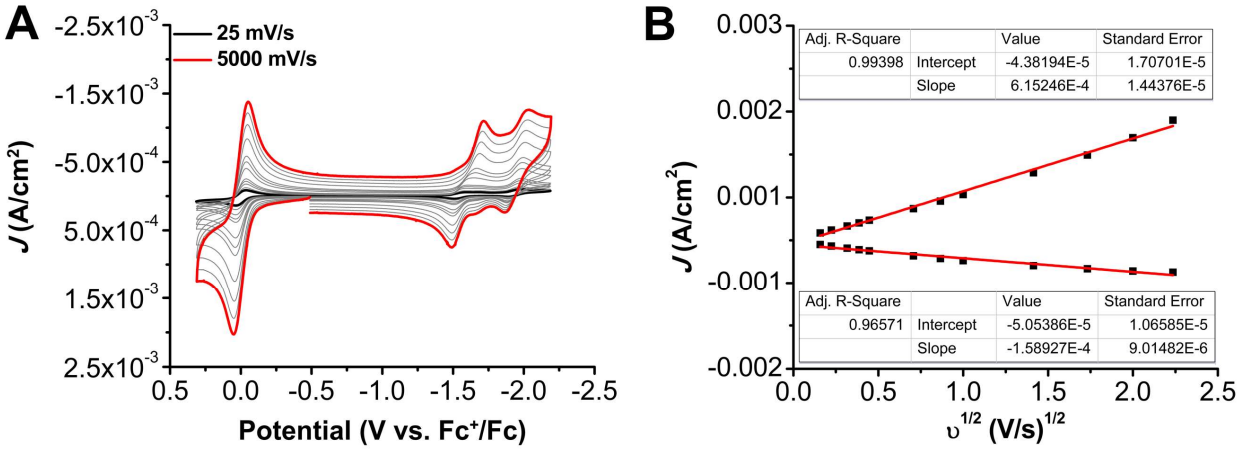

Figure S5.7. (**A**) CVs of Cr(^{tbu}dh^{Ph}phen)Cl(H_2O) **1** at variable scan rates ranging from 25 (black) to 5000 (red) mV/s, obtained under Ar saturation conditions. (**B**) Linear Fit of variable scan rate data from (**A**) demonstrating that Cr(^{tbu}dh^{Ph}phen)Cl(H_2O) **1** shows a diffusion-limited current response. The data in (**B**) was obtained from the reversible redox feature at −1.93 V vs Fc^+/Fc. Conditions: 1.0 mM **1**, 0.1 M $TBAPF_6$/DMF; glassy carbon working electrode, glassy carbon counter electrode, Ag/AgCl pseudoreference electrode; varied scan rate; referenced to internal ferrocene standard.

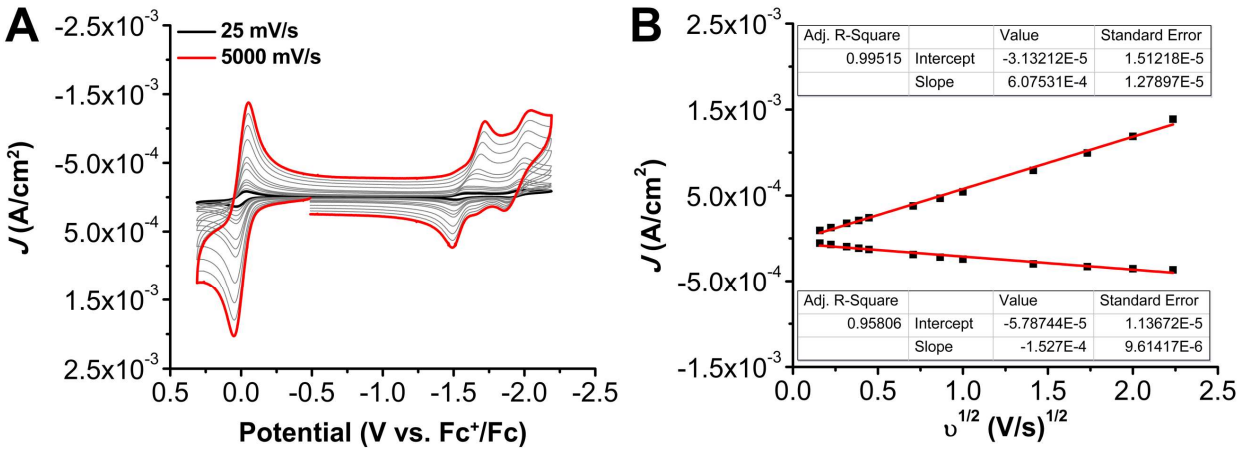

Figure S5.8. (**A**) CVs of Cr(^{tbu}dh^{Ph}phen)Cl(H_2O) **1** at variable scan rates ranging from 25 (black) to 5000 (red) mV/s, obtained under CO_2 saturation conditions. (**B**) Linear Fit of variable scan rate data from (**A**) demonstrating that Cr(^{tbu}dh^{Ph}phen)Cl(H_2O) **1** shows a diffusion-limited current response. The data in (**B**) was obtained from the reversible redox feature at −1.93 V vs Fc^+/Fc. Conditions: 1.0 mM 1, 0.1 M $TBAPF_6$/DMF; glassy carbon working electrode, glassy carbon counter electrode, Ag/AgCl pseudoreference electrode; varied scan rate; referenced to internal ferrocene standard.

At high scan rates in **Figures S5.7** and **S5.8**, the first two reduction features condense into a single feature, consistent with outcompeting a solvent-displacement equilibrium as summarized below, where L = ^{tbu}dh^{Ph}phen^{2-} and S = solvent and E_1^0 and E_2^0 are the first and second reduction features observed at 100 mV/s.$[Cr(L)Cl] + e^- \rightleftharpoons [Cr(L)Cl]^-$ E_1^0

$[Cr(L)Cl]^0 + S \rightleftharpoons [Cr(L)(S)]^+ + Cl^-$

$[Cr(L)(S)]^+ + e^- \rightleftharpoons [Cr(L)(S)]^0$ E_2^0

For all variable concentration studies without the presence of RMs (**Figures S5.9-S5.11**) analysis was adapted from Sathrum and Kubiak J. Phys. Chem. Lett. **2011**, *2*, 2372.[52] *F* is Faraday's constant, *A* is the electrode area, [*Q*] is the substrate concentration, k_{cat} is the catalytic rate, *D* is the diffusion constant of the catalyst, [*cat*] is the concentration of the catalyst, and n_{cat} is the number of electrons involved in the catalytic process.

$$\boldsymbol{i_{cat} = n_{cat}FA[cat](Dk_{cat}[Q]^y)^{1/2}}$$

For all concentration experiments in **Figure S5.9-S5.11**, only points where fully irreversible catalytic features and outside of the saturation range were included in the linear fits.

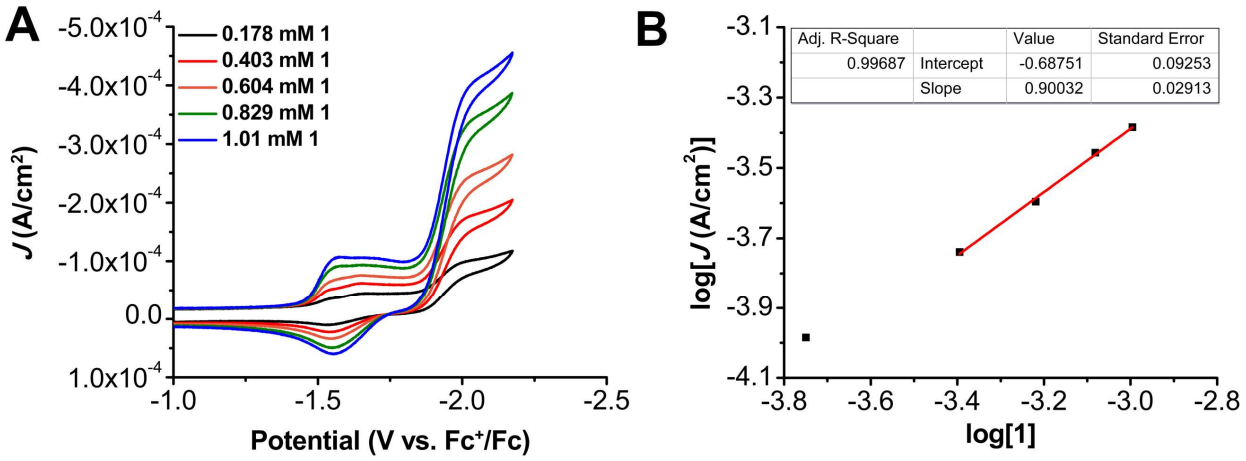

Figure S5.9. (**A**) CVs of Cr(^{tbu}dh^{Ph}phen)Cl(H_2O) **1** at variable concentrations, obtained under CO_2 saturation with 0.6 M PhOH. Conditions: 0.1 M $TBAPF_6$/DMF; glassy carbon disc working electrode, glassy carbon rod counter electrode, Ag/AgCl pseudoreference electrode; 100 mV/s scan rate; referenced to internal ferrocene standard. (**B**) Log-log plot from data obtained from CVs in **A** at −2.06 V vs. Fc^+/Fc.

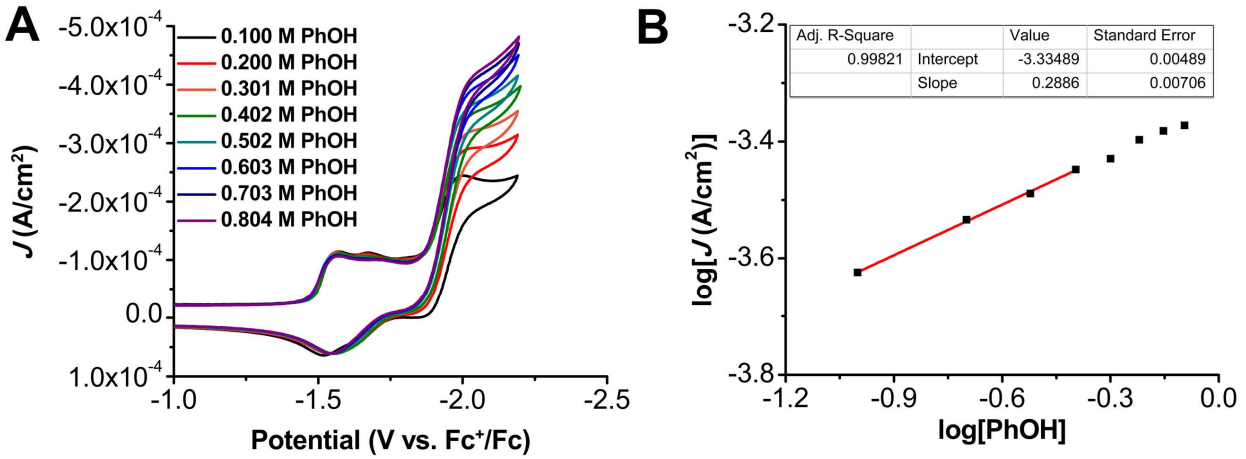

Figure S5.10. (**A**) CVs of 1.0 mM Cr(^{tbu}dh^{Ph}phen)Cl(H_2O) **1**, obtained under CO_2 saturation conditions with variable PhOH concentrations. Conditions: 0.1 M $TBAPF_6$/DMF; glassy carbon disc working electrode, glassy carbon rod counter electrode, Ag/AgCl pseudoreference electrode; 100 mV/s scan rate; referenced to internal ferrocene standard. (**B**) Log-log plot from data obtained from CVs in **A** at −2.06 V vs. Fc^+/Fc.

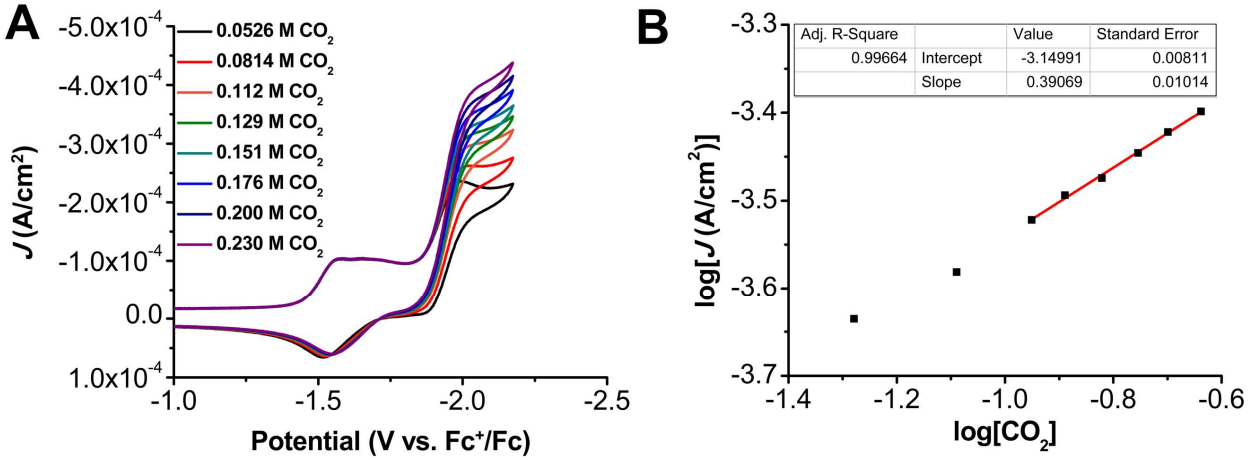

Figure S5.11. (**A**) CVs of 1.0 mM Cr(^{tbu}dh^{Ph}phen) **1** obtained under variable CO_2 concentrations with 0.6 M PhOH. Conditions: 0.1 M $TBAPF_6$/DMF; glassy carbon disc working electrode, glassy carbon rod counter electrode, Ag/AgCl pseudoreference electrode; 100 mV/s scan rate; referenced to internal ferrocene standard. (**B**) Log-log plot from data obtained from CVs in **A** at −2.06 V vs. Fc^+/Fc.

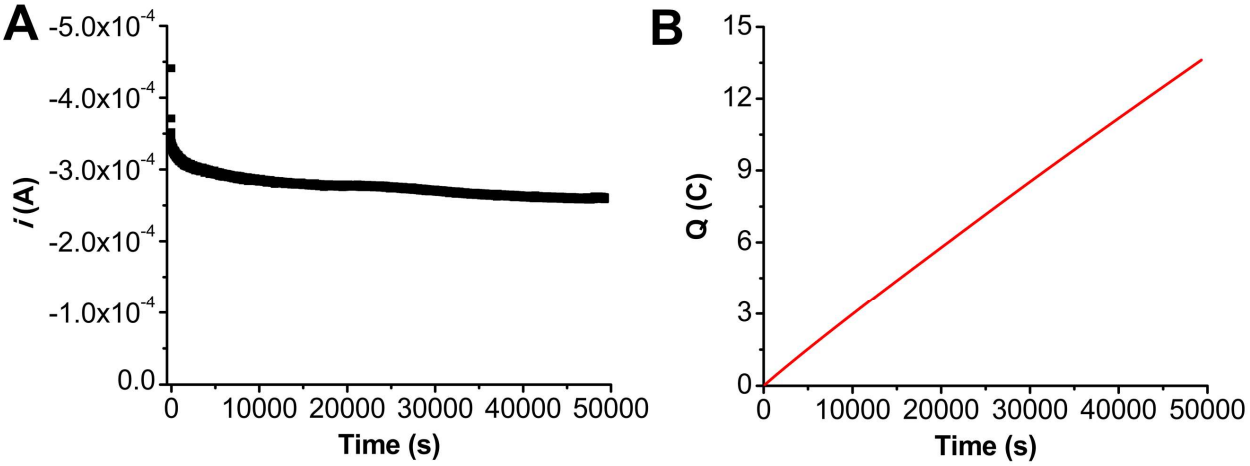

Figure S5.12. (**A**) Current versus time trace from CPE experiment for **1**+PhOH. (**B**) Charge passed versus time for the CPE experiment shown in **A**. Conditions were 0.5 mM Cr(^{tbu}dh^{Ph}phen)Cl(H_2O) **1** and 0.8 M PhOH under a CO_2 atmosphere at −2.10 V vs Fc^+/Fc in 0.1 M $TBAPF_6$/DMF; working electrode was a glassy carbon rod, counter electrode was a graphite rod, and the reference was a nonaqueous Ag/AgCl pseudoreference electrode; 0.075 M Fc was used as sacrificial oxidant.

Table S5.3. Results from CPE experiment in **Figure S5.12**, **1** + 0.8 M PhOH.

Time (s)	Charge (coulombs)	Moles (e^-)	Moles of CO	FE_{CO}	Moles of H_2	FE_{H2}
49329*	13.6	1.41×10^{-4}	6.58×10^{-5}	93.3	2.95×10^{-6}	4.18
49329*	13.6	1.41×10^{-4}	6.51×10^{-5}	92.2	4.67×10^{-6}	6.61
49329*	13.6	1.41×10^{-4}	6.40×10^{-5}	90.7	3.85×10^{-6}	5.45
49329*	13.6	1.41×10^{-4}	6.41×10^{-5}	90.9	2.17×10^{-6}	3.07
49329*	13.6	1.41×10^{-4}	6.06×10^{-5}	85.8	6.20×10^{-6}	8.79

*indicates a series of injections carried out upon completion of electrolysis

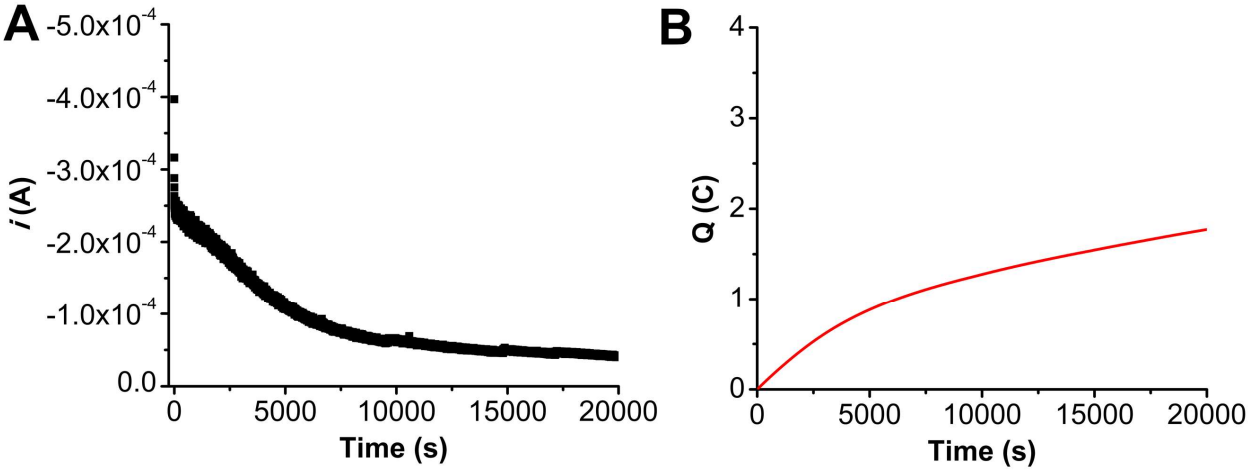

Figure S5.13. (**A**) Current versus time trace from CPE experiment for **1**. (**B**) Charge passed versus time for the CPE experiment shown in **A**. Conditions were 0.5 mM Cr(^{tbu}dh^{Ph}phen)Cl(H_2O) **1** under a CO_2 atmosphere at −2.10 V vs Fc^+/Fc in 0.1 M $TBAPF_6$/DMF; working electrode was a glassy carbon rod, counter electrode was a graphite rod, and the reference was a nonaqueous Ag/AgCl pseudoreference electrode; 0.075 M Fc was used as sacrificial oxidant.

Table S5.4. Results from CPE experiment in **Figure S5.13**, **1**.

Time (s)	Charge (coulombs)	Moles (e^-)	Moles of CO
9633	1.25	1.30×10^{-5}	< LOQ
14803	1.54	1.59×10^{-5}	< LOQ
17157	1.65	1.71×10^{-5}	< LOQ
19999	1.77	1.84×10^{-5}	< LOQ

5.5.4 Electrochemistry of BNTD

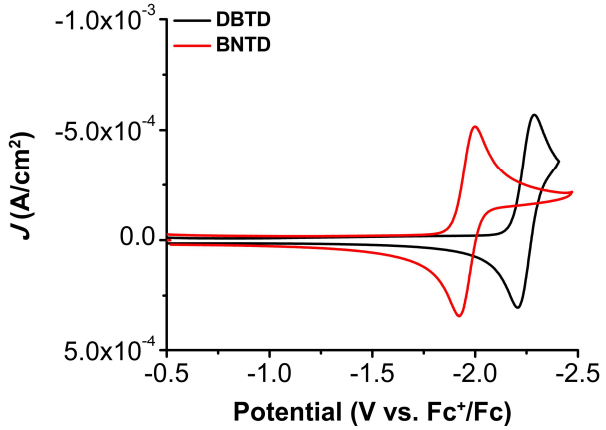

Figure S5.14. CVs of 2.5 mM DBTD and BNTD obtained under Ar saturation conditions.Conditions: 0.1 M $TBAPF_6$/DMF; glassy carbon disc working electrode, glassy carbon rod counter electrode, Ag/AgCl pseudoreference electrode; referenced to Fc^+/Fc internal standard; 100 mV/s scan rate.

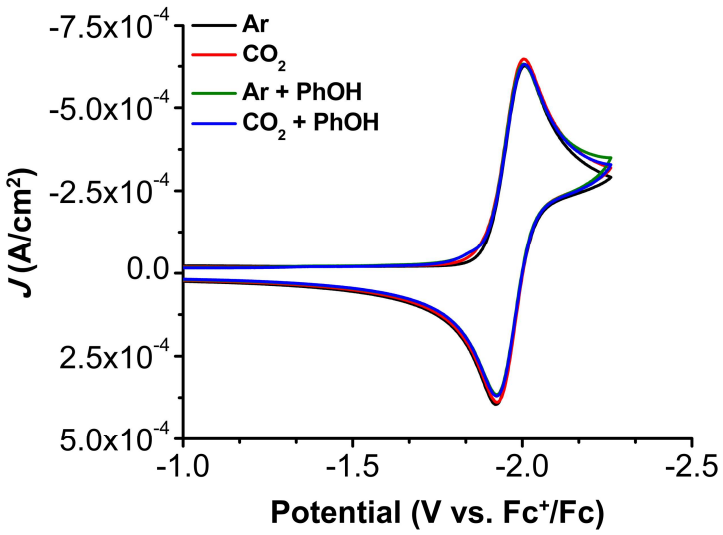

Figure S5.15. CVs of 2.5 mM BNTD both with and without 0.1 M PhOH obtained under Ar and CO_2 saturation conditions. Conditions: 0.1 M $TBAPF_6$/DMF; glassy carbon disc working electrode, glassy carbon rod counter electrode, Ag/AgCl pseudoreference electrode; referenced to Fc^+/Fc internal standard; 100 mV/s scan rate.

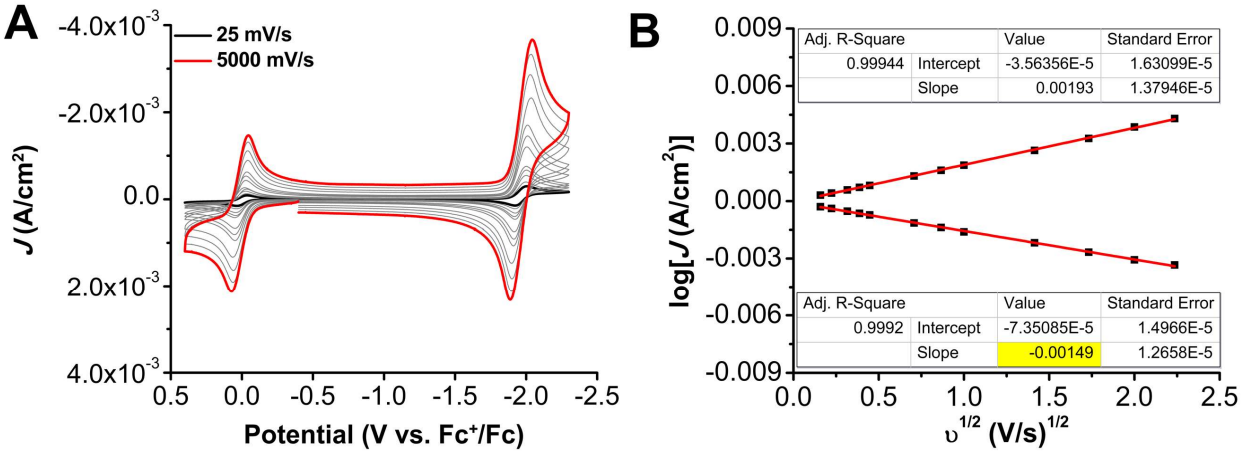

Figure S5.16. (**A**) CVs of 2.5 mM BNTD at variable scan rates ranging from 25 (black) to 5000 (red) mV/s, obtained under Ar saturation conditions. (**B**) Linear Fit of variable scan rate data from **A** demonstrating that BNTD shows a diffusion-limited current response. The slope highlighted in yellow was used to calculate the diffusion coefficient. The data in **B** was obtained from the reversible redox feature at −1.93 V vs Fc^+/Fc. Conditions: 0.1 M $TBAPF_6$/DMF; glassy carbon disc working electrode, glassy carbon rod counter electrode, Ag/AgCl pseudoreference electrode; varied scan rate; referenced to internal ferrocene standard.

5.5.5 Cyclic Voltammetry with Cr catalysts and RMs

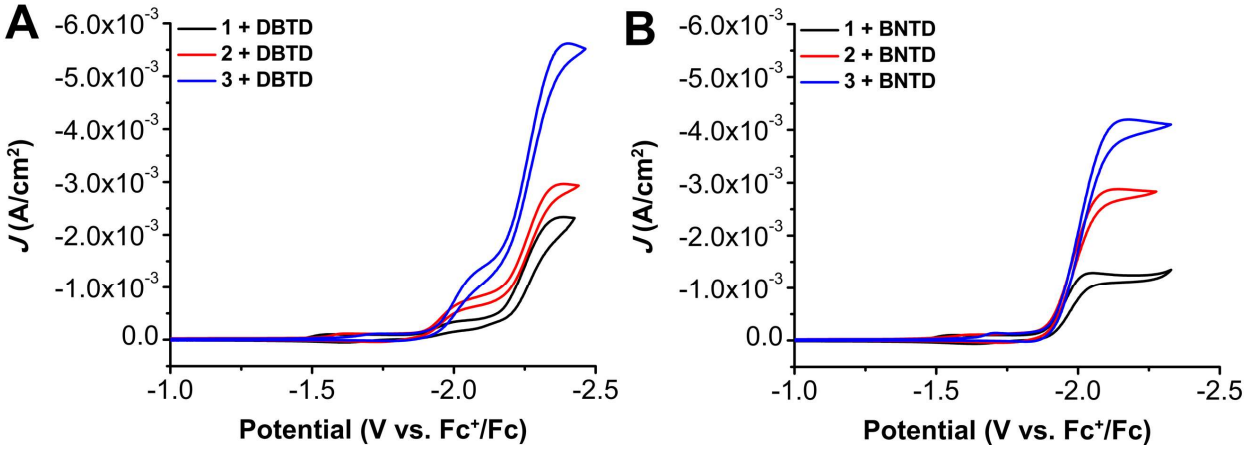

Figure S5.17. Comparison CVs of 1.0 mM Cr(^{tbu}dh^{Ph}phen)Cl(H_2O) **1**, Cr(^{tbu}dhphen)Cl(H_2O) **2**, and Cr(^{tbu}dh^{tbu}bpy)Cl(H_2O) **3** with (**A**) 2.5 mM DBTD and (**B**) BNTD and 0.5 M PhOH under CO_2 saturation conditions.Conditions: 0.1 M $TBAPF_6$/DMF; glassy carbon disc working electrode, glassy carbon rod counter electrode, Ag/AgCl pseudoreference electrode; referenced to Fc^+/Fc internal standard; 100 mV/s scan rate.

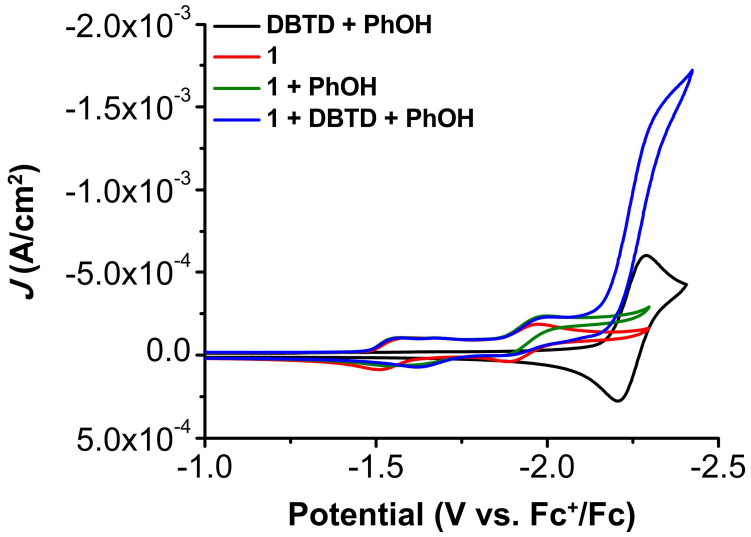

Figure S5.18. Comparison CVs of 1.0 mM Cr(^{tbu}dh^{Ph}phen)Cl(H_2O) **1** with and without 2.5 mM DBTD and 0.1 M PhOH under CO_2 saturation conditions.Conditions: 0.1 M $TBAPF_6$/DMF; glassy carbon disc working electrode, glassy carbon rod counter electrode, Ag/AgCl pseudoreference electrode; referenced to Fc^+/Fc internal standard; 100 mV/s scan rate.

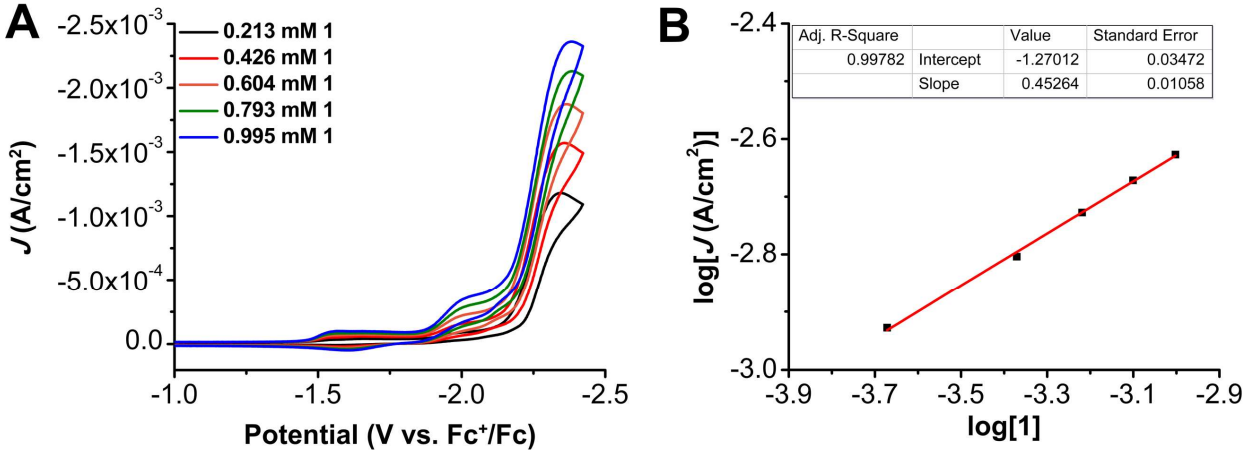

Figure S5.19. (**A**) CVs of Cr(^{tbu}dh^{Ph}phen)Cl(H_2O) **1** at variable concentrations, obtained under CO_2 saturation with 2.5 mM DBTD and 0.6 M PhOH. Conditions: 0.1 M $TBAPF_6$/DMF; glassy carbon disc working electrode, glassy carbon rod counter electrode, Ag/AgCl pseudoreference electrode; referenced to Fc^+/Fc internal standard; 100 mV/s scan rate. (**B**) Log-log plot from data obtained in **A** at –2.38 V vs. Fc^+/Fc.

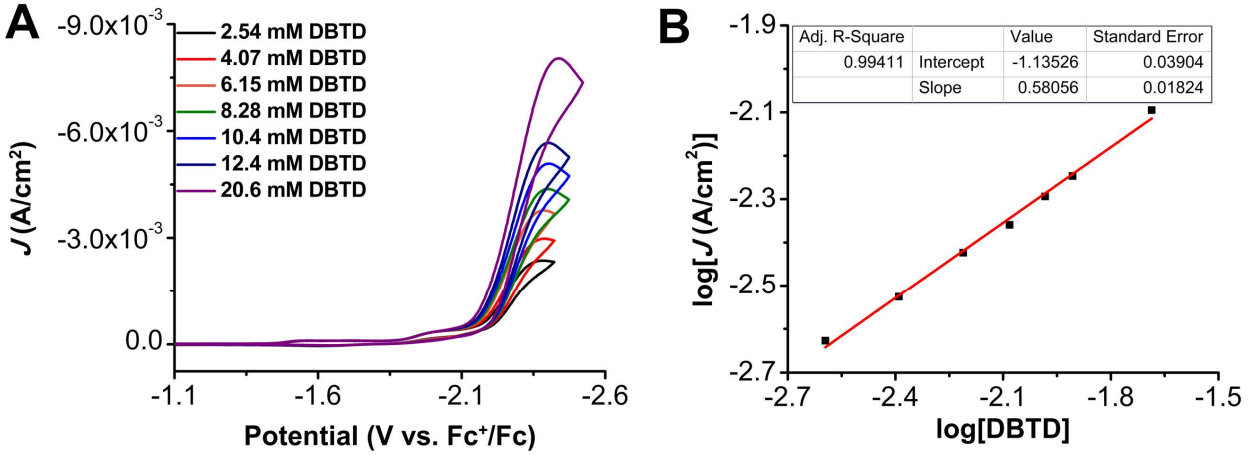

Figure S5.20. (**A**) CVs of 1.0 mM Cr(^{tbu}dh^{Ph}phen)Cl(H_2O) **1** with 0.6 M PhOH at variable DBTD concentrations, obtained under CO_2 saturation. Conditions: 0.1 M $TBAPF_6$/DMF; glassy carbon disc working electrode, glassy carbon rod counter electrode, Ag/AgCl pseudoreference electrode; referenced to Fc^+/Fc internal standard; 100 mV/s scan rate. (**B**) Log-log plot from data obtained in **A** at –2.37 V vs. Fc^+/Fc.

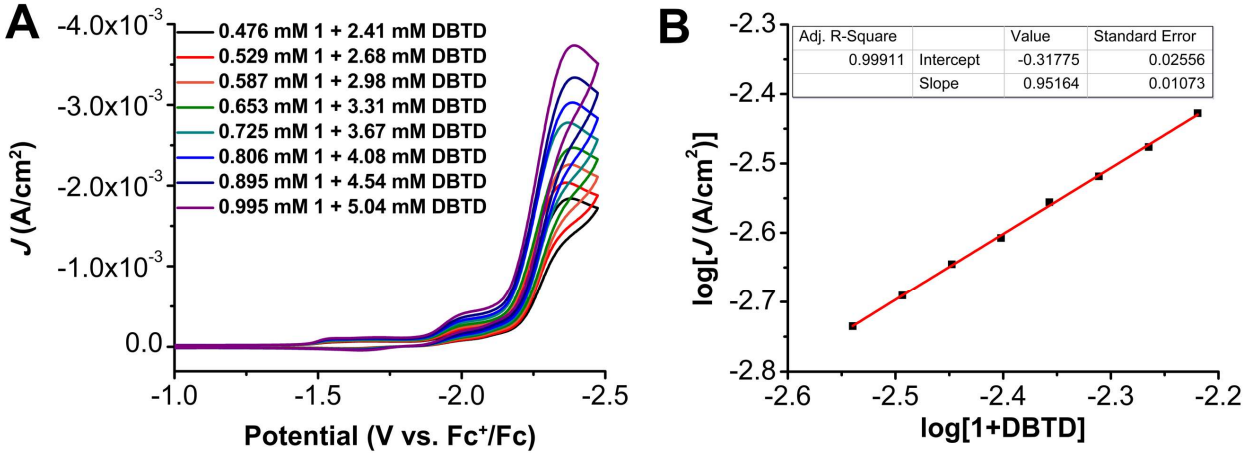

Figure S5.21. (**A**) CVs where the concentrations of Cr(^{tbu}dh^{Ph}phen)Cl(H_2O) **1** and DBTD were varied at a fixed 1:5 ratio of **1**:DBTD with 0.6 M PhOH under CO_2 saturation conditions.Conditions: 0.1 M $TBAPF_6$/DMF; glassy carbon disc working electrode, glassy carbon rod counter electrode, Ag/AgCl pseudoreference electrode; referenced to Fc^+/Fc internal standard; 100 mV/s scan rate. (**B**) Log-log plot from data obtained in **A** at –2.39 V vs. Fc^+/Fc.

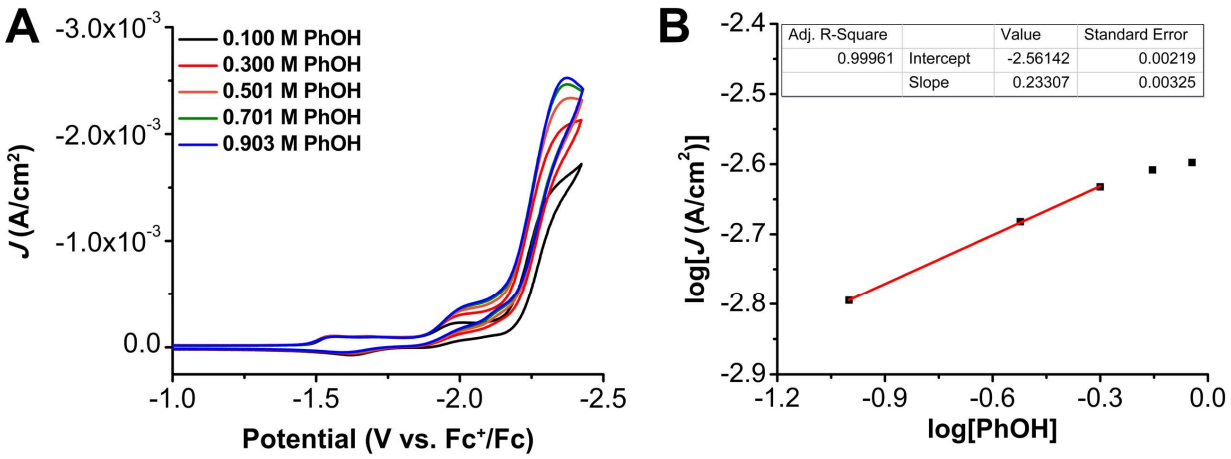

Figure S5.22. (**A**) CVs of PhOH at variable concentrations, obtained under CO_2 saturation with 1.0 mM Cr(^{tbu}dh^{Ph}phen)Cl(H_2O) **1** and 2.5 mM DBTD. Conditions: 0.1 M $TBAPF_6$/DMF; glassy carbon disc working electrode, glassy carbon rod counter electrode, Ag/AgCl pseudoreference electrode; referenced to Fc^+/Fc internal standard; 100 mV/s scan rate. (**B**) Log-log plot from data obtained in **A** at –2.37 V vs. Fc^+/Fc.

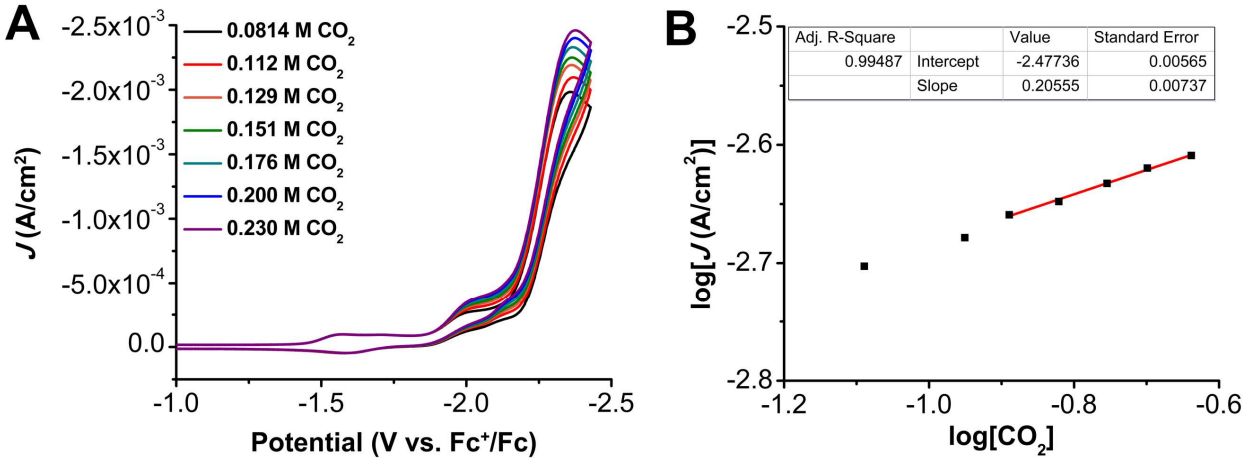

Figure S5.23. (**A**) CVs of 1.0 mM Cr(^{tbu}dh^{Ph}phen)Cl(H_2O) **1**, 2.5 mM DBTD, 0.9 M PhOH at varied CO_2 concentrations. Conditions: 0.1 M $TBAPF_6$/DMF; glassy carbon disc working electrode, glassy carbon rod counter electrode, Ag/AgCl pseudoreference electrode; referenced to Fc^+/Fc internal standard; 100 mV/s scan rate. (**B**) Log-log plot from data obtained in **A** at –2.36 V vs. Fc^+/Fc.

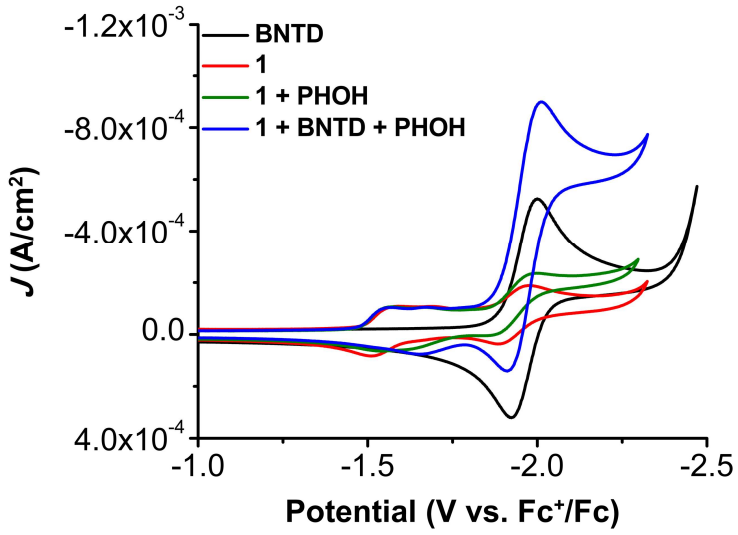

Figure S5.24. Comparison CVs of 1.0 mM Cr(^{tbu}dh^{Ph}phen)Cl(H_2O) **1** with and without 2.5 mM BNTD and 0.1 M PhOH under CO_2 saturation conditions. Conditions: 0.1 M $TBAPF_6$/DMF; glassy carbon disc working electrode, glassy carbon rod counter electrode, Ag/AgCl pseudoreference electrode; referenced to Fc^+/Fc internal standard; 100 mV/s scan rate.

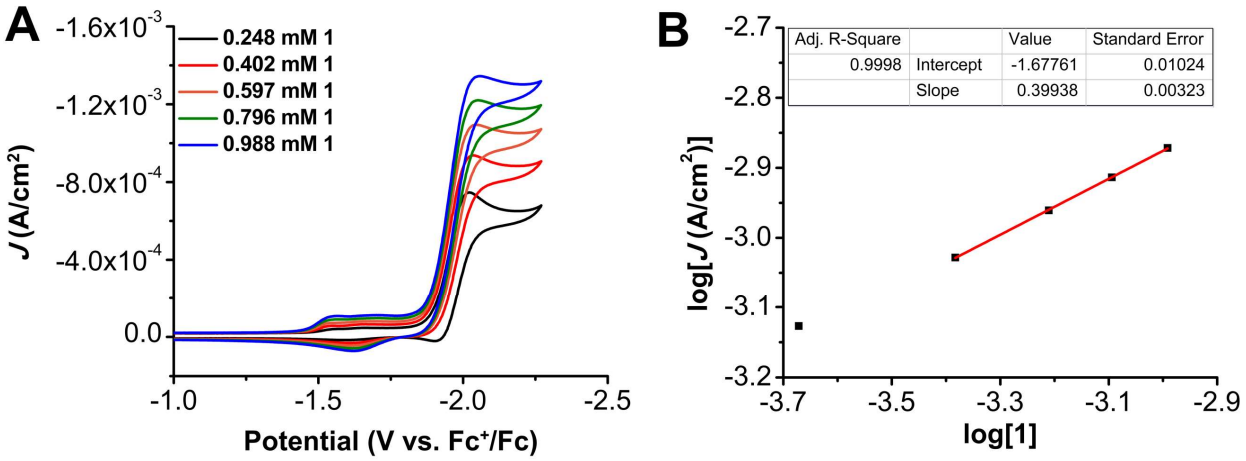

Figure S5.25. (**A**) CVs of Cr(^{tbu}dh^{Ph}phen)Cl(H_2O) **1** at variable concentrations, obtained under CO_2 saturation with 2.5 mM BNTD and 0.6 M PhOH. Conditions: 0.1 M $TBAPF_6$/DMF; glassy carbon disc working electrode, glassy carbon rod counter electrode, Ag/AgCl pseudoreference electrode; referenced to Fc^+/Fc internal standard; 100 mV/s scan rate. (**B**) Log-log plot from data obtained in **A** at –2.05 V vs. Fc^+/Fc.

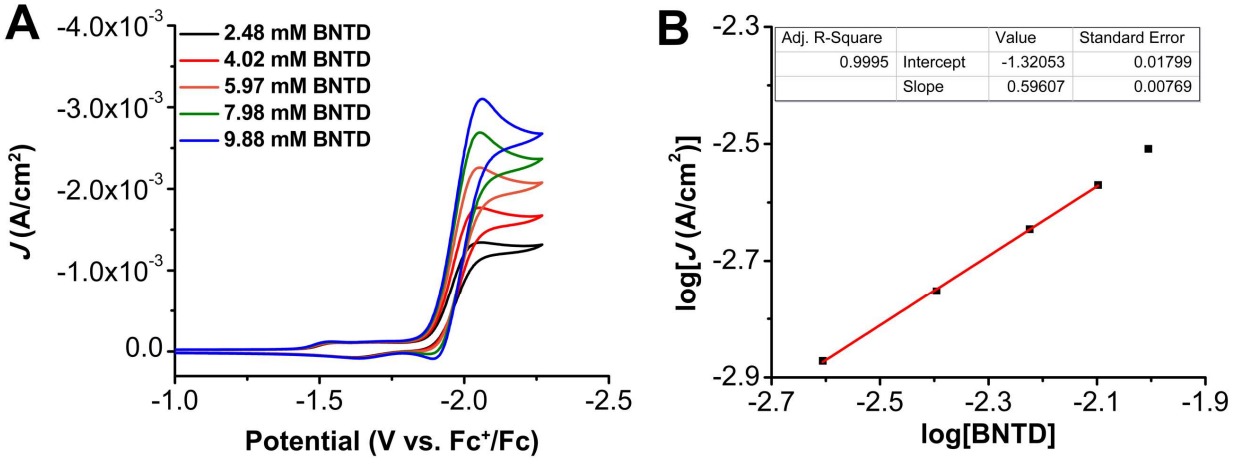

Figure S5.26. (**A**) CVs of 1.0 mM Cr(^{tbu}dh^{Ph}phen)Cl(H_2O) **1** with 0.6 M PhOH at variable BNTD concentrations, obtained under CO_2 saturation. Conditions: 0.1 M $TBAPF_6$/DMF; glassy carbon disc working electrode, glassy carbon rod counter electrode, Ag/AgCl pseudoreference electrode; referenced to Fc^+/Fc internal standard; 100 mV/s scan rate. (**B**) Log-log plot from data obtained in **A** at –2.06 V vs. Fc^+/Fc.

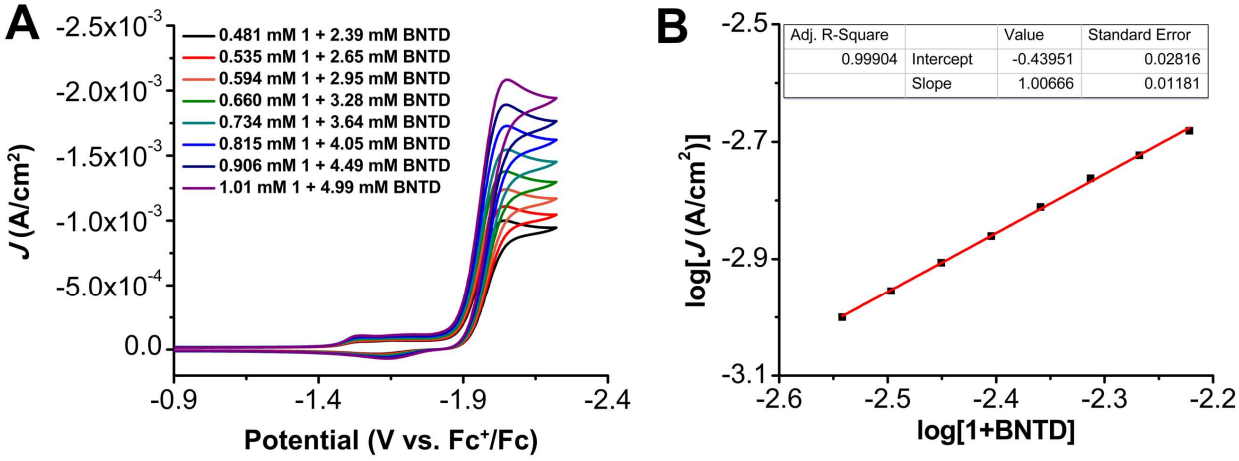

Figure S5.27. (**A**) CVs where the concentrations of Cr(^{tbu}dh^{Ph}phen)Cl(H_2O) **1** and BNTD were varied at a fixed 1:5 ratio of **1**:BNTD with 0.6 M PhOH under CO_2 saturation conditions. Conditions: 0.1 M $TBAPF_6$/DMF; glassy carbon disc working electrode, glassy carbon rod counter electrode, Ag/AgCl pseudoreference electrode; referenced to Fc^+/Fc internal standard; 100 mV/s scan rate. (**B**) Log-log plot from data obtained in **A** at –2.05 V vs. Fc^+/Fc.

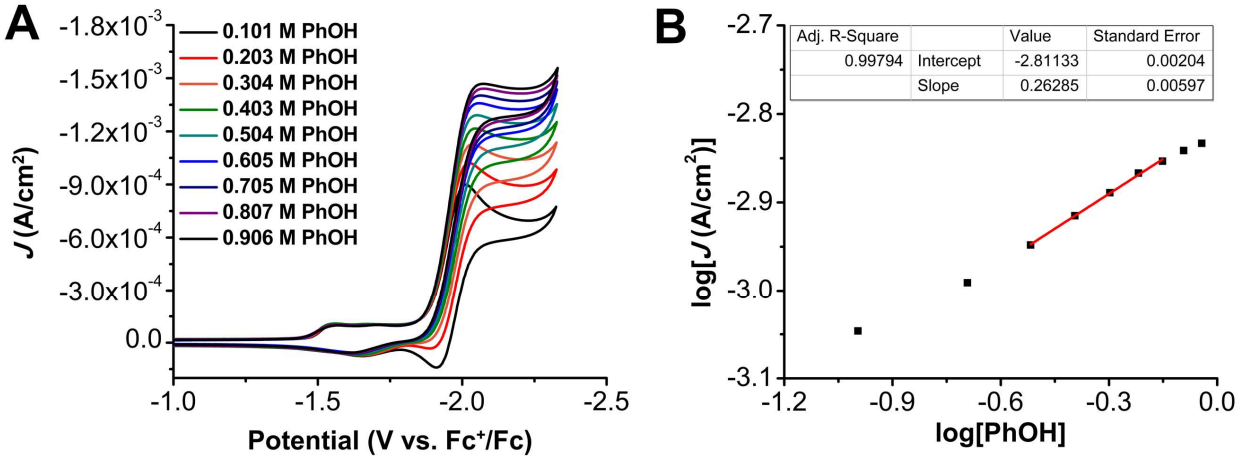

Figure S5.28. (**A**) CVs of PhOH at variable concentrations, obtained under CO_2 saturation with 1.0 mM Cr(^{tbu}dh^{Ph}phen)Cl(H_2O) **1** and 2.5 mM BNTD. Conditions: 0.1 M $TBAPF_6$/DMF; glassy carbon disc working electrode, glassy carbon rod counter electrode, Ag/AgCl pseudoreference electrode; referenced to Fc^+/Fc internal standard; 100 mV/s scan rate. (**B**) Log-log plot from data obtained in **A** at –2.07 V vs. Fc^+/Fc.

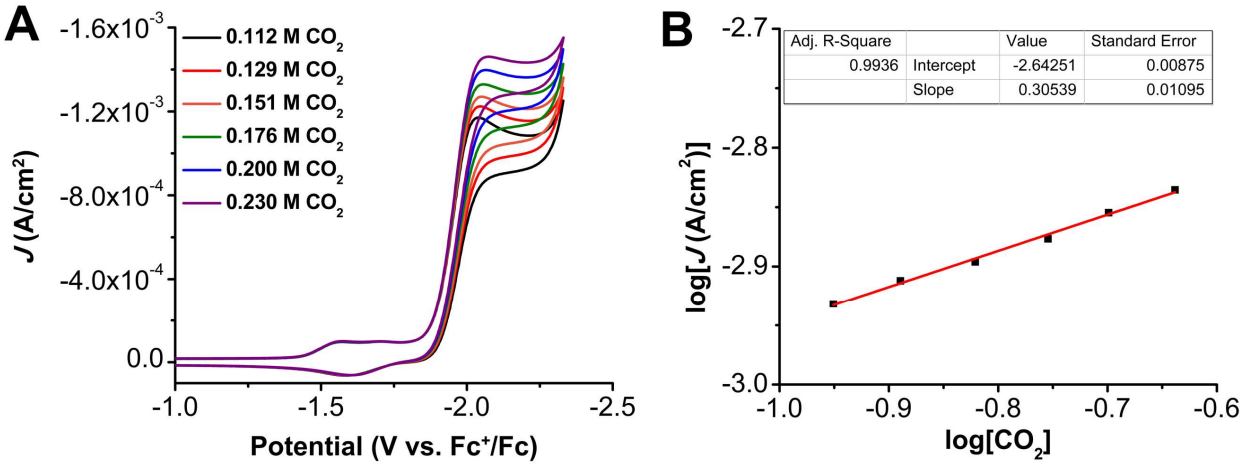

Figure S5.29. (**A**) CVs of 1.0 mM Cr(^{tbu}dh^{Ph}phen)Cl(H_2O) **1**, 2.5 mM BNTD, 0.9 M PhOH at varied CO_2 concentrations. Conditions: 0.1 M $TBAPF_6$/DMF; glassy carbon disc working electrode, glassy carbon rod counter electrode, Ag/AgCl pseudoreference electrode; referenced to Fc^+/Fc internal standard; 100 mV/s scan rate. (**B**) Log-log plot from data obtained in **A** at –2.07 V vs. Fc^+/Fc.

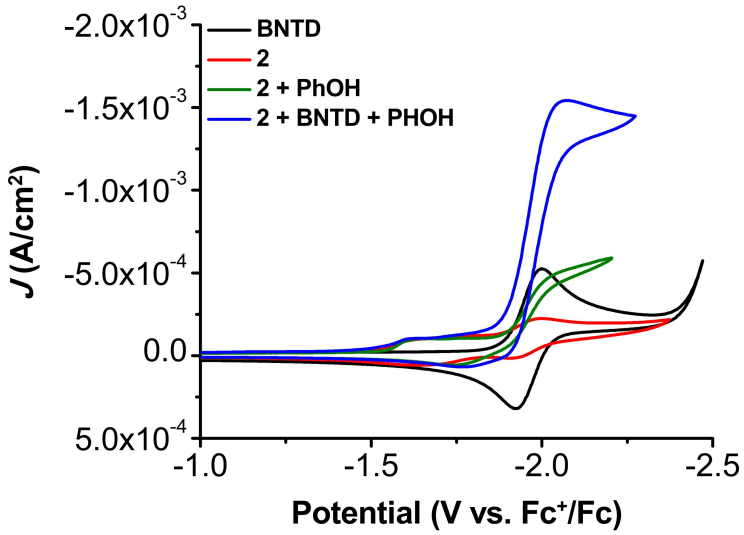

Figure S5.30. Comparison CVs of 1.0 mM Cr(^{tbu}dhphen)Cl(H_2O) **2** with and without 2.5 mM BNTD and 0.1 M PhOH under CO_2 saturation conditions. Conditions: 0.1 M $TBAPF_6$/DMF; glassy carbon disc working electrode, glassy carbon rod counter electrode, Ag/AgCl pseudoreference electrode; referenced to Fc^+/Fc internal standard; 100 mV/s scan rate.

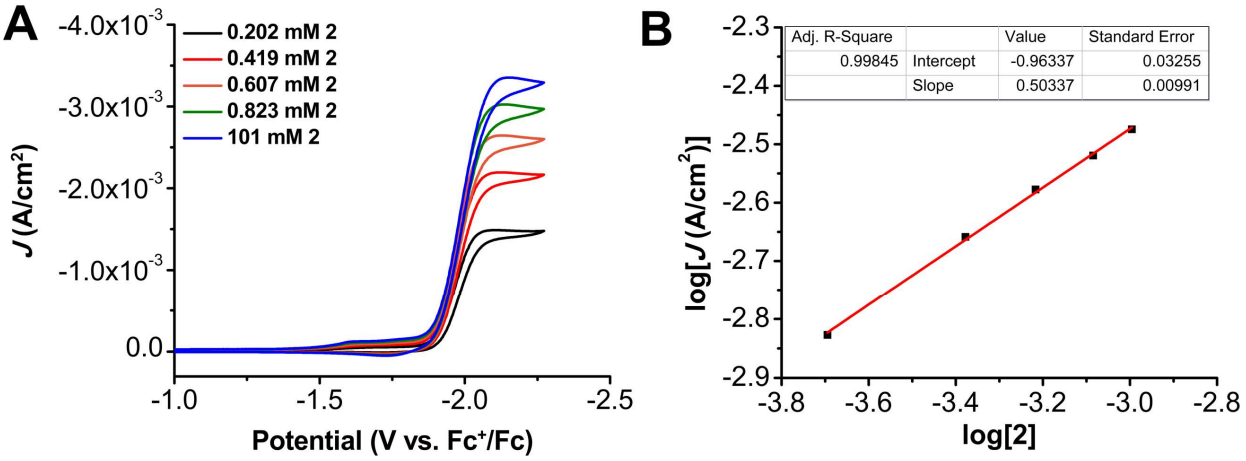

Figure S5.31. (**A**) CVs of Cr(^{tbu}dhphen)Cl(H_2O) **2** at variable concentrations, obtained under CO_2 saturation with 2.5 mM BNTD and 0.6 M PhOH. Conditions: 0.1 M $TBAPF_6$/DMF; glassy carbon disc working electrode, glassy carbon rod counter electrode, Ag/AgCl pseudoreference electrode; referenced to Fc^+/Fc internal standard; 100 mV/s scan rate. (**B**) Log-log plot from data obtained in **A** at –2.14 V vs. Fc^+/Fc.

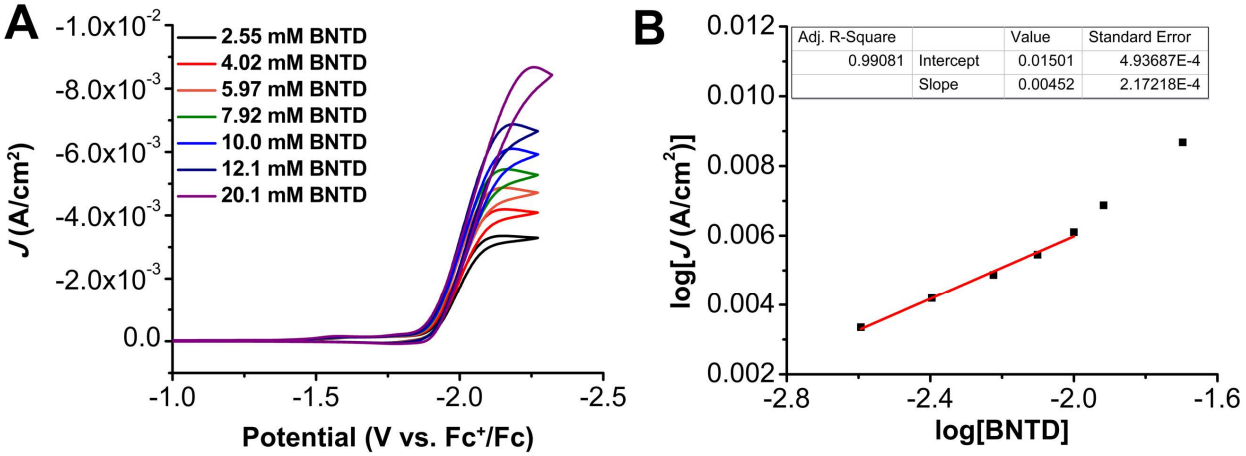

Figure S5.32. (**A**) CVs of 1.0 mM Cr(^{tbu}dhphen)Cl(H_2O) **2** with 0.6 M PhOH at variable BNTD concentrations, obtained under CO_2 saturation. Conditions: 0.1 M $TBAPF_6$/DMF; glassy carbon disc working electrode, glassy carbon rod counter electrode, Ag/AgCl pseudoreference electrode; referenced to Fc^+/Fc internal standard; 100 mV/s scan rate. (**B**) Log-log plot from data obtained in **A** at –2.16 V vs. Fc^+/Fc.

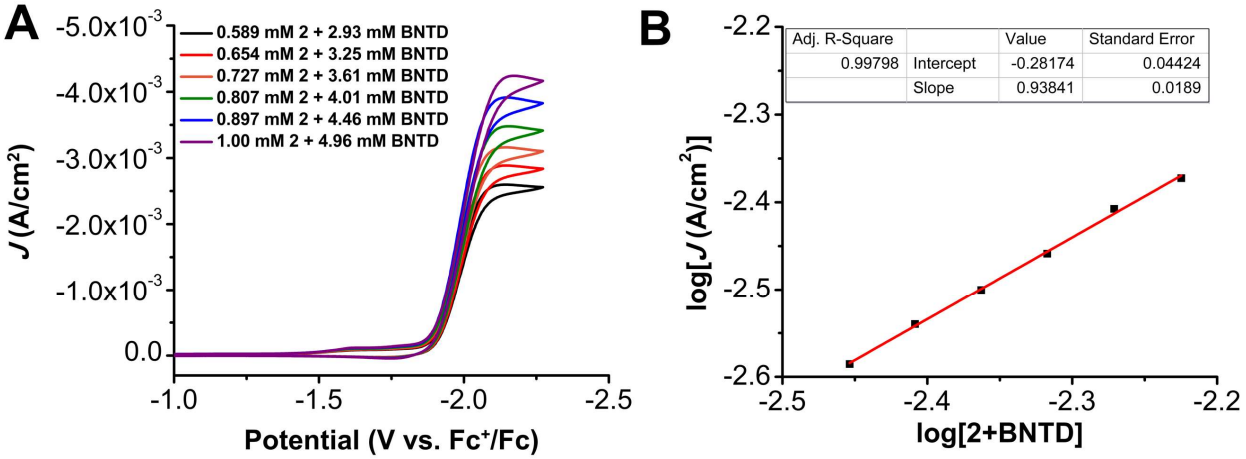

Figure S5.33. (**A**) CVs where the concentrations of Cr(^{tbu}dhphen)Cl(H_2O) **2** and BNTD were varied at a fixed 1:5 ratio of **2**:BNTD with 0.6 M PhOH under CO_2 saturation conditions.1 Conditions: 0.1 M $TBAPF_6$/DMF; glassy carbon disc working electrode, glassy carbon rod counter electrode, Ag/AgCl pseudoreference electrode; referenced to Fc^+/Fc internal standard; 100 mV/s scan rate. (**B**) Log-log plot from data obtained in **A** at –2.13 V vs. Fc^+/Fc.

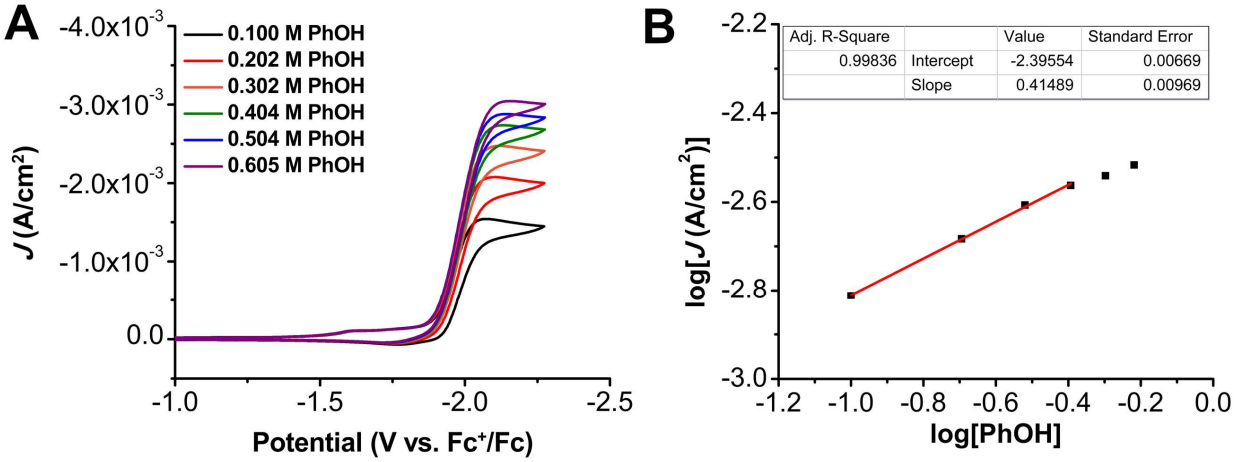

Figure S5.34. (**A**) CVs of PhOH at variable concentrations, obtained under CO_2 saturation with 1.0 mM Cr(^{tbu}dhphen)Cl(H_2O) **2** and 2.5 mM BNTD. Conditions: 0.1 M $TBAPF_6$/DMF; glassy carbon disc working electrode, glassy carbon rod counter electrode, Ag/AgCl pseudoreference electrode; referenced to Fc^+/Fc internal standard; 100 mV/s scan rate. (**B**) Log-log plot from data obtained in **A** at –2.12 V vs. Fc^+/Fc.

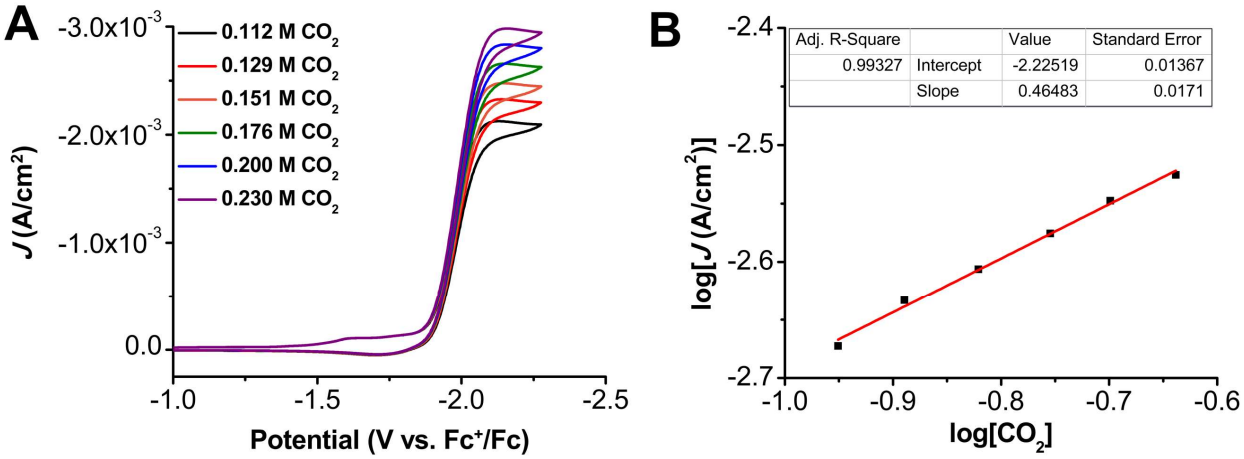

Figure S5.35. (**A**) CVs of 1.0 mM Cr(^{tbu}dhphen)Cl(H_2O) **2**, 2.5 mM BNTD, 0.6 M PhOH at varied CO_2 concentrations. Conditions: 0.1 M $TBAPF_6$/DMF; glassy carbon disc working electrode, glassy carbon rod counter electrode, Ag/AgCl pseudoreference electrode; referenced to Fc^+/Fc internal standard; 100 mV/s scan rate. (**B**) Log-log plot from data obtained in **A** at –2.14 V vs. Fc^+/Fc.

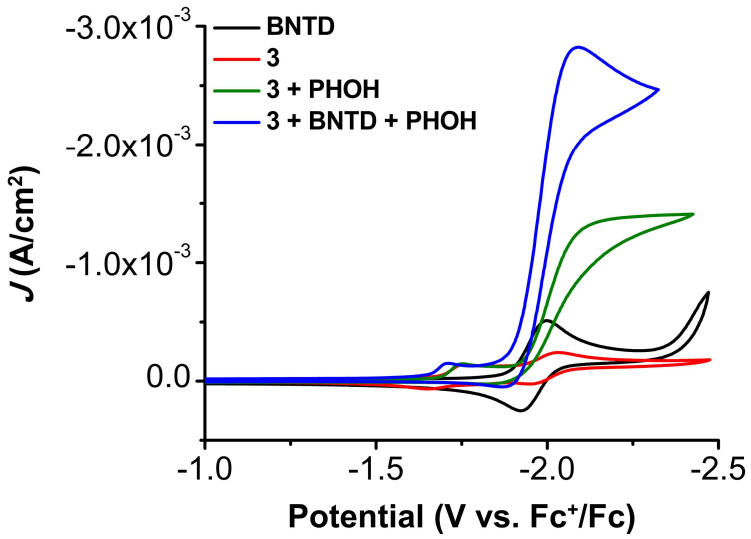

Figure S5.36. Comparison CVs of 1.0 mM Cr(^{tbu}dh^{tbu}bpy)Cl(H_2O) **3** with and without 2.5 mM BNTD and 0.1 M PhOH under CO_2 saturation conditions.Conditions: 0.1 M $TBAPF_6$/DMF; glassy carbon disc working electrode, glassy carbon rod counter electrode, Ag/AgCl pseudoreference electrode; referenced to Fc^+/Fc internal standard; 100 mV/s scan rate.

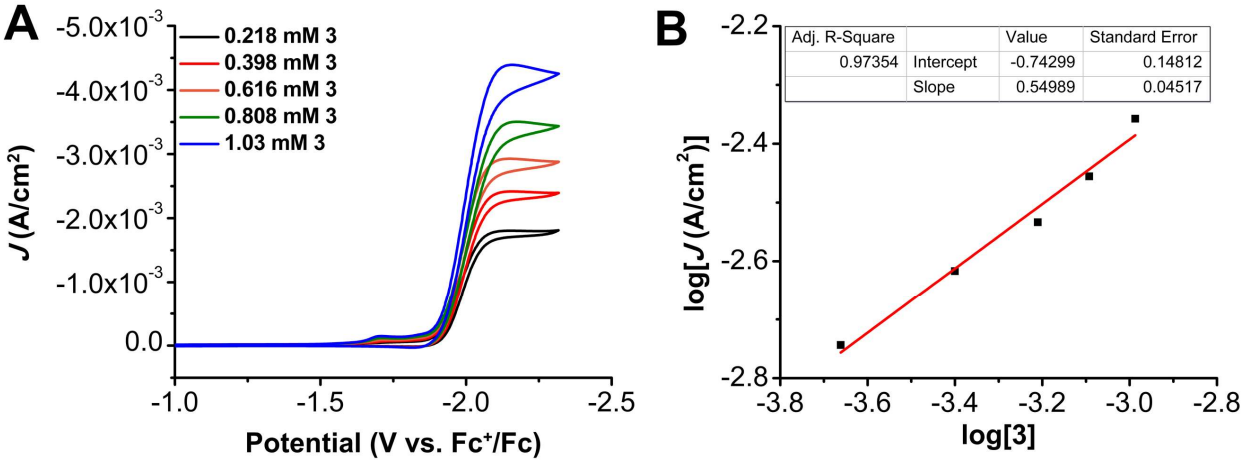

Figure S5.37. (**A**) CVs of Cr(^{tbu}dh^{tbu}bpy)Cl(H_2O) **3** at variable concentrations, obtained under CO_2 saturation with 2.5 mM BNTD and 0.5 M PhOH. Conditions: 0.1 M $TBAPF_6$/DMF; glassy carbon disc working electrode, glassy carbon rod counter electrode, Ag/AgCl pseudoreference electrode; referenced to Fc^+/Fc internal standard; 100 mV/s scan rate. (**B**) Log-log plot from data obtained in **A** at –2.15 V vs. Fc^+/Fc.

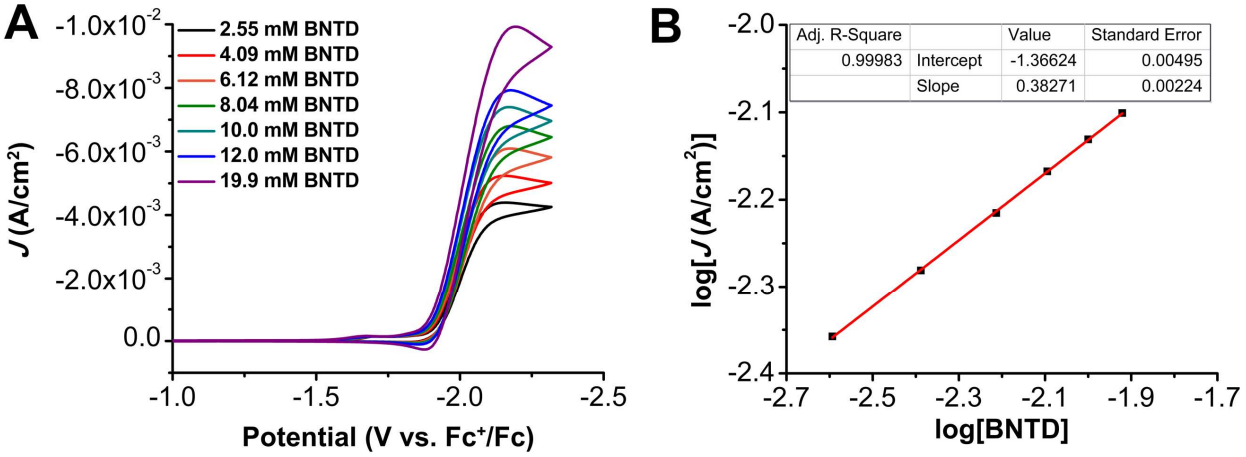

Figure S5.38. (**A**) CVs of 1.0 mM Cr(^{tbu}dh^{tbu}bpy)Cl(H_2O) **3** with 0.5 M PhOH at variable BNTD concentrations, obtained under CO_2 saturation. Conditions: 0.1 M $TBAPF_6$/DMF; glassy carbon disc working electrode, glassy carbon rod counter electrode, Ag/AgCl pseudoreference electrode; referenced to Fc^+/Fc internal standard; 100 mV/s scan rate. (**B**) Log-log plot from data obtained in **A** at –2.17 V vs. Fc^+/Fc.

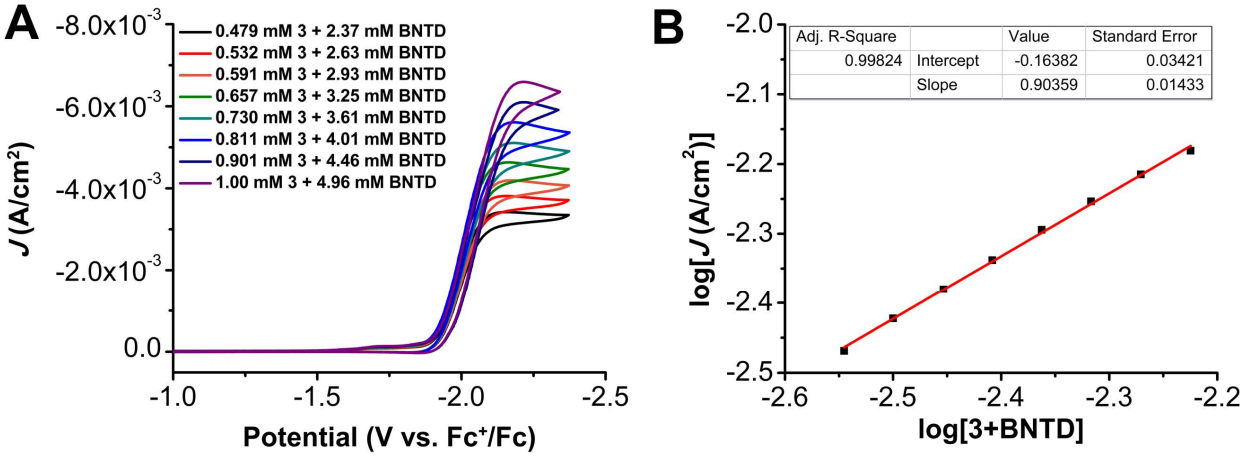

Figure S5.39. (**A**) CVs where the concentrations of Cr(^{tbu}dh^{tbu}bpy)Cl(H_2O) **3** and BNTD were varied at a fixed 1:5 ratio of **3**:BNTD with 0.5 M PhOH under CO_2 saturation conditions. Conditions: 0.1 M $TBAPF_6$/DMF; glassy carbon disc working electrode, glassy carbon rod counter electrode, Ag/AgCl pseudoreference electrode; referenced to Fc^+/Fc internal standard; 100 mV/s scan rate. (**B**) Log-log plot from data obtained in **A** at –2.22 V vs. Fc^+/Fc.

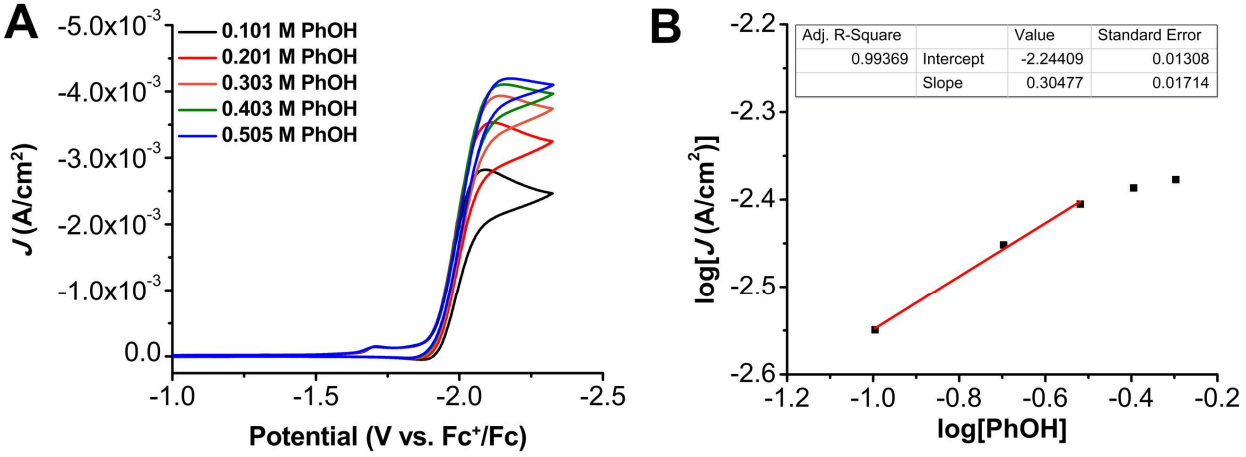

Figure S5.40. (**A**) CVs of PhOH at variable concentrations, obtained under CO_2 saturation with 1.0 mM Cr(^{tbu}dh^{tbu}bpy)Cl(H_2O) **3** and 2.5 mM BNTD. Conditions: 0.1 M $TBAPF_6$/DMF; glassy carbon disc working electrode, glassy carbon rod counter electrode, Ag/AgCl pseudoreference electrode; referenced to Fc^+/Fc internal standard; 100 mV/s scan rate. (**B**) Log-log plot from data obtained in **A** at –2.14 V vs. Fc^+/Fc.

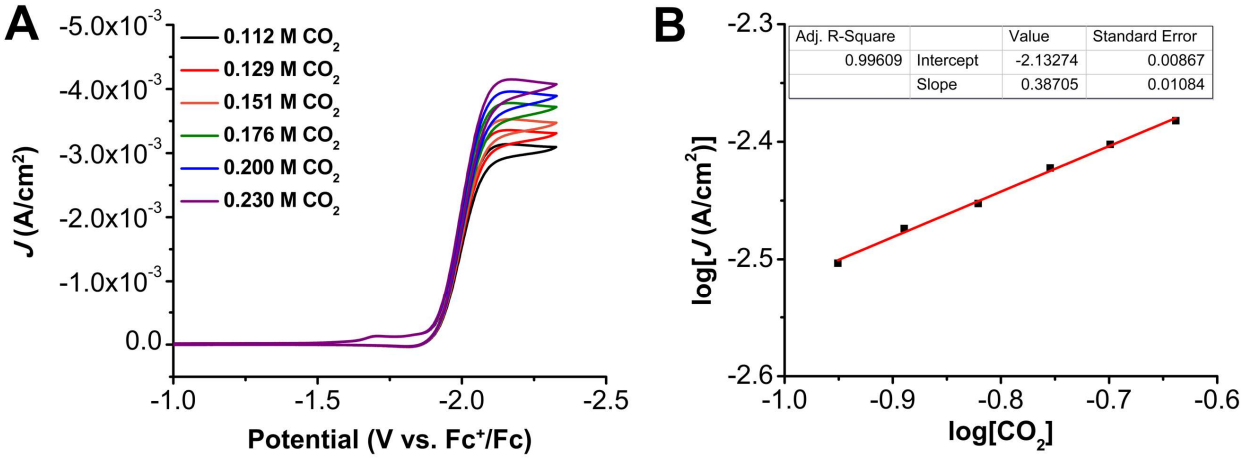

Figure S5.41. (**A**) CVs of 1.0 mM Cr(^{tbu}dh^{tbu}bpy)Cl(H_2O) **3**, 2.5 mM BNTD, 0.6 M PhOH at varied CO_2 concentrations. Conditions: 0.1 M $TBAPF_6$/DMF; glassy carbon disc working electrode, glassy carbon rod counter electrode, Ag/AgCl pseudoreference electrode; referenced to Fc^+/Fc internal standard; 100 mV/s scan rate. (**B**) Log-log plot from data obtained in **A** at –2.14 V vs. Fc^+/Fc.

5.5.6 CPE with Cr Catalysts and RMs

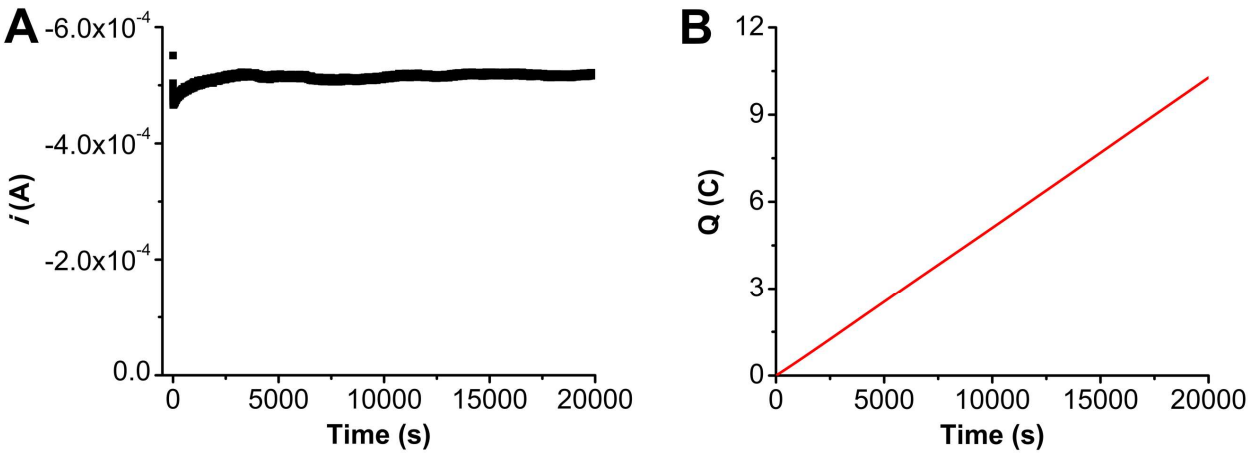

Figure S5.42. (**A**) Current versus time trace from CPE experiment for **1**+DBTD+PhOH. (**B**) Charge passed versus time for the CPE experiment shown in **A**. Conditions were 0.1 mM Cr(^{tbu}dh^{Ph}phen)Cl(H_2O) **1**, 0.5 mM DBTD, and 1.0 M PhOH under a CO_2 atmosphere at −2.30 V vs Fc^+/Fc in 0.1 M $TBAPF_6$/DMF; working electrode was a glassy carbon rod, counter electrode was a graphite rod, and the reference was a nonaqueous Ag/AgCl pseudoreference electrode; 0.075 M Fc was used as sacrificial oxidant.

Table S5.5. Results from CPE experiment in **Figure S5.42**, **1** + DBTD + PhOH.

Time (s)	Charge (coulombs)	Moles (e^-)	Moles of CO	FE_{CO}	Moles of H_2	FE_{H2}
20000*	10.3	1.07 x 10^{-4}	4.22 x 10^{-5}	79.2	1.05 x 10^{-5}	19.8
20000*	10.3	1.07 x 10^{-4}	4.02 x 10^{-5}	75.5	9.60 x 10^{-6}	18.0
20000*	10.3	1.07 x 10^{-4}	4.06 x 10^{-5}	76.1	9.32 x 10^{-6}	17.5

*indicates a series of injections carried out in triplicate upon completion of electrolysis

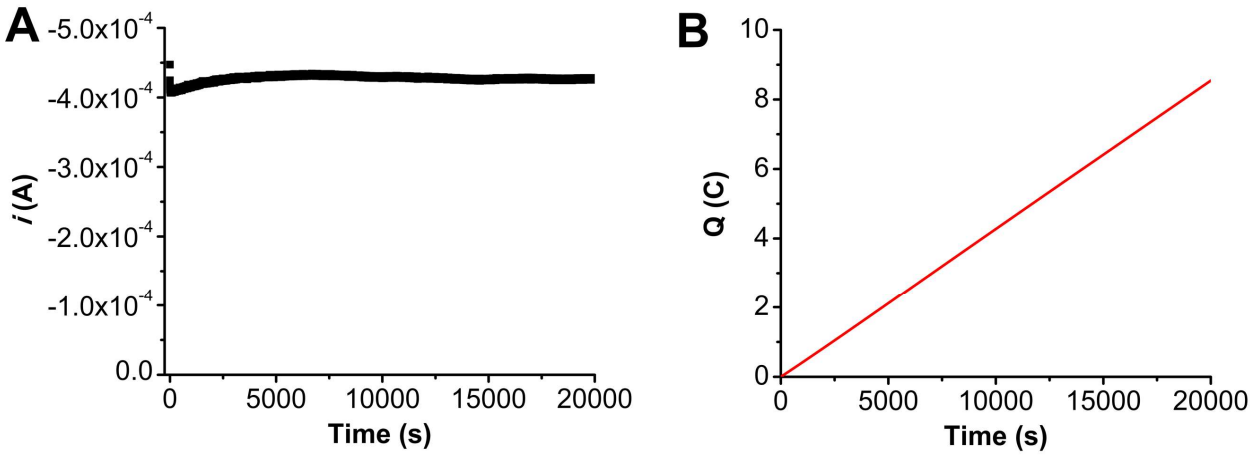

Figure S5.43. (**A**) Current versus time trace from CPE experiment for **1**+BNTD+PhOH. (**B**) Charge passed versus time for the CPE experiment shown in **A**. Conditions were 0.1 mM Cr(^{tbu}dh^{Ph}phen)Cl(H_2O) **1**, 0.5 mM BNTD, and 1.0 M PhOH under a CO_2 atmosphere at −2.20 V vs Fc^+/Fc in 0.1 M $TBAPF_6$/DMF; working electrode was a glassy carbon rod, counter electrode was a graphite rod, and the reference was a nonaqueous Ag/AgCl pseudoreference electrode; 0.075 M Fc was used as sacrificial oxidant.

Table S5.6. Results from CPE experiment in **Figure S5.43**, **1** + BNTD + PhOH.

Time (s)	Charge (coulombs)	Moles (e^-)	Moles of CO	FE_{CO}	Moles of H_2
13569	5.80	6.01×10^{-5}	2.80×10^{-5}	93.1	<LOQ
16528	7.06	7.32×10^{-5}	3.53×10^{-5}	96.6	<LOQ
19211	8.21	8.51×10^{-5}	4.22×10^{-5}	99.2	<LOQ
20791*	8.88	9.21×10^{-5}	4.53×10^{-5}	98.4	<LOQ
20791*	8.88	9.21×10^{-5}	4.52×10^{-5}	98.2	<LOQ
20791*	8.88	9.21×10^{-5}	4.52×10^{-5}	98.1	<LOQ

*indicates a series of injections carried out in triplicate upon completion of electrolysis

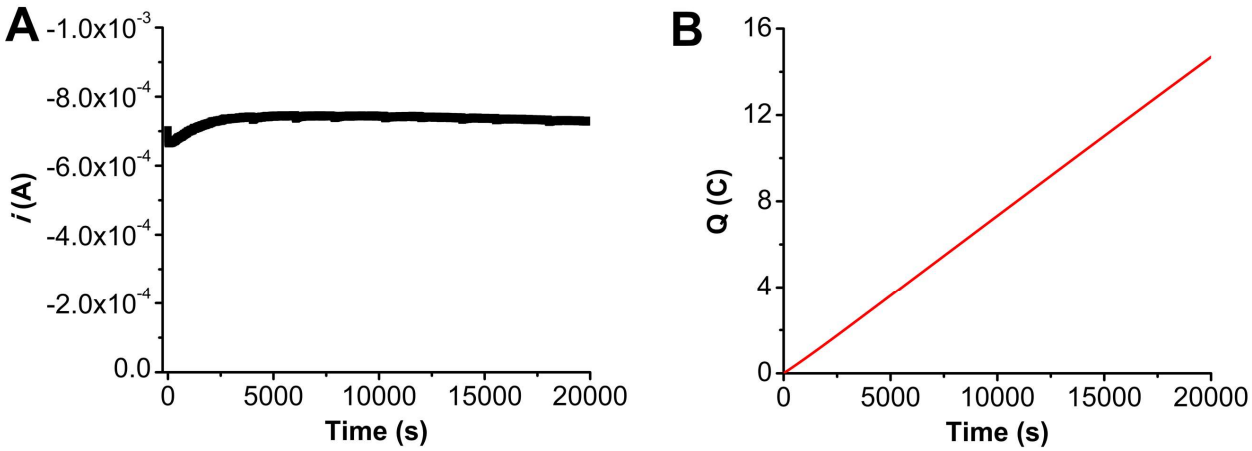

Figure S5.44. (**A**) Current versus time trace from CPE experiment for **2**+BNTD+PhOH. (**B**) Charge passed versus time for the CPE experiment shown in **A**. Conditions were 0.1 mM Cr(^{tbu}dhphen)Cl(H_2O) **2**, 0.5 mM BNTD, and 1.0 M PhOH under a CO_2 atmosphere at −2.20 V vs Fc^+/Fc in 0.1 M $TBAPF_6$/DMF; working electrode was a glassy carbon rod, counter electrode was a graphite rod, and the reference was a nonaqueous Ag/AgCl pseudoreference electrode; 0.075 M Fc was used as sacrificial oxidant.

Table S5.7. Results from CPE experiment in **Figure S5.44**, **2** + BNTD + PhOH.

Time (s)	Charge (coulombs)	Moles (e^-)	Moles of CO	FE_{CO}
11982	8.79	9.11×10^{-5}	4.33×10^{-5}	93.4
13926	10.2	1.06×10^{-4}	5.25×10^{-5}	95.1
15525	11.4	1.18×10^{-4}	6.30×10^{-5}	107
18025	13.2	1.37×10^{-4}	7.01×10^{-5}	102
20000*	14.7	1.52×10^{-4}	7.91×10^{-5}	104
20000*	14.7	1.52×10^{-4}	8.19×10^{-5}	108
20000*	14.7	1.52×10^{-4}	8.27×10^{-5}	109

*indicates a series of injections carried out in triplicate upon completion of electrolysis

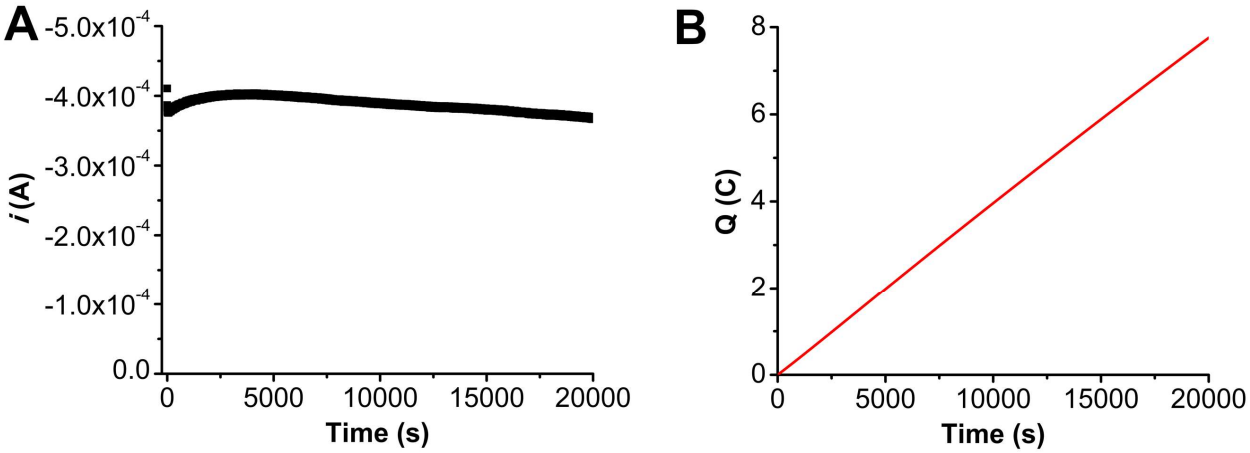

Figure S5.45. (**A**) Current versus time trace from CPE experiment for **3**+BNTD+PhOH. (**B**) Charge passed versus time for the CPE experiment shown in **A**. Conditions were 0.1 mM Cr(^{tbu}dh^{tbu}bpy)Cl(H_2O) **3**, 0.5 mM BNTD, and 0.12 M PhOH under a CO_2 atmosphere at −2.20 V vs Fc^+/Fc in 0.1 M $TBAPF_6$/DMF; working electrode was a glassy carbon rod, counter electrode was a graphite rod, and the reference was a nonaqueous Ag/AgCl pseudoreference electrode; 0.075 M Fc was used as sacrificial oxidant.

Table S5.8. Results from CPE experiment in **Figure S5.45**, **3** + BNTD + PhOH.

Time (s)	Charge (coulombs)	Moles (e^-)	Moles of CO	FE_{CO}
20000*	7.76	8.04 x 10^{-5}	4.16 x 10^{-5}	103
20000*	7.76	8.04 x 10^{-5}	3.99 x 10^{-5}	99.2
20000*	7.76	8.04 x 10^{-5}	3.92 x 10^{-5}	97.5

*indicates a series of injections carried out in triplicate upon completion of electrolysis

5.6 References:

1. Carbon dioxide now more than 50% higher than pre-industrial levels. https://www.noaa.gov/news-release/carbon-dioxide-now-more-than-50-higher-than-pre-industrial-levels.
2. De Luna, P.; Hahn, C.; Higgins, D.; Jaffer, S. A.; Jaramillo, T. F.; Sargent, E. H., What would it take for renewably powered electrosynthesis to displace petrochemical processes? *Science* **2019,** *364* (6438), eaav3506.
3. Aresta, M.; Dibenedetto, A.; Angelini, A., Catalysis for the Valorization of Exhaust Carbon: from CO_2 to Chemicals, Materials, and Fuels. Technological Use of CO_2. *Chem. Rev.* **2014,** *114* (3), 1709-1742.
4. Senftle, T. P.; Carter, E. A., The Holy Grail: Chemistry Enabling an Economically Viable CO2 Capture, Utilization, and Storage Strategy. *Acc. Chem. Res.* **2017,** *50* (3), 472-475.

5. Azcarate, I.; Costentin, C.; Robert, M.; Saveant, J. M., Through-Space Charge Interaction Substituent Effects in Molecular Catalysis Leading to the Design of the Most Efficient Catalyst of CO_2-to-CO Electrochemical Conversion. *J. Am. Chem. Soc.* **2016,** *138* (51), 16639-16644.
6. Cometto, C.; Chen, L.; Lo, P.-K.; Guo, Z.; Lau, K.-C.; Anxolabéhère-Mallart, E.; Fave, C.; Lau, T.-C.; Robert, M., Highly Selective Molecular Catalysts for the CO_2-to-CO Electrochemical Conversion at Very Low Overpotential. Contrasting Fe vs Co Quaterpyridine Complexes upon Mechanistic Studies. *ACS Catal.* **2018,** *8* (4), 3411-3417.
7. Froehlich, J. D.; Kubiak, C. P., Homogeneous CO_2 Reduction by Ni(cyclam) at a Glassy Carbon Electrode. *Inorg. Chem.* **2012,** *51* (7), 3932-3934.
8. Sampson, M. D.; Nguyen, A. D.; Grice, K. A.; Moore, C. E.; Rheingold, A. L.; Kubiak, C. P., Manganese Catalysts with Bulky Bipyridine Ligands for the Electrocatalytic Reduction of Carbon Dioxide: Eliminating Dimerization and Altering Catalysis. *J. Am. Chem. Soc.* **2014,** *136* (14), 5460-5471.
9. Beley, M.; Collin, J.-P.; Ruppert, R.; Sauvage, J.-P., Nickel(II)-cyclam: an extremely selective electrocatalyst for reduction of CO_2 in water. *J. Chem. Soc., Chem. Commun.* **1984,** (19), 1315-1316.
10. Beley, M.; Collin, J. P.; Ruppert, R.; Sauvage, J. P., Electrocatalytic reduction of carbon dioxide by nickel cyclam^{2+} in water: study of the factors affecting the efficiency and the selectivity of the process. *J. Am. Chem. Soc.* **1986,** *108* (24), 7461-7467.
11. Hawecker, J.; Lehn, J.-M.; Ziessel, R., Electrocatalytic reduction of carbon dioxide mediated by Re(bipy)$(CO)_3$Cl (bipy = 2,2′-bipyridine). *J. Chem. Soc., Chem. Commun.* **1984,** (6), 328-330.
12. Ishida, H.; Tanaka, K.; Tanaka, T., Electrochemical CO_2 reduction catalyzed by ruthenium complexes $[Ru(bpy)_2(CO)_2]^{2+}$ and $[Ru(bpy)_2(CO)Cl]^+$. Effect of pH on the formation of CO and HCOO. *Organometallics* **1987,** *6* (1), 181-186.
13. Hammouche, M.; Lexa, D.; Savéant, J. M.; Momenteau, M., Catalysis of the electrochemical reduction of carbon dioxide by iron("0") porphyrins. *J. Electroanal. Chem. Interf. Electrochem.* **1988,** *249* (1), 347-351.
14. Reid, A. G.; Machan, C. W., Redox Mediators in Homogeneous Co-electrocatalysis. *J. Am. Chem. Soc.* **2023,** *145* (4), 2013-2027.
15. Smith, P. T.; Weng, S.; Chang, C. J., An NADH-Inspired Redox Mediator Strategy to Promote Second-Sphere Electron and Proton Transfer for Cooperative Electrochemical CO_2 Reduction Catalyzed by Iron Porphyrin. *Inorg. Chem.* **2020,** *59* (13), 9270-9278.
16. Hooe, S. L.; Moreno, J. J.; Reid, A. G.; Cook, E. N.; Machan, C. W., Mediated Inner-Sphere Electron Transfer Induces Homogeneous Reduction of CO_2 via Through-Space Electronic Conjugation**. *Angew. Chem., Int. Ed.* **2022,** *61* (1), e202109645.
17. Reid, A. G.; Moreno, J. J.; Hooe, S. H.; Baugh, K. R.; Thomas, I. H.; Dickie, D. A.; Machan, C. W., Inverse Potential Scaling in Co-Electrocatalytic Activity for CO_2 Reduction Through Redox Mediator Tuning and Catalyst Design. *Chem. Sci.* **2022,** *13*, 9595-9606.
18. Reid, A. G.; Moberg, M. E.; Koellner, C. A.; Moreno, J. J.; Hooe, S. L.; Baugh, K. R.; Dickie, D. A.; Machan, C. W., Comparisons of bpy and phen Ligand Backbones in Cr-Mediated (Co-)Electrocatalytic CO_2 Reduction. *Organometallics* **2023,** *42* (11), 1139-1148.
19. Koellner, C. A.; Reid, A. G.; Machan, C. W., Co-electrocatalytic CO_2 reduction mediated by a dibenzophosphole oxide and a chromium complex. *Chem. Commun.* **2023,** *59* (42), 6359-6362.
20. Dey, S.; Masero, F.; Brack, E.; Fontecave, M.; Mougel, V., Electrocatalytic metal hydride generation using CPET mediators. *Nature* **2022,** *607* (7919), 499-506.
21. Anson, C. W.; Stahl, S. S., Cooperative Electrocatalytic O_2 Reduction Involving Co(salophen) with p-Hydroquinone as an Electron–Proton Transfer Mediator. *J. Am. Chem. Soc.* **2017,** *139* (51), 18472-18475.

22. Hooe, S. L.; Cook, E. N.; Reid, A. G.; Machan, C. W., Non-covalent assembly of proton donors and p-benzoquinone anions for co-electrocatalytic reduction of dioxygen. *Chem. Sci.* **2021,** *12*, 9733-9741.
23. Chalkley, M. J.; Del Castillo, T. J.; Matson, B. D.; Peters, J. C., Fe-Mediated Nitrogen Fixation with a Metallocene Mediator: Exploring p*K*a Effects and Demonstrating Electrocatalysis. *J. Am. Chem. Soc.* **2018,** *140* (19), 6122-6129.
24. Galvin, C. M.; Waymouth, R. M., Electron-Rich Phenoxyl Mediators Improve Thermodynamic Performance of Electrocatalytic Alcohol Oxidation with an Iridium Pincer Complex. *J. Am. Chem. Soc.* **2020,** *142* (45), 19368-19378.
25. McLoughlin, E. A.; Armstrong, K. C.; Waymouth, R. M., Electrochemically Regenerable Hydrogen Atom Acceptors: Mediators in Electrocatalytic Alcohol Oxidation Reactions. *ACS Catal.* **2020,** *10* (19), 11654-11662.
26. Badalyan, A.; Stahl, S. S., Cooperative electrocatalytic alcohol oxidation with electron-proton-transfer mediators. *Nature* **2016,** *535* (7612), 406-410.
27. Garrido-Barros, P.; Derosa, J.; Chalkley, M. J.; Peters, J. C., Tandem electrocatalytic N_2 fixation via proton-coupled electron transfer. *Nature* **2022,** *609* (7925), 71-76.
28. Derosa, J.; Garrido-Barros, P.; Li, M.; Peters, J. C., Use of a PCET Mediator Enables a Ni-HER Electrocatalyst to Act as a Hydride Delivery Agent. *J. Am. Chem. Soc.* **2022,** *144* (43), 20118-20125.
29. Gerken, J. B.; Stahl, S. S., High-Potential Electrocatalytic O_2 Reduction with Nitroxyl/NO_x Mediators: Implications for Fuel Cells and Aerobic Oxidation Catalysis. *ACS Cent. Sci.* **2015,** *1* (5), 234-243.
30. Chambers, G. M.; Wiedner, E. S.; Bullock, R. M., H_2 Oxidation Electrocatalysis Enabled by Metal-to-Metal Hydrogen Atom Transfer: A Homolytic Approach to a Heterolytic Reaction. *Angew. Chem., Int. Ed.* **2018,** *57* (41), 13523-13527.
31. Galvin, C. M.; Marron, D. P.; Dressel, J. M.; Waymouth, R. M., Coordination-Induced Bond Weakening and Electrocatalytic Proton-Coupled Electron Transfer of a Ruthenium Verdazyl Complex. *Inorg. Chem.* **2024,** *63* (2), 954-960.
32. Kertesz, M., Pancake Bonding: An Unusual Pi-Stacking Interaction. *Chem. Eur. J.* **2019,** *25* (2), 400-416.
33. Garcia-Yoldi, I.; Miller, J. S.; Novoa, J. J., Structure and Stability of the $[TCNE]_2^{2-}$ Dimers in Dichloromethane Solution: A Computational Study. *J. Phys. Chem. A.* **2007,** *111* (32), 8020-8027.
34. Garcia-Yoldi, I.; Miller, J. S.; Novoa, J. J., $[Cyanil]_2^{2-}$ dimers possess long, two-electron ten-center ($2e^-/10c$) multicenter bonding. *Phys. Chem. Chem. Phys.* **2008,** *10* (28), 4106-4109.
35. Mota, F.; Miller, J. S.; Novoa, J. J., Comparative Analysis of the Multicenter, Long Bond in $[TCNE]^{\cdot-}$ and Phenalenyl Radical Dimers: A Unified Description of Multicenter, Long Bonds. *J. Am. Chem. Soc.* **2009,** *131* (22), 7699-7707.
36. Hooe, S. L.; Dressel, J. M.; Dickie, D. A.; Machan, C. W., Highly Efficient Electrocatalytic Reduction of CO_2 to CO by a Molecular Chromium Complex. *ACS Catal.* **2020,** *10* (2), 1146-1151.
37. Pegis, M. L.; Wise, C. F.; Martin, D. J.; Mayer, J. M., Oxygen Reduction by Homogeneous Molecular Catalysts and Electrocatalysts. *Chem. Rev.* **2018,** *118* (5), 2340-2391.
38. Pegis, M. L.; Roberts, J. A. S.; Wasylenko, D. J.; Mader, E. A.; Appel, A. M.; Mayer, J. M., Standard Reduction Potentials for Oxygen and Carbon Dioxide Couples in Acetonitrile and *N,N*-Dimethylformamide. *Inorg. Chem.* **2015,** *54* (24), 11883-11888.
39. Nielsen, M. F.; Hammerich, O.; Rise, F.; Gogoll, A.; Undheim, K.; Wang, D. N.; Christensen, S. B., The Effect of Hydrogen Bonding between Methyl-Substituted Phenols and Dipolar Aprotic Solvents on the Rate Constants for. *Acta. Chem. Scan.* **1992,** *46*, 883-896.

40. Roy, S.; Sharma, B.; Pécaut, J.; Simon, P.; Fontecave, M.; Tran, P. D.; Derat, E.; Artero, V., Molecular Cobalt Complexes with Pendant Amines for Selective Electrocatalytic Reduction of Carbon Dioxide to Formic Acid. *J. Am. Chem. Soc.* **2017,** *139* (10), 3685-3696.
41. Matsubara, Y., Unified Benchmarking of Electrocatalysts in Noninnocent Second Coordination Spheres for CO_2 Reduction. *ACS Energy Lett.* **2019,** *4* (8), 1999-2004.
42. Costentin, C.; Drouet, S.; Robert, M.; Savéant, J.-M., Turnover Numbers, Turnover Frequencies, and Overpotential in Molecular Catalysis of Electrochemical Reactions. Cyclic Voltammetry and Preparative-Scale Electrolysis. *J. Am. Chem. Soc.* **2012,** *134* (27), 11235-11242.
43. Costentin, C.; Drouet, S.; Robert, M.; Savéant, J.-M., Correction to Turnover Numbers, Turnover Frequencies, and Overpotential in Molecular Catalysis of Electrochemical Reactions. Cyclic Voltammetry and Preparative-Scale Electrolysis. *J. Am. Chem. Soc.* **2012,** *134* (48), 19949-19950.
44. Baur, J. E., Chapter 19 Diffusion Coefficients. In *Handbook of Electrochemistry*, Zoski, C. G., Ed. Elsevier: 2007; pp 829-848.
45. Bruker *Saint; SADABS;TWINABS; APEX3*, Bruker AXS Inc.: Madison, Wisconsin, USA, 2012.
46. Krause, L.; Herbst-Irmer, R.; Sheldrick, G. M.; Stalke, D., Comparison of silver and molybdenum microfocus X-ray sources for single-crystal structure determination. *J. Appl. Crystallogr.* **2015,** *48* (1), 3-10.
47. Sheldrick, G., SHELXT - Integrated space-group and crystal-structure determination. *Acta Cryst.* **2015,** *71* (1), 3-8.
48. Dolomanov, O. V.; Bourhis, L. J.; Gildea, R. J.; Howard, J. A. K.; Puschmann, H., OLEX2: a complete structure solution, refinement and analysis program. *J. Appl. Cryst.* **2009,** *42* (2), 339-341.
49. Marshall-Roth, T.; Libretto, N. J.; Wrobel, A. T.; Anderton, K. J.; Pegis, M. L.; Ricke, N. D.; Voorhis, T. V.; Miller, J. T.; Surendranath, Y., A pyridinic Fe-N4 macrocycle models the active sites in Fe/N-doped carbon electrocatalysts. *Nat. Commun.* **2020,** *11* (1), 5283.
50. Grant, D. H., Paramagnetic Susceptibility by NMR: The "Solvent Correction" Reexamined. *J. Chem. Educ.* **1995,** *72* (1), 39.
51. Bain, G. A.; Berry, J. F., Diamagnetic corrections and Pascal's constants. *J. Chem. Educ.* **2008,** *85* (4), 532-536.
52. Sathrum, A. J.; Kubiak, C. P., Kinetics and Limiting Current Densities of Homogeneous and Heterogeneous Electrocatalysts. *J. Phys. Chem. Lett.* **2011,** *2* (18), 2372-2379.

Chapter 6

Summary and Outlook

Portions of this chapter originally published in:

Reid, A. G.; Machan, C. W., *Journal of the American Chemical Society* **2023**, *145* (4), 2013-2027.

6.1 Summary and Conclusions of Completed Research

The first portion of this Dissertation discussed Cr(tpy^{tbu}pho)Cl_2, a new Cr-centered catalyst with an N_3O ligand framework based on terpyridine that is capable of the carbon dioxide reduction reaction (CO_2RR). Cr(tpy^{tbu}pho)Cl_2 has quantitative selectivity for carbon monoxide (CO) when both phenol (PhOH) and water (H_2O) are used as proton sources (faradaic efficiency (FE_{CO}) of 93 ± 7% and 93 ± 4%, respectively). The electrochemical and kinetic properties of Cr(tpy^{tbu}pho)Cl_2 offer an interesting comparison to the previously reported Cr(^{tbu}dhbpy)Cl(H_2O) catalyst, which is based on a N_2O_2 ligand framework based on bipyridine (bpy).[1] The increased redox activity of the terpyridine-based N_3O ligand framework is consistent with experimental observations: Cr(tpy^{tbu}pho)Cl_2 must be reduced three times before the CO_2RR is observed compared to only two reductions with the bpy-based N_2O_2 complex. These redox events are assigned to two ligand-based reductions and one metal-based reduction with the active catalytic species consisting of a Cr^{II} center coupled to a doubly reduced ligand framework. The observed rate law of Cr(tpy^{tbu}pho)Cl_2 is zero-order with respect to proton concentration, based on which the rate-determining step (RDS) of the reaction is assigned to CO_2 binding. This is proposed to be the result of the increased anionic character of the active catalytic species which enhances the rate of protonation during C–OH bond cleavage, the rate-determining step for the N_2O_2 complex. This new mechanism is both different from the RDS of the N_2O_2 complex and uncommon during protic CO_2 reduction.

The remainder of this Dissertation discussed studies on the use of sulfone-based redox mediators (RMs) with Cr-centered catalysts for the CO_2RR. A previous report by our lab used the Cr(^{tbu}dhbpy)Cl(H_2O) complex with dibenzothiophene-5,5-dioxide (DBTD) as the RM, which led to the enhancement of the protic CO_2RR.[2] A new Cr catalyst was synthesized with *tert*-butyl groups substituted on the bpy backbone of the ligand framework (Cr(^{tbu}dh^{tbu}bpy)Cl(H_2O)) which lead to a more negative (50 mV) operating potential and about double the turnover frequency (TOF; 9.29

s^{-1}) compared to the parent bpy. Three additional sulfone RMs were synthesized, 2,8-dimesityldibenzothiophene-5,5-dioxide (Mes_2DBTD), 2,8-diphenyldibenzothiophene-5,5-dioxide (Ph_2DBTD), and triphenylothiophene-4,4-dioxide (TPTD), and the co-catalytic activity of all four RMs with both Cr catalysts was studied. All co-catalytic systems maintained quantitative selectivity for CO and enhanced the CO_2RR activity by up to 22-fold with a maximum observed TOF of 208 s^{-1}. This experimental data, along with computational results, supported a proposed mechanism for co-electrocatalysis that relies on an inner-sphere electron transfer mechanism where the reduced RM formally binds to the Cr center. This key intermediate is stabilized by a pancake bonding (PB) interaction between the radical in the bpy ligand backbone and the reduced RM. An unexpected inverse potential scaling relationship between the $E_{co\text{-}cat/2}$ and the TOF was observed: the RMs that were reduced at more positive potentials provided the greatest TOF enhancement. It was proposed that the reduction potentials were a qualitative measure of the relative frontier orbital energies which when closer in energy provided a more stable PB interaction.

In order to further optimize the co-catalytic association and tune the PB interaction a phenanthroline (phen) derivative of the Cr catalyst, $Cr(^{tbu}dhphen)Cl(H_2O)$, was synthesized. This catalyst has an almost identical $E_{cat/2}$ and TOF to the $Cr(^{tbu}dhbpy)Cl(H_2O)$ catalyst, which allowed for differences in co-catalytic enhancement to be pinned directly to the interaction of the catalyst with the RM and not the inherent catalyst activity which was the case in the previous study. The experimental electrochemical data as well as computational data supported the previous proposal of increased activity occurring when PB strength was increased favoring the formation of $[RM–Cr–COOH]^{2-}$. However, when adding steric bulk to both the RM and catalyst in order to tune their thermodynamic properties (reduction potential), the kinetic favorability of association was decreased and the restrictions on molecular alignment weakened the PB interaction which relies on direct atom-atom overlap. In these cases, this decrease in PB strength is compensated via

dispersive interactions between the RM and ligand backbone for interaction strength, but the enhancement on rate is limited compared to compounds with less hindrance.

The final portion of this Dissertation discussed the synthesis of a new RM, benzonaphthothiophene-7,7-dioxide (BNTD), and a Cr catalyst with phenyl groups substituted on the phenanthroline backbone, Cr(^{tbu}dh^{Ph}phen)Cl(H_2O). The reduction potential of BNTD was more positive than DBTD by 290 mV ($E_{1/2}$ = –1.96 V), while having a similar size and steric profile. This allowed for the study of co-electrocatalytic activity with three Cr catalysts that had reduction potentials more positive than, the same as, and more negative than the RM. In all cases, there is enhancement in the TOF when BNTD is present as the RM and this enhancement is maximized when the reduction potentials of both components are matched, supporting the proposals regarding strengthening the PB interaction made previously. This is the first and to this point only example of a system where co-catalysis for the CO_2RR is observed when a RM is reduced positive of the catalyst. Additionally, the $E_{co\text{-}cat/2}$ with BNTD present as the RM is the same as its $E_{1/2}$, no matter the $E_{cat/2}$ of the catalyst. This suggests that as long as the association of Cr complex and RM is favorable, the formation of any active catalyst will result in binding to the reduced RM to activate the co-catalytic pathway. Based on these results, future studies will need to incorporate an understanding of relative speciation to the molecular design of both RM and catalyst in addition to maximizing the PB interaction.

6.2 Future Directions

The research presented in this Dissertation has laid the foundation for understanding the co-electrocatalytic mechanism with Cr-N_2O_2 catalysts and sulfone-based RMs for the CO_2RR. Further optimization of these systems can likely be achieved by further structural modifications to both the ligand framework and RM structure (**Figure 6.1**). Since it is observed that matching the RM reduction potential to the catalyst reduction potential results in the highest activity of the co-catalytic systems discussed here, synthesizing a RM with a reduction potential that matches the

most active of the reported Cr-catalysts, Cr(^{tbu}dh^{tbu}bpy)Cl(H_2O), should result in an even larger TOF. This could be achieved by substituting BNTD with electron donating groups or DBTD with electron withdrawing groups. However, it is important to keep in mind that the synthetic design of these RMs should take into account the steric profile of the RM so that PB is not diminished by twisting out of an ideal vertical atom-atom overlap configuration.

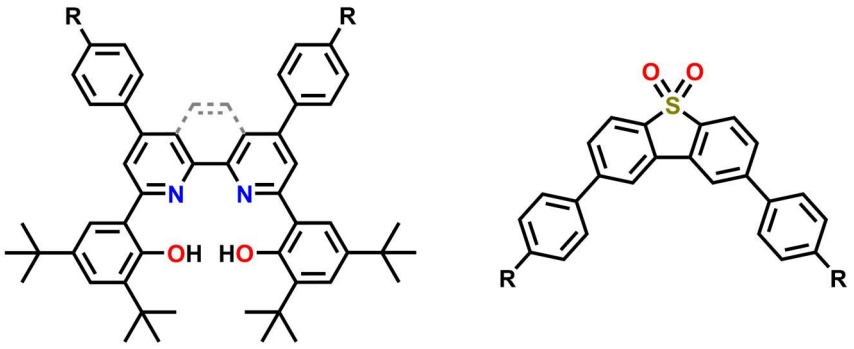

Figure 6.1. Potential new N_2O_2 ligand frameworks and DBTD-based RMs.

All of the RMs discussed here only transfer an electron equivalent and do not assist with the transfer of proton equivalents, even though proton transfer steps are important to the RDS of the proposed co-catalytic mechanism. The use of electron-proton transfer mediators (EPTMs) in co-catalytic CO_2RR[3, 4] and other electrocatalytic small molecule conversion[5-12] has been previously reported, however, these systems due not operate via an inner-sphere mechanism. Synthetically placing functional groups on DBTD or a similar derivative (**Figure 6.2**) could leverage the benefits of the inner-sphere pathway as well as the benefits of EPTMs. Preliminary studies with 4-pyridine and 4-aniline substituted DBTD derivatives have been conducted which have shown possible co-catalytic activity via cyclic voltammetry (CV). However, further study is needed to optimize and understand the nature of the co-catalytic interaction.

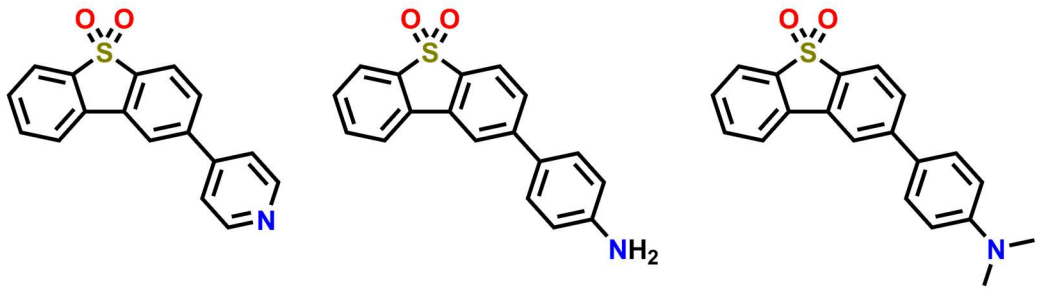

Figure 6.2. Proposed sulfone-based EPTMs.

Careful consideration must be taken to select a proton source with an appropriate pK_a to protonate the desired functional groups, but not interact with the reduced sulfone. Electroanalytical, spectrochemical, and computational analysis will be crucial to the understanding of changes in the co-catalytic mechanism. It is possible that the new EPTMs will enhance the proton-coupled electron transfer steps in the proposed mechanism, or the co-catalytic mechanism may change entirely. As discussed in **Chapter 1**, there are two pathways for the 2-electron/2-proton reduction of CO_2 which diverge based on whether the metal center first binds CO_2 or a proton. With the use of EPTMs there is a possibility that the formation of a M–H is favored and the selectivity of the catalyst is shifted as was the case in the study of Mn(bpy)$(CO)_3$Br with iron-sulfur clusters by Dey *et al.*[4]

6.3 Outlook on the Field

Overall, the relatively limited examples of molecular co-electrocatalytic systems suggest that the identification of simple thermodynamic values from catalytic cycles is of continuing importance to guide exploratory screening of possible mediators. The logical manifestation of this idea is found in the work of McLoughlin *et al.*, who have selected a series of parameters for the identification of possible RMs for the alcohol oxidation reaction.[7] Particularly compelling is their use of a transition metal complex as an EPTM, which they emphasize is attractive relative to organic molecules "…because the thermochemical properties (BDFE, pK_a, $E_{1/2}$) of these complexes can be readily modified by changing the nature of the ligand(s) and/or redox-active

transition metal."[7] The importance of understanding the reaction landscape and the most prominent features is essential for this approach, as it is no coincidence that many of the co-electrocatalytic strategies discussed in **Chapter 1** lower energy pathways by avoiding metal-based two-electron events to favor two distributed one-electron events. For kinetic and thermodynamic reasons, the movement of electrons with protons can also offer significant advantages, as can shifting the redox reactions from outer- to inner-sphere (**Figure 6.3**).

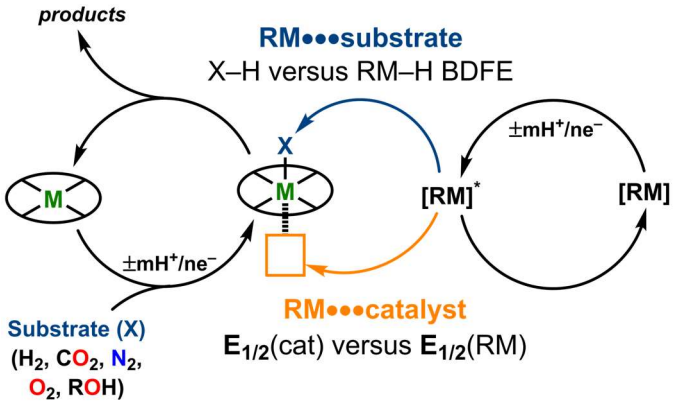

Figure 6.3. Overview of the ways in which RMs can interact with the catalytic species and parameters dictating this role.

The adaptation of aerobic reactions that use small molecule mediators to use electrodes to supply the necessary electrons or oxidizing equivalents has proven to be a powerful strategy for identifying new co-electrocatalytic electrochemical reactions.[5, 11, 13] However, there exists a multitude of molecular transformations that rely on the stoichiometric inclusion of reductants and oxidants that would benefit from electrification. Indeed, ferrocene derivatives have begun attracting attention as mediators in electrocatalytic oxidative transformations where the regeneration and stabilization of the catalytically active species is required[14, 15] or where catalyst-bound substrates can be activated.[16] As mentioned in **Chapter 1**, the ability of ferrocenes to function as catalytic electron-transfer mediators is also well established,[17-19] but these are not co-catalytic systems, and the mechanisms do not require inner-sphere electron transfer events.[20] It is important to emphasize again that the limitation of the 50 mV separation identified in biological systems does not necessarily exist in abiotic ones.[2, 21, 22] In biological systems with a variety of

overlapping reaction pathways, selectivity is enforced by establishing energy gradients with gradual steps. However, synthetic reaction conditions can be specifically tailored such that reactions with larger driving forces can selectively occur, assuming this has a benefit on kinetic parameters[23] and does not introduce large energy penalties. However, there are still additional challenges that must be addressed when designing co-electrocatalytic systems. As is the case with many complex chemical systems, there is the possibility of a competitive reaction pathway such as direct reaction of the RM with substrate or interaction of the RM with catalytic intermediates outside of the step of interest which can lead to side products or deactivation of the active catalyst.

An objection to these systems could be articulated thusly: why develop multicomponent co-catalytic systems instead of single component ones with ligand frameworks that directly incorporate RM elements? In redox-active catalyst systems, the coupling of redox-active moieties to active sites can indeed impact activity in a beneficial way;[24-27] however the intrinsic redox response of any molecule reflects electronic interactions between the two components prior to reduction. If the potential synthetic challenges are ignored, spatially co-locating multiple redox-active moieties can be a fundamental limitation to improving catalysis, given that the function of both the redox-active fragment and catalyst will change! Therefore, we believe there is continued value in developing a mechanistic understanding of catalytic cycles and using the principles of molecular design to select secondary components, which impact catalyst speciation and offer the possibility of shunting of reaction pathways, as described for the $[Fe(TPP)]^+$ catalyst in **Chapter 1**.[3, 28] Given the density of information available about aerobic catalytic processes and those which use stoichiometric reductants or oxidants, it is important for further studies on RM-based electrification of synthetic transformations. Likewise, with many well-established electrocatalysts for small molecule activation, it is surprising that so few co-catalytic examples exist, given the obvious precedents discussed in **Chapter 1**. Here, too, mechanistic information can allow for

analogous advances, as we begin to better understand how electrons and protons shift during a reaction such that we can better direct their selective transfer.

6.4 References

1. Hooe, S. L.; Dressel, J. M.; Dickie, D. A.; Machan, C. W., Highly Efficient Electrocatalytic Reduction of CO_2 to CO by a Molecular Chromium Complex. *ACS Catal.* **2020,** *10* (2), 1146-1151.
2. Hooe, S. L.; Moreno, J. J.; Reid, A. G.; Cook, E. N.; Machan, C. W., Mediated Inner-Sphere Electron Transfer Induces Homogeneous Reduction of CO_2 via Through-Space Electronic Conjugation**. *Angew. Chem., Int. Ed.* **2022,** *61* (1), e202109645.
3. Smith, P. T.; Weng, S.; Chang, C. J., An NADH-Inspired Redox Mediator Strategy to Promote Second-Sphere Electron and Proton Transfer for Cooperative Electrochemical CO_2 Reduction Catalyzed by Iron Porphyrin. *Inorg. Chem.* **2020,** *59* (13), 9270-9278.
4. Dey, S.; Masero, F.; Brack, E.; Fontecave, M.; Mougel, V., Electrocatalytic metal hydride generation using CPET mediators. *Nature* **2022,** *607* (7919), 499-506.
5. Badalyan, A.; Stahl, S. S., Cooperative electrocatalytic alcohol oxidation with electron-proton-transfer mediators. *Nature* **2016,** *535* (7612), 406-410.
6. Galvin, C. M.; Waymouth, R. M., Electron-Rich Phenoxyl Mediators Improve Thermodynamic Performance of Electrocatalytic Alcohol Oxidation with an Iridium Pincer Complex. *J. Am. Chem. Soc.* **2020,** *142* (45), 19368-19378.
7. McLoughlin, E. A.; Armstrong, K. C.; Waymouth, R. M., Electrochemically Regenerable Hydrogen Atom Acceptors: Mediators in Electrocatalytic Alcohol Oxidation Reactions. *ACS Catal.* **2020,** *10* (19), 11654-11662.
8. Chalkley, M. J.; Del Castillo, T. J.; Matson, B. D.; Peters, J. C., Fe-Mediated Nitrogen Fixation with a Metallocene Mediator: Exploring p*K*a Effects and Demonstrating Electrocatalysis. *J. Am. Chem. Soc.* **2018,** *140* (19), 6122-6129.
9. Derosa, J.; Garrido-Barros, P.; Li, M.; Peters, J. C., Use of a PCET Mediator Enables a Ni-HER Electrocatalyst to Act as a Hydride Delivery Agent. *J. Am. Chem. Soc.* **2022,** *144* (43), 20118-20125.
10. Chambers, G. M.; Wiedner, E. S.; Bullock, R. M., H_2 Oxidation Electrocatalysis Enabled by Metal-to-Metal Hydrogen Atom Transfer: A Homolytic Approach to a Heterolytic Reaction. *Angew. Chem., Int. Ed.* **2018,** *57* (41), 13523-13527.
11. Anson, C. W.; Stahl, S. S., Cooperative Electrocatalytic O_2 Reduction Involving Co(salophen) with p-Hydroquinone as an Electron–Proton Transfer Mediator. *J. Am. Chem. Soc.* **2017,** *139* (51), 18472-18475.
12. Hooe, S. L.; Cook, E. N.; Reid, A. G.; Machan, C. W., Non-covalent assembly of proton donors and p-benzoquinone anions for co-electrocatalytic reduction of dioxygen. *Chem. Sci.* **2021,** *12*, 9733-9741.
13. Wang, F.; Stahl, S. S., Electrochemical Oxidation of Organic Molecules at Lower Overpotential: Accessing Broader Functional Group Compatibility with Electron−Proton Transfer Mediators. *Acc. Chem. Res.* **2020,** *53* (3), 561-574.
14. Walker, B. R.; Manabe, S.; Brusoe, A. T.; Sevov, C. S., Mediator-Enabled Electrocatalysis with Ligandless Copper for Anaerobic Chan–Lam Coupling Reactions. *J. Am. Chem. Soc.* **2021,** *143* (16), 6257-6265.
15. Lee, K. J.; Lodaya, K. M.; Gruninger, C. T.; Rountree, E. S.; Dempsey, J. L., Redox mediators accelerate electrochemically-driven solubility cycling of molecular transition metal complexes. *Chem. Sci.* **2020,** *11* (36), 9836-9851.

16. Xiong, P.; Hemming, M.; Ivlev, S. I.; Meggers, E., Electrochemical Enantioselective Nucleophilic α-C(sp^3)–H Alkenylation of 2-Acyl Imidazoles. *J. Am. Chem. Soc.* **2022,** *144* (15), 6964-6971.
17. Lennox, A. J. J.; Nutting, J. E.; Stahl, S. S., Selective electrochemical generation of benzylic radicals enabled by ferrocene-based electron-transfer mediators. *Chem. Sci.* **2018,** *9* (2), 356-361.
18. Zhu, L.; Xiong, P.; Mao, Z.-Y.; Wang, Y.-H.; Yan, X.; Lu, X.; Xu, H.-C., Electrocatalytic Generation of Amidyl Radicals for Olefin Hydroamidation: Use of Solvent Effects to Enable Anilide Oxidation. *Angew. Chem., Int. Ed.* **2016,** *55* (6), 2226-2229.
19. Wu, Z.-J.; Xu, H.-C., Synthesis of C3-Fluorinated Oxindoles through Reagent-Free Cross-Dehydrogenative Coupling. *Angew. Chem., Int. Ed.* **2017,** *56* (17), 4734-4738.
20. Kellett, C. W.; Swords, W. B.; Turlington, M. D.; Meyer, G. J.; Berlinguette, C. P., Resolving orbital pathways for intermolecular electron transfer. *Nat. Comm.* **2018,** *9* (1), 4916.
21. Reid, A. G.; Moreno, J. J.; Hooe, S. H.; Baugh, K. R.; Thomas, I. H.; Dickie, D. A.; Machan, C. W., Inverse Potential Scaling in Co-Electrocatalytic Activity for CO_2 Reduction Through Redox Mediator Tuning and Catalyst Design. *Chem. Sci.* **2022,** *13*, 9595-9606.
22. Hooe, S. L.; Moreno, J. J.; Reid, A. G.; Cook, E. N.; Machan, C. W., Corrigendum: Mediated Inner-Sphere Electron Transfer Induces Homogeneous Reduction of CO_2 via Through-Space Electronic Conjugation. *Angew. Chem., Int. Ed.* **2022,** *61* (25), e202205139.
23. Saouma, C. T.; Mayer, J. M., Do spin state and spin density affect hydrogen atom transfer reactivity? *Chem. Sci.* **2014,** *5* (1), 21-31.
24. Md. Ahsan, H.; Breedlove, B. K.; Cosquer, G.; Yamashita, M., Enhancement of electrocatalytic abilities toward CO_2 reduction by tethering redox-active metal complexes to the active site. *Dalton Trans.* **2021,** *50* (38), 13368-13373.
25. Singha, A.; Mondal, A.; Nayek, A.; Dey, S. G.; Dey, A., Oxygen Reduction by Iron Porphyrins with Covalently Attached Pendent Phenol and Quinol. *J. Am. Chem. Soc.* **2020,** *142* (52), 21810-21828.
26. Mittra, K.; Chatterjee, S.; Samanta, S.; Dey, A., Selective $4e^-/4H^+$ O_2 Reduction by an Iron(tetraferrocenyl)Porphyrin Complex: From Proton Transfer Followed by Electron Transfer in Organic Solvent to Proton Coupled Electron Transfer in Aqueous Medium. *Inorg. Chem.* **2013,** *52* (24), 14317-14325.
27. Samanta, S.; Sengupta, K.; Mittra, K.; Bandyopadhyay, S.; Dey, A., Selective four electron reduction of O_2 by an iron porphyrin electrocatalyst under fast and slow electron fluxes. *ChemComm* **2012,** *48* (61), 7631-7633.
28. Costentin, C.; Robert, M.; Savéant, J.-M., Current Issues in Molecular Catalysis Illustrated by Iron Porphyrins as Catalysts of the CO_2-to-CO Electrochemical Conversion. *Acc. Chem. Res.* **2015,** *48* (12), 2996-3006.

Amelia Reid

agr8kd@virginia.edu

EDUCATION

University of Virginia — Charlottesville, VA
Ph.D. in Chemistry — **May 2024**
Advisor: Dr. Charles W. Machan
Thesis: Establishing Structure-Function Relationships for the Catalytic Reduction of Carbon Dioxide with Chromium-Based Molecular Catalysts with Redox Mediators

University of Georgia — Athens, GA
Bachelor of Science in Chemistry; *magna cum laude* — **May 2019**
Honors Program Graduate
Minor in Dance

RESEARCH EXPERIENCE

Graduate Research Assistant — **December 2019-July 2024**
Advisor: Charles W. Machan
University of Virginia, Department of Chemistry

Undergraduate Research Assistant — **May 2018-May 2019**
Advisor: Todd C. Harrop
University of Georgia, Department of Chemistry

PUBLICATIONS (*denotes co-first authorship)

1. Sarabamoun, E. S.; Bietsch, J. M.; Aryal, P.; **Reid, A. G.**; Curran, M.; Johnson, G.; Tsai, E. H. R.; Machan, C. W.; Wang, G.; Choi, J. J., "Photoluminescence switching in quantum dots connected with fluorinated and hydrogenated photochromic molecules" *RSC Adv.*, **2024**, 14, 424-432. DOI: 10.1039/d3ra07539g
2. **Reid, A. G.**; Moberg, M. E.; Koellner, C. A.; Machan, C. W.; Thornton, D. A.; Dickenson, J. C. Stober, J. J.; Turner, D. A.; Tarring, T. J.; Brown, C. A.; Harrison, D. P., "Sterically attenuated electronic communication in cobalt complexes of meridional isoquinoline-derived ligands for applications in electrocatalysis" *J. Chem. Phys.* **2023**, 159, 194306. DOI: 10.1063/5.0174177
3. Koellner, C. A.; **Reid, A. G.**; Machan, C. W., "Co-electrocatalytic CO_2 reduction mediated by a dibenzophosphole oxide and a chromium complex" *Chem. Comm.*, **2023**, 59, 6359-6362. DOI: 10.1039/D3CC00166K
4. **Reid, A. G.**; Moberg, M. E.; Koellner, C. A.; Moreno, J. J.; Hooe, S. L.; Baugh, K. R.; Dickie, D. A.; Machan, C. W., "Comparisons of bpy and phen Ligand Backbones in Cr-Mediated Co-Electrocatalytic CO_2 Reduction" *Organometallics,* **2023**, 42, 1139-1148. DOI: 10.1021/acs.organomet.2c00600
5. **Reid, A. G.**; Machan C. W. "Redox Mediators in Homogeneous Co-Electrocatalysis" *J. Am. Chem. Soc.* **2023**, 145, 2013-2027. DOI: 10.1021/jacs.2c10033
6. **Reid, A. G.***; Hooe, S. L.*; Moreno, J. J.; Dickie, D. A.; Machan, C. W. "Homogeneous Electrocatalytic Reduction of CO_2 by a CrN_3O Complex: Electronic Coupling with a Redox-Active Terpyridine Fragment Favors Selectivity for CO" *Inorg. Chem.* **2022**, 61, 16963-16970. DOI: 10.1021/acs.inorgchem.2c02013
7. **Reid, A. G.**; Hooe, S. L.; Moreno, J. J.; Baugh, K. R.; Thomas, I.; Dickie, D. A.; Machan, C. W. "Inverse potential scaling in co-electrocatalytic activity for CO_2 reduction through redox mediator tuning and catalyst design" *Chem. Sci.* **2022**, 13, 9595-9606. DOI:

10.1039/D2SC03258A

8. Hooe, S. L.*; Moreno, J. J.*; **Reid, A. G.**; Cook, E. N.; Machan, C. W. "Mediated Inner-Sphere Electron Transfer Induces Homogenous Reduction of CO_2 via Through-Space Electronic Conjugation**" *Angew. Chem. Int. Ed.* **2021**. DOI: 10.1002/anie.202109645
9. Hooe, S. L.; Cook, E. N.; **Reid, A. G.**; Machan, C. W. "Non-covalent assembly of proton donors and *p*-benzoquinone anions for co-electrocatalytic reduction of dioxygen" *Chem. Sci.* **2021**, 28, 9733–9741. DOI: 10.10139/D1SC01271A

PRESENTATIONS & POSTERS

1. "Comparisons of bpy and phen ligand backbones in Cr-mediated co-electrocatalytic CO_2 reduction" SERMACS Fall 2023, Durham, NC, October 27, 2023 (oral presentation).
2. "Comparisons of bpy and phen ligand backbones in Cr-mediated co-electrocatalytic CO_2 reduction" SERMACS Fall 2023, Durham, NC, October 25, 2023 (poster).
3. "Comparisons of bpy and phen ligand backbones in Cr-mediated co-electrocatalytic CO_2 reduction" UVA Department of Chemistry Annual Retreat, Charlottesville, VA, October 3, 2023 (poster).
4. "Comparisons of bpy and phen ligand backbones in Cr-mediated co-electrocatalytic CO_2 reduction" ACS National Meeting Fall 2023, San Francisco, CA, August 16, 2023 (oral presentation).
5. "Comparisons of bpy and phen ligand backbones in Cr-mediated co-electrocatalytic CO_2 reduction" ACS National Meeting Fall 2023, San Francisco, CA, August 13, 2023 (poster).
6. "Comparisons of bpy and phen ligand backbones in Cr-mediated co-electrocatalytic CO_2 reduction" Virginia Clean Energy and Catalysis Club 2023 Summit, Richmond, VA, August 7, 2023 (poster).
7. "Improving Co-Electrocatalytic Activity for CO_2 Reduction at Lower Overpotentials Through Redox Mediator Tuning and Catalyst Design" Gordon Research Seminar on Inorganic Reaction Mechanisms, Galveston, TX, March 5, 2023 (oral presentation).
8. "Improving Co-Electrocatalytic Activity for CO_2 Reduction at Lower Overpotentials Through Redox Mediator Tuning and Catalyst Design" Gordon Research Conference on Inorganic Reaction Mechanisms, Galveston, TX, March 5-10, 2023 (poster).
9. "Inverse Potential Scaling in Co-Electrocatalytic Activity for CO_2 Reduction Through Redox Mediator Tuning and Catalyst Design" Electrochemistry, ACS National Meeting Fall 2022, Chicago, Il, August 24, 2022 (oral presentation; **session presider**).
10. "Inverse Potential Scaling in Co-Electrocatalytic Activity for CO_2 Reduction Through Redox Mediator Tuning and Catalyst Design" **Sci-Mix**, ACS National Meeting Fall 2022, Chicago, Il, August 22, 2022 (**Division of Inorganic Chemistry invited poster**).
11. "Inverse Potential Scaling in Co-Electrocatalytic Activity for CO_2 Reduction Through Redox Mediator Tuning and Catalyst Design" Emerging Areas in Inorganic Chemistry, ACS National Meeting Fall 2022, Chicago, Il, August 21, 2022 (poster).
12. "Inverse Potential Scaling in Co-Electrocatalytic Activity for CO_2 Reduction Through Redox Mediator Tuning and Catalyst Design" Virginia Clean Energy and Catalysis Club 2022 Summit, Charlottesville, VA, August 8, 2022 (contributed poster).
13. "Inverse Potential Scaling in Co-Electrocatalytic Activity for CO_2 Reduction Through Redox Mediator Tuning and Catalyst Design" International Conference on Carbon Dioxide Utilization (ICCDU) 2022, Princeton, NJ, June 28, 2022 (**Outstanding Poster Award**).
14. "Inverse Potential Scaling in Co-Electrocatalytic Activity for CO_2 Reduction Through Redox Mediator Tuning and Catalyst Design" ICCDU 2022, Princeton, NJ, June 27, 2022 (contributed oral presentation).
15. "Developing Enhanced Co-Electrocatalytic System for CO_2 Reduction" UVA Department of Chemistry Annual Retreat, Charlottesville, VA, October 12, 2021 (**1st place oral presentation**).

16. "Through-Space Electronic Conjugation Enhances Co-Electrocatalytic Reduction of CO_2 to CO by a Molecular Cr Complex" ACS National Meeting, Atlanta, GA, August 22-26, 2021 (virtual oral presentation).
17. "Modulation of Co-electrocatalytic CO_2 Reduction by Cr Complexes and Dibenzothiophene 5,5-dioxide Derivatives" Virginia Clean Energy and Catalysis Club 2021 Summit, August 2, 2021 (virtual poster).
18. "Efficient Conversion of Carbon Dioxide (CO_2) to Useable Products for Fuels and Chemical Feedstocks" Research for Action Symposium for the University of Virginia's Environmental Research Institute's Climate Ambition Summit, March 31, 2021 (virtual poster).
19. "Synthesis and Properties of an H_2 Evolving Hydrogenase Mimic" University of Georgia Center for Undergraduate Research Opportunities Symposium, Athens, GA, April 9, 2019 (oral presentation).

HONORS & AWARDS

UVA Chemistry Lifetime Service Award	**April 2024**
UVA Chemistry Ritchie Research Award	**April 2024**
Best Poster Presentation Award (1st Place), VA Clean Energy & Catalysis Summit	**August 2023**
Graduate Student Symposium Travel Award, ACS Fall 2023	**August 2023**
Sci-Mix Poster Session Participant, ACS Fall 2022	**August 2022**
ICCDU Outstanding Poster Award	**June 2022**
First place oral presentation, UVA Department of Chemistry Retreat	**October 2021**
UVA Graduate School of Arts and Sciences Scholarship Recipient	**August 2019**
UGA Department of Chemistry 2019 L. B. "Buck" Rogers Award	**May 2019**
University of Georgia Honors Program	**Fall 2015-Spring 2019**
Zell Miller Scholarship Recipient	**Fall 2015-Spring 2019**
Phi Beta Kappa, University of Georgia	**November 2018**
Charter Scholarship Recipient	**August 2015**

TEACHING EXPERIENCE

Head Teaching Assistant, General Chemistry **January 2021-May 2021**
University of Virginia
- Prepared assignments and rubrics for the course, maintained electronic gradebook and assignments for all sections, managed 25 Teaching Assistants.

Teaching Assistant, Inorganic Chemistry **August 2020-December 2020**
University of Virginia
- Created and graded homework assignments to supplement course lectures.
- Facilitated review sessions for 75-100 undergraduate students.

Teaching Assistant, General Chemistry Lab **August 2019-May 2020**
University of Virginia
- Prepared pre-lab lectures, facilitated laboratory experiments for students, and graded lab reports.

INVOLVEMENT & OUTREACH

UVA Chemistry Graduate Student Council, President	**May 2023-April 2024**
UVA Chemistry Graduate Student Council, Social Co-chair	**May 2022-April 2023**
UVA Chemistry Department Open House Planning Committee, Co-chair	**2022**
UVA Chemistry Department Retreat Planning Committee	**2021**
UVA ChemSciComm, Member	**April 2021-May 2024**
Learning Ally, Volunteer in STEM books	**2016-2021**